Flinders University

Electric Machines for Electric Vehicles Considering Efficiency Map

By

Emad Roshandel
Master of Science (Electrical Machines and Drives)

Thesis
Submitted to Flinders University
for the degree of Doctor of Philosophy, Ph.D.

Ph.D. in Electrical Engineering
College of Science and Engineering
May 2023

TABLE OF CONTENTS

ABSTRACT

The electric machines (EMs) utilized in the electric vehicles (EVs) and hybrid electric vehicles (HEVs) must operate efficiently over a wide range of torque and speed. Hence, the design procedure of such EMs is involved with the performance parameters estimation over various operating points. Efficiency maps (EffMs) project the maximum efficiency of the machine in the torque-speed envelope as well as the torque-speed capability of EMs. So, the EffMs can be used for prediction of the energy consumption of an EM during operation over a driving cycle.

The main objective of this thesis is the design of EMs for EVs and HEVs. The thesis starts with a short discussion on the advantageous of EVs and HEVs utilization. The different transmission system components in EVs and HEVs are introduced for better understanding of such vehicles. The different factors affecting the various components of the loss in the electric machines and transmission system of the EMs are described. The literature review highlights the role of EMs efficiency in the propulsion system of EVs and HEVs.

The EMs operating region and the control techniques for operation in different operating regions is introduced in the third chapter of the thesis. The procedure of the calculation of the EffM is explained. Different calculation methods are discussed, and their strengths and weaknesses are clarified. The experimental procedure of the calculation of EffM for EMs is described and the EffM is obtained experimentally for a sample induction machine (IM). The comparison of different EffM methods, in terms of accuracy and computation time, enables the designer to choose an optimum technique for a certain application.

A step-by-step design procedure based on the finite element analysis (FEA) is introduced for design of the 100kW IM and interior permanent magnet machine (IPMSM) for a HEV. The design procedure not only considers the electromagnetic validity of the designed machines, but also it covers the thermal aspects during the design. The importance of the optimal selection of the number of poles is studied. The effect of the V-shape angle on the torque ripple and cogging torque of IPMSMs is studied. The role of the number of rotor bars on the torque ripple of IMs is another aspect of the study. The advantageous and disadvantages of the IM and IPMSMs are highlighted based on a comparison of their cost, torque density, and power density.

The design of 100kW and 200kW axial flux permanent magnet machines (AFPMSMs) is the subject of study in the fifth chapter of the thesis. This chapter designs the AFPMSMs for a HEV with the series propulsion system. Initially a design procedure using 3-D FEA is described and applied to design a 100kW AFPMSM, with optimal operation in the constant torque (CT) region. It is shown that the double stator design in double sided axial flux machines can offer a better performance compared to the double rotor designs. The higher power density of the axial flux machines is highlighted by comparison of the performance parameters with existing axial and radial flux designs. The role of the slot numbers, number of pole effect, torque ripple, THD, slot numbers, solid loss, axial force, stator negative stiffness, rotor eddy current loss, demagnetization, and thermal constraints are discussed and analysed during the design. The kriging technique and multi-objective optimization are employed to find the 100kW design with the optimal performance in the CT region.

The fifth chapter is continued by the optimal AFPMSM designs with capability of the operation in the constant power region. The axial flux interior PMSM (AFIPMSM), fractional slots topologies, and number of poles are the subjects of the study for improvement of the AFPMSM performance in the field weakening region. It is shown that AFIMPSM suffers from a low power factor and low power density. The rotor eddy current losses are investigated in axial flux PM machines which results in the limitation of the utilization of fractional slot designs to achieve an acceptable field weakening performance. The change of the number of poles is investigated as another alternative for the performance improvement in FW. Finally, the optimal 200kW design with the slot per pole of one and capability of delivery of maximum power up to 4 times of rated speed is obtained through an optimization study. The results demonstrate that the increase of the PM and iron losses is an important limiting factor for using higher number of poles in electric machines especially in higher speeds.

The lack of availability of a fast and accurate model for performance prediction of the EMs is underlined in chapter six. The subdomain technique is used to develop an accurate model for prediction of the performance parameters of the IMs. The model is further improved by adding the saturation consideration capability using the subdomains magnetic vector potentials. This model is validated using the 2-D FEA, 3-D FEA, and experimental results in this chapter.

The fast speed and high accuracy of the developed analytical model enables to define an optimization problem over the driving cycle points. In chapter seven, an accurate lumped thermal model is proposed to predict the temperature of the IMs during operation in a driving cycle. An optimization design approach for design of IMs with and without consideration of overload condition is introduced. The optimal designs are compared with each other in terms of the performance parameters, power density, and energy consumption over driving cycle. The effect of the consideration of the overload operation on the weight and energy consumption of IMs is discussed.

A 4kW axial flux induction machine (AFIM) is designed in a same size as a commercial AFPMSM. The challenges for construction of the AFIM rotor and its manufacturing is discussed. The AFIM is constructed for experimental analysis. The effect of the airgap length on the axial force and stiffness is studied through the 3-D FEA and experimental results. It is shown that the axial stiffness in lower airgaps is high which is a limitation for designing the axial flux machines with small airgaps. The optimum airgap with the minimum stiffness is chosen to redesign the AFIM. The locked rotor test is performed experimentally to extract the equivalent circuit parameters of AFIM and validate the 3-D FEA results. The performance parameters of the proposed AFIM are compared with the commercial AFPMSM. The results show the similar power density of both design and less torque density of the AFIM design in the torque-speed envelope.

In summary, this thesis investigates different types of electric machines and their design procedure for EVs and HEVs. The main contributions of the thesis are (1) Detailed analysis of different physical phenomena on the loss of the electric machines; (2) Analysis and development of different methods for efficiency map calculation of electric machines; (3) A step-by-step design process for design of induction and permanent magnet radial flux machines; (4) Optimal design of axial flux permanent magnet machines with the capability of acceptable operation in the field weakening region; (5)

Introduction of an analytical model for performance parameters prediction of induction machines; (6) Prediction of saturation level of induction machines using subdomain technique; (7) Optimal design of induction machine over driving cycle; (8) Design and construction of axial flux induction machine.

Keywords: Efficiency map, Electric machines, Electric vehicle, Hybrid Electric vehicle, Motor design, Optimization, Performance parameters estimation, Propulsion system, Thermal model.

DECLARATION

I certify that this thesis:

1. does not incorporate without acknowledgment any material previously submitted for a degree or diploma in any university

2. and the research within will not be submitted for any other future degree or diploma without the permission of Flinders University; and

3. to the best of my knowledge and belief, does not contain any material previously published or written by another person except where due reference is made in the text.

Signed.....Emad Roshandel.....

Date.....May 2023.....

ACKNOWLEDGEMENTS

I am grateful to Flinders University and the Australian Research Council for their invaluable financial support throughout my PhD, which enabled me to fully focus on my research. Their contributions have played a pivotal role in my academic journey and accomplishments. I extend my sincere appreciation to both institutions for their unwavering dedication to the pursuit of knowledge and for their support of my personal growth. Additionally, I would like to express my gratitude to the University of Adelaide for granting me three years of access to their well-equipped laboratories, which significantly contributed to my overall success.

I am pleased to appreciate Dr. Mahmoudi for his exceptional guidance and mentorship throughout my PhD thesis. His support and invaluable funding sources enabled me to participate in two groundbreaking industrial projects with MyModular Pty Ltd and Sovereign Propulsion System Pty Ltd, which significantly enriched my experience and knowledge in the field. I am also thankful for the opportunities he provided me for lecturing and tutoring, which allowed me to refine my teaching skills and gain valuable experience.

I would like to express my sincere gratitude to Dr. Wen L. Soong, who has played a crucial role in my professional growth. With a firm grip, he took my hand and led me towards success, step-by-step. His insightful guidance and thought-provoking questions have been instrumental in expanding my knowledge and skills. His unwavering support and scientific approach have provided me with the confidence to tackle new challenges and strive for excellence in all my endeavours. I am truly thankful for his impact on my career and his belief in my abilities. His guidance and support have been invaluable, and I am proud to have had such a dedicated and knowledgeable supervisor. My heartfelt appreciation goes out to him for everything he has done for me.

I am deeply grateful to my mother, who has been an unyielding source of support and love throughout my life. Her selfless devotion to my success and her constant encouragement have been a driving force in all my endeavours. Her teachings about hard work, determination, and resilience have had a profound impact on my life and have helped shape me into the person I am today. I am proud to call her my mother and am eternally grateful for her love and guidance. I would like to express my sincerest thanks and appreciation to her for everything she has done for me.

LIST OF FIGURES

LIST OF TABLES

PAPERS OUT OF THE THESIS

Journals

- **Roshandel, E.**, Mahmoudi, A., Kahourzade, S., & Soong, W. L. (2021). Saturation Consideration in Modeling of the Induction Machine using Subdomain Technique to Predict Performance. *IEEE Transactions on Industry Applications*, *58*(1), 261-272.

  Contributions: Conceptualization and decision of the selection of the methodology has been done by Emad Roshandel. The initial draft of the writing and the editions requested by supervisors have been applied by the Emad Roshandel. The mathematical modelling, coding, and finite element analysis have been developed and completed by the Emad Roshandel.

- **Roshandel, E.**, Mahmoudi, A., Kahourzade, S. & Soong, W. L., (2022). Efficiency Maps of Electrical Machines: A Tutorial Review. in *IEEE Transactions on Industry Applications*, Early Access, doi: 10.1109/TIA.2022.3210077.

  Contributions: Conceptualization and decision of the selection of the methodology has been done by Emad Roshandel. The initial draft of the writing and the editions requested by supervisors have been applied by the Emad Roshandel. The mathematical modelling, coding, and finite element analysis have been developed and completed by the Emad Roshandel.

- **Roshandel, E.**, Mahmoudi, A., Kahourzade, S., Yazdani, A., & Shafiullah, G. M. (2021). Losses in efficiency maps of electric vehicles: An overview. *Energies*, *14*(22), 7805.

  Contributions: Conceptualization and decision of the selection of the methodology has been done by Emad Roshandel. The initial draft of the writing and the editions requested by supervisors have been applied by Emad Roshandel. The mathematical modelling, coding, and finite element analysis have been developed and completed by Emad Roshandel.

- Kahourzade, S., Mahmoudi, A., **Roshandel, E.**, & Cao, Z. (2021). Optimal design of Axial-Flux Induction Motors based on an improved analytical model. *Energy*, *237*, 121552.

  Contributions: Emad Roshandel has carried out the mathematical modelling of the saturation effect in the subdomain model of axial flux induction machine and validation of the model using FEA. Also, he has done the collection of the relevant results related to the saturation effect.

Conferences

- **Roshandel, E.**, Mahmoudi, A., Kahourzade, S., & Soong, W. (2020, October). Analytical model and performance prediction of induction motors using subdomain technique. In *2020 IEEE Energy Conversion Congress and Exposition (ECCE)* (pp. 3815-3822). IEEE.

  Contributions: Conceptualization and discussion have been prepared by Emad Roshandel. The initial draft and the editions requested by supervisors have been applied by Emad Roshandel. The finite element model and analysis have been developed and completed by Emad Roshandel.

- **Roshandel, E.**, Mahmoudi, A., & Kahourzade, S. (2021, October). 2D Subdomain Model of the Ladder Linear Induction Machine with considering Saturation Effect. In *2021 IEEE Energy Conversion Congress and Exposition (ECCE)* (pp. 4127-4134). IEEE.

  Contributions: Conceptualization, discussion, and decision of the selection of the methodology have been done by Emad Roshandel. The initial draft of the writing and the editions requested by supervisors have been applied by Emad Roshandel. The required information, finite element analysis, and results preparation for publication are collected by Emad Roshandel.

- **Roshandel, E.**, Mahmoudi, A., Kahourzade, S., Tahir, A., & Fernando, N. (2021, September). Propulsion System of Electric Vehicles. In *2021 31st Australasian Universities Power Engineering Conference (AUPEC)* (pp. 1-6). IEEE.

  Contributions: Conceptualization and decision of the selection of the methodology have been done by Emad Roshandel. The initial draft of the writing and the editions requested by supervisors have been applied by Emad Roshandel. The required information and data for publication are collected by Emad Roshandel.

- Emami, S. P., **Roshandel, E.**, Mahmoudi, A., & Khaourzade, S. (2021, September). IPM Motor Optimization for Electric Vehicles Considering Driving Cycles. In *2021 31st Australasian Universities Power Engineering Conference (AUPEC)* (pp. 1-5). IEEE.

  Contributions: Emad Roshandel has written the introduction and collected the finite element analysis results of the paper. He has written the manuscript of the paper.

- **Roshandel, E.**, Mahmoudi, Soong, W., Khaourzade, S., Guo, Y., Lei, G. (2022). Design of a 100 kW Axial Flux Permanent Magnet Generator for a Hybrid Electric Vehicle. In *2022 32nd Australasian Universities Power Engineering Conference (AUPEC)* (pp. 1-6). IEEE.

  Contributions: Conceptualization and discussion have been prepared by Emad Roshandel. The initial draft and the editions requested by supervisors have been applied by Emad Roshandel. The finite element model and analysis have been developed and completed by Emad Roshandel.

Submitted journals

- **Roshandel, E.**, Mahmoudi, A. Soong, W., L., Kahourzade, S. Design of AC Electric Machines: 100 kW Electric Machine for a Hybrid Electric Vehicle, Submitted to Electrical Engineering.

  Contributions: Conceptualization, discussion, and decision of the selection of the methodology have been done by Emad Roshandel. The initial draft of the writing and the editions requested by supervisors have been applied by Emad Roshandel. The required information, finite element analysis, and results preparation for publication are collected by Emad Roshandel.

- **Roshandel, E.**, Mahmoudi, A. Soong, W. L., Kahourzade, S. Optimal Design of Induction Motors Over Driving Cycles for Electric Vehicles, Submitted to IEEE Trans. on Veh. Tech.

  Contributions: Conceptualization and decision of the selection of the methodology has been done by Emad Roshandel. The initial draft of the writing and the editions requested by supervisors have been applied by Emad Roshandel. The mathematical modelling, coding, and finite element analysis have been developed and completed by Emad Roshandel.

Chapter 1.

Introduction

1.1. Transportation Electrification Benefits

The environmental pollution and global warming as a result of greenhouse gas (GHG) emissions with conventional fossil-fuel cars are an aspect in political and scientific debates. A large number of reforms and new laws are aiming to reduce these emissions to protect the environment. For instance, reduction of the GHG emission to 80% of the 1990 levels by 2050 is the long term target in the United Kingdom [1]. In developed countries, about 30% of the energy generated by fossil fuels is consumed in the transportation sector [2] (see Fig. 1.1). Light and heavy vehicles consume 68% of the energy in the transportation sector. Among all available vehicles in transportation the trains are not categorized in the light and heavy vehicles.

Thus, transportation electrification, which has found popularity among government and researchers, allows significantly reducing GHG emissions. Electric vehicles (EVs) globally emitted around 38 MT[1] CO_2-eq throughout 2018 on a well-to-wheel basis, where equivalent internal combustion engine (ICE) vehicles would have emitted 78 MT CO_2-eq in the same period [3]. A comprehensive study on the substitution of EVs and light EVs (LEVs) for conventional cars demonstrated that GHG emissions can be reduced by up to 75% by 2050 [4]. The rated power of the electric motors in EVs and LEVs are respectively larger and smaller than 10kW. Therefore, electric-scooters, electric motorcycles, electric bikes, three-wheeled cars, and small electric cars are categorized within the LEV category. The vehicles with an electric motor larger than 10kW such as electric cars, trucks, and electric trains are in the category of EVs.

The efficiency of the EV drivetrain is about 77% which is more than 2.5 times of typical ICE based cars with about 30% efficiency [5]. Assuming that the efficiency of the electric motors in the current EVs is about 88%, a two percent efficiency improvement of the electric motor used in EVs will lead to improvement of the efficiency of the drive-train system by 1%. This improvement of the efficiency will reduce carbon emissions from 38 MT CO_2-eq to 37 Mt CO_2-eq. Thus, the study of the electric motors efficiency and improvement of the efficiency of the EVs propulsion system is a key factor in order to reduce the GHG emissions.

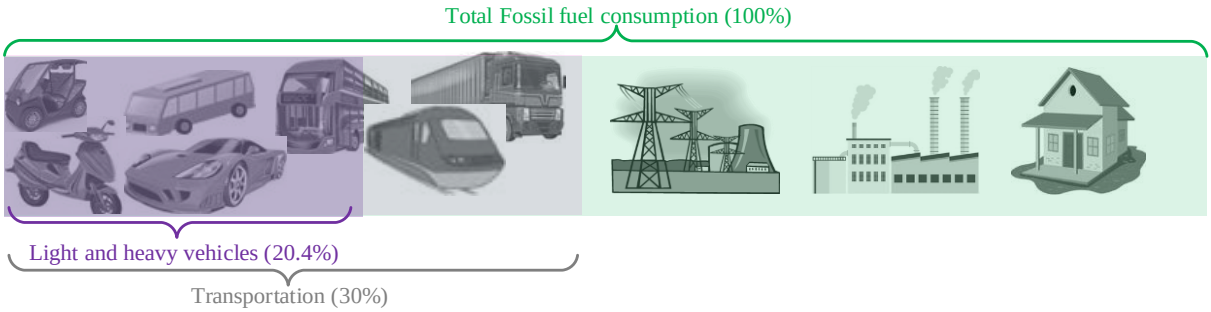

Fig. 1.1. Share of light and heavy electric vehicles in the consumption of the fossil fuels [6] © 2021 IEEE.

[1] Million Tonnes

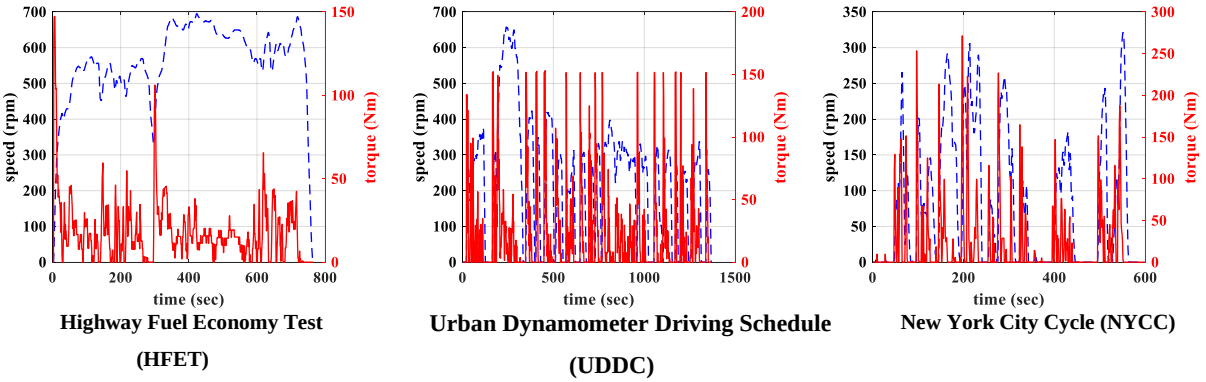

Fig. 1.2. Speed and torque versus time of three standard vehicle driving cycles used in the optimization studies in the literature [6] © 2021 IEEE..

1.2. Propulsion System of EVs and HEVs

The operating point of the electric motor in EVs depends on the vehicle speed and acceleration, the slope of road, the mas of vehicle, etc. Fig. 1.2 shows three standard vehicle driving cycles which are used to evaluate vehicle performance such as fuel economy. According to the driving cycle, the required torque and speed of a vehicle varies at different times. The propulsion system of EVs and hybrid electric vehicles (HEVs) should offer high efficiency over a range of different driving cycles.

Figs. 1.3a and 1.3b illustrates schematic diagrams for two typical propulsion systems of EVs. The propulsion system consists of the electric motor, transmission system (gearbox), battery package, and power electronics drives. The parallel and series HEV drivetrains presented in Figs. 1.3c and 1.3d are two typical transmission system in HEVs [7]. As shown in this figure, the electric machine and engine are placed on a same shaft where they deliver the power to the wheels through a gearbox. Normally, the electric drive of the car is designed to operate optimally in slow-moving city traffic, while the internal combustion engine takes over when the car moves in the highway. In the series HEV drivetrain, the engine and motor are connected to the shaft separately which enables each of them driving a car without any dependency on the other power source. Like parallel HEV drives, the electric motor normally is employed in urban regions while the engine is used for highway roads.

The use of electric motors in EVs became more practical with the development of low-cost, high performance power electronics and batteries. Power electronics are the heart of variable speed drives which can operate the electric motors over a wide range of torque and speed which is required for a propulsion system (see Fig. 1.2). The importance of batteries and power converters have led to a wide range of research and development work over the past decade [8]–[11]. The variation of the losses in power converters, batteries, and the transmission system is generally easier to predict compared to the electric machines (EMs) efficiency in a driving cycle. The efficiency of the EMs utilized in EVs and HEVs depends on various factors. For this reason, the loss analysis and loss reduction of electric machines over driving cycle have been subject of study in a wide range of researches [12]–[14].

The EM needs to offer high efficiency over different driving cycles. The contour plot of the maximum efficiency of an electric motor in the torque and speed plane is called the efficiency map (EffM). Also, the torque (or power) versus speed capability (envelope) of the entire propulsion system of an EV/HEV can be drown on the EffM [15], [16]. The EffM is used as a common means for comparing different electric machines for a given traction application and it provides insight into energy consumption over driving cycles. Fig. 1.4 illustrates a sample EffM of an interior permanent magnet synchronous motor (IPMSM) [17]. This thesis focuses on the EM design with respect to the EffM to achieve energy efficient propulsion systems for EVs and HEVs.

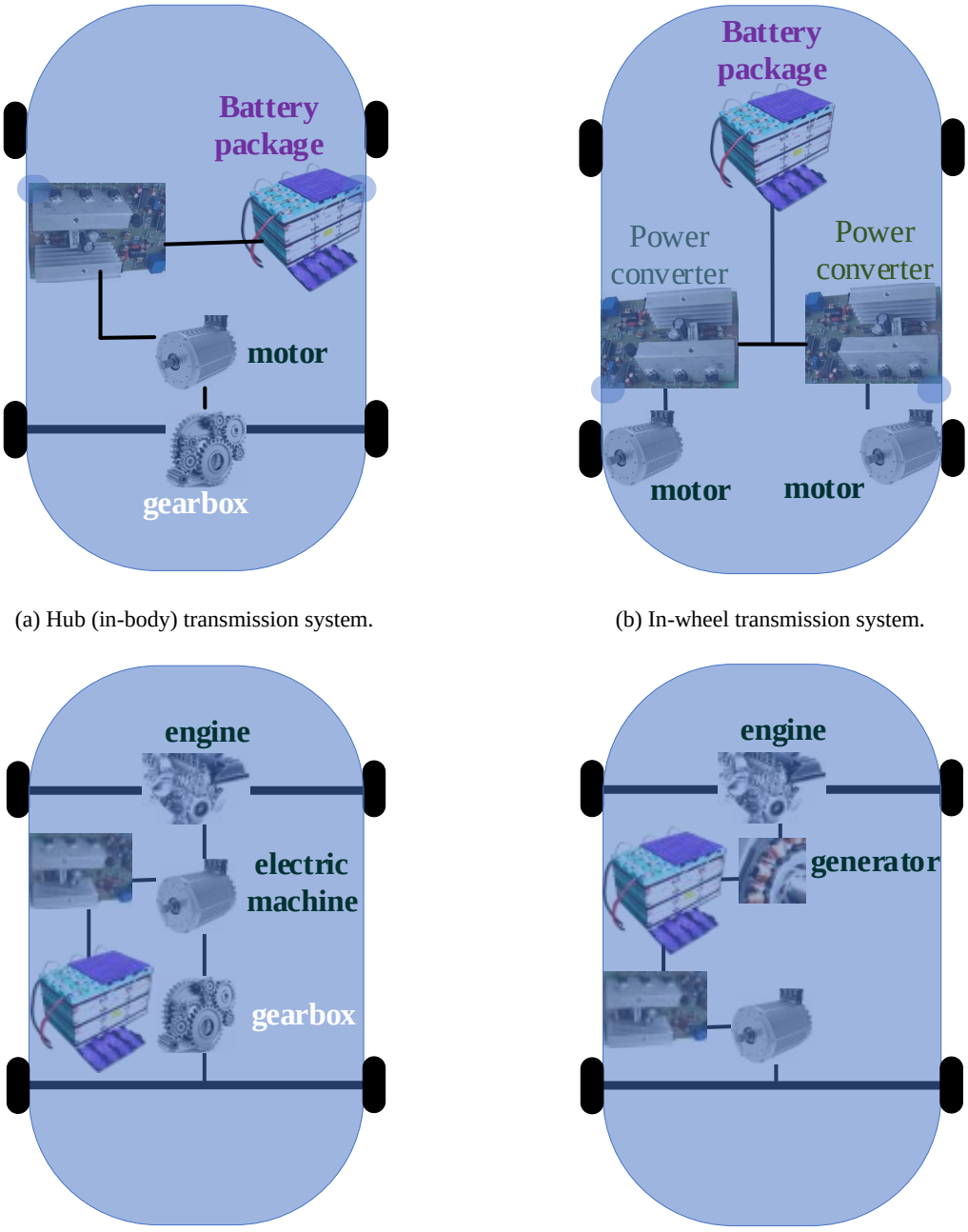

(a) Hub (in-body) transmission system.

(b) In-wheel transmission system.

(c) Parallel HEV drivetrain.

(d) Series HEV drivetrain.

Fig. 1.3. Simple schematic of the typical transmission systems of EVs and HEVs [6] © 2021 IEEE..

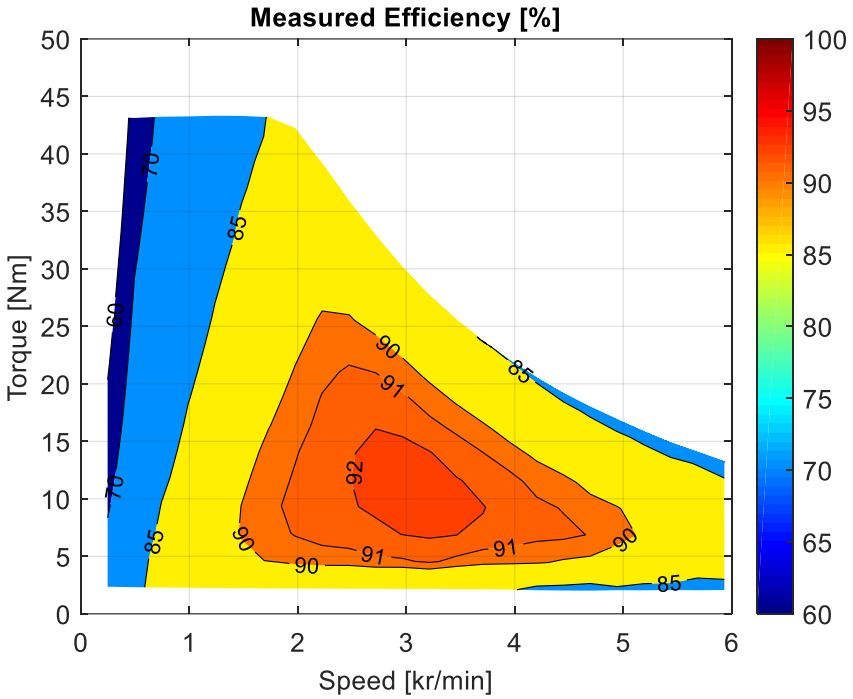

Fig. 1.4. Efficiency map of an IPMSM. The data of this plot has been collected from [6] © 2021 IEEE..

Some requirements of electric machines designed for EVs include high power density for small size and weight; high efficiency to reduce energy consumption; high reliability to reduce maintenance; and wide constant power speed range to minimize the need for variable gearbox between the machine and wheel. To satisfy the needs for simple control and a wide constant power speed range, DC machines were widely used in early traction applications. However, they have low power density and efficiency, and also require regular commutator maintenance.

Rapid developments in power electronics and control technology have allowed the use of AC drives for electric traction. Their advantages include the lack of a commutator and improved power density and efficiency. Induction machines were used initially as their design and manufacturing was well-understood. They offer moderate efficiency, power density, and constant power speed range. In recent years, permanent magnet (PM) machines have been the primary machine of choice for electric vehicles. They offer high efficiency and power density, and a wide constant power speed range. However, they use significant quantities of high-quality rare-earth magnets and the large variations in the cost of these magnets in recent years has been a major concern for manufacturers. This has produced significant interest in other electric machines with reduced or zero magnet requirements such as: induction machines, synchronous reluctance, switched reluctance, and switched flux machines. The characteristics and performance features of these machines are discussed in the thesis.

1.3. Aims and Motivations

The analysis of the loss in the propulsion system of EVs and HEVs and understanding the different factors on the variation of the loss is the preliminary objective of this thesis. This study allows recognizing the portion of the loss of each component over a wide range of torque and speed.

In addition to the physical factors such as temperature, frequency, current, and flux which play important roles in the variation of the loss, the EM loss is also affected by the type of the implemented control system in the drive. The understanding of the EM behaviour in different operating regions and control modes is another objective of the thesis.

The understanding of the loss and control roles allows calculating the IM and PMSM performance parameters in the torque-speed envelope. The efficiency map is a useful tool to understand the torque and speed characteristics of the EMs and the energy consumption of the system. The calculation of the efficiency map for different EMs is another important target of the thesis.

The EffM interpretation is important for understanding the EMs' behaviour in different operating points. It allows designing EMs by optimizing the EffM. The EffM detailed analysis and evaluation is another objective of this thesis.

The design of different types of EMs with respect to the EffM is the complementary objective of the thesis. In addition to the EffM consideration, the understanding of other physical factors such as the demagnetization of PMs, PM loss reduction, torque ripple of IMs and PMSMs, power factor, axial force in axial flux machines, and thermal limits are other objectives which are analysed in detail.

The analysis and understanding of the overload concept which deals with the EMs capability in delivering a larger torque than their rated torque for short duration is another objective of the thesis. This concept requires the temperature variation of the EMs to be modelled during the analysis. Hence, the thermal modelling of the EMs is another topic which is covered in the thesis.

According to the aforementioned explanations, the aims of this thesis are summarized as follows:

- The study of the effect of important factors on the losses in different parts of an EV/HEV propulsion system.
- The detailed analysis of the loss in EMs over a wide range of operating points.
- The discussion of the EM operating regions and role of the applied control approach in determining performance.
- The extraction and interpretation of the EffMs for PMSMs and IMs.
- The performance parameter calculation of IMs and PMSMs using finite element analysis.
- The electric machine design and optimization for HEVs considering optimal operation in both the constant power and constant torque regions.
- The development of an analytical model to accelerate the optimization of EM design for EVs.

- The analysis and understanding of the axial force in axial flux machines.

1.4. Original Contributions

1.4.1. Thesis contributions to the field

A comprehensive literature review is conducted to summarize the variation of EV drivetrain loss components in different loads. The analytical and numerical modelling of the drivetrain loss components is described and the experimental procedure for measurement of these losses is explained. The result of this study provides an overall view on the role of each part of the EV on the variation of the efficiency of EVs. Moreover, it shows the available research gaps which need to be studied in the performance analysis of EV drivetrains.

The calculation and measurement of the EffMs for different electric machines is presented as a tutorial in Chapter 3. This tutorial provides a "road map" for engineers and researchers in the field of EM design for transport electrification. It investigates the calculation of efficiency maps for AC electric machines and has the following areas of contribution:

(1) gives a brief tutorial of alternative EffM calculation methods and discusses their trade-offs;

(2) describes past research on EffMs and identifies research gaps and opportunities for future research.

In the literature review of Chapter 4, it is explained that there is a lack in the preparation of a proper baseline design in the literature. Hence, a systematic step-by-step design process for IPMSM, IM, and AFPMSM machines is developed. The proposed design process provides a baseline design with consideration of both the electromagnetic characteristics and thermal limits of the electric machines for a given cooling system. This allows to decrease the number of variables for optimization of a specific design and hence a reduction of the computational burden.

A fast and accurate subdomain model is proposed to reduce the time of optimal design of induction machines. Due to the capability of prediction of saturation effect, the proposed subdomain technique offers a higher accuracy compared to the earlier subdomain models in the literature. The optimal design of the induction machines requires an accurate thermal model. A lumped-circuit thermal model for the temperature prediction in induction machines is prepared. The availability of the accurate electromagnetic and thermal models enables executing a comprehensive optimization study with and without consideration of the overload capability in IMs. The result of this study shows the consideration of overload can increase the power density of IMs up to four times of a steady-state design but with the cost of the increase of energy consumption over driving cycle.

Chapter 8 explains the design and construction procedures of AFIMs. The results of the computation and measurement of the axial force in axial flux machines shows the importance of the selection of the optimal airgap for construction of these machines. The comparison of the performance

parameters of the designed AFIM and a commercial AFPMSM shows the lower torque density of the AFIM.

1.4.2. Minor contributions

- Interpretation of the EffM of electric machines.
- Analysis of the effect of number of poles on the power density and temperature rise of electric machines.
- Identification of the optimum structure for double-sided axial flux machines (double rotor vs. double stator designs).
- Analysis of the effect of the low radial permeability in tape-wound stators for axial-flux machines.
- Analysis of the importance of the slot number and number of poles on PM losses and field weakening characteristics.
- Investigation of PM segmentation effect in axial-flux machines.
- Demagnetization modelling and analysis of PM materials.
- Analysis of the interior permanent magnet rotor in an axial flux topology.
- Multi-objective optimization using surrogate models.
- Inter-bar rotor current analysis in induction machines.
- Analysis of the effect of a solid rotor on the performance of axial-flux induction machines.
- Analysis of the effect of number of rotor bars on the torque ripple of induction machines.

1.5. Thesis Outlines

Chapter 2 begins with a discussion on the advantages and disadvantages of different transmission systems and electric machines utilized in EVs. The popular electric motors used in EVs and HEVs are discussed, and their characteristics are emphasized. The losses in the entire propulsion system of the EVs and HEVs is studied in different operating points.

Although there are many papers discussing the EffM, there is a lack of clear steps/guidelines for the calculation of EffMs and discussion of the accuracy versus calculation effort trade-off between alternative techniques. The third chapter addresses this shortcoming by the provision of a tutorial for EffM calculation and measurement approaches. The fundamentals of the EMs operating regions (i.e., constant torque and constant power regions) are discussed in the stant of chapter 3. The characteristics of the machines and the concept of the voltage and current limits are explained to describe the necessity of the consideration of suitable control methods. A comprehensive study is conducted on the available methods for extraction of the EffMs. The advantages and disadvantages of these methods are discussed and the appropriate techniques in different situations are determined. The effect of different loss factors for both IMs and PMSMs are explained and finally the possible research opportunities in that field are introduced.

In Chapter 4, a step-by-step design approach is provided for the design of the IM and PMSM which are used in the propulsion system of a direct drive HEV. The design approach not only considers the electromagnetic performance of the EMs but also investigates the thermal performance. The increase of the number of poles leads to the increase of the operating frequency at a certain speed. The frequency increase result in more core losses in a smaller iron volume. So, the cooling system may fail in keeping the temperature in a reasonable range. The detailed discussion on the selection of the pole numbers for a given cooling system is discussed.

The introduced design process for the radial flux IPMSM and IM is used to design axial flux PMSMs (AFPMSM) in Chapter 5. A detailed analysis on the effect of the solid rotor for the designed AFPMSM is conducted. The demagnetization of the PMs due to the operation at higher temperature is another important factor which is analysed. Finally, to find the optimal design, a surrogate model for the machine is provided to conduct the multi objective optimization. An analysis of the effect of different number of poles and slots for 100kW and 200kW designs is performed to find an optimal design with the capability of the operation in the field weakening region up to four times of the rated speed.

The EM analysis and optimization study over a driving cycle requires an accurate and fast tool. In Chapter 6, a subdomain method (SDM) which solves the Maxwell equations of IMs in five subdomains is developed. The accuracy of the SDM is validated against 2-D and 3-DFEA, and experimental data. The superiority of speed of the proposed SDM model is demonstrated.

Chapter 7 discusses the differences between IM designs optimizing for various driving cycles with and without consideration of overload capability. As the temperature is a limiting factor in the overload analysis, a lumped thermal model is developed for prediction of the temperature of induction machines. The developed SDM model along with the proposed thermal model are utilized for the optimization.

In Chapter 8, a 4kW axial-flux induction machine is designed in a same dimension as a 4kW commercial AFPMSM. The effect of the number of slots is studied to select the optimum number of slots which offers the smallest torque ripple. The effect of the consideration of the solid rotor for the AFIM is studied to understand the performance difference compared to an AFIM designed with laminated rotor. The process of the construction of the AFIM is explained in detailed. The machine is constructed to validate the results of the 3-D FEA. The axial force analysis and the optimal airgap which gives a reasonable stiffness is determined using the experimental tests and 3-D FEA analysis.

Chapter 2. Literature review: the propulsion system of electric vehicles and losses

2.1. Chapter Overview

The first electric vehicles and locomotives were introduced in the mid-nineteenth century. However, the lack of reliable high capacity energy storage and a suitable drive system did not let them to be used in industry [18]. The development of the power electronics and appearance of rechargeable battery packages attracted researchers to spend time on the development of electric machines. EVs are environmentally friendly products because of their low noise and low GHG emissions during operation. So, they can be an appropriate substitute for the conventional ICE based vehicles for the future.

The propulsion system of EVs (including the electric motor, transmission system, battery package, and inverter) aims to offer high efficiency over a wide range of torque-speed operating points. Hence, the optimal design and performance improvement of such vehicles has attracted attention in the literature. The drivetrain systems in various EVs are reviewed in this chapter to highlight their advantages and disadvantages. The focus of this thesis is on the electric machines. Thus, the available batteries and power electronics devices are not reviewed. The popular electric motors used in the EVs are discussed and their characteristics are emphasized. This chapter briefly reviews the commercial transmission systems and electric machines of EVs. Then, an overview about the change of various loss components in the torque-speed envelope of EVs is rendered to show the role and significance of each loss component in a wide range of torque and speeds. The research gaps and future research subjects based on the conducted review are reported.

2.2. Review on the Type of Electric Machines and Transmission Systems

This section aims to highlight the advantages and disadvantages of the different transmission systems and electric machines utilized in EVs. The distinction of various propulsion systems provides the introductory knowledge about the significance of choosing proper transmission system. This section summarizes the key developments in the field and enable understanding the different types of propulsion systems available for EVs.

2.2.1. Electric machines in EVs

The electric motors are the beating heart of EVs. Electric machines have been used in traction applications for over a century. Some main requirements include high power density for small size and weight; high efficiency to reduce energy consumption; high reliability to reduce maintenance; capability to operate during overload conditions; and wide constant power speed range to minimize the need for a variable gearbox between the machine and wheels. Designing such machines require special attention since their operating points vary continuously during the driving cycle of EVs.

Due to their simple control and wide constant power speed range, DC machines were widely used in the earliest traction applications [19]. However, they lack sufficient power density and efficiency, and also require regular commutator maintenance. Rapid developments in power electronics and control technology allowed the use of AC drives for electric traction. Advantages include the lack of commutator and improved power density and efficiency. Induction machines (IMs) were used initially as their design and manufacturing was well-understood [20]. They offer moderate efficiency, power density, and constant power speed range [21].

In recent years, permanent magnet synchronous machines (PMSMs) and PM brushless DC machines (PMBLDCs) have been the primary machine of choice for electric vehicles. They offer high efficiency and power density, and a wide constant power speed range. Table 2.1 lists the types of electric machines used in commercial EVs. It confirms the popularity of the PM based machines in leading companies. It must be highlighted that interior PMSMs (IPMSMs) have higher popularity for EV traction applications than the surface mounted PMSMs (SPMSMs) owing to the following items [22], [23]:

- higher torque of IPMSMs due to reluctance torque;
- mechanical strength especially at high speeds;
- higher efficiency in the field weakening region;
- more robust against the demagnetization of the PMs;
- easier sensor-less control because of the larger difference between the *d*- and *q*- axes inductances.

Table 2.2 provides a qualitative comparison between different types of electric machines used in EVs and LEVs. The requirement of significant quantities of high-quality rare-earth magnets is a drawback for PM machines. The large variations in the cost of PMs in recent years has been a major concern for manufacturers. This has produced interest in other electric machines with reduced or zero magnet requirements such as: IMs, synchronous reluctance, switched reluctance machines (SRM), and switched-flux machines. Synchronous and switched reluctance motors [24]–[26] are two types of the magnet free machines which generate torque based on the inductance variation. The available topologies of the synchronous reluctance machines and SRMs do not have a comparable power density with the PM motors [27], [28].

The efficiency of the electric machines over a driving cycle can be extracted from the efficiency map of the machine. To illustrate the difference of the performance of the popular machines used in EVs, the efficiency map of two IPMSMs, an IM, and a SRM have been compared in [27]. The results prove the superiority of the IPMSM compared to the IM and SRM. The IPMSM peak efficiency occurs at the constant torque region and the beginning of the field weakening. The efficiency of the IPMSM drops because of the increment of the PM losses in larger speeds. On the contrary, the maximum efficiency of the IM and SRM occurred at the field weakening region. Compared to the IM

machine, the SRM has a greater efficiency in larger torques and speeds which is a need for the EVs operating with a single-speed transmission system.

Torque ripple, current ripple, difficult control, expensive drive system, and their acoustic noise are other reasons of the restriction of the SRMs commercialization in EVs [29]. Although the constant torque region of the IM is smaller than the IPMSM, it has a better overload capability compared to the IPMSM [30]. Therefore, the IM can be considered a good option for magnet free electric machine to be employed in EVs instead of the PM machines.

Table 2. 1. THE TYPES OF THE ELECTRIC MACHINES USED IN THE COMMERCIAL EVS [6] © 2021 IEEE..

Electric machine type	Company
DC	Fiat panda Ellatra, Citroën ë-Berlingo Électrique
SRM	Choloride lucas, converted GM prototype
PMSM	Nissan leaf, Toyota Prius, Citroen C-zero, BMW, Toyota, Hyundai, Chevrolet, JAC, Baic, Zotye
PMBLDC	Smart fortwo ED
IM	Tesla roadster, GM EV1

TABLE 2. 2. THE CHARACTERISTICS COMPARISON OF VARIOUS ELECTRIC MACHINES [6] © 2021 IEEE USED IN EVS [31]–[33].

	Motor type				
	DC	**PMBLDC**	**PMSM**	**SRM**	**IM**
Power density	low	very high	very high	medium	medium
Efficiency	low	very high	very high	medium	medium
Controllability	very high	high	high	medium	very high
Reliability	medium	high	high	very high	very high
Cost	low	high	medium	low	very low
Technology maturity	high	medium	high	high	very high
Noise levels	medium	low	very low	high	very low
Maintenance	high	low	low	low	low

2.2.2. Transmission systems

In conventional vehicles, multispeed transmissions are used as it provides different operating speeds, adequate acceleration, and smooth starting when the combustion engine works at its high efficiency region. Due to the fact that the electric motors offer a high efficiency over a wide range of torque-speed [34], both the single-speed and multi-speed transmission systems can be utilised in the propulsion system of EVs. Fig. 2.1 shows the graphical abstract of the single speed, two-speed, and continuously variable transmission (CVT) utilized in EVs and LEVs transmission systems.

In a single-speed transmission system, the required torque and speed is delivered to the wheels by the electric motor. The motor used in single speed transmission systems should operate efficiently in both low and high speeds. The non-magnet motors do not offer a high efficiency in lower speeds. So, the multi-speed transmission system is required to have a high efficiency in a wide torque-speed range. The multi-speed system benefits from the availability of the gearbox or pulley to convert the motor torque and speed to the required torque and speed. The tentative trade-off between the characteristics of the electric motor used along with different transmission systems is tabulated in Table 2.3.

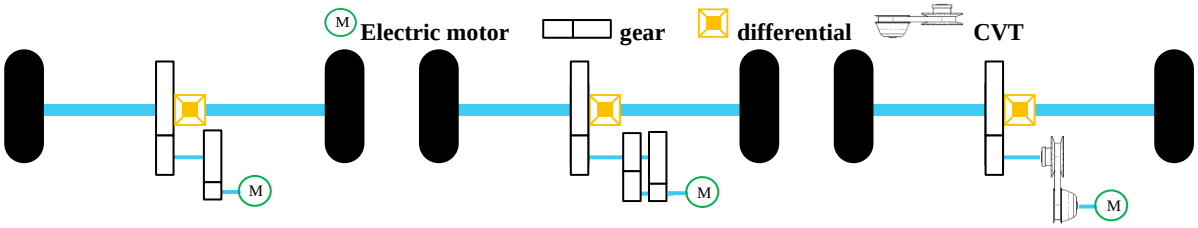

(a) single-speed transmission (b) two-speed transmission (c) CVT transmission

Fig. 2.1. The graphical illustration of three widely used transmission systems in EVs [6] © 2021 IEEE.

TABLE 2. 3. THE DIFFERENCES OF ELECTRIC MOTORS USED IN EVS AND LEVS ALONG WITH BOTH TYPES OF THE SINGLE-SPEED AND MULTI-SPEED TRANSMISSION SYSTEMS [6] © 2021 IEEE.

Electric motors characteristics	**Single-speed**	**Multi-speed**
Size/weight	Large/heavy	Small/light
Rotation speed	low	high
Load on the motor	high	low
Top speed	low	high
Acceleration	low	high
Maintenance	low	high
Reliability	high	low
Size/weight	Large/heavy	Small/light
Rotation speed	low	high
Load on the motor	high	low
Top speed	low	high

The in-wheel and in-body drivetrain systems are two typical drivetrain systems used in EVs. Reduction of mechanical losses due to the elimination of the transmission system and differential clutch are the advantages of the in-wheel drivetrains. The reduction of the total weight of the EV is the main superiority of the in-wheel drivetrains [35].

Although the use of the in-wheel topology removes the need for the transmission system, the total cost of the propulsion system is higher than the in-body drive trains. The higher cost results from the more expensive structure of the electric motor used for such a system [36]. Furthermore, the direct connection of the in-wheel motor to the wheels increases the unsprung mass which reduces the handling capability of the EVs. The limited available space in the wheels is a constraint for the design of an electric motors with the ability of the heavy braking at higher speeds [35].

The in-body drivetrains of EVs are like the transmission system of conventional cars with the ICE in which the mechanical energy is transferred to the wheels through a shaft. This drivetrain allows use of the gearbox to improve the acceleration time and maximum operating speed of the EV [34]. The literature shows the use of in-body drivetrains along with a multi-speed transmission system is very efficient option for the EVs and LEVs [37], [38]. Automatic, automated-manual, and continuously variable transmission (CVT) are the investigated transmission systems in the drivetrains of the in-body designs. The automatic transmission systems are categorized into the single-speed and multi-speed reduction gears. The characteristics of these transmission systems are discussed in this section.

2.2.2.1. Single-stage reduction gears

The reduction gears are used to provide larger torques in the presence of high-speed motors. The authors in [39], introduced the design of a high-performance gear and motor system for the LEVs application. The availability of the gear in this design is shown to decrease the required permanent magnet and iron volume of the electric motor. The performance of the reduction gears is improved by means of a planetary gear between the motor and wheels [40].

In addition to the reduction of the motor cost and weight, it was concluded that the overall efficiency of the drivetrain in the presence of the gear is higher than the efficiency of a gearless motor [41]. Furthermore, the gears reduce the stress on the motor during overload conditions which leads to the higher efficiency at overload. The noise, complexity of the design when multi-stage gear is required, and the high aspect ratio (i.e., high ratio of length to diameter) are the disadvantages of these types of gears.

2.2.2.2. Multi-speed reduction gears

Two-speed transmission systems improve the EV performance as compared to that of the single reduction gear system [42], [43]. In two-speed transmission systems, the first gear ratio is employed to increase the low-speed torque to speed-up the acceleration time. The second gear ratio aims to increase the operating speed range. Thus, the two-speed transmission can maintain high efficiency over a wider range of torque and speed.

The total efficiency of the drivetrain system over a wide range of the torque and speed is improved using the multi-speed transmission [44], [45]. But the total cost of the EV is the limiting factor for development of the gears with larger than a two-speed ratio system. The control of the multi-speed transmission system is more complex than the single-speed system due to the need for an automatic gearbox. Hence, the type of the gear is determined based on the operating driving cycle. It was demonstrated that a two-speed transmission system is efficient and cheap enough for the regular EVs with a wide range for torque-speed points [44].

The two-speed transmission system are widely used in EV as they offer a suitable balance between advantages of a transmission with multiple gears and the simplicity of a small /lightweight drivetrain [46], [47]. Their popularity leads to development of two-speed transmission systems. In [48], the torque converter was removed from the main part of the conventional two-speed automatic transmissions to improve the efficiency. In this upgrade, the planetary gear is substituted with a conventional hydraulic transmission system.

2.2.2.3. Automated-manual transmission (AMT) system

Automated manual is an efficient multi-speed transmission system used in EVs and LEVs. The conventional AMTs are composed of a clutch, gearbox, and an embedded control unit. The AMTs did not find popularity in commercialized EVs because of their intrinsic drawbacks like the interruption

of the traction and excessive wear of the clutch [49]. Literature has suggested clutch-less AMTs where the system uses a gear shift control strategy to achieve smoother shifts [50], [51]. However, the authors did not find a way to prevent the torque interruption during power transmission from motor to the shaft.

2.2.2.4. Continuously variable transmission

CVTs consists of a drive and a driven pulley which are linked together by a belt. The drive pulley and the driven pulley are connected to the motor shaft and wheel, respectively. It adjusts the delivered torque and speed to the wheels by changing the diameter of the drive pulley over a driving cycle. This capability allows the electric motor to operate at a certain speed where its efficiency is maximum [52] to generate the required torque.

The CVT not only improves the efficiency [53] of a drivetrain especially at low speeds [52], but also is a maintenance free device [54]. It has been demonstrated that the efficiency of an EV during operation is improved up to 12% in presence of the CVT [55]. CVT is a commercialized technology which has been used in Honda [56], Toyota [57], and Nissan [58].

2.2.2.5. Comparison of the performance of the popular drivetrains

The comparative study between the performance of a single-stage drivetrain and two-speed transmission conducted in [59] demonstrates the performance improvement of the EV in presence of the two-speed transmission. The comparison of the results of the two-speed with three- and four-speed transmission systems shows that the performance of all three systems is approximately similar [60]. Therefore, from the economical point of view, the two-speed transmission is an optimum system in the category of multi-speed transmissions. The performance of the single-speed, two-speed dual-clutch transmission, and CVT transmission systems have been compared with each other in [61]. The results indicate the CVT efficiency is higher than the two-speed transmission system. The superiority of the efficiency of the CVT over the multi-speed transmission systems was also proven in [60] and [62].

2.3. Losses in Electric Vehicles

The current motor efficiency standards are limited to the motors for single-speed applications such as fans, pumps, and compressors. NEMA standards [63] classifies the motor efficiencies into four categories named standard efficiency, high efficiency, premium efficiency, and super premium efficiency for 50 and 60 Hz three-phase and single-phase motors [63]–[65]. The IEC has a similar categorization for determination of the single speed motors efficiency which are known as IE1, IE2, IE3, and IE4 [63]. However, those machines designed for light and heavy electric and hybrid electric vehicles, which should offer a high efficiency over a wide range of torque and speed, are not subject to efficiency regulation [66].

The high-power density of the permanent magnet synchronous motors (PMSM) made them popular in the traction application [67], [68]. The high cost of the rare-earth magnet materials of the PMSM motivates researchers to improve the efficiency and performance of the induction [69], synchronous reluctance [25], and switched reluctance motors [26], [29], [70]. Nowadays, PMSMs are the main part of the propulsion system of the commercial EVs whereas some models of Tesla electric cars such as Tesla Roadster benefits from the low-cost induction machine in its propulsion system [71]. Therefore, the study of the synchronous and asynchronous EMs which are the most popular motors in the drivetrain system of the EVs is important to predict the EV performance over a wide operating range and perhaps specific driving cycles.

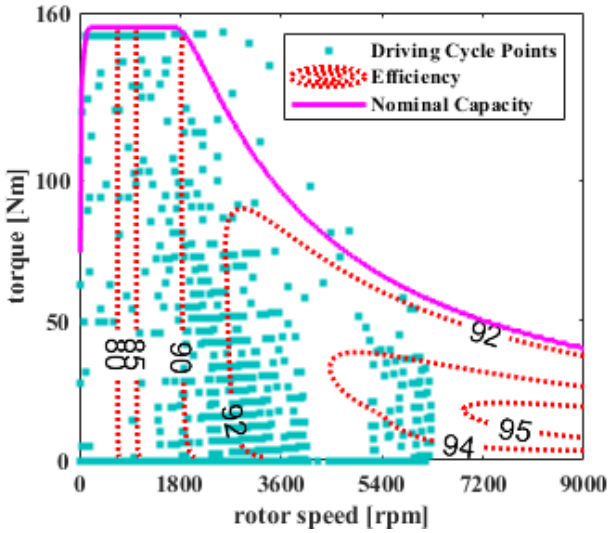

Fig. 2.2. Induction motor efficiency contour and the UDDS driving cycle operating points in the torque-speed envelope [72].

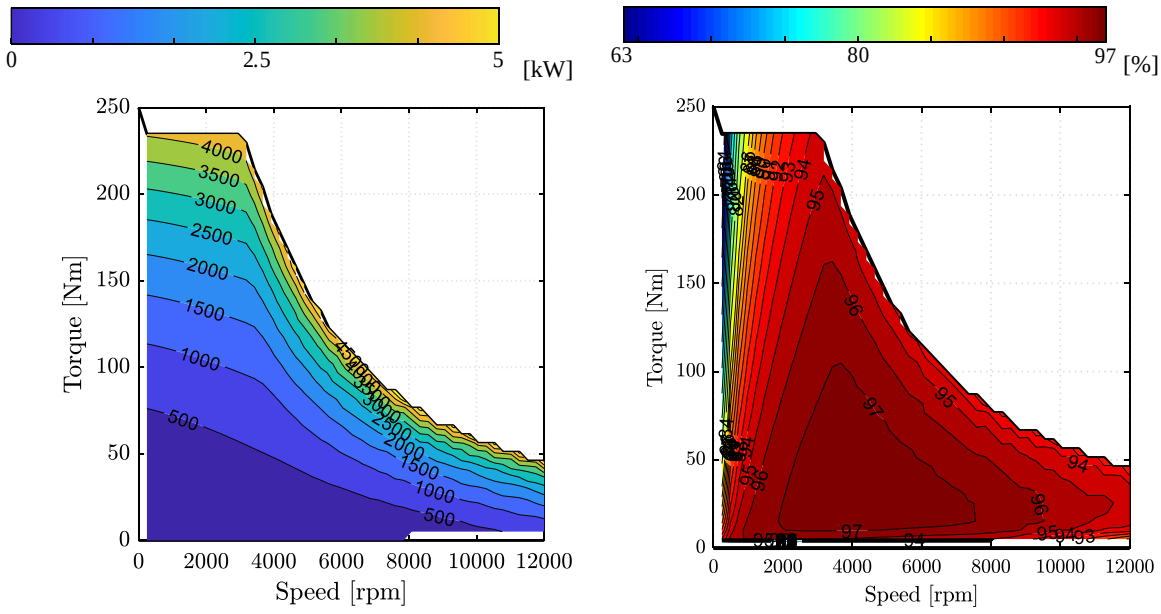

(a) Total loss map of an IPMSM. (b) Efficiency map of an IPMSM.

Fig. 2.3. Induction The loss and efficiency maps of a sample 50kW IPMSM subject to operation at its maximum efficiency in each operating point. The studied IPMSM is designed for EV application. The data of this plot has been collected from [16], [72], [73].

In traction applications, EffMs are widely utilized to estimate the total energy used by the propulsion system of the vehicle over a driving cycle. Fig. 2.2 projects the location of the urban dynamometer driving schedule (UDDS) driving cycle points in a sample efficiency map of an induction motor as per the dynamic model of a vehicle considering the motion equations and transmission coefficients.

The electric machine losses vary based on torque and speed operating points. In general, the reason for variation of the loss in different types of electric machines follows Ohm's law and other physics rules determining the core losses and mechanical losses. However, due to the dependency of the efficiency on the topology of the electric machines, the loss variation in different regions is not similar between them. Comparing the EMs of induction motors (IMs) with those of interior permanent magnet synchronous motors (IPMSMs), it is seen that different areas where the maximum efficiency is achieved are highlighted. In IMs, the rotor bar losses are high at lower speeds which leads to reduction of the efficiency. The reduction of the copper and core losses at higher speeds result in a high efficiency of IMs in the field weakening region (see Fig. 2.3). Above a certain speed, the windage and friction losses become dominant, and the efficiency of IMs start to decrease. The efficiency of the permanent magnet (PM) machines around the rated speed (half to two times of the rated speed) is at its highest level. In these machines, the losses are increased by increment of the speed because of the iron loss and permanent magnet loss increment. Also, the need for increment of the *d*-axis current in the field weakening region is the main reason of the increment of the copper losses in PM motors.

Identification of the major loss components and analysis of each component helps optimal design of a machine to reduce the losses in a wide-speed range. Fig. 2.4 shows the substantial types of the loss in the drive-train system of EVs. The machine loss splits and their role in in the efficiency of a machine over a wide torque-speed range are discussed. The review of the considered type of losses reveals which type of the loss has not been properly studied and modelled in literature.

The detailed analysis of the conductive and core losses of the PM and IM machines have been presented in a series of articles [74]–[76]. The core and ohmic losses in the torque-speed plane have been studied in [17], [21], [73]. A comprehensive literature review on the electric motor losses and their dependency on temperature has been conducted in [77]. However, there is no article summarizing the variation of all types of the losses in a wide range of torque and speed.

The content of this section covers a detailed overview of the sources of the losses in the drivetrain system of an EV. It is a conceptual framework to reconcile the previous works based on their studies and conclusions. The EV drive-train system consists of electric motor, electric drive, and transmission system. The loss of each part affects the overall efficiency of an EV. The details of the variation of each type of loss with different parameters such as voltage, current, speed, and torque are discussed. This overview and detailed loss discussion are a proper reference for the readers to understand the

role of losses in the converter, electric machine, and mechanical transmission system for traction system of EVs. The calculation procedure, measurement method, and role of different loss types as well as possible errors and difficulties of the measurement are explained to understand the behaviour and variation of the losses in a wide-torque speed range that is necessary for an optimum design of the drivetrain system of EVs.

The amount of power losses determines the efficiency of an electric vehicle. The ohmic losses, iron losses, permanent magnet (in PM motors), and converter losses are the main source of the electrical and magnetic losses in traction systems. The mechanical sources of the losses including friction, stray, and windage losses are placed in another category of the power dissipation. The transmission system loss is another source of the loss which is discussed in this section.

TABLE 2.4. THE TYPE OF LOSSES INVESTIGATED FOR EFFM CALCULATION DURING THE LAST THREE DECADES (1992 TO 2021) [72].

Reference number	Copper loss	Core loss	Friction loss	Windage loss	Stray stress	Converter loss	PM loss	Transmission system loss
[15], [78]–[92]	✓	✓	✓	✓	✓	×	×	×
[19], [21], [27], [28], [93]–[119].	✓	✓	×	×	×	×	×	×
[14], [120]–[133]	✓	✓	✓	✓	✓	✓	✓	×
[134]–[142]	✓	✓	✓	✓	✓	✓	✓	✓

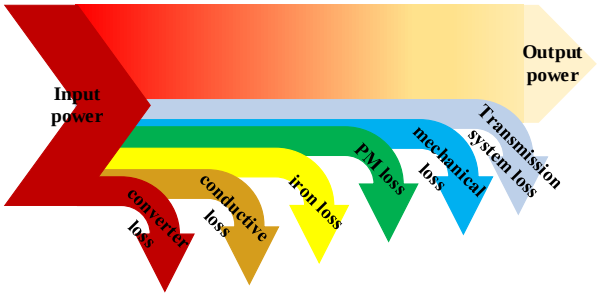

Fig. 2.4. The various loss components of an electric machine used in the propulsion system of EVs [72].

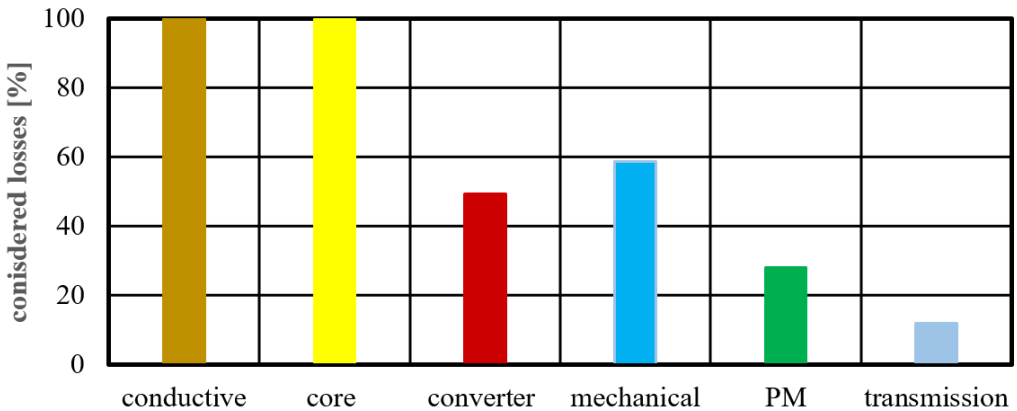

Fig. 2.5. The statistics of documented research focused on the impact of various types of losses on EffM of electrical machines during the last three decades (1992 to 2021) [72].

As shown in Fig. 2.5, except conductive and core losses, just about 50% of the literature have investigated the other sources of loss in the drivetrain (i.e., all mechanical and electrical parts) of an EV. The references used to extract the required data of Figure 4 are tabulated in Table 2.4. In practice,

precise measurement devices and power analyzers are used for the extraction of the efficiency maps [129]-[130]. It is obvious that in the experimental measurement all categories of losses are included for the EffM extraction. Comparison of the results of computational methods such as finite-element analysis (FEA) or analytical methods with the experimental tests shows that the most important sources of the losses belong to the conductive and iron losses [133]. Therefore, most of the finite element-based and analytical models used in the efficiency studies tried to model these two portions of the losses accurately [78], [85]. In this section, the sources of these type of losses and the determinative factors which affect the value of each loss are discussed. It explains how the losses play an important role in the prediction of efficiency maps.

2.3.1. Joule (Ohmic) loss

The stator winding losses in all types of electric machines and the rotor bar losses in squirrel-cage IMs are defined as the ohmic losses in electric machines [120]. The ohmic loss is proportional to the square of current flowing in the conductor ($P=RI^2$). Furthermore, the skin effect which is the tendency of forcing the alternating current towards the surface of the conductive material is significantly affected by the frequency, and the conductor temperature increases the amount of conduction losses. In AC electric motors, to a first approximation, the winding current has a directly proportion to the produced torque and the speed of the shaft has a direct relationship with the supply frequency. Thus, the ohmic loss varies by both the torque and speed. Figs. 2.6(a) and (b) illustrate the current map and ohmic loss map of a 50kW IPMSM motor over a driving cycle, demonstrating how the ohmic losses vary with the current amplitude. Such variations are linked with simultaneous changes in torque and speed. To illustrate the difference of the rotor bar and stator winding, Figs. 2.6(c) and (d) are presented. As expected, the effect of the increment of the current level increases the rotor bar and stator winding losses of the induction machines.

Researchers in [21], show that the copper losses have different relationships with the torque and speed in both constant torque and constant power regions. The finding indicated the copper losses can be approximated as a loss function ($T^m\omega^n$) where m and n determines the effect of the torque and speed on the copper loss of the machine. Table 2.5 summarizes the copper loss dependency on the torque and speed of IMs, surface-mounted PM (SPM), and interior-PM (IPM) machines. IMs and IMr represent the stator and rotor ohmic losses of the induction machines in Table 2.5. It must be highlighted that the powers of speed and torque give an acceptable estimation of the ohmic losses but not an exact value. Some literature [15], [91], [143] have sought to improve the accuracy of the loss function. The presented results in these papers have limited accuracy based on the authors' explanations. So, more investigations are required to improve the accuracy of loss function. Nevertheless, Table 2.5 can be used to approximately understand the relationship of the ohmic losses with the torque and speed.

In the electric equivalent circuit and 2D FEA models, the winding losses are modelled using the resistance of the stator in the electric equivalent circuit (EEC) or the excitation resistance in 2D FEA. Analytical, empirical equations, and experimental measurement using DC and AC tests are the conventional ways of the calculation of resistance. 3D FEA can calculate the resistive losses directly using the integration of the loss density over winding volume.

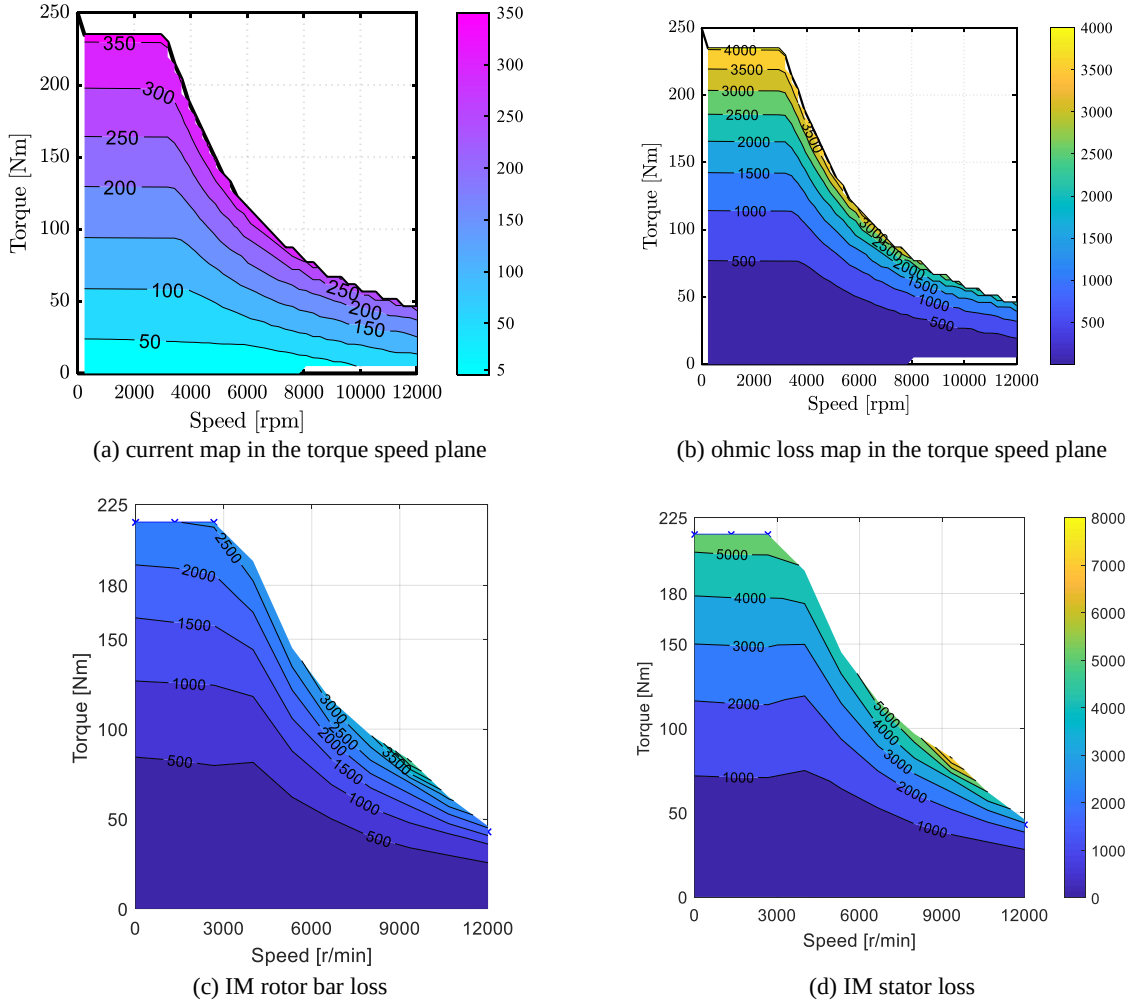

(a) current map in the torque speed plane

(b) ohmic loss map in the torque speed plane

(c) IM rotor bar loss

(d) IM stator loss

Fig. 2.6. current and ohmic loss maps of a 50kW IPMSM for operation over a wide torque speed range [16], [73] and the contour plot of a ohmic losses of a 60 kW induction machine (rotor bar and stator ohmic loss) [21]. These plots have been provided based on the collected data from [16], [21], [72], [73]

TABLE 2. 5. THE DEPENDENCY OF THE MACHINE OHMIC LOSSES ON THE TORQUE AND SPEED OF THE MACHINE RENDERING AN APPROXIMATION OF THE LOSS IN DIFFERENT OPERATING POINTS FOR EACH TYPE OF MACHINE [21], [72].

	Constant power region		Constant torque region		
T^2	IM_s, IPM, SPM	IM_r	IPM, SPM		IM_s, IM_r
T	IM_s IPM			IM_r	IM_s
1	IM_s		IPM, SPM		
	1	ω	1	ω	ω^2

In the analytical and FEA models, the effect of the temperature is investigated by determining a constant value of resistance at higher temperatures. Some commercial software like Ansys allows to link the electromagnetics analysis with the thermal transient analysis to calculate the temperature

variation effect in parallel with the operating condition of the machine [144]. However, such a process is computationally expensive and so is less practical for prediction of the efficiency map.

The effective copper area of a conductor is reduced by increase of the frequency which leads to the resistance increase. As formulated in (2-1), the skin depth depends on the resistivity and permeability of a conductor as well as the operating frequency [111]. Fig. 2.7 is to show the variation of the skin depth and resistance for a sample copper conductor. It is seen that at the 1.2kHz frequency the resistance is 7.5 times of the DC resistance. Thus, the consideration of the skin effect in analysis of the electric machines is an important factor. Normally, windings are designed based on the stranded conductors which helps to reduce the effect of the skin effect.

$$\delta = \sqrt{\frac{2\rho}{2\pi f_{eff}\mu_r\mu_0}} \tag{2-1}$$

FEA analysis enables considering the skin effect more precisely in higher frequencies [144]. However, it complicates the simulation and consequently increases the simulation time. Usually, the effect of the skin effect is separately analysed in FEA in different current levels and winding bundles. The calculated results are curve-fitted to correct the calculated losses during a postprocessing process.

Eddy current effect which is also known as the proximity effect is another source of the variation of the resistance in a conductor. It occurs when a conductor and a magnetic field are in relative motion, causing electric currents to flow within the conductor. This phenomenon increases the ohmic losses in higher frequency specially in thick conductors. FEA is the most reliable approach for prediction of this type of loss. The statistical modelling is another investigated approach to estimate the eddy current loss in the conductor [145].

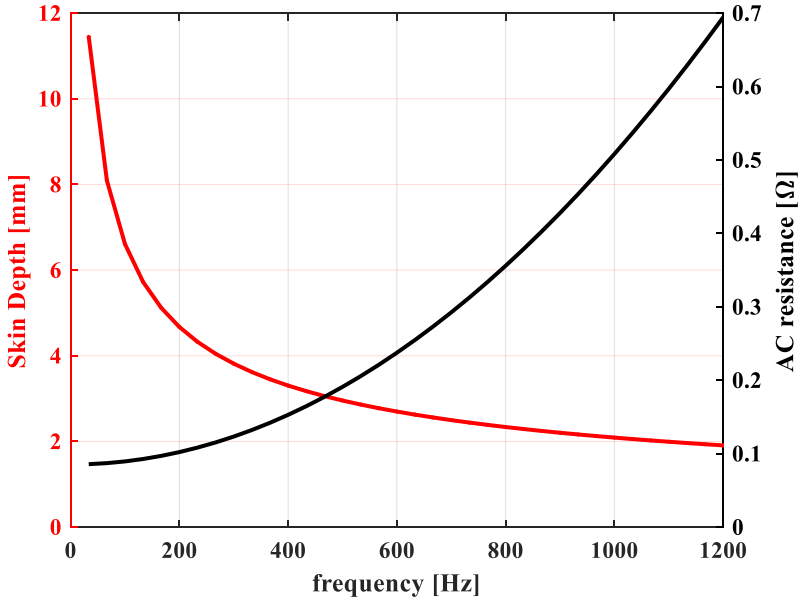

Fig. 2.7. Variation of skin depth and resistance of a sample conductor at 80°C versus frequency of operation.

2.3.2. Core loss

Core losses are another determinative factor in the efficiency calculations. The Steinmetz equation is the well-known method of the calculation of the core losses. Steinmetz showed that the core losses are varied with the frequency and flux density of the machine [146]. Later in [147] and [148], the generalized and improved generalized Steinmetz equation was introduced to take the hysteresis effect into account. These methods were new but did not consider the effect of the variation of the Steinmetz coefficients with the frequency. Thus, the core loss estimation using these techniques is not accurate when the supply voltage includes a wide range of harmonics. A loss separation model based on the Steinmetz equation was introduced and improved in [149]–[153]. The results of the research on the iron loss separation modelling introduced a loss model with three major components summarized in (2-2). The iron losses consist of the hysteresis (P_h), eddy current (P_{ed}), and excess losses (P_{ex}) are calculated by the Steinmetz equations presented in (2-2).

$$\begin{cases} P_h = k_h f B^2 V \\ P_{ed} = k_{ed} f^2 B^2 V \\ P_{ex} = k_{ex} f^{1.5} B^{1.5} V \end{cases} \tag{2-2}$$

where k_h, k_{ed}, and k_{ex} are the Steinmetz constants of hysteresis, eddy current, and excess losses which depend on the lamination material used in the structure of the rotor and stator. f, B, and V are the operating frequency, flux density, and iron volume, respectively. According to the Steinmetz equations, core losses are increased by the increment of the frequency and flux density [108].

There are several paper discussing the dependency of the Steinmetz coefficients on the operating temperature of the electric machine [154]–[156]. According to the presented results in [154], electric machine core losses are reduced by temperature increase. It is logical because of the reduction of the iron electric conductivity by increment of the temperature and consequently reduction of the eddy current losses in the iron parts.

The loss separation approach offers an acceptable accuracy for prediction of iron loss although it ignores the effect of the history of flux density waveform. Ignoring the history of the flux density waveform means that the instantaneous flux density and its rate of variation are the only responsible factors in determining the core loss. In the inverter driven systems where the high order harmonics distort the flux density, a minor hysteresis loops need to be taken into account [157]. Disregarding the minor hysteresis loop is another source of the inaccuracy in loss separation technique. To address this issue in the loss separation models, Preisach [158] and Jiles/Atherton [159] models, which are called hysteresis models, were introduced. The hysteresis loss density in the Presiach model is obtained using the integration of the multiplication of flux intensity by the rate of variation of flux density over a period. These models were also improved in several research papers to enhance the accuracy of the iron loss prediction [160]–[162]. These models offer higher accuracy compared to the loss separation

model but require more computational and mathematical efforts which complicates the iron loss modelling.

Most of the commercial finite element software like Ansys Electromagnetics [144] and Motor-Cad [163] employ (2-1) to predict the core losses. To improve the accuracy of the core loss prediction, JMAG [164] uses a frequency separation approach in the post processing [165]. The frequency separation allows to investigate the minor loop hysteresis losses. This software uses time series data of magnetic flux density to consider the size of the hysteresis loops and predict the hysteresis losses [166].

The loss separation technique for estimation of the core losses is not limited to the FEA based software. Some analytical models which can estimate the flux density in the iron parts have employed (2-1) to predict the core loss [20], [167], [168]. The estimation of the flux density based on the sizing equation and magnetic equivalent circuit of the electrical machines also allows to find the core loss by (2-1) [22], [169], [170].

The no-load test of the induction motor and combination of the open circuit and short circuit tests in the synchronous motor are the common experimental ways of the measurement of core losses [94]. The core loss is usually modelled with a resistance in the electric equivalent circuit of the electric motors. So, authors estimate the core losses for a certain frequency and voltage level to find a proper value of the core resistance in the EEC and find the core loss by solving the circuit in different supply voltages and frequencies [171].

In the variable speed applications like EVs, electric motors are driven by inverters. The core loss value is changed by the variation of the carrier frequency because of the appearance of the high order harmonics in the output pulses of the power converter. According to the conducted study in [76], the core losses of an inverter driven PM motor can be increased by 45% compared to a sinusoidal supply voltage.

The dependency of the core losses on various factors complicates the accurate prediction of the core losses over a driving cycle [172]. The introduction of a loss function in [21] was a fast and fairly accurate approach to predict the electric machine core losses in the torque speed plane. Table 2.6 summarizes the core loss variation in IM, SPM, and IPM motors in different operating regions.

The dependency of the core loss on the frequency and supply voltage of the machine affects this value over a driving cycle. Fig. 2.8 illustrates the voltage map and core loss maps of a 50kW IPMSM and 45kW SPMSM. As expected in the field weakening region where the machine works in higher speeds and the voltage level is at its maximum level, the core losses are significant [120]. The comparison of the core loss maps of these machines shows that SPMSM has a much larger core losses at higher speeds. For this reason, the IPMSM is more popular in EV applications.

TABLE 2.6. THE DEPENDENCY OF THE MACHINE CORE LOSS ON THE TORQUE AND SPEED OF THE MACHINE RENDERING AN APPROXIMATION OF THE LOSS IN DIFFERENT OPERATING POINTS FOR EACH TYPE OF THE MACHINE [21], [72].

	Constant power region			Constant torque region		
T^2		IPM	IM, IPM			
T			IM	IM		
1		IPM, SPM	IM, IPM, SPM	IM, IPM, SPM		IPM
	1	ω	ω^2	1	ω	ω^2

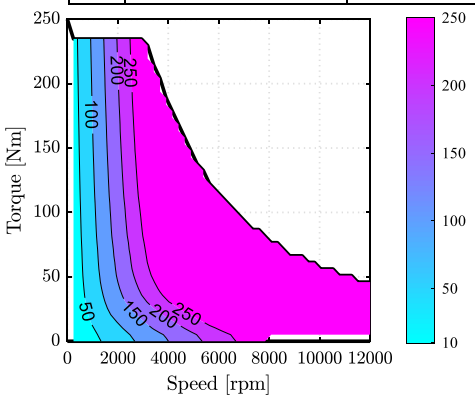

(a) voltage map in the torque speed plane for the IPMSM

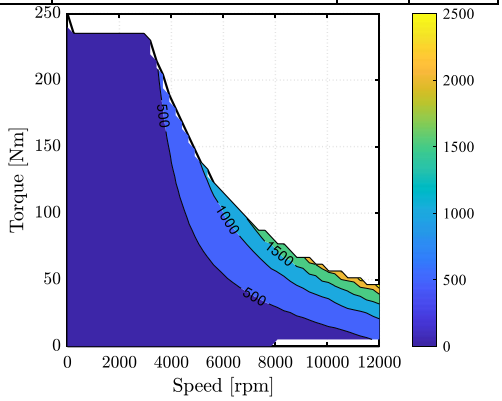

(b) core loss map in the torque speed plane for the IPMSM

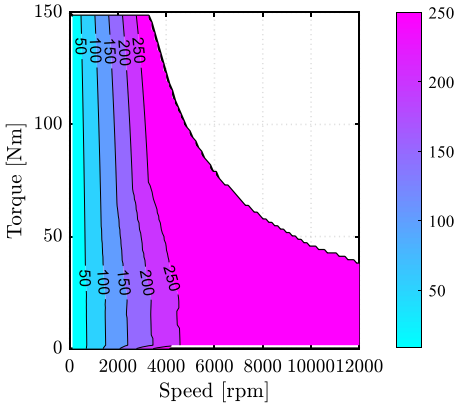

(c) voltage map in the torque speed plane for the SPMSM

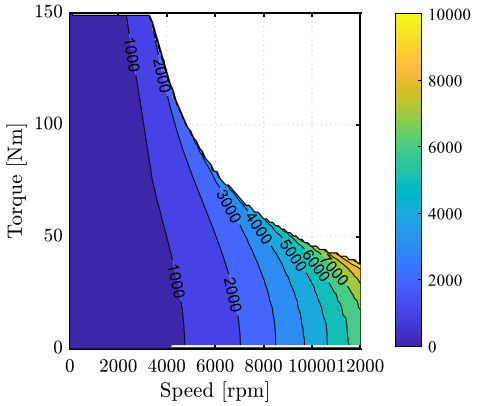

(d) core loss map in the torque speed plane for the SPMSM

Fig. 2.8. Voltage and core loss maps of a 50kW IPMSM and 45 kW SPMSM for operation over a wide torque speed range. These plots have been provided based on the collected data from [16], [72], [73].

2.3.3. Power converter loss

The power converters (electric drive system) losses are other sources of the electrical losses considered in the efficiency studies [126]. The switch losses are composed of the conductive loss ($P_{sw,rms}$), switching at turn on and off losses ($P_{sw,on}$ and $P_{sw,off}$), output capacitance loss ($P_{sw,oss}$), and gate loss ($P_{sw,gate}$). As shown in (2-3), the conductive loss depends on the rms current (I_{rms}) where the switch conducting resistance (R_{sw}) is assumed constant. The rising time, falling time, energy stored in the output capacitance, and gate charge of a switch shown by t_{on}, t_{off}, E_{oss}, and Q_g are constants. According to (2-4) to (2-7), the switching losses depend on the switching frequency (f_{sw}), DC-link voltage (V_{DC}), and I_{rms}.

$$P_{sw,rms} = R_{sw}.I_{rms}^2 \tag{2-3}$$

$$P_{sw,on} = 0.5.I_{rms}.V_{DC\_link}.t_{on}.f_{sw} \tag{2-4}$$

$$P_{sw,off} = 0.5.I_{rms}.V_{DC\_link}.t_{off}.f_{sw} \quad (2\text{-}5)$$

$$P_{sw,oss} = E_{oss}.f_{sw} \quad (2\text{-}6)$$

$$P_{sw,gate} = V_g.Q_g.f_{sw} \quad (2\text{-}7)$$

The voltage is at its maximum level in the constant power region (see Fig. 2.8(a)). Thus, $P_{sw,on}$, $P_{sw,off}$, $P_{sw,oss}$, and $P_{sw,gate}$ are increased by increment of the shaft speed [173]. The temperature of the switches in the power converter is another important factor which affects the converter switching loss. The conduction losses ($P_{sw,rms}$) are increased by the temperature rise due to higher value of the switch series resistance (R_{sw}) [174]. Literature shows that the influence of the temperature variation on the conduction losses is much smaller than the switching losses ($P_{sw,on}$ and $P_{sw,off}$) [175]. It was shown that under half of the rated current, the switching losses are increased up to 20% when the temperature varies from 25°C to 200°C [175]. The change at larger currents is bigger. The switching losses are increased from 60% to 140% of the rated switching losses when the temperature changes from 25°C to 200°C during the operation at rated current [175]. This significant variation of the losses necessitates a proper cooling system for safe operation of the power converters at various ambient temperatures.

Existing methods usually ignore the converter losses in estimation of the efficiency maps. However, literature shows that the semiconductor losses in the constant torque and field weakening regions can be approximately at least one-third of the total losses [135]. The results presented in [135] shows the semiconductor loss in the field weakening region is much larger than the conductive losses and at least half of the core losses. Fig. 2.9 [135] compares the value of the drive (converter) losses with the conductive and core losses in different driving cycles. It shows the converter losses are a large portion of the total losses and hence needs to be considered for an exact efficiency map.

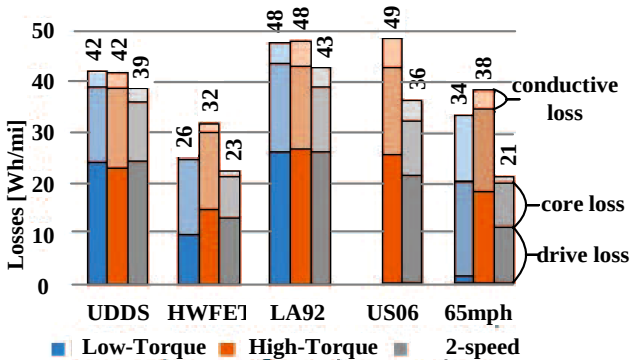

Fig. 2.9. The measured copper, core and drive (converter) losses per mile for three different machine/gearbox combinations in 4 drive cycles and constant-speed of 65 mph operation reported in [72], [135].

2.3.4. Permanent magnet loss

The conductivity of the PM materials allows eddy currents to flow within the magnet [176]. The induced current in the PMs is high when the magnet volume is large. Although in large electric

motors the segmented sintered rare-earth magnets are used to reduce the eddy-current, the PM loss can be still large. According to the results presented in [27], the PM eddy current loss increases by 50 times above 5000rpm. Fig. 2.10 visualizes the effect of the variation of the rotor speed on PM loss [177]. Thus, it is important to estimate the PM losses when the machine efficiency is reported over a wide speed range.

The time and frequency domain FEA are the widely used approaches for the calculation of PM losses. The PM loss calculation by 2D FEA is fairly accurate in radial flux machines [178]. The 3D FEA is necessary for calculation of the PM loss in axial-flux machines [179]. In some specific dimensions and topologies, the 2D FEA cannot predict the PM loss properly. In general, axial-flux machines necessitate 3D FEA if precision is required [180]. Fig. 2.10 shows the difference between the 2D and 3D FEA results for a 16-pole machine [177]. Although the machine is radial flux, there is a large difference between the 2D and 3D FEA results. In addition, when the segmented or skewed magnet structures are utilized in the rotor the 3D FEA is required to accurately find the PM losses as well as the machine performance [181], [182].

The FEA models are accurate but computationally expensive. Hence, authors have devoted time and energy to estimate the PM loss using the fast analytical models [183]. The available analytical models only considered the armature reaction [184] and slot effects [77] for calculation of the PM loss. In these models, the eddy current loss is the only investigated portion of the PM loss and the hysteresis PM loss is ignored [77]. It was shown that the hysteresis losses are approximately two times of the eddy current losses in PMs [185]. Therefore, consideration of the PM loss without investigation of hysteresis loss is not accurate. The loss mapping technique is a type of the analytical modelling to the PM losses [176], [177], [186]. It is fast, but limited to a given type of the magnet, shape of the rotor, and shape of the stator. For this reason, the PM loss mapping and the developed loss functions are limited to a specific machine and geometry.

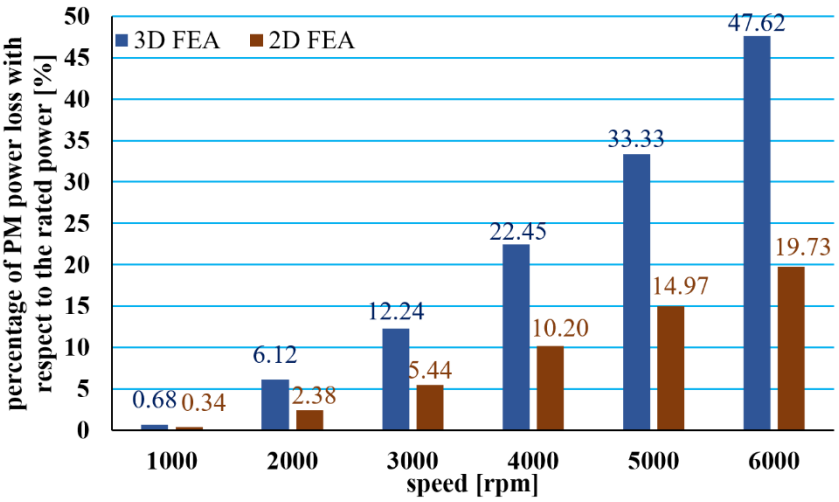

Fig. 2.10. Non-segmented PM power loss in different operating speeds and comparison of the accuracy of the 2D and 3D FEA results for a 14.7kW 4000rpm 16 pole machine. The data to plot this figure was collected from [72], [177].

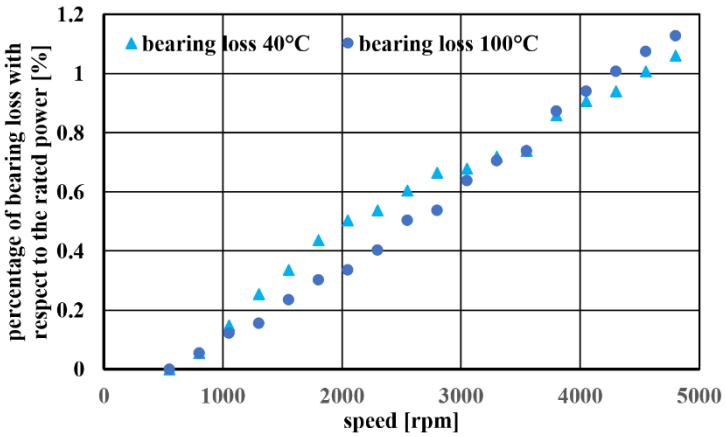

Fig. 2.11. The mechanical loss variation in a 14.9kW axial-flux PM motor against speed of two different temperatures. The data to plot this figure was collected from [72].

2.3.5. Mechanical Losses

In addition to the electrical and magnetic losses mentioned in previous sections, the mechanical losses including windage [187], friction [80] (mechanical losses [108]), and stray losses [119] are other sources of the power dissipation in the efficiency studies of the electrical machines. The friction and windage losses value depends on the mechanical speed, shaft radius, shaft length, and the environment in which machine works in [187]. According to the Mack's equation shown in (2-8), the mechanical loss which is the summation of the friction and windage losses is related to the cube of the operating speed. In (2-8), the first terms represent the windage loss whereas the second term shows the friction loss.

$$P_{mech} = \pi C_f \rho \Omega^3 r_{rot}^4 L + C_f \Omega \tau_{load} \quad (2\text{-}8)$$

In this equation, ρ and C_f are the fluid density around the rotor and friction coefficient, respectively. The rotor speed and its radius are shown by Ω and r_{rot} where L is the rotor axial length. The load torque is shown by τ_{load} in this equation. According to the reported findings in [108], the mechanical and stray losses have a direct relationship with the speed of the machine and the output power. The mechanical losses consideration in most of the analytical calculations are ignored because they include a small portion of the total losses. Moreover, the modelling of temperature effect on the efficiency of bearings is not easy and hence often ignored. In [188], the effect of the speed and temperature on the variation of the mechanical losses was studied. According to Fig. 2.11, the effect of the speed is dominant compared to the temperature effect. This figure shows the maximum value of 200W mechanical loss for a 14.9kW axial-flux PM motor. If the maximum efficiency of this machine is 90% [188], the mechanical loss is about 12% of the total losses at high speeds which is not a negligible value in the efficiency calculation.

2.3.6. Transmission system (mechanical drivetrain) losses

Efficiency maps are widely studied in electrical machine design for EVs where the motor must operate in different speeds. Therefore, the analysis of the transmission system losses in different torques and speeds are important to precisely estimate the efficiency maps of an EV.

The in-wheel and in-body are two types of transmission systems used in EVs. Single-stage transmission, multi-stage transmission, and continuously variable transmission (CVT) are the widely used mechanical systems in the drivetrain of EVs [6]. The availability of these transmissions systems is necessary to distribute and deliver the generated power to the wheels of an EV with the in-body drivetrain. Although the transmission can be removed from the in-wheel drivetrain, literature has suggested the utilization of a reduction gear in this system [189] because of the higher efficiency of the electric machines during operation at the field weakening region (e.g. see the efficiency maps in Figs. 2.2 and 2.3).

Gearbox, propeller shaft, differential, and drive shaft are the main components of the single and multi-speed transmission systems. The comparison of the single-speed and two-speed transmission systems, shown in Fig. 2.1, demonstrates that they differ in the number of gears. Although increment of the number of gears leads to the increase of the mechanical losses in transmission system, the overall efficiency of the machine in the presence of multi-speed transmission system is higher [44]. This improvement of the efficiency resulted from the operation of the electric machine in the field weakening region where its efficiency is higher. CVT is the most widely used transmission system in commercialized EVs like Honda, Nissan, and Toyota. The efficiency of the CVT is significantly higher than the other types of the transmission system. Moreover, it offers a continuous torque where its counterpart (multi-speed transmission system) suffers from torque interruptions during the operation [6].

2.3.6.1. Loss and efficiency in the single and multi-speed transmission systems

The gear mesh and bearing efficiency are two main factors in determination of the gearbox efficiency [190]. If N_{bg} and N_{gmg} are the number of the bearings and gear meshes respectively, the efficiency of the gear box is obtained by (2-9); where the bearing and gear mesh efficiency are shown by η_{bg} and η_{gmg}, respectively [191].

$$\eta_{gbox} = \eta_{bg}^{N_{bg}} \times \eta_{gmg}^{N_{gmg}} \tag{2-9}$$

The torque is transmitted from the gearbox to the axle through the propeller shaft [192], [193]. The propeller shaft efficiency depends on the number of bearings (N_{bp}) and universal joints (N_{up}) and their efficiency. The total efficiency of the propeller shaft is calculated by (2-10) where $\eta_{bp}$and η_{up} are the bearing and universal joints efficiencies in the structure of the propeller, respectively.

$$\eta_{psh} = \eta_{bp}^{N_{bp}} \times \eta_{up}^{N_{up}} \quad (2\text{-}10)$$

The differential splits the torque to be applied to the right and left wheels. So, it is considered as the last gear reduction part of the in-body transmission system [194]. The efficiency of the differential, shown in (2-11), depends on its gear mesh efficiency (η_{gmd}) and bearing efficiency (η_{bd}). In (2-11), N_{bd} is the number of differential bearings.

$$\eta_{diff} = \eta_{bd}^{N_{bd}} \times \eta_{gmd} \quad (2\text{-}11)$$

The driveshaft is the last part of the transmission system which delivers the differential torque to each wheel. A constant velocity joint is located at each end of the driveshafts to compensate the relative motion between the differential and wheel [195], [196]. The efficiency of the drive shaft, which is dependent on the constant velocity joints (i.e., tripod and Rzeppa), is obtained by (2-12).

$$\eta_{dsh} = \eta_{Tripod} \times \eta_{Rzeppa} \quad (2\text{-}12)$$

Considering the efficiency of each part of a mechanical drivetrain system for an in-body transmission system, the total efficiency is obtained by (2-13).

$$\eta_{drivetrain} = \eta_{gbox} \times \eta_{psh} \times \eta_{diff} \times \eta_{dsh} \quad (2\text{-}13)$$

Note that the obtained efficiencies for each part are not constant in practice and they highly depend on the temperature of these parts and the operating speed [197]. For instance, the bearings efficiency of each part is at its lowest value at low temperatures (high viscosity of oil) and the highest operating speed. Also, the universal joint and driveshaft efficiencies are changed by the offset (angle) between their ends. The offset for the universal joint is the angle between the front and rear angles, whereas the offset for the driveshaft is the angle between the differential and wheels. Literature shows the significance of the speed in determination of the transmission system efficiency [198] in comparison to the role of other factors. It has been shown that the maximum efficiency of transmission systems is not higher than 95% [44], [198]. Thus, this portion of the loss must not be ignored when the total efficiency of an EV is studied.

In multi-speed transmissions, the friction, viscous, and clutch losses during changing from single to two or more is about 4% to 5% [199]. The losses per gear is 2% to 3% [199]. According to the comparative study results presented in [199], the efficiency of single, two, and three -speed transmission systems are 93%, 86%, and 83%, respectively.

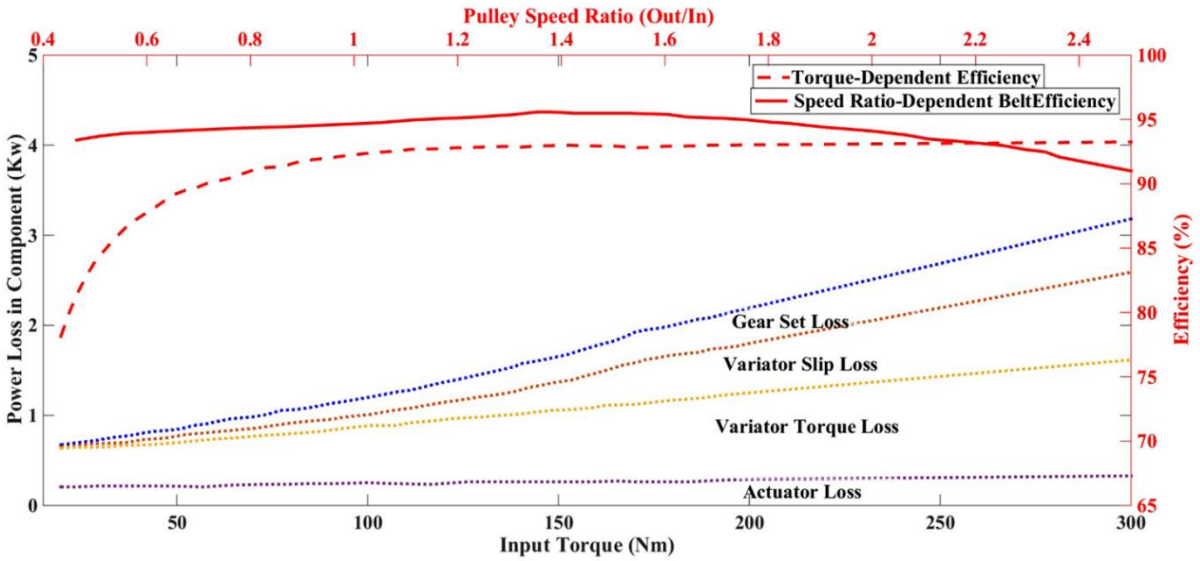

Fig. 2.12. The variation of the losses and efficiency in CVT [72], [199].

2.3.6.2. Losses and efficiency in CVT

The drive and driven pulleys are the main components of a CVT which are connected to each other through a metal belt [200]. As shown in Fig. 2.1, the CVT delivers power to the wheels through a reduction gear [6]. Literature shows the CVT efficiency depends on the torque and speed ratio. Fig. 2.12 shows how the different portion of losses in the CVT vary during various loadings. This figure demonstrates the low efficiency of the CVT at small torques (i.e., 79%). Also, it is seen that the CVT efficiency is reduced by increment of the speed ratio. A simple comparison between the efficiency of the multistage transmission system and the CVT shows their maximum efficiency is not larger than 95% in various torque-speed operating points [199].

2.3.6.3. Loss and efficiency for in-wheel transmission system

A reducer is used in the topology of the in-wheel EVs to utilize the electric machine in its field weakening region where it offers a high efficiency. The topology of the integration of the reducer with an in-wheel electric machine is explained in [189]. The input shaft of the reducer is connected to the shaft of electric machine and its output shaft delivers power to the wheel. According to the EffM of the reducers presented in [189], the efficiency of the reducer is larger than 95% which is higher than efficiency of the multi-speed transmission system and CVTs used in in-body drivetrains. Hence, the utilization of in-wheel drivetrain in the EVs have found popularity among researchers and industries [201].

2.4. Discussion on the Loss Analysis

Literature show that the efficiency map and loss map of a certain electric machines can be scaled up and down for different power ratings [98], [101]. Therefore, it is possible to estimate the losses over a driving cycle based on the scaling laws for different power ratings of the machines [101], [202]. According to Equations (3) to (12) in [101], the core, ohmic, and PM losses of a PMSM have a

direct relationship by variation of the machine stack length and diameter. Copper loss is proportional to the change of radial and axial directions. The core loss is proportional to the axial direction and square of the radial direction changes. The PM loss has a relationship with the fourth and third power of the radial and axial direction changes, respectively. Therefore, the losses in the PM machines can be estimated based on the variation of the dimensions of the machine for different power ratings when the rating torque/power of the machine is proportional to the axial direction and square of the radial direction changes. Based on the scaling, if the axial and radial dimensions of a machine become two times of a benchmark machine, the core, ohmic, and PM losses will be 6, 2, and 128 times larger than the losses of the losses of the benchmark machines. The scaling law for the IM is also discussed in [202] which determines the relationship of the ohmic and core losses with the variation of the machine geometry.

The variation and characteristics of each portion of the loss in an electric vehicle has been discussed in Section 2.2. The IM and PM machines are the most popular machines in EVs. Table 2.7 summarizes the percentage of each type of loss for these two machines in the constant torque and field weakening regions. It must be highlighted that the reported values are not absolute and have been determined based on the available data in the collected references. The size of the wire and number of strands can change the ohmic losses in a specific design [203]. The type and thickness of the laminated materials can change the core losses [204]. The type of the magnet and their number of segments vary the PM losses [181]. The type of the switches, converter, and control system can lead to change of the converter loss [124], [205]. Mechanical losses can be changed by the type of the bearings.

Due to the availability of the rotor bars in IMs, the ohmic loss range of variation in IMs is larger than the PM machines. The winding current which determines the ohmic losses is increased by increment of the torque. So, the minimum and maximum ohmic losses tabulated in Table 2.7 is the percentage of the ohmic loss in lower and higher torques, respectively. Because of the current constraints of the electric machines, the maximum current cannot generally be used in the field weakening region. Hence, the maximum value of the ohmic loss in the constant power region is generally less than the constant torque region [98], [121].

As explained in Section 2.2, core loss is a function of the voltage and frequency. For this reason, it is seen that the percentage of the core loss in the field weakening region is much larger than the core loss of the constant torque region for IPMSMs. Note that the SPM core loss is larger than the IPMSMs and its higher band can be increased to 18% of the maximum power at higher speeds [16], [99]. The maximum value of the core losses in the IMs in both of constant torque and field weakening is similar. The larger frequency of operation in the field weakening region increases the minimum core losses of IMs compared to the constant torque region.

PM losses are increased by increment of the speed because of the increase of the induced eddy current in PMs. In the SPM machines, the PM is closer to the windings which leads to the increment of the eddy currents on their surface. For this reason, in the field weakening region, the PM losses can be increased to 6% or even higher for SPMSMs [21].

The lower power factor of IMs compared to the PM motors leads to the increment of the converter losses in both constant torque and constant speed regions. The large DC-link voltage at the field weakening region increases the switching losses [124], [206].

Mechanical and transmission system losses are the other portion of losses in EVs which highly depend on the operating speed. As it is tabulated in Table 2.7, their values in the constant power region are much larger than those of value in constant power region [188], [189].

TABLE 2.7. RANGE OF THE VARIATION EACH TYPE OF LOSS AS A PERCENTAGE OF THE MAXIMUM POWER OF THE MACHINE IN THE CONSTANT TORQUE AND CONSTANT POWER REGIONS FOR IMS AND IPMSMS [72].

Operating Regions	Machine Type	Ohmic Loss	Core Loss	PM Loss	Converter Loss	Mechanical Loss	Transmission System Loss
Constant torque	PM	$0.1\% - 13\%$	$0.01\% - 1.5\%$	$0.001\% - 0.5\%$	$0.01\% - 6\%$	$0.1\% - 1\%$	$5\% - 6\%$
	IM	$0.1\% - 15\%$	$0.01\% - 2.5\%$	0	$0.01\% - 7\%$	$0.1\% - 1\%$	$5\% - 6\%$
Constant power	PM	$0.1\% - 5\%$	$1\% - 15\%$	$0.001\% - 1\%$	$1\% - 12\%$	$0.5\% - 3\%$	$4\% - 15\%$
	IM	$0.1\% - 10\%$	$1\% - 2.5\%$	0	$1.5\% - 15\%$	$0.5\% - 3\%$	$4\% - 15\%$

2.5. Experimental Setup for Loss Measurement

The experimental calculation of the losses is carried out based on the efficiency extraction IEEE and IEC standards (i.e. IEEE 1812, IEC60034-2-1-2A, IEEE 112, and IEC 60034-2-1-1B [136]). The flowchart of the calculation of the motor efficiency based on these methods are shown in Fig. 2.13. In these methods, the speed and load are changed such that the machine meets its rated temperature.

Considering the standard methods for calculation of the electric machine efficiency, an experimental setup measuring the input and output power of the machine is required to find the machine losses by subtraction of the input power and output power. The efficiency and losses of each part of an EV drive system is found by proper placement of measuring devices in the system. Fig. 2.14 shows the entire drive-train system of an EV along with the monitoring/measuring devices which are required for experimental loss separation of the different parts.

2.5.1. Measurement of converter loss

As shown in Fig. 2.14, the converter losses are found by measuring the input power and output power of the converter using two power analyzers (the difference between the input power and output power results in the loss in the power converter).

2.5.2. Electric machine loss

Although the total machine loss is obtained by subtraction of the input and output power of the machine, the calculation of the split losses consisting of conductive, core, PM, and mechanical losses needs more details to be considered [64].

2.5.2.1. Separation of ohmic losses

In induction machines, ohmic losses result from the stator windings and rotor bars. A simple way for calculation of the ohmic losses is excitation of the windings at rated current in the locked rotor condition [65]. The stator and rotor resistances are obtained by conducting this test. However, this method is not accurate for an inverter driven IM because the skin effect and harmonics are ignored if the measurement is done at a single operating point. Hence, it is suggested to supply the machine in different current levels and frequencies at the locked rotor condition and measure the consumed active power which gives two variable resistances for both of stator windings and rotor bars.

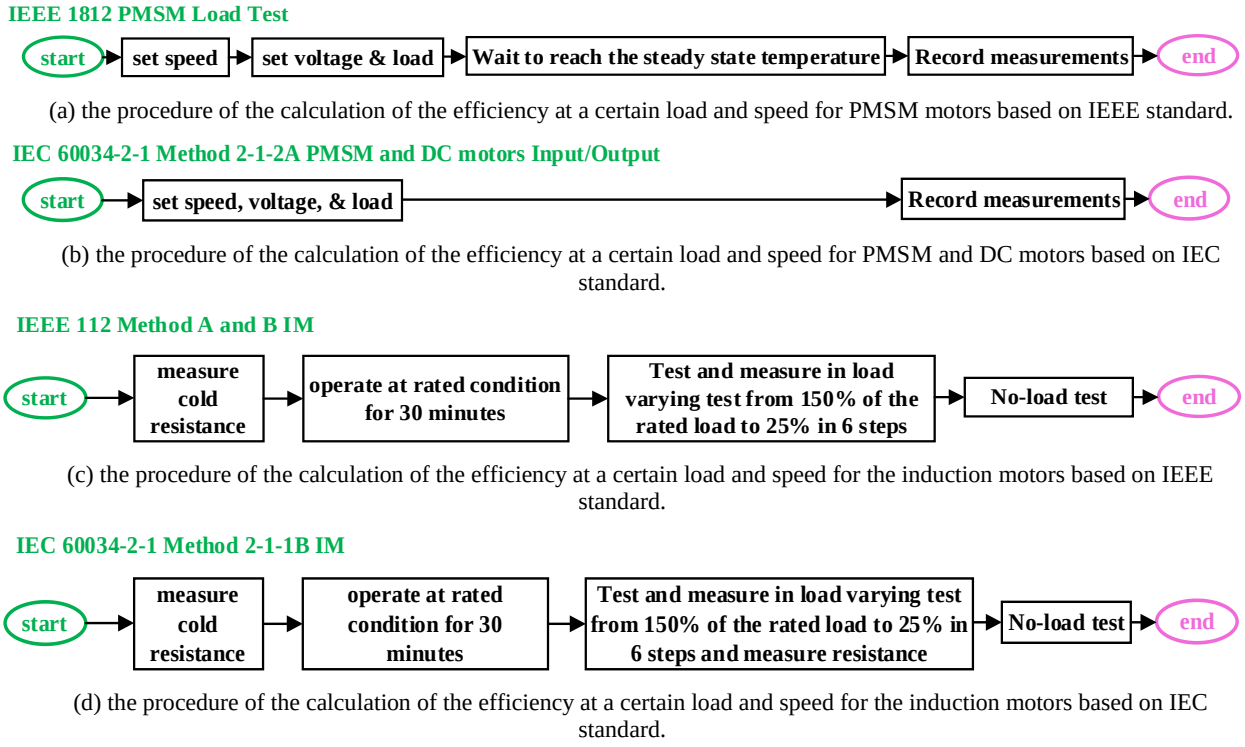

(a) the procedure of the calculation of the efficiency at a certain load and speed for PMSM motors based on IEEE standard.

(b) the procedure of the calculation of the efficiency at a certain load and speed for PMSM and DC motors based on IEC standard.

(c) the procedure of the calculation of the efficiency at a certain load and speed for the induction motors based on IEEE standard.

(d) the procedure of the calculation of the efficiency at a certain load and speed for the induction motors based on IEC standard.

Fig. 2.13. The conventional methods for the extraction of the motor's efficiency experimentally based on IEEE and IEC standards [72].

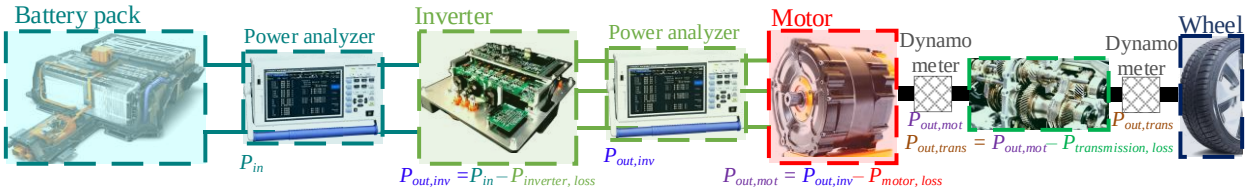

Fig. 2.14. The placement of power analysers and dynamometers to measure each loss component of the EV propulsion system [72].

The temperature rises of the machine windings, which lead to the increment of the resistance, should be considered. The temperature effect is considered by applying the DC test when the winding resistance is cold and when it is at the rated operating temperature. This variation of the measured resistance is considered as a coefficient to update the resistances from the previous test (locked rotor). Having a variable stator and rotor resistance based on the frequencies allows to find the ohmic loss based on the EEC in different loadings. The rotor loss of the induction machine is proportional to the motor slip. In the next paragraphs, it will be explained that the core losses can be extracted independently from the slip. Therefore, the conductive rotor loss of induction motor is found by (2-14) when the stator resistance (R_s), core loss (P_{Fe}), winding current (I_{ph}), and slip (s) are measured experimentally [207].

$$P_{rotor,IM} = (input\ power - R_s I_{ph}^2 - P_{Fe})s \quad (2\text{-}14)$$

The resistance of the synchronous motors at different operating frequencies is found through a similar procedure. As the synchronous machines have no rotor bars, their rotor can be locked or even removed from the stator to extract the winding losses and estimate DC resistance. The AC resistance can be obtained if the stator is supplied by an inverter which includes all the harmonics at a certain fundamental frequency.

2.5.2.2. Core loss

If the no-load input active power of the induction machine is subtracted by its no-load winding loss, the result is the summation of the core and mechanical losses. The standard tests for inverter driven machines segregate the core losses into two portions to investigate the harmonic effect separately [208], [209]. The difference of the obtained core loss from the inverter driven machine with the extracted core loss when a pure sinusoidal supply is applied to the winding is determined as the core loss resulting from the harmonics.

The mechanical loss varies by speed. The core loss is a function of the voltage amplitude and frequency. If the IM is run at a constant speed with different voltage levels, the extrapolated interception points of the summation of core loss and mechanical loss (the measured input power of an electric machine at the no-load condition) plot versus voltage squared represents the mechanical loss. In other words, when the voltage is zero the machine loss just includes the mechanical loss of the machine at that speed. Note that at least a small voltage should be applied to the induction motor winding to reach the no-load speed. So, the experimental measurement of the mechanical loss when voltage is zero seems to be impossible. However, the machine at small supply voltage operates on the linear section of the B-H curve of the iron characteristic. Thus, to find the interception point with the y-axis (i.e., summation of the core and mechanical losses) it is logical to assume that the curve is linear and estimate the mechanical loss. It is more accurate to consider V^2 instead of a linear curve to find the interception point because the core loss is the function of voltage square.

Applying the no-load test for determination of the core loss of the synchronous machines using a similar approach to the IM machine is a way to find the core and mechanical losses at different operating speeds and voltage levels. It has been proven that the core losses can be found using an open circuit test for synchronous PM machines. To apply the open circuit test, a prime mover rotates the shaft at a constant speed and the input mechanical power is recorded at each speed [210]. As the copper loss is zero, the measured mechanical power is equal to the summation of the core and mechanical losses of the synchronous PM machine.

2.5.2.3. PM losses for permanent magnet motors

The PM losses are another portion of the loss in the PM machines. There is an indirect technique for measurement of the PM losses. When the core loss, mechanical loss, and ohmic losses of a machine are extracted, the PM loss is found by subtraction of the total input power at loading condition with the summation of total output power and measured losses. To achieve a more accurate value for the PM losses through the indirect measurement technique, the ohmic losses of the stator should be collected when the rotor is removed from the stator. The indirect method is not accurate because some portion of the stray losses may be added to the PM loss. The amplitude and frequency of the induced eddy current on the PMs affects the PM temperature. In [211], the temperature of the PM parts was measured and (2-15) was used to find the PM losses.

$$P_{PM} = \rho \times c \times N_{PM} \times V_{PM} \times (\frac{\Delta\theta}{\Delta t}) \quad (2\text{-}15)$$

In this equation, ρ and c are the specific mass density and heat capacity of the PMs. Number of PM elements and volume of a single PM part are shown by $N_{PM}$and V_{PM}. The rate of the variation of the temperature shown by $\frac{\Delta\theta}{\Delta t}$ which can be taken directly from the measured temperature curve.

2.5.2.4. Transmission system losses

The transmission system losses are the last portion of the loss in the propulsion system of an EV. As shown in Fig. 2.14, this portion is obtained by subtraction of the mechanical input power to the transmission system and its mechanical output power.

The EffM of electric machines is accurate if it is plotted with a sufficiently large number of points, e.g. 300 to 1600 points [212], [213]. On the other hand, the efficiency map calculation requires a sweep between different pairs of *d*- and *q*- axes currents to find the minimum loss point for each set of torque and speed values. Thus, the loss separation over a driving cycle would be a time-consuming process because an accurate loss map for each portion of the loss is obtained when at least the above-mentioned details are considered for 300 operating points over a driving cycle.

2.6. Research Gap

2.6.1. Technology of electric machines

As discussed, the electric motor cost, weight, reliability, mechanical strength, and robustness of the electric motors are of great importance in selection of electric machine type for EVs. However, these variables are by no means the only required properties of the EV electric motor. The other aspects of the electric machines which has not been studied enough in the literature are listed below:

- Overload capability improvement beyond 2 per unit has not been addressed in the current literature. This is important for electric vehicles where it provides a significant opportunity to reduce the size/weight of electric machines in electric cars/trucks while still meeting the desired driving cycle capability.
- The capability of the brake system for available electric motors used in the in-wheel application is affected. It is useful to direct the researchers to address this issue for the in-wheel systems.
- Literature shows the axial-flux designs offer higher power density than the radial-flux machines. Despite existing commercial axial-flux motors for EV applications, the manufacturing aspect of such motors are not fully addressed in the literature. In fact, cost-effective fabrication of the axial-flux line-start motor requires innovative manufacturing techniques yet to be discussed.
- The commercial EVs employ a mechanical transmission system between the motor and wheels. The transmission system is required to handle the starting of the EVs. Introduction of the hybrid electric machines may help to remove the need of the mechanical transmission system. For instance, a switched reluctance motor can be used as the starter and accelerator of the machine where the IPMSM part of the hybrid electric machine is used for operation at higher speeds. Also, it can be a cost-efficient option because of the removal of the mechanical transmission system.
- Most of the electric machines introduced for EVs use a cooling system in their structure. Sometimes, in the LEVs like scooters, electric bikes, and electric motorcycles, the space limit does not allow to add an appropriate cooling system on the motor. For this reason, most of the current LEVs benefit from the expensive high-power density PMBLDC and PMSM machines. As a result of the high cost of PM material, a gap in the development and use of magnet-less motors for LEVs exist.

2.6.2. Transmission system of EVs

Literature show the CVT is the most efficient type of transmission system of the current EVs. However, CVTs are vulnerable to heat and require an additional cooling system. Moreover, the volume of the CVTs is larger than the two-speed transmission system. So, although the efficiency of

the CVTs is higher, they have a lower power density compared to the two-speed transmission systems. Thus, future research may focus on the introduction of new transmission systems or improved version of CVTs reducing the losses as well as increasing the power density.

2.6.1. Loss investigation

In addition to the electric machine losses, the power converter and transmission system losses have a significant value as a part of a propulsion system of an EV. Therefore, all types of the losses must be modeled with an acceptable accuracy for design of optimal electric machines for EVs. The review shows that many studies have been conducted on the estimation of the copper and core losses in electric machines. However, the power converter losses, PM losses, and transmission losses which can significantly change during operation at high speeds on a wide torque-speed range have not been studied sufficiently.

Most of the proposed analytical models for the copper and core losses ignore the effect of the higher order harmonics that the power converters injected to the windings. So, the improvement of the accuracy of the losses based for the inverter driven machines in a wide torque speed range is an important topic of study. The optimal machine design can consider the inverter model to improve the efficiency. The switching modes of the inverters can be optimized to maximize the efficiency over a driving cycle.

Most of the analytical design methods of the electric machines ignore the converter losses which play an important role especially at higher speeds. Therefore, accurate modelling of the converter losses can be a prominent topic of the study. Adding an additional term to the loss function, proposed in [21], can be considered as a possible way for estimation of converter losses.

Literature has covered the role of cross-saturation to improve the calculation of the efficiency maps for synchronous machines [15]. The cross-saturation effect on the loss of the induction machine is small but can be studied to improve the calculated efficiency.

Temperature has a significant role on the amount of each loss component. As discussed in [77], the need for a multi-physics simulation environment and other computationally expensive numerical methods are the main challenges of the consideration of the temperature effect in analytically calculated EffMs. The investigation of the loss variation with the temperature and the accurate thermal analytical models are other significant subjects for future works.

Most of the conducted studies overlook the effect of the high order harmonics of the induced current on the PM parts, temperature effect, and variation of the physical characteristics of the PMs in different temperatures. The utilization of the multi-physics finite-element software to model the electromagnetic behavior of the PM machines along with the thermal and structural variations (i.e., any change in the shape of PMs and air barriers) at different speeds is useful to improve the accuracy of the PM loss modelling. The need of the computationally expensive 3D FEA simulation for the

accurate estimation of the PM losses restricts the researchers in studying PM losses in the torque-speed envelope of the electric machines. Introduction of a fast combined analytical-FEA method or an accurate loss function is helpful to model PM loss in a wide torque speed range.

The artificial intelligence modelling and machine learning approaches have recently found popularity because of their ability in prediction and estimation of the physical characteristics of a system based on the real datasets. Some literature have used large datasets to predict losses and efficiency maps of electric machines [107], [141]. The required dataset for these models is huge which can cause difficulties in the provision of the dataset. Moreover, the application of these models is limited to the type of the motor with a specific shape of the magnet, slots, and barriers. These models can be mixed with the analytical models to reduce the amount of the required data. Combination of the loss function and computational intelligence models is another useful approach to develop a precise computational method for loss estimation of the electric machines with different sizes in a wide torque-speed range.

2.7. Conclusion

This chapter reviewed various electric machines and possible transmission systems for the propulsion system of electric vehicles. The advantages and disadvantages of each type of electric machine considering cost and performance were discussed. A brief history along with the characteristics of the electric machines used in EVs and LEVs was reported to show how their performance differs over a driving cycle. The role of the transmission system in the efficiency of EVs was explained. The characteristics of each type of transmission system and their performance and efficiency in the drivetrains of the EVs were explained.

It was explained that the design of electric machines to achieve the maximum efficiency requires an accurate prediction of the losses. To design the machine for optimal operation over a driving cycle, the loss prediction is more challenging because of the dependency of the losses on different operating points and supply factors.

The dependency of each loss component on the efficiency of the electric machines at different operating regions was reviewed. The machine loss measurement and calculation methods were explained. The difference between the loss variation in different electric machines were described to show the weakness and strength of different electric machines for operation over a wide torque-speed range.

In addition to the electric machines, power converters play an important role in the drivetrain system of electric vehicles. Hence, the role of the converter losses and their significance in the total efficiency of the propulsion system of EVs was discussed. It was explained that the converter losses become more significant when the electric machine operates at higher speeds.

Based on the conducted literature review, the design of an optimal propulsion system for EVs needs many considerations. On one hand, the electric machines offer a high efficiency when they operate in higher speeds (field weakening region). On the other hand, the efficiency of the power converters and transmission systems are reduced by increment of the speed. Thus, it is necessary to investigate the performance of all sections of an EV propulsion system during the design process.

The research gaps based on the conducted literature review were highlighted and the possible future research subjects in the electric machine designs, transmission system improvement, and loss analysis of electric machines were introduced.

Chapter 3. Efficiency maps

3.1. Chapter Overview

This chapter aims to describe different calculation techniques and experimental procedure based on the literature. The electric machines' operating regions and the current and voltage limit concepts are briefly explained. The maximum torque per ampere (MTPA), maximum torque per voltage (MTPV), and the field weakening control are described. Then, the detailed procedure for extraction of EffM of AC EMs is explained. The accuracy versus calculation effort trade-off for different methods is discussed. Finally, the EffM of a sample 2.2kW motor is extracted experimentally to demonstrate the agreement of the experimental results with the calculations.

3.2. EM operating regions

3.2.1. Voltage and current limits

The operating points of the inverter driven EMs are restricted with the voltage and current limits. The voltage limit is determined by the maximum of the DC-link voltage of the inverters. The current limit is restricted to the maximum permitted temperature of the windings. The available winding insulations are divided into for different category of class A, B, F, and H. The maximum permitted temperature for class A, B, F, and H are respectively 105°C, 130°C, 155°C, and 180°C.

The current limit and voltage limits of the induction and permanent magnet synchronous machine are presented in Figs. 3.1a and 3.1b, respectively. Electrical equivalent circuits (EEC) of the synchronous and induction machine in *d-q* axes are presented in Fig. 3.2. The *d-q* axes voltage and flux equations are considered to predict the machine performance in each operating region.

The current limitation of both the induction and synchronous machine is a circle with the radius of the rated current in *d-q* stator current frame ($I_d^2 + I_q^2 \leq I_s^2$). The voltage limit (i.e., $v_d^2 + v_q^2 \leq {V_s}^2$) must be met in each frequency and current. Considering the phasor diagrams of the PMSM and IM presented in Fig. 3.3, the *dq*-axes voltages are found by (3-1) It must be highlighted that the voltage limit ovals are calculated based on their voltage equations when the stator resistance is ignored.

$$\begin{array}{cc} \text{Synchronous machine} & \text{Induction machine} \\ \begin{cases} v_d = R_s i_d + \dfrac{d\lambda_d}{dt} - \omega\lambda_q \\ v_q = R_s i_q + \dfrac{d\lambda_q}{dt} + \omega\lambda_d \end{cases} & \begin{cases} v_d = R_s i_d + \dfrac{d\lambda_d}{dt} - (\omega - \omega_r)\lambda_q \\ v_q = R_s i_q + \dfrac{d\lambda_q}{dt} + (\omega - \omega_r)\lambda_d \end{cases} \end{array} \quad (3\text{-}1)$$

Where R_s is the stator resistance. ω and ω_r show the synchronous speed and rotor electrical speed, respectively. λ_d and λ_q are the *d-q* axis fluxes and for the synchronous and induction machine can be calculated by the presented equation in (3-2); where φ_m, L_d, L_q are magnet flux, *d*-axis inductance, and *q*-axis inductance of the synchronous machines. Note that φ_m is zero in the *d*-axis equation of the synchronous reluctance machines. Magnetizing inductance, stator leakage inductance, and the rotor

leakage inductance transferred to the stator side of the induction machine has been shown by $L_m, L_s,$ and L_{lr}, respectively.

Synchronous machine Induction machine

$$\begin{cases}\lambda_d = \varphi_m + L_d i_d \\ \lambda_q = L_q i_q\end{cases} \quad \begin{cases}\lambda_d = L_s i_d \\ \lambda_q = \sigma L_s i_q\end{cases}, where\ \sigma = 1 - \frac{L_m^2}{L_s L_r}, L_s = L_{ls} + L_m, L_r = L_{lr} + L_m \quad (3\text{-}2)$$

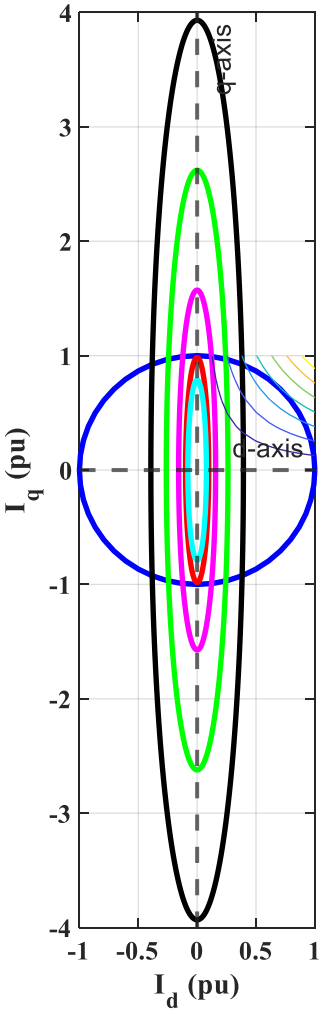

Circle: current limit
Oval: voltage constraint
Black oval: rated speed
Green oval: 2 pu speed
Pink oval: 3 pu speed
Red oval: 5 pu speed
Cyan oval: 6 pu speed

(a) the voltage and current constraints of and induction machine

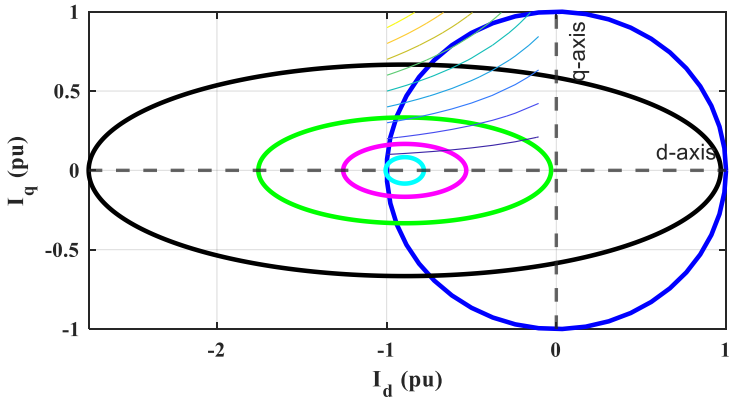

(b) the voltage and current constraints of an interior permanent magnet synchronous machine; blue circle: current limit. Ovals: voltage limits in different speeds.

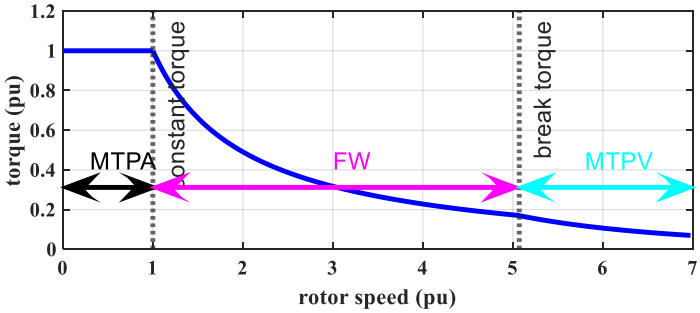

(c) torque vs. speed curve

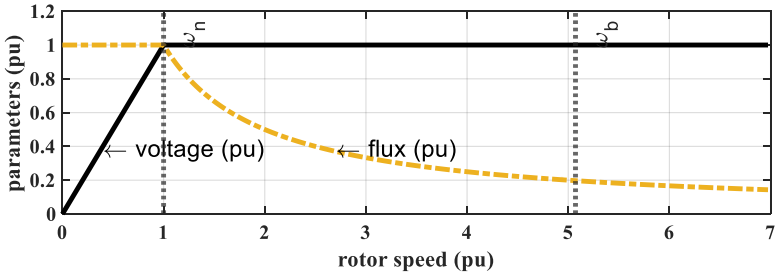

(d) voltage and flux variation in different operating regions.

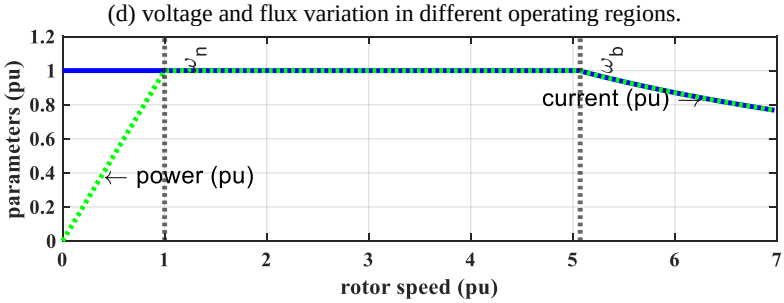

(e) current and power variations in different operating regions.

Fig. 3.1. The different operating regions of the AC electric machines.

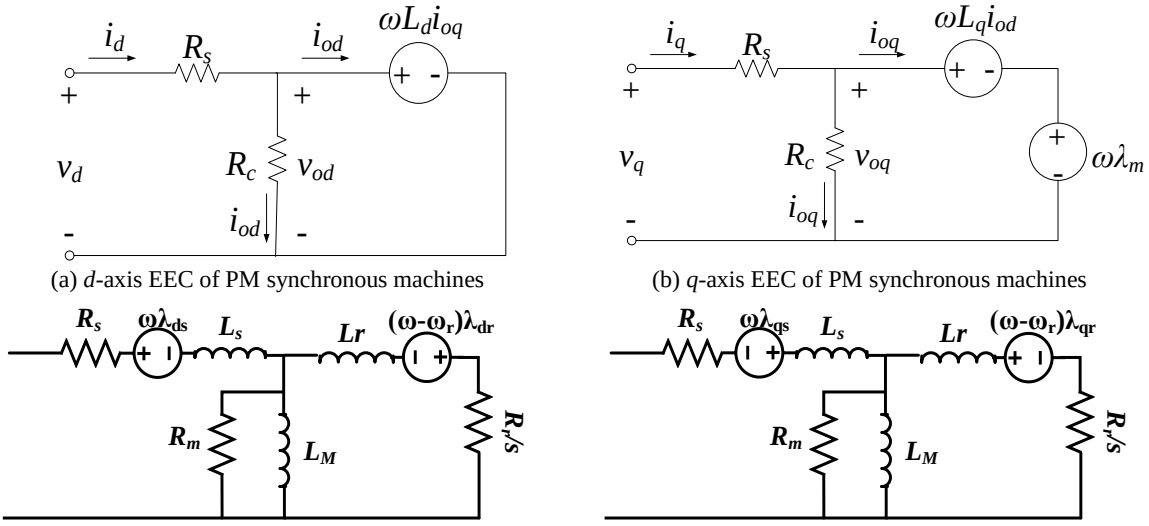

(a) *d*-axis EEC of PM synchronous machines

(b) *q*-axis EEC of PM synchronous machines

(c) *d*-axis EEC of induction machine

(d) *q*-axis EEC of induction machine

Fig. 3.2. the equivalent circuits of the synchronous and induction machines.

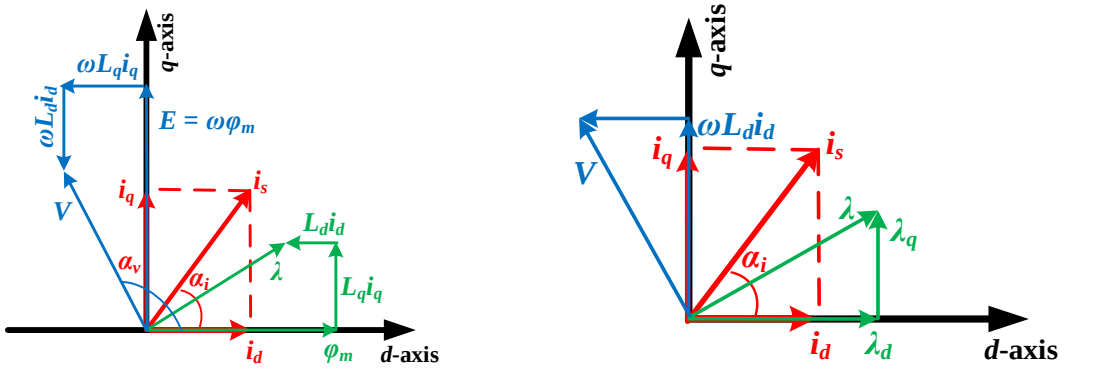

(a) the phasor diagram of the PM synchronous machines in absence of the stator resistance.

(b) the phasor diagram of the induction motor in absence of the stator resistance.

Fig. 3.3. The PM synchronous machine and induction machine phasor diagrams without consideration of the voltage drop of the stator resistance.

3.2.2. Operating regions

The constant torque and constant power regions are two well-known operating regions of the EMs. Fig. 3.1c shows the torque speed characteristics of a sample IM. The constant torque region includes the first portion of this curve (below 1pu speed where the torque is constant). As shown in Figs. 3.1d and 3.1e, the power and voltage are increased by the speed increment for less than 1pu speeds.

Fig. 3.4 is provided for further clarifications on the voltage and current limits and the operating regions. The vertical lines are the ovals of the voltage limit where the current limit is presented by blue line (see left side figure in Fig. 3.4). According to the right-side figure in Fig. 3.4, the MTPA is achieved when the *d*- and *q*- currents are equal for the speeds less than ω_1. Moreover, comparison of the loss and torque contours shows that the minimum loss point are also matched with the MTPA points in this region (see A, A_1, A_2, and A_3).

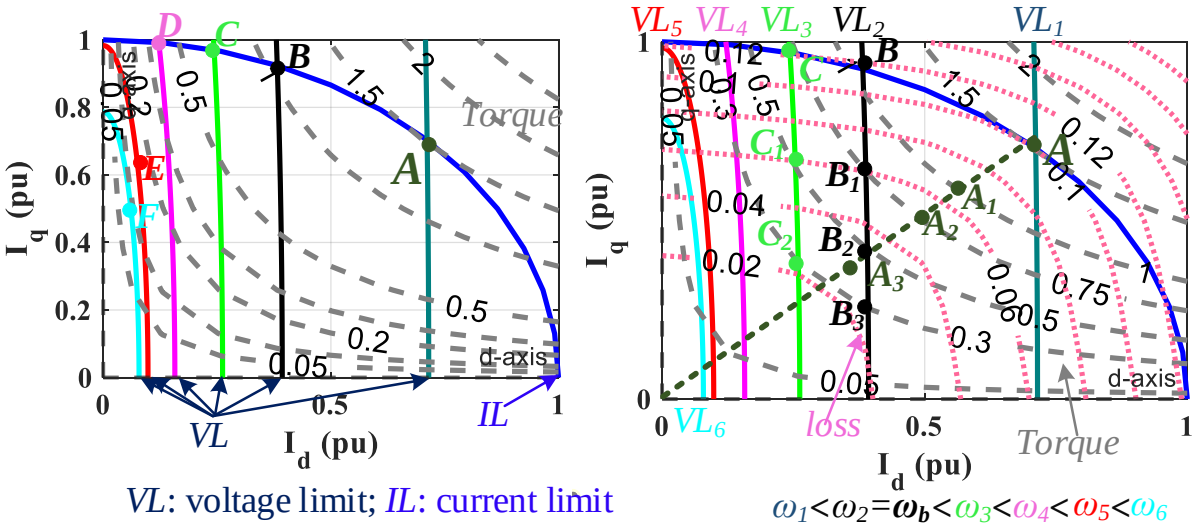

Fig. 3.4. Sample MTPA, FW, and MTPV operating point trajectories in the *dq*- axes current plane for an IM.

Once the voltage reaches its limit, the flux should be reduced by increment of the speed to be able to operate within in the voltage limit. Hence, the operating region above the 1pu speeds is called filed weakening region (FW) or constant power region. Fig. 3.1. shows the flux reduction by increase of the speed in the constant power region. According to Fig. 3.4, for the speed higher than the rated speed (*VL2* to *VL5* curves) the maximum torque occurs at the boundary of current limit where the maximum efficiency is obtained on the boundary of voltage limit.

Above a certain speed in the FW region, the maximum current cannot be injected to the winding. Because the injection of the maximum current will lead to the over voltage problem. For this reason, the current amplitude is decreased to meet the voltage limit requirement. This region is called maximum torque per voltage (MTPV) region (see Fig. 3.1). The cyan oval shown in Fig. 3.4 points out the MTPV region.

3.3. Efficiency Map

Fig. 3.5 summarizes various methods for obtaining efficiency maps of EMs along with the number of research papers based on about 100 papers published in the last thirty years (1992-2022). It is seen although other methods becoming popular, the main techniques for calculations of the EffMs are experimental, finite element analysis (FEA), and analytical techniques, respectively. The accuracy of experimental setups and FEA [214], the flexibility of FEA and analytical methods [107], and the fast speed of analytical methods [102] are the main reasons for the popularity of these techniques. The focus of this paper is on the experimental, FEA, analytical, and corrected analytical methods.

The calculation of the EffM using scaling techniques [85], [115], [141] and artificial intelligence [98], [100], [101] is employed in a few papers. The scaling technique uses the EffM of a certain geometry to estimate the EffM of scaled machines. These methods are generally not reliable when the shapes and material types of some parts of a motor like rotor bar, magnets, and winding structure are changed during the design process. The artificial intelligence-based techniques can avoid this problem

if a large data set consisting of the EffM of different geometries and materials are provided. However, the provision of such a data set is generally not possible.

Although there are many papers discussing the EffM, there is a lack of clear steps/guidelines for the calculation of EffM and discussion of the accuracy versus calculation effort trade-off between alternative techniques.

This section provides a "road map" for engineers and researchers in the field of EM design for transport electrification. It investigates the calculation of efficiency maps for AC electric machines and has the following areas of contribution:

- gives a brief tutorial of alternative EffM calculation methods and discusses their trade-offs;
- describes past research on EffMs and identifies research gaps and opportunities for future research.

3.3.1. General procedure for EffM extraction

The efficiency of the electric motor (η) for a given torque (τ) and speed (ω) is obtained by (3-3) where the total losses (P_{loss}) of the EM are a function of torque and speed.

$$\eta = \frac{\tau\omega}{\tau\omega + P_{loss}(\tau, \omega)} \tag{3-3}$$

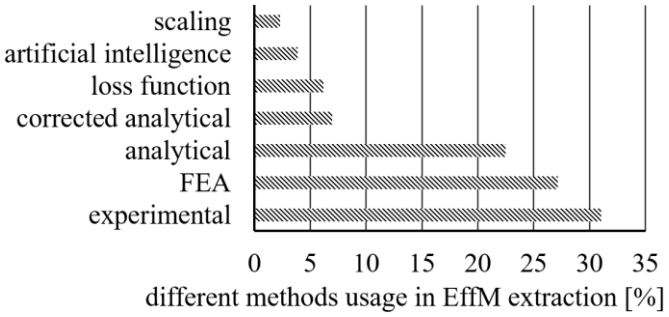

Fig. 3.5. The Summary of the frequency of different approaches used to calculate EffMs based on 100 papers in the period 1992-2022 (based on the reported references in Table 2.4) [215] © 2023 IEEE.

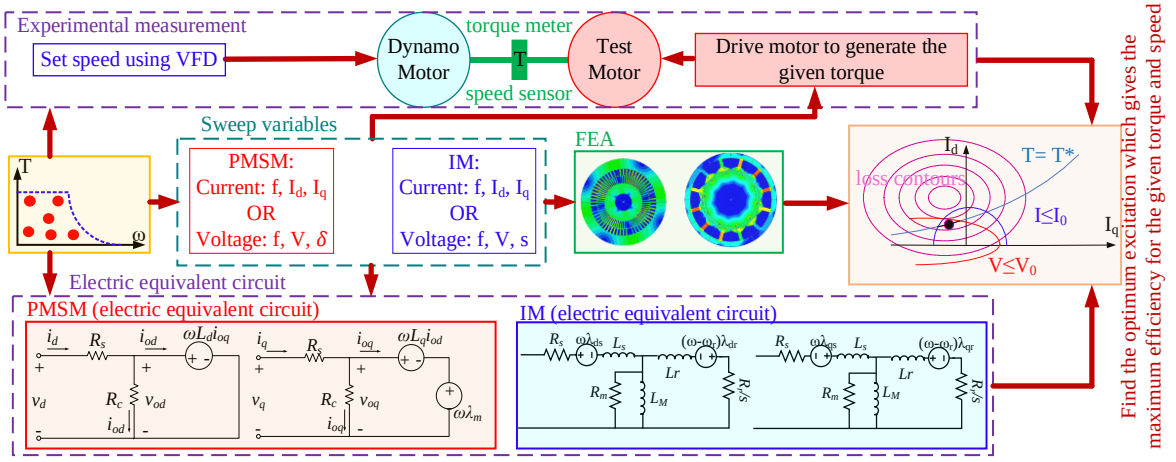

Fig. 3.6. The general process of the calculation of efficiency maps based on the equivalent circuit, FEA, and experimental measurements. The enlarged version of the equivalent circuit of EMs are shown in Fig. 3.2 [215] © 2023 IEEE.

Normally the efficiency map is defined in terms of the maximum efficiency (or minimum loss) for each torque/speed operation point. In some literature, the EffMs have been calculated based on the MTPA control [19], [114], [171] which corresponds to the minimum stator current and stator winding loss. The MTPA operating points do not necessarily match with the maximum efficiency points especially in the field weakening region. The results of the consideration of these two different control techniques are discussed in this chapter. Other efficiency map definitions are also possible such as minimum copper loss or minimum iron loss.

There are multiple ways for obtaining the EffMs of electric machines. These can be classified firstly in terms of their approach:

- experimental methods
- equivalent-circuit approaches
- finite-element analysis

Fig. 3.6 shows the process of the measurement and calculation of the EffMs using the experimental, FEA, and equivalent circuit calculation methods. Accordingly, Table 3.1 summarizes the general steps toward calculation of EffMs. It is seen depending on the considered type of excitation in FEA and electric equivalent circuit modelling, the sweep variables are chosen. For instance, the sweep variable for the voltage-driven PMSM and induction motor (IM) are the power angle (γ) and slip frequency (sf_s), respectively. For a current driven PM and IM, the sweep variables are current (I) and current angle (δ). For a given torque and speed, the loss and efficiency of the motor are obtained through an iterative procedure at different sweep values. The efficiency of the motor in each iteration is recorded when the voltage and current limits are met. Among the collected efficiency values for each torque-speed point, the value which offers the highest efficiency (or smallest loss) is selected to plot the EffM.

As shown in Fig. 3.6, the experimental test follows a similar process where the given speed is set by the dynamo motor drive. The test motor drive works on the torque control mode while it can use voltage-driven or current driven control method to find the maximum efficiency point for each pair of τ and ω.

TABLE 3.1. GENERAL PROCESS OF CALCULATION OF EFFMS [215] © 2023 IEEE.

- **Determine the sweep variables based on the considered power source and type of EM**
  - For synchronous EM, the sweep parameters are either (V and γ) or (I_d and I_q) or (I and δ).
  - For IM, the sweep variables are (V and sf_s) or (I_d and I_q) or (I and δ).
- **Create torque and speed matrices**
  - Create a matrix in the range of the minimum and maximum values for torque and speed.
  - Select one torque (τ) and speed (ω) point for calculation.
- **Calculate efficiency for a given pair of torque and speed**
  - Vary one of the sweep parameters over a range.
  - For the given τ and ω, find the values of the other sweep variable.
  - Find the maximum efficiency while meeting voltage and current constraints.
- **Report the efficiency at the minimum loss point (i.e., maximum efficiency)**

It also possible to classify efficiency maps methods as:

- indirect methods: torque is predicted, usually from flux-linkage, losses are predicted using a simplified model, such as the iron loss is only a function of speed. This can be done using equivalent-circuit or finite-element methods.
- direct methods: torque and losses are directly predicted or measured. This can be done using finite-element or experimental methods.

The calculation and experimental procedures will be explained in details in the next two sections.

3.4. Indirect Efficiency Map Estimation

3.4.1. Principles

When explaining the principles of indirect efficiency map calculation using equivalent circuits it is useful to consider a synchronous machine driven by *d*- and *q*-axis currents (I_d, I_q). It is desired to find the corresponding *dq*-axes flux linkages (λ_d, λ_q). These allow calculating the torque (τ) given the number of phases *m* and pole-pairs *p*,

$$\tau = mp\left(\lambda_d I_q - \lambda_q I_d\right) \tag{3-4}$$

From the stator resistance R_s and the electrical frequency ω_e the *dq*-axes voltages can be found,

$$\begin{aligned} V_q &= R_s I_q + \lambda_d \omega_e \\ V_d &= R_s I_d - \lambda_q \omega_e \end{aligned} \tag{3-5}$$

The stator current *I* and voltage *V* are thus given by,

$$I = \sqrt{I_d^2 + I_q^2} \quad \text{and} \quad V = \sqrt{V_d^2 + V_q^2} \tag{3-6}$$

When calculating efficiency maps, the selected operating point must meet the requirement that both the current and voltage are within the rated current I_0 and rated voltage V_0,

$$I \leq I_0 \quad \text{and} \quad V \leq V_0 \tag{3-7}$$

The stator copper losses are given by,

$$P_{cu} = mI^2 R_s \tag{3-8}$$

There are three methods for obtaining the *dq*-axes flux linkages [15]:

linear: $\lambda_d(I_d)$ and $\lambda_q(I_q)$ where the functions are linear (see the red lines in Fig. 3.7) which correspond to constant values for the inductances L_d and L_q

saturation: $\lambda_d(I_d)$ and $\lambda_q(I_q)$ where the functions are non-linear (see the black lines in Fig. 3.7) due to magnetic saturation, this corresponds to varying inductances $L_d(I_d)$ and $L_q(I_q)$

cross-saturation: for highly saturated electric machines it can be necessary to consider cross-saturation where I_q affects λ_d, and hence $\lambda_d(I_d, I_q)$ and similarly $\lambda_q(I_d, I_q)$. Thus, $L_d(I_d, I_q)$ and $L_q(I_d, I_q)$. This phenomenon for an interior permanent magnet synchronous machine (IPMSM) is shown by cyan dot-points in Fig. 3.7.

3.4.2. Synchronous machine equivalent circuit models

Equivalent circuits can be used with the linear, saturation, and cross-saturation flux-linkage/inductance models.

The equivalent circuit for IPMSMs has the following relationships,

$$\begin{aligned} \lambda_d &= \Psi_m + L_d I_d \\ \lambda_q &= L_q I_q \end{aligned} \tag{3-9}$$

Thus, the main equivalent-circuit parameters are the stator resistance (R_s), PM flux linkage (Ψ_m), and the *dq*-axis inductances (L_d and L_q). These equivalent circuit parameters can be found:

- analytically or from finite-element analysis: based on stator and rotor dimensions, lamination and permanent magnet properties, stator winding information etc.
- experimentally: resistance, inductance/flux-linkage measurements in either stationary or rotating conditions.

These equivalent-circuit parameters can then be used with the equivalent circuit to estimate the flux-linkage from (3-9) and hence torque and voltage using (3-4) and (3-5). From this, the efficiency map can be found.

When using equivalent circuits, the stator iron losses (P_{fe}) can be estimated as a function of speed using an open-circuit test ($P_{oc}(\omega)$). It is done using either finite-element analysis or experimental testing. For the latter this will also include mechanical losses P_{mech} such as friction and windage losses [108], [187]. The total loss $P_{loss} = P_{cu} + P_{fe} + P_{mech}$ is used to find the efficiency (η) by (3-3).

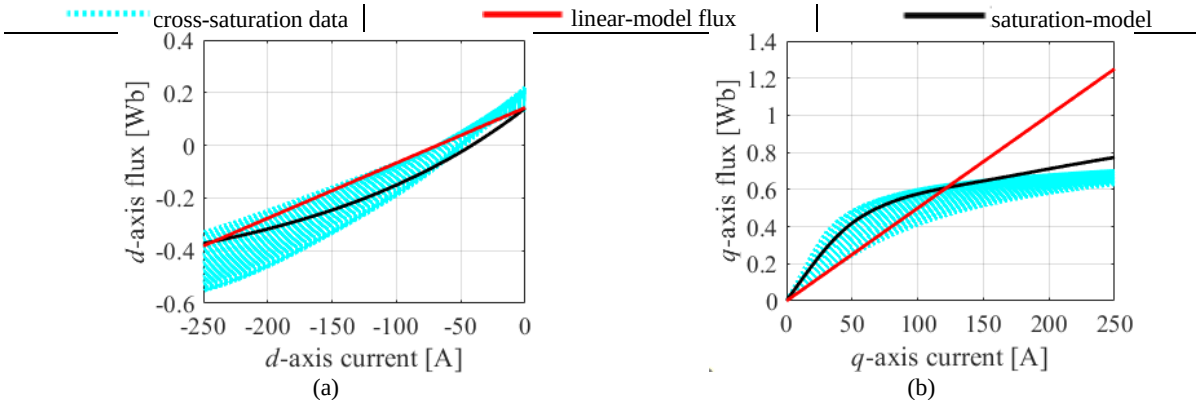

Fig. 3.7. The variation of *d*-axis and *q*-axis flux vs. current. (a) The *d*-axis flux variation. (b) The *q*-axis flux variation [215] © 2023 IEEE.

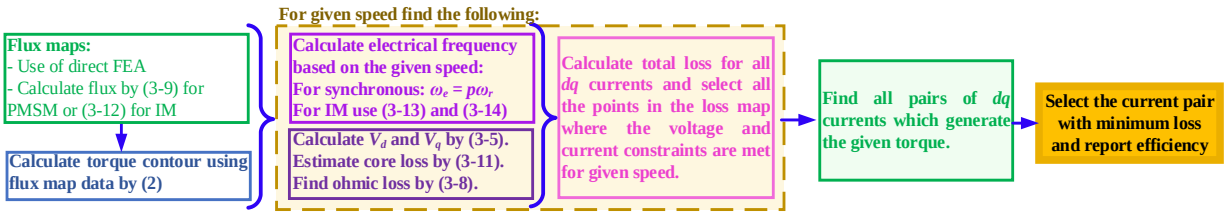

Fig. 3.8. The summary of procedure of the calculation of EffMs using the equivalent circuit for IM and PMSM [215] © 2023 IEEE.

In the equivalent circuit, the stator iron losses can be approximated as only a function of speed $P_{fe} = P_{oc}(\omega)$ and is often subtracted from the output torque. Alternatively, the stator iron loss is modelled as a parallel resistance in the equivalent circuit and hence as an increased electrical input power.

Fig. 3.8 illustrates the general process for obtaining efficiency maps using either equivalent circuit or FEA. According to this figure, the following steps should be investigated to find the EffM of a synchronous machine:

- The first step is to identify the operating limits. The rated voltage V_O and current I_O are given. For synchronous machines there are two control variables (I_d, I_q) and for conventional PM and reluctance machines, the normal ranges are presented in (3-10).

$$-I_0 \leq I_d \leq 0 \quad \text{and} \quad 0 \leq I_q \leq I_0 \tag{3-10}$$

- Secondly, matrices of torque and speed operating points covering the desired operating range (τ,ω) are generated, given the operating speed (ω), the electrical frequency ($\omega_e = p\omega$).
- Thirdly, for each operating point, a vector of (negative) d-axis current (I_d) points in the allowable range given by (3-10) is considered. Eqs. (3-4) and (3-9) are used to identify the required (positive) q-axis current values (I_q) to generate the required torque. From these the corresponding total current, voltage, losses, and hence efficiency are determined. This allows finding the maximum efficiency for that operating point, within the required current and voltage constraints in (3-7). This is repeated for all operating points to find the efficiency map.

3.4.3. Finite-element mapping

A more accurate means for efficiency map calculation, particularly for highly saturated machines, is to avoid using the approximations associated with the equivalent circuit in (7) and instead directly use the flux-linkage $\lambda_d(I_d, I_q)$ and $\lambda_q(I_d, I_q)$. Generally, a large number of finite-element simulations is used to create flux-linkage "maps" of λ_d and λ_q on the (I_d, I_q) plane. In [216], a 15×15 mesh of (I_d, I_q) points were used. The flux-linkage maps can also be found experimentally. As illustrated in

Fig. 3.8, for a given (I_d, I_q) the flux maps are used to find λ_d, λ_q, and hence find torque and voltage using (3-4) and (3-5).

Similarly, to the flux-linkage maps, maps of the stator hysteresis, stator eddy-current, and rotor magnet eddy-current loss maps are found in the (I_d, I_q) plane at a reference speed ω_0 using finite-element analysis. Then, for given values of (I_d, I_q) and the actual speed (ω), actual losses can be found by scaling the loss map results appropriately [217],

$$\begin{aligned} P_{hys}(I_d, I_q, \omega) &= P_{hys}(I_d, I_q, \omega_0) \cdot (\omega/\omega_0) \\ P_{eddy}(I_d, I_q, \omega) &= P_{eddy}(I_d, I_q, \omega_0) \cdot \left(\frac{\omega}{\omega_0}\right)^2 \end{aligned} \tag{3-11}$$

3.4.4. Induction machine efficiency maps

A similar process shown in Fig. 3.8 can be used for induction mchines. For induction machines, the equivalent circuit has three inductances, the magnetising inductance (L_m), the stator leakage inductance (L_{ls}), and the referred rotor leakage inductance (L'_{lr}). From these, the stator and rotor inductances can be defined as $L_s = L_m + L_{ls}$ and $L_r = L_m + L'_{lr}$. These values can be found analytically [162], from finite-element analysis [218], or experimentally [219].

For induction machines, the *dq*-axes fluxes are estimated using (3-12) knowing the machine *dq*-axes inductances.

$$\begin{cases} \lambda_d = L_d I_d; \text{where } L_d = L_s \\ \lambda_q = L_q I_q; \text{where } L_q = (L_s - \dfrac{L_m^2}{L_r}) \end{cases} \tag{3-12}$$

The torque is estimated using (2). The stator electrical frequency (ω_e) is required to obtain the stator voltage using (3). As shown in (11), the value of ω_e depends on slip speed (ω_{slip}).

$$\omega_e = p(\omega + \omega_{slip}) \tag{3-13}$$

where the slip speed is defined in terms of the referred rotor resistance $R_r{}'$ and rotor inductance (L_r) [220],

$$\omega_{slip} = \frac{R_r{}'}{L_r}\frac{I_q}{I_d} \tag{3-14}$$

For induction machines, the typical operating values of slip speed is between zero and the value corresponding to maximum torque, $\omega_{slip(Tmax)}$,

$$\omega_{slip(Tmax)} = \frac{\omega_s R'_2}{\left|R_1 + j\omega_s(L_{ls} + L'_{lr})\right|} \tag{3-15}$$

where $\omega_s = 2\pi f_s/p$ is the rated synchronous speed with rated supply frequency f_s.

For each torque-speed operating point, a range of slip speeds in the above range is considered and the corresponding values of I_d and I_q are determined using (3-4), (3-12) and (3-14). Then, the voltage, ohmic loss, and core loss are calculated. The core loss is modelled as a parallel resistance, and the ohmic loss including the stator winding and rotor cage losses is modelled by series resistances in the equivalent circuit. Based on this, the maximum efficiency for the torque-speed points, while meeting the voltage and current constraints in (3-7), can be found.

For induction machines, the saturation of the magnetising inductance (L_m) is important to consider. It is normally modelled as a function of the magnetising current (I_m) and this can be determined by a no-load test in either finite-element analysis or experimental testing.

The rotor resistance can also depend on the slip frequency due to deep bar effects [221]. This dependency can be found using locked-rotor tests at different slip speeds (either using finite-element analysis or experimental tests) [222].

3.4.5. Voltage control vs. current control

Variable-speed electric machines are normally current-controlled using a field-oriented control technique. It allows rapid control of instantaneous torque and fast over-current protection. This technique is generally less sensitive to motor parameter variations at low speeds. On the other hand, line-operated machines are inherently voltage controlled. Voltage control is simpler to implement while over-current protection is more difficult. It is simpler to control during high-speed field-weakening operation but has generally poorer dynamics.

For voltage control of synchronous machines normally the voltage magnitude $V$and power angle γ between the voltage and the q-axis (which is the back-emf for permanent magnet machines). This defines the dq-axis voltages as,

$$V_q = V\cos\gamma \quad \text{and} \quad V_d = -V\sin\gamma \tag{3-16}$$

If magnetic saturation and stator resistance is neglected, then (3-5) and (3-9) can be used to find a closed-form solution for the dq-axis currents. However, in general, an iterative approach is required to solve for the dq-axis currents. For voltage control of induction machines, normally the slip (s) or slip frequency (sf_s) is used instead of the rotor angle

3.4.6. Core loss models

At higher speeds, EM core losses become more significant. They also affect the stator current and so cause a small increase in the winding losses [108]. The induction machine core loss modelling was discussed in [223]. In [223], authors introduced an iron loss scaling technique. This model is used to update the Foucault eddy current loss obtained from a single frequency and scaled it to find iron loss in other frequencies.

In [224], an improved analytical core loss model based on the short circuit and open circuit characteristics of the PM motors was proposed. The approach is summarized in Fig. 3.9. It is seen that the stator iron loss is considered the superposition of the loss from the main magnetizing flux and from the PM flux. The main magnetising flux is related to the magnetising voltage (V_m) which is the induced stator voltage, and this loss is found from the open-circuit test. The PM flux is directly related to the demagnetising voltage (V_d) and this loss is found from the short-circuit test. This method is more accurate than the simple equivalent circuits for the calculation of efficiency in both rated flux and field-weakening operating regions. It was later improved by including saturation and cross-saturation effects [176].

In this method, the magnitude of the former flux and hence its associated iron loss is directly related to the magnetising voltage (V_m) which is the induced stator voltage. The magnitude of the latter flux and hence its associated iron loss is directly related to the demagnetising voltage (V_d). Therefore, it is assumed that the iron loss associated with the main magnetizing flux path and demagnetizing flux path are approximated as a polynomial function of the magnetising voltage (V_m) and demagnetising voltage (V_d) respectively:

$$P_{fe1} = g_1(V_m)$$
$$P_{fe2} = g_2(V_d) \quad (3\text{-}17)$$

The magnetizing and demagnetizing voltages used in (3-17) are determined from the direct-quadrature (*d*-*q*) axes phasor diagram describing operation of the PM machine as indicated in Fig 3.9. The stator iron losses for a given design using two term version of modified Steinmentz equation equivalent hysteresis and eddy current coefficients a_h , a_e , b_h , b_e are obtained in the form:

$$P_{loss,fe}^{OC} = a_h f + a_e f^2$$
$$P_{loss,fe}^{SC} = b_h f + b_e f^2 \quad (3\text{-}18)$$

More accurate stator iron losses are obtained from:

$$P_{loss,fe}^{OC} = a_h f + a_e f^2 + a_{ex} f^{1.5}$$
$$P_{loss,fe}^{SC} = b_h f + b_e f^2 + b_{ex} f^{1.5} \quad (3\text{-}19)$$

The above equations are for the open-circuit and short-circuit conditions, respectively. By separating the iron loss into three components; hysteresis, classical Joule eddy current and excess losses the constants in ((3-18) & (3-19)) can be found from the FE field solution evaluated at a single arbitrary frequency. The iron loss at open circuit is the iron loss when $i_d = 0$ and $i_q = 0$ and the iron loss at short-circuit is the iron loss when $i_d = -I_{sc}$ and $i_q = 0$. The loss functions are found by substituting for the frequency (f) in (3-18) as follows:

$$g_1(V_m) = \frac{a_h}{2\pi\lambda_m(i_q)} V_m + \frac{a_e}{2\pi\lambda_m^2(i_q)} V_m^2 + \frac{a_{ext}}{2\pi\lambda_m^{1.5}(i_q)} V_m^{1.5}$$
$$g_2(V_d) = \frac{b_h}{2\pi\lambda_m(i_q)} V_m + \frac{b_e}{2\pi\lambda_m^2(i_q)} V_m^2 + \frac{ab_{ext}}{2\pi\lambda_m^{1.5}(i_q)} V_m^{1.5} \quad (3\text{-}20)$$

It is to be noted that

$$\lambda_m(i_q) = \lambda_d(0, i_q) \quad (3\text{-}21)$$

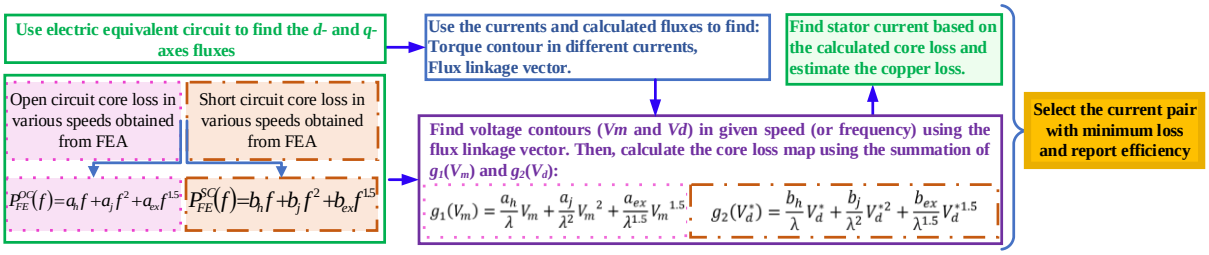

Fig. 3.9. The computationally efficient FEA approach for efficiency map calculation of PMSMs. Magnetising and demagnetising voltages are shown by V_m and V_d, respectively. The flux linkage is shown by λ [215] © 2023 IEEE.

From the phasor diagram and equivalent circuit:

$$V_d = -2\pi f\left[\lambda_d(i_d, i_q) - \lambda_m(i_q)\right] \tag{3-22}$$

and

$$V_m = -2\pi f\left[\lambda_d(i_d, i_q) - \lambda_m(i_q)\right] \tag{3-23}$$

The total iron loss is then calculated at any operating point from the sum of as

$$P_{loss,fe} = g_1(V_m) + g_2(V_d) \tag{3-24}$$

Parameters obtained from these analyses are used alongside the standard *d-q* equivalent circuit to generate a map for the iron loss across the entire machine working envelope.

$$P_{loss}(i_d, i_q) = \frac{3}{2}(i_d^2 + i_q^2)R_s + g_1(V_m) + g_2(V_d) = \frac{3}{2}(i_d^2 + i_q^2)R_s + P_{fe,loss}(i_d, i_q) \tag{3-25}$$

3.4.7. Effect of temperature

Temperature can significantly affect the efficiency of an electric machine. As shown in (3-26) and Fig. 3-10a, the resistance of windings has a direct relationship with temperature [225].

$$R = R_{ref}\left(1 + \alpha(\theta - \theta_{ref})\right) \tag{3-26}$$

In (3-26), the reference resistance (R_{ref}) is the value of the resistance measured at reference temperature (θ_{ref}). The temperature coefficient of the material is shown by α; and θ is the average temperature of the conductors. The temperature co-efficient of copper is about 0.39%/°C which means that, for instance, a 100°C temperature rise would result in a 39% increase in the stator winding resistance and hence losses. In a similar fashion the temperature co-efficient of resistance of aluminium (0.40%/°C) needs to be considered in the rotor resistance of induction machines. In addition, the increase in temperature also increases the resistivity of the permanent magnets which will generally increase the rotor magnet losses.

The properties of permanent magnets are significantly affected by temperature including their remanent flux density B_r, their coercivity H_c and their demagnetisation knee point [226], [227]. This causes the PM flux linkage Ψ_m of PM machines to reduce significantly with temperature resulting in the torque reduction and copper losses increase at higher temperatures. For instance, the temperature co-efficient of the commonly used NdFeB rare-earth magnet material is typically in the range -0.45

[228] to -0.65%/°C and hence a 50°C temperature increase will reduce the PM flux linkage and hence PM torque by about 25-30%.

Iron losses of lamination materials generally reduce slightly with temperature partially due to the increase in the resistivity of the material reducing the eddy-current losses [72]. For example, for a particular lamination material at 1,000 Hz [229], the iron loss reduced by about 10% for a 60°C increase in temperature which corresponds to a temperature co-efficient of about -0.2%/°C.

For machines using rolling-element bearings, temperature substantially affects the grease viscosity and hence bearing losses [230].

For equivalent-circuit and finite-element-based efficiency map estimation, it is useful to have estimates of the operating temperatures in the machine either from design information or from a reliable thermal model.

3.4.8. AC winding loss effect

The resistance of the winding also increases with frequency due to the skin effect (see Fig. 3-10b). Increasing frequency reduces the skin depth and hence the effective area of the wire. This can be modeled using the skin effect equation [231] to improve the accuracy of the ohmic loss estimation. Fig. 3-10c shows the variation of the equivalent resistance of a sample phase winding at different temperatures and frequencies.

In addition to skin effect, another frequency related winding loss is called proximity effect. This is associated with AC losses in a conductor due to it being exposed to magnetic fields created by AC currents flowing in other nearby conductors [145].

The above effects can be modelled to a first approximation by a stator resistance which is a function of frequency.

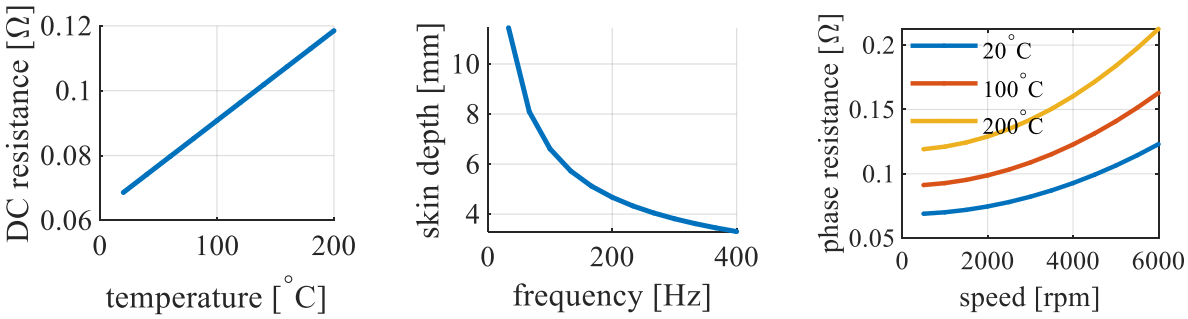

(a) (b) (c)

Fig. 3.10. The temperature and frequency variation effects on the resistance of a conductor. (a) the resistance variation vs. temperature. (b) reduction of the effective area of a wire dure to skin effect by increment of the frequency. (c) resistance variation due by temperature and frequency [215] © 2023 IEEE.

3.4.9. Effect of inverter harmonics

Analytical and FEA methods generally assumes sinusoidal voltages. The core loss increases when an EM is supplied by inverter due to the injection of high order harmonics. Inverter voltage harmonics increase the ohmic loss (i.e., skin and proximity loss) in induction motors and the eddy current PM loss in PM machines.

The electric equivalent circuit models can be solved for different harmonics of the inverter when the amplitude of the harmonics is determined analytically. These methods are not accurate because the equivalent circuit parameters are found based on the fundamental frequency [232]. The inverter harmonics can be modelled in FEA by coupling a circuit simulator with the FEA or use of predefined inverter waveforms [233]. However, these approaches substantially increase the simulation time. An analytical model considering the effect of the high-order harmonics for correct estimation of the conductive, core, and PM losses is complex and yet to be presented.

3.5. Direct Efficiency Map Estimation Technique

In a direct method for estimation of EffMs, torque, voltage, and losses are directly found for the operating condition (I_d, I_q, ω). It can be performed using either:

finite-element analysis: a simulation model is run at the operating conditions and the finite-element predictions of torque, voltage and losses are used.

experimental testing: a prototype machine is run on a dynamometer at the operating conditions and the measurements are taken for voltages, currents, input and output power.

These direct efficiency map results are more accurate than indirect estimation methods but are slower and for experimental measurements requiring a prototype machine and significant experimental equipment.

As shown in Fig. 3.6, experimental measurement of the efficiency map of a test machine involves loading it with a dynamometer machine and finding its minimum input power when producing each desired torque and speed operating point.

Both the test and load machines need to be controlled by variable-frequency drives. One drive is normally in speed control mode and the other in torque control mode to allow stable operation. The test machine generally acts as a motor and the dynamometer machine as a generator. The generated power can be dissipated in a resistive load bank or regenerated to the AC mains. A more efficient approach is to connect the DC link of the two drives together to allow recirculation of the power. This means that the only input power required is that to supply losses in the system.

An electric power analyser is normally used to measure the voltage, current, and power at the input of the test motor. A brushless torque transducer allows measurement of the torque and speed signals. For synchronous machines, the stator current frequency can also be used for speed estimation.

The measurement of the EffMs can be carried out using a hardware in the loop (HIL) system [136], [213], [234]. In such a system, the collection of the measured data and setting the drive torque-speed references is done using devices like field-programmable gate array (FPGA) boards [212] or general purpose control hardware such as a dSPACE MicroLabBox [219].

There are two approaches when experimentally measuring the efficiency for a given operating point. Firstly, searching for the optimum (I_d, I_q) within the voltage and current constraints, likely starting from a pre-calculated optimum reference (I_d, I_q) value found using analytical or numerical methods. Secondly, just applying the pre-calculated reference values, checking that the torque is achieved and voltage/current limits are maintained, and then measuring the efficiency [219].

The number of torque-speed operating points required for an accurate efficiency map calculation has been investigated. One researcher used 1,600 operating points [235], while a later work indicated that 300 operating points may be sufficient for calculation of an EffM up to 5 times of the rated speed [234].

In an standard efficiency measurement process [136], [235], data should normally be collected at a constant temperature. At the start of the test the machine is normally loaded at the rated torque allowing to reach its rated temperature. During the EffM measurement process, the loading can be varied to seek to maintain the motor temperature within acceptable limits [136].

3.6. Calculation of EffM using Commercial software

Commercial finite-element software such as Ansys Electromagnetics [144], JMAG [164], and Motor-CAD [163] have introduced toolboxes to calculate the EffMs of the EMs. In this section, the methods that these toolboxes use to calculate EffMs are briefly explained.

These toolboxes compute the fluxes and losses over a range of current magnitudes and current angles for PM machines. A process similar to that described in Section III.C is then used to find the EffMs. Where JMAG and Ansys electromagnetics use a complete FEA to find these data, motor-CAD uses a combination of FEA and an analytical solver to build the loss maps of the EMs [236]. Hence, the EffM calculation time of the motor-CAD is less than the others. JMAG and motor-CAD use the current-driven model to predict the EffM of induction machines. Ansys electromagnetic uses a voltage-driven model for induction machine EffM calculation. In this model, the voltage magnitude, slip, and frequency are variables.

Ansys Electromagnetics offers various control methods including minimum total loss, MTPA, minimum copper loss, or minimum iron loss. Stator current control ($I_d = 0$), MTPA, maximum torque per flux, and maximum efficiency are the available control methods provided by JMAG. MotorCAD only reports the EffMs calculated by MTPA control.

These toolboxes use a similar approach to consider the additional loss factors. The resistance values are updated analytically before loss calculation in these packages. The skin and proximity effects on stator resistance can be considered. However, these effects are applied analytically to update the losses. The mechanical losses are based on a user-defined input. These toolboxes ignore the effect of the inverter harmonics for loss computation.

3.7. Discussion on EffMs calculation models

This section discusses EffMs of induction and permanent magnet motors and compares the results of different methods with consideration of the various factors in EffMs calculation.

3.7.1. EffM of IMs

This section compares the calculated efficiency maps for an example 2.2kW IM investigating the effects of using linear versus saturation models and maximum efficiency versus MTPA control. The studied IM electrical characteristics and geometry are tabulated in Table 3.2.

Fig. 3.11 shows calculated efficiency maps (first column) and corresponding required control parameter of slip frequency (second column) for three cases based on the equivalent circuit model. The first two rows use maximum efficiency control with row 1 showing a constant (equal to its rated value) magnetising inductance and row 2 including saturation. Row 3 uses MTPA control and includes saturation.

The effect of magnetising inductance saturation (comparing rows 1 and 2), is to slightly reduce the low-speed torque capability, reduce the efficiency over most of the operating range and to increase the required slip frequency at higher torques in the low-speed region. The effect of MTPA versus maximum efficiency control (comparing rows 2 and 3) is a small reduction of efficiency at low to medium torque values at higher speeds with a significantly different slip frequency used.

In some literature and commercial software, like Motor-CAD [163], MTPA control is used to calculate the EffM instead of the maximum efficiency control. The obtained EffM from Motor-CAD software for the same 2.2kW induction machine is presented in Fig. 3.12 and shows a good agreement with the equivalent-circuit results with MTPA (Fig. 3.11e).

TABLE 3.2. STUDIED IM ELECTRICAL CHARACTERISTICS AND GEOMETRY [215] © 2023 IEEE.

Electrical Characteristics			
Rated line voltage [V]	415	Rated power [W]	2200
Frequency [Hz]	50	Number of poles	4
Geometry and dimensions			
Stator outer diameter [mm]	165	Stator inner diameter [mm]	105
Rotor outer diameter [mm]	104	Rotor inner diameter [mm]	38
Number of stator slots	36	Number of rotor slots	28
Lamination material	M19	Stator winding [AWG]	18

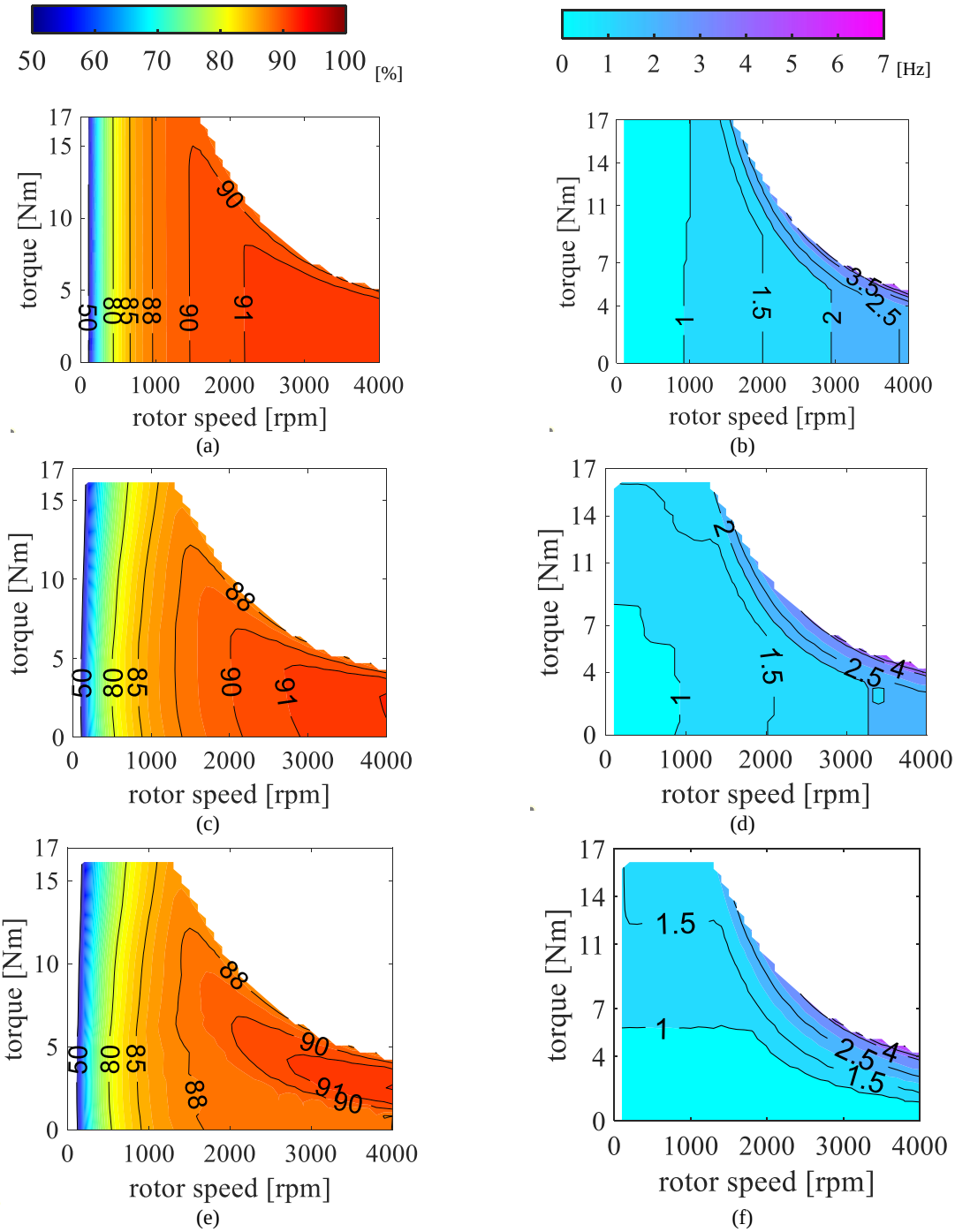

Fig. 3.11. The calculated efficiency maps (left column) and corresponding required control parameter of slip frequency (right column) for an example 2.2kW IM based on the equivalent circuit model. Rows 1 and 2 are using a linear (Row 1) and saturating (Row 2) magnetizing inductance with maximum efficiency control. Row 3 is using a saturating model but with MTPA control [215] © 2023 IEEE.

In Figs. 3.11 and 3.12, the mechanical loss was ignored during calculation of EffM. Figs. 13a shows that the investigation of the mechanical losses can change the shape of the EffM dramatically. In larger speeds, the mechanical losses are increased which leads to the reduction of the efficiency. Hence, the maximum efficiency happens at the middle speeds around the end of the constant torque region and beginning of the field weakening when the flux is maximum, and the machine produces the maximum torque.

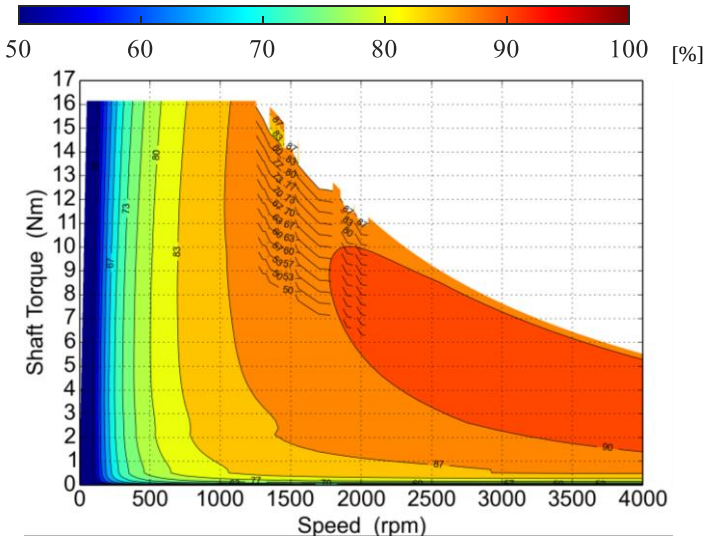

Fig. 3.12. Efficiency maps of the 2.2kW IM obtained by MotorCAD using MTPA control [215] © 2023 IEEE.

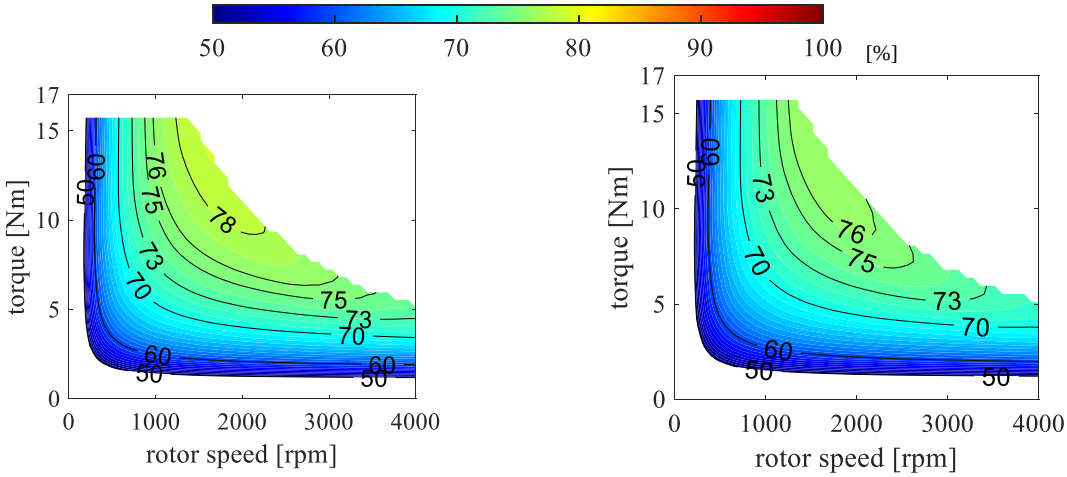

Fig. 3.13. Calculated EM of the 2.2kW IM from saturation considered electric equivalent circuit with consideration of mechanical loss and temperature effect. (a) mechanical loss effect. (b) mechanical loss effect and temperature increment from 60°C to 120°C.

As explained in section 3.4.7, the temperature plays an important role in the efficiency of EffMs. Fig. 13b is to show the effect of the consideration of the temperature. The values of the resistances in the electric equivalent circuit (stator and rotor resistance) are updated by (3-26) and it is assumed that the machine operates at 120°C. Two percent efficiency drop in all operating regions is seen in the results.

3.7.2. EffM of PMSMs

The efficiency map of a 50kW interior permanent magnet motor (i.e., 2nd generation IPMSM in [237]) is presented in Fig. 3.14. Several 2-D FEA simulations are executed to find the equivalent circuit parameters with and without saturation consideration. Also, the *dq*-fluxes required for the flux mapping technique are obtained in different pairs of *dq*-currents using 2-D FEA.

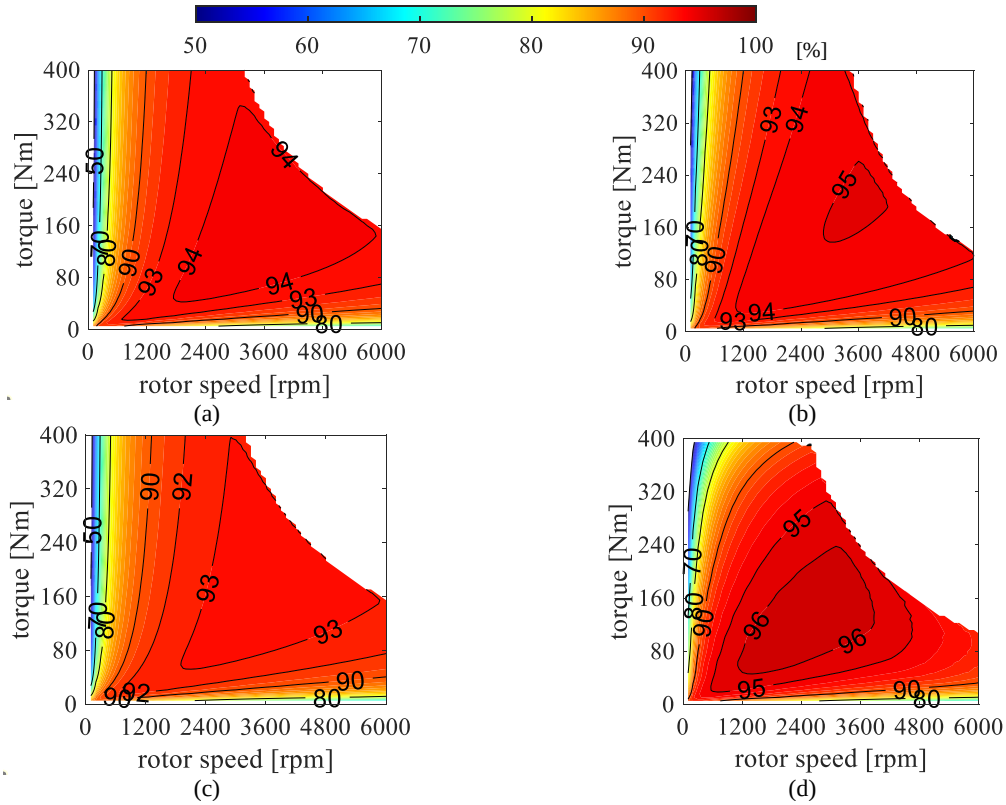

Fig. 3.14. Calculated EffM of a 50kW IPMSM using (a) linear electric equivalent circuit, (b) including saturation model, (c) corrected core loss approach with electric equivalent circuit. (d) flux mapping technique [215] © 2023 IEEE.

Comparison of the efficiency map calculated with the linear electric equivalent circuit (Fig. 3.14a) and with consideration of the saturation (Fig. 3.14b) shows the smaller efficiency of the machine in the constant torque region and a higher efficiency in the field weakening region. A constant value of the core resistance in the electric equivalent circuit was considered to estimate the core losses in the linear model. The Steinmetz equation was used for core loss prediction in the saturation model. In Fig. 3.14(c), the core losses were estimated using the corrected analytical model with FEA explained in Section 3.4.6 and Fig. 3.8. It is seen that the obtained efficiency map using this technique is mostly like the linear model since the inductances are constant in the performance estimation.

The flux mapping technique is used to calculate the EffM in Fig. 3.14d, the maximum torque in the constant torque region is slightly reduced due to the *q*-axis flux reduction at higher currents. The flux-linkage results for this machine were given earlier in Fig. 3.7 which shows when the *d*-axis current is zero and *q*-axis current is at its maximum value, the *q*-axis flux is less than the saturation model and the linear electric equivalent circuit. As shown in Fig. 3.7, the *d*-axis flux reduces significantly at larger currents in comparison to the linear and saturation models. This reduction on one hand leads to reduction of the efficiency because of the increase of the core losses in the field weakening region. On the other hand, it limits the torque generation. As shown in Fig. 3.14d, at the end of the field weakening region, the obtained torque is less than the saturation and linear models.

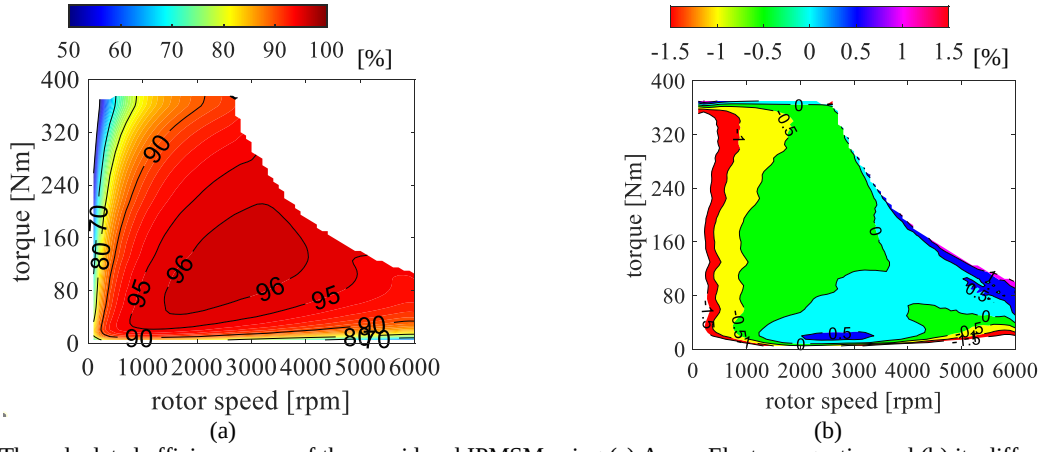

Fig. 3.15. The calculated efficiency map of the considered IPMSM using (a) Ansys Electromagnetics and (b) its difference by the flux mapping method [215] © 2023 IEEE.

TABLE 3.3. COMPARISON OF THE CLASSICAL METHODS IN TERMS OF ACCURACY AND SPEED OF CALCULATION FOR AN EXAMPLE ANALYSIS [215] © 2023 IEEE.

Methods	Max error %	FE Simulations	FE simulations time	Calculation time
Linear equivalent circuit	20%	2	0.17 h	0.01 m
Saturation equivalent circuit	10%	41	3.7 h	0.38 m
Corrected core loss	15%	80	7.4 h	0.87 m
Flux mapping technique	1.5%	225	19 h	0.6 m
Ansys Electromagnetics	0%	500	43 h	4 m

Table 3.3 compares the above EffM calculation techniques in terms of accuracy and time. The accuracy is reported based on the comparison of the results in Fig. 3.14 with the FEA predicted efficiency maps from Ansys Electromagnetics [144]. In this table, the simulation time for the linear equivalent circuit is the time for running open-circuit and short-circuit FEA simulations to find the equivalent circuit parameters. The time for the saturation equivalent circuit includes the FEA simulation times for loading tests at 40 points to find the *d*- and *q*-axis inductances and an open-circuit test to find the core loss value. The time for the corrected core loss models includes 40 open-circuit and 40 short-circuit FEA simulations at different operating speeds to find the core loss variation. Finally, the flux mapping technique preparation time covers the collected data for 15×15 pairs of *d*- and *q*-axis currents to find the flux and loss maps. The required simulation time is an important factor for selection of the method in each application. In this table, the calculation time is the required time for estimation of EffM for all considered pairs of torque and speed.

The calculated EffM from the Ansys Electromagnetics and its difference with the results of the flux mapping technique are presented in Figs. 3.15a and 3.15b, respectively. A comparison of Figs. 3.14d and 3.15a shows that the maximum produced torque in the constant torque region is about 5% less than the flux mapping technique. The difference map shown in Fig. 3.15b demonstrate these two methods have less than 1.5% efficiency difference in the torque-speed envelope.

3.8. Experimental Test and Discussion

This section explains the details of an experimental setup which is prepared for the efficiency mapping of the 2.2 kW IM introduced in section 3.7.1 and Table 3.3. The prepared test rig and its electrical schematic are presented in Fig. 3.16.

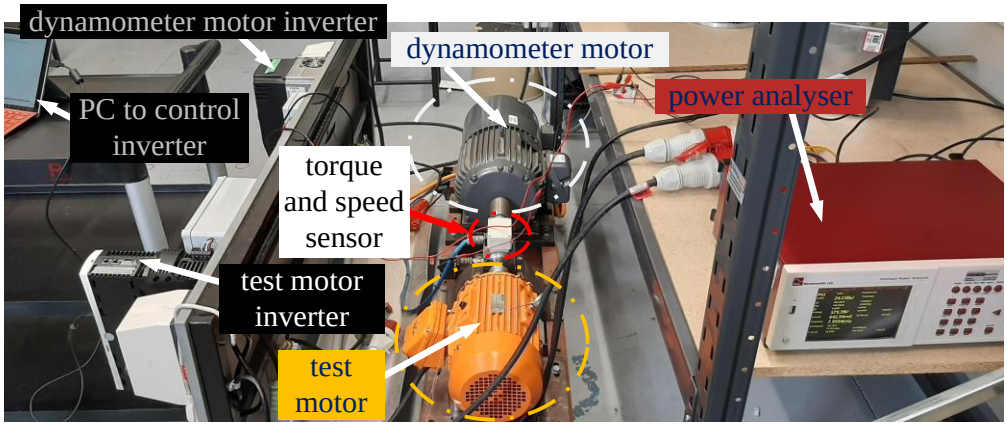

(a)

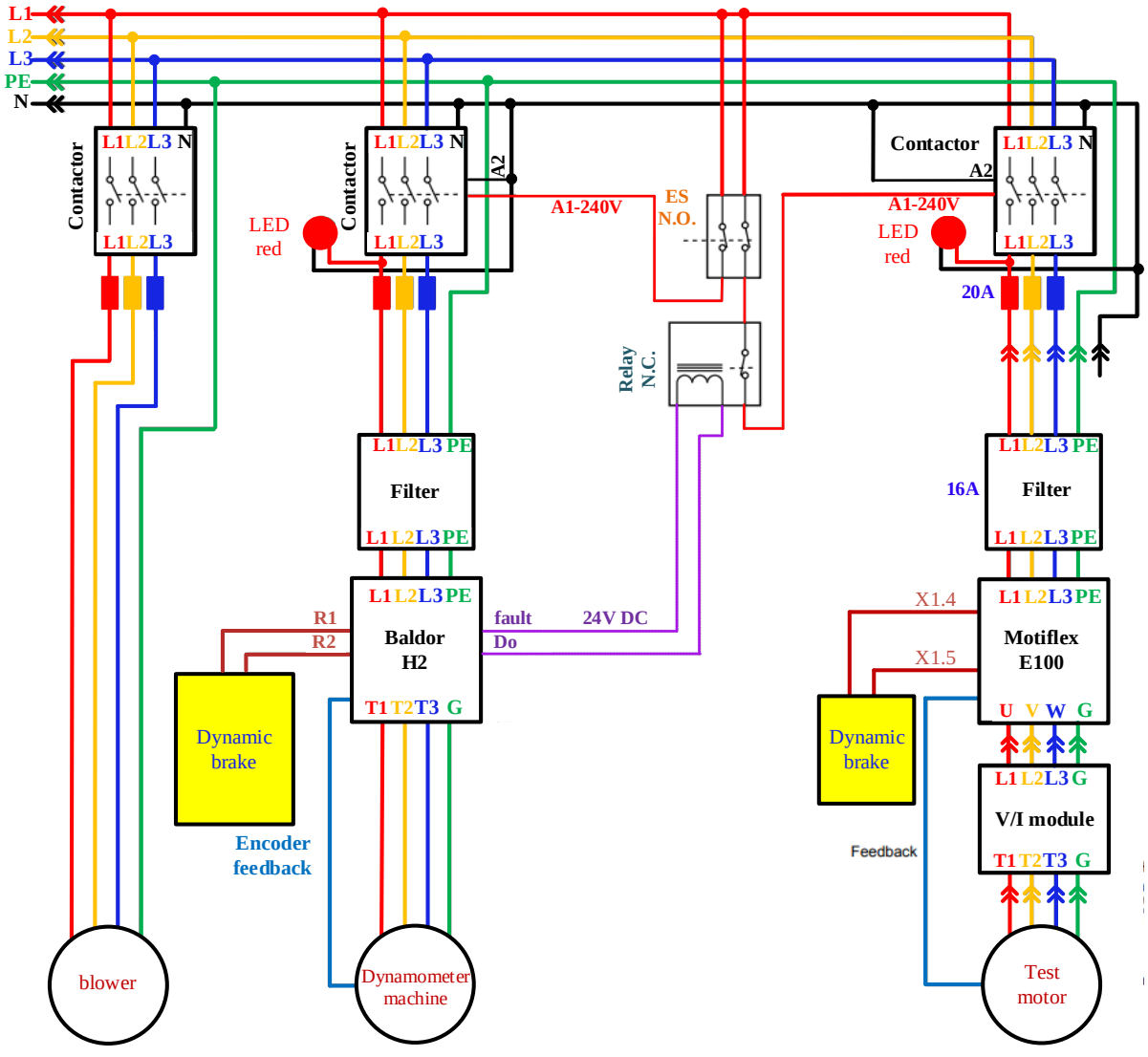

(b)

Fig. 3.16. (a) test rig and its components. (b) wiring schematic of the test rig.

3.8.1. Test rig components EffM measurement of IM

In Fig. 3.16, The Motiflex e100 and 7.5kW Baldor H2 voltage frequency drives (VFDs) are used to control the test motor and dynamometer motor, respectively. A 415V, 7.5hp (5.5kW), 14.4A, 50Hz, 37Nm induction machine is used as the dynamometer motor.

A sinusoidal encoder with the accuracy of 60 pulses per revolution is used for the speed sensing. The output of the speed sensor is analog and the voltage amplitude is proportional to speed. The peak-to-peak voltage of the speed sensor at 5krpm is 3V.

A strain gauge torque sensor (i.e., Himmelstein torque transducer) with the capability of the measurement of the torque for two different ranges is used to measure the torque. The full-scale torque is 5V. So, for the low range output of 11.3Nm, the torque scale is 11.3Nm/5V = 2.26Nm/V. Similarly, for the high-range output torque of 56.6Nm, the torque scale is 11.32Nm/V.

The utilized power analyser to measure the voltage and current and also monitor torque and speed values is PPA 5500.

The speed feedback has been prepared for the dynamometer motor drive. For this reason, a speed limit of 3000rpm is set to protect the system against over speed operation. In addition to the regenerative bank considered for the dynamometer inverter, a 60Ω regenerative resistive bank is also used for the test motor VFD. The regenerative resistive bank of the test motor drive protect drive against possible DC-link over voltage fault.

3.8.2. Test process for EffM measurement of IM

The voltage current characteristics of the test motor in different voltage levels in a constant frequency is obtained at no-load. This curve is used to predict the magnetizing current for efficiency map calculation. The equivalent circuit parameters including the stator and rotor resistances as well the leakage inductances are obtained using the locked rotor test. The explained procedure in the section 3.4.4 is employed to calculate the efficiency map of the test machine using the experimentally extracted equivalent circuit parameters.

The calculated efficiency map is validated by measurement of the efficiency for 10 points by means of the experimental setup. The considered operating point for testing are shown by green points in the Fig. 3.17. As shown in this figure, the maximum test point has a speed of 1600rpm because the rated speed of the test motor is 1440rpm and driving such a machine under load in higher speeds increases the risk of mechanical fault.

The frequency and slip of operation for each pair of torque and speed is extracted from all considered operating points. Figs. 3.18a and 3.18b show the variation of rotational speed and frequency in different torque points, respectively. The rotational speed of the dynamometer electric machine is set on the calculated speed. To generate the slip, the rotational speed of the test motor is

set based on the obtained operating frequency. The V/f control is applied to the test motor. The shaft speed is forced by the dynamometer EM. Thus, the torque is generated on the shaft by the test motor.

The validity of the estimated operating point which are supposed to offer the maximum efficiency is examined experimentally. To achieve this aim, the slip search is executed for a given operating point experimentally. Figs 3.19 to 3.23 show the conducted search for each given rotational speed. Figs. 3.19, 3.20, 3.21, and 3.22 are the search points for the 480, 960, 1280, and 1440 rpm, respectively. All of these points are located within the constant torque region. Although there is a small difference (about 1%) between the estimated efficiency and the measured efficiency, in most of the considered pairs of torque and speed the maximum efficiency point is determined accurately by the calculation.

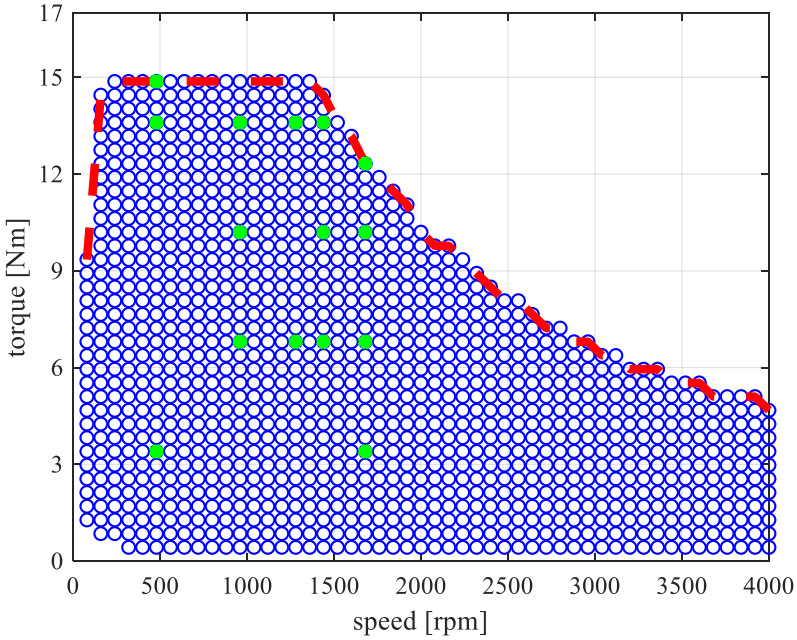

Fig. 3.17. Blue circles are the calculated operating points which gives the maximum efficiency for the given torque and speed. The green dots show the selected operating point for experimental validation.

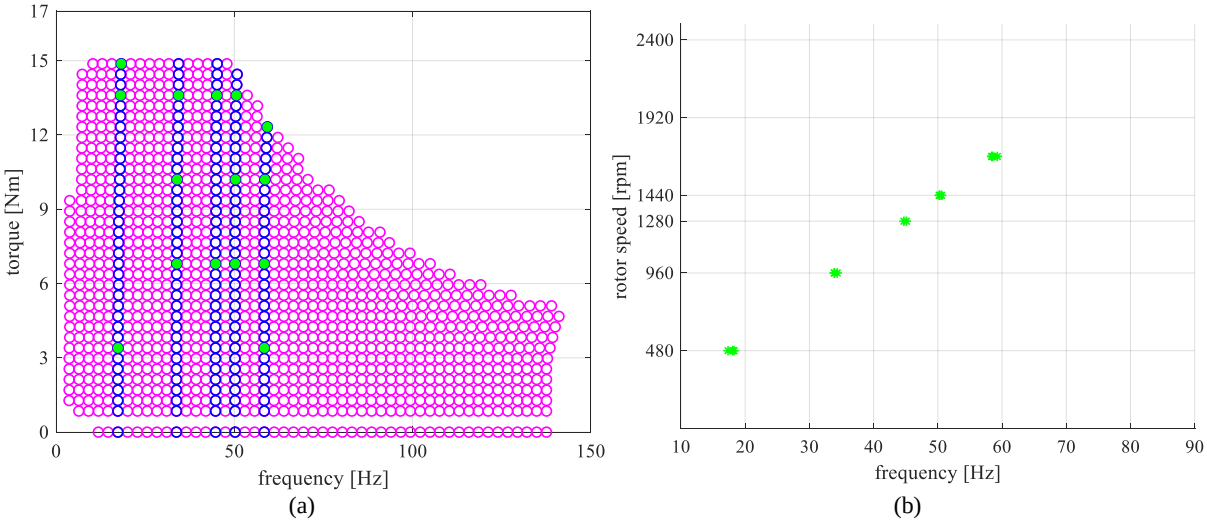

(a) (b)

Fig. 3.18. (a) the torque vs frequency of the selected points. (b) the shaft speed vs. speed of the selected operating points for experimental validation.

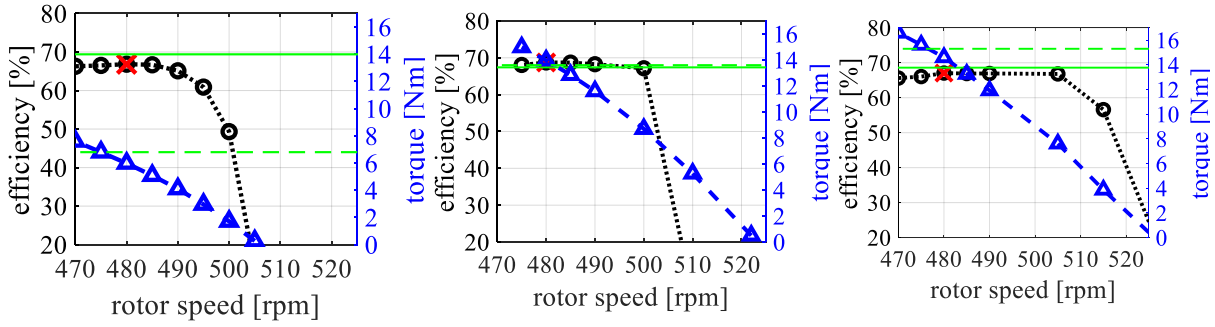

Fig. 3.19. The black and blue symbolized lines are the efficiency and torque, for different slips. The green solid line and dashed line are the calculated efficiency and torque for the maximum efficiency target which occurs at 480rpm. The red cross shown the point with maximum efficiency obtained experimentally. The frequency of the operation in (a), (b) and (c) are 16.84Hz, 17.45Hz, and 17.54Hz.

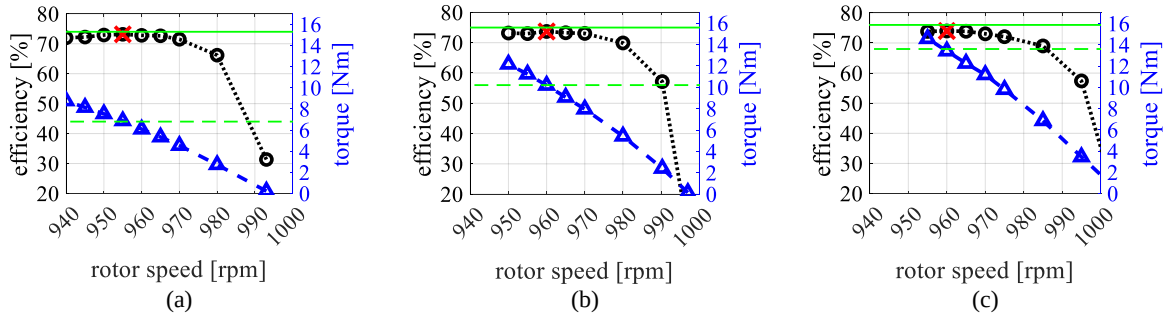

Fig. 3.20. The black and blue symbolized lines are the efficiency and torque, for different slips. The green solid line and dashed line are the calculated efficiency and torque for the maximum efficiency target which occurs at 960rpm. The red cross shown the point with maximum efficiency obtained experimentally. The frequency of the operation in (a), (b) and (c) are 33.16Hz, 33.33Hz, and 33.54Hz.

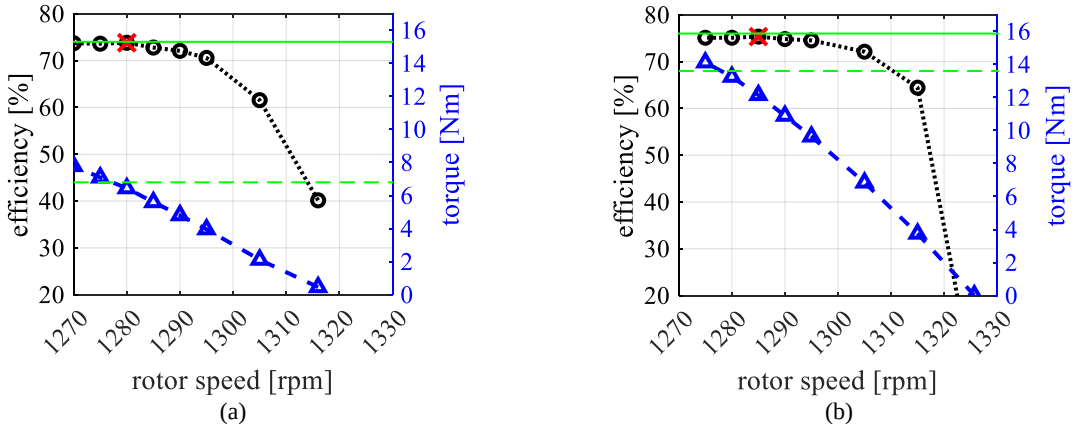

Fig. 3.21. The black and blue symbolized lines are the efficiency and torque, for different slips. The green solid line and dashed line are the calculated efficiency and torque for the maximum efficiency target which occurs at 1280rpm. The red cross shown the point with maximum efficiency obtained experimentally. The frequency of the operation in (a), (b) and (c) are 43.94Hz and 44.26Hz.

The speed limit of the torque transducer is a restriction which does not allow to operate at higher speeds. For this reason, the 1680rpm is the only examined speed in the field weakening region. According to the presented results in Fig. 3.23, the predicted maximum efficiency points are close to the experimentally measured data. In Figs. 3.23a, 3.23b, and 3.23c, the measured maximum efficiency point (red cross) has 5rpm difference with the expected speed of 1680rpm. The rotor temperature

cannot be monitored during the test. So, there is a possibility of the slight difference of the rotor temperature from its expected value of 60°C. This difference changes the rotor resistance and leads to the speed change. It should be highlighted that the difference between the measured maximum efficiency and the expected point efficiency have less than 0.2% difference which is ignorable.

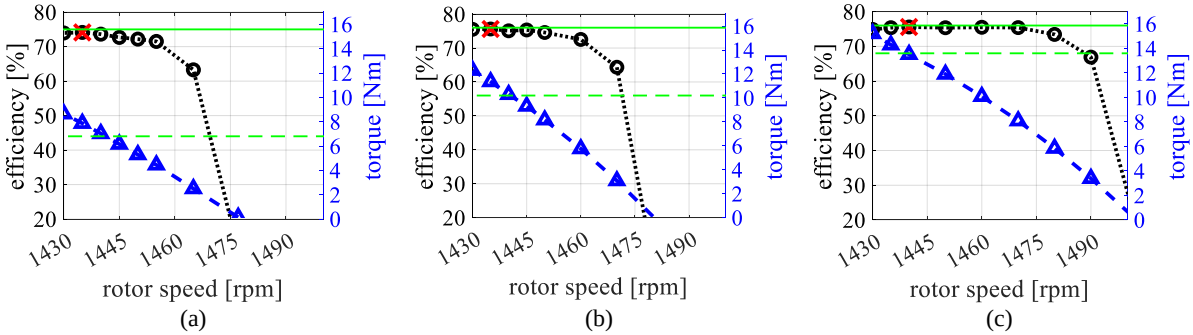

Fig. 3.22. The black and blue symbolized lines are the efficiency and torque, for different slips. The green solid line and dashed line are the calculated efficiency and torque for the maximum efficiency target which occurs at 1440rpm. The red cross shown the point with maximum efficiency obtained experimentally. The frequency of the operation in (a), (b) and (c) are 49.33Hz, 49.43Hz, and 50.15Hz.

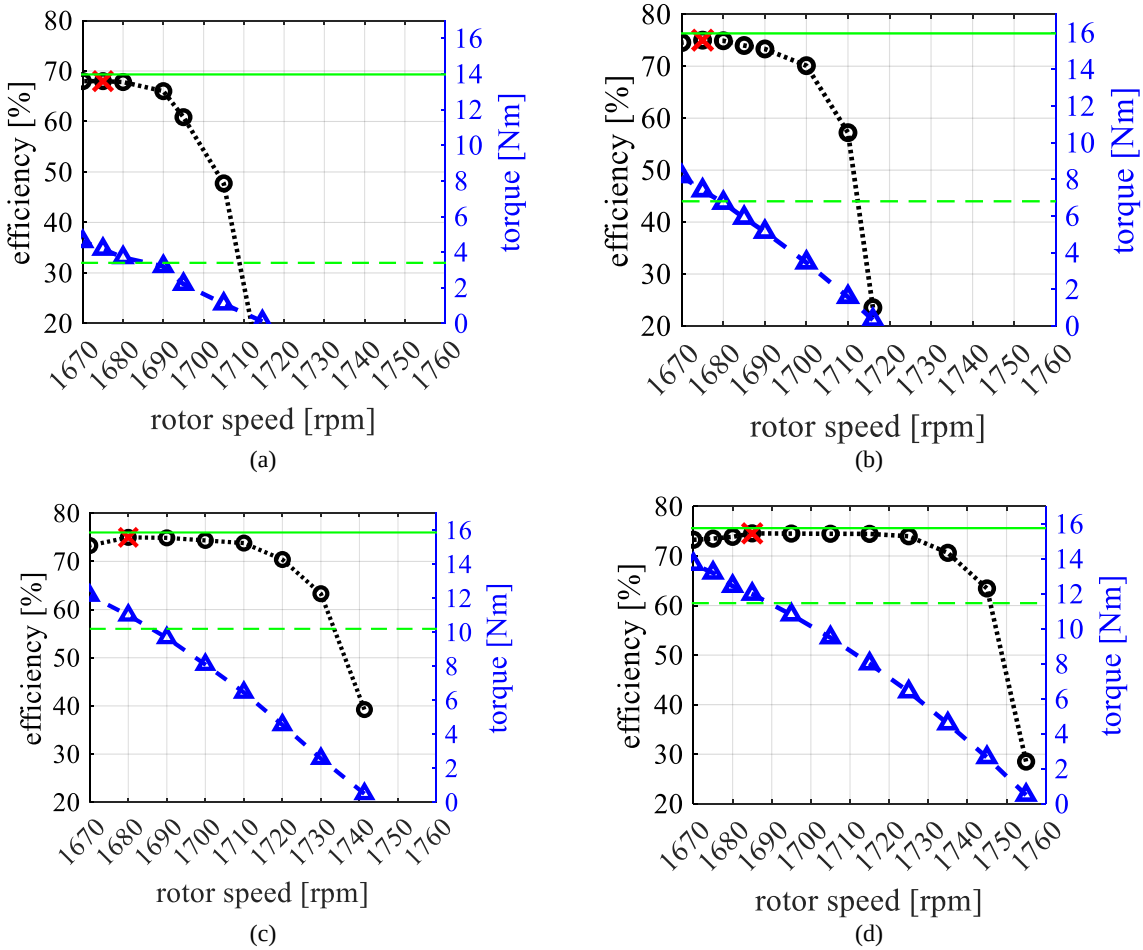

Fig. 3.23. The black and blue symbolized lines are the efficiency and torque, for different slips. The green solid line and dashed line are the calculated efficiency and torque for the maximum efficiency target which occurs at 1680rpm. The red cross shown the point with maximum efficiency obtained experimentally. The frequency of the operation in (a), (b), (c), and (d) are 57.32Hz, 57.37Hz, 58.15Hz, and 58.7Hz.

3.8.3. Test rig components EffM measurement of PMSM

The test rig of the PMSM and the required measurement devices are exactly similar to the test setup explained in Section 3.8.1. Depending on the capability of the available VFD for the drive of the test machine one of the following pairs of excitation variables is selected for searching the maximum efficiency point:

- ✓ V and γ
- ✓ I_d and I_q
- ✓ I and δ

The dynamo meter VFD drives the dynamometer motor on the torque control mode to set the given torque of operation. The test motor control operating frequency is set based on the required speed. Then, the excitation variables which can be one of the above pages are varied at the test motor VFD. Among those pairs which deliver the required torque within the voltage and current limit, an excitation pair with the minimum loss (maximum efficiency) is selected. The efficiency map for the PMSM can be reported after extraction of 300 operating point in the torque-speed envelope of the test machine.

3.9. Research Opportunities

Although many studies on the calculation of the efficiency maps have been conducted, some aspects of the losses have not been studied in detail. For instance, in most of the calculation methods, the converter losses which play an important part especially at higher speeds have been ignored. It has been shown that the converter losses can be equal to the core losses at higher speeds under light load conditions [135]. Therefore, it is useful to include the effect of this type of loss for EffMs calculation. The inverter operation also leads to injection of high-order harmonics into the winding which can affect the ohmic and core losses of EMs is another important factor to improve the accuracy of the estimated EffM.

It is possible to include the inverter in a multi-physics simulation for analytical and FEA. However, it substantially increases the computation time. The development of an analytical model for calculation of the inverter losses can improve the accuracy of the analytical and combined analytical-FEA calculation of EffMs.

The improvement of the accuracy of the estimation of core loss is another important subject for further study. Although the Steinmetz and Bertotti equations offer good accuracy in the estimation of the core losses, they ignore the effect of high order harmonics, especially in tooth. In addition to the discussed models, literature has introduced loss function to predict the efficiency maps. However, loss functions do not predict the core losses with an acceptable accuracy [99].

The available temperature effect consideration is usually done based on the machine temperature for a certain operating point. However, the machine temperature changes with the load. As discussed in [77], the challenges of multi-physics simulation using computationally-expensive numerical methods are the main challenges consideration of temperature effects in EffMs. A fast dynamic modelling of the thermal behavior of the machine is useful to update the machine model parameters during a vehicle driving cycle.

3.10. Conclusion

In this chapter, the efficiency map calculation techniques were reviewed and the advantageous and disadvantageous of each method was described. The applied methods which have been considered to improve the accuracy and speed of the calculation of the EffMs were introduced. The novel techniques which allow to estimate the efficiency map were reviewed and their shortages were discussed. The use of finite element software for calculation of the EffM and the error sources included was the title of a section which discussed the software capabilities and shortcomings. Finally, the future research opportunities which can improve the accuracy of the calculation of the EffMs were introduced based on the literature review.

Chapter 4. Design of AC Electric Machines for a HEV

4.1. Chapter Overview

This chapter describes the step-by-step design procedure of electric machines using FEA. The proposed method uses the available findings in the literature and FEA results for design procedure. In addition to the electromagnetic analysis, thermal analysis is executed to guarantee the capability of the designed machines for handling the load in terms of thermal limits. It allows to consider the normal and overload performance of the electric machines during design. The proposed design procedure is exploited for designing of a 100-kW induction machine (IM) and interior-permanent magnet synchronous machine (IPMSM) for a parallel hybrid-electric vehicle (HEV). The differences between the performance parameters of the studied machines are discussed and the advantageous and disadvantageous of each design are highlighted. The designed machines are compared with the commercially available electrical machines (i.e., products of EMRAX and YASA companies) in terms of performance and power density. The comparison demonstrates the designed machines can offer a comparable performance with other designs. It should be highlighted that the presented EffM in this chapter are obtained using flux mapping technique.

4.2. Problem Description and Motivation

The preparation of a suitable base-line design is necessary to reduce the optimization variables and speed up the design and analysis process [238]. The electromagnetic characteristics and temperature consideration are two main factors for preparation of a reliable base line design [239].

This chapter describes a step-by-step design procedure for preparation of base-line design of interior permanent magnet synchronous machine (IPMSM) and induction machine (IM) for a hybrid electric vehicle (HEV) application. The proposed designed process benefits from the accuracy of the 2-D and 3-D finite element analysis in design of electric machines. The introduction is divided to four subsections including the design process, IPMSM designs, IM designs, and contributions section.

4.2.1. Background Information and Literature Review

Sizing equations [240], subdomain models (SDMs) [162], magnetic equivalent circuit (MEC) [25], and finite element analysis (FEA) [241] are the methods which consider the electromagnetic design aspects of the electric machines.

Sizing equations are based on the empirical equations developed by engineers and researchers. These equations are usually suitable for a specific geometry and material. Hence, they cannot predict the electric machine performance parameters with an high accuracy specially in a wide range of dimensions and machine sizes [167], [242].

In SDMs, Maxwell equations are solved in different parts of an electric machine. The obtained magnetic vector potentials from the solution of the Maxwell equations are utilized to find the flux density in each region. The flux density is used to estimate performance parameters [20], [243], [244].

In the past decade, researchers have proposed the SDMs for induction machine [20], switched reluctance [244], and permanent magnet machines [243]. Researchers demonstrated the accuracy of SDMs in prediction of performance parameters of electric machines. The SDMs implementation is mathematically complex and needs a deep understanding of the electric machines. Hence, it has not become popular in engineering practice.

In MEC models, the electromagnetic reluctance and magnetic motive force (mmf) are obtained under a pole, Then, the MEC is solved to find the mmf and flux in each region. The estimation enables to prediction the performance parameters [245]–[247]. MECs are inaccurate if limited flux paths are investigated in the MEC model [245]. They can become more accurate by the increase of the number of equivalent circuit elements. However, the consideration of a larger number of elements increases the computational burden [246], [247].

FEA is one of the most precise tools for prediction of the electric machines' performance parameters [248], [249]. FEA is computationally expensive which limits its application for design of a machine for a given geometry [162]. On the other hand, the appearance of the commercial and open-source software has led to the popularity of FEA.

Literature has discussed the design procedure for IPMSMs. The available literature discusses about the optimization of the IPMSMs with different objective functions to design a machine with the desired performance characteristics [7], [250], [251]. These studies normally use the available commercialized geometries as the baseline for their studies. Some literature has updated rotor or stator parameters to improve performance based on the results of the sensitivity analysis [252]. The update of winding configuration for design improvement has been another subject of study [253]. The rotor design and PM location and structure have been a popular method for improvement of the IPMSM performance. The rotor of an IPMSM can include permanent magnets arranged in various patterns, including a single V-shape, or double V-shape, delta shape, W-shape, U-shape, and spoke type. Gilsu has introduced an electromagnetic design procedure for double V-IPMSM [254]. They used the results of the sensitivity analysis of different parameters of the stator and rotor to prepare a base-line design for their optimization study. The temperature effect which is a crucial factor for design of electric machines was ignored in [254].

A comprehensive comparative analysis was conducted in [255] to determine the optimum shape of the IPMSM rotor among the single V-shape, double V-shape, and delta shape configurations. Authors concluded single V-shape not only has the highest efficiency in a wide range of torque and speed, but also the risk of the demagnetization is less in this topology. Comparison of the V-shape, U-shape, and spoke type IPMSMs reveals the spoke type offers better performance in higher speeds, but it has a lowest torque density [256]. Larger saliency ratio of the V-shape configuration compared to the U-shape is another advantageous of the V-shape for production of larger reluctance torque [257]. The

advantageous of the V-shape design do not limit to the electromagnetic performance parameters. It has been shown that they are more robust against the demagnetization issue [255], [258].

The overall superiorities of the V-shape PMs encourage researchers to work on the dimensions and V-angle in several studies [259]. The V-angle has been usually investigated as a variable in an iterative optimization study [7], [260]. In [261], the performance variation by changing the V-angle was studied. It was shown that the increment of the V-angle can increase the torque in the constant torque region but reduce the maximum operating speed of the machine.

The induction machine is a well-established technology. NEMA and IEC have standardized IMs for single operating point applications and the required geometry, number of rotor and stator slots, and slot types are specified to achieve the required performance while meeting the thermal and mechanical constraints [262].

Literature showed IM can be a suitable choice to be utilized in the propulsion system of the EVs and HEVs. They not only offer a comparable efficiency with the PMSMs in the field weakening region, but also are cheaper due to the absence of PM in their rotor.

A large amount of literature discusses the design of IM based on the sizing equations [170]. These methods are not useful for design of IM in EVs because they are optimal for operation at a single operating point. Some literature employs sizing equations in a population based iterative optimization studies. These studies cannot bring about a real optimal design because the considered sizing equation are not reliable for a wide range of dimensions and loading levels [240].

The number and shape of the rotor bars play an important role in the performance parameters of IMs. Different optimization problems have been defined to achieve desired outputs such as high torque or efficiency [263], [264]. An optimization study for axial-flux IM was executed in [167] and [171]. Although optimal designs were determined, the effect of slot shape on the performance parameters have not been discussed.

In [262], authors showed that the optimal number of rotor bars depends on the type of the supply (line-starting or inverter driven) and number of pole pairs. The round rotor slots reduces the vibration and noises as compared to the sharp edge rectangular slots [265]. It has been shown that the deep and wide rotor bars increase the efficiency where the larger starting and power factor are obtained by shorter and wide bars [266]. Thirteen different shape of rotor slots was studied in [267] to find the optimal shape of the bars which offer the highest efficiency and starting torque was determined. These studies discussed the characteristics for a certain operating point and miss the performance analysis for a wide range of torque and speed. Moreover, these papers just describe the effect of their considered variables on the case studies and miss the procedure of the preparation of base line design.

The aforementioned design processes ignore the temperature effect or assume some constant values to guarantee the feasibility of the design in terms of the thermal stress [171], [250]. For

instance, a constant current density depending on the cooling is assumed to determine the slot area [268]. Or it is assumed that the stator will not be over heated for a specific operating frequency [269].

Considering the discussed limitations of the available design procedures, there is a lack of a systematic design procedure for preparation of a baseline design for PMSMs and IMs.

4.2.2. Significance and contribution of the chapter

This chapter proposes a systematic step-by-step design process for both IPMSM and IM. The proposed design process allows to provide a reliable baseline design because it considers both the electromagnetic characteristics and thermal limits of the electric machines during the design. To the best of authors knowledge, literature has not introduced any design process considering the machine temperature for a given cooling system. The proposed method allows to consider the performance of any given cooling system during the design. The proposed design procedure uses the Motor-CAD thermal module analysis in one of its steps to provide a design which meets the thermal limits.

The literature findings such as the flux density value in different parts of the machine, the relationship of the number of slots and poles for having an optimum design, and selection of number of rotor bars for an IM machine are used as a recommended values in the suggested design procedure. This information is useful to design quickly without the need of doing time consuming population based iterative optimization. Also, the chapter results shows that the preparation of design based on this information allows to have a comparable baseline design with the commercially available machines and the electric machines in the literature.

Although lots of studies have been conducted on the design of V-shape IPMSMs in different angles, there is no article discussing the advantageous of using deep V-shape PM against the conventional deep shape. This chapter compares the deep shape PM with two other sample angles to show the deep PM not only allows to increase the torque density but also it reduces the torque ripple.

The previously conducted comparative studies ignore the IM over temperature [27], [270]. This ignorance allows them to reach a same torque as an equivalent PM machine in the constant torque region which is impractical. This chapter clarifies the difference between the capability of the torque generation in both machines by consideration of the temperature limits.

The increment of the number of poles increases the core losses resulting in higher temperature in iron parts. This chapter shows the limitations on the selection of number of poles which should be investigated due to the possible over temperature.

The proposed design procedure is used for designing of 100 kW IM and IPMSM for a hybrid electric vehicle (HEV). The different ways of the placement of the PMs in the rotor of an IPMSM are studied. The role of the number of rotor bars on the performance parameters of the IM is another investigated factor in this chapter. Finally, the performance parameters of these designs are obtained

over a wide range torque and speed and compared with each other to discuss the advantageous and disadvantageous of each topology.

4.3. Design Specifications for the HEV

4.3.1. Direct drive electric machine

The industry partner requirement mandates a 100-kW electric machine which is directly coupled to the combustion engine of a hybrid electric vehicles (HEVs) with parallel hybrid-electric drive (see Fig. 4.1) [271]. Note that most of the electric machines are connected through a gearbox to the engines. In the presence of a gearbox, the constant power region characteristics of the electric machine are important to be able to provide enough torque in different speeds. The electric machine in this case study is directly coupled to the shaft of the engine. Thus, the machine should be able to deliver its highest torque in all operating speeds of the engine. This electric machine should be able to operate at ± 355 Nm up to the speed of 2800rpm. The limited available space for the installation of the machine necessitates the introduction of high-power density designs. The DC-link voltage is 750V. The requirements of the considered HEV are summarized in Table 4.1.

The considered stator and rotor materials is laminated silicon iron (SiFe) with the commercial name of M250-35A. The electric conductivity and density of M250-35A are $59 \mu\Omega.\mathrm{m}$ and $7650 \mathrm{kg/m^3}$, respectively.

The standard copper with the conductivity of 58MS/m at 20°C is assumed for preparation of the winding of both machines. Class A, B, F, and H are the defined standard insulation classes for the electric machines. The Class F insulation which is usually used for operation at hotspot of 155°C is applied in this study. This selection determines the maximum operating temperature of the machine.

Considering the hot available coolant (80°C), Sm_2Co_{17} magnet is used to reduce the risk of demagnetization. The selected PM has a magnetic flux remanence of 1.13T at 20°C.

For the IM, the copper cage is selected instead of aluminium cage due to the higher conductivity of copper and as a result production of larger torque. It is noted that most of the available IMs use the aluminium cage due to lower cost.

TABLE 4.1. THE SPECIFIC REQUIREMENTS FOR THE PARTICULA HEV.

Normal speed	2800 rpm	**Maximum speed**	3200 rpm
Power	100 kW	**Overload capability**	2pu current for 30s
liquid flow rate	40 lit/min	**Coolant**	80°C mixture of 50/50 water/glycol
Axial length	150 mm	**Outer diameter**	400 mm

TABLE 4.2. THE SELECTED MATERIALS FOR DESIGN PROCEDURE.

	Winding	**Rotor and stator lamination material**	**PM**	**Cage**
IM	Copper with class F insulation layer	M250-35A	--	Copper
IPMSM	Copper with class F insulation layer	M250-35A	Sm_2Co_{17}	--

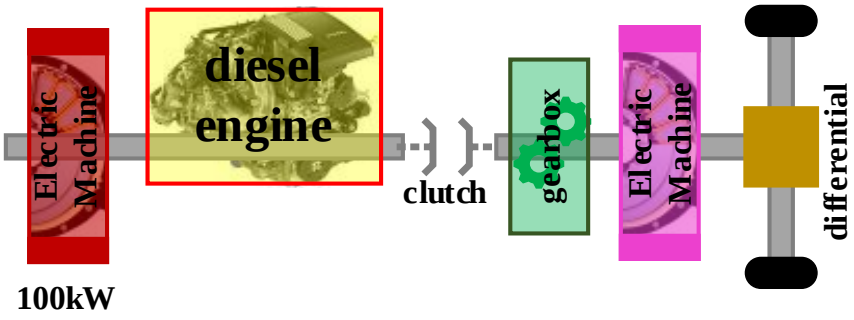

Fig. 4.1. The schematic of the transmission system of the considered parallel hybrid electric vehicle.

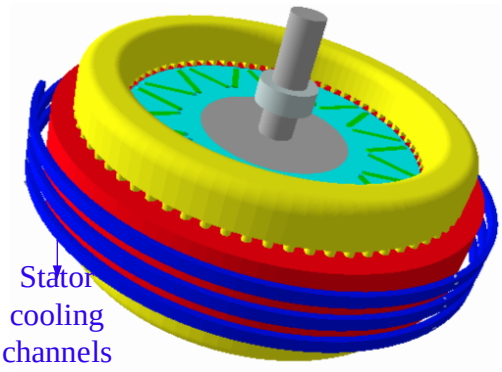

Fig. 4.2. The schematic of the considered spiral cooling system for the stator of both machines.

4.3.2. Thermal model and cooling system

The electric machine thermal analysis is usually performed by the lumped equivalent circuit and finite element analysis [249], [272]. Literature shows these models can predict the average temperature of the different parts in an electric machine with an acceptable accuracy. 2-D and 3-D FEA are other approaches used in prediction of the machine temperature [225]. Motor-CAD software provides a thermal analysis package employing FEA to find the temperature of the machine. The boundary conditions and material characteristics for thermal analysis are adjusted by the software based on the empirical equations obtained from electric machine designers [163], [236]. So, this adjustment results in more realistic temperature estimation of the electric machines. The conducted thermal analysis benefits from the accuracy of Motor-Cad for modelling of the given cooling system.

A similar cooling system is assumed for stators of both IM and IPMSM stators. The literature shows the spiral cooling jackets not only offers a better performance for heat removal from the stator, but also it enables uniform temperature distribution. As shown in Fig. 4.2, the stator is surrounded with cooling channels [273]. The considered height and width of the water channels are 5 mm. As presented in Table 4.1, 80°C mixture of 50/50 water/glycol with fluid flow rate of 40 l/min is injected to the inlet of the channels.

Rotor bars in induction machines conduct large currents which leads to the generation of large amount of loss at the rotor side. Normally, the cage losses are comparable with the stator winding losses. This fact necessitates the consideration of a proper cooling system for IM rotors. In this

chapter, similar cooling system which was introduced for Tesla induction motor is assumed for the IM machine [274].

4.4. Design Procedure

The available active space for design of the electric machines is determined at the first step. Then, the design procedure of IPMSM and IM are explained in two different sections.

4.4.1. Available space for design

The geometry limit is the main challenge of this design. Given 400mm for housing outer diameter, 370mm is considered for stator OD to allow 15mm radial thickness for housing with 10mm spiral cooling channels. Given a 150mm axial length requirement, it is assumed that the housing thickness occupies 2.5mm of axial length on each side. The end winding length reduces the available axial space for design of the machine. Based on the chosen number of poles, slots, and winding design which will be explained later, a 3D printed stator was provided for the coil winder to do a sample winding to estimate the length of end winding which was 40mm. Thus, the maximum machine stack length would be only 65mm.

4.4.2. IPMSM Design

Fig. 4.3 shows the flowchart of the proposed design procedure for the IPMSM. The number of poles and slots are selected at the first step. A higher number of poles reduces the required stator and rotor yoke thicknesses and hence achieves higher torque density. However, increasing the number of poles leads to increasing the operating frequency and hence core losses of the machine for a fixed operating speed. For reasonable lamination thicknesses, the optimal operating frequency is normally selected in the range of 250Hz to 500Hz [72], [229], [275].

It is generally preferred to use a larger number of narrower slots to improve the stator winding cooling. This is limited by mechanical strength of the stator laminations and achieving reasonable winding fill factors for narrow slots. The number of slots is selected based on observations of commercial designs to guarantee the feasibility of the lamination.

The literature shows that IPMSMs with a number of slots per pole per phase (SPP) of two introduces less torque ripple and cogging torque compared to the SPP of one and fractional values [276]. This SPP value also has low total harmonic distortion of the back-emf. Thus, the number of poles is selected based on the selected number of slots to reach an SPP of two.

The generated torque is proportional to the product of the airgap area, magnetic loading, and electric loading. Increasing the airgap diameter increases the airgap area but reduces the slot cross-sectional area and hence electric loading. In most IPMSMs with normal aspect ratios like the IPMSM

studied in [237], the ratio of the inner to outer diameter is 0.6. When the available axial length is limited, it is reasonable to increase this ratio to 0.7 [237].

After the determination of the machine geometry, slot number, and number of poles, the machine slot dimensions, and PM volume should be found. An initial magnet design with pole pitch of 80% and thickness of 6mm was used. The literature shows that optimum IPMSM designs generally have a flux density of 1.2-1.4T in their back-iron at no-load [22]. So, the average airgap flux density (B_{ag}) is checked to be in the range of 0.8T to 0.9T, and the PM amount is adjusted if necessary to achieve this.

After adjustment of B_{ag}, the depth of slots is adjusted to reach the flux density of 1.2T to 1.4T in back-iron. Then, the stator teeth width is adjusted to obtain 1.5T to 1.6T flux density in the teeth [277]. The stator teeth should be roughly 50% to 66% of the slot pitch at the mean stator slot diameter.

The voltage equation presented in (4-1) is used to determine the number of turns. The airgap flux density (B) is assumed to be 0.85T.

$$E = 4.44BANf \tag{4-1}$$

The considered copper diameter is equal to 1mm which is easier for winding. Assuming a copper slot fill factor of 0.45, the number of parallel branches for the obtained number of turns is determined.

High-power PMSMs normally offer a high efficiency and power factor in their constant torque region. If it is assumed that the product of power factor ($\cos(\varphi)$) and efficiency (η) for this machine should be around 0.95 [278], the following equation is used to find the machine current (I_s) for generation of maximum torque:

$$I_s = \frac{P_{out}}{\sqrt{3}V_{ll}\eta\cos(\varphi)} \tag{4-2}$$

In (4-2), P_{out} and V_{ll} are the output power at the maximum speed in the constant torque region (i.e., 2800rpm) and maximum rms value of line voltage. Ignoring voltage drops on power components and inverter harmonics, this value for a pure sinusoidal waveform is equal to $\frac{750}{\sqrt{2}}$ when DC-link voltage is 750V. This value is used to find the current.

The Class F insulation standard allows operating temperature of 145°C with the hotspot temperature of 155°C. The current is increased to reach the hotspot temperature limit in the windings (i.e., 155°C) [279].

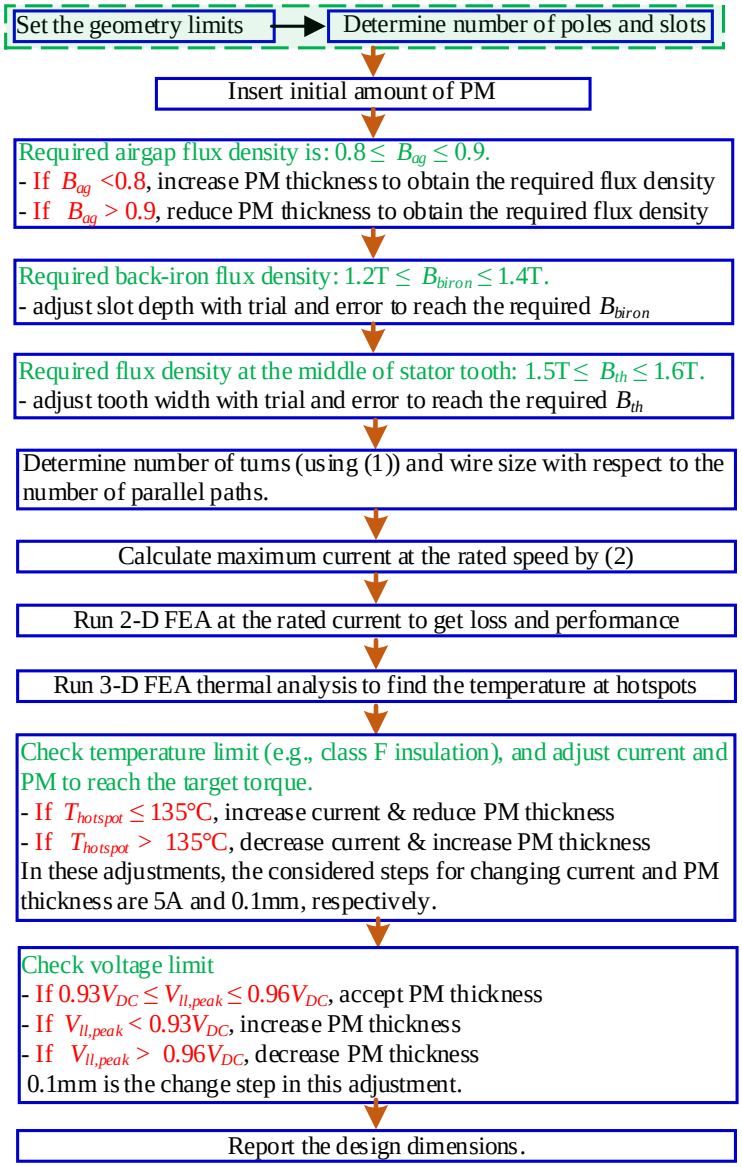

Fig. 4.3. The design flowchart of the studied 100kW interior permanent magnet synchronous machine (IPMSM).

The determination of the maximum current allows to find the required PM volume by means of a sensitivity analysis in FEA. The literature shows V-shaped magnets offer sinusoidal back-emf and smaller cogging torque compared to the other IPMSM rotors. In addition, the PM volume in the V-shaped topology is smaller than the delta shaped and W-shaped structure [280]. Hence, the V-shaped topology is selected for this design. The machine is rotated at 2800 rpm while the computed rated current from the previous step flows through the winding. The minimum PM volume which provides maximum voltage of the 750V and gives the required torque at that operating condition is chosen.

For more clarification, The V-angle is changed from 180° to 60 degrees and the airgap flux density is monitored when the PM volume keeps constant. To show the effect of the variation of the V-angle, Fig. 4.4 is provided for three different sample angles. Fig. 4.4 showing the effect of the selection of the V-shape angle in the back-emf waveform and cogging torque of the machine is provided. It is

shown that a deeper V-shape allows increasing the power density per volume of the IPMSM. Comparison of the 150° V-shape with the 180° V-shape (straight slots) PM shows the decrease of the V-shape angle initially reduces the power density of the machine. To compensate this reduction, a larger PM volume should be inserted into the rotor. The 60° V-shape achieves the 100kW output power with an increased PM volume. Its back-emf is more sinusoidal than the other two designs.

The efficiency of the three designs is comparable and the bar graph of the stacked losses is presented in Fig. 4.5 which shows that the majority is due to stator copper losses, followed by stator iron losses and only small rotor iron and magnet losses.

The 60° V-angle cross-section presented in Fig. 4.4 is the geometry of final design. Table 4.3 summarizes the dimensions of the designed 100kW IPMSM.

TABLE 4.3. THE DIMENSIONS OF THE DESIGNED IPMSM.

Parameter	value	Parameter	value
Outer diameter [mm]	370	Inner diameter [mm]	260
Slot depth [mm]	38	Tooth width [mm]	7.3
PM thickness [mm]	6	PM length [mm]	43
Length of air barriers [mm]	2	Airgap length [mm]	1
Shaft diameter [mm]	130	Stator stack length [mm]	65
Winding overhang length [mm]	40	Number of poles	12
Number of turns per slot	6	Number of slots	72

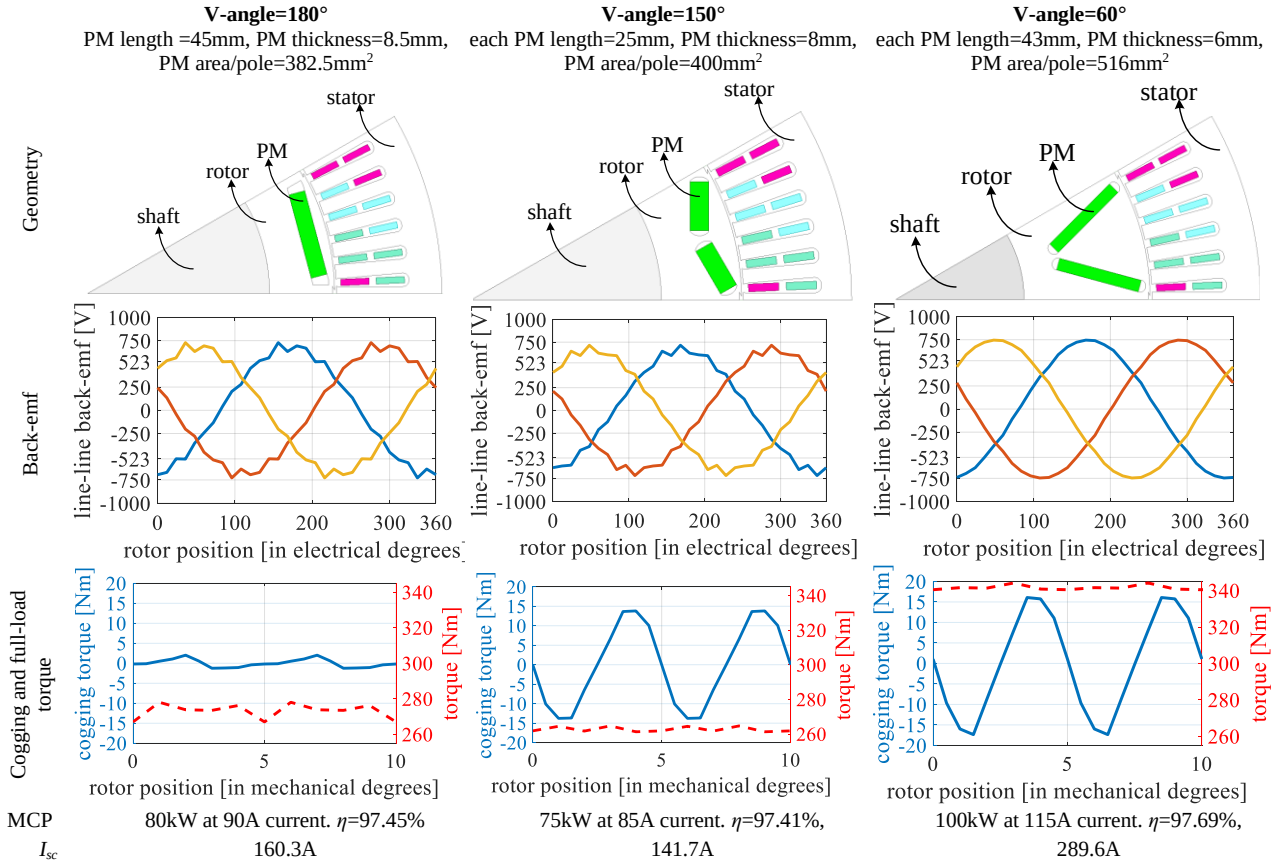

Fig. 4.4. 2-D FEA results of the studied rotors toward achieving the maximum power based on the V-shape angle. The maximum continuous power (MCP) is reported @2,800rpm with Class F temperature rise. Isc is short circuit current.

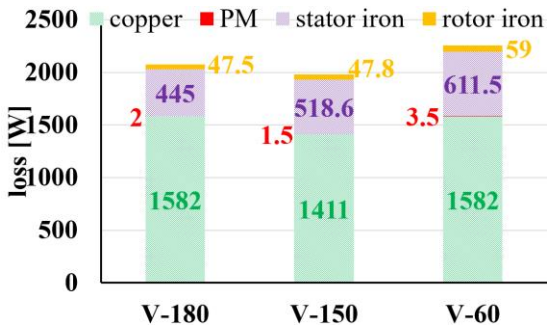

Fig. 4.5. Stacked losses of all presented PMSM designs obtained from 2-D FEA.

4.4.3. IM Design

The considered space limit is applied for design of IM. The design flowchart is presented in Fig. 4.6. According to the explanation for selection of the number of poles and slots of the IPMSM design, a 72 slots 12 poles IM is designed in this section.

The inner to outer diameter ratio of 0.6 is a typical value for electrical machines (like IM in Tesla model S [281]). Because the available space requires a small aspect ratio machine. The chosen inner to outer diameter ratio for design is set on 0.7. Considering a maximum DC-link voltage of 750V, the number of turns per slots are calculated using (1) for 0.7T average airgap flux density and 280Hz frequency. Considering these values, the obtained number of turns per slot is 6 turns.

According to [262], it is reasonable to select the number of rotor bars (N_R) in the following range:

$$0.5N_S \leq N_R \leq 1.5N_S, \tag{4-3}$$

where N_S is the number of stator slots. The results of the analysis in [282] demonstrates the torque ripple is zero and machine cannot be line started when $N_S = N_R$. Because the line start operation of the IM is not an important criterion for the considered HEV, the initial N_R is assumed to be equal to the stator slots ($N_R = 72$). An arbitrary reasonable value (i.e., 10%-15% of the rotor radius) is assumed for the bars and their width is kept equal to the stator width.

The power factor of the induction machines is normally in the range of 0.7 to 0.9. So, it is reasonable to assume $\eta\cos(\varphi) = 0.65$ for IMs. Considering this value, a possible rated current for the IM is calculated at this stage. Normally, the no-load current in IMs is 40% to 60% of the rated current. It is assumed that the no-load current in this design is 50% of the rated current. The calculated no-load current is injected to the winding in the 2-D FEA when the rotor is rotated at the no-load speed. The no-load 2-D simulation is executed for different slots height and width to reach the required back-iron and tooth fluxes in both rotor and stator. The required values have been indicated in Fig. 4.6 which has been selected based on the information in [277], [281]. This process is adopted for the case study to obtain stator tooth width and back-which are found to be equal to 7mm and 17mm, respectively. The selected value for the rotor tooth width is 1 mm less than the stator tooth width in all variations during the analysis. In this stage the rotor slot height remains constant (for the

case study 20mm is selected). The final rotor bars shape will be determined in the next stage under a full-load analysis study.

In the optimal IM designs for EVs and HEVs, the IM operates at 0.1%-1% slip over a wide range of torque and speed. Hence, the rotor of the machine is rotated with 0.5% slip when a current driven IM is simulated using 2-D FEA at rated frequency. The amplitude of the current is increased to reach the limits of the Class F insulation standard. Note that the stator voltage is always checked to guarantee that the machine does not exceed the DC-link voltage limit. This current is selected as the rated current of the designed IM.

The dimensions of the rotor bars are determined with respect to the obtained current limit with the assumed 72 number of rotor bars. The reduction of the rotor side resistance not only reduces the losses, but also allows to have a less torque ripple. On the other hand, it reduces the tooth flux path which can lead to the earlier saturation of the rotor tooth and hence torque reduction. Hence, the width of the rotor bar is started to find the optimum bar width where the torque has not started to decrease because of saturation. The reduction of the rotor side resistance is continued by increment of the bar depth. The increase of the bar depth leads to the increment of the length of flux path and consequently torque drop and additional core loss.

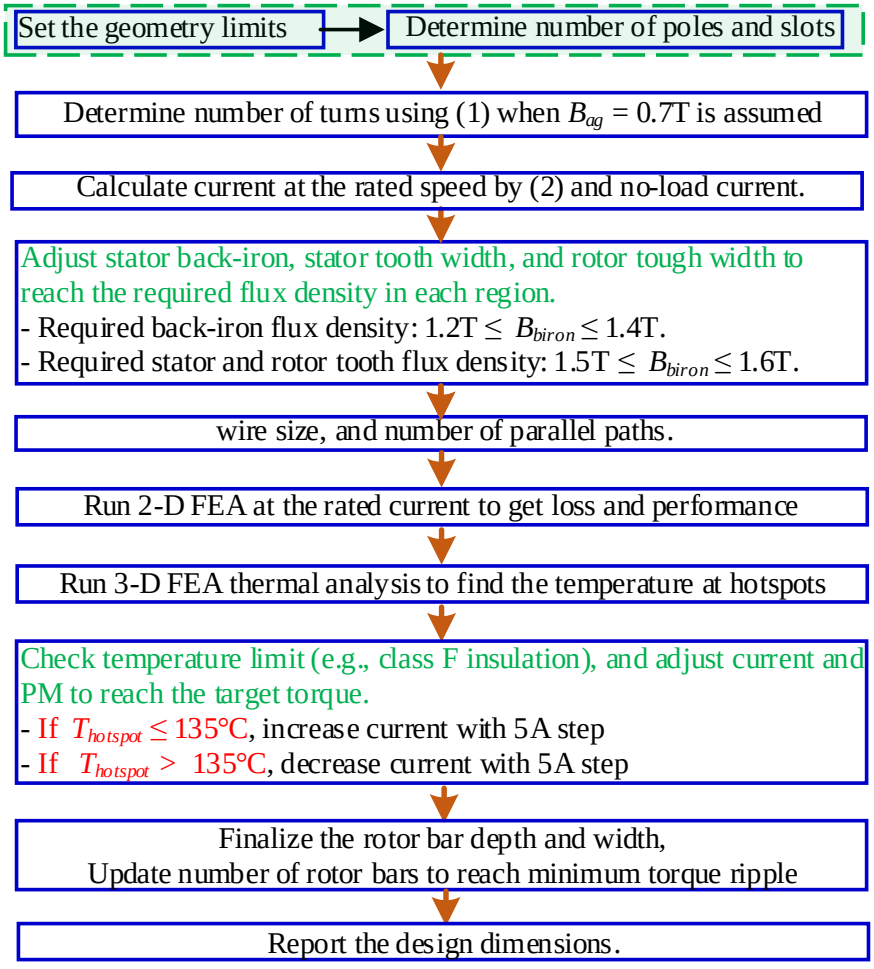

Fig. 4.6. The proposed step-by-step design process for the induction machine design.

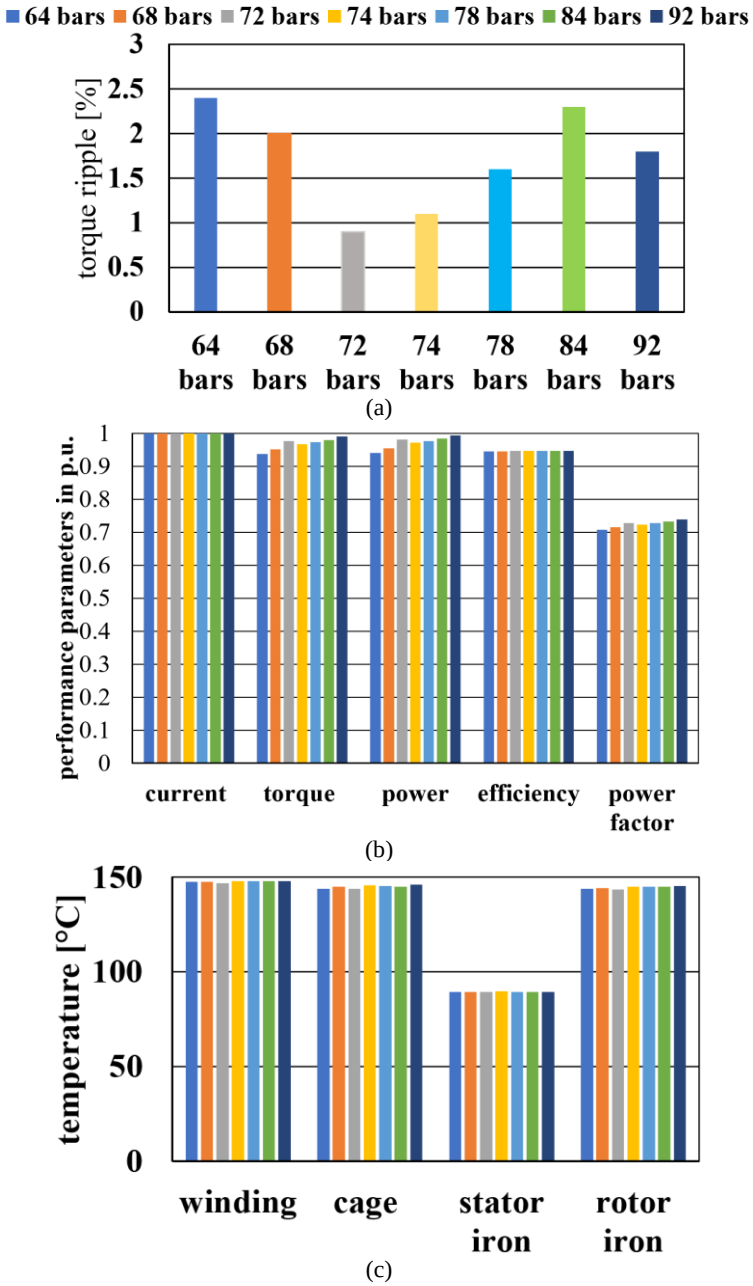

Fig. 4.7. (a) 2-D FEA results of torque ripple at rated torque (b) 2-D FEA results of performance parameters of the case studies. (c) 3-D FEA results of hot spot temperature of the case studies in different parts. Current, torque, and output power are per unitized based on their rated values which are 120A and 260Nm, and 80 kW, respectively.

The tradeoff between the reduction of the rotor resistance and increment of the length of flux path should be controlled to find the optimum depth for the slot through several 2-D FEA simulations. The obtained rotor tooth width and bar depth are 5.7 mm and 24.5 mm for the case study.

The number of rotor bars is determined using the obtained dimensions for the rotor bars in previous step. The bar depth is kept constant, and the width is updated by variation of the number of rotor bars to maintain rotor iron to copper ratio at a constant value. Fig. 4.7 shows the effect of the variation of number of rotor bars on the performance parameters of the IM when the designed IM operates at rated condition. Fig. 4.7a shows that the torque ripple becomes larger when the difference

between the rotor and stator slots is increased. The minimum torque ripple occurs when number of rotor bars is 72 and it is similar to the conclusion of the previous works conducted by Joksimovic [262], [282]. As shown in Fig. 4.7b the generated torque, output power, and power factor are increased by increase of the number of rotor bars because the rotor contributes more flux to the airgap. Larger amount of the airgap flux increases the core loss and consequently increment of iron temperature. Fig. 4.7c shows in larger number of rotor bars (i.e., 78 to 92 bars) the rotor iron temperature is slightly (1°C) higher compared to the machine temperature with a smaller number of rotor bars. The stacked loss of the machine with different number of rotor bars is presented in Fig. 4.8. As expected, the loss is increased slightly by the increase of number of rotor bars. The 2-D FEA results show the rotor core loss which is increased by 1.05% from 64 to 92 slots is the largest increase. These results show the design with 78 bars offer an acceptable performance with small torque ripple. Hence, it is selected for further analysis. The geometry and cross section of the designed machine are presented in Table 4.4 and Fig. 4.9, respectively.

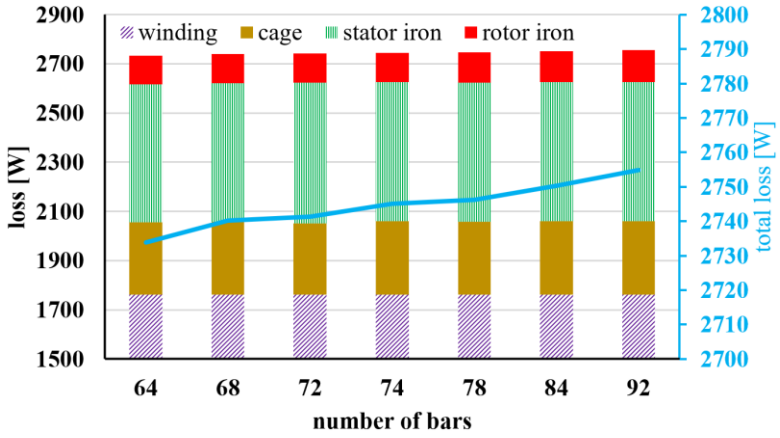

Fig. 4.8. 2-D FEA results of loss in different regions of IMs with different rotor bars.

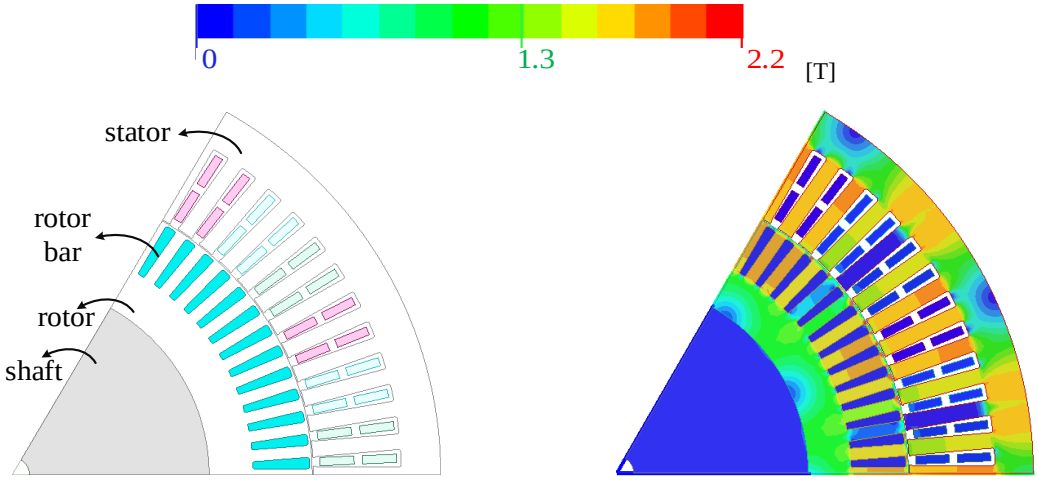

(a) (b)

Fig. 4.9. (a) cross-section of the designed induction machine. (b) flux density distribution on the IM at full-load operating condition.

TABLE 4.4. THE DIMENSIONS OF THE DESIGNED IM.

Parameter	value	Parameter	value
Outer diameter [mm]	370	Inner diameter [mm]	260
Slot depth [mm]	42	Stator tooth width [mm]	6.9
Rotor bar depth [mm]	24.5	Rotor tooth width [mm]	5.3
Airgap length [mm]	0.5	Shaft diameter [mm]	170
Winding overhang length [mm]	40	Stator stack length [mm]	65
Number of rotor bars	78	Number of poles	12
Number of stator slots	72	Number of turns per slot	6

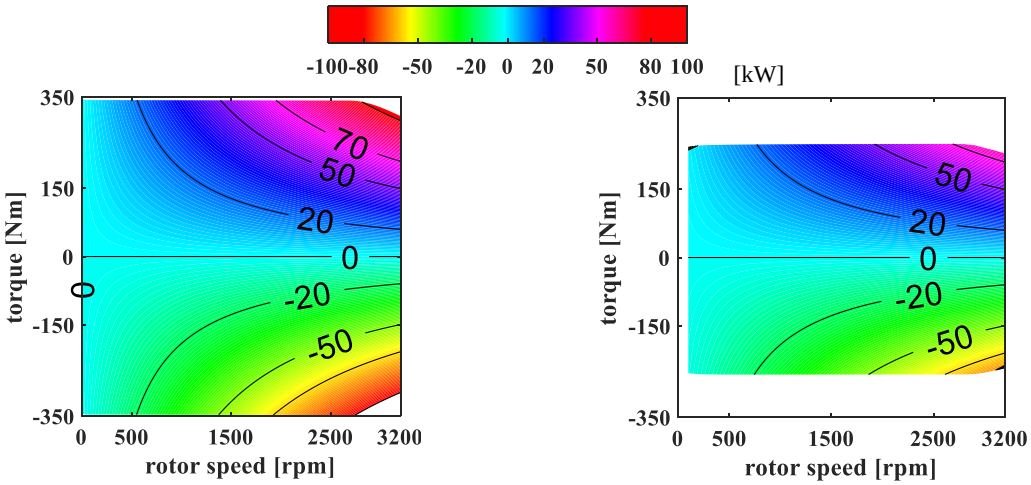

Fig. 4.10. 2-D FEA results for comparison of the output power of both machines. (a) IPMSM (b) IM.

4.5. Simulation Results and Discussion

The performance parameters of these machines over a wide range torque and speed in the required operation region and over-load condition are compared. Finally, the proposed design procedure is used to design these machines with different number of poles to study the selection of the pole numbers.

4.5.1. Performance Parameters

Although the machine has been designed for operation as a generator in the considered HEV, the performance parameters in this section are provided in motoring and generating conditions. This allows to see the possible differences between the performance parameters of an electric machine in different operating conditions.

The power map, efficiency map, and power factor maps of the designed IPMSM and IM are discussed in this section. Fig. 4.10 compares the output power of both machines. It is seen that the IPMSM offer a higher power (larger torque) at lower speeds. The maximum power of the IPMSM is 103kW when the IM maximum power is limited to 75kW. It should be highlighted that the induction machine offers 81kW power during operation at generative mode at rated speed which is 6kW larger

than the power at motoring condition. The maximum output power of the IPMSM at motoring mode is 2 kW larger than its output power at generative mode.

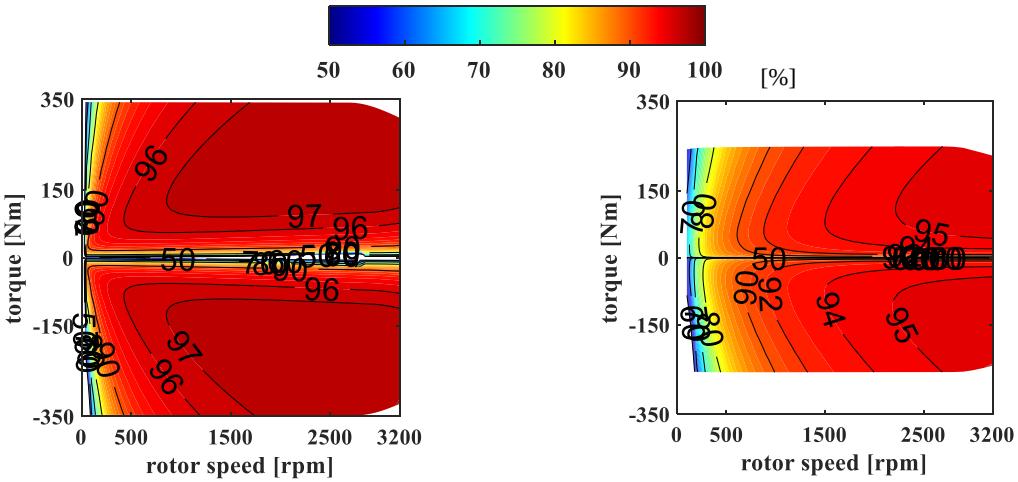

Fig. 4.11. 2-D FEA results for comparison of the efficiency map of both machines. (a) IPMSM (b) IM.

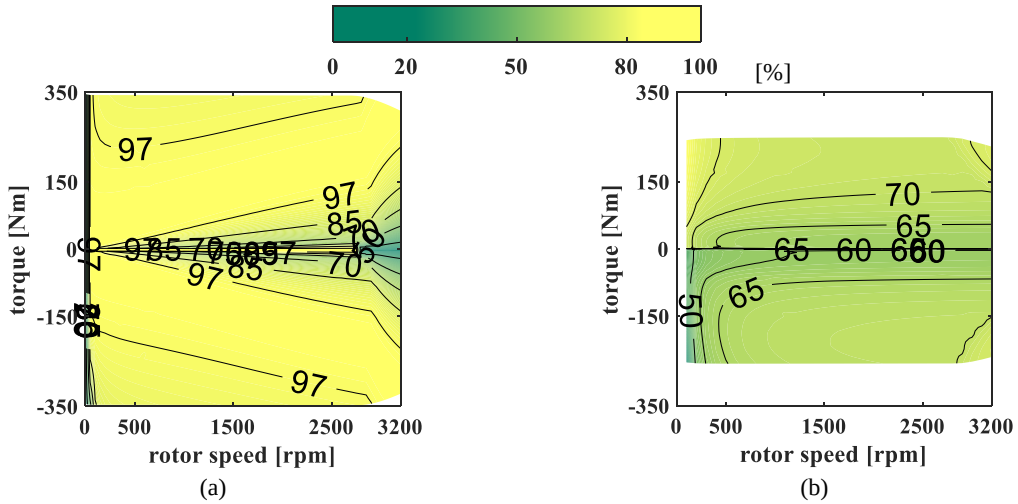

Fig. 4.12. 2-D FEA results for comparison of the power factor of both machines. (a) IPMSM (b) IM.

TABLE 4.5. COMPARISON OF THE IPMSM MACHINE WITH DESIGNED IM

	Weight [kg]				Power [kW]		Efficiency [%]	
	winding	cage	iron	PM	rated	peak	rated	peak
IPMSM	12.0	--	34.4	3.0	103	206	97	91
IM	12.0	13.1	31.4	--	81	162	95	92

The efficiency maps of designed machines are compared with each other in Fig. 4.11. This result shows the efficiency of the IPMSM is at least 2% larger the IM in both motoring and generating modes. Note that in lower speeds this difference reaches 7% which is significant amount of power.

Table 4.5 compares the designed machines weight, power, and efficiency from each other. The IM machine is approximately 10 kg heavier than the IPMSM because of the weight of the copper cage at

its rotor. According to the information of this table, the power density of IPMSM and IM are 2.08 kW/kg and 1.43 kW/kg, respectively.

The comparison of the power factor of the designed electric machines demonstrates the larger power factor for IPMSM in most of the operating points. In larger torques this difference is about 37%.

4.5.2. Overload Condition

A transient temperature analysis is executed to examine the machines capability for handling 2pu overload power for 30 seconds. It is assumed that the machines operate at rated load (i.e., 345Nm for IPMSM and 255Nm for IM) and rated speed of 2800rpm from t=11 seconds to t=360 seconds. Then, 2pu load is applied for 30 seconds. After t=390 seconds, the machine continues its operation at full load for 350 seconds. The operation scenario for both machines are shown by red line in Fig. 4.13a and 13b. Fig. 4.13a shows the transient of the IPMSM temperature variation when the windings are then energized to produce 2pu power. This figure shows the IPMSM temperature is increased from 108°C to 114°C within 30 seconds. The slope of the temperature increase shows the machine will not reach the limitation of the class F insulation temperature (i.e., 155°C) after 30 seconds overload. The transient temperature analysis of the IM with 2pu overload power (Fig. 4.13b) also shows the capability of the IM for handling the 2pu overload.

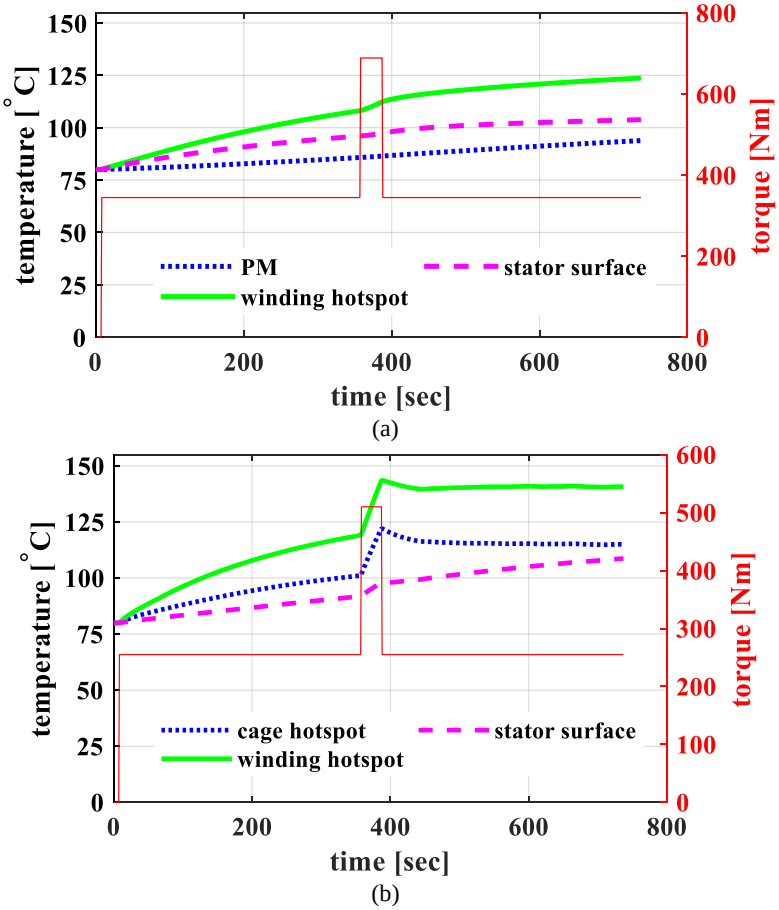

Fig. 4.13. 3-D FEA results of the transient thermal analysis of the designed machines. (a) IPMSM. (b) IM.

4.5.3. Number of Poles

Because the number of poles was initially selected based on an initial choice for the number of slots, an analysis for understanding of the importance of the number of poles is conducted. The proposed procedure is to consider machines with 10 to 20 poles while keeping a slot per pole per phase of 2. The output power of the designed machines is compared with each other with respect to the temperature limit.

Fig. 4.14 shows that the increment of the number of poles does not necessarily allow obtaining higher power from the induction machine because of the temperature limits. The increase of the core losses by increment of the number of poles (see Fig. 4.14b) increases the temperature. It is seen that the rate of the reduction of the iron volume is much smaller than increase of the core loss.

4.5.4. Comparison of the Designed Machines with the Commercially Available Products

Given the tight axial length constraint, axial-flux PM designs are an important alternative to the radial-flux PM and IM designs covered in this paper for this traction application. Thus, the performance of the designed radial-flux machines are compared with four axial-flux PM designs, two commercially available designs and two designs described in the literature, as shown in Table 4.6.

The radial-flux IPMSM and IM designs use Class F insulation and with the assumed 80°C liquid coolant, are designed for operation at 130°C during steady-state operation. The application requirement is a 2,800 rpm rated speed. To provide a fair comparison, the four benchmark axial-flux machines are derated for this cooling arrangement and this rated speed. Due to the limited information provided by the manufacturers, the following assumptions are made in the derating: the machines operate with a steady-state temperature of 130°C and the available cooling is directly proportional to the difference between this and the fluid temperature; at this low speed only the copper loss is considered so the loss is proportional to the square of current; and the torque is proportional to current.

The YASA-750 is a commercial axial-flux PM machine which is rated at 70 kW and 3,000rpm with 40°C coolant [283]. Using the above approximations, with 80°C coolant, the derated output power is estimated at 49 kW at 2,800rpm.

The EMRAX 268CC [284] is another commercial axial-flux PM design and can deliver 105 kW at 4,500rpm with 50°C coolant. The derated power for this machine is estimated at 60.8kW at 2,800rpm.

Two different axial flux PM synchronous machines (AFPMSM) have been studied in the literature in [285] and [249]. The coolant inlet temperature for the designed machines in [285] and [249] are 25°C and 20°C, respectively, and have rated powers at 2,800 rpm of 20 kW and 82 kW, respectively. The winding temperature in [285] at rated current is 75°C (i.e., the Class A insulation limit). If this

insulation level is changed to Class F, the 45°C increase in the inlet coolant temperature is compensated and no derating is required. This can also be applied to the machine in [249].

Table VI compares the power density of the considered electric machines in the literature with the designed IPMSM and IM in this paper. According to this comparison, the designed machines offer a promising performance. Note that the reported efficiency values for the designed IPMSM and IM does not include bearing/windage losses. Also, the power density does not include the housing, shaft, and bearings etc. unlike the commercial machines [283], [284] and the AFPMSM in [285]. The reported weight in [249] does not cover the housing, shaft, and bearing weights.

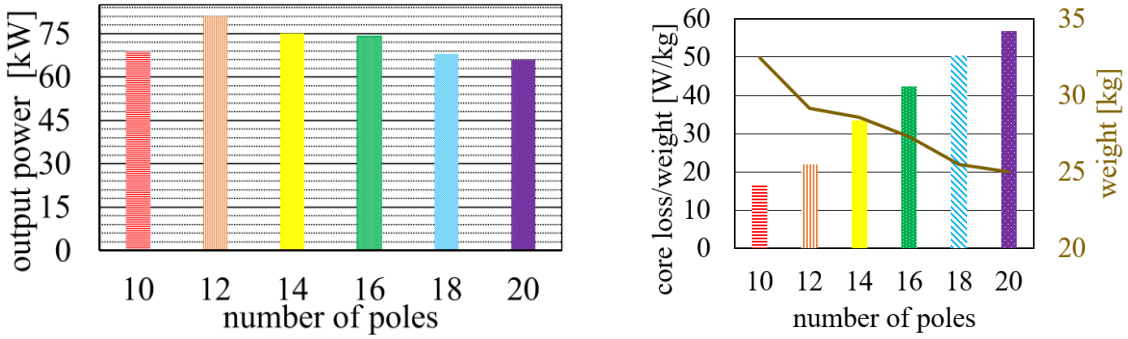

(a) (b)

Fig. 4.14. 2-D FEA results for comparison of the power factor of both machines. (a) IPMSM (b) IM.

TABLE 4.6. COMPARRISON OF THE PERFORMANCE PARAMETRES IOF THE DESIGNED IPMSM AND IM AT 2800 RPM SPEED WITH FOUR OTHER AVAILABLE DEISNGS IN LITERAURE AND MARKET.

	Inlet coolant temperature	Max. Continuous Power	Max. Efficiency	Power density
Proposed IPMSM	80°C	103kW	97%	2.08 kW/kg
Proposed IM	80°C	75kW	95%	1.43kW/kg
YASA-750 [283]	40°C	70kW	97%	1.89kW/kg
	80°C	49kW	≤ 97%	1.32kW/kg
EMRAX 268CC [284]	40°C	105kW	98%	5.12kW/kg
	80°C	60.8kW	≤ 98%	2.96kW/kg
AFPMSM [285]	80°C	20kW	91.5%	0.88kW/kg
AFPMSM [249]	80°C	82kW	94%	2.3kW/kg

4.6. Conclusion

A step-by-step design procedure for the design of interior permanent magnet and induction machines was proposed in this paper. The design procedure employs the existing values, assumptions and finite element analysis for optimal design of the machines. The proposed methods include checking the temperature limit for a given cooling system during the design. It provides a reliable baseline design for further optimization.

A 100-kW direct-drive electric machine for a hybrid electric vehicle was considered for explanation of the design procedure. An IPMSM and an IM were both designed for the HEV, and their performance were compared.

The effect of different rotor magnet V-angles in the IPMSM was studied and the advantages of using the deeply embedded PMs were described. The sensitivity of the performance of the induction machine on the number of rotor bars was examined to highlight the importance of this value.

The effect of the selection of the pole number was another subject of the study. It was demonstrated that although it is expected to increase the power density by increasing the number of poles the temperature limit can limit reaching larger torques/power by increasing of the number of rotor bars.

The comparison of the design with the performance of commercial designs and two designs in the literature showed the developed designs are competitive in power density and efficiency and can be used as a baseline for further optimization. For instance, the optimization can be conducted by consideration of the slot widths and depths, or PM dimensions as studied in various former works.

Chapter 5. AFSPMSM Design for HEV

5.1. Chapter Overview

This chapter describes the design procedure of a 100kW and 200kW axial flux permanent magnet synchronous machine (AFPMSM) for a hybrid-electric vehicle (HEV). Although there are general guidelines for design of electrical machines, there is no specific standard design procedure, and hence it is useful to consider case studies. Those case studies reporting the step-by-step design process of the electric machines are limited in the literature despite many papers thoroughly reporting the performance of their designed machines. This section describes the electric machine design process for an industrial heavy electric vehicle application considering the project requirements, practical limitations, thermal behaviour, space limitations, etc.

The chapter explains the requirements for operation of these machines at regular and overload conditions. The temperature analysis of the machine at full load and over-load condition is another aspect which is taken into account. The machine design optimizes the amount of the permanent magnet (PM) considering the lowest volume and losses. The machine performance over a wide range of torque and speed is analysed using the simulation study. It should be highlighted that the steady state performance of all design is analysed using flux mapping technique. The designed machines are constructed, and their performance parameters are analysed and validated experimentally.

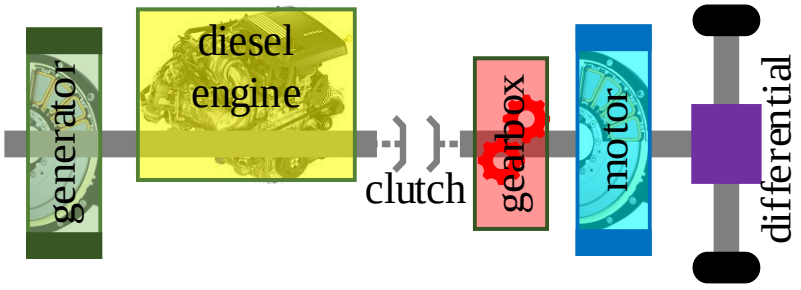

(a)

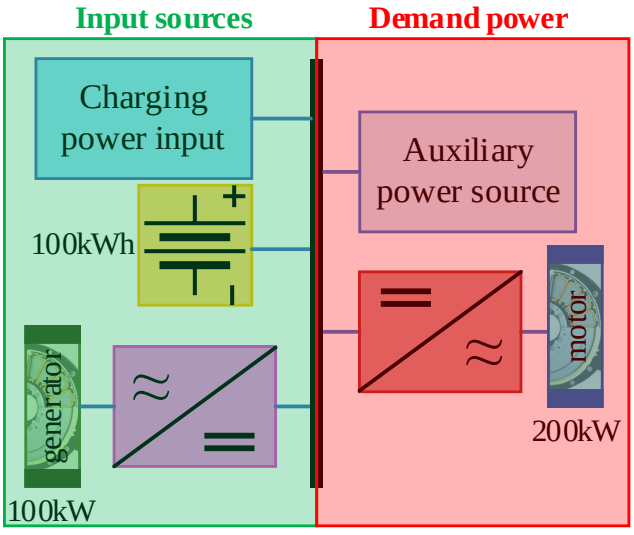

(b)

Fig. 5.1. The drive train of the investigated HEV and the electrical network. (a) Simplified block diagram of traction system arrangement, (b) single line block-diagram of the power network.

TABLE 5.1. THE SPECIFIC REQUIREMENTS FOR A PARTICULAR VEHICLE

Optimum speed of engine	2800 rpm	**Maximum speed**	3200 rpm
Generator rated power	100kW	**Generator overload capability**	200kW in 30 sec.
Motor rated power	200kW	**Motor overload capability**	400kW in 30 sec.
Cooling	70°C mixture 50/50 water/glycol	**Liquid flow rate**	40 lit/min
Axial length	Should be minimized	**Outer diameter**	550mm

5.2. Problem Definition

Two electric machines are designed for a heavy hybrid electric vehicle with a specific requirement tabulated in Table 5.1. The investigated HEV is a parallel hybrid-electric drive with a 100kW generator and 200kW electric motor (see Fig. 5.1a). In this application, the internal combustion engine and electric machines are directly coupled. The electric motor can handle the machine load when the engine is off. The generator charges the battery packages when the engine operates in the propulsion system. As shown in Fig. 5.1b, the battery is charged and discharged through the DC link. The auxiliary power is the required power of other electric components such as cooler, heater, fan, and refrigerator.

The optimum operating speed of the engine is 2800rpm and its maximum speed does not exceed 3200rpm. The generator not only must produce 100kW during continuous operation, but also it should have the capability of generating 200kW for 30sec during operation at over-load condition. A 200kW motor which must be able to deliver 400kW power at overload condition is another electric machine which is designed in this section. The cooling system delivers 70°C mixture of water/glycol at the inlet of each electric machine. The considered liquid flow rate for this HEV is 40lit/min. The maximum diameter of 550 and the minimization of the axial length are other requirements of the design.

5.3. Initial Design

As the PM machines offer a high efficiency in the end of the constant torque and starts of the constant power regions [15], the machine is designed for operation in the constant torque region up to 2800rpm which is the optimum speed of the operation of engine. This selection allows to use the machine high efficiency until the maximum speed of the operation of the engine (i.e., 3200rpm).

The design flowchart of the considered AFSPMSM is shown in Fig. 5.2. The geometry and operation at high temperatures must be investigated for proper design of the machine. Because the use of larger outer diameters permits larger airgap area and consequently more torque production, the design will investigate the largest outer diameter for design purpose.

5.3.1. Geometry determination

Literature show a 100kW AFPMSM can be designed with 155mm stack length and outer diameter of 350mm [247], [249]. The considered inner diameter to locate the end winding is 240mm. If it is assumed that the shaft is occupied 35mm space in the stator to reach the bearing, the considered end winding length is 85mm. The considered inner diameter for the initial design of the AFSPM is 300mm. This allows 115mm space for the end winding length. An equal length is considering for the outer side length of the winding. Considering 5mm thickness for the housing thickness and 115mm end winding length, inner steel diameter can be 430mm. Thus, the machine should be designed in this dimension.

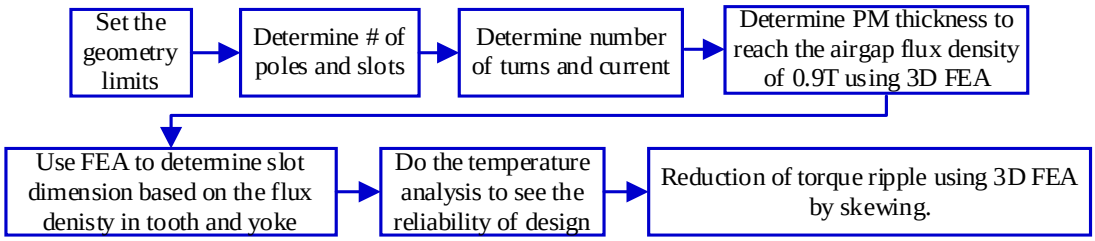

Fig. 5.2. The design flowchart of the studied 100kW interior permanent magnet synchronous machine (IPMSM).

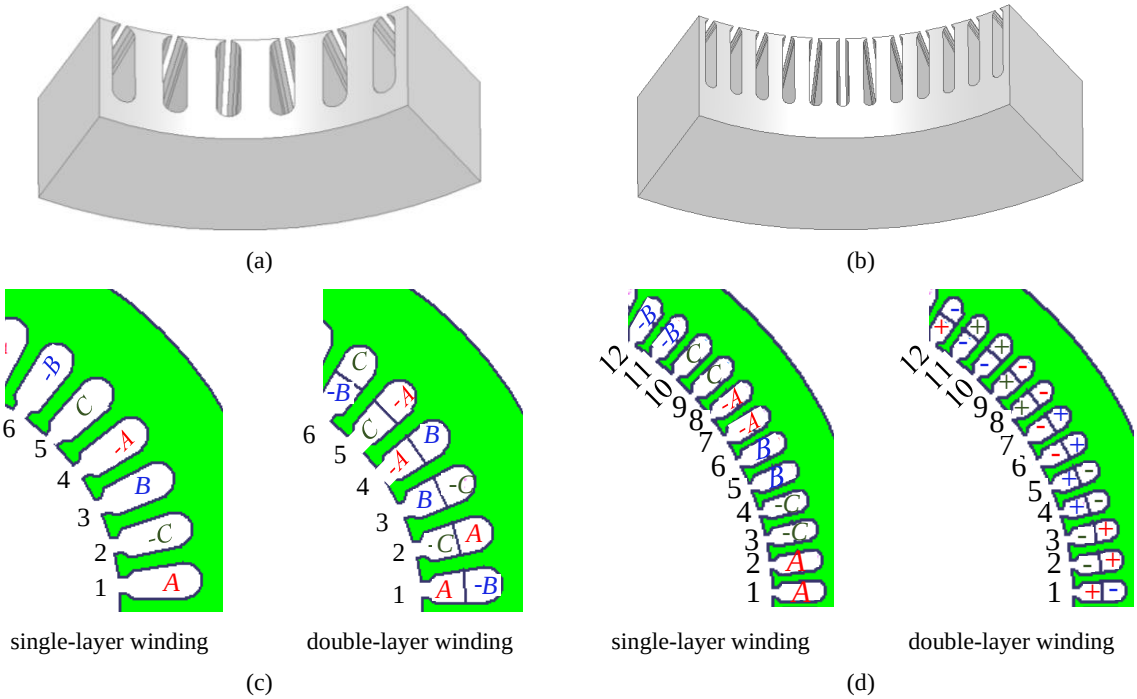

Fig. 5.3. The difference between the tooth thickness and slot width with two different SPPs. (a) a 12 poles stator with 36 slots (SPP=1), the slot width is 12mm. (b) a 12 poles stator with 72 slots (SPP=2), the slot width is 6mm. (c) coil path for a 36-slot stator with single-layer and double-layer windings. (d) winding path for a 72-slot stator with single-layer and double-layer windings.

5.3.2. Determination of number of poles and slots

A higher number of poles reduces the required stator and rotor iron parts and hence higher power density. The operating frequency of the machine is increased by increment of the number of poles.

Consequently, the core losses are increased. For reasonable lamination thicknesses, the optimal operating frequency is normally selected in the range of 250Hz to 500Hz [286]. Given 3200rpm as the maximum speed of the machine, the number of poles can be a value in the range of 10 to 20 poles.

The HEV system operates in high temperature level. The increase of the number of poles reduces the iron volume and consequently increment of the temperature density in the whole machine. For this reason, 12-pole is assumed for the initial design. The use of narrower slots improves the cooling of the machine. However, the use of narrow slots reduces the mechanical strength of the axial flux machine at inner diameter.

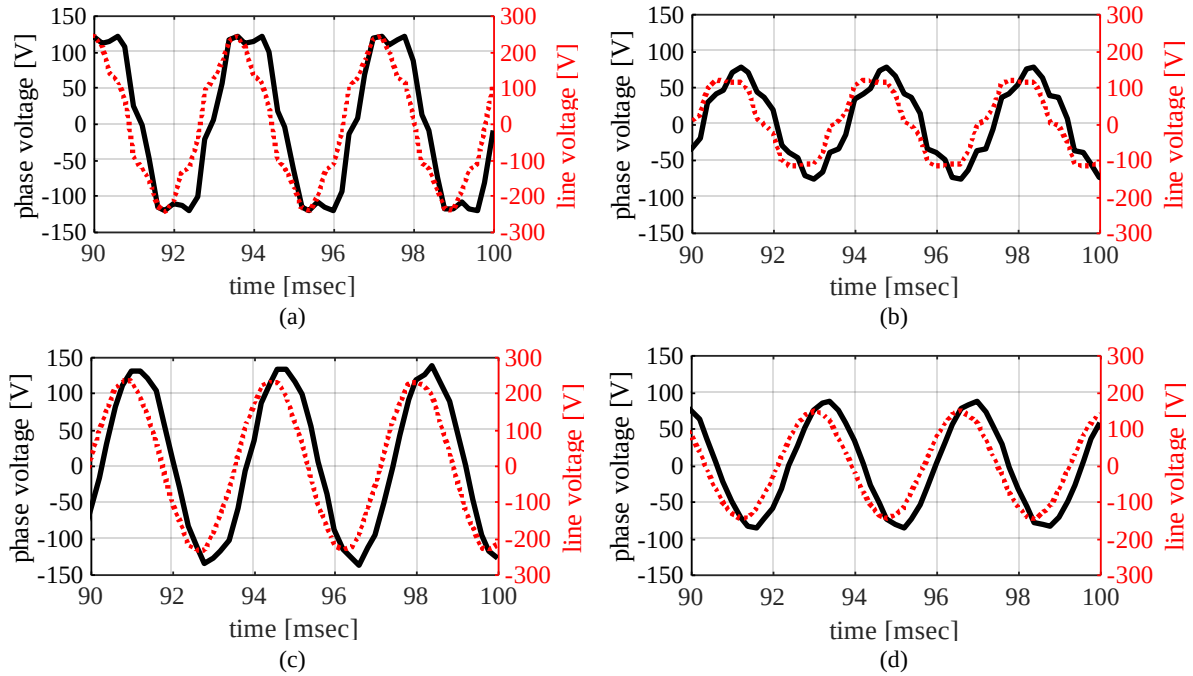

Fig. 5.4. Back-emf analysis of the design with SPP = 1 and 2 and similar skewing angle of 5 degrees. (a) back-emf waveform for SPP = 1 with single-layer winding structure which exhibits 11.11% THD. (b) back-emf waveform for SPP = 1 with distributed winding structure which exhibits 13.65% THD. (c) back-emf waveform for SPP = 2 with single-layer winding structure which exhibits 9.1% THD. (d) back-emf waveform for SPP = 2 with distributed winding structure which exhibits 0.5% THD.

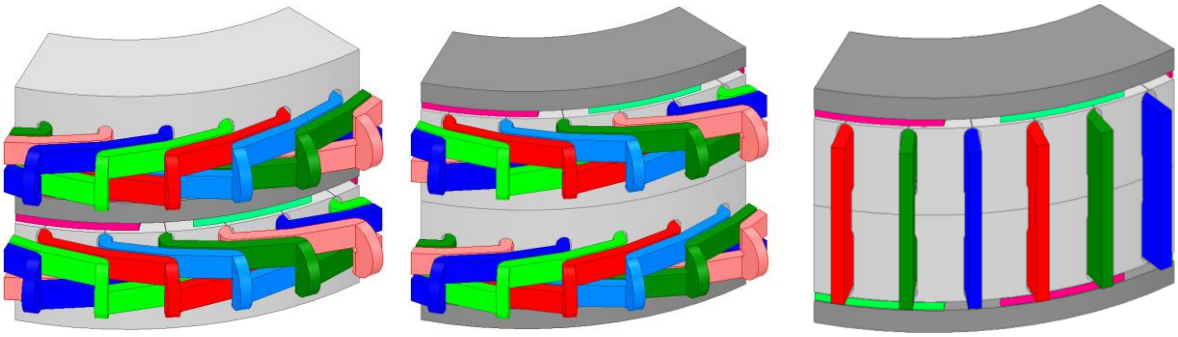

Fig. 5.5. The possible options for design of the machine. (a) double-stator AFSPMSM. (b) double rotor AFSPMSM with distributed winding. (c) double rotor AFSPMSM with ring winding (act as a single-layer winding).

The stator and their possible winding configurations are shown in Fig. 5.3. The back-emd waveform and total harmonic distortions (THD) of these winding structures are reported in Fig. 5.4. According to this figure the THD of the waveforms of the stator with double-layer winding is much smaller than the other winding configuration. The preparation of the winding for this structure is not easy at the inner diameter of the axial flux machine. On the other hand, the preparation of 72 slots in the inner diameter weakens the mechanical strength of the stator. Hence, the total slot per pole (SPP) of one is chosen for initial design of the machine. At the end of the analysis, a comparison between the performance of the machine with these two SPPs is executed for better understanding on the selection of SPP.

5.3.3. Determination of the number of turns and PM volume

The double-rotor and double-stator AFSPMSM are the targeted topologies for design of the system. The consideration of the double-rotor topology with a ring winding is another option for investigation. The shape of each consider design is presented in Fig. 5.5.

Due to the fact that the portion of the core loss at the stator side of the machine is much larger than the rotor, the preparation of a proper cooling system for the stator is mandatory. The availability of the two stators at each side of a rotor in the double-stator topology eases the preparation of a cooling system for the stator. The double-rotor topology can be in two different shapes shown in Figs. 5.5a and 5.5b. The machine shown in Fig. 5.5b benefits from the distributed winding configuration. As shown in Fig. 5.4, distributed windings offer a lower THD compared to the single-layer winding configuration used in Fig. 5.5c. Moreover, the stator of the double-rotor topology shown in Fig. 5.5c is surrounded by the windings which hardens the preparation of the cooling system for the stator. Hence, the presented topologies shown in Figs. 5.4a and 5.4b are considered for further analysis and selection of the appropriate option.

For further analysis the 12-poles machine with the SPP of one and distributed winding structure at the stator side is prepared in the form of double-stator and double-rotor topologies (i.e., Figs. 5.5a and 5.5b). The windings of each side of a stator in each topology will be connected in series with each other. The machine will be supplied by a 700V battery package. Thus, the output line voltage of the machine should be slightly larger than DC-link voltage to be able to charge the battery. The assumption of having 700V as the peak of line voltage means that the peak of phase voltage for each stator is equal to:

$$V_{ph,peak} = \frac{1}{2}\frac{V_{LL}}{\sqrt{3}} = \frac{1}{2}\frac{700}{\sqrt{3}} = 202\text{V} \tag{5-1}$$

The number of turns per phase (N_{ph}) for each stator is obtained by (5-2) [247].

$$N_{ph} = \frac{p \times V_{ph,peak}}{B_{ag} \times f \times (1 - \lambda_D^2) D_O^2} \tag{5-2}$$

In (5-2), p represents the pole-pairs of the machine. The other diameter and average airgap flux density are shown by D_O and B_{ag}, respectively. The ratio of the inner diameter (D_i) over D_O is shown by λ_D. For a 12-pole machine with outer diameter of 430m and inner diameter of 300mm, the number of turns per phase should be equal to 96, to reach phase voltage of 202V at airgap flux density of 0.9T. Therefore, the number of turns per phase per slot for double-layer winding (Fig. 5.3c) is equal to 4 turns.

The total power of the machine is 100kW, and the rms phase voltage values is $\frac{700}{\sqrt{2}\sqrt{3}} = 285\text{V}$. Therefore, the rms current of the machine by consideration of 96% efficiency (η) and 96% power factor (PF) is obtained as follows:

$$I_{ph} = \frac{P_{out}}{3 \times \eta \times PF \times V_{ph}} = \frac{100 \times 10^3}{3 \times 0.96 \times 0.96 \times 285} \approx 130\text{A} \qquad (5\text{-}3)$$

The calculation of the number of turns and current allows to determine the slot size of the stator. 5A/mm^2 current density with slot fill factor of 0.45 are safe values to make sure that the machine is cool. These values are achieved by 8mm and 38mm slot width and heights. These values can be updated later during the second step of the design. Equal back-iron of 15mm is considered for both rotor and stator at initial stage to be able to run 3D FEA analysis to determine the size of PM.

A 3D FEA analysis is run to find the required PM thickness which gives 0.9T average flux density at the middle layer of the machine while the magnet arc remains constant. It is seen that this value is achieved by 6mm PM thickness when the arc of the PM covers 70% of the pole-pitch. Note that the investigated PM type is SmCo28 PM material. The SmCo is chosen to reduce the risk of the demagnetization due to high temperature. The type of the PM can be changed to higher grades of NdFeB in the second design to reduce cost, if the rotor temperature in the experimental tests become lower than the 145°C which is considered for the design.

5.3.4. Determination of the machine topology

The initial loading results of the designed machine shows the rated torque in the considered geometry is achieved by injection of 165A. Hence, the width of the slots is increased from 8mm to 10mm to keep the current density constant. In this section, this amount of current is injected to the winding for collecting the loading data for different machine topologies. The effect of the stator and rotor back-iron, PM thickness, and PM arc are studied. The result of the analysis shows the capability of the double-stator topology in generation of the larger torque/power density compared to the double-rotor structure.

The variation of the torque and line voltage with the stator and rotor thicknesses of each design are presented in Figs. 5.6 and 5.7. Although Fig. 5.6, shows the torque production drop of the double-stator design in smaller stator back-iron, it demonstrates the double-stator can produce larger

torque/power in an optimal size of stator back-iron. According to Fig. 5.7, the performance of the double-rotor design is highly sensitive to the rotor thickness and in the larger rotor thicknesses the performance of this machine becomes close to the double-stator design performance. Fig. 5.8 shows that the torque capability production of the double-stator design in larger PM volumes is better than the double rotor design. It occurs due to the saturation of the rotors in the double-rotor topology. The results of the increment of the PM arc which is presented in Fig. 5.9 confirms the weakness of the double-rotor design in larger amount of PM.

According to the obtained results from 3D FEA analysis the double stator topology offers better electromagnetic performance in different geometries. Moreover, because it shares two area of two stators at its outer surface, the provision of the cooling system for this machine is easier. Considering these facts, it seems rational to select the double-stator to select the double-stator topology for this application.

5.3.5. Consideration of the skewing effect

The skewing effect is used to improve the torque ripple of the system. A view of the skewed rotor is presented in Fig. 1.9a. The results of the torque and torque ripple variation in different skewing angles presented in Fig. 1.9b demonstrate the trade of between the torque ripple and average produced torque. On the basis of the collected data, 5 degrees skewed rotor which provides a high torque with a small torque ripple is chosen for the designed AFPMSM.

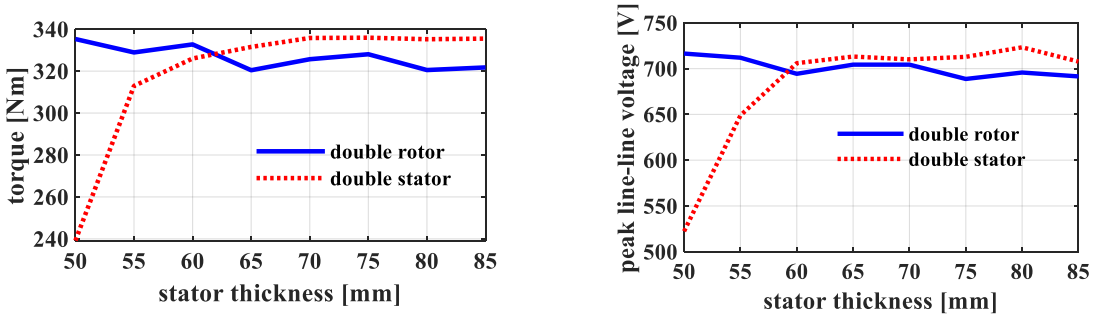

(a) (b)

Fig. 5.6. The 3D FEA results for comparison of the effect of the variation of stator back iron on the torque and induced voltage of both designs at 2800rpm operation speed and current of 165A. PM arc ratio, PM thickness, skewing angle are 0.7, 6mm, and 5 degrees, respectively. (a) torque. (b) induced voltage.

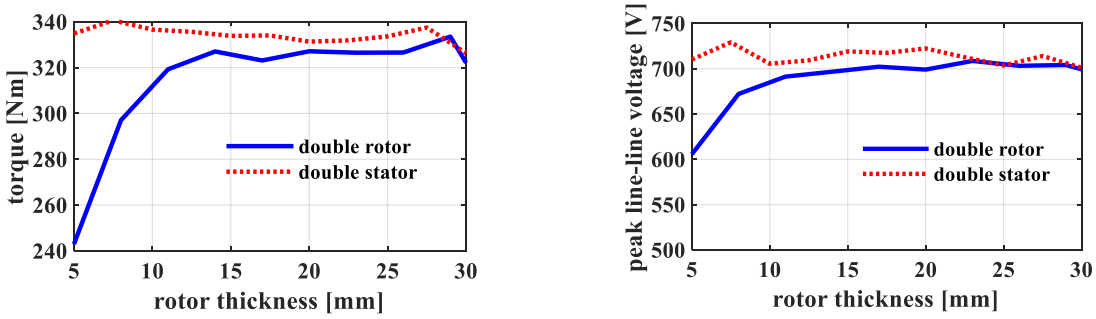

(a) (b)

Fig. 5.7. The 3D FEA results for comparison of the effect of the variation of rotor back iron on the torque and induced voltage of both designs at 2800rpm operation speed and current of 165A. PM arc ratio, PM thickness, skewing angle are 0.7, 6mm, and 5 degrees, respectively. (a) torque. (b) induced voltage.

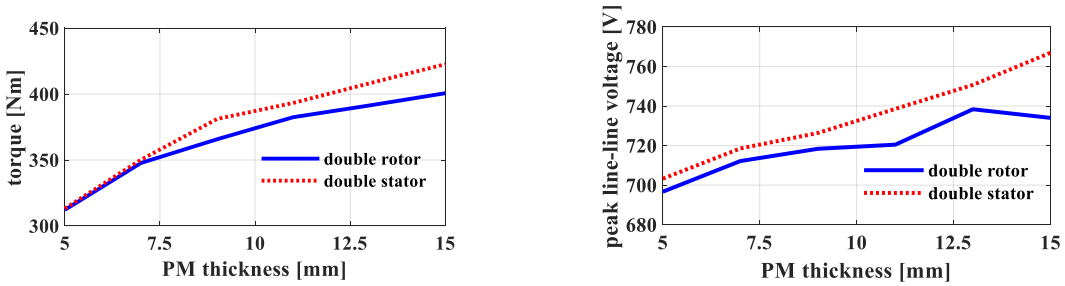

(a) (b)

Fig. 5.8. 3D FEA results for comparison of the effect of the variation of PM thickness on the torque and induced voltage of both designs at 2800rpm operation speed and current of 165A. PM arc ratio and skewing angle are 0.7, and 5 degrees, respectively. The stator and rotor thicknesses are 60mm and 15mm, respectively (a) torque. (b) induced voltage.

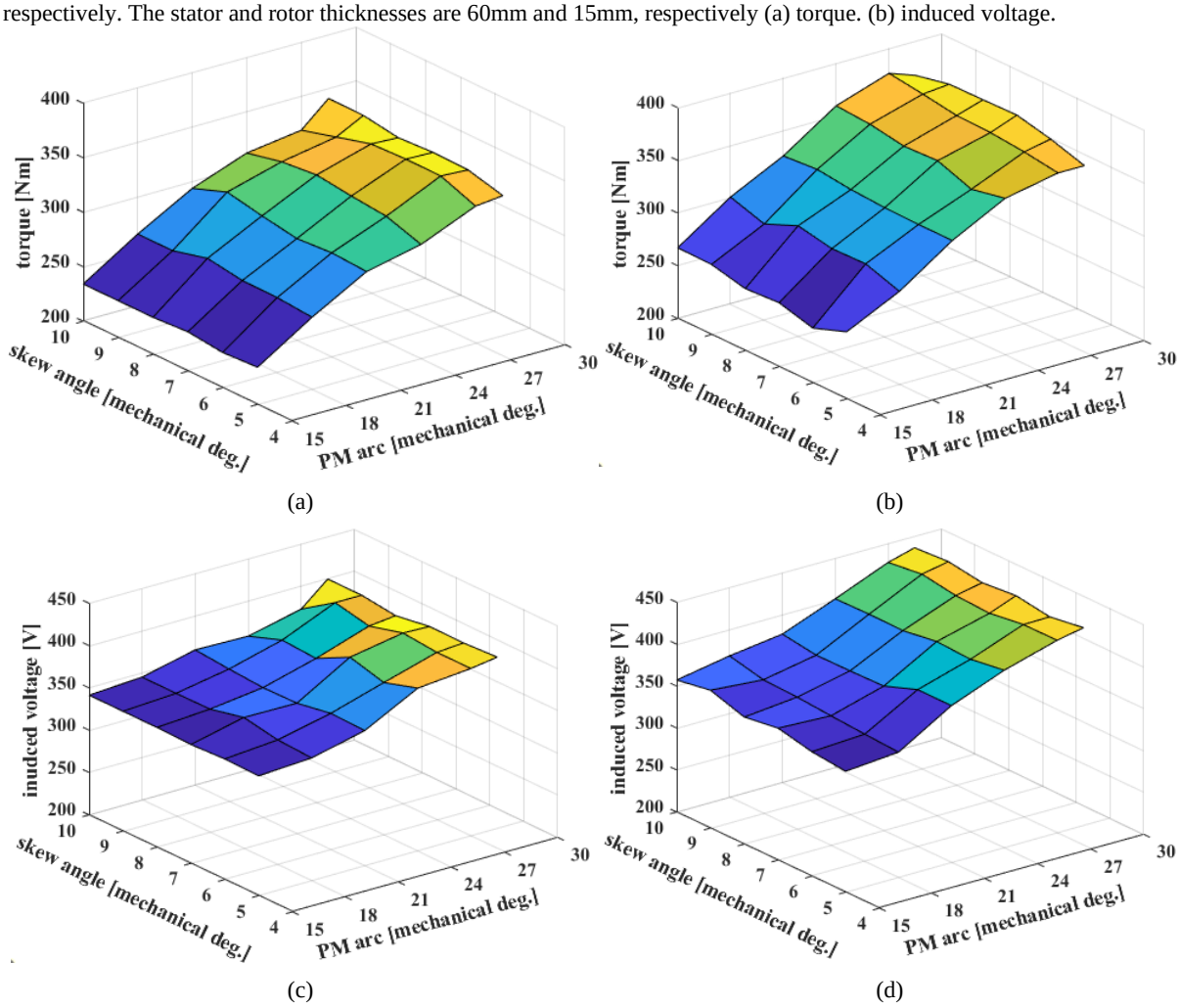

(a) (b)

(c) (d)

Fig. 5.9. 3D FEA results to see the effect of PM arc and skewing angle on the torque in constant stator and rotor lengths for both designs. (a) double rotor torque. (b) double stator torque. (c) double rotor induced voltage (d) double stator induced voltage.

5.3.1. Determination of the slot size

The determination of the initial size of the machine based on the current and assumption of slot width and height values to reach a targeted current density with a specific fill factor is not a proper way of finalization of slot dimension. Literature shows an optimum IPMSM designs have a flux density of 1.2-1.4T in their back-iron [277]. These values can be a proper option for the design of the AFSPMSM.

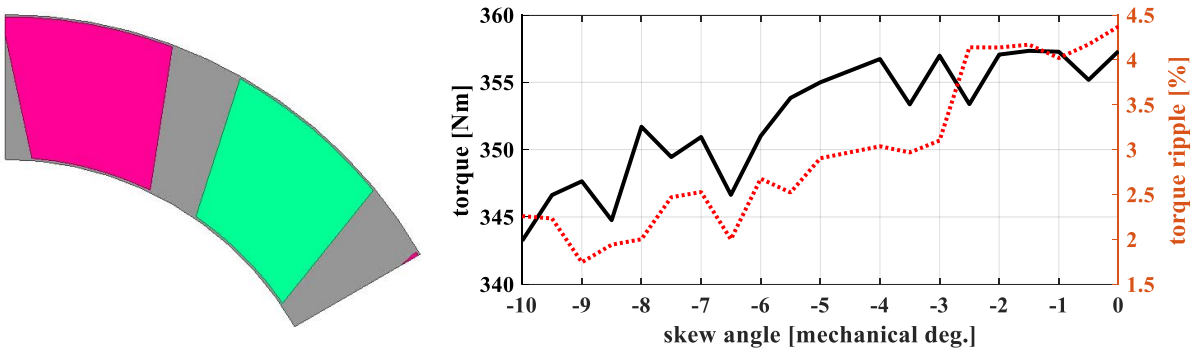

(a) (b)

Fig. 5.10. A view of the skewed PMs on the rotor and the effect of skewing on torque and torque ripple. (a) skewed rotor view. (b) 3D FEA results of the torque and torque ripple in different skewed angles.

The larger slot width and height are led to the increase of the core reluctances and consequently iron losses. The reduction of the height of slots allows to achieve a higher power density machine due to the decrease of axial-length. The current density in the slot can remain constant when the slot width is increased, and its height is reduced. Therefore, a 3D FEA analysis under full-load operation of the machine is executed and the width and heights of the slots are increased and decreased, respectively. The total slot area and the back-iron length are the constant values when the width and heights of the slot are varied. The torque values for several pairs of slot width and height in a constant current and current density is presented in Table 5.2. Based on the presented results in this table, a slot with 12mm width and 28mm height which offers the lowest torque ripple and highest power is considered for the machine. The flux density distribution contour is shown in Fig. 5. 11.

Fig. 5.11c shows the tooth flux path is not equal to the back-iron which means the machine has not been properly optimized. For this reason, some further analysis on the size of the slots and back-iron is carried out. It is seen that the oval shape of the end of slots tightens the flux path area by increment of the of the slot width. For this reason, the optimization results presented in Table 5.2 with those slots are not reliable. The shape of the slots is changed, and the increment of the slot width is continued to reach approximately same flux pathing area at the middle layer of the machine. The final shape of the slots and the flux density distribution in the final design is presented in Fig. 5. 12.

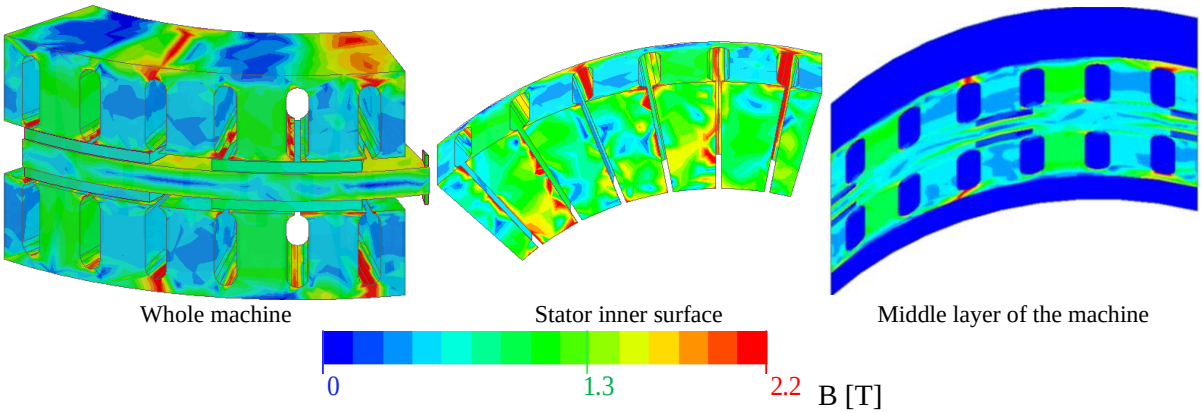

Fig. 5.11. The flux density distribution on different parts of the machine during operation at full load.

TABLE 5.2. EFFECT OF VARIATION OF SLOT HEIGHT AND WIDTH ON TORQUE AND CORE LOSS

Slot dimension	8mm width & 44mm height	10mm width & 35mm height	12mm width & 28mm height	14mm width & 22.3mm height	15mm width & 20.5mm height
Torque [Nm]	338.73	322.28	345.95	324.10	320.89
Torque ripple [%]	17.5	16.09	14.21	18.36	16.91
Torque [Nm] – dq	356.79	342.01	367.78	336.62	341.67
Torque ripple [%] - dq	3.38	2.38	2.54	2.95	1.2
Core loss [W]	735.27	736.71	721.75	610.88	645.01
Efficiency [%]	97.05	96.94	97.16	97.03	97.03

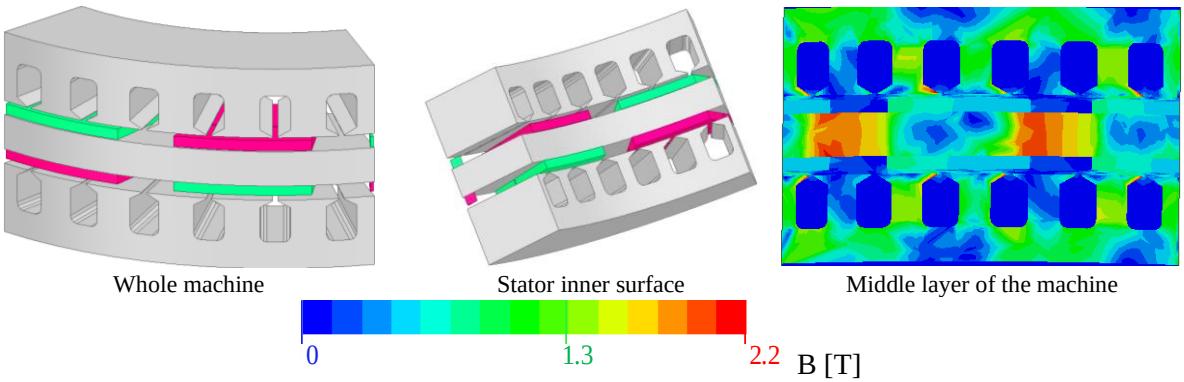

Fig. 5.12. The 36-slot design slot shape form the outer and inner views as well as the flux density distribution in the core.

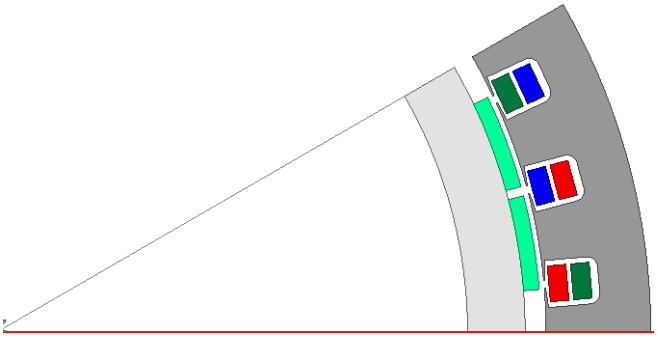

Fig. 5.13. The prepared 2D FEA model of the radial flux machine for checking the calculated solid loss.

The geometry and performance parameters of 36 slot designs are presented in Tables 5.3. The analysis of the slid loss is highly dependent on the mesh sizes in rotor and PM parts. To show that the calculated solid loss in 3D simulation of the axial flux machine is reliable, a radial flux machine, shown in Fig. 5.13, is simulated and the value of the obtained solid losses are compared with each other. The considered airgap radius is equal to the radius of the middle layer of the axial-flux machine. The outer diameter and stator inner diameter are 500mm and 420mm, respectively. The slot height is the dimensions of the slots, stator, and rotor back-iron are equal to their respective dimensions in axial flux design. The 2D FEA analysis shows that the summation of the eddy current losses on the rotor and PM are equal to 730W. This value in the designed axial flux machine is 507W.

5.3.2. Thermal analysis of the design

The temperature analysis of the design is carried out using the thermal analysis module of the Motor-CAD software. This software does not have the capability of the analysis of the axial flux machines. For this reason, a dual radial flux model of the designed AFSPMSM is prepared for thermal analysis. The considered thermal model can provide an acceptable estimation when the considered stator back surface area and the amount of the loss in the radial flux design are equal to the axial flux machine. However, this model cannot be considered as an accurate model because it cannot properly estimate the rotor temperature which is located between two stators in the axial flux design.

The Motor-CAD thermal module corrects the FEA results of the temperature analysis using the experimental data and engineering experiences [163]. This capability of the software allows to estimate the temperature with an acceptable accuracy.

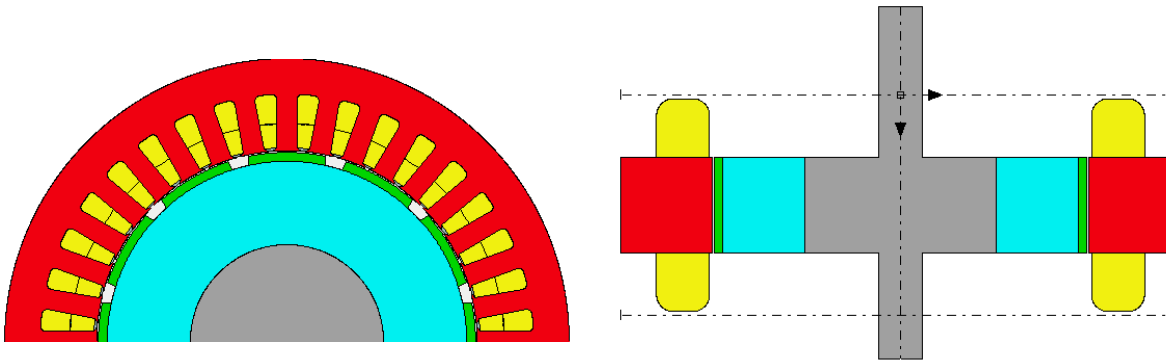

Stator lam diameter = 380 mm
Stator bore diameter = 256 mm
Airgap length = 1 mm

Stack length = 65 mm
PM thickness = 6 mm
Tooth width = 14 mm

Fig. 5.14. The geometry of the model in motor-cad.

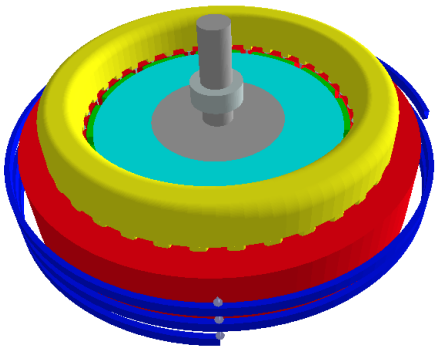

Fig. 5.15. The 3D view of the prepared dual radial flux machine for the designed AFSPMSM. The blue spiral pipes are the considered fluid path around the stator.

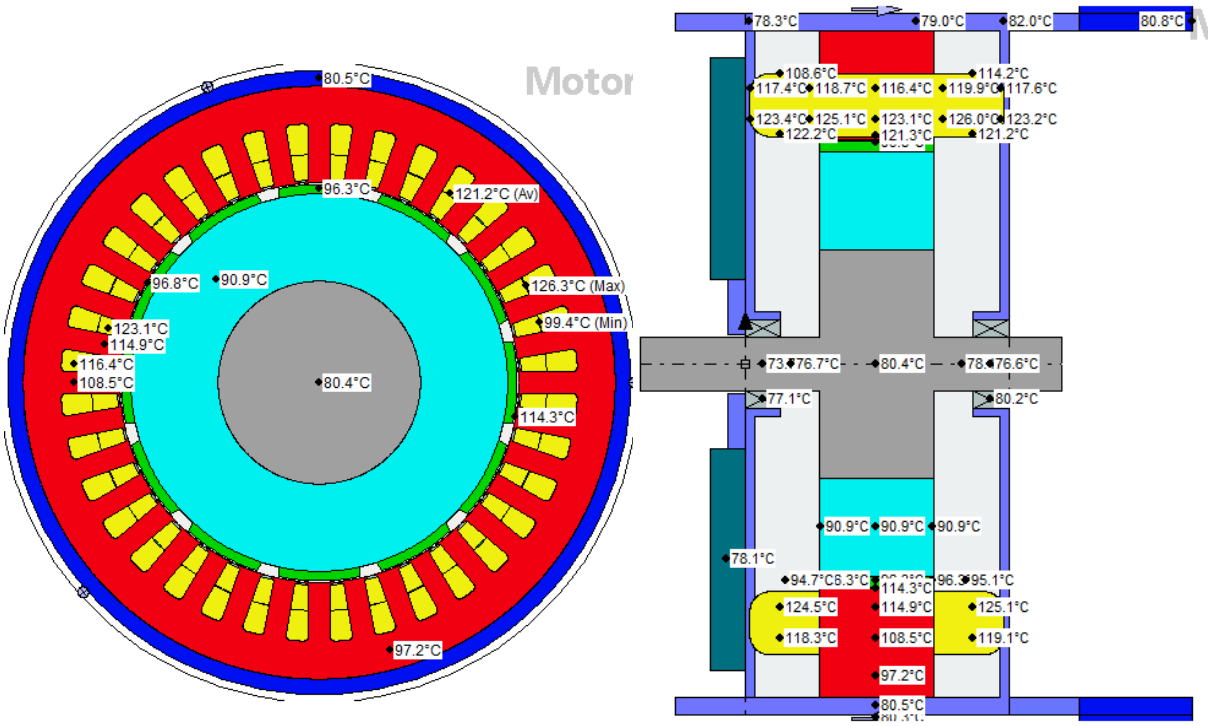

(b) (c)

Fig. 5.16. Thermal analysis results. (a) overall geometry. (b) cross-section view. (c) axial view

TABLE 5.3. GEOMETRY, PREFORMANCE AND MATERIALS OF THE DESINGED 100KW MACHINE.

Geometry				
Number of poles	12	Number of slots		36
Outer diameter [mm]	420	Inner diameter [mm]		300
Each stator height [mm]	40	Rotor thickness [mm]		20
PM thickness [mm]	6	PM arc [deg]		21
Skew angle of PM [deg]	5	Number of turns per phase per slot		4
Stator slot opening height [mm]	0.5	Number of turns per phase		48
Stator slot depth [mm]	16	Stator slot opening width [mm]		3
Airgap length [mm]	2.2	Fill factor		0.49
Materials				
PM relative permeability	1.0797	PM bulk conductivity [S/m]		1252800
PM magnetic coercivity [A/m]	-684169.12	PM type: SmCo20		
Winding: copper		Rotor and stator material: M250-50		
Performance parameters				
Rated torque @ rated current [Nm]	349.91	Rated current [A]		140
Torque ripple [%]	10.57%	Current density [A/mm^2]		6
Rated speed [rpm]	2800	Power @ rated current [kW]		102.6
Peak line voltage [V]	730.3	Copper loss [W]		1951.4
Core loss [W]	524.97	Solid loss [W]	Axial model	507.5
			Radial model	733
Total axial length [mm]	116	Efficiency [%]		97.17

Note that, only one of the stators of the designed AFSPMSM are modelled in the Motor-CAD. To prepare the dual model of the designed AFSPMSM the following items are taken into account:

- Similar slot area to have a same current density
- Similar stack length
- Similar back iron and tooth height
- Similar surface area per outer stack (Just for a single stator)
- Similar PM volume

Fig. 5.14 shows and summarizes the cross-sections and considered dimensions for the radial flux model. It is assumed that the stator of the radial-flux machine is surrounded with the fluid pipes of a spiral cooling system which carries 80°C mixture of the glycol/water at its inlet. The considered flow rate of 40lit/min is assumed for the fluid. A 3D view of the prepared radial flux model with fluid pipes is shown in Fig. 5.15.

NEMA is categorized the motor winding insulation to four classes consisting of class A. B, F, and H. The winding maximum insulation temperature for class A, B, F, and H are 105°C, 130°C, 155°C, and 180°C. The Class F insulation standard allows operating temperature of 145°C with the hotspot temperature of 155°C.

According to the presented thermal analysis results shown in Fig. 5.16, the maximum temperature of the winding is 126°C which meets the required temperature for the Class B and F insulations. Note that this temperature is very closed to the boundary of the hotspot temperature for class B insulation. So, class F insulation is selected for the winding of the machine. The 20°C temperature with the allowable hotspot temperature allows to reach the overload within the insulation temperature limit.

5.4. Further Analysis

The effect of the low radial permeability in tape-wound stator is investigated to see the possible performance drop by investigation of this effect. To simulate this effect an anisotropic material with the relative permeability of 300 in theta and z axes are defined. The radial relative permeability is updated for different stacking factors using (5-4).

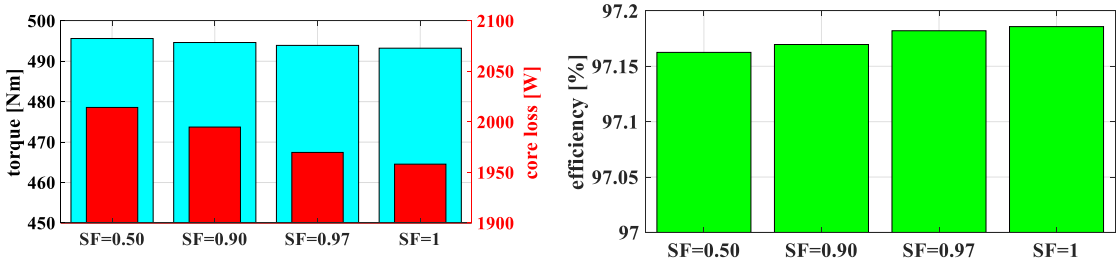

(a) (b)

Fig. 5.17. 3D FEA results to show the effect of the variation of the radial relative permeability on the performance of the machine the injected current and frequency of operation in all studied stacking factors are 165A and 280Hz, respectively.

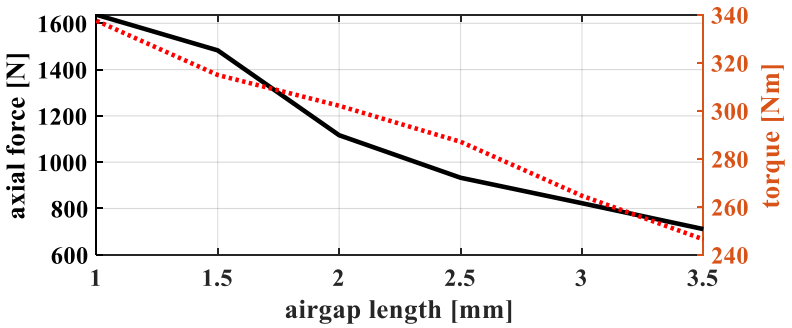

Fig. 5.18. Axial force and torque of the double stator design in different airgap lengths.

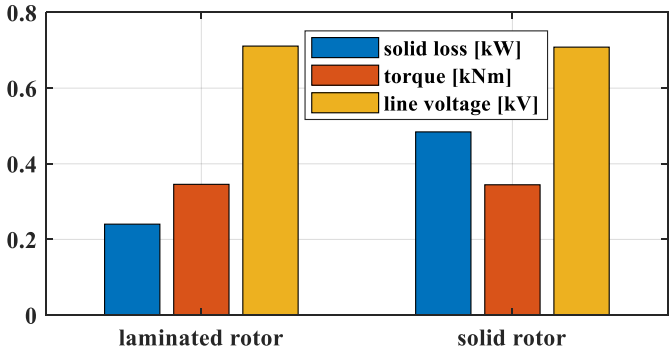

Fig. 5.19. Investigation of the difference between the solid and laminated rotor for double stator design.

$$\text{relative radial permeability} = \frac{1}{1 - SF} \tag{5-4}$$

Fig. 5.17 is to analyse the effect of the low radial relative permeability of the laminated stator. The presented results in this figure demonstrate that the machine performance is changed slightly in larger stacking factor due to the variation of the relative permeability.

Another phenomenon which is investigated in the machine is the rotor stiffness. For this purpose, the negative axial-force applied to the stator at full-load condition is obtained (see Fig. 5.18). According to (5-5), the force is defined as the integration of the flux density (B_{z-axis}) over the entire surface at the stator. Fig. 5.18 shows that the negative axial force on the stator is about 1600N which should be investigated during selection of bearing.

$$F_{z-axis} = \frac{0.5}{\mu_0} \oiint B_{z-axis}^2 ds \tag{5-5}$$

The effect of the consideration of the solid rotor instead of the laminated rotor is studied in the full-load operation of the machine when the machine is excited with 140A current source and rotates at 2800rpm. The reported solid loss in the laminated rotor condition is the PM eddy current losses. In the solod rotor condition, the reported solid loss is the summation of the rotor and PM ohmic losses as a result of eddy current. As shown in Fig. 5.19, the solid loss at solid rotor condition is 230W larger than the laminated rotor condition. In this power level, this amount of extra loss is acceptable because the solid rotor offers better mechanical strength.

5.5. Compare Performance of the Machine with Other Possible Options

5.5.1. 72-slot design analysis

Comparison of the back-emf waveforms of the distributed windings in SPP of 1 and 2 in Fig. 5.4 demonstrates that the 72-slot design has more sinusoidal with a small THD back-emf. It allows to have a higher power factor and possibly better efficiency during operation. In this subsection, a 72-slot AFPMSM is designed, and its performance is compared with the 36-slot design to see the effect of SPP on the performance of the machine.

The 3D FEA analysis shows that there is an opportunity of the increment of the stack length when the machine SPP is changed. This opportunity is achieved because of the smaller peak voltage of the machine with 72-slot. The increment of the stack length provides higher power in a same current density in the available space. On the other hand, it allows to reduce the slots current density and get a same power as the 36-slot design.

The updated dimension of the machine with increase of the number of slots are reported in Table 5.4. It shows the rated current of the machine with the update of the geometry is reduced for 10A which leads to the reduction of the copper loss. The loss reduction allows to have a cooler machine compared to the 36-slot design.

The comparison of the thermal analysis presented in Fig. 5.16 with the results of the 72-slot design shows that the 72-slot is a cooler machine. The winding hotspot in the 72-slot design is approximately 10°C less than the 36-slot design. Because the hotspot temperature of the Class F wires is 155°C, it is possible to use the machine at the rated power.

A transient analysis for 30 seconds overload is conducted to see if the machine is capable of the handling the overload for meeting the HEV requirement. The transient analysis assumes the inlet coolant temperature of 70°C, flow rate of 40lit/min, and ambient temperature of 80°C. Fig. 5.21a shows the hotspot temperature of the windings after 30 minutes operation reaches 300°C which means the machine has not been designed for continues operation at that power level. According to Fig. 5.20, the hotspot temperature of the winding when the machine operates at its rated point is 110°C. If it is assumed that the overload condition is occurred when the machine operates at its rated condition (i.e., 110°C), Fig. 5.21b proves the machine is capable of handling the 2pu overload for 95secs which meets the HEV requirement. Note that the hotspot temperature of the class F insulation is 155°C.

TABLE 5.4. GEOMETRY, PREFRORMANCE AND MATERIALS OF THE DESINGED 100KW MACHINE WITH 72 SLOTS.

Geometry				
Number of poles	12	Number of slots		72
Outer diameter [mm]	430	Inner diameter [mm]		300
Each stator height [mm]	40	Rotor thickness [mm]		20
PM thickness [mm]	6	PM arc [deg]		21
Skew angle of PM [deg]	5	Number of turns per phase per slot		2
Stator slot opening height [mm]	0.5	Number of turns per phase		48
Stator slot depth [mm]	16	Stator slot opening width [mm]		3
Airgap length [mm]	2	Fill factor		0.41
Materials				
PM relative permeability	1.0797	PM bulk conductivity [S/m]		1252800
PM magnetic coercivity [A/m]	-684169.12	PM type: SmCo28		
Winding: copper		Rotor and stator material: M250-50		
Performance parameters				
Rated torque @ rated current [Nm]	352.5	Rated current [A]		130
Torque ripple [%]	6.7%	Current density [A/mm^2]		5.45
Rated speed [rpm]	2800	Power @ rated current [kW]		103.36
Peak line voltage [V]	740.5	Copper loss [W]		1471.8
Core loss [W]	577.4	Solid loss [W]	Axial model	172.07
			Radial model	180.89
Total axial length [mm]	116	Efficiency [%]		97.89

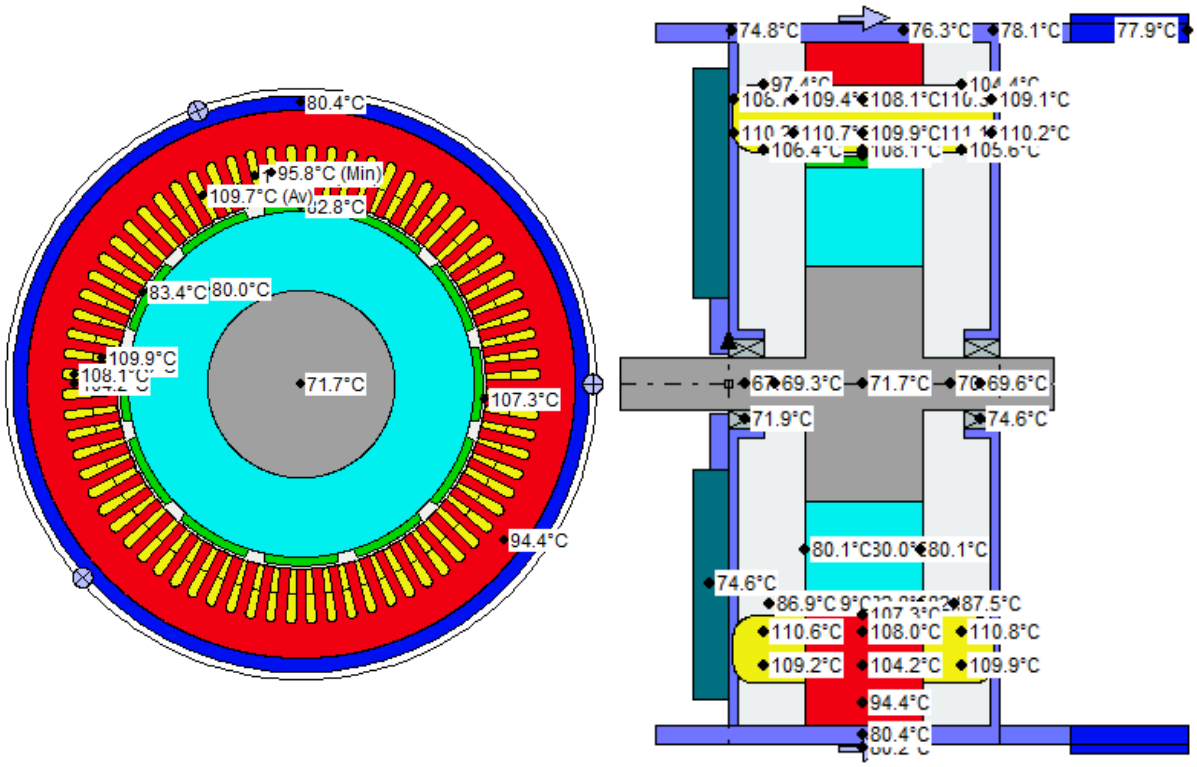

Fig. 5.20. The equivalent radial flux model of the designed 72-slot machine to check the designs temperature.

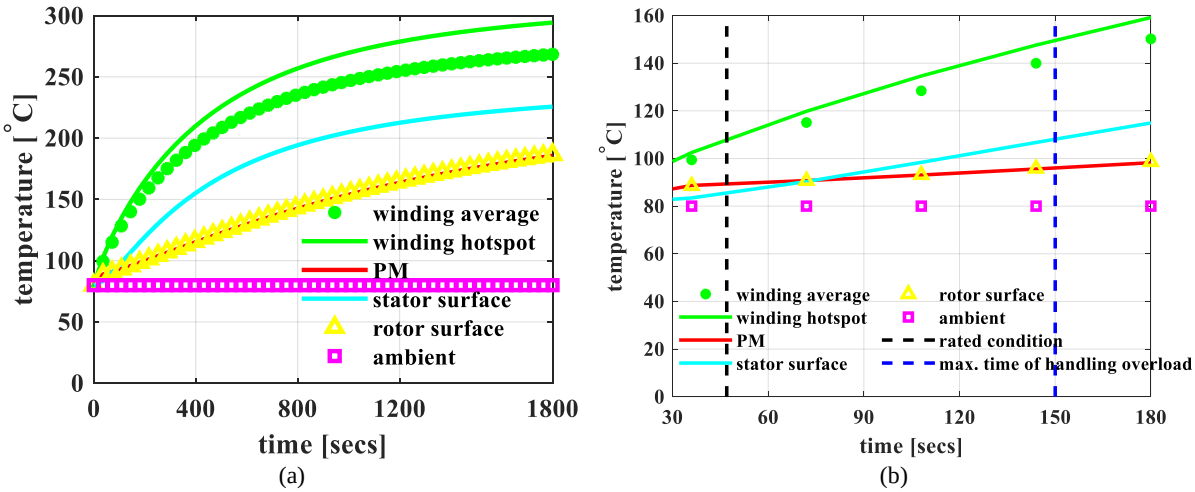

(a) (b)

Fig. 5.21. The temperature transient during the time when it operates at 2pu overload condition. (a) 30 minutes transient. (b) transient from 110°C to 160°C at 2pu overload.

5.5.1. Performance of the designed axial-flux machines over a wide range of torque and speed

The designed axial flux machines are analysed through a wide range of torque and speed. The data *dq*-axes flux is collected from 3D FEA analysis in different *dq*- axes currents. The flux mapping technique is used to plot the efficiency map and power map presented in Figs. 5. 22 and 5. 23. To understand the effect of the mechanical loss 0.5% of the maximum torque is assumed as a mechanical loss torque at each speed. The presented results in Fig. 5. 22(a) and (b) are the 36-slot machine

performance parameters when the mechanical losses are ignored. The efficiency map and power map with consideration of the mechanical loss are presented in Figs. 5.22 (c) and (d), respectively. Comparison of the Figs. 5. 22 and 5. 23 shows that the AFPMSM with 72-slot is capable of offering higher power and larger constant torque region.

The effect of airgap on the variation of the solid loss in both AFPMSMs is analyzed. Fig. 5. 24 demonstrates that in both machines the increment of the length of airgap reduces the solid loss as well as the torque. The lower solid loss of the 72-slot in all airgap lengths is useful to reduce the PM temperature and protect them against demagnetization. The comparison of the full-load and no-load losses presented in Figs. 5.24 (b) and (d) demonstrates the importance of the selection of the optimum number of slots. Fig. 5.24(d) shows the largest portion of the rotor solid losses is resulted from the slotting effect.

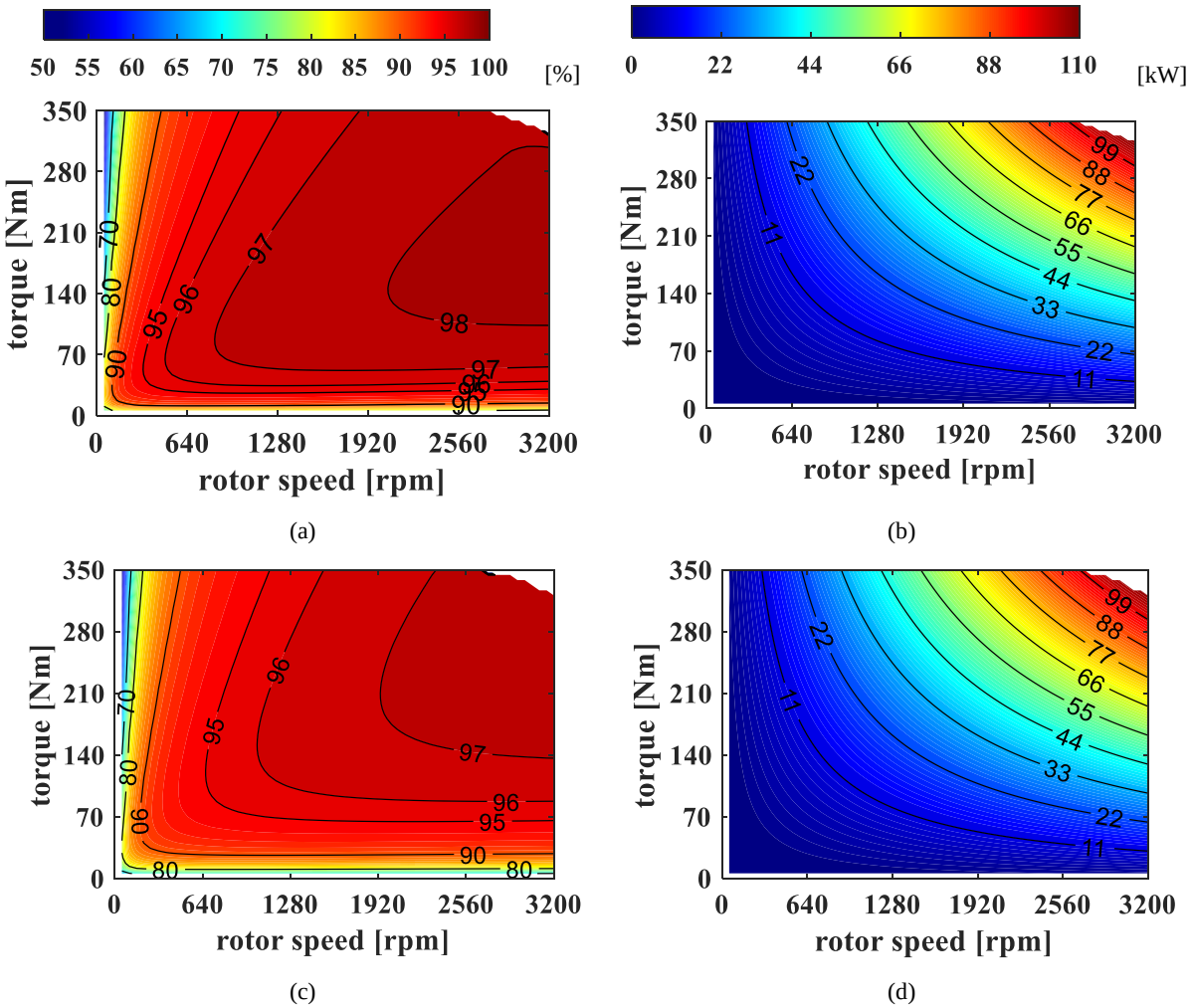

Fig. 5.22. The efficiency map and power maps of the designed axial flux machines. (a) efficiency map of 36-slot design, (b) power map of the 36-slot design, (c) efficiency map of 36-slot design with consideration of mechanical loss. (d) power map of the 36-slot design with consideration of mechanical loss.

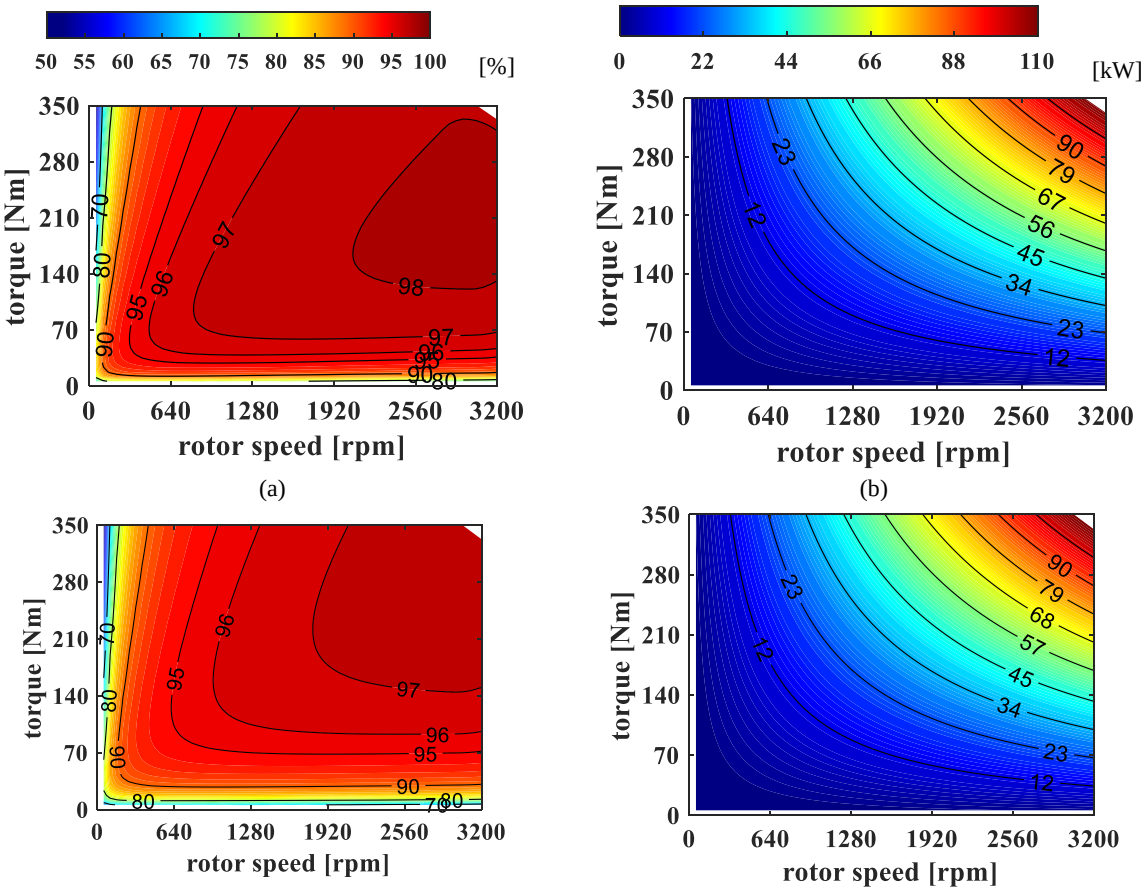

Fig. 5.23. The efficiency map and power maps of the designed axial flux machines. (a) efficiency map of 72-slot design, (b) power map of the 72-slot design, (c) efficiency map of 36-slot design with consideration of mechanical loss. (d) power map of the 72-slot design with consideration of mechanical loss.

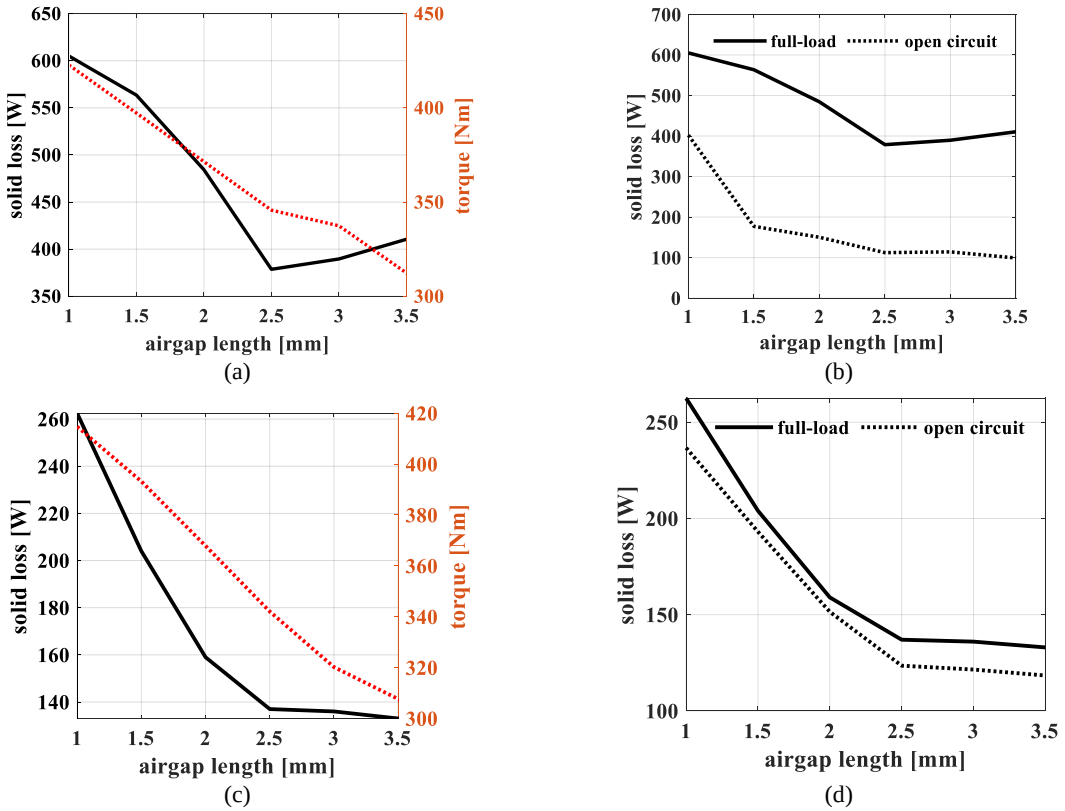

Fig. 5.24. The variation of the rotor solid loss and torque with airgap. (a) and (b) 36-slot design. (c) and (d) 72-slot design.

5.5.2. 100kW radial flux machine

The maximum available outer diameter (500mm) is assumed for the initial design of an equivalent radial-flux machine. The considered tooth thickness, back-iron, and equal current density for the designed AFPMSM is considered for the design of radial-flux machine. The radial flux machine geometry and performance parameters are tabulated in Table 5.5. According to the presented results in this Table, it is possible to reach the 100kW machine with a same current density as the AFPMSM when the assumed axial length is 150mm. The end-winding length is the main reason of having large axial-length compared to the designed axial-flux machines. The presented temperature analysis results (Fig. 5.25) at maximum load shows that the design meets the Class F requirement.

The designed FFPMSM not only has a larger power density in terms of volume compared to the both 36-slot and 72-slot AFPMSMs, but its temperature is also at the boundary of the class F insulation which endangers threatens the machine safe operation. The temperature issue can be addressed by reduction increment of the stack length and reduction of the current density. However, this change will lead to increment of the machine volume.

Table 5.6 is to compare the material volume and cost of these designs. This table shows the 72-slot design has a smaller weight and volume compared to other designs. The advantageous of the 72-slot design are not limited to its higher power density and efficiency. It delivers 100kW power in a lower temperature. Thus, the best option for construction is the 72-slot design. The smaller torque ripple and its THD are other superiorities of the 72-slot AFPMSM.

TABLE 5.5. GEOMETRY, PREFRORMANCE AND MATERIALS OF THE DESINGED 100KW RADIAL-FLUX MACHINE WITH 72 SLOTS.

Geometry			
Number of poles	12	Number of slots	72
Outer diameter [mm]	480	Inner diameter [mm]	377
Stator slot depth [mm]	32	Shaft diameter [mm]	300
PM thickness [mm]	6	PM arc [deg]	21
Skew angle of PM [deg]	5	Number of turns per phase per slot	3
Stator slot opening height [mm]	0.5	Number of turns per phase	72
Airgap length [mm]	2	Stator slot opening width [mm]	3
Materials			
PM relative permeability	1.0797	PM bulk conductivity [S/m]	1252800
PM magnetic coercivity [A/m]	-684169.12	PM type: SmCo20	
Winding: copper		Rotor and stator material: M250-50	
Performance parameters			
Rated torque @ rated current [Nm]	342.1	Rated current [A]	150
Torque ripple [%]	7.2%	Current density [A/mm^2]	5.42
Rated speed [rpm]	2800	Power @ rated current [kW]	100.25
Peak line voltage [V]		Copper loss [W]	2675
Core loss [W]	754	Solid loss [W]	363
Total axial length [mm]	150	Efficiency [%]	96.3

TABLE 5.6. COMPARISON OF THE DESINGED MACHINES IN TERMS OF WEIGHT AND VOLUME

	AFPMSM 36-slot		**AFPMSM 72-slot**		**RFPMSM 72-Slot**	
	Volume [lit]	**Weight [kg]**	**Volume [lit]**	**Weight [kg]**	**Volume [lit]**	**Weight [kg]**
Stator iron	3.78	28.91	3.54	27.08	2.98	22.86
Rotor iron	0.18	1.37	0.18	1.37	2.08	15.98
Permanent magnet	0.6	4.50	0.6	4.50	0.372	2.79
Copper	1.54	13.79	0.93	8.38	1.25	11.12

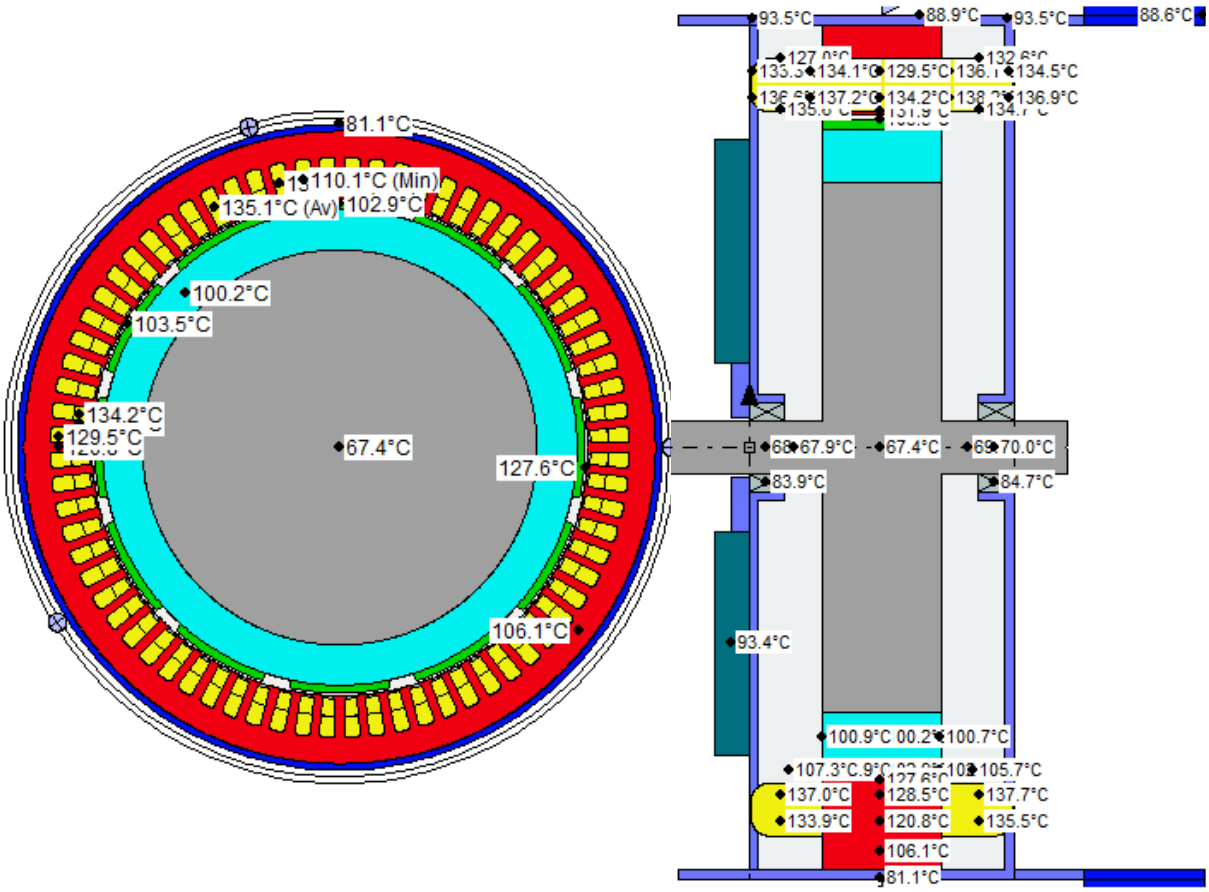

Fig. 5.25. The temperature analysis of 72-slot radial-flux model for checking the axial length where it gives an equivalent performance with the axial flux design.

5.6. Comparison with Reference Designs

5.6.1. Comparison with a machine in literature

A 60kW double-stator AFSPMSM was designed and studied in [249] with outer and inner diameters of 350 and 240, respectively. In [249], the reported ohmic and core losses are 1723W and 760W, respectively. The available surface behind of each stator in this design is 0.051m^2. Authors showed that the machine can operate safely with current density of 10A/mm^2 when 60°C glycol solution passes through the inlet with 20L/min flow rate.

The designed machine in this report, shares 0.074m^2 surface area behind each stator which enables a better heat transfer with the outer regions and cooling channels. Moreover, the considered current density for the machine is 5.45A/mm^2 which is almost half of the current density of the reference machine. The ohmic and core loss of the designed machine are 2232.5W and 721.75W, respectively. Although the summation of the total losses in the designed machine is approximately 400W larger than the reference machine, the machine can be cooled down using a proper cooling system because of the larger outer surface which it shares with the cooling channels. This conclusion was achieved during the thermal modelling of the system.

5.7. Demagnetization Analysis

The short circuit fault occurrence can lead to the demagnetization of the PM materials due to the invers magnetic field that is applied to the PMs. The demagnetization concept and analysis have been the subject of various literature [287]–[289]. In this section, the demagnetization of the considered SmCo 2:17 material considered for the design of AFPMSM at 120°C is analysed through FEA.

5.7.1. The calculation of B-H curve of PM using manufacturer data

The BH curve of the PM material is calculated using the datasheet of the SmCo and the presented equations in [290]. Datasheets and catalogues report the remanence (B_r) and intrinsic coercivity (H_{ci}) of the permanent magnets for a certain temperature (T_0). Maximum energy which can be provided by the PM at the given temperature is shown by BH_{max}. This parameter reports the maximum output energy of PM per unit volume. The last point where $B = \mu_r H$ on the intrinsic BH curve of the considered magnet at the given temperature is named the knee point remanence and shown by B_t. The coercivity of the PM at the knee point of the normal curve, shown by (H_t), is obtained by (5-6). The relative permeability of the PM in the linear section of its B-H curve is shown by μ_r.

$$H_t = \frac{B_t - B_r}{\mu_r} \tag{5-6}$$

The calculation of the H_t and having μ_r and B_r from the datasheet, the flux density in the linear section of the normal curve is obtained by (5-7).

$$B_i = B_r + \mu_r H \; \forall \; H \geq H_t \tag{5-7}$$

Knowing the intersection point of the intrinsic B-H curve with the flux strength axis (i.e., defined by H_{ci}) enables to calculate the amount of the remanence flux (B_{r0}) when the intrinsic curve reaches its knee point using (5-8)

for value is used to estimate the linear section of the B-H curve of the PM The calculation of this value allows to determine the slope of the linear section of the normal BH curve at the given temperature by (5-8) [289].

$$a_0 = \frac{B_r - \mu_r(H_t - H_{ci})}{B_r - \mu_r(\frac{H_t}{H_c} - 1)H_t}$$
$$B_{r0} = \frac{B_t(a_0 H_t - H_{ci})}{H_t - H_{ci}} \tag{5-8}$$

This allows to find the B variation on the intrinsic B-H curve using the following equation:

$$B_i = \frac{B_{r0}(H - H_{ci})}{a_0 H - H_{ci}} \quad \forall \; H < H_t \tag{5-9}$$

Thus, the intrinsic B-H curve for different H is obtained by (5-7) and (5-9), respectively. The normal B-H is finally obtained using (5-10) for all values of coercivities.

$$B_n = B_i + \mu_r H \tag{5-10}$$

The temperature effect is applied to the coercivity, and calculated flux densities based on (5-11). In this equation α and β are the thermal constant and can be found in datasheets.

$$H_{new} = H(1 + \beta(T - T_0))$$
$$B_{n.new} = B_i(1 + \alpha(T - T_0)) \tag{5-11}$$
$$B_{i.new} = B_{n.new} + \mu_r H_{new}$$

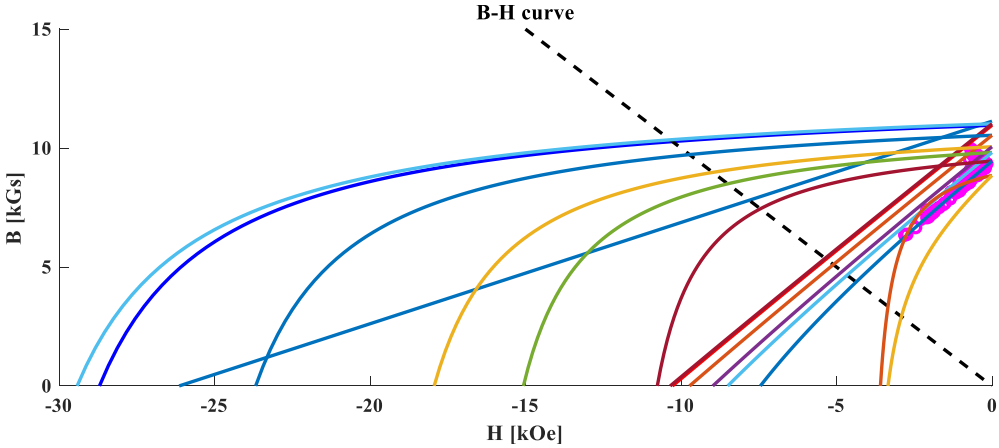

Fig. 5.26. The calculated B-H curves of the SmCo 2:17 material. Light blue: 20°C, Navy blue: 60°C, yellow: 100°C, green: 120°C, brown: 150°C, and orange: 200°C.

TABLE 5.7. THE GIVEN CHARACTERSITICS OF THE CONSIDERED PERMANENT MAGNET BY THE DATASHEET.

	B_r [T]	B_t [T]	H_{ci} [kA/m]	BH_{max}	μ_r	α [°C]	β [°C]
SmCo 2:17	1.13	0.1	-2080	20.4×10^6	1.02	-0.11	-0.5

The physical characteristics of the considered SmCo 2:17 are tabulated in Table 5.7. The B-H curves of this material for a wide range temperature are calculated using the abovementioned procedure and plotted in Fig. 5.26. The 20°C, 60°C, 100°C, 120°C, 150°C, and 200°C are the considered temperatures for this plot. The dark blue is the B-H curve of the material at 25°C. It is seen that the increment of the temperature reduces the range of safe operating region for the PM. Because the datasheet temperature is 25°C, it is seen that the light blue which represent the 20°C B-H curve interests the x-axis in a bigger coercivity.

5.7.2. The demagnetization analysis

The calculated B-H curves can be used to execute the demagnetization analysis in FEA. The demagnetization depends on the rotor temperature as well as the stator current which produces the inverse field. The maximum flux density produced by the windings is happened at the short circuit fault when the amplitude of the current is maximum. Therefore, the short circuit current is obtained

through the FEA analysis which is equal to $I_{sc}^{peak} = 375\text{A}$. This value is about 2.67 times of the rated current which is an acceptable value for a proper design.

In the first set of the analysis the set of current defined in (5-12) are injected to the windings. The currents waveforms are shown in Fig. 5.27. As shown in this figure, the current is gradually increased up to the short circuit current. A portion of the PM shown if Fig. 5.28 is selected and the flux density and the coercivity over this volume is obtained in each time step (see (5-13)). The collected $B_{PM.mag}$ and $H_{PM.mag}$ are plotted on the B-H curve of the PM shown in Fig. 5.26. According to this figure, all the plotted pink points are located below the knee point of the 120°C and 150°C B-H curves (green and brown lines). Therefore, the demagnetization will not be happened when the short circuit current flows through the windings and the rotor temperature is at its highest value.

$$I_a = I_{sc}^{peak}\cos(\omega t)\,(1-e^{-250t})$$
$$I_b = I_{sc}^{peak}\cos\left(\omega t-\frac{2\pi}{3}\right)(1-e^{-250t}) \quad (5\text{-}12)$$
$$I_c = I_{sc}^{peak}\cos\left(\omega t-\frac{4\pi}{3}\right)(1-e^{-250t})$$

$$B_{PM.mag} = \frac{\int B(x,y,z)dV}{\int dV} \quad (5\text{-}13)$$
$$H_{PM.mag} = \frac{\int H(x,y,z)dV}{\int dV}$$

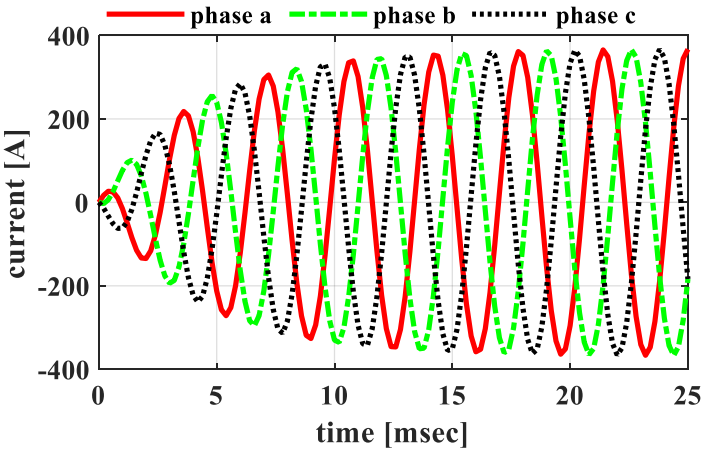

Fig. 5.27. The injected current for the first set of analysis.

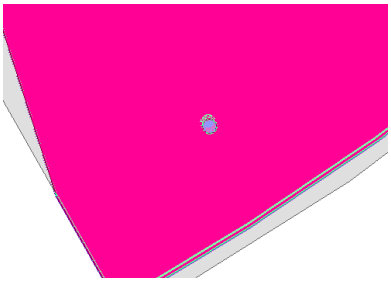

Fig. 5.28. The considered PM volume for demagnetization analysis.

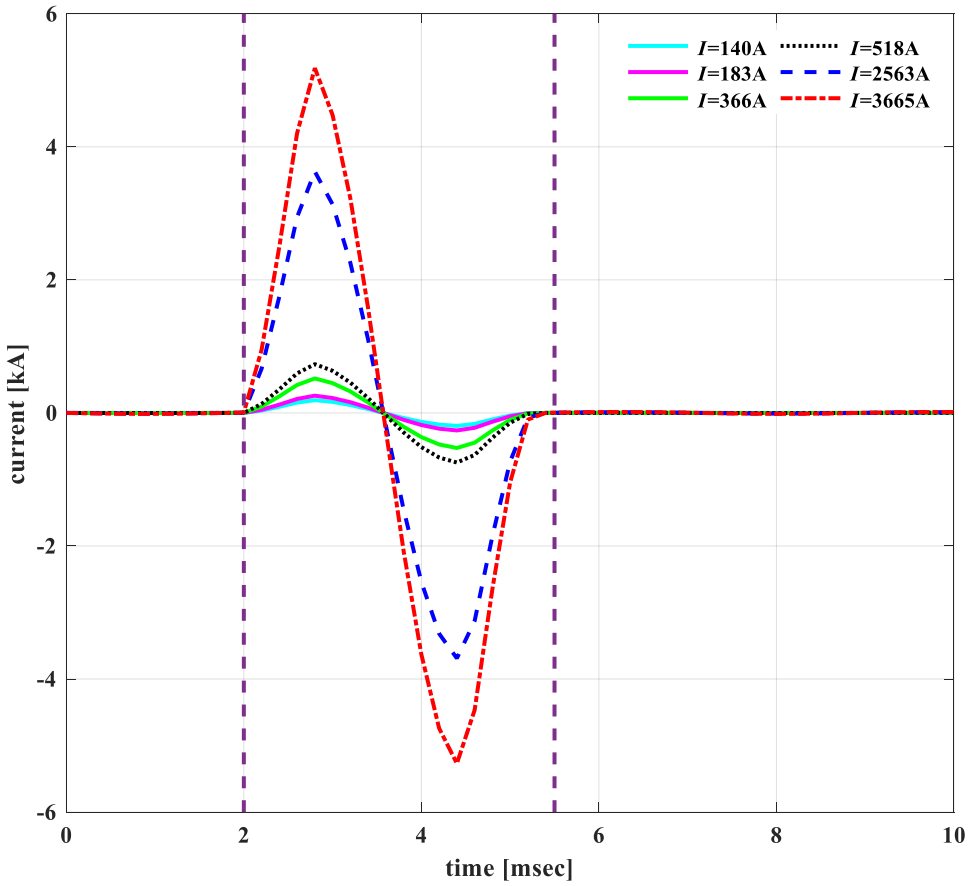

Fig. 5.29. The defined current for demagnetization analysis through the second process. The amplitude of the current before 2 msec and after 5.5msec are equal to 1A.

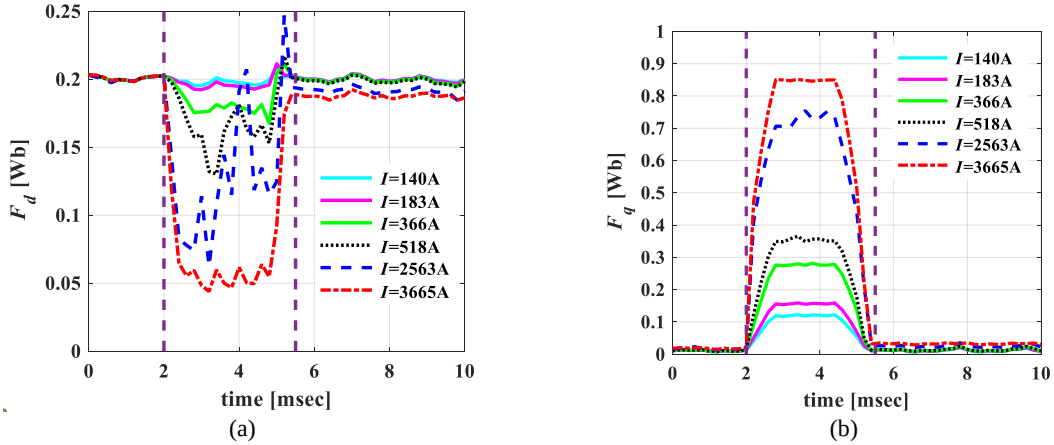

(a) (b)

Fig. 5.30. The *d-q* axes fluxes for demagnetization analysis by applying different currents. The reported current values in the legend are the rms current value which the result are obtained.

In the second type of the analysis, the B-H curve of the PM at 120°C is defined for the PM material in the FEA analysis. A set of current are defined shown in Fig. 5.29 are defined and injected to the windings. The *d-q* axes fluxes and torque are collected for each current. As shown in Fig. 30 the PM material is completely recovered after the short circuit occurrence. The green line, which shows the instantaneous demagnetization at short circuit (366A) condition, comes back to its normal value after fault removal at 5.5msec. To understand the capability of the model in prediction of the demagnetization some larger currents are applied to the windings. It is observed that the *d*-axis flux

for larger current was not able to reach its initial value after disconnection of large current at 5.5msec. To monitor the effect of the variation of the flux and torque after demagnetization 1A current are injected into the windings before 2msec and after 5.5msec. As shown in Fig. 5.30b, the *q*-axis current for the larger currents is larger than the smaller currents. It means the PM magnetization direction has been changed permanently after applying the larger currents. For this reason, the *q*-axis flux has some values. The 3D FEA results of the flux density distributions on the surface of the PM for different case studies, in which PM is not demagnetized and is demagnetized, are reported in Fig, 5.31. The comparison of Figs. 3.31a and 5.31b shows the flux density distribution after applying the rated current and short-circuit current are unified and similar to each other. In contrary, the demagnetization is observed when large impulse currents are injected through the winding. According to Figs. 5.31c and Figs. 5.31d, the PMs are demagnetized at 10 and 20 times of the short circuit currents. Fig. 5.32 is to show the effect of the demagnetization on the back-emf of the machine after applying large impulse current. It is seen that the amplitude of the back-emf after applying 3665A is 20V less than the back-emf after applying the rated current. This value is expected because of 0.015Wb *d*-axis flux drop after injection of 3665A. Considering 0.015Wb at speed of 2800rpm, the voltage drop should be in the range of $0.012\times2\pi\times280=21.11$V which is observed in Fig. 5.32b.

Further investigation is carried out on the demagnetization and understanding of the marginal current and temperature when the machine is seriously demagnetized. For this purpose, 150°C and 200°C B-H of the PM are considered as the physical characteristics of the PM and the short circuit current is injected to the winding. Fig. 5.33 shows the back-emf is hugely dropped after short circuit impulse when the PM temperature is 200°C.

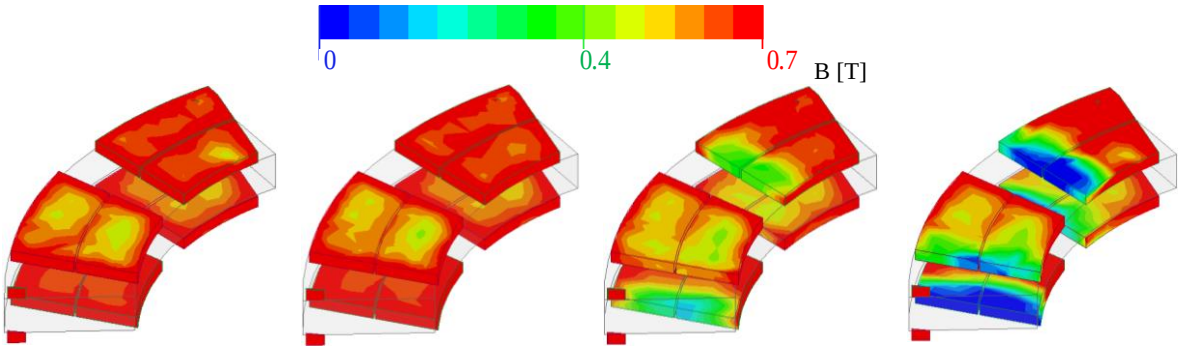

Fig. 5.31. PM flux density distribution after applying different current pulses, (a) flux density at 10msec after applying rated current (140A). (b) flux density at 10msec after applying short circuit current (366A). (c) flux density at 10msec after applying 10 times of short circuit current (3665A). (d) flux density at 10msec after applying 20 times of short circuit current (7330A).

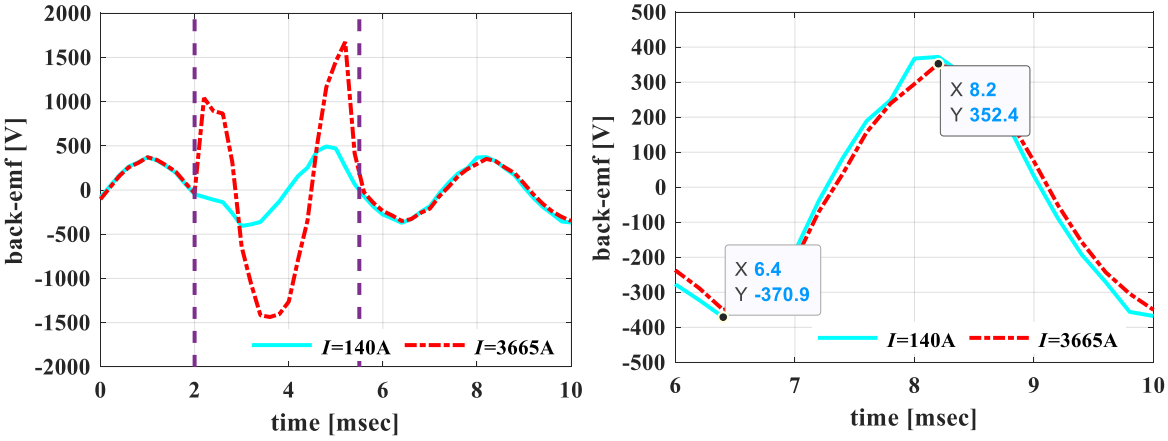

(a) (b)

Fig. 5.32. The back-emf waveform after current impulse. (a) the waveform in the whole period. (b) zoom-in view.

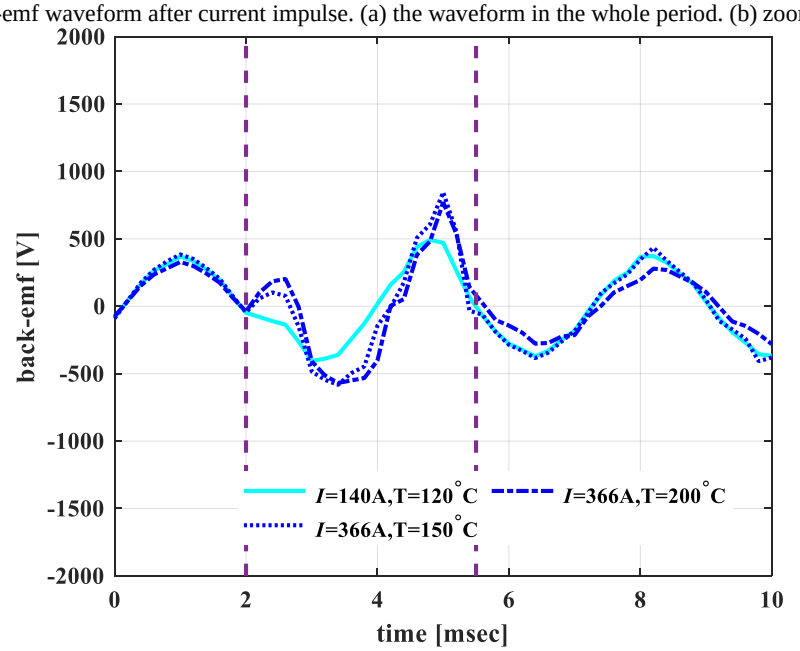

Fig. 5.33. The back-emf drop of the machine because of the effect of demagnetization in different PM temperatures.

5.8. The Optimization of AFSPMSM

5.8.1. Single objective optimization for 36 slots machine

An optimization study with the objective function of the maximization of the efficiency over the total axial length is executed to find the optimum dimensions which gives 100kW power for 36 slot stators. The slot width, stator thickness, PM arc, and PM thickness are considered as the variables of the optimization problem. Table 5.8 reports the range of the variation of variables and the optimal solutions. It should be highlighted that the slot height is an independent variable in the optimization problem changing with the variation of the slot width to keep the current density constant.

TABLE 5.8. THE CONSIDERED RANGE OF VARIABLES AND THE OPTIMAL SOULUTIONS AFTER OPTIMIZATION.

	Slot width [mm]	Stator thickness [mm]	PM arc [degrees]	PM thickness [mm]
Range of variation	14-18	35-60	21-23	5-10
Optimum results	15.39	36.50	21.60	5.40

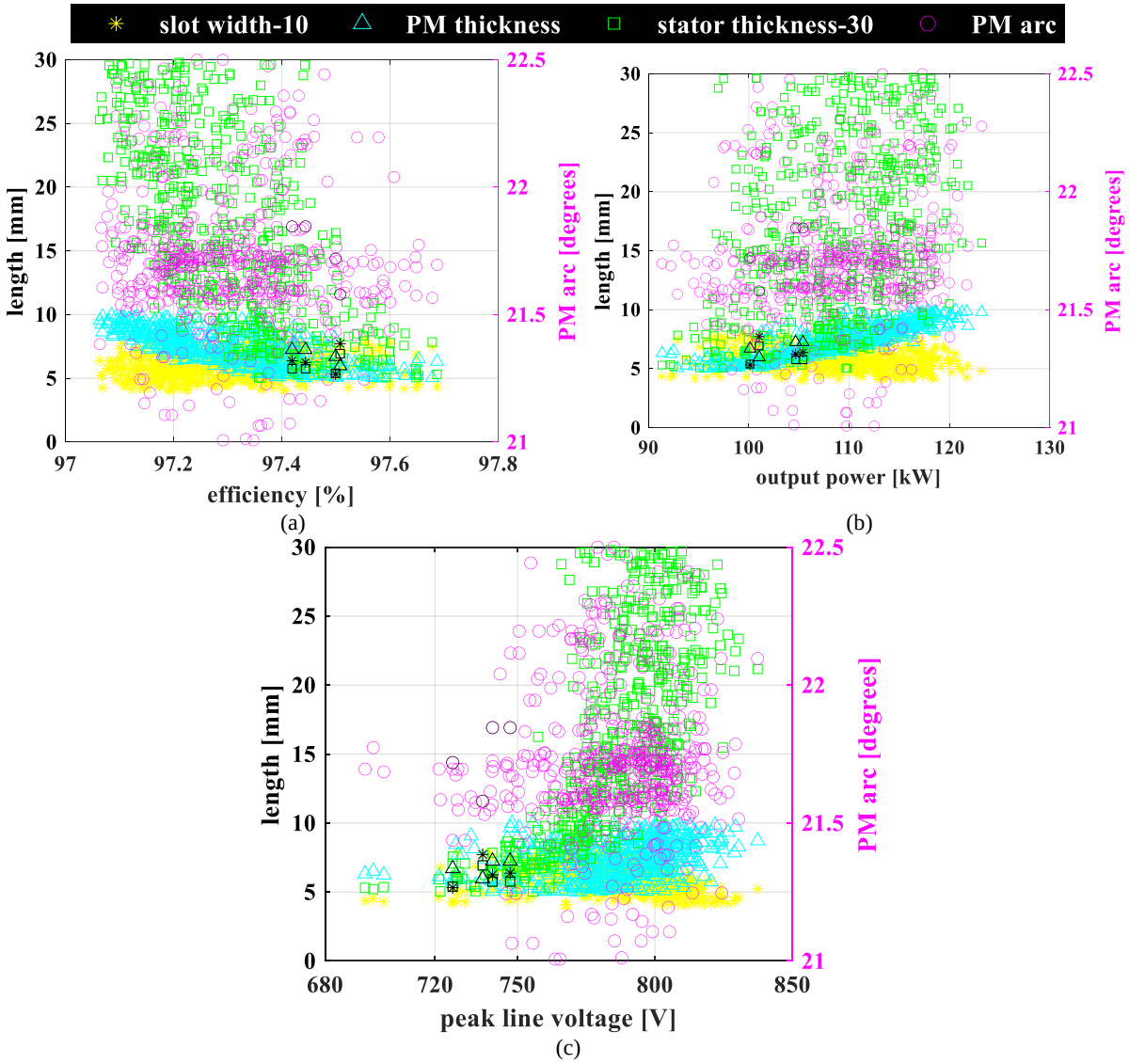

Fig. 5.34. The optimization variables against efficiency, power, and voltage at rated condition. The black points are the optimal length point where the total axial length is less than 100mm. (a) efficiency; (b) output power; (c) peak of line-voltage.

TABLE 5.9. GEOMETRY AND PREFORMANCE PARAMETERS OF THE OPTIMIZED AFPMSM.

Geometry			
Number of poles	12	Number of slots	36
Outer diameter [mm]	420	Inner diameter [mm]	300
Stator slot depth [mm]	17.67	Rotor thickness [mm]	20
PM thickness [mm]	5.40	PM arc [deg]	21.6
Skew angle of PM [deg]	5	Number of turns per phase per slot	4
Stator slot opening height [mm]	0.5	Number of turns per phase	48
Airgap length [mm]	2	Stator slot opening width [mm]	3
		Fill factor	0.45
Performance parameters			
Rated torque @ rated current [Nm]	349.79	Rated current [A]	140
Torque ripple [%]	5.4%	Current density [A/mm^2]	6
Rated speed [rpm]	2800	Power @ rated current [kW]	102.56
Peak line voltage [V]	740.45	Copper loss [W]	1952.41
Core loss [W]	670.38	Solid loss [W]	474.13
Total axial length [mm]	107.78	Efficiency [%]	97.07

Fig. 5.26 is to clarify the effect of variation of the considered variables in the specified solution space on the efficiency and output power. The black points in the presented plots in Fig. 5.26 highlights the designs which have an axial length smaller than 110mm and minimum output power of 100kW. According to Fig. 5.26c, the maximum peak line voltage of the 730V is achieved for the selected designs. This peak voltage allows to charge a 700V battery package when the machine operates at the generator motor.

The dimension and the performance parameters of the designed AFPMSM are reported in Table 5.9. Comparison of this table with the reported design in table 5.4 reveals that the optimal design offers offer a higher efficiency in a smaller axial flux. The flux density distribution and the machine shape are presented in Fig. 5.34.

5.8.1. Multi-objective optimization for 72 slots machine

A multi-objective optimization problem is defined with three different sets of objectives to design 3 machines and compare their performance parameters. The considered objective functions and the considered constraint in each optimization process are tabulated in Table 5.10. According to (5-14) to (5-16), the axial length is the main objective function which has been appeared in all defined problems. The second objective function is changed to the maximization of efficiency, achievement of required torque, and minimization of PM volume in (5-14) to (5-16). Since the required torque at 2800rpm for a 100kw machine is 341Nm, this value is considered as a constraint in the optimization study. In (5-15), achieving the exact value of 345Nm at minimum axial length is the objective. Hence, the minimum value of the torque is not limited in the constraints.

TABLE 5.10. THE CONSIDERED OBJECTIVE FUCNTION AND CONSTRAINT FOR THE MULTIOBJECTIVE OPTIMIZATION STUDY.

First optimization	Objective	$Min: \begin{cases} f_1 = Axial\ length \\ f_2 = 100 - \eta \end{cases}$	(5-14)
	Constraint	$subject\ to: \begin{cases} g_1 = \tau \leq 360 \\ g_2 = \tau \geq 341 \\ g_3 = \eta \geq 97 \end{cases}$	
Second optimization	Objective	$Min: \begin{cases} f_1 = Axial\ length \\ f_2 = 341 - \tau \end{cases}$	(5-15)
	Constraint	$subject\ to: \begin{cases} g_1 = \tau \leq 360 \\ g_2 = Axial\ length \leq 110 \\ g_3 = \eta \geq 97 \end{cases}$	
Third optimization	Objective	$Min: \begin{cases} f_1 = Axial\ length \\ f_2 = Amount\ of\ PMs \end{cases}$	(5-16)
	Constraint	$subject\ to: \begin{cases} g_1 = \tau \leq 360 \\ g_2 = \tau \geq 341 \end{cases}$	

TABLE 5.11. THE CONSIDERED RANGE OF VARIABLES AND THE OPTIMAL SOULUTIONS AFTER OPTIMIZATION FOR 72 SLOTS MACHINE.

	Slot width [mm]	**Stator thickness [mm]**	**PM arc [degrees]**	**PM thickness [mm]**
Range of variation	5-9.5	35-45	19.5-28.5	4-10
First optimization	9.31	37.89	22.82	4.38
Second optimization	9.48	35.08	28.33	4.01
Third optimization	9.17	36.01	24.64	4.03

A sensitivity analysis is executed on 800 geometries in the 3D FEA analysis. The considered variables in the sensitivity analysis are slot width, stator thickness, PM arc, and PM thickness. The range of variation of these values are summarized in the first row of the table 5.11. Note that the slots height is a dependent variable with the slot width. This value is automatically changed by variation of the slot width to keep the current density constant. Kriging as a surrogate model is applied to the collected data based on the provided model in [291]. This surrogate model allows to model the machine in based on the collected data to reduce the computational time. The multi-objective genetic algorithm (MOGA) is executed on the model in the range of the variables for the described objective functions. The optimal dimensions obtained from the executed MOGA on each objective function is summarized in Table 5.11.

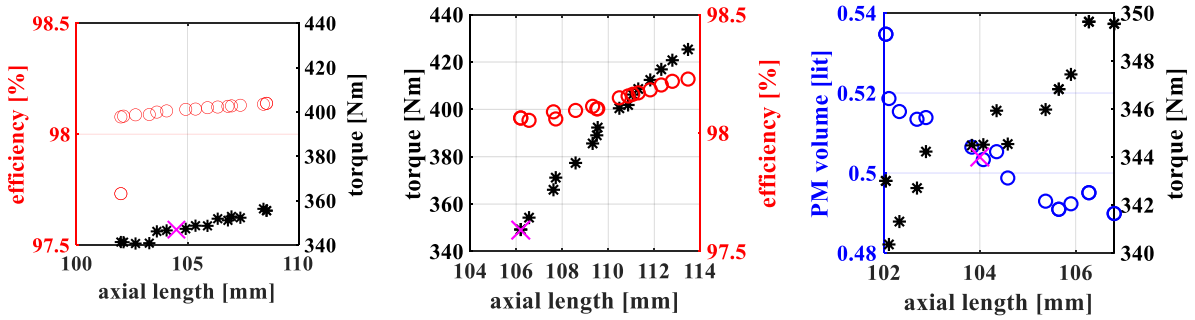

(a) (b) (c)

Fig. 5.35. The obtained pareto-front after implementation of each objective function. (a) results of first objective. (b) results of second objective. (c) results of third objective.

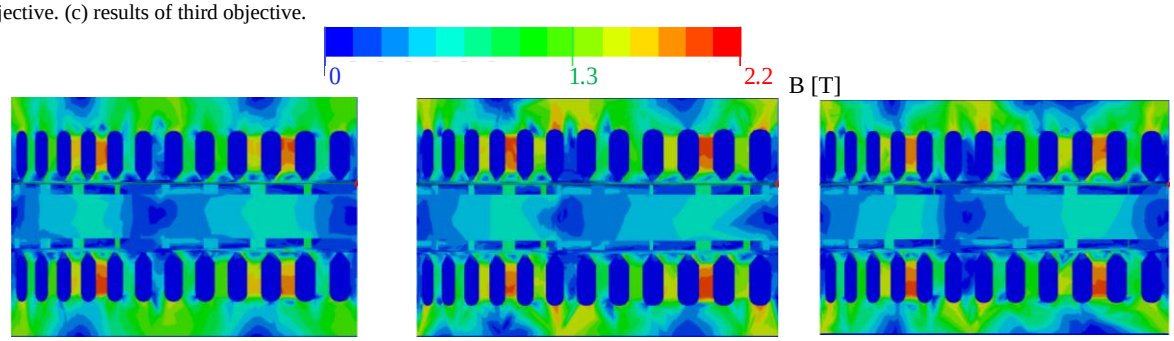

(a) (b) (c)

Fig. 5.36. The flux density distribution on each design during operation at rated condition of 130A and 2800rpm operating speed. (a) results of first objective. (b) results of second objective. (c) results of third objective.

TABLE 5.12. GEOMETRY AND PREFRORMANCE PARAMETERS OF THE OPTIMIZED 72 SLOTS AFPMSM WITH MAXIMUM EFFICIENCY AND MINIMUM LENGTH OBJECTIVE

Geometry			
Number of poles	12	Number of slots	72
Outer diameter [mm]	430	Inner diameter [mm]	300
Stator slot depth [mm]	13.74	Rotor thickness [mm]	20
PM thickness [mm]	4.38	PM arc [deg]	22.82
Skew angle of PM [deg]	5	Number of turns per phase per slot	2
Stator slot opening height [mm]	0.5	Number of turns per phase	48
Airgap length [mm]	2	Stator slot opening width [mm]	3
		Fill factor	0.45
Performance parameters			
Rated torque @ rated current [Nm]	340.96	Rated current [A]	130
Torque ripple [%]	4.2%	Current density [A/mm^2]	6
Rated speed [rpm]	2800	Power @ rated current [kW]	100.01
Peak line voltage [V]	725.85	Copper loss [W]	1262.3
Core loss [W]	660.2	Solid loss [W]	154.3
Total axial length [mm]	108.54	Efficiency [%]	98.11

TABLE 5.13. GEOMETRY AND PREFRORMANCE PARAMETERS OF THE OPTIMIZED 72 SLOTS AFPMSM WITH MAXIMUM TORQUE AND MINIMUM LENGTH OBJECTIVE

Geometry			
Number of poles	12	Number of slots	72
Outer diameter [mm]	430	Inner diameter [mm]	300
Stator slot depth [mm]	13.74	Rotor thickness [mm]	20
PM thickness [mm]	4.38	PM arc [deg]	28.33
Skew angle of PM [deg]	5	Number of turns per phase per slot	2
Stator slot opening height [mm]	0.5	Number of turns per phase	48
Airgap length [mm]	2	Stator slot opening width [mm]	3
		Fill factor	0.45
Performance parameters			
Rated torque @ rated current [Nm]	352.70	Rated current [A]	130
Torque ripple [%]	6.8%	Current density [A/mm^2]	6
Rated speed [rpm]	2800	Power @ rated current [kW]	103.6
Peak line voltage [V]	721.78	Copper loss [W]	1269.8
Core loss [W]	797.60	Solid loss [W]	165
Total axial length [mm]	106.2	Efficiency [%]	98.04

TABLE 5.14. GEOMETRY AND PREFRORMANCE PARAMETERS OF THE OPTIMIZED 72 SLOTS AFPMSM WITH MINIMUM AMOUNT OF PM AND MINIMUM LENGTH OBJECTIVE.

Geometry			
Number of poles	12	Number of slots	72
Outer diameter [mm]	430	Inner diameter [mm]	300
Stator slot depth [mm]	13.74	Rotor thickness [mm]	20
PM thickness [mm]	4.38	PM arc [deg]	24.64
Skew angle of PM [deg]	5	Number of turns per phase per slot	2
Stator slot opening height [mm]	0.5	Number of turns per phase	48
Airgap length [mm]	2	Stator slot opening width [mm]	3
		Fill factor	0.45
Performance parameters			
Rated torque @ rated current [Nm]	341.1	Rated current [A]	130
Torque ripple [%]	3.52%	Current density [A/mm^2]	6
Rated speed [rpm]	2800	Power @ rated current [kW]	100.02
Peak line voltage [V]	725.81	Copper loss [W]	1267.4
Core loss [W]	714.8	Solid loss [W]	159.1
Total axial length [mm]	104	Efficiency [%]	98.05

The obtained pareto fronts after each optimization are presented in Fig. 5.35. The pareto-fronts show the relationships of the axial length, efficiency, PM volume, and generated torque with each other with respect to the investigated objective function. As shown by magenta cross on Fig. 5.35a, the design with 108.5mm axial length which offers the required torque and a high efficiency compared to the other designs is selected as the output of the selected design for first objective function. The magenta cross shown in Fig, 5.35b shows the chosen design for the second objective function formulated in (5-15). This design is selected because it offers the required torque in a relatively high efficiency at the minimum axial length. The magenta cross depicted at Fig. 5.35c demonstrate the selected design based on the third objective function (i.e., (5-16)). This design is selected because it meets the required torque in the minimum axial length with a reasonable PM size. The designed machines are simulated at rated condition. Fig. 5.36 shows the flux density distribution

on each design. The uniform flux density distribution in the tooth and yoke of designs shows their optimality and suitability.

The performance parameters analysis of each design is reported in Tables 5.12 to 5.14. According to these tables, the axial length of all designs is approximately equal. Moreover, the amount of PM used in these machines does not have a large difference. Comparison of these tables demonstrate the designed machine with the third objective function offers the required power in the minimum axial length and in a fairly small PM amount.

The performance parameters of the designed machine, with the third objective function, over a wide torque speed range are presented in this Fig. 5.37. Although the maximum operating speed of the machine is 3200rpm (the vertical dotted-line in the presented figures), the performance parameters are reported until 5000rpm for further discussion. These results show the machine produces the required torque at the rated speed of 2800 rpm with the highest efficiency. The maximum power is about 102kW occurring at the beginning of field weakening region. As expected, the copper loss is increased with increase of the torque because a higher current is injected to the winding. The core loss is enhanced by speed increment due to the higher operating frequency.

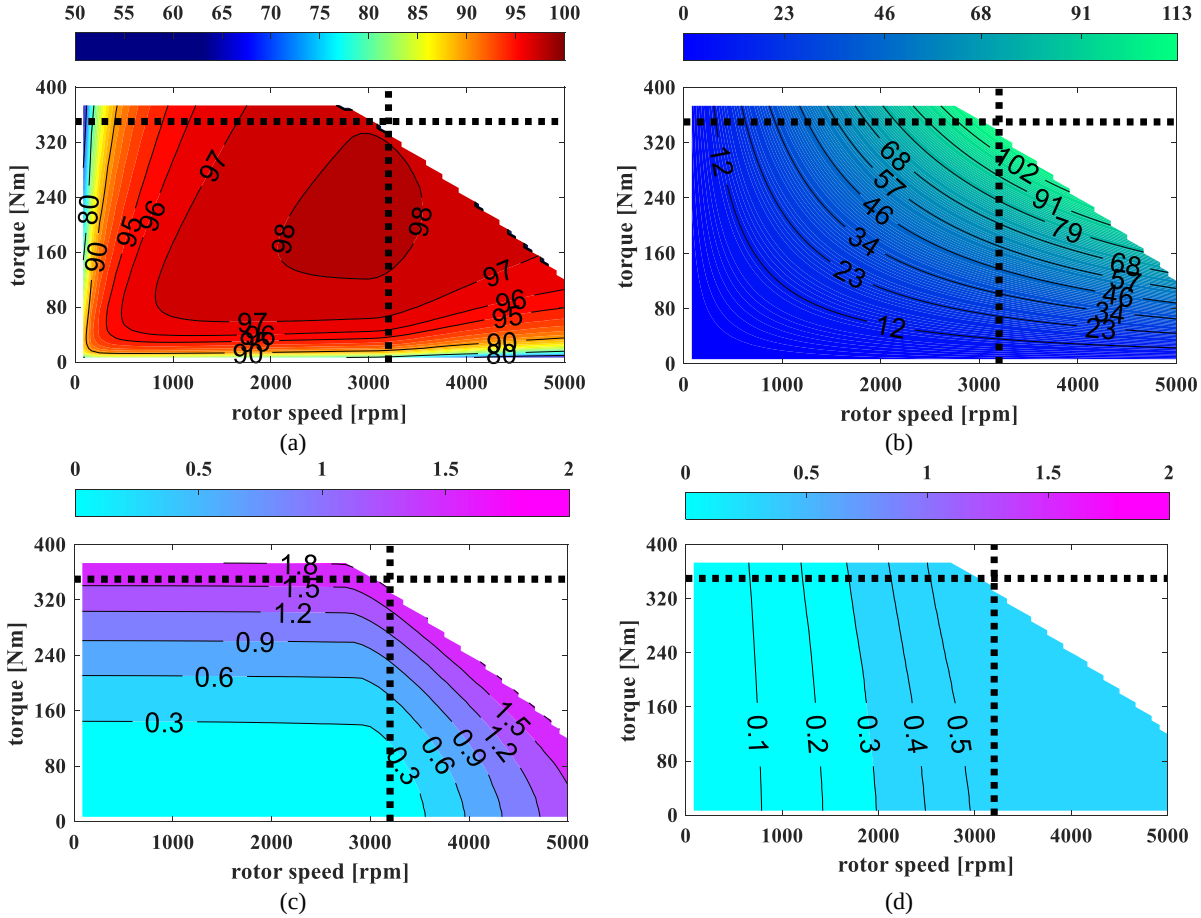

Fig. 5.37. Performance parameters of the designed machine in the torque speed envelope. (a) efficiency map in [%], (b) output power map in [kW], (c) ohmic loss map in [kW] (d) core loss map in [kW].

Due to the fact that the machine uses the surface mounted permanent magnet rotor, it cannot operate in the deep field-weakening region. The *d*-axis inductance is small and PM flux is dominant in the *d*-axis direction. Hence, the negative injected current cannot weaken the PM field successfully in the constant power region.

5.8.1. Comparison with commercialized machine

The products of two companies are presented in this section to be compared with the proposed design. Table 5.15 summarizes the characteristics of each commercial design against our design. Because the information provided in the commercialized machine catalogue depends on the operating condition, this information is updated for each machine based on the following paragraphs.

The best product of the YASA-Motor company is YASA-750 with the highest power of 70kW [283]. According to the presented table in [283], their machine offers 70kW at 3000rpm. So, the power at 2800 rpm is 70kW × 2800/3000 = 65.3 kW. The machine rating is reduced if the coolant temperature is increased from 40°C to 80°C because the machine must operate on lower current to protect the magnets against demonization and meets the thermal insulation. Assume that the machine generates 70kW at 120°C. Therefore, we should reduce the losses to 50% of the rated loss if we increase the temperature of the coolant for 40°C. Ignoring the core losses, the copper loss should become half which means the current must not be larger than 70% of the rated current. Therefore, the power of the machine will be 49kW with 80°C coolant.

EMRAX 268CC [284] is another available commercial product which has been designed in a same rating as the proposed design in this report. The end of the constant torque region for this machine is 4500rpm where it delivers 105kW power. Therefore, the rated power of the machine at 2800rpm is around 78kW. The reported performance is for an inlet cooling of 50°C. The increase of the inlet cooling liquid to 80°C leads to the reduction of the maximum power of the machine, the total losses should be reduced by 62.5% to provide a safe operating condition. If the effect of the core loss is ignored, in the best condition the current should be reduced by 78%. Therefore, the maximum power of the machine at 2800rpm is 60.8kW.

Comparison of the designed machine dimensions with the commercialized design and literature shows the machine can be an initial point for further improvement and analysis. The considered current density in this version of the machine is 5.45A/mm^2. However, this value can be increased if the machine temperature in the experimental tests does not meet the thermal insulation tolerances. The increment of the current density allows to achieve less axial length and consequently reduction of the machine volume.

Table 5.15 compares the power density of the designed machine with the YASA-750 and EMRAX 268CC. According to this table, the power density of the optimal design of AFPMSM is almost three times of the YASA-750. It is mainly because of the low torque of the YASA at the considered speed.

The power density of the optimal design is 6kW/lit smaller than the EMRAX machine in a same coolant temperature. However, the optimal design torque density is 6Nm/lit higher which makes it suitable for the targeted application.

TABLE 5.15. COMPARRISON OF THE DESIGNED MACHINE WITH THE COMMERCIALLY AVAILABLE DESIGNS.

	YASA-750 @ 2800rpm speed		EMRAX 268CC @ 2800rpm speed		Proposed design @ 2800rpm speed
Temperature of inlet liquid	40°C	80°C	50°C	80°C	80°C
Power	70kW	49kW	78kW	60.8kW	100.1kW
Efficiency	97%	≤ 97%	98%	≤ 98%	97%
Continuous power density [kW/lit]	9.11	6.38	33.1	25.7	19.6
Continuous torque density [Nm/lit]	52.1	36.4	106	61.4	67.1
Axial length	98mm		90.6mm		104mm
Diameter	368mm		268mm		550mm

5.9. Improvement of the design for operation in the field weakening region

The designed machine up to this point offers a high performance for the operation in the constant torque region. Thus, it is optimum for direct connection to the HEV engine. The EffM presented in Fig. 5.37 demonstrate the weakness of that machine in production of a high torque in the field weakening region. The capability of the operation in a wide range of speed in the constant power region is necessary for those EMs which are connected to the engine of HEV through a gearbox. This section investigates different rotor topologies and slots number for improvement of the machine performance in the field weakening region.

5.9.1. Possibility of the use of interior PM rotor

The use of the interior PM in the topology of the radial flux machines is a common practice to achieve a PMSM machine with an acceptable performance in higher speeds. The IPM topology allows to reduce the *d*-axis flux. As a results of this reduction, the required current to generate an equal torque as a SPM design with a same amount of PM material is increased. The less *d*-axis flux and higher rated current allows to have a better field weakening performance where the negative *d*-axis current should be injected to mitigate the flux.

The per-unit characteristics current (I_{ch_pu}) presented in (5-17) is used as an index to show the capability of the PMSMs for operation in the field weakening region. In (5-17), the PM flux and rated current are shown by λ_{PM} and I_{rated}, respectively.

$$I_{ch} = \frac{\lambda_{PM}}{L_d} \tag{5-17a}$$

$$I_{ch,pu} = \frac{I_{ch}}{I_{rated}} \tag{5-17b}$$

Radial PMSMs with I_{ch_pu} of 1pu can operate at their maximum power at least at three times of their rated speed [292]. Although there is a large number of articles discussing different aspects of the radial flux IPMSMs, there is a limited number of studies on the IPM topology for AFPMSMs. The AFIPMSMs have not found popularity because of the difficulty of the manufacturing and low mechanical strength. Moreover, literature has not introduced a completed interior PM machine. The PMs of the proposed AFIPMSMs are sit into the rotor where the PMs' face is in contact with the airgap.

In this section, a rotor topology which covers all faces of the PMs is considered (see Fig. 5.38). As shown in Fig. 5.38 the PM parts are placed into the iron. The thickness of the steel on top of the PMs is 1mm and the considered airgap is 1mm. An optimization study considering the variables tabulated in Table 5.12 is executed to find the optimum AFIPMSM based on the objective function and constraints presented in (5-14). The pareto front obtained from the optimization study and the 3-D view of the optimal design is shown in Fig. 5.39. The performance parameters of this design are summarized in Table 5.16. Comparison of Tables 5.13 and 5.16 reveals that the AFIPMSM axial length is about 40mm larger than the AFPMSM. It is because of the depth of the slots which is used to keep the current density constant. Another point which deserves to be mentioned is the larger rotor eddy current losses of the AFIPMSM design compared to the AFPMSM. The larger loss at the rotor side increases the possibility of the PMs demagnetization due to the over temperature at higher loads.

The EffM of the designed AFIPMSM shows the capability of the design for operation in higher speeds (see Fig. 5.40a). Fig. 5.40b shows the output power of the machine which is increased to 150kW in the constant power region. The smaller power factor of AFIPMSM compared to the AFPMSM is another disadvantageous of this machine. The small power factor increases the cost and size of the inverter which is not desirable from the HEV designer point of view (see Fig. 5.41).

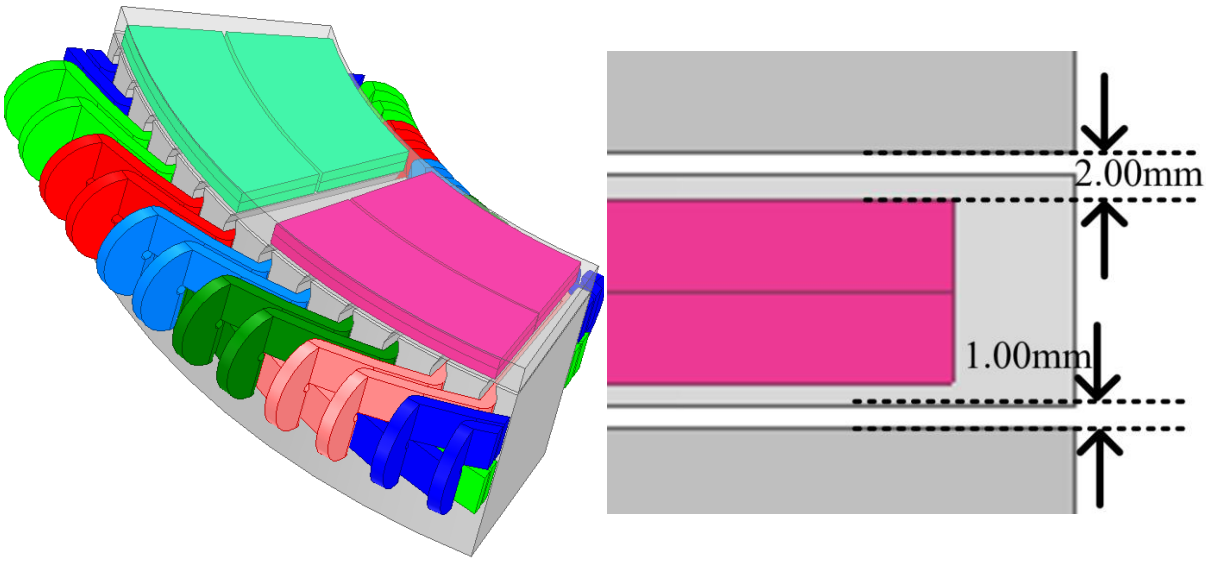

(a) (b)

Fig. 5.38. 3-D view and dimensions of the considered AIPMSM topology.

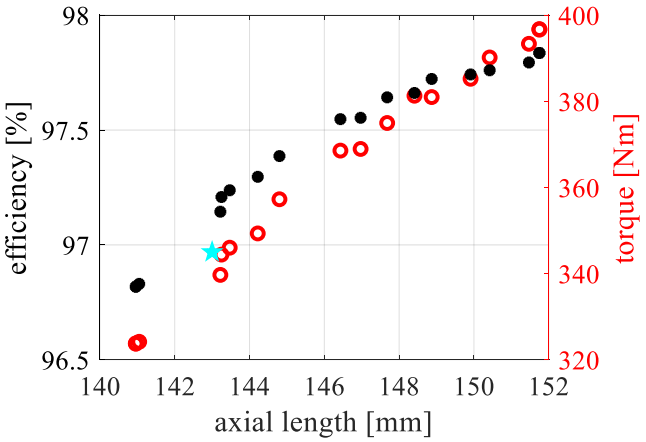

Fig. 5.39. The obtained pareto front from the multi-objective optimization based on the cost function and constrained of (5-13). The cyan star is the selected AIPMSM design for further investigation.

TABLE 5.16. GEOMETRY AND PREFORMANCE PARAMETERS OF THE OPTIMIZED 72 SLOTS AFIPMSM.

Geometry			
Number of poles	12	Number of slots	72
Outer diameter [mm]	430	Inner diameter [mm]	285
Stator slot depth [mm]	34.9	Rotor thickness [mm]	10
PM thickness [mm]	4×2	PM arc [deg]	25.2
Skew angle of PM [deg]	5	Number of turns per phase per slot	1
Stator slot opening height [mm]	0.5	Number of turns per phase	24
Airgap length [mm]	1	Stator slot opening width [mm]	3
		Fill factor	0.45
Performance parameters			
Rated torque @ rated current [Nm]	342.5	Rated current [A]	280
Torque ripple [%]	3.74%	Current density [A/mm^2]	5.7
Rated speed [rpm]	2800	Power @ rated current [kW]	101.02
Peak line voltage [V]	698.57	Copper loss [W]	990.8
Core loss [W]	1757.6	Solid loss [W]	914.1
Total axial length [mm]	143.8	Efficiency [%]	96.5

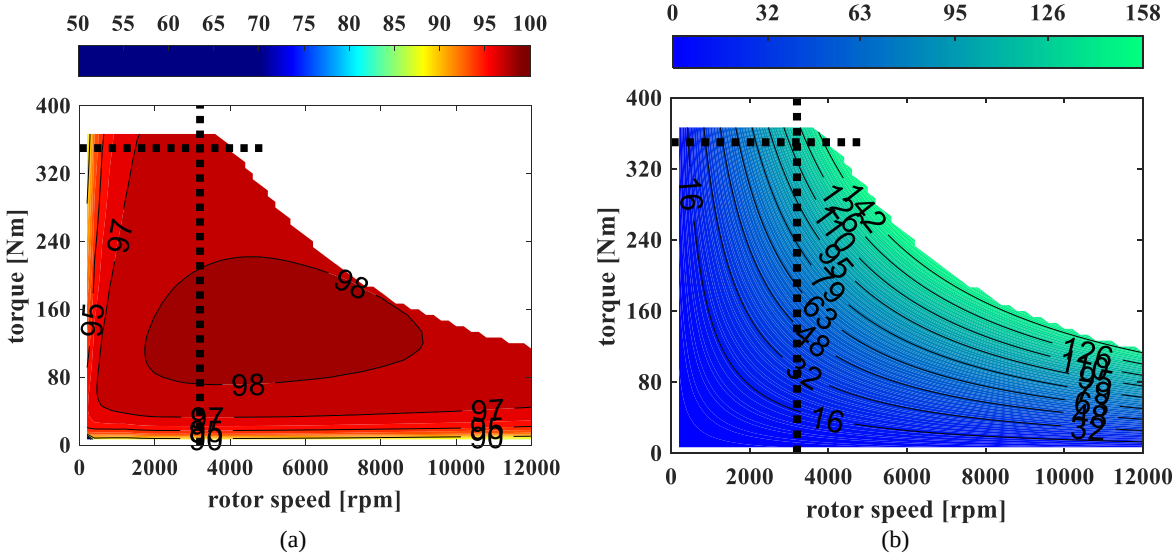

(a) (b)

Fig. 5.40. (a) EffM in [%] and (b) power map in [kW] of the optimal 100kW axial flux AFIPMSM.

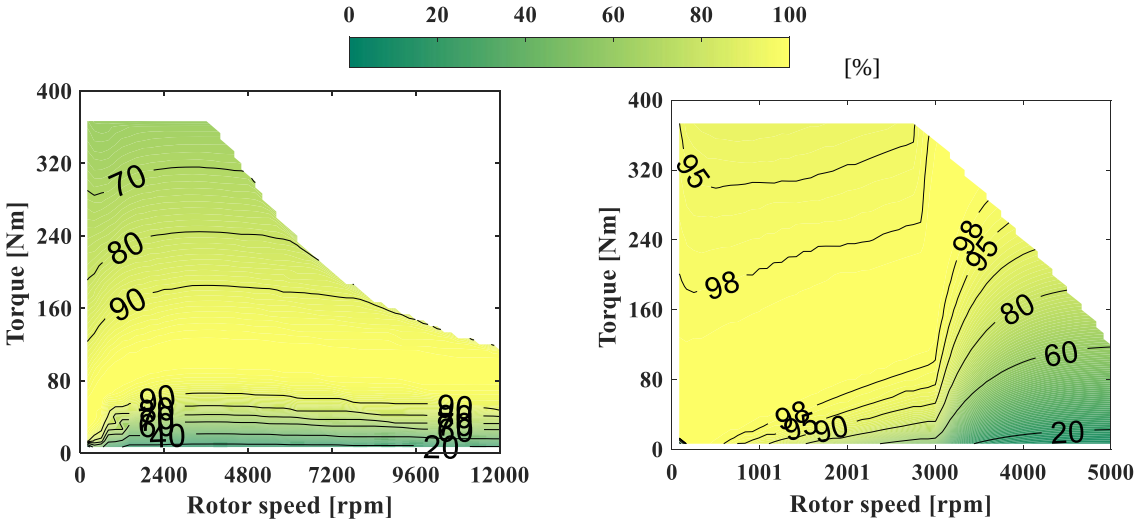

(a) (b)

Fig. 5.41. Comparison of the power factor between the optimal AFIPMSM and AFPMSM. (a) AIFPMSM, (b) AFPMSM.

5.9.2. Effect of slots to improve the field weakening region

The low power factor of the AFIPMSM design discussed in previous subsection reduces the possibility of the utilization of that design in the HEVs. In fact, low power factor not only increases the size and losses of the inverter, but also it leads to the slow charge and fast discharge of the battery packages.

The use of fractional slots winding is another approach investigated for improvement of the characteristics current in the design of EMs. Hence, in addition to the 36-slot design (shown in Fig. 5.5a), 72-slot design (designed in section 5.8), and the AFIPMSM (designed in 5.9.2), an 18-slot stator (i.e., shown in Fig. 5.42) is designed in this section. These designs are compared with respect to the characteristics current and rotor eddy current loss. It should be highlighted that 18-slots machine is designed based on the introduced design procedure in section 5.3. The machine dimensions are summarized in Table 5.17. According to the table, the copper losses of the machine is 300W less than the AFIPMSM and 1000W smaller than the previously designed AFPMSMs. It is mainly because of the reduction of the length of the wires in each phase. However, it mainly suffers from a high rotor eddy current loss with two PM segments. This huge increase in the amount of the loss is due to the large $\frac{dB}{dt}$ on top of the PMs' surface which is concluded by comparison of the no-load and full-load results presented in Fig. 5.43a.

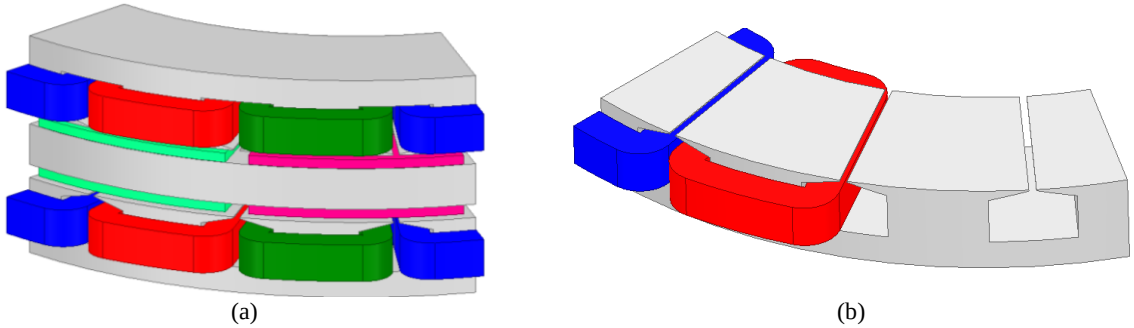

(a) (b)

Fig. 5.42. 3-D view of the designed 18-slots AFPMSM for further investigation.

TABLE 5.17. GEOMETRY AND PREFRORMANCE PARAMETERS OF THE OPTIMIZED 18-SLOTS AFPMSM.

Geometry			
Number of poles	12	Number of slots	18
Outer diameter [mm]	430	Inner diameter [mm]	305
Stator slot depth [mm]	20	Rotor thickness [mm]	10
PM thickness [mm]	4.5	PM arc [deg]	27
Skew angle of PM [deg]	5	Number of turns per phase per slot	7
Stator slot opening height [mm]	0.5	Number of turns per phase	42
Airgap length [mm]	1	Stator slot opening width [mm]	3
		Fill factor	0.45
Performance parameters			
Rated torque @ rated current [Nm]	342.6	Rated current [A]	135
Torque ripple [%]	4.13%	Current density [A/mm^2]	5.4
Rated speed [rpm]	2800	Power @ rated current [kW]	100.4
Peak line voltage [V]	700	Copper loss [W]	645.06
Core loss [W]	662.22	Solid loss [W]	4871
Total axial length [mm]	107	Efficiency [%]	94.2

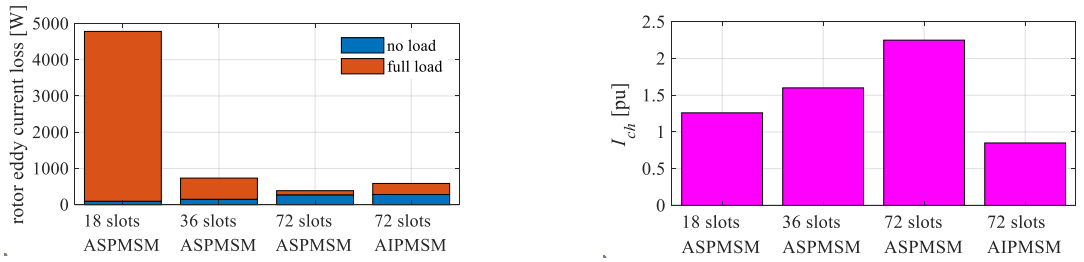

(a) (b)

Fig. 5.43. (a) comparison of the full-load and no-load rotor losses four all studied cases. (b) comparison of the characteristics current of the studied cases.

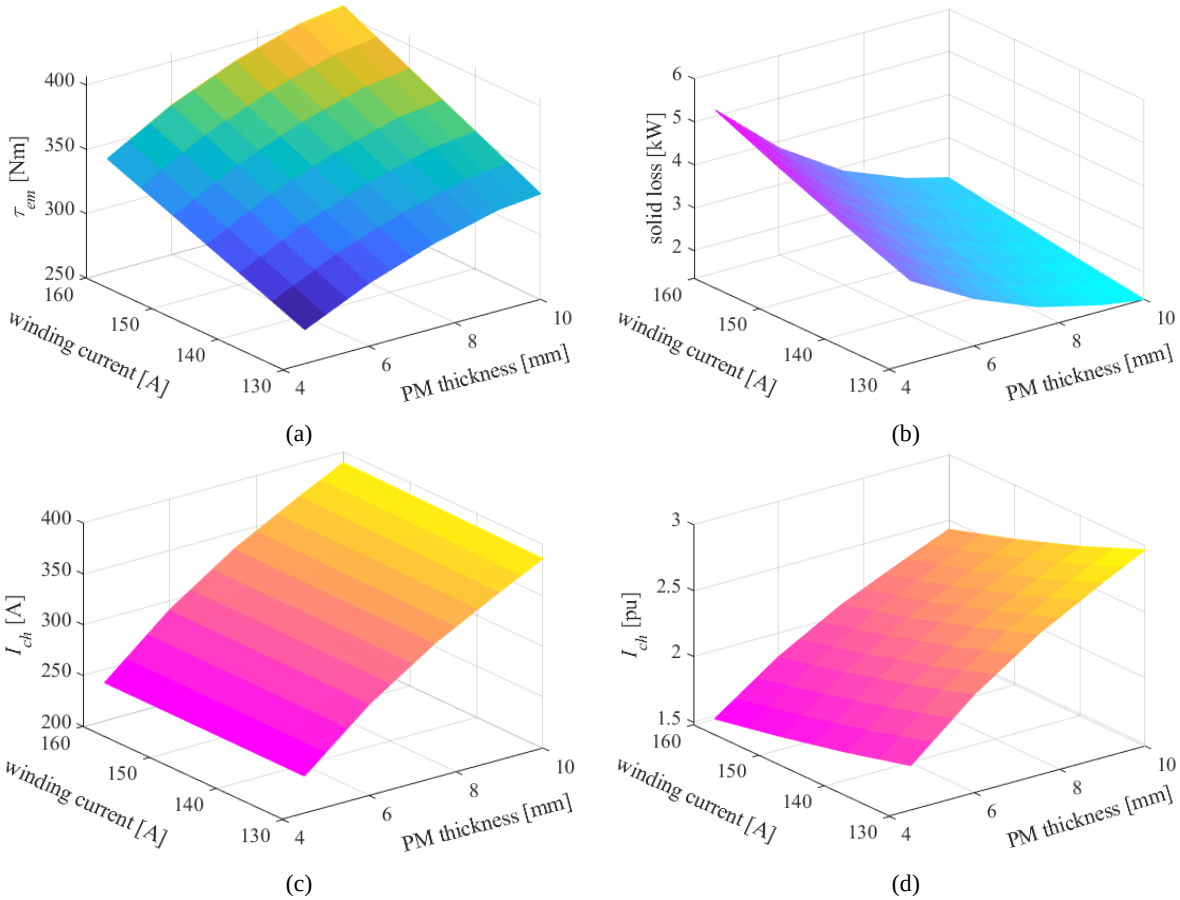

(a) (b)

(c) (d)

Fig. 5.44. The analysis of the effect of PM thickness on the rotor loss and characteristics current. (a) torque in different PM thicknesses and current. (b) rotor eddy current losses variation by variation of the PM thickness and current. (c) and (d) variation of characteristics current and its per unit value.

The characteristics current of the 18-slots design is close to 1pu and is much smaller than the 36- and 72-slots AFPMSM (see Fig. 5.43b). Hence, it is tried to reduce the rotor eddy current losses by increment of the PM thickness at the first step. Although the rotor eddy current losses are reduced to 1kW by changing the PM thickness from 4.5mm to 10mm, the characteristics current is increased dramatically (see Fig. 5.44). Thus, the increment of the PM thickness is not an appropriate approach to have an 18-slots machine with low rotor loss and capability of the operation in the field weakening region.

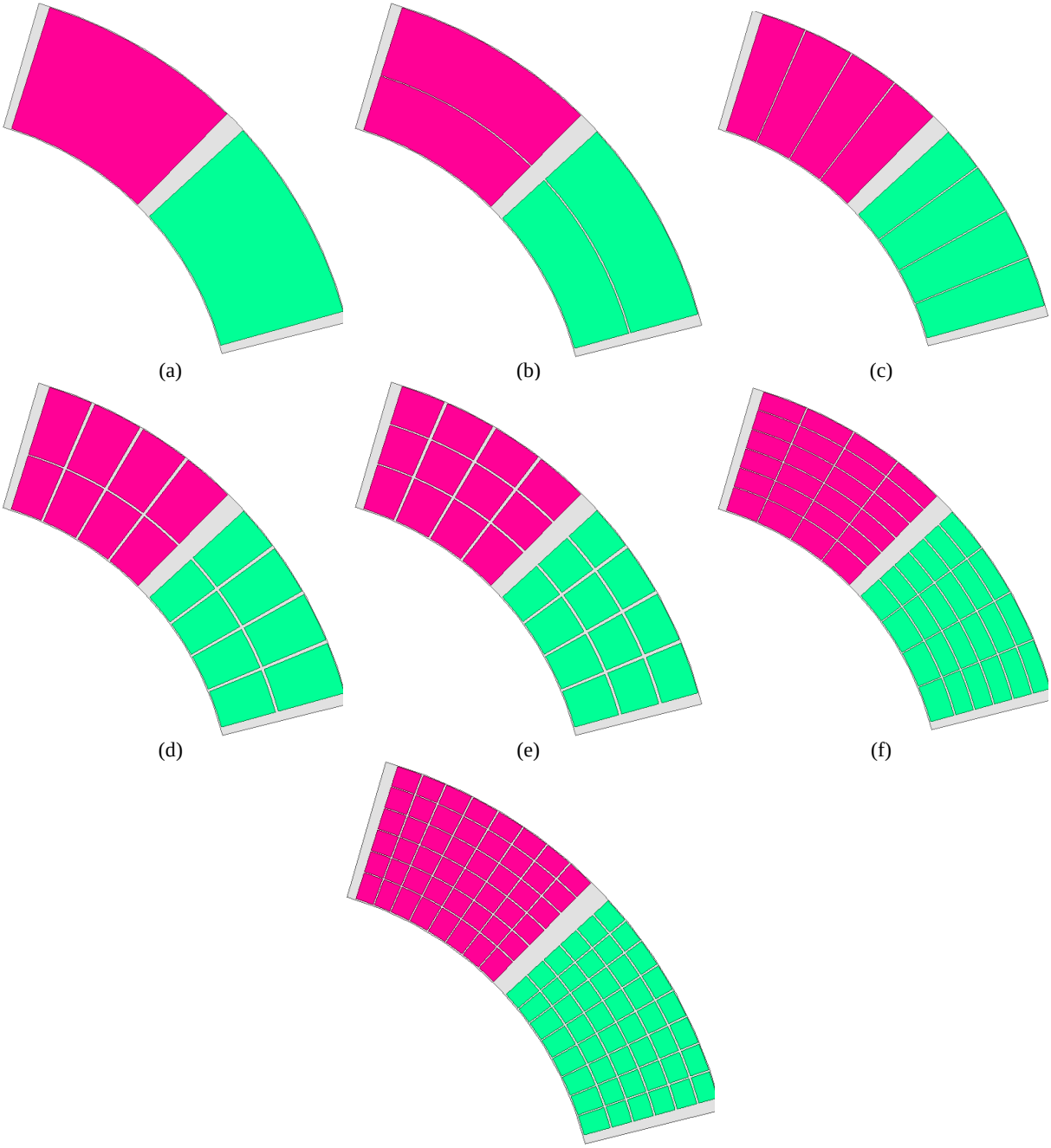

Fig. 5.45. Rotor shape with segmented PMs. (a) Single segment, (b) two segments, (c) four segments, (d) eight segments, (e) twelve segments, (f) twenty four segments, (g) forty eight segments.

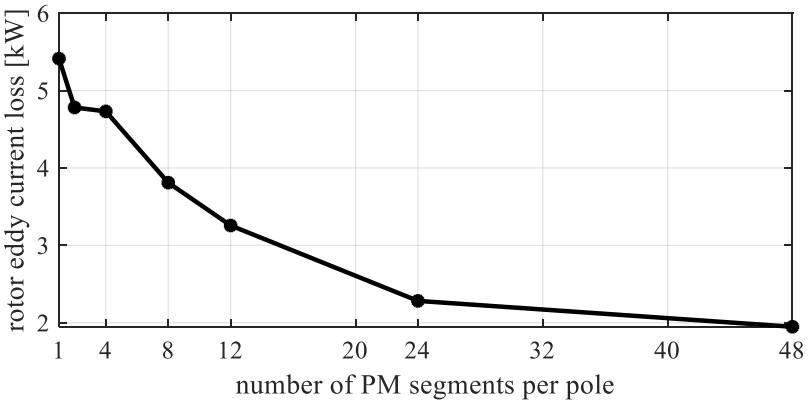

Fig. 5.46. Rotor eddy current losses in different PM segments.

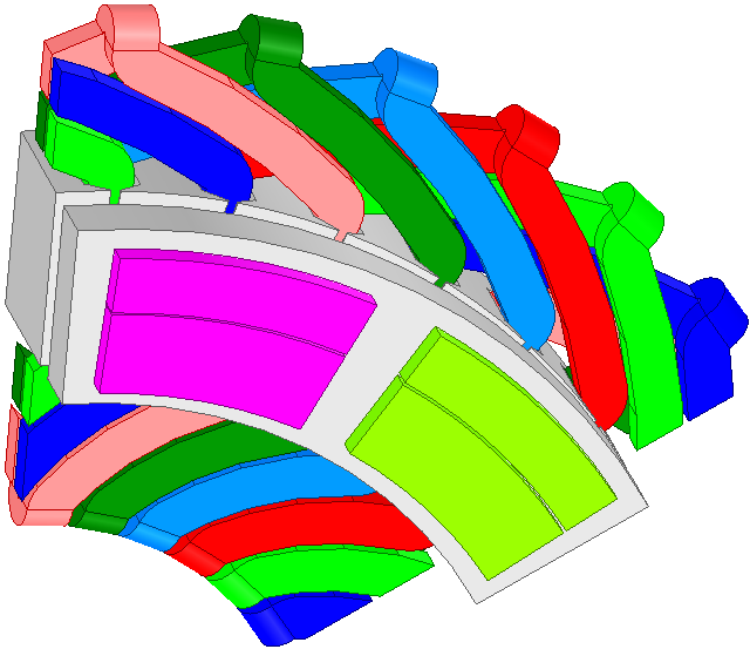

Fig. 5.47. The consideration of new rotor topology for 36-slots AFPMSM for possible improvement of the characteristics current.

The PM segmentation is another considered approach for reduction of the rotor eddy current loss. The considered number of segments and rotor shape are shown in Fig. 5.45. The presented results of the segmentation shown in Fig. 5.46 demonstrates a huge amount of rotor eddy current loss (i.e., 2kW) even with investigation of the very small pieces of PM (48 Segments). The availability of the large amount of loss on the rotor increases the risk of PMs demagnetization due to high temperature. Considering this, the 18-slots design is not a suitable choice for an AFPMSM in this size even though it offers an acceptable performance in the field weakening region.

The rejection of 18-slots AFPMSM and AFIPMSM enforces designer to use the 36-slots design which has a smaller characteristics current compared to the 72-slots AFPMSM to have an extended constant power region. According to the results of the analysis presented in Fig. 5.43b, the available 36-slots design has $I_{ch,pu}$ of 1.65pu. In this section, it is tried to reduce the characteristics current by increment of the *d*-axis inductance when the PM flux is constant.

It is expected to reach the larger *d*-axis inductance in constant flux by reduction of the PM radial length (see Fig. 5.47) and compensation of the flux by a possible increase of the PM arc or its height. This change allows having a larger flux pathing area in the rotor and stator. The larger diameter of the stator will also contribute to the generation of the higher flux in a constant current.

The initial trial and error analysis to get the 342Nm torque at rated speed of 2800rpm results in a promising result of 1.42pu for characteristics current. Hence, an optimization study is executed to find the optimal amount of PM which gives the required power in a small characteristic current. The considered objective function and constraint are formulated in (5-18). The PM arc, PM thickness, and PM inner and outer radii, and rated current of the machine are considered as the variables of the optimization. Table 5.18 shows the range of the variation of these variables in creation of the search space for the optimization.

$$\begin{aligned} &\text{Objective} && Min: \begin{cases} f_1 = I_{ch,pu} \\ f_2 = \text{total loss} \end{cases} \\ &\text{Constraint} && subject\ to: \begin{cases} g_1 = \tau \leq 360 \\ g_2 = \tau \geq 341 \\ g_3 = PF \geq 75\% \end{cases} \end{aligned} \tag{5-18}$$

A sensitivity analysis is executed using the reported variables and their range of variation in Table 5.18. The Kriging model is developed to train the system using the collected torque, characteristics current, power factor, and total loss. The MOGO is employed to find the optimum design based on the presented objective function in (5-18). The optimal pareto front is plotted in Fig. 5.48. The red square operating point shown in Fig. 5.48 which offers a low characteristic current (i.e., 1.49pu) within a reasonable amount of loss is selected as the optimal design. It should be highlighted that the rotor eddy current losses are ignored in calculating the performance parameters in the optimization study. Thus, the obtained total loss does not include the rotor eddy current loss. The optimal solutions are reported in the second row of Table 5.18. The general dimension and performance parameters of the optimal design are tabulated in Table 5.19. Due to the larger current pathing through the winding, the ohmic loss of this design is larger than previous designs.

The efficiency map, power map, and power factor map of this design plotted in Fig. 5.49 demonstrate the capability of the design in generating the required torque of 342Nm at lower speeds and delivery of 100kW power up to 12000rpm.

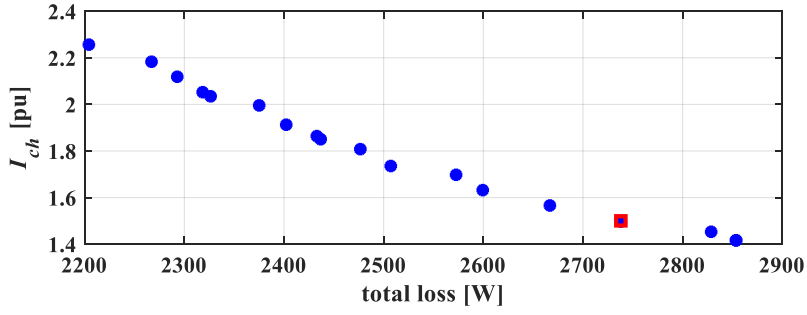

Fig. 5.48. The optimal pareto front for the 36-slot AFPMSM design.

TABLE 5.18. THE CONSIDERED RANGE OF VARIABLES AND THE OPTIMAL SOULUTIONS AFTER OPTIMIZATION FOR 36-SLOTS MACHINE CONSIDERING THE FIELD WEAKENING PERFORMANCE.

	current [A]	**PM distance form inner and outer edges of rotor [mm]**	**PM arc [degrees]**	**PM thickness [mm]**
Range of variation	130-160	5-15	20-28	4-7
Optimal solution	158	7.5	27	4.5

TABLE 5.19. GEOMETRY AND PERFRORMANCE PARAMETERS OF THE OPTIMIZED 36-SLOTS AFPMSM DESIGNED FOR OPERATION IN HIGHER SPEEDS.

Geometry			
Number of poles	12	Number of slots	36
Outer diameter [mm]	420	Inner diameter [mm]	305
Stator slot depth [mm]	20.5	Rotor thickness [mm]	10
PM thickness [mm]	4.5	PM arc [deg]	27
Skew angle of PM [deg]	5	Number of turns per phase per slot	4
Stator slot opening height [mm]	0.5	Number of turns per phase	48
Airgap length [mm]	2	Stator slot opening width [mm]	3
		Fill factor	0.45
Performance parameters			
Rated torque @ rated current [Nm]	344.8	Rated current [A]	158
Torque ripple [%]	7.4%	Current density [A/mm^2]	5.6
Rated speed [rpm]	2800	Power @ rated current [kW]	101.1
Peak line voltage [V]	681.38	Copper loss [W]	2012.2
Core loss [W]	700.9	Solid loss [W]	566.5
Total axial length [mm]	102	Efficiency [%]	97.4

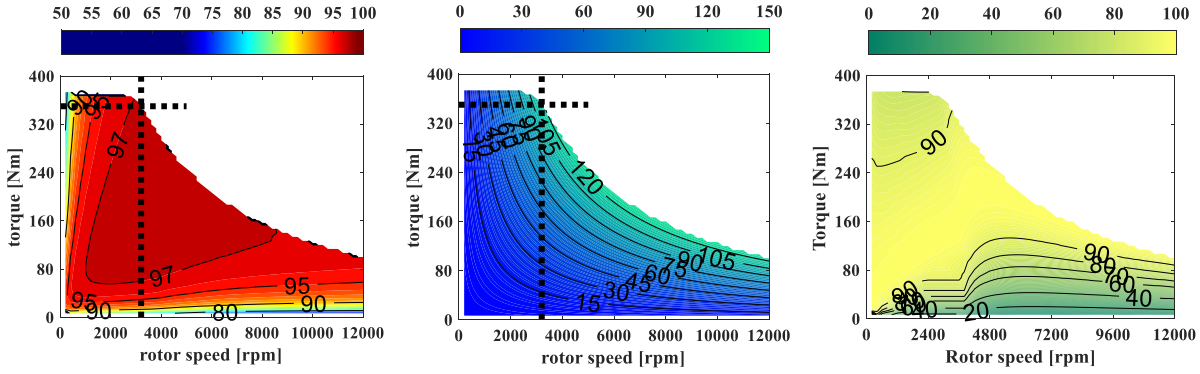

(a) (b) (c)

Fig. 5.49. (a) EffM, (b) power map, (c) power factor map of the optimal 36-slots design AFPMSM considering its performance in the field weakening region.

Comparison of the AFIPMSM and 36-slot AFPMSM efficiency map, power factor and axial length is useful to decide about the suitability of on of these designs for design of axial flux machines with the capability of the operation in the deep field weakening region (i.e., up to four times of the rated speed). Their EffM comparison presented in Figs. 5.40a and 5.49a shows that the AFIPMSM offers 1% higher efficiency in most of the operating points. However, the power factor of AFIPMSM is much lower than the 36-slot AFPMSM in lots of operating points. For instance, the AFIPMSM power factor is 20% less than the 36-slots design at maximum torque (see Figs. 41a and 49c). The large axial length of the AFIPMSM resulted from the requirement of having deep stator slots is another disadvantageous of this design where the power density matters. Considering these issues, the 36-slot design is selected as the best option for achieving a good performance in the FW region.

The result of this section shows it is possible to have an AFPMSM capable of operating in a wide range of speeds. This flexibility in design for higher speeds is employed for design of the 200kW machine which is coupled to the engine through the gearbox (see Fig. 5.1).

5.10. Design of 200kW AFPMSM

The 200kW machine should be offer a good performance in both constant torque and constant power region. The gear ratio has not been determined by the company. Hence, the objective of this section is to find a machine which have can operate in highest speed in the constant power region.

5.10.1. Stator cooling

Similar to the 100kW designs, the current density of 5.5A/mm^2 is initially assumed for the design of 200kW machine. This value may not be reliable for the 200kW design because of the current amplitude increase which lead to the increase of copper loss. For this reason, the machine temperature is initially checked, and a proper current density is chosen before further analysis.

Based on the conducted study in section 5.9, 36-slot AFPMSM with the introduced rotor topology is the initial choice for design of the required 200kW machine and thermal analysis. Firstly, the required 200kW machine is designed based on the procedure explained in section 5.3. Secondly, the thermal analysis is conducted for possible corrections of the considered current density. Fig. 5.50a shows the initial 200kW machine with 5.5A/mm^2 current density. The thermal analysis results show the maximum temperature of the winding is 180°C which is 25°C higher than the permitted temperature of the class F winding insolation (see Fig. 5.50). Note that the available stator surface in the equivalent radial model is equal to the outer surface of the AFPMSM design. Also, the ohmic and iron losses of the radial model are 3.4kW and 2.1kW, respectively, which are equal to the AFPMSM design.

The copper losses can be reduced by decrease of the current density. Hence, the permitted current density of the design is set on 4.5 A/mm^2 and the slot depth is updated to reach this value. The thermal analysis is executed on the equivalent radial flux machine. Fig. 5.51 shows that the hotspot temperature of the winding with this current density is still 3°C higher than the permitted maximum temperature in class F insulation. It is not reasonable to reduce the current density more than this because the cost of the wire and machine axial length is increased. Moreover, this machine should be capable of handling 2pu overload for 30 seconds. Operation of the machine at this high temperature will not permit the overload operation. Considering these points, the idea of the reductio of current density is rejected.

The current density is set back to 5.5 A/mm^2, but an oil spray is added as a part of cooling system. Fig. 5.52 shows the success of the spray cooling in reduction of the temperature form 185°C to 120°C. The considered spray cooling has a nuzzle at each side of end windings and sprays the liquid with

flow rate of 1.79 l/min. The considered liquid has thermal capacity of 0.0125 W/m/°C and specific heat capacity of 1880 J/kg/°C.

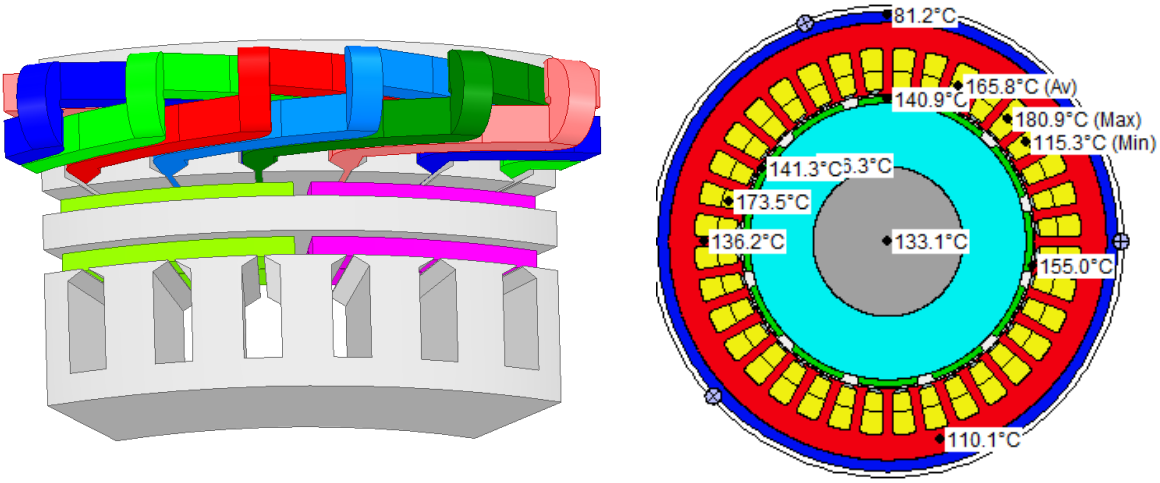

(a) (b)

Fig. 5.50. (a) the 3-D view of the initial design of double stator 200kW 36-slots AFPMSM. (b) the results of the thermal analysis for the design.

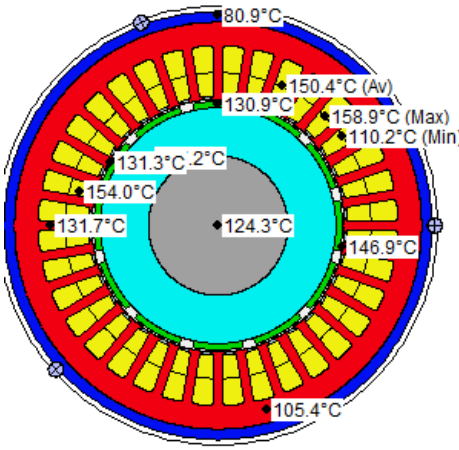

Fig. 5.51. Results of the thermal analysis for 200kW machine with consideration of 4.5 A/mm^2 current density.

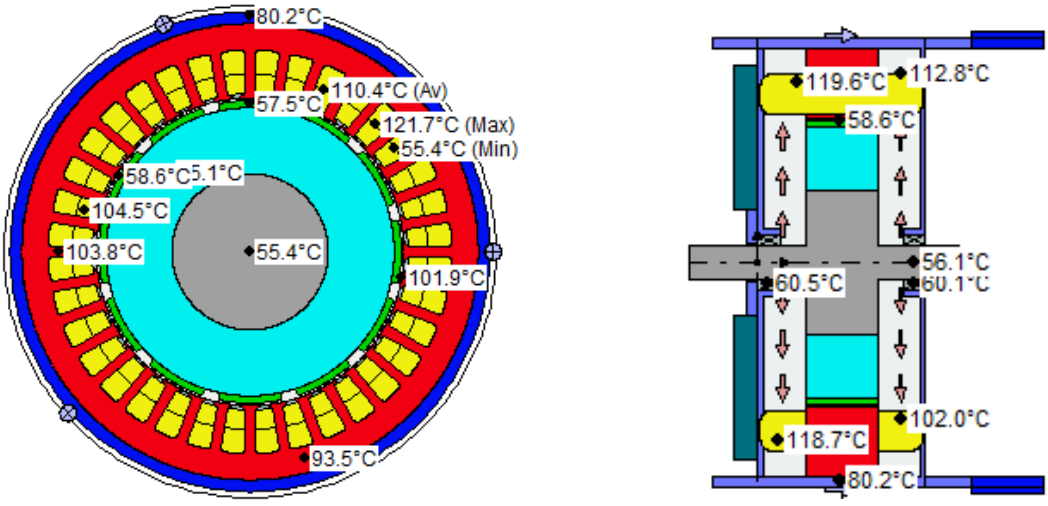

(a) (b)

Fig. 5.52. The cross-section view of the radial flux machine which is equivalent with the 200kW AFPMSM with the current density of 5A/mm^2. In these results both the spiral cooling system and the spray cooling are considered to cool down the machine. (a) temperature of different parts in radial view. (b) axial view of the model which shows temperature. Arrows in this figure shows the direction of the spray from shaft to end winding.

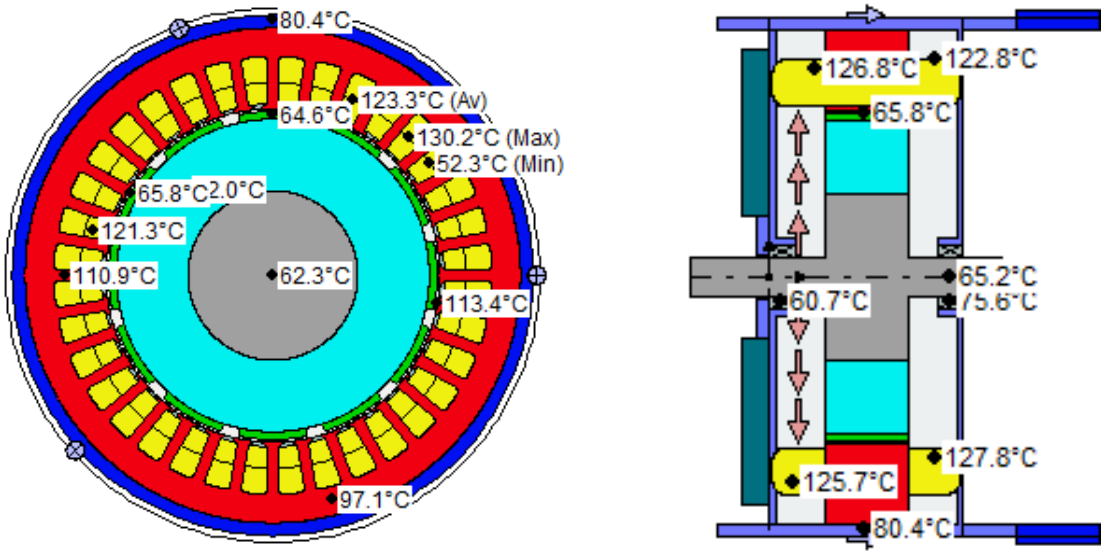

(a) (b)

Fig. 5.53. The cross-section view of the radial flux machine which is equivalent with the 200kW AFPMSM with the current density of 5A/mm^2. In these results both the spiral cooling system and the spray cooling are considered to cool down the machine. However, the fluid is sprayed on one of the end windings. (a) temperature of different parts in radial view. (b) axial view of the model which shows temperature. Arrows in this figure shows the direction of the spray.

The inner end winding in AFPMSMs is close to the shaft and there is not enough space to insert the spray cooling nozzles. For this reason, the spray cooling is only considered for the outer end winding of AFPMSM. Fig. 5.53 shows that the maximum temperature of the winding is increased to 131°C when the end winding is cooled down from one side. However, this temperature is acceptable because the hotspot temperature is 24°C less than the maximum Class F temperature limit. This cooling system is selected for the 200kW design. The performance of the cooling system in handling the overload is studied after the optimization study in the continuation of this section.

5.10.2. Optimal design of the 12-pole machine with 36-slots

This part discusses the optimal design of the 12-pole machine with 36-slots with consideration of the design capability for operation up to four times of the rated speed (2800rpm) in the FW region. According to (5-19) the characteristic current and total losses of the machine are considered as the objectives of the optimization study. The rated current, PM thickness, PM arc, and PM distance from each edge of the rotor (PM length) are the considered optimization variables. Table 5.20 summarizes the investigated range of variables in the optimization study.

$$\begin{aligned} &\text{Objective} && Min: \begin{cases} f_1 = I_{ch,pu} \\ f_2 = \text{total loss} \end{cases} \\ &\text{Constraint} && subject\ to: \begin{cases} g_1 = \tau \leq 720 \\ g_2 = \tau \geq 683 \\ g_3 = PF \geq 75\% \end{cases} \end{aligned} \qquad (5\text{-}19)$$

The optimal pareto front of this design and the flux density distribution on the middle layer of the optimal design are shown in Fig. 5.54. The selected optimal design, shown by red square, has a characteristic current of 1.24pu. Thus, this design is capable of delivery of 200kW power at 12000rpm. The EffM, power map, ohmic loss map, and core loss map of the optimal design showing the machine performance in the entire expected operating points are presented in Fig. 5.55. It is seen that the machine can at least operate at 250kW until 12000 rpm. The dimensions and performance parameters of this design are summarized in Table 5.21.

TABLE 5.20. THE CONSIDERED RANGE OF VARIABLES AND THE OPTIMAL SOULUTIONS AFTER OPTIMIZATION FOR 36-SLOTS MACHINE CONSIDERING THE FIELD WEAKENING PERFORMANCE.

	current [A]	**PM distance form inner and outer edges of rotor [mm]**	**PM arc [degrees]**	**PM thickness [mm]**
Range of variation	360-400	5-20	20-28	7-10
Optimal solution	362	7	26.8	9.41

TABLE 5.21. GEOMETRY AND PERFRORMANCE PARAMETERS OF THE OPTIMIZED 12-POLES, 36-SLOTS 200KW AFPMSM DESIGNED FOR OPERATION IN HIGHER SPEEDS.

Geometry			
Number of poles	12	Number of slots	36
Outer diameter [mm]	430	Inner diameter [mm]	300
Stator slot depth [mm]	40	Rotor thickness [mm]	10
PM thickness [mm]	9.5	PM arc [deg]	27
Skew angle of PM [deg]	5	Number of turns per phase per slot	4
Stator slot opening height [mm]	0.5	Number of turns per phase	48
Airgap length [mm]	2	Stator slot opening width [mm]	3
		Fill factor	0.45
Performance parameters			
Rated torque @ rated current [Nm]	805	Rated current [A]	362
Torque ripple [%]	3.4	Current density [A/mm^2]	5.27
Rated speed [rpm]	2800	Power @ rated current [kW]	236.1
Peak line voltage [V]	689	Copper loss [W]	3681.7
Core loss [W]	2014.6	Solid loss [W]	5115.2
Total axial length [mm]	151.82	Efficiency [%]	97.7

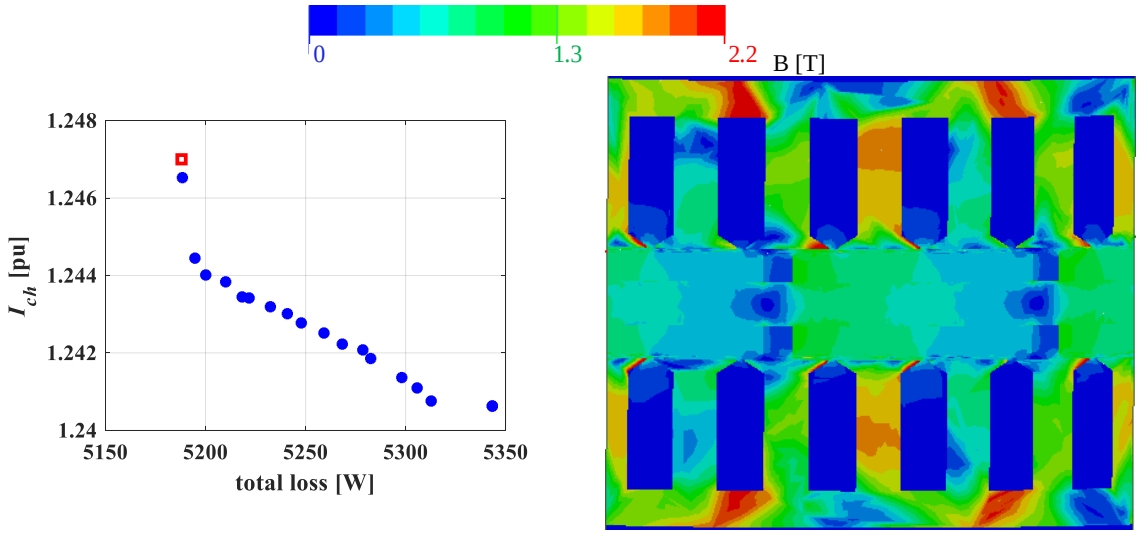

(a) (b)

Fig. 5.54. (a) the 3-D view of the optimal 200kW 12-pole AFPMSM with 36-slots. (b) the flux density distribution at the middle layer of the optimal design.

It is seen that the core losses at 12000rpm reach 4kW which results in a temperature increment if the machine operates continuously at that speed. It is mainly because of the operation of the machine at 1000Hz which is a high-end value for the laminated steels. Another risk factor of the selection of 12-pole design is its high rotor losses. It is seen that the rotor losses are reached to 5kW the segmented PM (two segments) shown in Fig. 5.47. The PMs are broken to five radial segments shown in Fig. 5.56a. The results of the variation of the solid losses against speed with five segments are shown in Fig. 5.56b. Although the amount of the rotor losses are a fifth of the two segmented rotor at 2800 rpm, having 1.2kW loss at this speed and such increase at higher speeds will lead to the rotor temperature increment drastically. The PMs temperature increment not only reduces the machine torque due to the flux drop, but also it leads to the demagnetization. Because of these issues, it is decided to reduce the number of poles to 8 and redesign a machine with the same performance as the designed 12-pole in the next part.

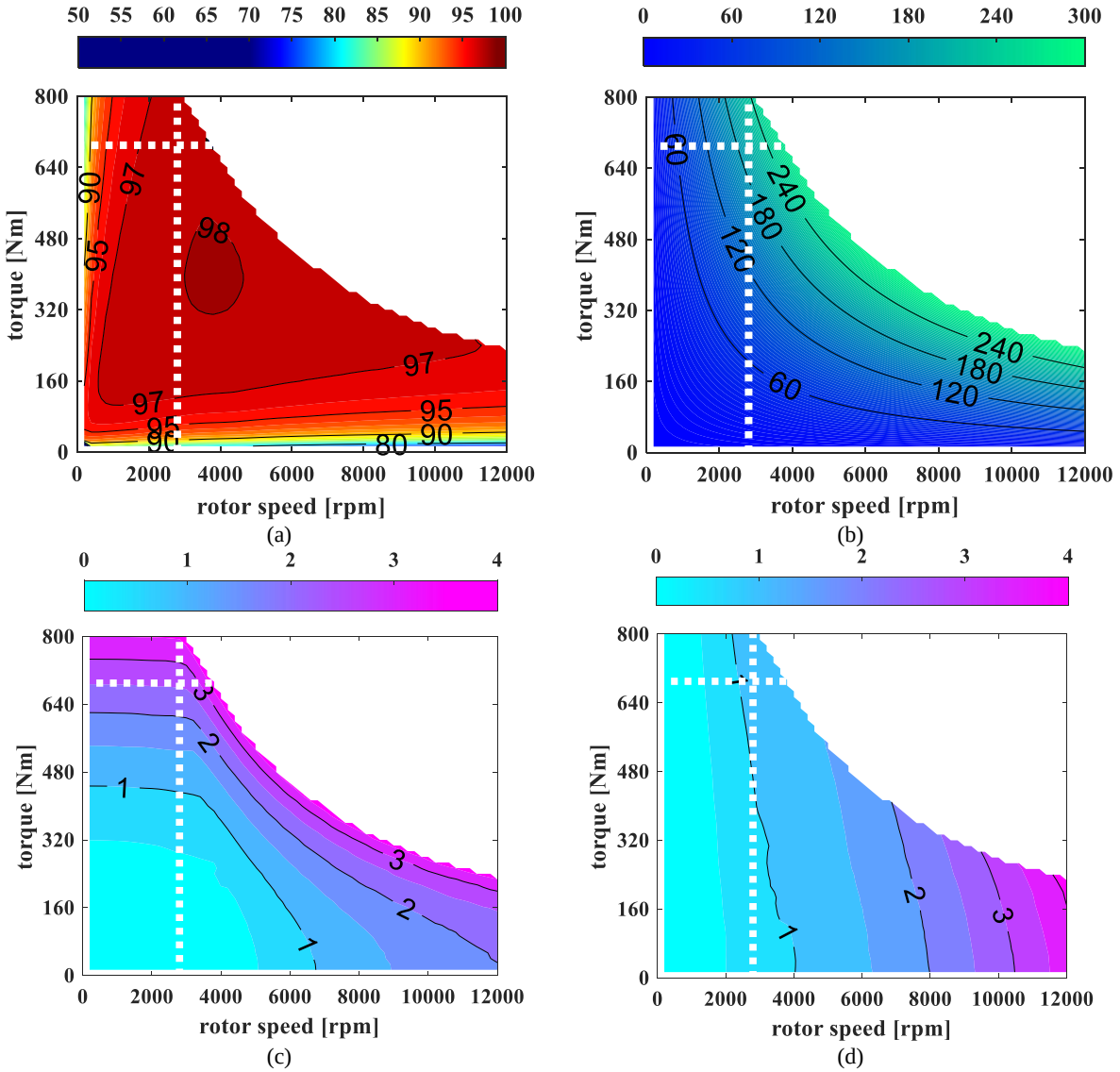

Fig. 5.55. performance parameters of the optimal 200kW 12-pole design with 36-slots in the torque speed plane. (a) EffM, (b) power map, (c) ohmic loss map, (d) core loss map

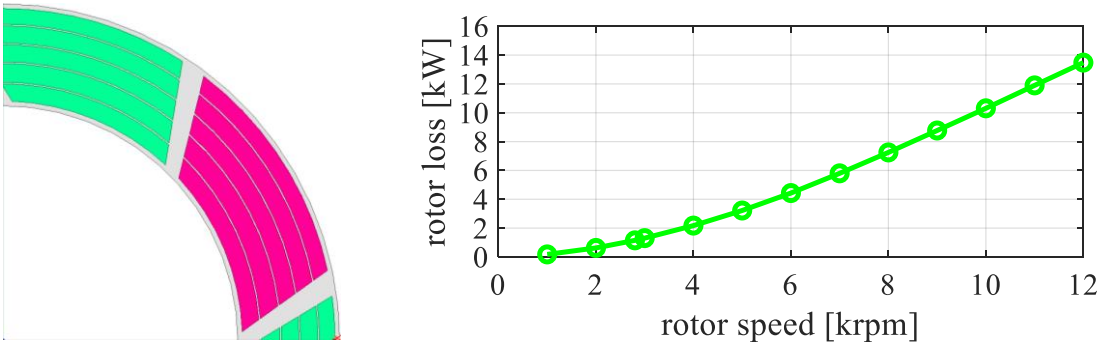

(a) (b)

Fig. 5.56. (a) PM with 5 radial segments. (b) eddy loss variation in 12-pole design in 5-radially segmented PM.

5.10.3. Eight pole design

The eight pole AFPMSM design process is carried out in a same manner as 12-pole design explained in section 5.3. A 24-slots stator is chosen at the first step to achieve two slots per pole for the eight-pole design.

As explained in section 5.3, the 430mm and 300mm are considered for the outer and inner diameters. Number of turns per phase by consideration of 0.85T for the airgap flux density (B_{ag}) is obtained by (5-2). The PM thickness in a constant PM arc of 36 degrees is increased to reach the targeted flux density in the airgap. The rated current with assumption of the efficiency of 0.97 and power factor of 0.75 is calculated by (5-3). The rated current value is used to adjust the size of the slot to reach the current density of 5.5 A/mm^2. The limitation for the increase of the slot width is the tooth flux density. When the rated current is injected to the winding the maximum tooth flux density should be set on 1.7T. The thickness of the back-iron is adjusted to reach a maximum flux density of 1.8T. Fig. 5.57 shows the 3-D view and the middle layer flux density distribution of the machine. The finalized dimension and performance parameters of this design are reported in Table 5.22.

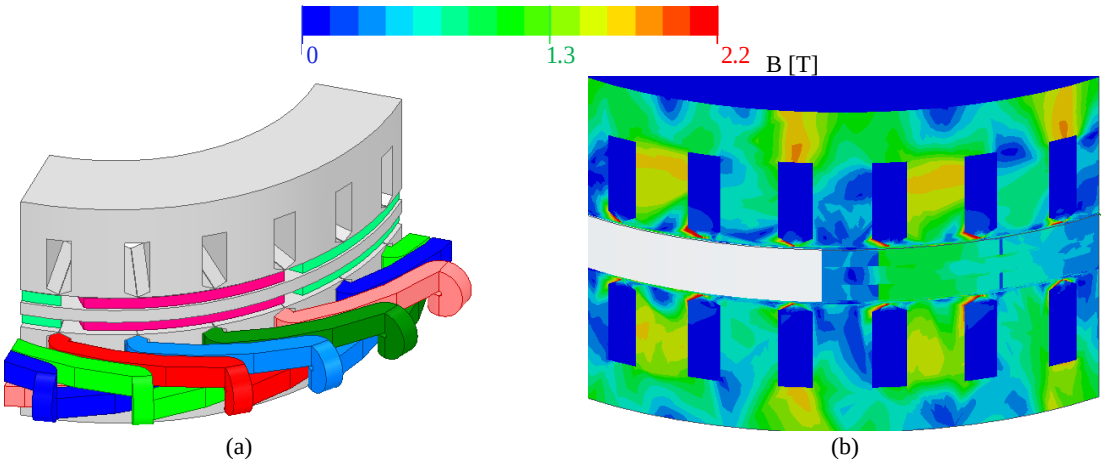

(a) (b)

Fig. 5.57. (a) the 3-D view of the optimal 200kW 8-pole AFPMSM with 24-slots. (b) the flux density distribution at the middle layer of the optimal design.

TABLE 5.22. GEOMETRY AND PERFRORMANCE PARAMETERS OF THE 8-POLES, 24-SLOTS 200KW AFPMSM DESIGNED FOR OPERATION IN HIGHER SPEEDS.

Geometry			
Number of poles	12	Number of slots	24
Outer diameter [mm]	430	Inner diameter [mm]	300
Stator slot depth [mm]	41.5	Rotor thickness [mm]	10
PM thickness [mm]	8.5	PM arc [deg]	40.5
Skew angle of PM [deg]	5	Number of turns per phase per slot	4
Stator slot opening height [mm]	0.5	Number of turns per phase	64
Airgap length [mm]	2	Stator slot opening width [mm]	3
		Fill factor	0.45
Performance parameters			
Rated torque @ rated current [Nm]	683.3	Rated current [A]	300
Torque ripple [%]	3.12%	Current density [A/mm^2]	5.45
Rated speed [rpm]	2800	Power @ rated current [kW]	200.3
Peak line voltage [V]	691	Copper loss [W]	3208.7
Core loss [W]	440.5	Solid loss [W] (PMs are segmented to five)	4240.5
Total axial length [mm]	179	Efficiency [%]	96.2

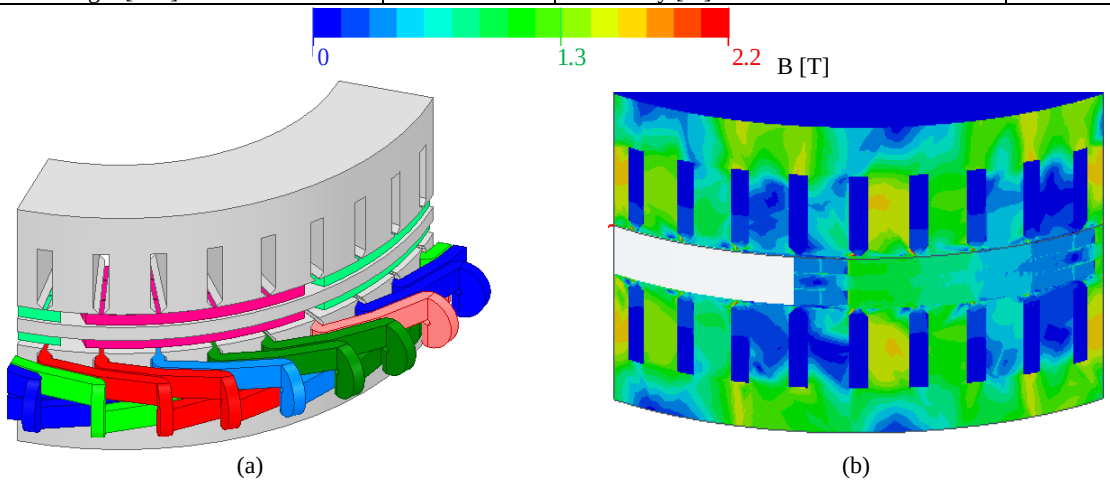

(a) (b)

Fig. 5.58. (a) the 3-D view of the optimal 200kW 8-pole AFPMSM with 36-slots. (b) the flux density distribution at the middle layer of the optimal design.

The rotor eddy current losses of this design with two segments of PM is large due to the high induced eddy current on the PM surface. Based on the segmentation effect discussed in 5.9.2, breaking the PM to smaller portions is not much helpful when the eddy current losses are in this range. For this reason, the design is updated to 36-slots to achieve 4.5 slots per pole.

To reach an equivalent 36-slot design as the 24-slot, the iron volume in the stator is kept constant. It means the total flux pathing area at the stator side in the 24-slots and 36-slots designs are same. The 36-slots design 3-D view and flux density distribution at the middle axial layer are shown in Fig. 5.58. The 3-D FEA results demonstrate the effectiveness of this change in reducing the rotor eddy current losses. Table 5.23 tabulates the dimension and performance parameters of the 36-slots design during operation at the maximum torque at the end of constant torque region. The rotor losses are decreased to 25% of the rotor loss in 24-slots design.

In the eight-pole design the PM arc is large and each PM portion is located under four stator slots. Therefore, the radial segmentation of the PMs is more useful to diminish the total induced current. To show the importance of the radial segmentation, the induced eddy current on the PMs with different segments are shown in Fig. 5.59. As shown in Figs. 5.59a to 5.59c, the segmentation is increased from

two segments to three and four. By increment of the number of segments the peak eddy current is reduced (see Figs. 5.59d to 5.59f) because of the reduction of the available PM surface. This reduction of the conductivity of the PM segments reduces their eddy current losses. These losses in the 2-segment, 3-segment, and 4-segments rotor are respectively equal to 3.3kW, 2.3kW, and 1.5kW.

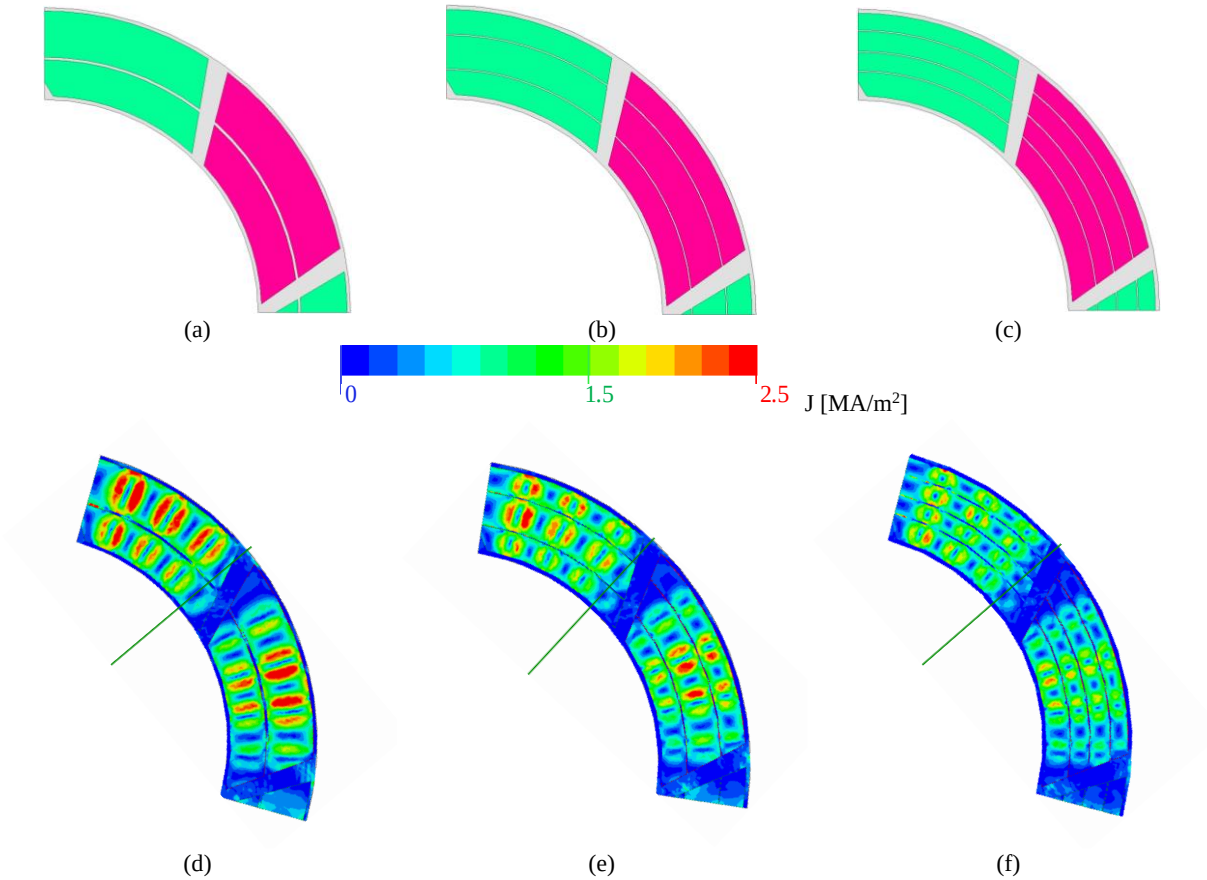

Fig. 5.59. (a), (b), and (c) shows the 2-segment, 3-segment, and 4-segment PMs. (d), (e), (f) are the current density distribution on the rotor elements of the 8-pole, 200kW design with 36-slots with 2-segment, 3-segment, and 4-segment PMs.

TABLE 5.23. GEOMETRY AND PERFRORMANCE PARAMETERS OF THE 8-POLES, 36-SLOTS 200KW AFPMSM DESIGNED FOR OPERATION IN HIGHER SPEEDS.

Geometry			
Number of poles	12	Number of slots	36
Outer diameter [mm]	430	Inner diameter [mm]	300
Stator slot depth [mm]	40.5	Rotor thickness [mm]	10
PM thickness [mm]	8	PM arc [deg]	40
Skew angle of PM [deg]	5	Number of turns per phase per slot	2
Stator slot opening height [mm]	0.5	Number of turns per phase	48
Airgap length [mm]	2	Stator slot opening width [mm]	3
		Fill factor	0.45
Performance parameters			
Rated torque @ rated current [Nm]	685	Rated current [A]	400
Torque ripple [%]	2.15	Current density [A/mm^2]	5.6
Rated speed [rpm]	2800	Power @ rated current [kW]	200.8
Peak line voltage [V]	561.87	Copper loss [W]	2816
Core loss [W]	1300	Solid loss [W] (PMs are segmented to five)	1054.2
Total axial length [mm]	176	Efficiency [%]	97.3

The axial segmentation in small numbers (2 to 3 axial cuts) does not have much effect on the reduction of the rotor eddy losses because they cannot successfully reduce the PM surface under the slots. For instance, the eddy current loss of the rotors shown in Figs. 5.60a and 5.60b are 1.52kW and 1.51kW, respectively. Although the axial segmentation is not helpful form the loss reduction point of view, it can ease the PM mounting on rotor. The smaller pieces can be simply screwed to the rotor. The variation of the 8-pole 36-slot rotor eddy current loss vs. speed is shown in Fig. 5.61. Comparison of Figs. 5.56 and 5.61 shows 20% smaller loss of the 8-pole design in all operating speeds. It is mainly due to the reduction of the operating frequency (smaller $\frac{dB}{dt}$) in 8-pole design.

Although the 8-pole machine with 36-slot offers smaller rotor loss compared to the 12-pole design with 36-slots, the rotor losses are still high. Hence, the number of slots in 8-pole design is increased to 48. Note that the flux pathing area in tooth and back-iron in the 48-slot design is equal to the 36-slot design. The dimensions and performance parameters of the 48-slot design are reported in Table 5.24.

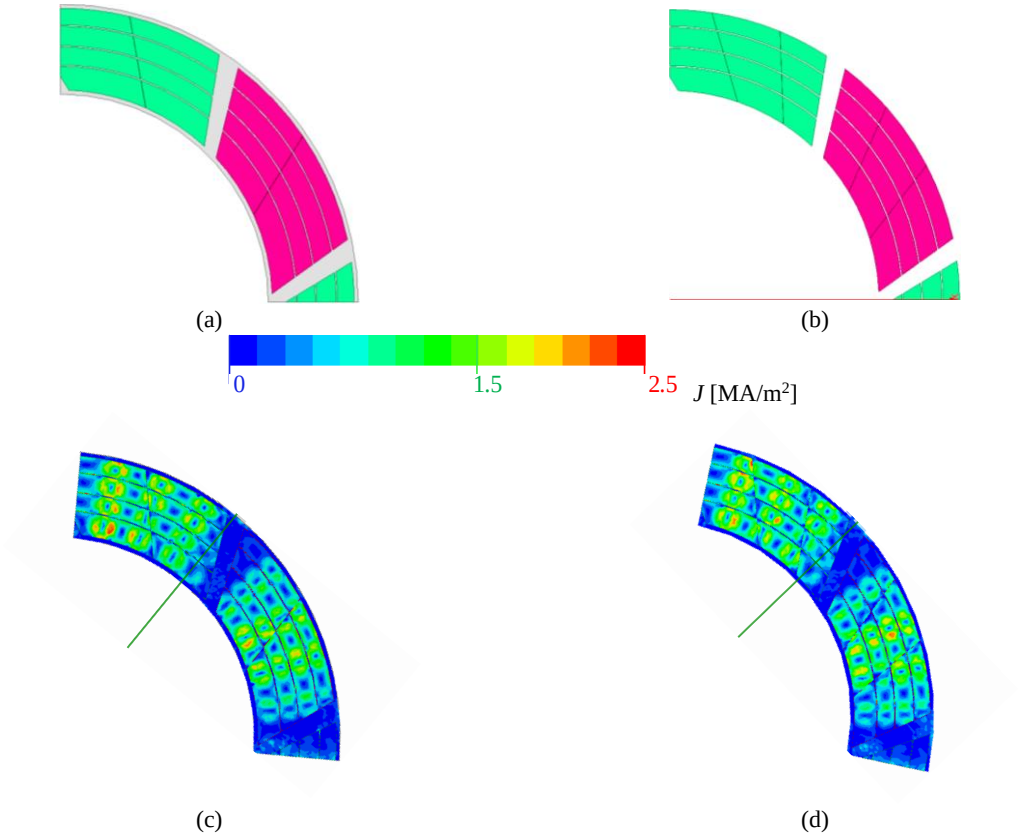

Fig. 5.60. (a) and (b) are two considered axial cuts on the PMs on the PM segments shown in Fig. g.58c. The induced eddy current on the rotors shown in (a) and (b) are shown in (c) and (d).

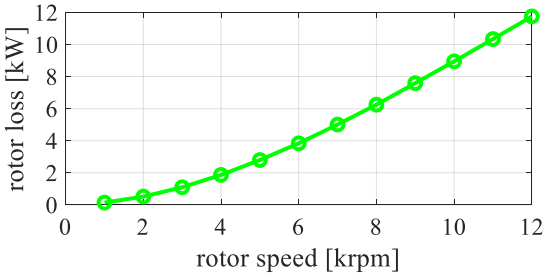

Fig. 5.61. rotor eddy loss variation in 8-pole design with 36-slot.

TABLE 5.24. GEOMETRY AND PERFRORMANCE PARAMETERS OF THE 8-POLES, 48-SLOTS 200KW AFPMSM DESIGNED FOR OPERATION IN HIGHER SPEEDS.

Geometry			
Number of poles	8	Number of slots	48
Outer diameter [mm]	430	Inner diameter [mm]	300
Stator slot depth [mm]	42	Rotor thickness [mm]	10
PM thickness [mm]	9	PM arc [deg]	40
Skew angle of PM [deg]	5	Number of turns per phase per slot	2
Stator slot opening height [mm]	0.5	Number of turns per phase	32
Airgap length [mm]	2	Stator slot opening width [mm]	3
		Fill factor	0.45
Performance parameters			
Rated torque @ rated current [Nm]	691	Rated current [A]	355
Torque ripple [%]	2.91	Current density [A/mm^2]	5.7
Rated speed [rpm]	2800	Power @ rated current [kW]	202.6
Peak line voltage [V]	655.74	Copper loss [W]	2853.1
Core loss [W]	1165	Solid loss [W] (PMs are segmented to five)	326
Total axial length [mm]	177	Efficiency [%]	97.8

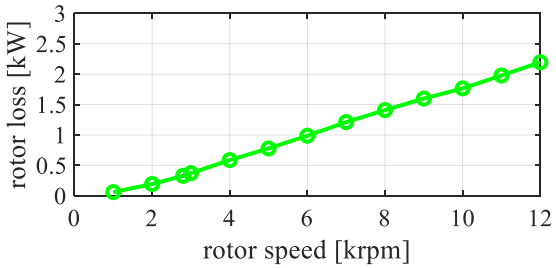

Fig. 5.62. rotor eddy loss variation in 8-pole design with 48-slot.

Table 5.24 shows the amount of rotor losses in 8-pole 48-slots design is a fourth of the 8-pole 36-slot design presented reported in Table 5.23. This small rotor loss is acceptable to select this machine for operation at higher speeds.

The curve of the variation of the rotor loss vs. speed of 8-poles, 48-slots machine is presented in Fig. 5.62. The important point which should be highlighted is the danger of demagnetization owing to the huge amount of loss at higher speeds. The only way to cool down the rotor is the consideration of a shaft groove with cooling channel. If 60m is considered for the inner side end winding, the shaft radius will be 90mm. Considering 10mm thickness for the shaft wall the groove radius (r_{gr}) is 80mm. Thus, the available contacting surface of the cooling channel with rotor (S_{rotor}) is 0.011m^2 which is obtained by (5-20). In (5-20), the rotor axial length is shown by l_{rot}.

$$S_{rotor} = 2\pi r_{gr} l_{rot} \tag{5-20}$$

The demagnetization analysis showed that the PMs can operate at 120°C safely. So, all operating speed in which the rotor temperature is less than 120°C in presence of the cooling system are considered as the valid operating point. The considered cooling system for the stator demonstrate its success in removal of the heat up to 5kW at the stator side. The stator shares a surface area of 0.018m^2 with the cooling jackets. The available cooling surface of the rotor is 60% of the stator. Thus, the cooling system can remove the rotor heat optimistically up to 60% of the 5kW which is 3.5kW. According to Fig. 5.62, the rotor losses does not reach the limit of 3.5kW until 12krpm. Therefore, this machine can operate safely up to four times of the rated speed in the FW region.

The 8-pole 48-slot total rotor loss is approximately a fourth of the other 8-pole designs, 12-poles 36-slot, and 12-pole 18-slot design. Although the rotor losses of 12-pole 72-slot design is half of the 8-pole 48-slot design, it suffers from the small characteristic current which limits its operation in the FW region. Thus, the low rotor loss and characteristic current of the 8-pole design make it a suitable option to be used as the required 200kW machine which is connected through a gearbox to the HEV engine. The analysis of the rotor temperature requires a valid FEA model which is out of scope of this chapter. However, the estimation of the rotor temperature based on the losses and available cooling system allows to select the maximum speed of 12000 rpm for the machine. Note that the axial length of the 200kW, 8-pole design is 22mm larger than the 200kW, 12-pole design. It is mainly because of the requirement of the larger flux path of the machines with smaller number of poles.

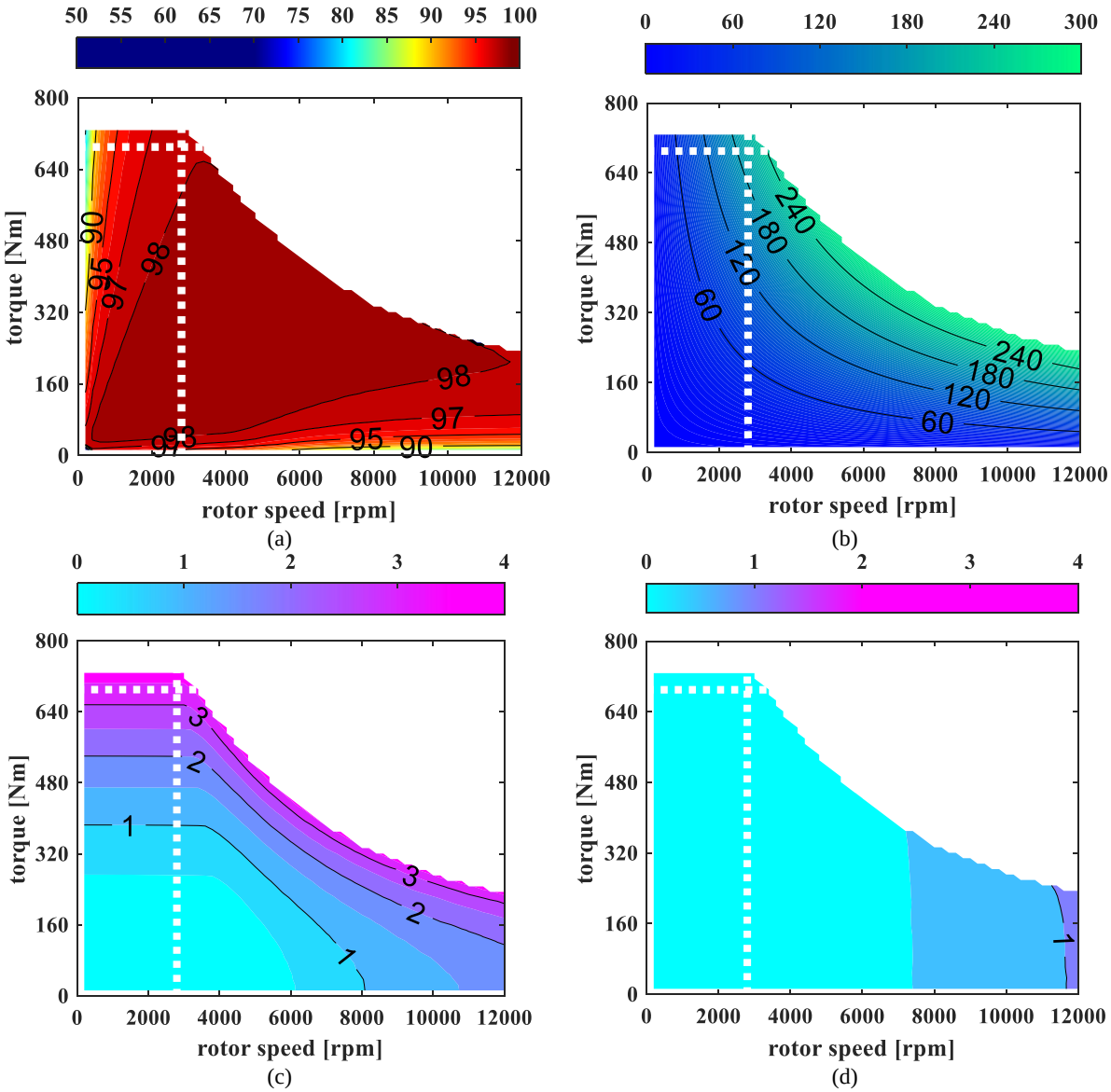

Fig. 5.63. performance parameters of the optimal 200kW 8-pole design with 48-slots in the torque speed plane. (a) EffM, (b) power map, (c) ohmic loss map, (d) core loss map

The performance parameters map of this design including EffM, power map, and loss maps are presented in Fig. 5.63. The comparison of Figs. 55 and 63 shows that the torque of the 8-pole design in the constant torque region is almost 50Nm less than the 12-pole design. According to the EffMs shown in Figs. 55a and 5.63a, the EffM of the 8-pole design is 1% higher than efficiency of the 8-pole design in most of the operating point. Figs. 55b and 63b shows that the maximum power of the 8-pole design in the FW region reaches 295kW which is 3kW less than the 12-pole design. So, the output power of both designs in the field weakening region is almost same. The copper losses of both designs are in a same range (see Figs. 55c and 63c). However, the core loss of the 8-pole design is 3kW less than the 12-pole design (see Figs. 55d and 63d). The less core loss not only brings about a higher efficiency, but also it allows to have a cooler stator compared to the 12-pole design.

The EffM of the design 8-pole machine with 48 slots when two times of the rated current is injected to the winding is shown in Fig. 5.64a. According to this figure, the machine generates 1kNm at 2800rpm when it runs at 2pu current. At the same current level, the maximum torque of 1.3kNm is achieved at 2100rpm. The power factor of the machine in the torque speed envelope is presented in Fig. 5.64b. If the user plans to drive the machine at the maximum current of 2pu, it is necessary to select an inverter which can handle this current with respect to the power factor and efficiency. The inverter rating current is obtained by (5-21) where ŋ and PF are the efficiency and power factor when 1.3kNm torque is generated at 2100rpm. Considering ŋ and PF of 94% and 51%, the inverter should be able to operate at 1481A during the overload condition.

$$I_{inv} = \frac{2 \times I_{rated}}{\eta PF} = \frac{2 \times 355}{0.94 \times 0.51} = 1481\text{A} \qquad (5\text{-}21)$$

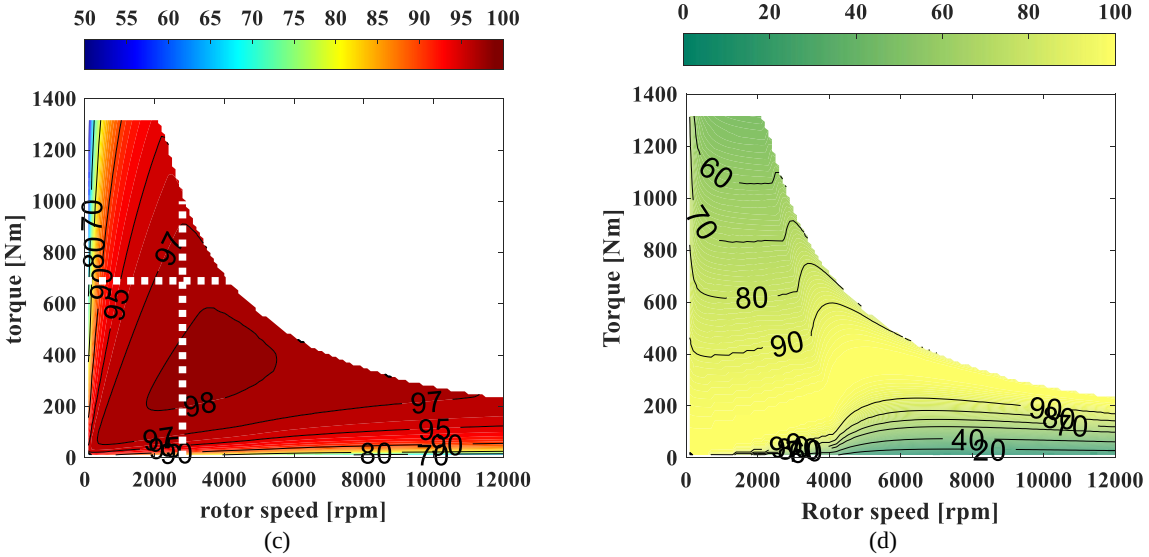

(c) (d)

Fig. 5.64. performance parameters of the optimal 200kW 8-pole design with 48-slots in the torque speed plane. (a) EffM, (b) power factor map

5.11. Conclusion

This chapter investigates the feasibility of the 100kW and 200kW axial-flux machines for an HEV. An analysis was conducted to select an optimal option between the double-stator and double-rotor designs. The double stator design was selected due to the slightly better performance that it offered in various geometries.

A design procedure based on the 3-D FEA was introduced to provide a baseline design for AFPMSMs. For thermal analysis, the introduced design process used an equivalent radial flux machine of the AFPMSM. This assumption is feasible when the available cooling surface in both axial flux and its equivalent radial flux machine are same. It should be highlighted this is necessary to have a same slot depth and tooth width in both of axial and radial flux machines. The equivalent radial flux machine was analysed using the thermal module of the Motor-CAD software. The demagnetization model of the PMs was developed to study the safety of the PMs during operation at highest current and occurrence of short circuit faults.

Gaussian process regression (kriging) was used to train the collected data from the 3-D FEA sensitivity analysis. The trained model was used to find the optimal 100kW AFPMSM. The performance parameters of the optimal 12-poles 72-slots AFPMSM were reported in the torque speed envelope to show the capability of the design in delivering the required torque in the constant torque operating region.

The designed 12-pole AFPMSM with 72-slot was selected as the proper choice for utilization as the required directly coupled 100kW machine for the targeted HEV due to the following reasons:

- It offers its maximum torque up to optimum speed of the engine (2800 rpm) and produces enough torque at the maximum engine speed (3200 rpm).
- Its maximum rotor losses are less than 120W which allows to have a cold rotor and reduces the risk of PMs demagnetization.
- It can operate at 2pu overload condition for 60 seconds which meets the requirements of HEV.
- It is torque ripple is about 3% which is an acceptable value for the direct drive electric machines.
- It operates at a high-power factor (greater than 95%) at higher torques which allows to select an optimum inverter.

A study was conducted to find a 100kW design with the capability of operation in the FW region for possible connection of the 100kW design to the engine through a gearbox. It was shown that the 100kW 12-poles design could not offer a good performance in the constant power region. Different type of rotors and stator slots were studied to find the feasible designs which offer an acceptable performance in the field weakening region. A comprehensive analysis on the effect of the slots on the

performance of the 12-pole design was conducted. It was shown that the rotor eddy current losses can be dramatically increased by reduction of the number of slots (fractional winding). The effect of the use of a smaller number of slots per pole was described and analysed. It was demonstrated that the 12-pole design with 36-slots has a promising capability for operation in the constant power region. The interior PM AFPMSM was another design with the capability of the operation in FW. However, this design was rejected for further analysis due to the large rotor losses and low power factor.

The design of the 200kW machine was started by selection of the 12-poles 36-slots design to benefit from its performance in the field weakening region. The optimization study was executed to find the optimal 200kW 12-pole design. Although the optimal design offered a good performance up to four times of the rated speed, this machine was rejected due to the large rotor losses and core losses at higher speeds. It was concluded that the 12-pole could not be a proper choice for design of 200 kW AFPMSM.

The introduced design procedure in this chapter was one more time used to design an 8-pole AFPMSM with 24-slots and 36-slots. These two designs were refused because of their large rotor losses. An 8-pole AFPMSM with 48-slot was designed and accepted as the final design for the 200-kW machine. According to the 3-D FEA results, the 48-slots design not only had smaller rotor losses (i.e., 25% less than 8-pole 36-slots design), but also it offered a characteristic current of 1.4pu. These features make it suitable for reliable operation in the field weakening region, The performance parameters of the design in the torque-speed envelope were presented and the possible shortcomings and weaknesses of the design were discussed.

The conducted analysis on the effect of slot/pole for the designed machines in this chapter showed the effectiveness of the increase of number of slots in reduction of the eddy current losses of the rotor. It was seen that the rotor losses in the 100kW design with SPP of 0.5 is ten times of the rotor loss with SPP of 1 (i.e., 500W vs 5000W). Thus, in a certain torque and speed, the efficiency of the design with SPP of 0.5 is approximately 3.5% smaller than the SPP of 1. This efficiency drops of 1% is also seen by comparing the 200kW 8-pole designs with SPP of 1 against the 200kW design with SPP of 2.

Chapter 6. Analytical model of IMs

6.1. Chapter Overview

An exploded view of induction motor is presented in Fig. 6.1. The housing and the cap region are considered as the mechanical parts of an electric motor which has no relationship with the electromagnetic behaviour of an electric motors. So, the stator dimension, rotor geometry, and cage dimensions, and number of turns of the winding section are the main parts of an IM which are contributing to the electromagnetic performance. So, the performance of an electrical machine depends on these parts and an IM is studied and modelled by study of their details.

As discussed in the previous chapters, the design and study of the performance of electric motors using the numerical methods like FEA is not computationally efficient. For this reason, researchers have devoted more time and energy to develop the accurate analytical models comparable with the results of the FEA. In the first section of this chapter, a brief description of analytical models is provided. A new analytical model which uses the solution of the Maxwell equations in different regions of an induction motor is introduced and the performance of the model is validated using the FEA results. Finally, the model is used to calculate the efficiency map of induction motor.

6.2. Introduction on the Analytical Models

The non-numeric models of the electric machines are categorized in two different groups called empirical models and analytical techniques [171], [293], [294]. The empirical methods developed based on the experiment cannot be reliable to be applied to all types of the induction machine in different sizes and rated powers [170].

The magnetic equivalent circuit (MEC) modeling and Maxwell equation-based techniques are two other types of the analytical models. Many nodes and reluctances must be considered to prepare an accurate MEC model. The increase of the number of elements in a model not only intricate the modelling process but also increases the processing time of the simulation like a numeric method. Moreover, the MEC is not much accurate without the consideration of the saturation effect where the investigation of the nonlinear characteristics of the magnetic materials complicates MECs [246].

Analytical methods solve Maxwell equations of an electric machine in the airgap. The slotting effect consideration in different parts of the machine has been the difficulty of the researcher for writing the Maxwell equation [295], [296]. The slotting effect has been modeled using some permeance dependent models since 1984 [295] to 2007 [297]. The definition of the Carter's coefficient, conformal transformation, and Schwarz-Christoffel mapping techniques are the main contributions of the researchers in modeling the slotted parts in the analytical methods. Although some simplifications have been done to reduce the complexity of these models and improve the accuracy of the analytical models, an acceptable accuracy has not been obtained. These techniques intricate the analytical model and lack the ability of the accurate prediction of the machine performance [298]. Moreover, these models (permeance related techniques) are suffered from an

accurate investigation of the nonlinearity of the magnetic parts and saturation [299].

The subdomain models (SDM) [300], [301] were introduced to consider the slotting effect directly as a solution of the Maxwell equations. The SDM, which is also called semi-analytical model, separates machine in different regions and solve the Maxwell equation for each region based on the boundary conditions. The SDM has been comprehensively studied for the permanent magnet machines [302]. Due to the difficulty of the eddy-current estimation on the rotor bars of a squirrel cage induction machine (SCIM), there are limited literature for this case [303]–[308].

A current sheet has been considered in [303] to [305] to compute the rotor bar currents of the SCIM. The introduced model in [303] was not only accurate enough in the estimation of the spatial flux density but also it requires a simulation time approximately equal to an FEA study.

In [306], the stator flux linkage was calculated at the first step when the authors assume that the rotor bars cannot conduct any current. Then, they calculate the voltage of the rotor bars by calculation of the derivation of the flux linkage. Finally, the eddy current was calculated by dividing the induced voltages by the bar resistances. Because of the consideration of a constant resistance for each harmonic, the skin effect of the rotor bars was approximately calculated using the analytical expressions. The introduced model, in [306], was improved by simultaneously calculation of the subdomain equation and electric equivalent circuit (EEC) equations with a time stepping method in [307]. Authors demonstrate that this method is computationally efficient compared to FEA. The consideration of the required transient time of this technique increases the time of a study of the analysis. For this reason, a method which considers both the slotting effect of the rotor and stators was introduced in [308] to solve the Maxwell equations at the steady-state without any need to consider the numerical transient. This method solves the Helmholtz equation and uses the time stepping to simulate the rotor motion.

The discussed literatures are focusing on the calculation of the eddy current of the rotor bars to predict the SCIM performance. The previous literature has had a focus on the transient operation of the machine when the high order harmonics are high at the rotor bars. It must be highlighted that skin effect and high order harmonics has a higher impact on the performance of the machine at the smaller slips. It has been proven the steady state performance of the SCIM can be predicted with an acceptable accuracy using its EEC [309].

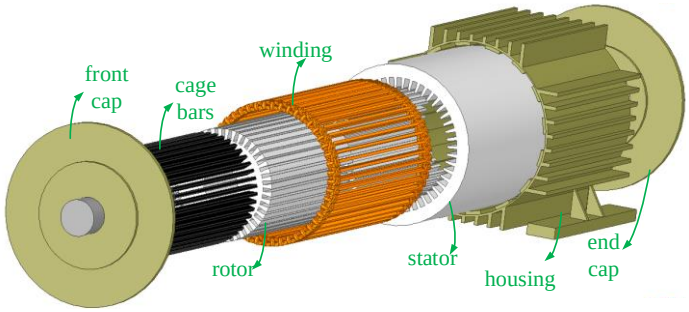

Fig. 6.1. The exploded view of the induction motor [20] © 2020 IEEE.

6.3. The Proposed Analytical Model

The proposed model consists of three main calculation steps to model an SCIM and assess its performance. Fig. 6.2 shows the overall flowchart of the proposed analytical model. The machine geometry and electrical characteristics of the machine are the initial values used in the electrical study. In the next step, the quasi-magnetostatic equations of the machine are obtained which are written for the different radiuses. The consideration of the five subdomains allows the investigation of all the slotted areas, which has not been considered previously for SCIMs. The calculated vector potentials in different areas of the model are used to find the flux density in different subdomains. Flux density allows to calculate the core loss. The electric equivalent circuit (EEC) is used to calculate the machine performance parameters, losses, and efficiency.

6.3.1. Quasi-magnetostatics problem

The SCIM is represented using a 2D model in the cylindrical coordinate system. The boundary values of MVPs for all five subdomains presented in Fig. 6.3 are required to solve the fundamental partial differential equations of the machine.

Maxwell's equation for a machine is obtained based on Gauss law presented in (6-1) [310].

$$\nabla . B = 0;\ B = \mu_0 \mu_r H + \mu_0 M \tag{6-1}$$

where B, H and M are the magnetic flux density, magnetic field strength and magnetization, respectively. On the other hand, the Laplacian of a vector potential like A is defined as follow:

$$\nabla^2 A = \nabla(\nabla . \mathrm{A}) - \nabla \times (\nabla \times \mathrm{A}) \tag{6-2}$$

where $\mathrm{B} = \nabla \times A$ and $\nabla . A = 0$. Thus, Laplacian of the magnetic vector potential is formulated by (6-3) where the current density is shown by J and is calculated by (6-4).

$$\nabla^2 A = -\mu_0 \mu_r J - \mu_0 \nabla \times M \tag{6-3}$$

$$\nabla \times H = J \tag{6-4}$$

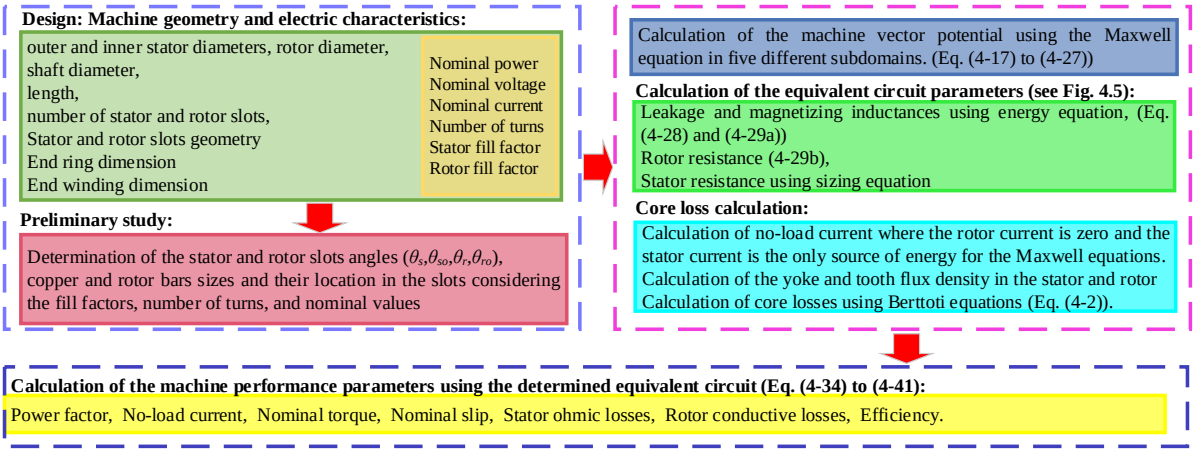

Fig. 6.2. The flowchart of the proposed analytical model [20] © 2020 IEEE.

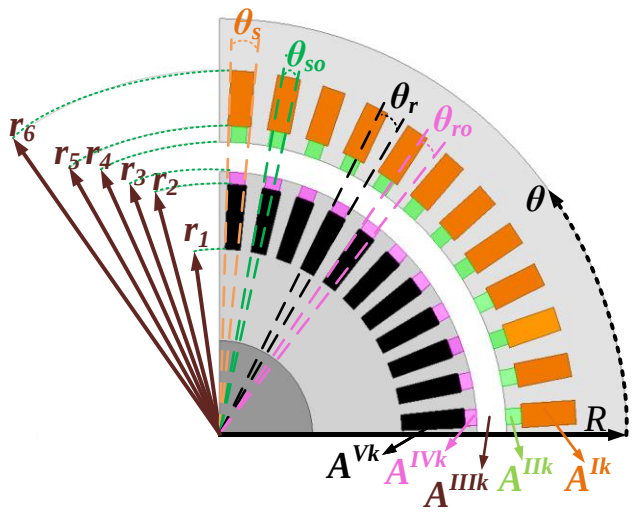

θ_s: slot angles of the stator
θ_{so}: slot opening angle of the stator
$r_1 to\ r_5$: the radius of the different subdomains
θ_r: slot angles of the rotor
θ_{ro}: slot opening angle of the rotor
$A^{Ik} to A^{Vk}$: the magnetic vector potentials inside of each subdomain

Fig. 6.3. A sample cross-section of a SCIM with the exaggerated airgap which shows the considered subdomains and parameters to write the Maxwell equations in $R-\theta$ plane [162] © 2022 IEEE.

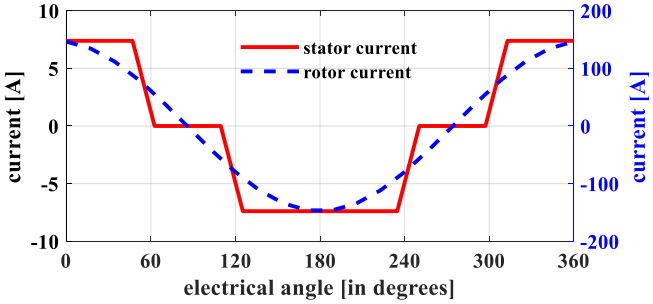

Fig. 6.4. The assumed current distribution for the stator and rotor slots of the machine under an electrical pole [162] © 2022 IEEE.

The *A*, *J*, and *M* are considered by the following vectors for a two-dimensional analysis of a machine.

$$\begin{cases} A = [0, 0, A_Z(r,\theta)] \\ J = [0, 0, J_Z(r,\theta)] \\ \mathrm{M} = [M_r(r,\theta), M_\theta(r,\theta), 0] \end{cases} \tag{6-5}$$

Note that the absence of any permanent magnetic part in the structure of an induction machine leads to the elimination of *M* matrix in the equations. Thus, the magnetic vector potential's Poisson equation in the different areas can be summarized by (6-6) for the rotor and stator slots. The Poisson equation for the other regions (i.e. airgap, slot openings and yoke) is shown by (6-7) [310].

$$\nabla^2 A_z = \frac{1}{r}\frac{\partial}{\partial r}\left(r\frac{\partial A_z}{\partial r}\right) + \frac{1}{r^2}\frac{\partial^2 A_z}{\partial \theta^2} = -\mu_0 J_z \tag{6-6}$$

$$\nabla^2 A_z = \frac{1}{r}\frac{\partial}{\partial r}\left(r\frac{\partial A_z}{\partial r}\right) + \frac{1}{r^2}\frac{\partial^2 A_z}{\partial \theta^2} = 0 \tag{6-7}$$

The general solution of the Poisson equation presented in (6-8) is considered to solve the above differential equations in the different studied subdomains.

$$A_z(r,\theta) = A_0 + B_0 lnr + \sum_{k=1}^{\infty}\left(A_k r^{\frac{-k\pi}{\beta}} + B_k r^{\frac{k\pi}{\beta}}\right)cos\left(\frac{k\pi}{\beta}(\theta-\theta_i)\right) \tag{6-8}$$

The boundary conditions of the different subdomains are obtained based on the continuity of the magnetic flux density and Ampere's law. The boundary condition for the rotor and stator slots are shown in (6-9) and (6-10), respectively [171].

Between slot and slot opening in rotor $(0 \le r \le r_1)$:

$$\begin{cases} \left.\frac{\partial A^{Vk}}{\partial r}\right|_{r=r_1} = \begin{cases} -j_{kr}\mu_0 & \theta\ under\ the\ k^{th}\ tooth\ tip \\ \left.\frac{\partial A^{IVk}}{\partial r}\right|_{r=r_1} - j_{kr}\mu_0 & otherwise \end{cases} \\ \left.\frac{\partial A^{Vk}}{\partial r}\right|_{r=0} = 0 \\ \left.\frac{\partial A^{Vk}}{\partial \theta}\right|_{\theta\ on\ the\ sides\ of\ the\ k^{th}\ rotor\ slot} = 0 \end{cases} \quad (6\text{-}9)$$

Between airgap and rotor's slot opening $(r_1 \le r \le r_2)$:

$$\begin{cases} \left.\frac{\partial A^{IVk}}{\partial r}\right|_{r=r_2} = \begin{cases} 0 & \theta\ under\ the\ k^{th}\ tooth\ tip \\ \left.\frac{\partial A^{IIIk}}{\partial r}\right|_{r=r_2} & otherwise \end{cases} \\ \left.\frac{\partial A^{IVk}}{\partial \theta}\right|_{r=r_1} = \left.\frac{\partial A^{Vk}}{\partial \theta}\right|_{r=r_1}, \left.\frac{\partial A^{IVk}}{\partial \theta}\right|_{r=r_2} = \left.\frac{\partial A^{IIIk}}{\partial \theta}\right|_{r=r_2} \\ \left.\frac{\partial A^{IVk}}{\partial \theta}\right|_{\theta\ on\ the\ sides\ of\ the\ k^{th}\ rotor\ slot} = 0 \end{cases} \quad (6\text{-}10)$$

Equation (6-11), (6-12), and (6-13) give the boundary condition for the rotor slots' opening, stator slots' opening, and the airgap region [171].

Airgap $(r_2 \le r \le r_3)$:

$$\left.\frac{\partial A^{IIIk}}{\partial r}\right|_{r=r_3} = \begin{cases} 0 & \theta\ under\ the\ k^{th}\ tooth\ tip \\ \left.\frac{\partial A^{IIk}}{\partial r}\right|_{r=r_3} & otherwise \end{cases} \quad (6\text{-}11)$$

$$\left.\frac{\partial A^{IVk}}{\partial r}\right|_{r=r_2} = \begin{cases} 0 & \theta\ under\ the\ k^{th}\ tooth\ tip \\ \left.\frac{\partial A^{IIIk}}{\partial r}\right|_{r=r_2} & otherwise \end{cases}$$

Between airgap and stator's slot opening in stator $(r_3 \le r \le r_4)$:

$$\begin{cases} \left.\frac{\partial A^{IIIk}}{\partial r}\right|_{r=r_4} = \begin{cases} 0 & \theta\ under\ the\ k^{th}\ tooth\ tip \\ \left.\frac{\partial A^{IIk}}{\partial r}\right|_{r=r_4} & otherwise \end{cases} \\ \left.\frac{\partial A^{IIIk}}{\partial \theta}\right|_{r=r_3} = \left.\frac{\partial A^{IVk}}{\partial \theta}\right|_{r=r_3}, \left.\frac{\partial A^{IIIk}}{\partial \theta}\right|_{r=r_4} = \left.\frac{\partial A^{IIk}}{\partial \theta}\right|_{r=r_4} \\ \left.\frac{\partial A^{IIIk}}{\partial \theta}\right|_{\theta\ on\ the\ sides\ of\ the\ k^{th}\ rotor\ slot} = 0 \end{cases} \quad (6\text{-}12)$$

Between slot and slot opening in stator $(r_4 \le r \le r_5)$:

$$\begin{cases} \left.\frac{\partial A^{Ik}}{\partial r}\right|_{r=r_4} = \begin{cases} -j_{ks}\mu_0 & \theta\ unther\ the\ k^{th}\ tooth\ tip \\ \left.\frac{\partial A^{IIk}}{\partial r}\right|_{r=r_4} - j_{ks}\mu_0 & otherwise \end{cases} \\ \left.\frac{\partial A^{Ik}}{\partial \theta}\right|_{r=r_5} = 0 \\ \left.\frac{\partial A^{Ik}}{\partial \theta}\right|_{\theta\ on\ the\ sides\ of\ the\ k^{th}\ rotor\ slot} = 0 \end{cases} \quad (6\text{-}13)$$

The continuity of the vector potential considered in (6-14) is necessary to calculate the MVP where it is not a function of radius (r) or θ.

$$A^{Vk}\big|_{r=r_1} = A^{IVk}\big|_{r=r_1}, A^{IVk}\big|_{r=r_2} = A^{IIIk}\big|_{r=r_2}$$
$$A^{IIIk}\big|_{r=r_3} = A^{IIk}\big|_{r=r_3}, A^{IIk}\big|_{r=r_4} = A^{Ik}\big|_{r=r_4} \quad (6\text{-}14)$$

The stator and rotor currents are assumed sinusoidally distributed in the machine slots for the magnetostatics analysis. Fig. 6-4 shows the assumed current distribution with a single layer winding for a stator phase and rotor current under a pole.

The general solution of Maxwell's partial differential equations in the machine airgap are obtained by the consideration of sinusoidal functions in the determined pole-pairs. It must be noted that the general solution in the slot areas is attained based on the zero tangential magnetic field on the sides of the slots [304]. The unknown variables (i.e. *a, b, A, B, C, D*) in the general solutions for the different subdomains presented in Table 6.1 can be solved using the boundary conditions. For the simplicity the functions presented in (6-15) and (6-16) are adopted. The equations presented in Table 6.2 are the extended version of the general solution which are used to find the Fourier coefficients. Appendix I includes the procedure of the calculation of the unknowns available in Table 6.1.

$$P(n,r,rx) = (r/rx)^n + (rx/r)^n \quad (6\text{-}15)$$
$$E(n,r,rx) = (r/rx)^n - (rx/r)^n \quad (6\text{-}16)$$

TABLE 6.1. GENERAL SOLUTION OF THE VECTOR POTENTIAL FOR EACH SUBDOMAIN OF THE SCIM [162] © 2022 IEEE.

stator slot
$$A^{Ik} = \sum_n A_n^{Ik} \frac{\theta_s}{n\pi} \frac{\mathrm{P}\left(\frac{n\pi}{\theta_s}, r, r_5\right)}{\mathrm{E}\left(\frac{n\pi}{\theta_s}, r_5, r_4\right)} \cos\left(\frac{n\pi}{\theta_s}(\theta - \theta_s^{0k})\right) + a_{1k} - \mu_0 j_{sk}\left(\frac{1}{4}r^2 - \frac{1}{2}r_5^2 \ln r\right) \quad (6\text{-}17)$$

stator slot opening
$$A^{IIk} = \sum_n \left(A_n^{IIk} \frac{\mathrm{E}\left(\frac{n\pi}{\theta_{so}}, r, r_4\right)}{\mathrm{E}\left(\frac{n\pi}{\theta_{so}}, r_3, r_4\right)} + B_n^{IIk} \frac{\mathrm{E}\left(\frac{n\pi}{\theta_{so}}, r, r_3\right)}{\mathrm{E}\left(\frac{n\pi}{\theta_{so}}, r_4, r_3\right)} \right) \cos\left(\frac{n\pi}{\theta_{so}}(\theta - \theta_{so}^{0k})\right) + b_{2k} \ln r + a_{2k} \quad (6\text{-}18)$$

airgap
$$A^{III} = \sum_n \left[A_n^{III} \frac{1}{nN_p} \frac{\mathrm{P}(nN_p, r, r_4)}{\mathrm{E}(nN_p, r_3, r_4)} \sin nNp\theta + B_n^{III} \frac{1}{nN_p} \frac{\mathrm{P}(nN_p, r, r_3)}{\mathrm{E}(nN_p, r_4, r_3)} \sin nNp\theta + C_n^{III} \frac{1}{nN_p} \frac{\mathrm{P}(nN_p, r, r_4)}{\mathrm{E}(nN_p, r_3, r_4)} \cos nNp\theta + D_n^{III} \frac{1}{nN_p} \frac{\mathrm{P}(nN_p, r, r_3)}{\mathrm{E}(nN_p, r_4, r_3)} \cos nNp\theta \right] \quad (6\text{-}19)$$

rotor slot opening
$$A^{IVk} = \sum_n \left(A_n^{IVk} \frac{\mathrm{E}\left(\frac{n\pi}{\theta_{ro}}, r, r_2\right)}{\mathrm{E}\left(\frac{n\pi}{\theta_{ro}}, r_3, r_2\right)} + B_n^{IVk} \frac{\mathrm{E}\left(\frac{n\pi}{\theta_{ro}}, r, r_3\right)}{\mathrm{E}\left(\frac{n\pi}{\theta_{ro}}, r_2, r_3\right)} \right) \cos\left(\frac{n\pi}{\theta_{ro}}(\theta - \theta_{ro}^{0k})\right) + b_{4k} \ln r + a_{4k} \quad (6\text{-}20)$$

rotor slot
$$A^{Vk} = \sum_n A_n^{Vk} \frac{\theta_r}{n\pi} \frac{\mathrm{P}\left(\frac{n\pi}{\theta_r}, r, r_1\right)}{\mathrm{E}\left(\frac{n\pi}{\theta_r}, r_2, r_1\right)} \cos\left(\frac{n\pi}{\theta_r}(\theta - \theta_r^{0k})\right) + a_{5k} - \mu_0 j_{rk}\left(\frac{1}{4}r^2 - \frac{1}{2}r_1^2 \ln r\right) \quad (6\text{-}21)$$

j_{rk}, j_{sk}, P	current density of the k^{th} rotor/stator slots, and number of pole pairs	$\theta_r^{0k}, \theta_s^{0k}$	starting angles of the k^{th} rotor/stator slots
$\theta_{ro}^{0k}, \theta_{so}^{0k}$	starting angles of the k^{th} rotor/stator slot openings	*a, b, A, B, C, D*	coefficients of the Fourier series

TABLE 6.2. SOLVING THE GENERAL FORM OF THE VECTOR POTENTIALS BASED ON THE BOUNDARY CONDITIONS PRESENTED IN (6-9)-(6-14) AND VECTOR POTENTIALS OF EACH SUBDOMAIN WRITTEN IN TABLE 6.1 [162] © 2022 IEEE.

r_5: consider the effect of winding in the stator slots and use (6-12), (6-13) and (6-14) to calculate parameters:

$$(I): \quad \sum_{n_2} A_{n_2}^{Ik} \cos\left(\frac{n_2\pi}{\theta_s}(\theta-\theta_s^{0k})\right) = \begin{cases} \sum_{n_1}\left(A_{n_1}^{IIk}\frac{n_1\pi}{\theta_{so}}\frac{2}{\mathrm{E}\left(\frac{n_1\pi}{\theta_{so}},r_5,r_4\right)} + B_{n_1}^{IIk}\frac{n_1\pi}{\theta_{so}}\frac{\mathrm{P}}{\mathrm{E}}\left(\frac{n_1\pi}{\theta_{so}},r_4,r_5\right)\right)\cos\left(\frac{n_1\pi}{\theta_{so}}(\theta-\theta_{so}^{0k})\right) + b_{2k} + \frac{1}{2}j_{kv}\mu_0(r_4^2-r_5^2) \\ \frac{1}{2}j_{kv}\mu_0(r_4^2-r_5^2) \end{cases} \tag{6-22}$$

$$(II): \quad \sum_{n_1}\frac{n_1\pi}{\theta_{so}}B_{n_1}^{IIk}\sin\left(\frac{n_1\pi}{\theta_{so}}(\theta-\theta_{so}^{0k})\right) = \sum_{n_2}A_{n_2}^{Ik}\frac{n_2\pi}{\theta_s}\frac{\theta_s}{n_2\pi}\frac{\mathrm{P}}{\mathrm{E}}\left(\frac{n_2\pi}{\theta_s},r_5,r_4\right)\sin\left(\frac{n_2\pi}{\theta_s}(\theta-\theta_s^{0k})\right)$$

r_4: refers to the stator opening section and uses (6-11), (6-12), (6-13) and (6-14) to calculate parameters

$$(III): \quad \sum_n B_n^{III}\sin nN_p\theta + D_n^{III}\cos nN_p\theta = \begin{cases} \sum_{n_1}\left(A_{n_1}^{IIk}\frac{n_1\pi}{\theta_s}\frac{\mathrm{P}}{\mathrm{E}}\left(\frac{n_1\pi}{\theta_{so}},r_4,r_3\right) + B_{n_1}^{IIk}\frac{n_1\pi}{\theta_{so}}\frac{2}{\mathrm{E}\left(\frac{n_1\pi}{\theta_{so}},r_3,r_4\right)}\right)\cos\left(\frac{n_1\pi}{\theta_{so}}(\theta-\theta_{so}^{0k})\right) + b_{2k} \\ 0 \end{cases} \tag{6-23}$$

$$(IV): \quad \sum_{n_1}\frac{n_1\pi}{\theta_{so}}A_{n_1}^{IIk}\sin\left(\frac{n_1\pi}{\theta_{so}}(\theta-\theta_{so}^{0k})\right) = \sum_n -A_n^{III}\frac{2}{\mathrm{E}(nN_p,r_2,r_3)}\cos nNp\theta - B_n^{III}\frac{\mathrm{P}}{\mathrm{E}}(nN_p,r_3,r_2)\cos nNp\theta + C_n^{III}\frac{2}{\mathrm{E}(nN_p,r_2,r_3)}\sin nNp\theta + D_n^{III}\frac{\mathrm{P}}{\mathrm{E}}(nN_p,r_3,r_2)\sin nNp\theta$$

r_3: refers to the airgap area and uses (6-10) and (6-14) to calculate parameters

$$(V): \quad \sum_n A_n^{III}\sin nN_p\theta + C_n^{III}\cos nN_p\theta = \begin{cases} \sum_{n_1}\left(A_{n_1}^{IVk}\frac{n_1\pi}{\theta_{ro}}\frac{\mathrm{P}}{\mathrm{E}}\left(\frac{n_1\pi}{\theta_{ro}},r_2,r_3\right) + B_{n_1}^{IVk}\frac{n_1\pi}{\theta_{ro}}\frac{2}{\mathrm{E}\left(\frac{n_1\pi}{\theta_{ro}},r_3,r_2\right)}\right)\cos\left(\frac{n_1\pi}{\theta_{ro}}(\theta-\theta_{ro}^{0k})\right) + b_{4k} \\ 0 \end{cases} \tag{6-24}$$

$$(VI): \quad \sum_{n_1}\frac{n_1\pi}{\theta_{ro}}A_{n_1}^{IVk}\sin\left(\frac{n_1\pi}{\theta_{ro}}(\theta-\theta_{ro}^{0k})\right) = \sum_n -A_n^{III}\frac{\mathrm{P}}{\mathrm{E}}(nN_p,r_3,r_2)\cos nNp\theta - B_n^{III}\frac{2}{\mathrm{E}(nN_p,r_2,r_3)}\cos nNp\theta + C_n^{III}\frac{\mathrm{P}}{\mathrm{E}}(nN_p,r_3,r_2)\sin nNp\theta + D_n^{III}\frac{2}{\mathrm{E}(nN_p,r_2,r_3)}\sin nNp\theta$$

r_2: refers to the rotor opening section area and uses (6-9) and (6-14) to calculate parameters

$$(VII): \quad \sum_{n_2} A_{n_2}^{Vk}\cos\left(\frac{n_1\pi}{\theta_r}(\theta-\theta_r^{0k})\right) = \begin{cases} \sum_{n_1}\left(A_{n_1}^{IVk}\frac{n_1\pi}{\theta_{ro}}\frac{2}{\mathrm{E}\left(\frac{n_1\pi}{\theta_{ro}},r_1,r_2\right)} + B_{n_1}^{IVk}\frac{n_1\pi}{\theta_{ro}}\frac{\mathrm{P}}{\mathrm{E}}\left(\frac{n_1\pi}{\theta_{ro}},r_2,r_1\right)\right)\cos\left(\frac{n_1\pi}{\theta_{ro}}(\theta-\theta_{ro}^{0k})\right) + b_{4k} + \frac{1}{2}j_{kv}\mu_0(r_1^2-r_0^2) \\ \frac{1}{2}j_{kv}\mu_0(r_1^2-r_0^2) \end{cases} \tag{6-25}$$

$$(VIII): \quad \sum_{n_1}\frac{n_1\pi}{\theta_{ro}}B_{n_1}^{IVk}\sin\left(\frac{n_1\pi}{\theta_{ro}}(\theta-\theta_{ro}^{0k})\right) = \sum_{n_2}\frac{n_2\pi}{\theta_r}A_{n_2}^{Vk}\frac{\theta_r}{n_2\pi}\frac{\mathrm{P}}{\mathrm{E}}\left(\frac{n_2\pi}{\theta_r},r_1,r_0\right)\sin\left(\frac{n_2\pi}{\theta_r}(\theta-\theta_r^{0k})\right)$$

According to the presented relationships in Table 6.2, $A_{n_1}^{IIk}$, A_n^{III}, $A_{n_1}^{IVk}$, $A_{n_2}^{Vk}$, $B_{n_1}^{IIk}$, B_n^{III}, $B_{n_1}^{IVk}$, C_n^{III}, and D_n^{III} are the unknown coefficient of the MVP in the different subdomains. The MVP coefficients are categorized into excitation dependent and geometry dependent terms. For instance, in part (*I*) and

part (*VII*), b_{2k} and b_{4k} are the excitation dependent parameters of their related terms which vary for different exciting currents. The geometry dependent terms are extracted from each equation and located in a specific array which is shown by *G*. Matrix *G* is calculated for a certain geometry. The excitation dependent terms create the excitation vector shown by *K*. According to (6-26), vector *X* consists of the unknown constants and is computed based on these matrices.

$$GX = K \rightarrow X = G^{-1}K \tag{6-26}$$

The curl of the calculated MVP represents the flux density for each region. So, the radial and tangential flux densities are determined by (6-27a) and (6-27b), respectively.

$$B_r(r,\theta) = \frac{1}{r}\frac{\partial A_z}{\partial \theta} \quad \text{(a)}$$
$$B_\theta(r,\theta) = -\frac{\partial A_z}{\partial r} \quad \text{(b)} \tag{6-27}$$

6.3.2. Use of Energy Equation to find the EEC parameters

The calculated magnetic vector potential is utilized to find the magnetic energy. According to (6-28), the magnetic energy results from the integration of the products of half of the current density by MVP's over the volume of the slots. So, the value of magnetic energy is required to determine the parameters of the machine EEC shown in Fig. 6.5.

The turn ratio of the induction machine (n_{rs}) is used to transform the rotor side elements to the stator side of the equivalent circuit. Three independents linear equation are required to find the three unknown inductances (L_{ls}, L_{lr}, L_m) in (6-28). So, three sets of independent arbitrary excitation currents (i.e. (i_{st},*0*), (*0*,i_{rt}), and (i_{st},i_{rt})) are assumed to form the needed linear equations. The arbitrary stator and rotor test currents are shown by i_{st} and i_{rt}, respectively. The presented set of the equations in (6-29) includes three independent values of W_{ms}, W_{mr}, and W_{msr} which are the magnetic energy produced by each set of the excitation. The constant values of k_s, k_r, and k_m are defined to calculate the performance parameters. The equivalent circuit helps to calculate the stator current and the rotor slip which are required for the calculation of the machine torque. It must be noticed that the coefficient matrix is independent of the stator currents. Therefore, the inverse of the matrix is only calculated once which, in turn, leads to higher processing speed for the model.

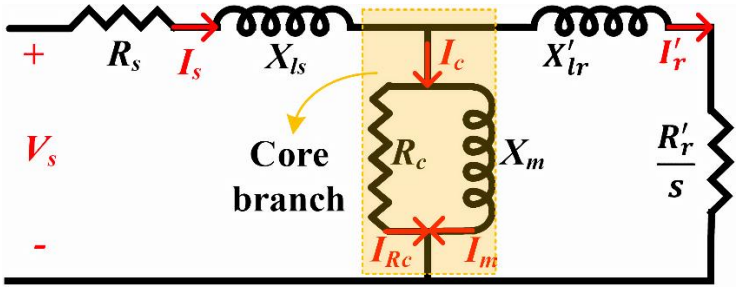

Fig. 6.5. Electric equivalent circuit of the induction machine [20] © 2022 IEEE.

TABLE 6.3. EQUIVALENT CIRCUIT PARAMETERS OF THE STUDIED RFIM AS PER THE PROPOSED ANALYTICAL MODEL [162] © 2022 IEEE.

magnetic energy equation: $W_m = \frac{1}{2}\sum_k \iiint_{\mathcal{V}} (j_{sk}A^{\mathrm{I}k} + j_{rk}A^{\mathrm{V}k})\mathrm{d}v = \frac{3}{2}\left(\frac{1}{2}(L_{ls}+L_m)i_{ms}^2 + \frac{1}{2}(L'_{lr}+L_m)n_{rs}^2 i_{mr}^2 + n_{rs}L_m i_{mr} i_{ms}\right)$ (6-28)

reactances
$$\begin{aligned} &X_{ls} + X_m = 4\omega W_{ms}/3i_{st}^2 = k_s \\ &X'_{lr} + X_m = 4\omega W_{mr}/(3i_{rt}^2 n_{rs}^2) = k_r/n_{rs}^2 \\ &X_m = 2\omega(W_{mrs} - W_{ms} - W_{mr})/(3i_{st}i_{rt}n_{rs}) = k_m/n_{rs} \end{aligned}$$ (6-29)

$$\begin{cases} X_{ls} + X_m = k_s \\ X'_{lr} + X_m = k_r/n_{rs}^2 \end{cases} \xrightarrow{X_{ls}=X'_{lr}} n_{rs} = \sqrt{\frac{k_r}{k_s}} \xrightarrow{considering\ (4-29)} X_m = n_{rs}k_m\ , X_{ls} = X'_{lr} = k_s - X_m$$ (6-30)

k_s, k_r, k_m: constants used for performance parameters calculations

L_{ls}, L'_{lr}, L_m, X_{ls}, X_{lr} ', X_m: stator and equivalent rotor leakage, and magnetizing inductances and reactances

W_{ms}, W_{mr}, W_{mrs}: magnetic energy when the currents are $(i_{st}, 0)$, $(0, i_{rt})$, (i_{st}, i_{rt}), respectively

ρ, N_b, p: rotor conductivity, number of bars, number of pole pairs, and n_{rs}: turns ratio

R_r, R'_r: rotor resistance seen from rotor and stator side

H_{er}: height of the end ring

A_b, A_{er}: bars and end ring cross section area

R_b, R_{er}: bar and end ring resistances

i_{mr}, i_{ms}: rotor and stator currents

TABLE 6.4. PERFORMANCE CALCULATION FROM THE EEC.

$$Z_{in} = (R_s + jX_{ls}) + \left(\frac{R'_r}{s} + jX'_{lr}\right) \Big\| (jX_m)$$ (6-31)

$$I_s = V_s/Z_{in}$$ (6-32)

$$I'_r = I_s(jX_m/\left(\frac{R'_r}{s} + jX'_{lr}\right) + jX_m)$$ (6-33)

$$\tau = 3R'_r I_s^2/s\omega_s$$ (6-34)

$$P_{out} = \tau\omega_m$$ (6-35)

$$P_{cu} = 3R_s I_s^2 + 3R'_r I_r'^2$$ (6-36)

$$S_{in} = 3V_{ph}I_s^* \rightarrow P_{in} = real(S_{in}), PF = P_{in}/S_{in}$$ (6-37)

$$\eta = \frac{P_{out}}{P_{out} + P_{cu} + P_{fe}}$$ (6-38)

The turn ratio of the machine is a critical value for further investigations of the machine. It can be assumed that the value of the stator and rotor leakage inductances are approximately equal. Considering the equality of the inductances and value of k_s and k_r, the turn ratio of the machine can be calculated by (6-30).

The determination of n_{rs} eases the machine analysis based on T-model equivalent circuit. Table 6.4 presents the related formulas of the machine performance parameters calculation. The machine equivalent impedance is calculated by (6-31) for each value of slip. After that, the stator current and the rotor current transferred to the stator side are calculated using (6-32) and (6-33), respectively. Determination of these parameters and consideration of slip variation enables calculation of the machine output power, copper losses, power factor, and efficiency using (6-34) to (6-38).

6.3.3. Improvement of the calculation of the EEC parameters using updated energy equation

The accuracy of the estimation of the equivalent circuit parameters is improved when the effect of the mutual inductance between the stator winding is considered in the energy equation. To consider this effect, (6-28) is updated by a term in the stator related equation (see (6-39)). In (6-29), M_{ss} is the mutual inductances between the stator windings. β is defined to consider the number of the responsible inductances for different current distributions on winding.

$$W_m = \frac{3}{2}\left(\frac{1}{2}(L_{ls} + \beta M_{ss} + L_m)i_{ms}^2 + \frac{1}{2}(L'_{lr} + L_m)n_{rs}^2 i_{mr}^2 + n_{rs}L_m i_{mr} i_{ms}\right) \quad (6\text{-}39)$$

In the updated energy equation shown in (6-39), the number of unknowns is increased by one compared to (6-28). So, another set of equation is needed to find the additional value which is obtained by definition of a series excitation. Fig. 6.6 shows the considered excitations for creation of the four required equations to find four unknowns in (6-39).

Considering (6-39), the summation of the stator leakage and linkage inductances are obtained when the rotor current (I_{mr}) is zero and i_{ms} is injected to the stator winding. A single layer winding structure is assumed for the distribution of the current on the slots to simulate this condition. The red solid line (I_{st}) in Fig. 6.6(a) shows the distributed current for the calculation of the energy by (6-39). Note that the current of the phase C is zero in this excitation and consequently β is 1. So, the calculated energy (W_{ms}) is equal to the summation of the stored energy in a leakage inductance, mutual inductance, and a linkage inductance. Considering the rated frequency (f) and the synchronous speed ($\omega = 2\pi f$), the first equation of the four required equations is obtained as follow:

$$X_{ls} + X_{Mss} + X_m = 4\omega W_{ms}/3I_{st}^2 \quad (6\text{-}40)$$

A sinusoidal current (I_{rt}) shown in Fig. 6.6(b) is distributed on the rotor bars when the stator current is zero ($I_{st} = 0$). In this excitation condition, the second term of the energy equation (W_{mr}) is non-zero. It enables writing the second required equation which is presented in (6-41).

$$X'_{lr} + X_m = 4\omega W_{mr}/(3I_{rt}^2 n_{rs}^2) \quad (6\text{-}41)$$

The third set of the combination of excitation is prepared when the stator slots are supplied by the solid red lines in Fig. 6.6(a) and rotor bars are excited by the current presented in Fig. 6.6(b). The resulted equation (W_{msr}) from this excitation is employed to write the third required equation presented in (6-42).

$$X_m = 2\omega(W_{mrs} - W_{ms} - W_{mr})/(3I_{st}I_{rt}n_{rs}) \quad (6\text{-}42)$$

The above three equations are driven from the equation (6-39) in different excitation condition. In the single layer excitation shown with red line in Fig. 6.6(a), the flux encompasses a pole (see Fig. 6.7(a)). Hence, the resulted mutual inductance is the inductance between the windings of phase A and B. If an excitation is defined to create a flux pass like the single layer winding excitation, the mutual inductance will be equal to the summation of several mutual inductances, leakage inductances, and magnetizing inductance when the machine operates at no-load condition. Hence, the blue line excitation which is called series excitation (I_{ser}) is defined to calculate the energy from (6-39). In this excitation, the flux linkage equation is written by (6-43) and the energy equation calculated from the integral of the flux linkage is shown in (6-44).

$$\begin{aligned}\lambda = {} & L_{ls}I_{sera} + M_{ss}I_{serc} + M_{ss}I_{serb} + L_m I_{sera} + L_{ls}I_{serb} + M_{ss}I_{serc} + M_{ss}I_{sera} + L_m I_{serb} \\ & + L_{ls}I_{serc} + M_{ss}I_{sera} + M_{ss}I_{serb} + L_m I_{serc}\end{aligned} \quad (6\text{-}43)$$

$$W_{mse} = \frac{3}{2}(L_{ls} + 2M_{ss} + L_m)I_{ser}^2 \quad (6\text{-}44)$$

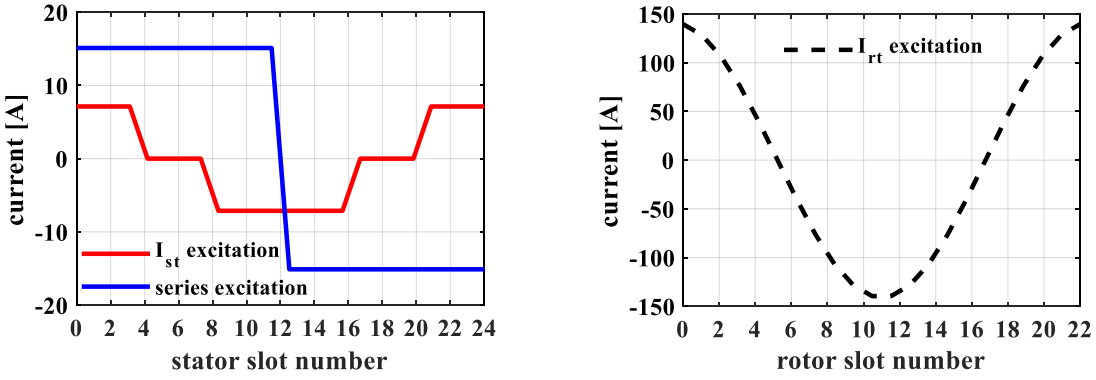

(a) stator excitations (b) rotor excitation

Fig. 6.6. the distributed currents on the stator and rotor slots to write the energy equations [162] © 2022 IEEE.

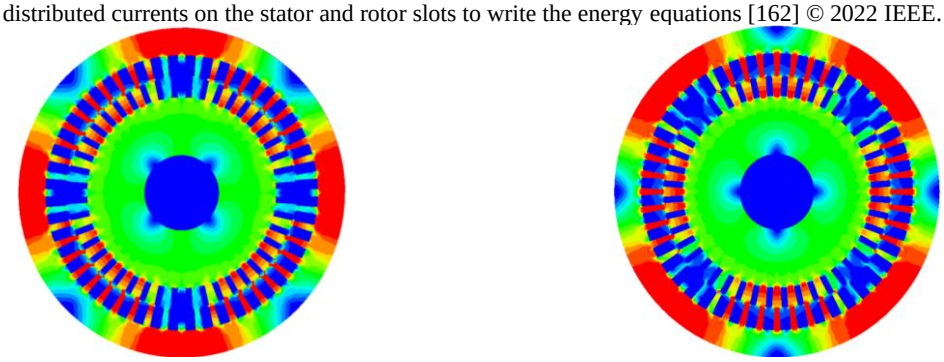

(a) The flux density distribution when the I_{st} is injected to the windings in magnetostatics analysis.

(b) The flux density distribution when the I_{ser} is injected to the windings in magnetostatics analysis.

Fig. 6.7. The flux density distribution with different excitations [162] © 2022 IEEE.

The resulted energy is equal to the stored energy in three phase inductances. The flux density distribution presented in Fig. 6.7(d) shows the similarity of flux pass in both excitations (red line and blue line when they are distributed on the stator slots). The calculated energy (W_{mse}) is used as the fourth required equation to write the four-equation system. The relationship between the calculated energy and the inductances is written in (6-45).

$$\boldsymbol{X_{ls} + 2X_{Mss} + X_m = 2\omega W_{mse}/3I_{ser}^2} \tag{6-45}$$

All the driven equations ((6-40) to (6-42) and (6-45)) are solved to attain the leakage and linkage inductances required for the EEC. The stator and rotor resistances (i.e., R_s and R_r) are other important parameters of the equivalent circuit. The stator resistance is calculated based on the presented equation in (6-46).

$$\boldsymbol{R_s = (1 + \alpha\Delta\theta)\frac{\rho((r_5 + r_6)\pi/2P + 2L)N_{ss}P}{3\theta_s(r_6{}^2 - r_5{}^2)k_{fs}}} \tag{6-46}$$

Where $\boldsymbol{\alpha}$ is the temperature coefficient and $\boldsymbol{\Delta\theta}$ is the difference of the stator winding temperature with 25˚C. $\boldsymbol{\rho}$ is specific copper resistance temperature coefficient. P represents the number of pole pairs. L and N_{SS} are the stack length and number of stator slots, respectively. and K_{fs} is the fill factor of the windings. The rotor bars resistance ($\boldsymbol{R_b}$) and end-ring equivalent resistance ($\boldsymbol{R_{er}}$) are obtained by (6-47) where number of bars is shown by (N_b) and the bars and end ring cross section areas are indicated by $\boldsymbol{A_b}$, $\boldsymbol{A_{er}}$, respectively. Also, the rotor fill factor is presented by k_{fr}.

$$R_b = \rho L_{bar}/\left(\theta_r(r_2^2 - r_1^2)k_{fr}\right) \tag{6-47}$$

$$\boldsymbol{R_{er}} = \left(\frac{\boldsymbol{2\pi r_2}}{\boldsymbol{N_b}}\right) + \left(\frac{\boldsymbol{H_{er}}}{\boldsymbol{2}}\right)/\left(\boldsymbol{4A_{er}\, sin^2(p\pi/N_b)}\right)$$
$$R'_r = (R_b + R_{er})/n_{rs}^2 = R_r/n_{rs}^2$$

$\boldsymbol{R_r}$, $\boldsymbol{R'_r}$ are rotor resistance seen from rotor and stator side, respectively. The height of the end-ring and length of a bar are presented by $\boldsymbol{H_{er}}$ and $\boldsymbol{L_{bar}}$. The core resistance (R_C) will be the last element of the EEC which is computed by the calculation of the core loss at the no-load condition. The core loss computation method is discussed in the next section.

6.4. The Core Loss Calculation

The calculation of the core losses can be done using the prepared machine model by applying the time stepping method to the magnetostatics analysis. Due to the rotation of the rotor in the time stepping, the geometry matrix (G) is changed in each rotor position. So, all the calculations must be done again which increases the analysis time. To reduce the simulation time, two different excitations called sinusoidal and cosinusoidal excitation are distributed on the stator slots (see Fig. 6.8). The consideration of the two different excitation allows seeing the variation of the fluxes in different subdomains. The average value of the calculated core losses from these two types of excitations is reported as the core loss.

The Berttoti equations presented in (6-48) are used for the iron loss calculations in different subdomains. In (6-48), the hysteresis, eddy, and excess losses are shown by P_h, P_{ed}, P_{ex}, respectively.

$$\begin{cases} P_h = k_h f(B_{ts}^2 V_{ts} + B_{ys}^2 V_{ys} + B_{tr}^2 V_{tr} + B_{yr}^2 V_{yr}) \\ P_{ed} = k_{ed} f^2 (B_{ts}^2 V_{ts} + B_{ys}^2 V_{ys} + B_{tr}^2 V_{tr} + B_{yr}^2 V_{yr}) \\ P_{ex} = k_{ex} f^{1.5} (B_{ts}^{1.5} V_{ts} + B_{ys}^{1.5} V_{ys} + B_{tr}^{1.5} V_{tr} + B_{yr}^{1.5} V_{yr}) \end{cases} \quad (6\text{-}48)$$

where k_h, k_{ed}, and k_{ex} are the hysteresis, eddy current, and excess losses Steinmetz constants which depends on the lamination material used in the structure of the rotor and stator. f is the rated frequency of the machine, because it is assumed that the fundamental harmonic of the no-load current is distributed on the winding. The tooth and yoke flux densities are shown with B_t and B_y, respectively. The s and r indices show the stator and rotor related values. The tooth and yoke volumes are shown by V_t and V_y. The total iron losses should be calculated by (6-49).

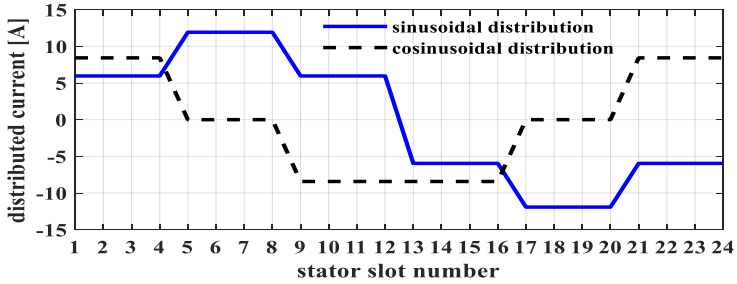

Fig. 6.8. Sinusoidal and cosinusoidal distribution of the current under a pole used for calculation of the core losses [162] © 2022 IEEE.

$$P_{fe} = (P_h) + (P_{ed}) + (P_{ex}) \quad (6\text{-}49)$$

The calculated core loss from (6-49) is used to find the equivalent core resistance (R_C) in the EEC by (6-50).

$$R_C = \frac{3(|V_{ph} - R_s I_s - j2\pi f L_{ls} I_s|)^2}{P_{fe}} \quad (6\text{-}50)$$

6.5. The Proposed Saturation Model

In this section, the saturation effect, which has not been studied in previous SDM related literature about the SCIM, is modelled to increase the accuracy of the calculation of the core loss and machine performance using the SDM and EEC. The magnetic flux density of an ideal core is similar to a motor with a real steel core with a same supply voltage because the flux density is a function of voltage and frequency. Therefore, the magnetic flux density of the motor with the real steel core can be calculated based on its B-H curve. The calculated magnetic field strength is required to estimate the saturation level of the motor cores and correct the saturation-related values in the EEC parameters.

According to Fig. 6.9(a), an Ampere loop is assumed around a pole in the proposed estimation method of the saturation effect. In an ideal core, with infinite permeability, the ampere-turns produce the magnetic field in the air subdomain. However, in a steel core, in addition to the air subdomain, the iron parts are magnetized according to Ampere's law formulated in (6-51). So, Ampere's law should be separately written for both iron and air areas.

The flux density in the iron parts depends on the core relative permeability in the stator and rotor teeth and yokes (μ_{rt} and μ_{ry}). According to (6-51), these values are required to find the exact value of the mmf in each region (i.e., rotor and stator teeth and yokes). In the proposed method, the flux density of the iron parts is calculated when the relative permeability of the core is equal to infinity (shown by X_1 in Fig. 6.9(b)). Then, the corresponding magnetic field strength (H_2 in Fig. 6.9(b)) of the calculated flux density based on the real B-H curve is obtained. In other words, the method ignores the relative permeability of the core to find the flux density (i.e., assuming an ideal core) but updates the magnetic field strength value based on the flux density of the real B-H curve.

The ampere-turns (mmf) for the stator/rotor teeth and yoke are demonstrated in (6-51a) and (6-51b), respectively. Because some of the rotor/stator teeth under a pole are saturated, especially at higher magnetic loadings, the magnetic flux density of the airgap is usually distorted. Therefore, the average value of the neighbouring teeth under a pole is considered to increase the accuracy of the estimation of the magnetic flux density in this modelling method.

The ampere-turns in the air regions consisting of airgap and rotor slots are formulated in (6-51c) and (6-51d). In (6-51c) and (6-51d), flux density is calculated based on the radial component of the curl of magnetic vector potential in the relevant subdomain. Then, the integral of the magnetic field strength over the closed loop gives the required ampere-turns.

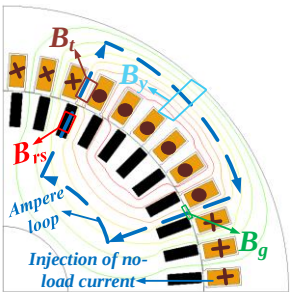

(a) ampere loop for no-load condition

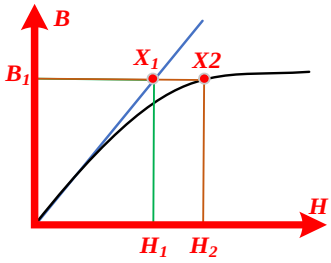

(b) an abstract of the proposed saturation model.

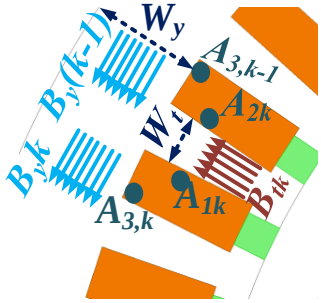

(c) magnetic flux density distribution of the stator yoke and teeth.

Fig. 6.9. The considered ampere loop and the strategy of the saturation modelling using the MVPs [162] © 2022 IEEE.

TABLE 6.5. AMPERE LAW EQUATION FOR A SINGLE POLE AS ILLUSTRATED IN FIG. 6.9 (THE REQUIRED VECTOR POTENTIALS FOR (6-51) ARE PRESENTED IN APPENDIX II) [162] © 2022 IEEE.

$$\sum_k T_s I_{sk} = \underbrace{\frac{r_6-r_4}{\mu_0}\left(\frac{B_{ts\pi}}{\mu_{rts\pi}}+\frac{B_{ts0}}{\mu_{rts0}}\right)+\frac{r_3-r_1}{\mu_0}\frac{B_{tr0}}{\mu_{rtr0}}}_{\text{(a) AT in rotor/stator teeth}} + \underbrace{\left(\frac{2\pi}{N_s\mu_0}\right)\sum_k\frac{B_{ysk}}{\mu_{rysk}}+\left(\frac{2\pi}{N_b\mu_0}\right)\sum_k\frac{B_{yrk}}{\mu_{ryrk}}}_{\text{(b) AT in rotor/stator yoke segn}} + \underbrace{\frac{1}{\mu_0}\int_{r_3}^{r_4}(B_{g0}-B_{g\pi})\mathrm{d}r}_{\text{(c) AT in the airgap regior}} + \underbrace{\frac{1}{\mu_0}\int_{r_1}^{r_2}B_{rs}\mathrm{d}r}_{\text{(d) AT in the rotor slot}} \quad (6\text{-}51)$$

$$\Downarrow \qquad \Downarrow \qquad \Downarrow \qquad \Downarrow$$

$$\frac{r_6-r_4}{\mu_0}\left[\frac{(A_{1,\pi s}-A_{2,\pi s})}{\mu_{rts\pi}W_{ts}}+\frac{(A_{1,0s}-A_{2,0s})}{\mu_{rts0}W_{ts}}\right]+\frac{r_3-r_1}{\mu_0}\frac{(A_{1,0r}-A_{2,0r})}{\mu_{rts\pi}W_{tr}} \quad \frac{2\pi}{N_s\mu_0}\sum_k\left[\frac{A_{3,ks}}{\mu_{ryks}W_{ys}}\right]+\frac{2\pi}{N_b\mu_0}\sum_k\left[\frac{A_{3,ks}}{\mu_{ryks}W_{yr}}\right] \quad \sum_n\left[\frac{(A_n^{III}-B_n^{III})(1-(-1)^n)}{n}\right]\sum_n\left[\frac{A_n^{Vk}\theta_r(-1)^n}{n\pi}\right]$$

$$k_{sat} = \left(\int_{in\ core}\vec{H}.\mathrm{d}\vec{l}+\int_{in\ air}\vec{H}.\mathrm{d}\vec{l}\right)\Big/\left(\int_{in\ air}\vec{H}.\mathrm{d}\vec{l}\right) \quad (6\text{-}52)$$

$$X_m^{new} = X_m/k_{sat};\ X_{ls}^{new} = X_{ls}/k_{sat};\ X_{lr}^{new} = X_{lr}/k_{sat} \quad (6\text{-}53)$$

A_1, A_2, A_3: vector potential values at the positions indicated in Fig 6.9(c). other indexes indicate rotor/stator, and position of tooth or yoke segment (eg. start/end of pole or kth).

AT, T_s, I_{sk}: ampere-turn, number of turns per slot, no-load current of turns in kth slot

$B_{ts\pi}$, B_{ts0}: magnetic flux density in the first and last stator teeth of a pole. (Fig 6.9(a))

B_{tr0}: magnetic flux density in the first rotor tooth of a pole. (Fig 6.9(a))

B_{g0}, $B_{g\pi}$: axial component of magnetic flux density in the start and end of a pole (Fig. 6.9(a))

W_{ts}, W_{tr}, W_{ys}, W_{yr},: width of stator and rotor teeth and yokes. (Fig 6.9(c))

B_{yrk}, B_{ysk}, μ_r,: magnetic flux density of kth stator and rotor segments, relative permeability

k_{sat}: saturation factor

N_s, N_b, k_{sat}: number of stator slots and rotor bars, saturation factor

The saturation factor is defined around an Ampere loop which includes the mmf drops in the rotor and stator teeth and yokes as well as the airgap (see Fig. 6.9(a)). In each saturation level, the magnetic field strength in the iron parts (stator/rotor yokes and teeth) are obtained through the explained procedure for derivation of (6-51a) and (6-51b). As the considered Ampere loop shown in Fig. 6.9(a) includes a rotor slot, the mmf drop in the airgap and rotor slot are obtained using (6-51c) and (6-51d). The summation of the calculated mmfs in the core and iron regions results in the numerator of (6-52). The denominator of (6-52) is the sum of the calculated mmfs in only the air regions.

As indicated in (6-53), the EEC magnetizing and leakage reactances are updated by dividing the magnetizing and stator/rotor leakage reactance values by k_{sat}. The following pseudocode summarizes the procedure of the estimation of the saturation level in SCIMs using the proposed method.

- Find MVPs at each subdomain at no-load condition. The no-load current is found using the calculated reactances before consideration of saturation.
- Calculate A_1, A_2, A_3 using the presented equations in Appendix II at each position in the considered Ampere loop.
- Calculated the required flux densities in each region ($B_{ts\pi}$, B_{ts0}, B_{tr0}, B_{ysk} , B_{yrk}). The relationship of the flux densities with the calculated A_1, A_2, A_3 are formulated in (6-51a) and (6-51b).
- Find the magnetic field strength associated with the calculated flux density in each region from the real iron B-H curve.
- Find ampere-turns by multiplication of the obtained magnetic field strength with the length of the iron for each area of iron.
- Calculate the summation of obtained ampere-turns in each region to obtain iron mmf drop (i.e., $\int_{in\ core} \vec{H}.\overrightarrow{dl}$).
- Use (6-51c) and (6-51d) to find the mmf drop in the air regions (i.e., $\int_{in\ air} \vec{H}.\overrightarrow{dl}$).
- Calculate saturation factor using (6-52).
- Update inductances by means of the obtained saturation factor using (6-53).

The core B-H characteristic and the estimated permeability of the studied machine is presented in Fig. 6.10(a) to show the variation of the core permeability as a function of magnetic field strength. The red rectangle in Fig. 6.10 (a) shows the initial flux density and the corresponding magnetic field strength for an ideal core. The green rectangle is the updated magnetic field strength obtained from the real B-H curve.

Fig. 6.10(b) shows how the iron and airgap mmfs and saturation factor changes as a function of magnetizing current. At low values of current, the flux density is low, and the iron has a high value of permeability and hence the airgap mmf drop is dominant. At higher values of current, the iron permeability is reduced by saturation which brings about an increase of the iron path reluctance and hence a larger iron mmf drop. The saturation factor is thus near unity at low values of current but increases significantly at higher values of current.

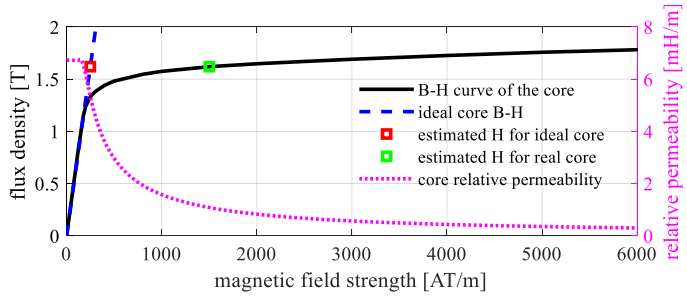

(a) B-H curve of the core lamination materials and the estimated core relative permeability on the basis of the B-H curve .

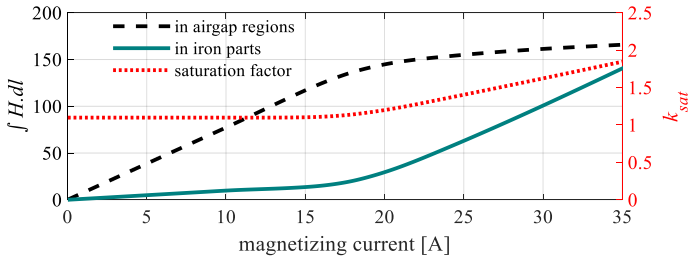

(b) The airgap and iron mmf drops and the saturation factor as a function of magnetizing current.

Fig. 6.10. The The graphical description of the proposed saturation model [162] © 2022 IEEE.

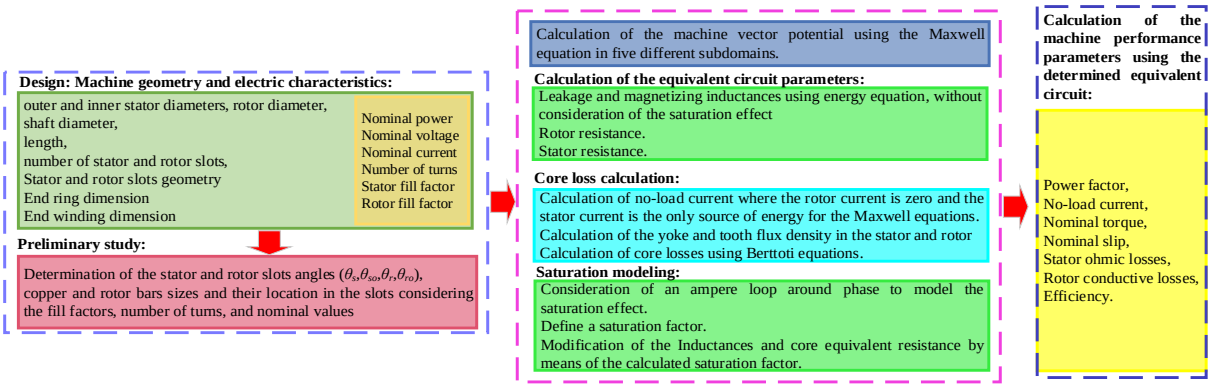

Fig. 6.11. The flowchart of the analytical model when the saturation effect is considered in the model [162] © 2022 IEEE.

The values of the leakage and magnetizing inductance depend on the saturation level of the core. So, these values are modified by the saturation factor (k_{sat}) defined in (6-52) to achieve a more precise EEC. As written in (6-53), these values are updated by dividing the previously extracted values by k_{sat}. The flowchart of the analytical model with consideration of the saturation effect is presented in Fig. 6.11.

6.6. Validation of the Proposed Model using Finite Element Analysis

A 7.5kW machine with a rated frequency and voltage of 50 Hz and 380 V is considered for the validation of the model. The machine geometry and specifications are reported in Table 6.6. The validation of the proposed model is carried out through a comparative study with FEA results. The software used is Ansys Electromagnetics 2020® [144] which executes the time-domain based FEA model. The time step used is 0.2 ms for both 3D and 2D FEA simulations. A three-phase sinusoidal voltage source was used to model the supply. The effect of inter-bar and in-plane currents are ignored in the FEA model.

The rotor bar end connection resistance (R_{er}) was calculated using (6-47) and used as the user-defined end ring resistance in 2D FEA model. The effect of the end ring resistance is automatically considered in 3D FEA. Table 6.6 includes the height and width of the end rings used for the 3D FEA model. The stator resistance is calculated from (6-46). The Ansys FEA package uses the Steinmetz equations to estimate the core losses. Similar Steinmetz equations and constants are used to estimate the core losses in the analytical model.

6.6.1. Validation of the model in estimation of field and EEC parameters

In the first step, the airgap radial and axial flux density estimated by the proposed method is compared with the 2D and 3D FEA results. Fig. 6.12 shows that the model can successfully predict the radial and tangential airgap flux density.

To validate the accuracy of the model in the estimation of the saturation level of the core, the magnetization current versus no-load voltage is obtained and compared with the 2D FEA results (see

Fig. 6.13(a)). The variation of the magnetizing and leakage reactances with the magnetizing current is plotted in Fig 6.13(b). It shows the effectiveness of the saturation factor to estimate a correct value for the inductances.

TABLE 6.6. THE GEOMETRY AND PROPERTIES OF THE INVESTIGATED MACHINE FOR THE MODEL VERIFICATION [162] © 2022 IEEE.

Core material	M19-24
Number of turns per slot	14
Number of pole pairs	2
Air gap [mm]	0.5
Stack length [mm]	250
Outer diameter [mm]	210
Inner diameter [mm]	148
Shaft diameter [mm]	48
Number of stator slots per pole pair	48
Number of rotor slots per pole pair	44
Stator slot height (Hss) [mm]	12.9
Rotor slot height (Hrs) [mm]	12
Rotor bar length [mm]	254.5
Rotor bar height [mm]	10.8
Stator yoke height [mm]	18.1
Rotor yoke height [mm]	37
Stator wedge height [mm]	0.8
Rotor half-wedge width [mm]	0.5
Rotor inner end ring width [mm]	8
Rotor inner end ring height [mm]	8

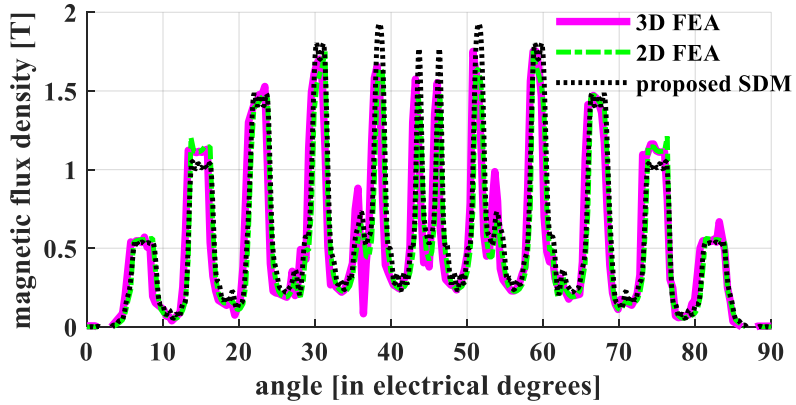

(a) analytical result comparison of the airgap radial flux density with 2D and 3D FEA.

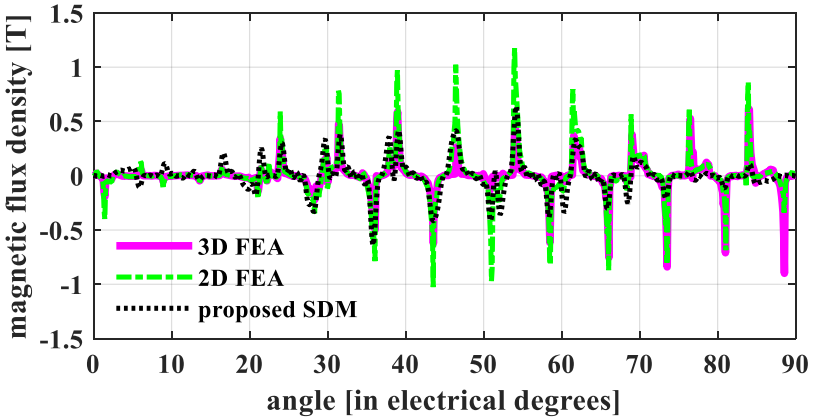

(b) analytical result comparison of the airgap tangential flux density with 2D and 3D FEA.

Fig. 6.12. The airgap flux density at the full-load condition; comparison of the results of SDM with 2D and 3D FEA [162] © 2022 IEEE.

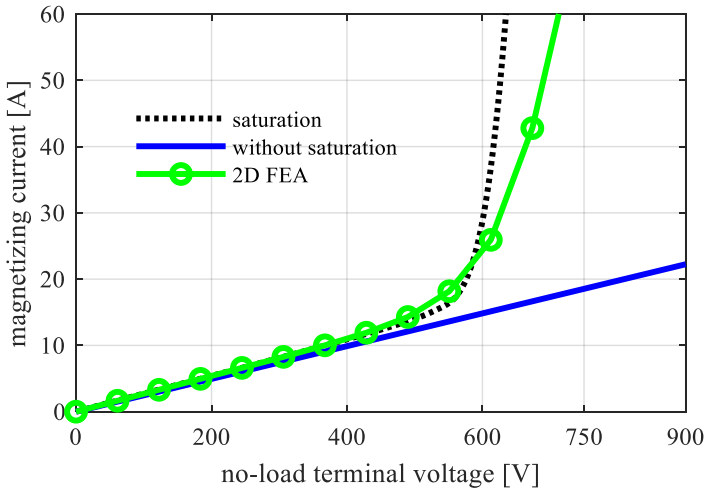

(a) magnetizing current versus no-load line voltage

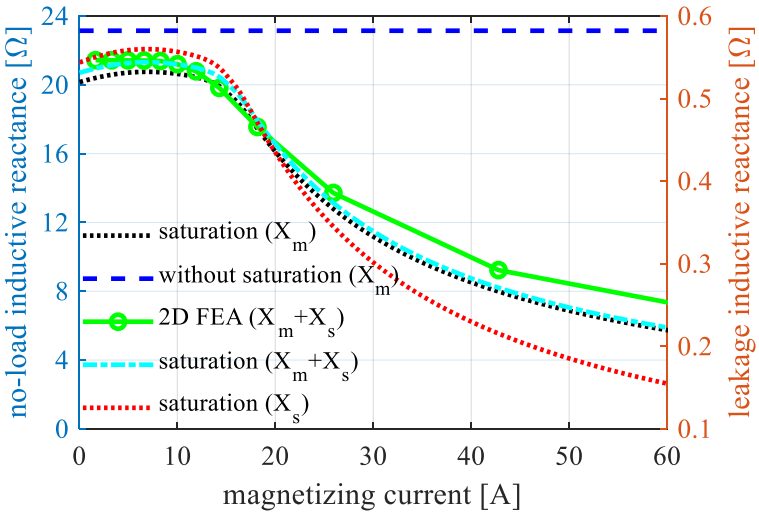

(b) magnetizing and leakage reactance variation vs. magnetizing current changing as the result of core saturation.

Fig. 6.13. The performance of the proposed SDM in prediction of the core saturation level [162] © 2022 IEEE.

6.6.2. Validation of the proposed model in prediction of the performance parameters

The extracted performance parameters of the studied 7.5 kW SCIM from 3D FEA, reported in Table 6.7, are investigated as the rated values of the machine. Table 6.8 shows the calculated values of the equivalent circuit parameters for the case study. Having these parameters enables the calculation of the machine performance parameters using the EEC model used in [20]. A bar graph is provided to compare the results of the proposed model with the conventional analytical model and 2D FEA. The bar graph presented in Fig. 6.14 demonstrates the proposed model accuracy in the prediction of the SCIM performance. Note that all values are per unitized where the 3D FEA results are considered as the base value.

The stator current and electromagnetic torque against speed of the machine are presented in Fig. 6.15(a) and (b), respectively. These curves demonstrate the ability of the proposed model to predict the performance parameters. Note that the torque is not completely matched in low speeds because of

the rectangular shape of the considered slots which affects the flux paths and increases the high order harmonics at the current of the bars. The crawling effect resulting from the presence of the high- order harmonics of the rotor bar currents cannot be predicted because only fundamental harmonic is considered in EEC model.

The model can be improved by the consideration of the three-cage model [20]. However, the prediction of the torque at lower speeds is not so important when the steady-state loaded performance of a machine is the main objective of the study.

Fig. 6.16 shows the machine performance with different loads. The EEC results with consideration of the saturation effect has an acceptable accuracy. The current of the machine with consideration of the saturation at no-load matches well with the FEA results. It shows that the magnetizing current and stator leakage inductance are properly calculated. Also, the phase current has a good agreement with the 2D FEA results which shows the appropriate calculation of the rotor branch elements. Fig. 6.16(b) shows the efficiency variation in different loads and demonstrates the acceptable ability of the saturation model in the calculation of the efficiency. Efficiency can be correctly calculated when the ohmic and core losses are computed correctly. It must be highlighted that the correct estimation of the rotor side losses shows the correct estimation of the slip because the value of the slip determines the amplitude of the current in different loads.

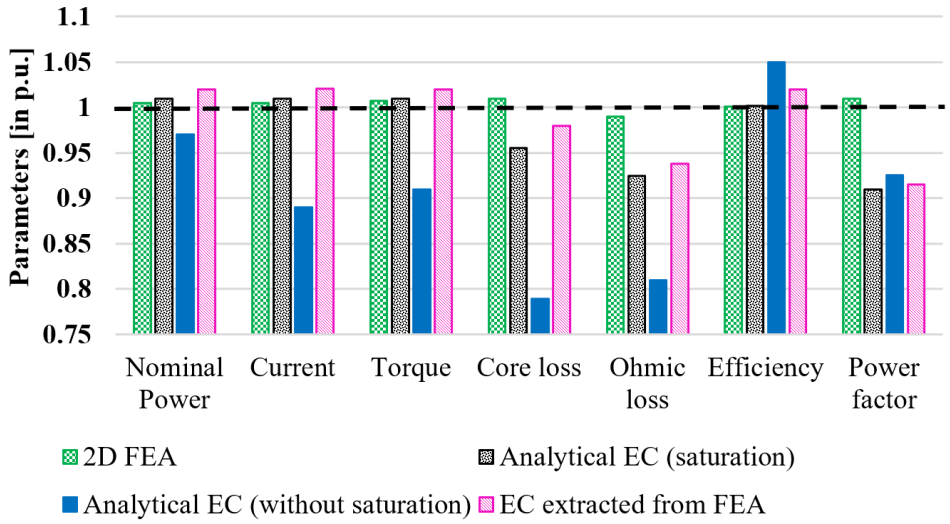

Fig. 6.14. The performance parameter values compared to the 3D FEA results (dashed line shows the 3D FEA results in p.u.) [162] © 2022 IEEE.

TABLE 6.7. DESIGN PARAMETERS OF THE STUDIED 7.5 KW SCIM [162] © 2022 IEEE.

Parameter	Value	Parameter	Value
Nominal power [kW]	7.5	Nominal frequency [Hz]	50
rms line voltage [V]	380	Number of pole pairs	2
Current [A]	17.4	Torque [Nm]	51
Efficiency [%]	83	Speed [rpm]	1418
Core loss [W]	131	Power factor [%]	86
Conductive loss [W]	1381	--	--

TABLE 6.8. EQUIVALENT CIRCUIT PARAMETERS FOR THE STUDIED MODELS [162] © 2022 IEEE.

EEC parameters	SDM model (without saturation consideration)	SDM model (with saturation consideration)	FEA EEC parameters (Results of locked rotor and no-load simulations)
R_s (stator side)	0.4 Ω	0.4 Ω	0.4 Ω
R_r (rotor side)	0.0131 Ω	0.0131 Ω	0.0137 Ω
R'_r (stator side)	0.86 Ω	0.86 Ω	0.90 Ω
X_{ls} (stator side)	0.62 Ω	0.51 Ω	0.48 Ω
X_{rp} (stator side)	0.62 Ω	0.51 Ω	0.48 Ω
X_{mn} (stator side)	23.1 Ω	19.3 Ω	19.6 Ω
R_c (stator side)	1585 Ω	1310 Ω	1251 Ω

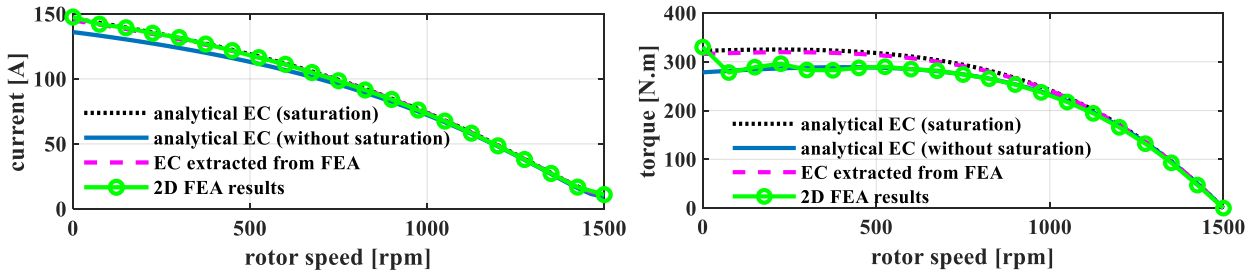

(a) Rotor current versus speed (b) Torque versus speed

Fig. 6.15. The performance prediction of the machine as a function of speed (comparison of the 2D FEA with the proposed model) [162] © 2022 IEEE.

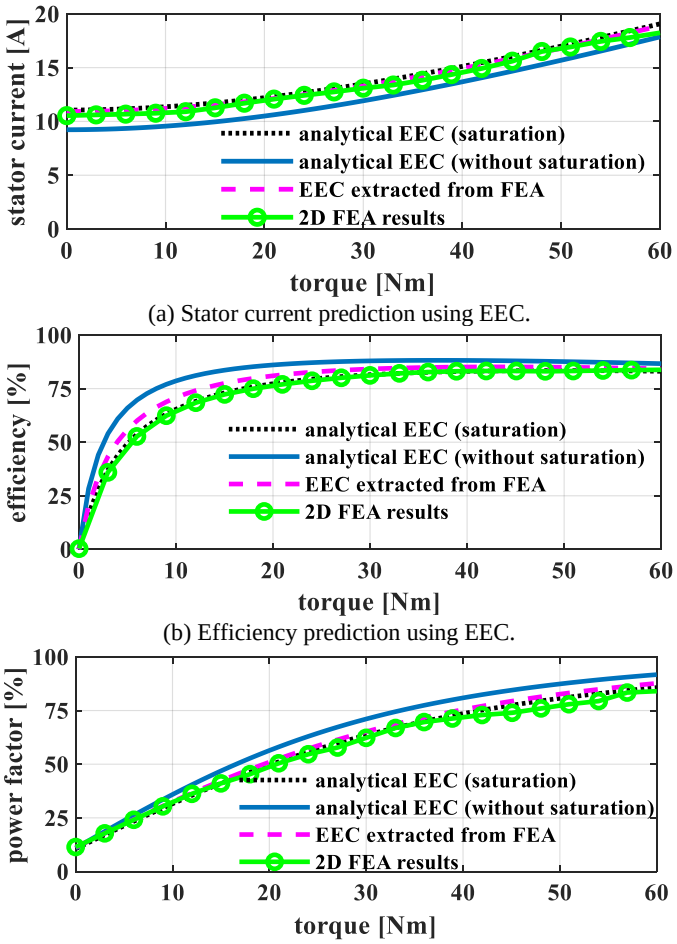

(a) Stator current prediction using EEC.

(b) Efficiency prediction using EEC.

(c) Power factor prediction using EEC.

Fig. 6.16. Comparison of the predicted performance parameters using the saturation considered model and non-saturation model with the 2D FEA results [162] © 2022 IEEE.

A sensitivity analysis was carried out by changing the machine length, machine outer diameter, airgap, and number of turns resulting in 75 machine design variations. The 2D FEA results of 75 designs are compared with the saturation and non-saturation proposed models as shown in Fig. 6.17. The results of the analytical model have a good agreement with the results of the 2D FEA in prediction of the performance parameters. The error of the output power is not exceeding 3% for different geometries. Also, the efficiency error of the proposed model is lower than 5% in all considered geometries which demonstrate the low difference in the value of the machine losses and calculated EEC parameters. Also, error of 10% for the power factor is shown in Fig. 6.17(c).

The comparison of the required simulation times of the proposed analytical model against 2D FEA demonstrates the analytical model's superiority in terms of speed. A Core i9-7900X (3.30GHz) computer with 128 GB RAM completes each 2D FEA analysis in about 1,000 seconds. In comparison, the performance prediction of a SCIM is completed in 12 seconds using the proposed SDM. The ability of the model for the fast prediction of the machine behavior helps speed up the process of the design of an optimum machine for a specific application.

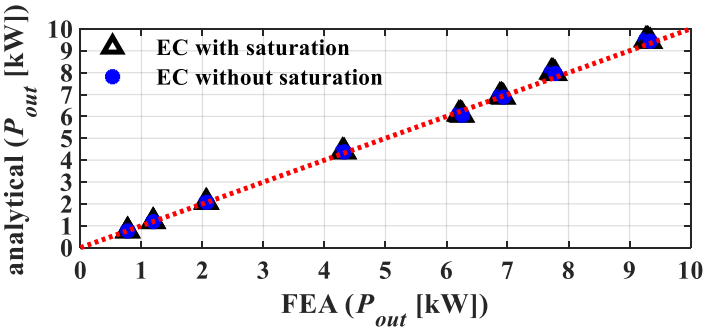

(a) the accuracy of the model in prediction of output power

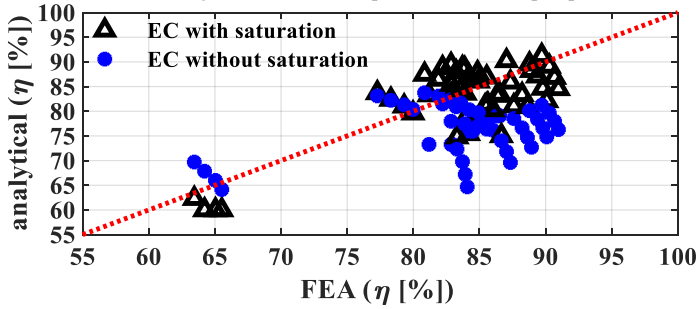

(b) the model accuracy in prediction of efficiency

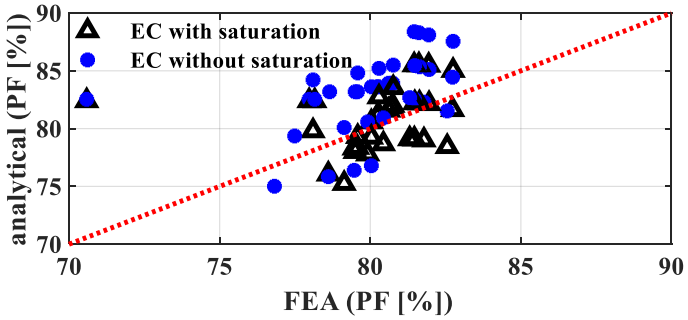

(c) the accuracy of model in the prediction of power factor

Fig. 6.17. The capability of the saturation and non-saturation models in performance prediction of the induction machines with 75 different geometries via 2D FEA analysis [162] © 2022 IEEE.

6.6.3. Validation of the model in prediction of the performance parameters in presence of the inter-bar current

The current which flows through the core material between the adjacent rotor bars is defined as the inter-bar current [311]. The amount of the inter-bar current depends on the conductivity of the rotor core material. The influence of inter-bar currents on the performance of the case study is examined in this part.

As the inter-bar current distribution varies with the slip of the machine [312], the 3D FEA is performed both at locked rotor and 1450 rpm (about three-quarters of rated load). A conductivity of 2 MS/m was used for the core material [312]. Fig. 6-18(a) shows the 3D FEA current density distribution on the surface of the core materials at locked rotor condition. The current density is plotted in the axial middle section of the machine in different operating conditions to show their differences with more details. Comparison of Figs. 6-18(b) and (c) shows that the core conductivity does not affect the current distribution on the rotor at the locked rotor condition. Fig. 6-19 is to compare the current density distribution of the case study during operation at the speed of 1450 rpm. Although the current density between the rotor bars is high, the 3D FEA results demonstrate that there is a small difference (less than 1%) between the calculated performances with and without consideration of the inter-bar currents. The study of the inter-bar current in 3D FEA increases the computational burden. A Core i9-7900X (3.30GHz) computer with 128 GB RAM reports the performance parameters of the 3D FEA results after 64 hours when the analytical model finds the performance after 12 seconds. Although the analytical model sacrifices the 1% accuracy, but its speed makes it suitable for an optimization study.

The 3D FEA calculated torque, current, and rotor bar losses performance results with and without consideration of the inter-bar currents are reported in Table 6.9. In general, inter-bar currents were found to produce only a small effect on the performance. The most sensitive parameter is the input current at locked rotor which increased by about 2% when including inter-bar currents. Therefore, the proposed analytical model which ignores the effect of the inter-bar current is fairly accurate.

It should be noted that the proposed model is not intended for transient performance simulation of SCIMs. The time-stepping based models proposed in [304], [305] are slow, but can be used in the real-time simulation when the transient performance is required.

TABLE 6.9. COMPARISON OF 3D FEA RESULTS OF THE CASE STUDY WITH AND WITHOUT CONSIDERATION OF THE INTER-BAR CURRENTS [162] © 2022 IEEE.

Rotor core conductivity [MS/m]	0.00		2.00	
Rotor speed [rpm]	0.00	1450	0.00	1450
Torque [Nm]	325.9	36.61	326.6	36.60
Current [A]	134.3	9.28	137.1	9.20
Bar loss [kW]	45.83	0.190	45.56	0.189

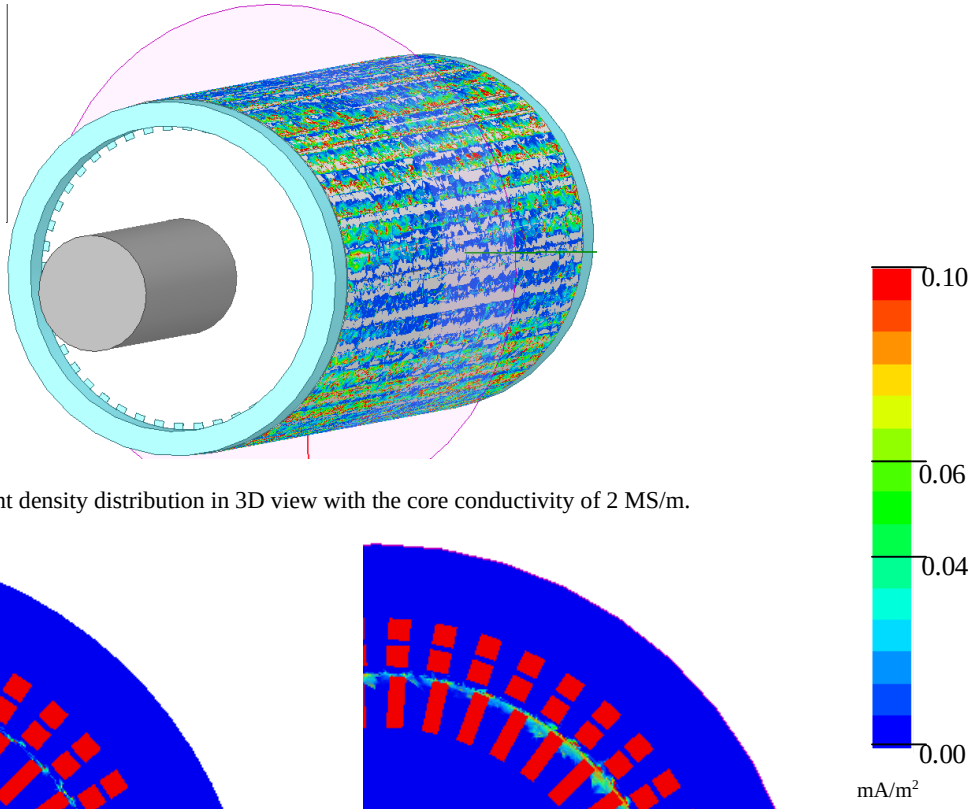

(a) current density distribution in 3D view with the core conductivity of 2 MS/m.

(b) current density distribution on the case study when the core conductivity is 0 S/m.

(c) current density distribution on the case study when the core conductivity is 2 MS/m.

Fig. 6.18. The 3D FEA results of the current density distribution with and without consideration of the inter-bar currents with the stacking factor of 95% at locked rotor condition.

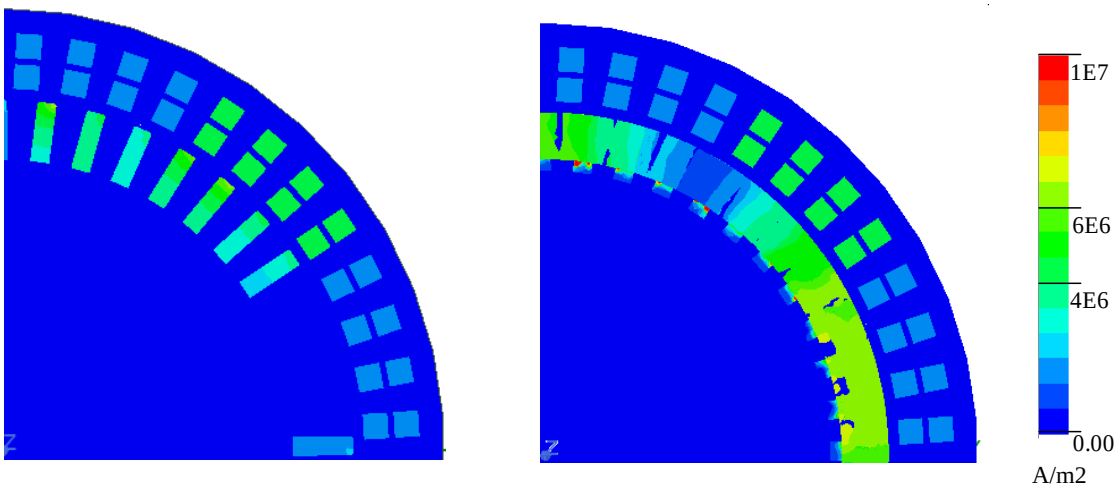

(a) current density distribution on the case study when the core conductivity is 0 S/m.

(b) current density distribution on the case study when the core conductivity is 2 MS/m.

Fig. 6.19. The 3D FEA results of the current density distribution with and without consideration of the inter-bar currents with the stacking factor of 95% when rotor rotates at 1450 rpm.

6.7. Validation of the Proposed Model using Experimental Data

A 2.2kW, 4 poles, 415V induction machine available at the machine laboratory of the University of Adelaide is chosen for validation of the proposed model. The dimensions and characteristics of the case study are tabulated in Table 6.10. Fig. 6.20 shows the prepared experimental setup including a dynamo motor, understudy motor, dynamometer, and high precision power analyser. The dynamo motor acts a load for the motor and is controlled with a voltage frequency drive (VFD). Dynamometer provides the torque and speed feedbacks for the VFD as well as the measurement data for the power analyser. The understudy motor is supplied by an auto transformer. The input power of the test machine is measured using PM3000ACE which is high accuracy power analyser [313]. PM3000ACE accepts the speed and torque inputs in addition to the electric signals for measurement of the output power.

Table 6.11 presents the experimentally obtained 2.2kW equivalent circuit parameters from the no-load and locked rotor tests. The presented result in this paper shows the appropriate agreement of the experimentally calculated equivalent circuit parameters with the proposed model. The experimental data have been collected when the stator and rotor windings temperatures were 60°C. This temperature is considered for calculation of the resistance in 2D-FEA and analytical model.

The capability of the model to predict the saturation curve of the understudy motor is validated by collecting the no-load test data. To provide a precises saturation curve the shaft of the case study is rotated at 1500rpm using the dynamo motor and the supplied voltage of the machine is varied from zero to 500V line voltage. Fig. 6.21a shows the proposed model capability in the prediction of the magnetizing current in different supply voltages. According to this figure, the error of the proposed model at rated voltage is less than 1% and in the worth case condition the error of the proposed model is about the 11%. The model is further analysed through a frequency variation analysis.

The motor is supplied by California Instrument CSW Series AC Power Source (CIPS). This device allows to prepare a pure sinusoidal waveform for supplying the machine in different frequencies and voltage levels. The machine is supplied with 40Hz, 50Hz, and 60Hz by the CIPS at no-load condition. The obtained stator reactance in the no-load test in these frequencies and different winding currents are plotted in Fig. 6.21b. This figure demonstrates the proposed model capability prediction of the machine inductance. Note that due to the large slip in the lower voltage supply voltage levels, in small magnetizing current the experimentally collected reactance is not accurate. For this reason, a strange variation of the reactance in small currents is seen in Fig. 6.21b.

The collected experimental data in different operating slips are compared with proposed model in Fig. 6.22. The loading current, shaft speed, output power, and efficiency of the machine shown in this figure have an acceptable agreement with the calculated values. The maximum error of the current

does not exceed 6% (around the rated load of 14.5Nm). The error in the current resulted from the slight difference between the estimated magnetizing inductance (see Fig. 6.21a).

TABLE 6.10. STUDIED IM ELECTRICAL CHARACTERISTICS AND GEOMETRY

Electrical Characteristics			
Rated line voltage [V]	415	Rated power [W]	2200
Frequency [Hz]	50	Number of poles	4
Geometry and dimensions			
Stator outer diameter [mm]	165	Stator inner diameter [mm]	105
Rotor outer diameter [mm]	104	Rotor inner diameter [mm]	38
Number of stator slots	36	Number of rotor slots	28
Stator slot height [mm]	12.8	Width of stator slot opening [mm]	2.8
Airgap length [mm]	0.47	Rotor slot height [mm]	18.21

TABLE 6.11. EQUIVALENT CIRCUIT PARAMETERS FOR THE STUDIED 2.2KW MACHINE OBTAINED FROM THE NO-LOAD AND LOCKED ROTOR TEST IN EXPERIMENT, FEA ANALYSIS, AND THE PROPOSED MODEL

EEC parameters	Experimental results	2D FEA	Proposed model
R_s (stator side) @ 60°C	2.52 Ω	2.52 Ω	2.71 Ω
R'_r (stator side) @ 60°C	2.77 Ω	2.56 Ω	2.46 Ω
X_{ls} (stator side)	3.29 Ω	3.37 Ω	3.39 Ω
X_{rp} (stator side)	3.29 Ω	3.37 Ω	3.45 Ω
X_{mn} (stator side)	122.51 Ω	127.4 Ω	127.4 Ω
R_c (stator side)	2057.13Ω	2011.87Ω	1967.16Ω

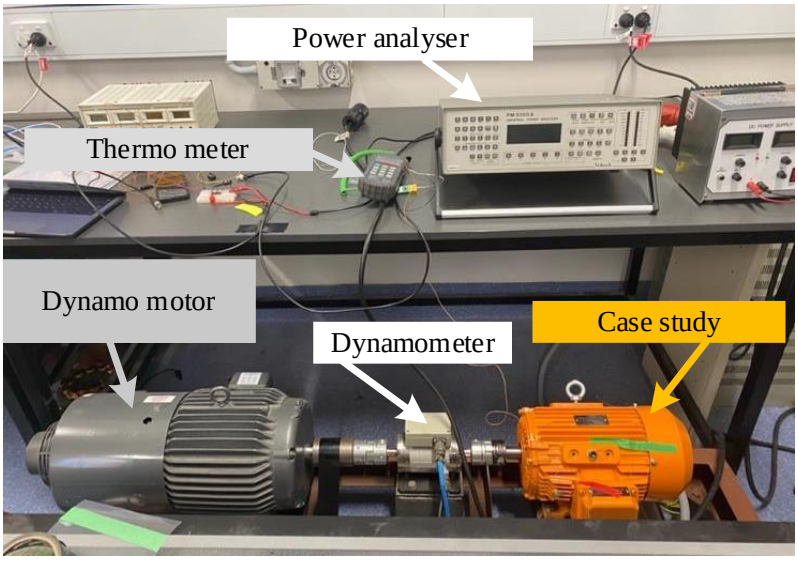

Fig. 6.20. The prepared experimental setup for verification of the proposed SDM model. A 2.2kW induction machine is used for validation.

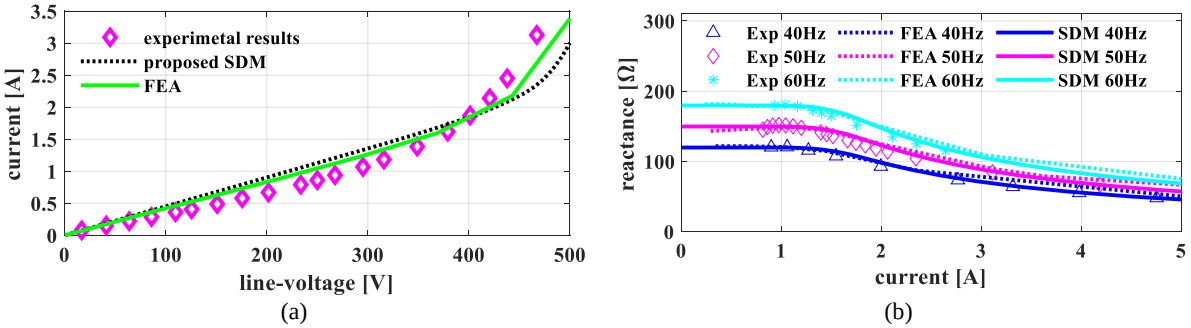

(a) (b)

Fig. 6.21. The no-load experimental results. (a) no-load current in different voltage. (b) the stator reactance variation in different frequencies vs. no-load current.

The difference between the calculated current and measurement at larger torques is due to the increment of the rotor frequency at higher slips. In fact, the rotor resistance is dropped at higher slips and this drop is more obvious in larger currents [314]. The error of the estimated speed and power are less than 1%. The maximum error of the 3% happens at 14.8Nm point in the efficiency curve. This efficiency error resulted from the larger current flowing through the winding and rotor cage.

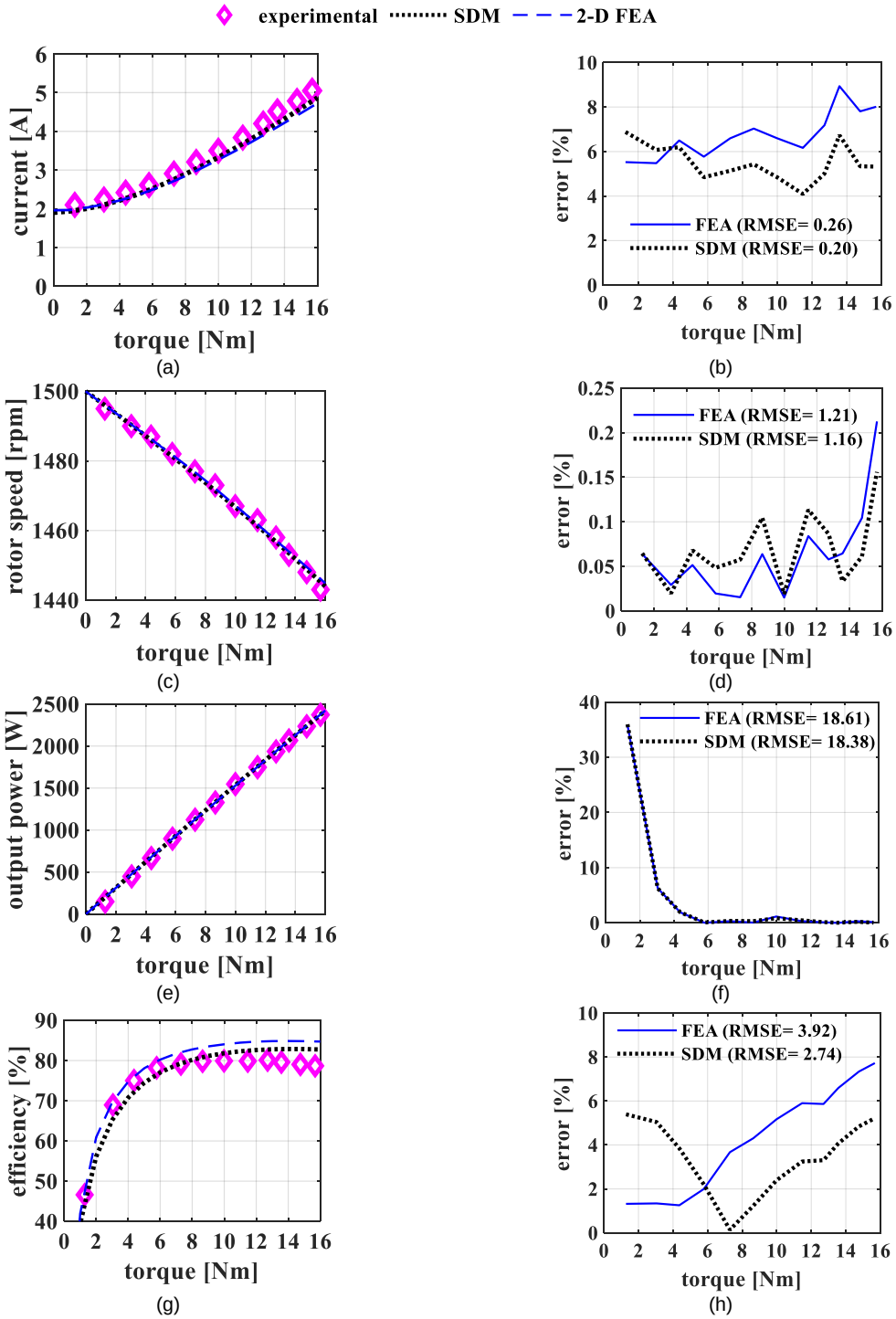

Fig. 6.22. Loaded performance validation: (a) and (b) current and current error variations vs. load; (c) and (d) speed and speed error variations vs. load; (e) and (f) output power and output power error variations vs. load; (g) and (h) efficiency and efficiency variations error vs. load.

6.8. Conclusion

A subdomain model with capability of the consideration of the saturation effect in iron parts was introduced in this chapter. The leakage, magnetizing, and stator mutual inductances were calculated using the magnetic vector potentials (MVPs) obtained from the induction motor (IM) subdomain model. The iron loss was predicted based on the calculated flux density in different parts of the iron based on the magnetic vector potentials at the no-load condition. The electric equivalent circuit was used to study the machine performance. To improve the accuracy of the model, the saturation of the core was estimated using the MVPs at different voltage levels. A saturation factor was defined to find the different values of the saturation dependent components of the IM electric equivalent circuit at different saturation levels. The capability of the model in the prediction of the machine inductances was validated using finite element analysis (FEA).

The proposed model was used to predict the performance of a 7.5kW induction motor under different loading conditions. The model was compared and validated against the results of 2D and 3D FEA. The results demonstrate that the higher capability of the saturation model in performance parameters prediction of SCIM.

A sensitivity analysis was conducted using different machine geometries and used to demonstrate the generality of the model. The effect of inter-bar currents was also investigated using 3D FEA analysis and found to be small. Thus, the proposed model showed acceptable accuracy and fast execution time suitable for optimal design of induction machines with different variables.

Finally, a 2.2kW induction machine was prepared on the test rig. The no-load and full load test was accomplished on the machine. The collected experimental data was compared with the results of the proposed saturation model to show the reliability of the proposed model in a real case study.

The proposed model is fast and accurate in prediction of the performance of SCIMs. Thus, this machine can be a proper tool for prediction of the efficiency map of induction machine. A framework consisting of the proposed SDM, and an optimization algorithm is developed in the next chapter. The optimum SCIMs in different driving cycles are designed using the developed framework. The characteristics of the designed machine are compared with each other.

Chapter 7. Optimal Electric Machines Considering Overload

7.1. Chapter Overview

Consideration of the overload (OL) performance of electric machines designed for EVs enables increasing the power density of the propulsion system. This chapter aims to show the characteristics and advantages of the optimal IMs which have the capability of handling OL. A subdomain model with the capability of the saturation prediction is developed and validated using experimental data. A lumped thermal model is developed to predict the transient temperature variation of the IMs. The thermal model is validated using the Motor-CAD transient thermal analysis. The fast speed and accuracy of the applied SDM allows to select twelve variables in a large search space for the optimization purpose. Initially, an optimization procedure is proposed to design three IMs over three different driving cycles. The optimal designs are validated from the electromagnetic and thermal aspects by the finite element analysis. IMs are then designed optimally with consideration of the OL capability. A transient thermal analysis is carried out to validate the designs. The optimal designs with and without consideration of OL are compared in terms of the machine parameters and geometry to understand how dimensions and equivalent circuit parameters of the IMs vary according to the driving cycles. The comparison allows more intuition about the consideration of OL capability in design.

It should be highlighted that all the obtained EffMs in this chapter are calculated using the saturation considered model of the IMs which was explained in Chapter. The validation of this model has been carried out using the obtained EffM from Motor-CAD software.

7.2. Background and Contribution

IMs could be a suitable choice for utilization in the propulsion systems of electric vehicles and hybrid electric vehicles. The absence of rare-earth permanent magnet materials in the IMs leads to reduction of the machine cost in comparison to the PMSMs [315]. The literature shows that the performance parameters and efficiency of IMs during operation in the constant power region is comparable or even better than PMSMs [316].

The design of the IMs for the industrial line-starting or single point operation applications is a well-established subject. Unlike operation over a wide range speed range, NEMA and IEC have standardized the design of IMs for line-start applications [63], [317]. The optimum geometry and dimensions to achieve the required performance in line-starting applications has been described in the literature.

The literature has introduced sizing equations of IMs for various geometries and power ratings [238]. These empirical formulae are prone to errors due to poor estimation of IM equivalent circuit parameters. On the other hand, these equations are developed based on the machine performance during operation at a single operating point (i.e., certain saturation level). So, the obtained model based on these equations is not valid for a wide range of operating points when saturation phenomenon in iron parts is involved. Consequently, the previous optimization studies, which have

utilized sizing equations, were not able to provide an optimal IM for operation over a wide range of loads.

FEM-based motor optimization techniques have been the subject of extensive research. For PM machine optimization, FEA and electric equivalent circuits were used for optimal design of PM machines using a differential evolution algorithm [318]. The authors optimize a coreless linear PM machine using FEA and a genetic algorithm in a multi-objective optimization study [319]. Multi-objective optimization problems were simplified using the aggregation tree method, as suggested in [320]. The dependency of these articles on FEA is the main drawback because of their computational burden.

Surrogate models like the Gaussian Process (Kriging), which are a type of supervised machine learning, has been used as an effective tool in the design of electric machines [241], [321], [322]. These models have been used for reduction of the time of optimization study while using FEA [269]. These models require the previously collected data to predict the behavior of an electric machine. A number of FEA simulations are executed to gather the initial data from a case study [321]. Then, the collected data is used to predict the performance parameters in different geometries. The trained model by the surrogate model is used in a single- or multi-objective optimization problem to design the target machine based on the objective function (OF) and constraints [7], [323], [324]. In [325], a comprehensive study on the robust optimization of the electric machine were conducted. The authors showed that the robust optimization allows finding the optimum design which meets all the constraints with greater computational cost compared to the conventional optimization methods. The preparation of the required sample data for the surrogate models is computationally expensive because it needs the execution of a larger number of simulations. To reduce the number of simulations, previous studies have limited the number of the variables and their range of variation. The limited range of search however produces a design which may not be the global optima in the entire search space.

The use of analytical models like MEC [326], [327] and SDMs [328], [329] can be considered as a substitute for FEA to decrease the computational time of the optimization study. A MEC model will become more accurate if the number of considered permeances are increased in the airgap and iron parts [245]. The increase of the number of elements leads to the increase of computational time. Most of the previously introduced MECs and SDMs ignore the saturation effect during the machine modelling [20], [308], [330]. The ignorance of the saturation reduces their accuracy for predicting the performance parameters over a driving cycle, particularly in the overload condition.

There are several references which introduced an approach for saturation modelling in SDMs [162], [167], [171], [331]–[333]. Only in [167], [171], the saturation model of the AFIM was employed in the optimization problems. The optimal design of line-start AFIMs have been discussed in [167] which means the results are not optimal for operation over driving cycles. In [171], the

authors have considered a limited region near the nominal points for saturation modelling. Hence, the predicted performance cannot be reliable for all operating points in a driving cycle. The maximum torque per ampere control has been employed for the optimization in [171]. The maximum torque per ampere control cannot find the maximum efficiency points in the constant power region [215]. So, the designed AFIMs in [171] are not the optimal designs from the maximum efficiency perspective.

The effect of rotor losses on the machine temperature is another important factor which has been ignored in [167], [171]. Rotor losses in induction machines are often high which leads to a higher rotor temperature rise. The optimization studies in [171] assume a cooling system similar to the radial flux machines for their designs. Even if the assumed cooling system works successfully for the stator of the axial flux IMs, it cannot be used for the cooling of the rotor. This is because the available contact surface between the cooling channel and rotor in AFIM is less than the radial rotors, but also as the heat distribution on the disk (axial flux IM rotor) is different to a cylinder (radial flux IM rotor).

The SDM can be a fast and accurate modelling technique for performance prediction of IMs. This chapter employs the proposed SDM in Chapter Six [162] to introduce an optimization procedure for design of IMs over driving cycle. The saturation approach used in the considered SDM model has not been validated through the experimental results in former work. This model is developed and validated using the experimental results for a sample 2.2 kW IM. To the best of authors' knowledge, there is no previous work which uses a saturation considered SDM for design of IMs over a driving cycle based on maximum efficiency control.

The literature lacks a comprehensive study between the design of the IMs with and without consideration of the OL capability during the design. The overload consideration requires an appropriate thermal model with the capability of the transient temperature prediction. This chapter proposes a lumped thermal model using the thermal modules of MATLAB/SIMULINK which is integrated with the SDM to predict the IM design temperature variation over driving cycles.

This chapter aims to highlight the importance of the consideration of OL during the design. Hence, the benefits of the consideration of the OL capability for IM design with respect to the size and performance is discussed and evaluated.

The fast speed of the SDM allows choosing twelve different variables in the optimization study. A similar cooling system as the 150 kW e-mobility IM [163], [334] is assumed for the design process. In the optimization study, the maximum loss of the rotor and stator are set as constraints to guarantee the success of the cooling system at the rated condition. The loss constraint is determined based on the maximum loss per outer stack of the stator and rotor of the benchmark design (i.e., 150 kW e-mobility IM). A single-speed transmission system with a gear ratio of 9.6 is assumed between the motor shaft and wheels. An optimization problem to obtain the maximum efficiency over the driving cycle in the minimum volume is defined. The optimal designs are validated against the FEA results in terms of

their electromagnetic and thermal performance. In the second stage, the proposed optimization procedure is utilized to design IMs with consideration of the OL capability over the driving cycle. The developed lumped model is used to predict the hotspot temperature of the winding in the optimization study to check the temperature limit. The obtained results clarify how the OL capability consideration can reduce the IM volume while the thermal constraints over the studied driving cycle are met.

7.3. Lumped Circuit Thermal Model

7.3.1. Introduction of thermal model

A lumped parameter model, shown Fig. 7.1, is developed to predict the thermal behavior of the induction machine over the driving cycle. The generated heat because of the stator winding loss, stator core loss, and rotor cage and iron losses are represented by the heat flow sources in the model. The convection heat transfer, thermal conductance, and thermal masses are utilized to develop the thermal model.

The thermal mass which is the material's capability in absorbing and releasing the thermal heat is used for different parts of the machine including winding, stator iron, motor housing, rotor iron, bearings, and flange. A conduction path is considered between those parts which are physically connected with each other. Convection heat transfer is used where the heat is transferred through the air.

The heat flow due to the thermal mass as a function of time (t) is defined by (7-1) where Q is the heat flow, C_p is the specific heat of the mass of material, m is the material mass, and T is the temperature. The considered specific heat and the density of each material are reported in Table 7.1.

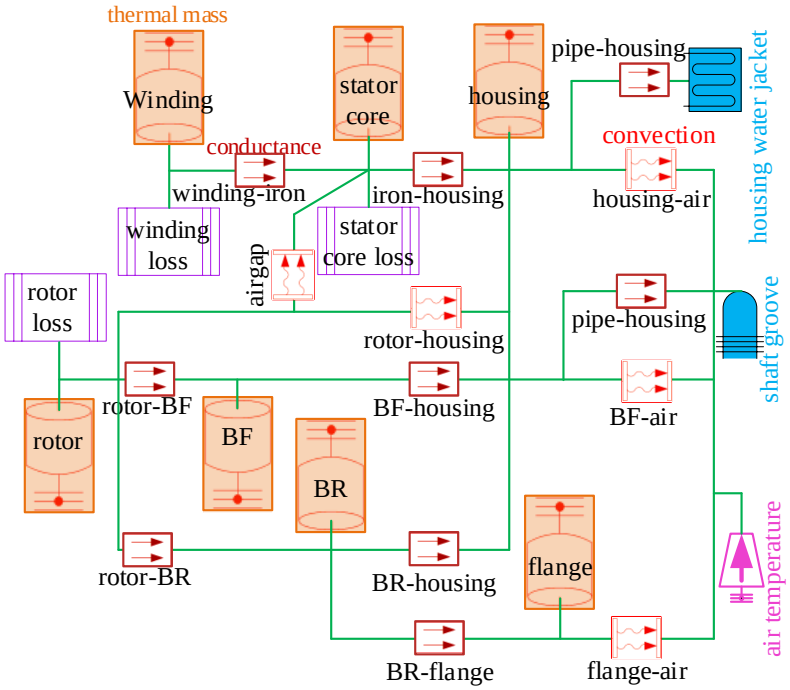

Fig. 7.1. The developed lumped thermal model for the transient thermal analysis of the induction machine.

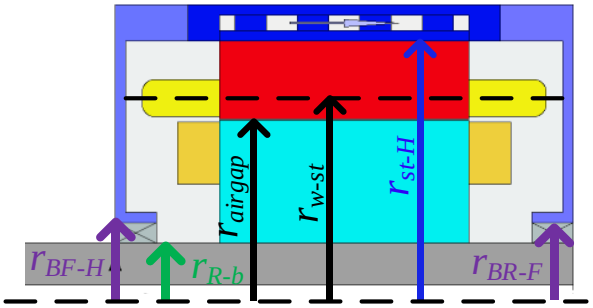

Fig. 7.2. The considered radii for calculation of the area for each part of the machine.

TABLE 7.1. THE THERMAL PARAMETERS USED FOR THE THERMAL ANALYSIS

Specific heat for each part (C_p)			
Winding [J/kg/K]	385	Housing [J/kg/K]	733
Stator iron [J/kg/K]	460	Bearing [J/kg/K]	447
Rotor iron [J/kg/K]	460	Flange [J/kg/K]	447
Thermal conductivity of each part (k_{cd})			
Winding – Iron [W/(m×K)]	401	Bearing – Housing [W/(m×K)]	80.2
Iron – Housing [W/(m×K)]	80.2	Bearing – Flange [W/(m×K)]	25.5
Rotor – Bearing [W/(m×K)]	25.5		
Convection heat transfer coefficient (k_{con})			
Airgap [W/(m^2×K)]	250	Bearing – Air [W/(m^2×K)]	125
Housing – Air [W/(m^2×K)]	26.8	Flange – Air [W/(m^2×K)]	125
Reynolds (Re) and Prandtl (Pr) numbers for cooling channels			
Re	16E5	Pr	11.7

$$Q(t) = mC_p \frac{dT}{dt} \tag{7-1}$$

The Fourier law presented in (2) is utilized to describe the conductive heat transfer. The thermal conductivity of each material (k_{cd}) used in this chapter is tabulated in Table 7.1. In (7-2), A is the area of material normal to the heat flow direction. This area for each section is found using (7-3) where r is the considered radius for calculation of the area and l is the axial length of each part. The winding to stator radius, stator to housing radius, rotor to bearing radius, front bearing to case radius, and rear bearing to flange radius are shown by r_{w-st}, r_{st-H}, r_{R-b}, r_{BF-H}, r_{BR-F}, respectively in Fig. 7.2. The material thickness between layers A and B and the temperatures at layers A and B are shown by Th, T_A, and T_B.

$$Q(t) = k_{cd} \frac{A}{Th} (T_A(t) - T_B(t)) \tag{7-2}$$

$$A = 2\pi rl \tag{7-3}$$

The convection heat transfer is modelled by Newton's law of cooling formulated in (7-4). In (7-4), k_{con} is the convection heat transfer coefficient. Note that the S is the effective area of each motor component. For instance, the rotor area is $S = 2\pi(r_{airgap}^2 - r_{R-b}^2)$; two times the effective rotor surface is considered because the rotor convection to the housing occurs at both ends of the rotor. The reported k_{con} for air is the considered coefficient for the flange, bearing, and housing convection.

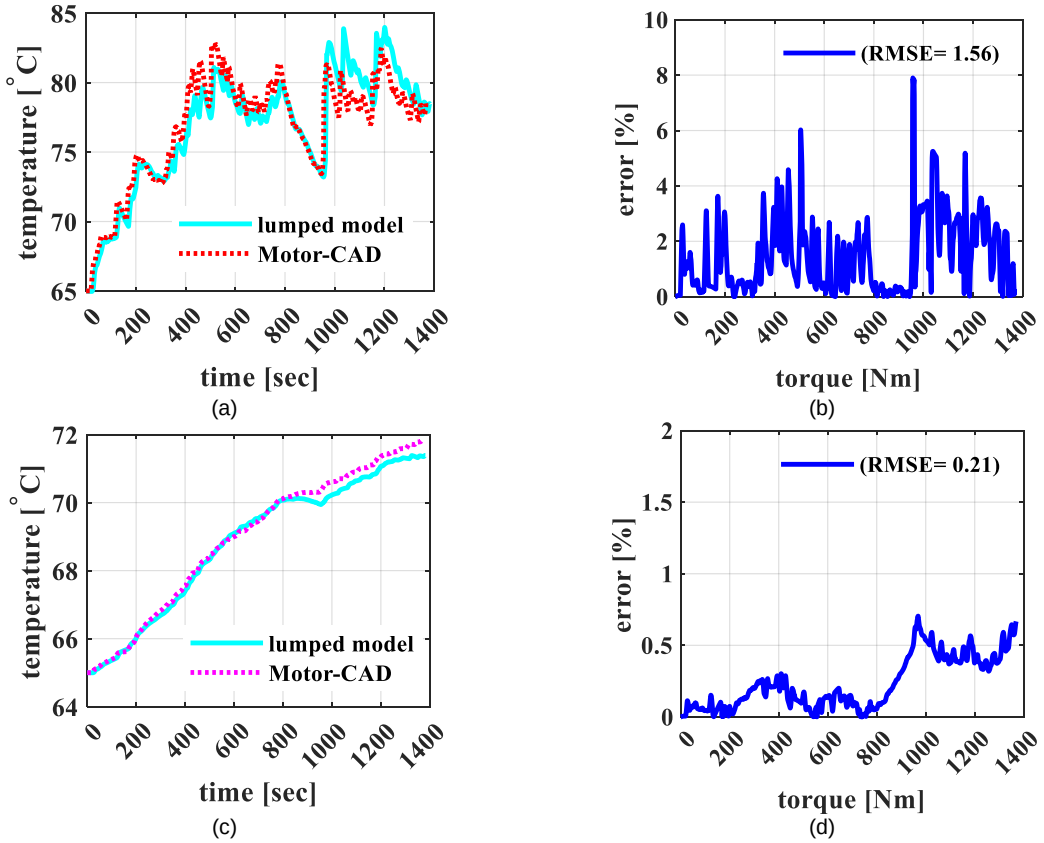

Fig. 7.3. Transient thermal analysis results for the developed lumped-circuit model versus the Motor-CAD predictions for the benchmark IM over the UDDC: (a) stator hotspot temperature, (b) corresponding error, (c) rotor temperature, (d) corresponding error.

According to Taylor and Gazler [335], for Taylor numbers less than 41, the heat transfer is only conductive in the airgap and the Nusselt number (Nu) is equal to 2 [335], [336]. Considering this, k_{con} in the airgap is found by multiplication of the air convection coefficient and 2 (i.e., the Nusselt number).

$$Q(t) = k_{con} S (T_A(t) - T_B(t)) \tag{7-4}$$

It is assumed that the ethylene glycol-water mixture flows through the spiral cooling channel and shaft groove with a constant flow rate. The pipe (TL) block from the MATLAB SIMULINK library is used to model the heat transfer at the pipe wall. This block uses the Dittus-Boelter correlation which estimates the Nu as a function of the Reynolds (Re) and Prandt (Pr) numbers. The laminar flow and rectangular channel equations presented in [337] are used to find the Nusselt number for the rotor groove cooling and stator spiral cooling. The values of the Re and Pr in calculating Nu are given in Table 7.1.

7.3.2. Validation of thermal model

The thermal model is validated through a transient thermal analysis. It is assumed that the benchmark machine is operated over the urban dynamometer driving schedule (UDDS) [338]. The performance parameters of the machine are calculated using the Motor-CAD software.

The Motor-CAD transient thermal analysis module is utilized to predict the machine temperature variation over the UDDS operating points. The obtained losses over the driving cycle are considered as the input for the introduced thermal model. The predicted results shown in Fig. 7.3 shows an acceptable agreement between Motor-CAD and the developed model results.

7.4. Problem Definition

7.4.1. Introduction of Benchmark IM

An IM with a rating of 100 kW continuous power (at current density of 16A/mm^2 and DC-link voltage of 400V) and 150 kW peak power (at 50A/mm^2 current density) is considered as the benchmark machine in this study [163], [334]. This commercial machine has 72 stator slots and 84 copper rotor bars. The lamination material M250-35A is used in the construction of stator and rotor.

The stator of this machine is cooled by a 50/50 water/glycol mixture which flows through a spiral cooling jacket. The coolant inlet temperature is 65°C and a 6.5 l/min flow rate is used. A spiral groove is assumed into the shaft which carries coolant at 2 l/min.

The stator loss of the benchmark design at rated power is 1.8 kW. The available outer surface of the machine cooled by the spiral cooling is 0.094 m^2. Thus, the maximum permitted loss per outer stack for this machine 15.2 kW/m^2 which will be used as a limiting factor in the optimization study. It is assumed that the diameter of the rotor spiral groove of the designed machines in this chapter is equal to the benchmark groove diameter (15mm). So, the active length of the rotor which is in contact with the cooling system plays an important role to successfully remove the heat from the rotor. As the axial stack length (L_{st}) of the benchmark design is 0.12m, 3.3 kW/m is considered as the allowable loss per length for the rotor.

The benchmark machine was designed for operation in a vehicle with 1,961 kg weight. The motor transfers power to the wheels through a single-speed gear box with a 9.6 gear ratio. This gear ratio is assumed for the design of the IMs in this chapter.

7.4.2. Definition of Optimization Problem without Consideration of Overload Condition

This section describes an optimization procedure to find an optimal design without consideration of transient performance. The designed machine will be able to continuously operate at all operating points of a driving cycle.

The flowchart of the defined optimization problem including the detailed steps have been presented in Fig. 7.4. The fast speed of calculation of the SDM allows increasing the number of optimization variables. As shown in the first block of Fig. 7.4, twelve independent variables are considered for the optimization.

Particle swarm optimization (PSO) [339] is the proposed evolutionary algorithm for solving the problem. The literature shows PSO has a good convergence rate when the number of particles is equal to five times of the number of parameters (variables) [340]. Thus, considering the twelve variables in this study, the number of particles is set on 60. The inertia weight and damping factor for the particle search are set to 0.9 and 0.3, respectively. The individual and social co-speed of particles are set on 1.6 [341]. The problem is defined for a certain number of iterations which is shown by it_{max} in the flowchart and a value of 50 was chosen for this.

The initial variables are randomly generated, and the problem is solved to provide the initial data for the first iteration. As the height of the rotor end ring (H_{er}) is a maximum of 0.9 times of the rotor bar height (RS_h), this value is checked in each iteration. If the selected value for H_{er} is larger than RS_h, the selected H_{er} value is limited to this value. If the outer diameter (D_O) exceeds the maximum value of 290mm, the algorithm rejects the design.

The developed SDM is used to find the magnetic vector potentials in each iteration. The core loss, saturation curve (i.e., voltage vs. current curve of the machine at no-load), and electric equivalent circuit parameters are found using the SDM. Based on the stator slot area in each iteration, the value of the maximum operating current of the machine is determined from the assumed 16A/mm^2 current density.

The obtained current is set as the rated current for the machine. Considering this current and DC-link voltage of 400V, the maximum efficiency control is applied to obtain the efficiency map (EffM). The maximum loss per outer stack and maximum rotor loss per length are calculated under rated condition. If these values exceed the loss limits, the rated stator winding current density is reduced, and this process is repeated. Once the loss limit is met, the algorithm directs analysis into the next stage.

The calculated EffM is used to find the efficiency of each of the operating points in the considered driving cycle. The first cost function ($CF1$) aims to maximize the efficiency of the operating points. To find $CF1$, the average efficiency over driving cycle (S_η) is found and then is subtracted from 100%.

The designed machine should be able to operate continuously at each single operating point. The red line shown in Fig. 7.5 shows the torque-speed characteristics of an example design in the optimization iteration. The constant torque (CT) and field weakening (FW) regions of this design are determined based on its torque speed curve on the given driving cycle.

The optimization algorithm should find the optimum design with the green line torque speed characteristics shown in Fig. 7.5. This objective is achievable when the machine volume is increased. If the volume is not considered as the second objective function, the PSO will apply a large increase in volume to find the optimum design. This large increase may result in convergence to a local

minimum. To reduce the risk of being trapped in local minima, the volume is penalized in the CT and FW regions.

The number of operating points located above the CT and FW regions are separated and counted by N_{CT} and N_{FW}, respectively. N_{CT} and N_{FW} are highlighted by yellow and green in Fig. 7.5. The volume of the IM which is evaluated in the current iteration is shown by Vol_m, which is the summation of the volumes of the rotor, stator and end winding. The considered penalty for the N_{CT} points is calculated by (7-5).

$$P_{CT} = N_{CT} \times Vol_m \tag{7-5}$$

The compensation of the torque at the field weakening (FW) region by increasing the current is limited due to the voltage limit. Hence, the penalty volume (P_{FW}) for the N_{FW} points is applied by a larger volume factor. According to (7-6), two times of N_{FW} is applied to the volume penalty.

$$P_{FW} = 2N_{FW} \times Vol_m \tag{7-6}$$

To make the second cost function the Vol_m is summed up with the obtained penalties applied to volume ($CF2 = Vol_m + P_{FW} + P_{CF}$). The objective function is defined by the multiplication of the $CF1$ and $CF2$ (i.e., $OF = CF1 \times CF2$). Finally, the objective function is minimized by the PSO optimisation.

7.4.1. Consider Overload Capability During Optimization

In a given driving cycle, there are many operating points where the machine torque is low that provides time for cooling. This allows increasing the loss limit of the machine in the transient operation over the driving cycle. According to Fig. 7.4, the process of the consideration of the OL capability follows a different step compared to the normal design based on maximum power.

In the OL consideration procedure, a similar current density as the benchmark IM (i.e., 50A/mm^2) is assumed at the first step. The rotor loss, stator winding loss, and stator core loss maps and EffM of a machine in each iteration are calculated.

The transient loss estimation is feasible if all operating points of the driving cycle are covered by the EffM. Thus, if N_{CT} and N_{FW} are exist, the IM is rejected when its OF is set on infinity. This decision process is summarized in (7-7).

$$\begin{cases} N_{CT} = N_{FW} = 0 \rightarrow accept\ design \\ N_{CT} \neq 0 \text{ or } N_{FW} \neq 0 \rightarrow reject\ design\ (i.e., OF = \infty) \end{cases} \tag{7-7}$$

The transient loss variation of each part of the machine over a driving cycle is extracted from the loss map. The proposed thermal model is used to predict the machine temperature variation using the transient loss data.

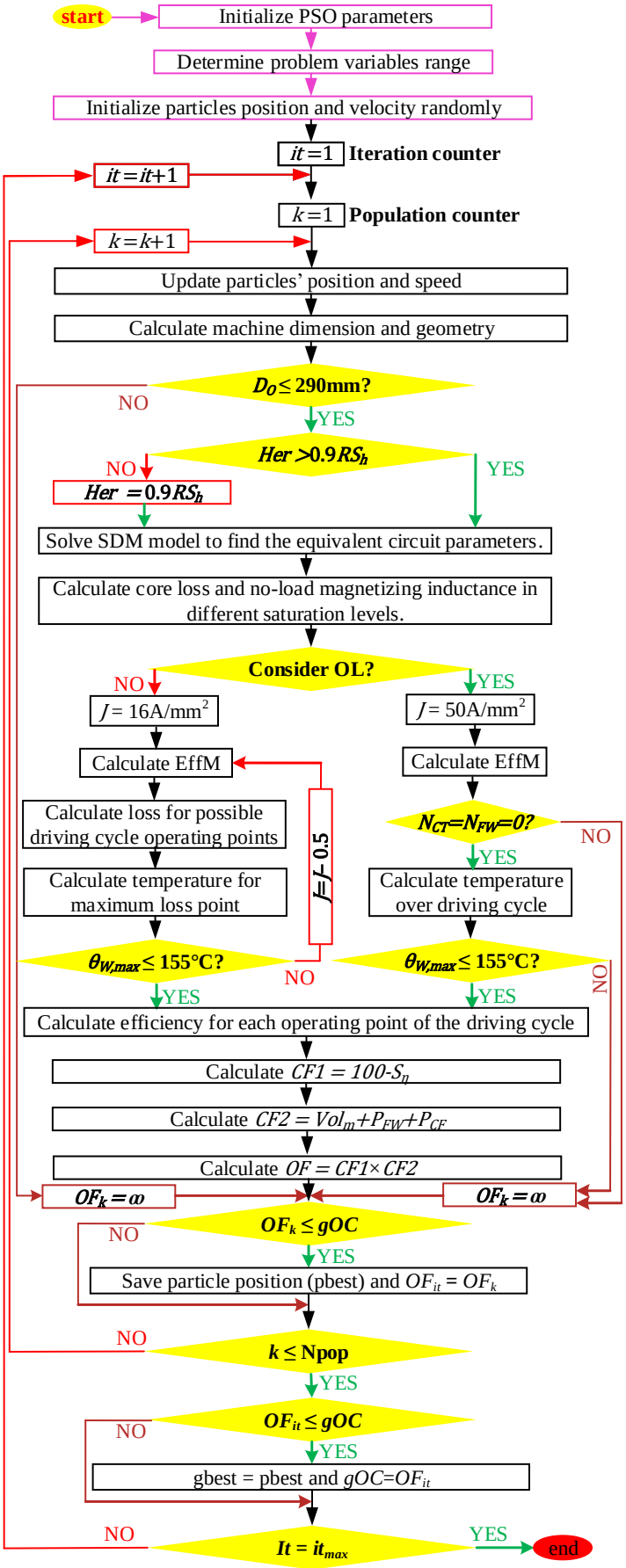

Fig. 7.4. The optimization study flowchart for consideration of the normal and overload condition.

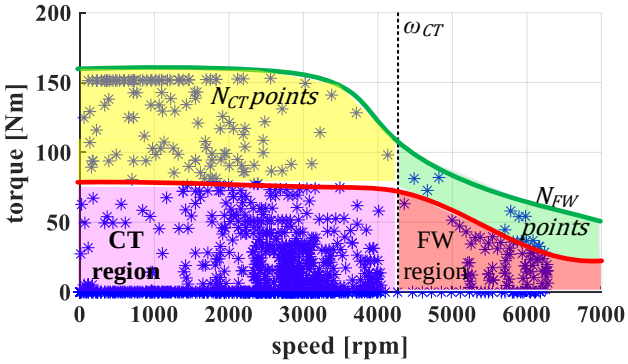

Fig. 7.5. Torque speed curve of a sample machine showing the CT and FW regions as well as the N_{CT} and N_{FW} points in a driving cycle.

The considered condition for selection or rejection of a design in each iteration is defined by (7-8). In (7-8), the maximum winding hotspot temperature during transient analysis is presented by $\theta_{W,max}$.

$$\begin{cases} \theta_{W,max} \leq 155℃ \rightarrow accept\ design \\ \theta_{W,max} \geq 155℃ \rightarrow reject\ design\ (i.e., OF = \infty) \end{cases} \quad (7\text{-}8)$$

If the design is accepted based on (7-7), the algorithm continues its process to find $CF1$ and $CF2$ using the same procedure as the normal design described in the previous section. In the case of the rejection of the design, the algorithm sets OF to infinity to reject the design.

7.5. Results and Discussion

7.5.1. Normal Optimization

Three driving cycles including HFET, UDDC, and NYCC are considered for the optimization study [6]. The normal optimization approach for the design of the IMs over the three driving cycles is executed to find the optimal IMs. The variables and their selected ranges in the solution space are reported in Table 7.2.

The trend of the variation of the average efficiency over the driving cycle against volume during the optimization is presented in Fig. 7.6. According to this figure, the higher efficiency is achieved by increasing the volume. It is expected because with larger volumes the airgap area is larger which allows generating more torque with smaller currents. The reduction of the current decreases the ohmic losses which are a large portion of the losses in IMs. Thus, the efficiency will generally be increased by increasing the volume.

The grey rows in Table 7.2 shows the obtained dimensions of the optimal designs for each driving cycle. The stator inner and outer diameters (D_i and D_O) which are indirectly obtained from the optimization solutions are also reported in this table. It is seen that the optimization process tends to maximize the outer diameter which is expected as this allows reducing the ohmic losses due to the larger airgap area.

The designed machines are also simulated by the electric machine analysis Motor-CAD package to validate the accuracy of the SDM using FEA results. Fig. 7.7 shows the difference between the EffM of the designs calculated by the SDM with the EffM obtained from FEA. It is observed that the largest difference between the predicted efficiency is less than 5%.

Fig. 7.8 shows that the thermal limits (i.e., total loss per outer stack area and rotor loss per rotor length) are considered during the optimization study and these values are approximately equal to the benchmark design.

The reliability of the design for operation with regards to temperature limits is another point which is studied in this section. A thermal analysis is executed on the designed machines in Motor-CAD. The results of the analysis shown in Fig. 7.9 demonstrate that the applied power loss limits used in the optimization produces optimum design with acceptable temperature limits. This figure shows the rotor of the designed IM for the HFET operates at a higher temperature at full load. Fig. 7.9 demonstrates that the rotor is the hottest part of all three designs. It shows the importance of the proper selection of the cooling system for the IM rotor.

The EffMs of the designs are calculated without considering mechanical losses and are presented in the third column of Fig. 7.9. It is seen that the designed machines offer an efficiency larger than 90% in most of the driving cycle points in all designs. As increasing the current density leads to the increase of the ohmic losses, the optimization algorithm tries to keep the current density of these designs at moderate values (see Table 7.2).

According to Fig. 7.9, the maximum torque of the designed machines is higher than the maximum torque of the driving cycle. However, this high current is required to generate the required torque in the field weakening region.

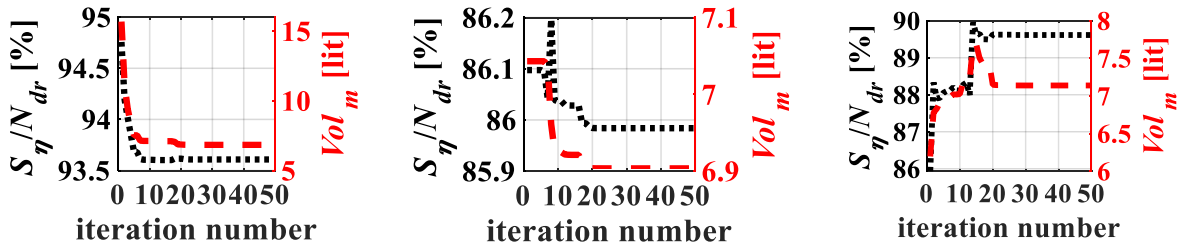

Fig. 7.6. The The variation of the efficiency over driving cycle and the active part of the at each iteration of the optimization. (a) HFET; (b) UDDC; (c) NYCC

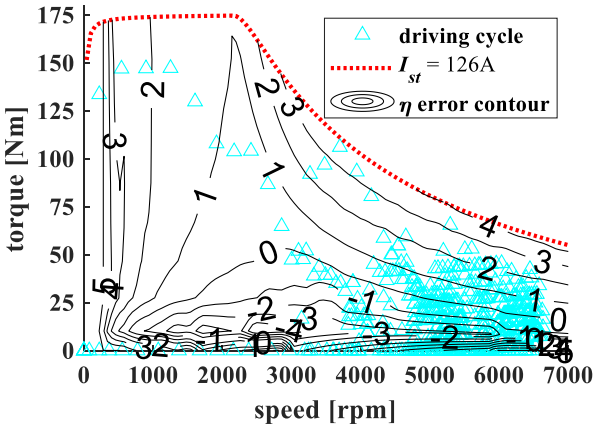

(a)

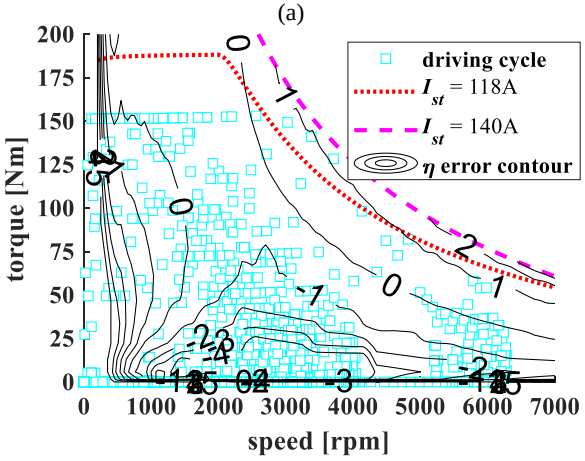

(b)

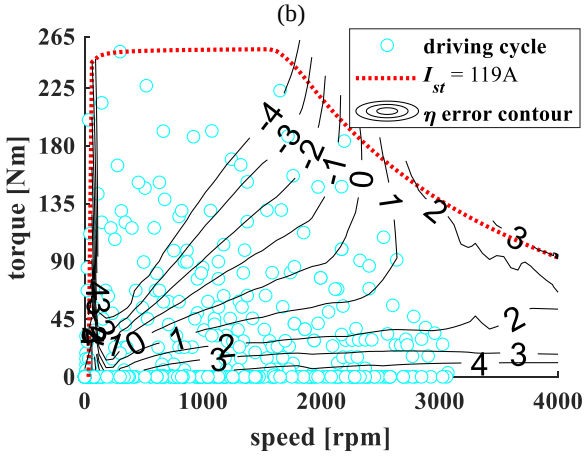

(c)

Fig. 7.7. (a), (b), and (c) the difference between the obtained EffMs from the analytical model and the Motor-CAD software results. The red dot-lines are the rated current determined by normal optimization study. The cyan points are the considered driving cycle points.

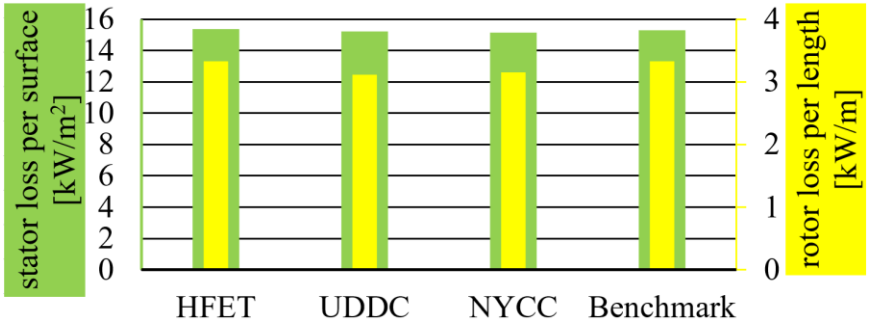

Fig. 7.8. The full load 2-D FEA results of the rotor and stator loss distribution on the designed machines and comparison with benchmark.

TABLE 7.2. THE OPTIMIZATION VARIABLES CONSIDERED RANGES FOR DETERMINATION OF SOLUTION SPACE.

			Number of turns per slot	Number of rotor bars	Rotor slot pitch	Stator slot pitch	L_{st} [mm]	Shaft diameter [mm]	Stator back-iron [mm]	Rotor back-iron [mm]	Rotor Slot height [mm]	Stator slot height [mm]	End-ring width [mm]	End-ring height [mm]	D_O [mm]	D_i [mm]	Rated current density [A/mm^2]	Maximum current density [A/mm^2]
Variable ranges			2-15	40-100	0.2-0.7	0.5-0.8	100-350	30-150	10-100	10-100	10-50	10-50	5-50	5-50	--	--	--	--
Optimal solutions	Norm	HFET	3	66	0.39	0.58	152	63.6	21.4	22.0	23.9	20.9	10.1	12.3	243	157	11.4	--
		UDDC	3	96	0.26	0.56	148	71.0	17.5	30.1	31.4	23.1	12.6	18.5	277	196	8.86	--
		NYCC	3	78	0.47	0.55	230	98.9	16.7	31.2	21.1	25.7	15.3	19.8	287	201	8.96	--
	OL	HFET	4	78	0.36	0.64	116	45.6	10.5	14.2	11.1	14.0	11.8	8.11	145	95.4	16.0	50.0
		UDDC	4	64	0.66	0.51	103	45.1	10.1	15.5	10.4	21.2	7.34	9.06	158	94.1	16.0	50.0
		NYCC	4	60	0.28	0.62	101	85.9	14.2	27.1	13.6	10.0	6.16	11.3	216	166	16.0	50.0

7.5.2. Overload consideration

The proposed design process with consideration of the OL capability is employed in this section. The optimal solutions of the optimization study over the three considered driving cycles are tabulated in Table 7.2. The results demonstrate a smaller depth of the rotor and stator slots compared to the normal optimization results dimensions. The smaller back-iron and L_{st} are other factors which can be seen as the results of the consideration of the OL capability (see the axial views in Fig. 7.9).

The EffM of the designed machines over each investigated driving cycle are shown in Fig. 7.9. The rated current and maximum current to cover all the operating points of the considered driving cycles is highlighted in each presented EffM. It is seen that the maximum current of these designs is almost three times the rated value.

7.5.3. Comparison of the Designed IMs

A comparison between the optimal designs with and without consideration of the OL condition is carried out to highlight their differences.

A transient thermal analysis during operation in the driving cycles is executed to check the reliability of the designs based on the suggested design process. The results of the transient thermal analysis are presented in Fig. 7.10. The class F insulation permits a hotspot temperature of 155°C for the winding. As shown in Fig. 7.7, all the designs operate within the temperature constraint of the Class F insulation. This figure shows the designed machines without consideration of OL have peak temperatures of less than about 80°C which is quite low. When larger torques are required in the driving cycle, the temperature of the machine significantly increases because of the higher currents which flow through the rotor bars and windings.

The results of the proposed thermal model used during the optimization has been compared with the Motor-CAD transient thermal analysis results in Fig. 7.10. These results show the success of the thermal model in prediction of the temperature.

Table 7.3 shows the weight of the active materials consisting of the iron parts and copper in both the stator and rotor in the optimal designs. The designs using the OL capability are much lighter than their counterparts. Fig. 7.11a compares the weight of the active materials including end-winding of the designed IMs using the normal optimization and OL consideration optimization. It demonstrates the weight of designed IMs for HFET, UDDC, and NYCC using normal optimization are respectively about 3.8, 5.1, and 4.4 times of the designed IMs with consideration of OL. This reduction of the weight leads to the increase of the power density which is reported in Fig. 7.11b. The consideration of OL allows to reach about 4 to 5 times larger power density for the designed IMs for the HFET, UDDC, and NYCC driving cycles.

It should be noted that while using the overload capability of the machines can significantly reduce the machine size for a given driving cycle, there are likely other practical constraints like gradeability and continuous power requirements which may limit the ability to implement this fully in practice.

Fig. 7.11c shows the efficiency drop when the IM designs based on OL are utilized in the EV instead of the normal optimal designs. It is seen that the energy consumption for the HFET is about four percent higher while for the UDDC and NYCC designs this is increased by 28% and 31%. This is because there are more operating points in the UDDC and NYCC which require larger torque than the rated power of the designs. As shown in the EffM of the OL-based design, the efficiency is substantially lower (e.g., 5-20%). Hence, in those driving cycles in which the EV requires large torque, the energy consumption increases significantly.

Table 7.4 reports the electrical equivalent circuit parameters to show the difference and similarities of the designed IMs. It is seen that the leakage inductances of the IMs designed based on the normal optimization process and OL consideration procedure are close to each other for all three driving cycles. However, there is a large difference between the rotor and stator resistances with and without consideration of OL.

The reported current values in the third column of Fig. 7.9 showed that the current increase can be a reason for the efficiency drop. The higher resistance value of the OL considered designs against the normal designs is another reason for the efficiency reduction in the OL based designs (see Table 7.4). The maximum power in the torque-speed plane of each design is considered for the loss shown in Fig. 7.12. This figure shows at the considered operating point the amount of the loss in the OL considered designs is at least three times of the IMs designed without considered of OL.

Front view Axial view EffM

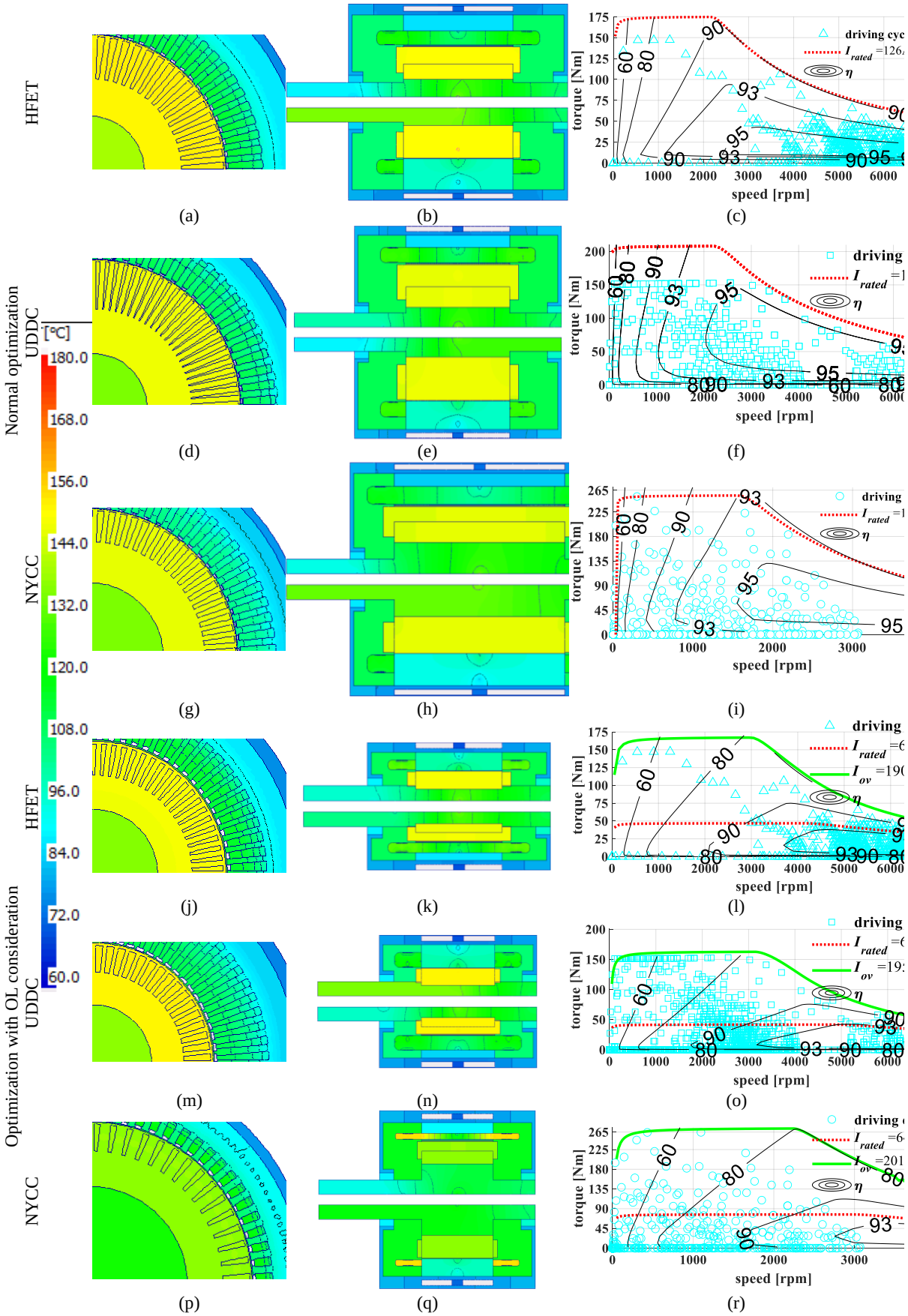

Fig. 7.9. Steady-state 3-D FEA results of thermal analysis at the rated current and EffMs of all designs.

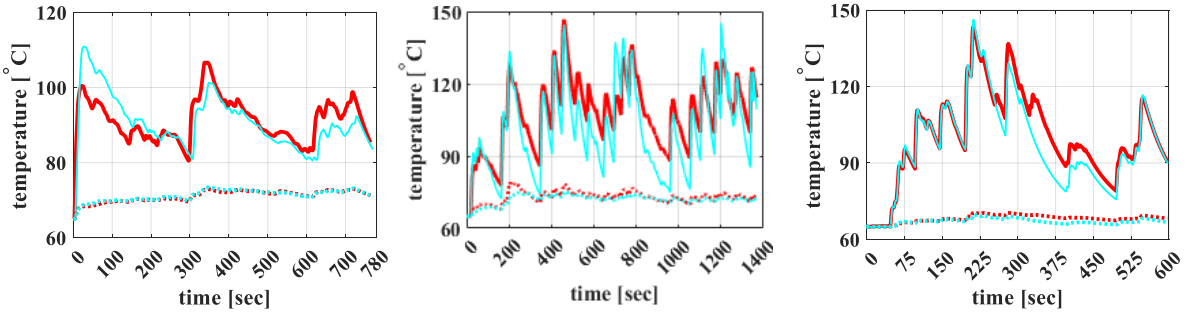

(a) (b) (c)

Fig. 7.10. Motor-CAD and lumped model results of the transient thermal analysis of the stator winding hotspot of the designed machines with and without consideration of OL (a) HFET, (b) UDDC, (c) NYCC.

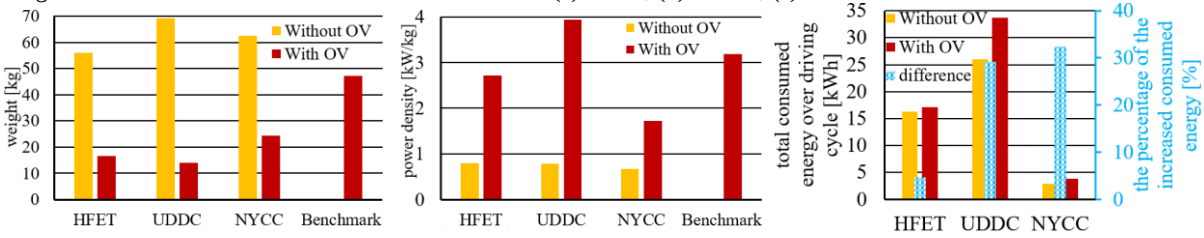

(a) (b) (c)

Fig. 7.11. Comparison of the (a) weight and (b) power density of the optimal designs with and without consideration of the overload during optimization against benchmark.

TABLE 7.3. THE MASS OF THE ACTIVE MATERIALS IN THE OPTIMAL DESIGNS WITHOUT CONSIDERATION OF THE OVERLOAD.

Part	HFET		UDDC		NYCC	
	Norm.	OL.	Norm.	OL.	Norm.	OL.
Stator lamination [kg]	23.5	5.56	23.9	6.36	39.6	9.04
Stator copper [kg]	6.15	1.96	9.16	1.95	14.1	2.29
Rotor lamination [kg]	12.6	3.61	22.8	2.79	29.9	8.72
Rotor copper cage [kg]	8.82	2.14	11.6	2.02	17.4	2.99
Shaft steel [kg]	7.64	5.02	8.38	4.63	17.3	9.56
Total weight [kg]	58.7	18.3	75.9	17.7	118	32.6

TABLE 7.4. EQUIVALENT CIRCUIT PARAMETERS OF THE OPTIMAL DESIGNS WITHOUT CONSIDERATION OF THE OVERLOAD.

EEC parameters	HFET		UDDC		NYCC	
	Norm.	OL.	Norm.	OL.	Norm.	OL.
R_s @ 140°C [Ω]	0.035	0.081	0.028	0.072	0.029	0.095
R'_r @ 140°C [Ω]	0.012	0.041	0.011	0.028	0.015	0.021
L_{ls} [mH]	0.111	0.144	0.114	0.175	0.172	0.105
L'_{lr} [mH]	0.202	0.231	0.209	0.194	0.271	0.263

7.5.1. Computation time comparison

The proposed optimization procedure utilizes a SDM model and a thermal model in each iteration. For a certain design, the required time for the SDM model to calculate the EffM is 23 seconds using a Core i9-7900X (3.30 GHz) computer with 128 GB RAM. The estimated driving cycle loss data are the inputs for thermal model. These data are extracted from in 1 second from the output data of the SDM model. The thermal model predicts the temperature variation over a driving cycle in 28 seconds. Thus, the total required time for the proposed model to predict the electromagnetic and thermal behavior of a certain design is less than one minute.

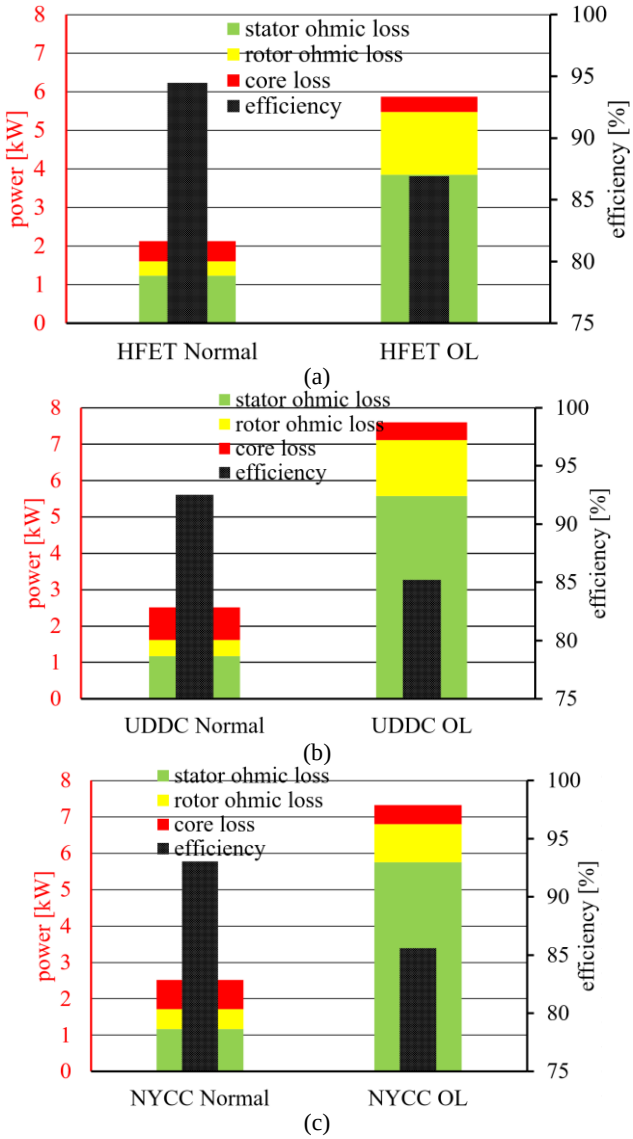

Fig. 7.12. Comparison of the loss breakdown and efficiency at the maximum power point operation of the optimal normal designs against OL designs for (a) HFET at 42.5kW, (b) UDDC at 47.2kW, and (c) NYCC at 46.4kW.

On the same computer, FEA modeling in Motor-CAD requires 140, 180, 63, and 154 seconds for the saturation modelling, core loss modelling, efficiency map estimation, and driving cycle data extraction, respectively. The transient thermal analysis takes about 14 minutes to be completed in Motor-CAD. Thus, the total required time for analysis of an induction machine over driving cycle and estimation of its temperature variation is about 22 minutes for a certain design in Motor-CAD.

In the optimization procedure, around 3,000 designs are analyzed for each driving cycle. Therefore, the total time of the simulation using the proposed analytical model is about 43 hours. On the other hand, Motor-CAD needs about 1,100 hours for such an optimization study which is about 26 times of the proposed analytical model. Thus, the proposed analytical model is a computationally-efficient technique for the optimization of induction machines for traction applications

7.6. Conclusion

This chapter discussed the optimization of induction motors over three specific vehicle driving cycles. An accurate multi-physics model was developed for performance parameter and temperature estimation of the IMs. The performance parameters were calculated using a subdomain model with capability of the prediction of saturation level at different operating points. The temperature variation was predicted using a lumped-circuit thermal model.

The fast and accurate multi-physics model allowed defining optimization problems to find the optimal design over different driving cycles. Two sets of optimizations were executed. Firstly, the IMs were optimized for maximum efficiency in the minimum possible volume. Secondly, the IMs were optimized only for minimum volume while meeting the thermal limitations during the driving cycle. This resulted in increasing the power density by up to four times but also reduced the machine efficiency and increased the driving cycle energy consumption by about 30% for some cases. Note that the capability to use this approach to reduce the motor size will likely be limited by other vehicle constraints such as gradeability.

Although the OL performance is considered in the design of the electric motors in industrial applications, there is limited reported data on investigation of the OL effect in the literature. The presented results in this Chapter show that the energy consumption increases by consideration of OL in highway driving cycles (i.e., HFET) is only about 2.5% larger than the normal design. So, it is more reasonable to consider the minimum volume objective function for the EVs which are designed for highway applications. Although the results showed it is possible to achieve 4 times higher power density in the IMs designed for operation in urban area, the 30% increase in energy consumption is a limit to design for minimum volume. The energy consumption constraint can be added to the problem to cover this trade-off.

The proposed optimization model can be used for design of any electric machines if precise and fast electromagnetic and thermal models are available for that machine. Although the proposed algorithm can be applied in a full FEA analysis, it is not reasonable to be applied because it will be computationally expensive.

Chapter 8. Design and Construction of a Small Sized AFIM

8.1. Chapter Overview

The axial-flux electric machines designed for electric vehicles offer higher efficiency and power density compared to the radial flux machines. The AF induction machine (AFIM) can be a proper substitute for the AF permanent magnet (AFPM) machines. This chapter aims to design a single-sided AFIM in a same size as a commercialized AFPM to shed light on the possible differences of these machines in terms of performance and manufacturing difficulties.

The performance parameters of the designed AFIM are compared with the commercial AFPMSM over a wide range of torque and speed based on 3-D FEA results. The simulation results show the promising performance of the designed AFIM compared to the AFSPMSM. The manufacturing of the closed slots rotor for AFIM has been challenging issue among researchers. This chapter discusses the possible approaches for the construction of AFIM and the manufacturing challenges of each approach. The available cutting and drilling methods are described, and their advantages and disadvantages are discussed. The designed AFIM is constructed using the cheapest and fastest available technique. An experimental test setup is provided to compare the axial forces of the AFIM and AFPMSM. The importance of the selection of the airgap length to suppress the axial stiffness is studied experimentally and 3-D FEA. The design is updated using the new airgap length and the performance of the new designed is obtained to be compared with the initial AFIM design and AFPMSM.

The saturation considered EffM calculation method for IM machines is the adapted method for calculation of AFIMs' EffMs in this Chapter. The flux mapping technique is employed for EffM calculation of AFPMSM.

8.2. Chapter Introduction

Axial-flux motors become popular due to their high-power density. Manufacturing of AF motors is not only more complex than the radial flux motors, but also it is more expensive. Among different types of AF motors, construction of surface mounted permanent magnet synchronous motors (SPMSM) is easier. Hence, most of available commercialized AF machines are AFSPMSMs [342]. The availability of the permanent magnet (PM) materials in the structure of permanent magnet motors increases the cost of the electric motors. So, it is reasonable to study PM free electric motors as a substitute for them. Considering the PM cost and high-power density of AF machines, the AF induction motor (AFIM) is an appropriate option for the electric vehicles (EVs) [171].

Lots of literature have studied the design and analysis of AFIM for EV applications. However, the construction of a proper cage for the rotor has not been reported in the literature when AFIM was designed for EV. This is mainly due to the difficulties and cost involved in machining the internal slots and cavities in the rotor. There are only three papers which have prototyped the AFIM. Their topologies offer benefits for the line-starting performance which does not have value for EV applications. In [343], a separated aluminium cage was constructed and placed into an open slot rotor.

The proposed wide-open rotor slot with a few numbers of bars introduces large torque ripple. This machine can be used as a line-start motor where the torque ripple is not important. The copper bar insertion in open slots rotor and provision of the end-ring by welding was the subject of the study in another paper [344]. The circular shape of the slots in their design allows drilling the slots and inserting the copper bars. Such rotor topology is not strong enough for operation at higher speeds. In [345] to construct an AFIM the authors suggest to build the rotor using the iron wires and copper matrix. The use of copper matrix reduces the total area of the conductors in each rotor slots resulting an increased rotor resistance. Such rotor offers a high torque value at the starting suitable for the line-start applications but reduces the efficiency at steady state operation.

This study adapts a commercialized AFSPMSM as a benchmark for our case study. As such the stator of our case study is not subject of a design and hence the design variables are rotor parameters. The finite element analysis (FEA) [346], analytical models [162], and empirical equations [170] are the methods to design an axial-flux machines. In this study, the number of the rotor bars, rotor back-iron, and bars dimensions are determined using 3D FEA. The possible approaches for construction of a proper cage for the rotor are investigated by focusing on the feasibility of implementation of the available mechanical approaches. The limitation of the available methods for provision of the rotor cage in terms of cost and time of the construction are explained. The designed motor is fabricated and tested. It was found that the performance parameters of the designed AFIM are comparable with the AFSMPM making it suitable for operation in a small EV.

8.3. Design Process and Performance Analysis

8.3.1. AFIM design

The stator of the commercial AFSPMSM with 151.5mm and 85mm outer and inner diameters with 24 slots is used for the design of AFIM. The number of turns per phase of the commercial stator is 28 turns. When the stator geometry is determined, the optimal number of rotor slots, their dimension, and rotor back-iron are found out using 3-D FEA. In an initial value of 20 rotor slots, the dimension of the rotor bars and back-iron are determined to reach the no-load peak flux density of 1.7T and 1.4T in the middle layer of the rotor tooth and rotor back-iron, respectively. Literature shows these levels of the flux density in tooth and yoke allow the machine to operate optimally at full-load [277], [281].

The determination of proper tooth dimension in presence of 20 rotor bars enables to analyze the effect of the number of rotor bars. The number of rotor bars are varied in a sensitivity analysis from 16 to 24 bars. In any number of rotor bars, the summation of the iron volume in the rotor teeth keeps constant. The machine torque and torque ripple are monitored in any number of rotor bars. As shown in Fig. 8.1, the generated torque and torque ripple with 18 rotor bars are close to the larger number of bars. Although the torque ripple in both 18 and 22 rotor bars are very close, the smaller number of rotor bars reduces the manufacturing cost. Hence, the rotor with 18 rotor bars is selected for further

analysis and manufacturing procedure in this chapter. The assembled and exploded views of the designed machine are shown in Fig. 8.2. The designed machine geometry and properties are tabulated in Table 8.1 where the cross section of rotor slot and its dimensions are shown in Fig. 8.3.

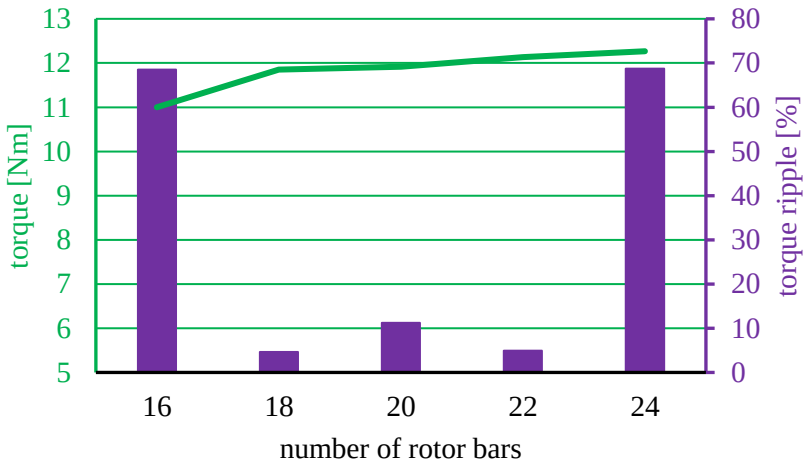

Fig. 8.1. 3-D FEA results showing the effect of number of rotor bars on torque and torque ripple. The reported data are related to 333Hz operating frequency and rotational speed of 4955rpm.

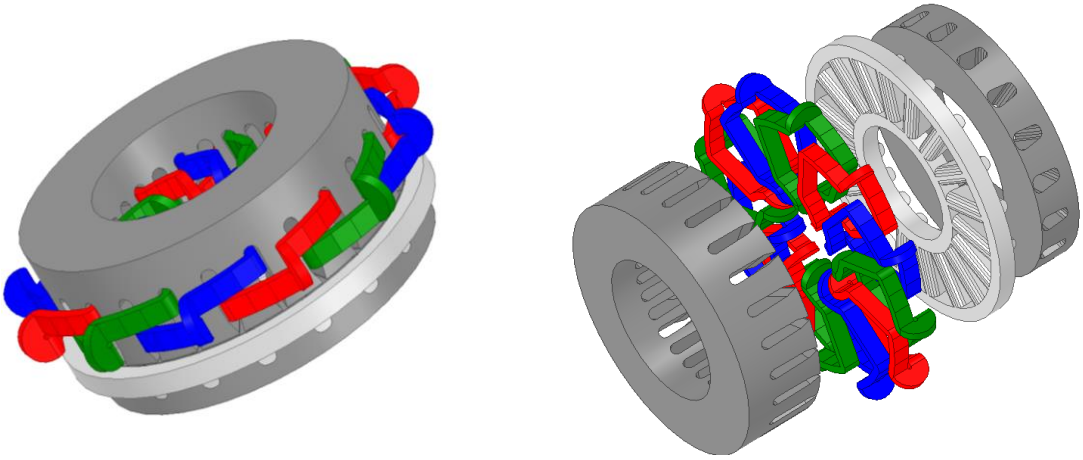

(a) (b)

Fig. 8.2. (a) 3-D assembled view and (b) exploded views of the designed AFIM.

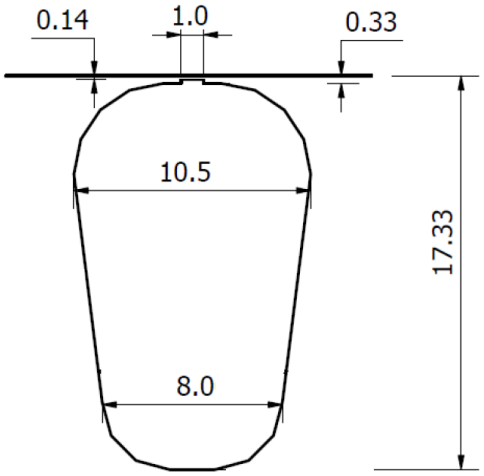

Fig. 8.3. Rotor slot dimensions of the designed AFIM.

TABLE 8.1. THE CHARACTERISTICS OF THE AFIM DESIGNED FOR CONSTRUCTION.

Parameter	value	Parameter	value
Number of stator slots	24	Number of rotor slots	18
Number of poles	8	Number of turns per phase	28
End ring height [mm]	12	End ring width [mm]	14
Outer diameter [mm]	151.5	Inner diameter [mm]	85
Stator height [mm]	48	Rotor height [mm]	25
Total stator slot height [mm]	28.7	Stator slot width [mm]	6.5
Stator slot opening height [mm]	1	Stator slot opening width [mm]	2.5
Stator lamination material with 35mm thickness of each layer	M085-23P	Solid rotor steel	1010
Airgap length [mm]	0.5	Winding line-line resistance [Ω]	0.025
DC bus voltage [V]	96	Maximum current [A]	80

8.3.2. Performance parameters of the AFIM and ASPMSM

3-D FEA is used to derive the equivalent circuit parameters of the designed AFIM and the saturation curve of the machine in different supplied voltage in a constant frequency. The stator resistance and the rotor resistance transferred to the stator side at 60°C are 0.0125Ω and 0.029Ω, respectively. The calculated stator and rotor leakage inductances from the locked rotor test are 0.08mH. The magnetizing inductance of the machine obtained from no-load test is 0.41mH. The summation of the leakage and magnetizing inductances in different magnetizing currents at 200Hz operation are shown in Fig. 8.4. This curve is used to calculate the EffM of AFIM using the explained method describe in chapter 3.

The flux-map and core loss of the commercialized AFSPMSM (benchmark model) are also extracted through 3-D FEA. The collected data are used to calculate the performance parameters of the AFIM and ASPMSM over a wide torque-speed range. Fig. 8.5 demonstrates the capability of the designed AFIM in production of higher torque in the constant torque region. It should be highlighted that the mechanical losses are ignored in the reported performance parameters in Fig. 8.5. The promising performance of the designed AFIM is a good reason to construct the machine and test its performance experimentally.

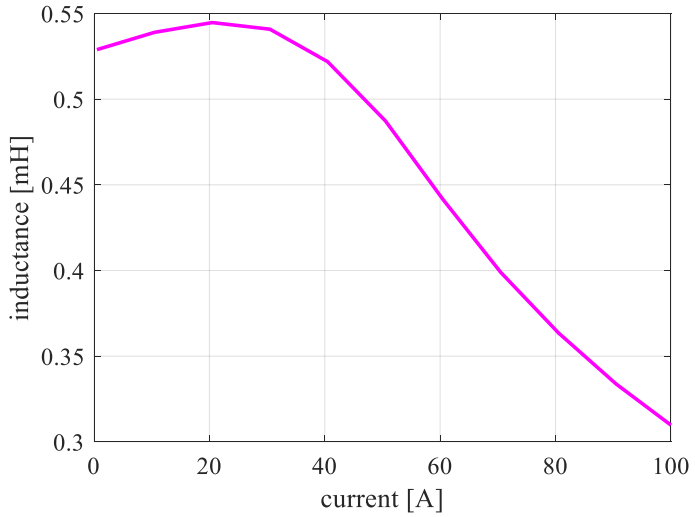

Fig. 8.4. Inductance variation of the designed AFIM in different no-load currents at 250Hz.

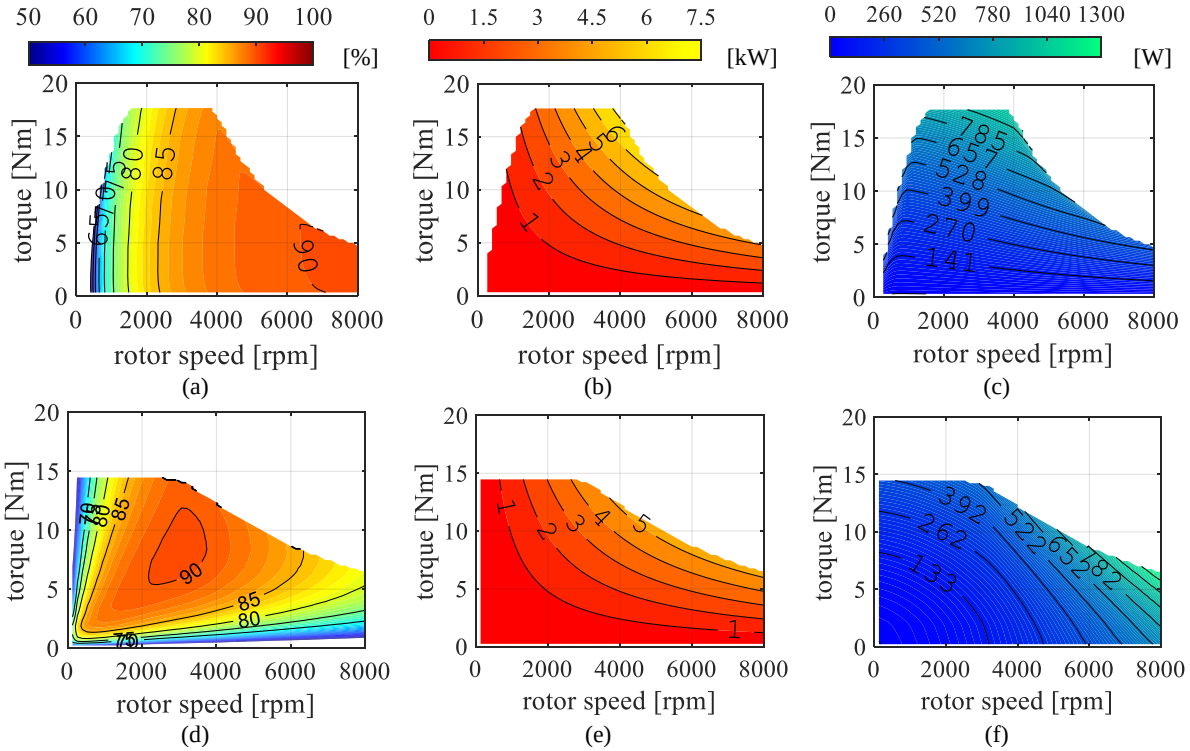

Fig. 8.5. Performance parameters of the AFIM and ASPMSM calculated using the 3D FEA results and analytical model. (a) efficiency map of AFIM; (b) Power map of AFIM; (c) total losses of AFIM; (d) efficiency map of AFSPMSM; (e) Power map of AFSPMSM; (f) AFSPMSM loss map.

8.4. Methods for Manufacturing of AFIM

The stator, rotor, and rotor cage are the most challenging parts of an AFIM construction. This part explains the details of the available technologies and optimum approach for manufacturing of AFIMs.

8.4.1. Approach of stator fabrication

The available laminated steel rolls are the best option for the stator fabrications. It enables to cut the designed slots of the stator in different stator radiuses using the laser cutting or stamping process. After the creation of the stamped layers the stator is rolled, and all layers are punched to each other to make the stator. The laser cutting is slow and expensive. Nowadays, the stamp cutting devices have been commercialized and are widely used to prepare the laminated axial flux stator.

8.4.1. Approaches of rotor fabrication

The rotor fabrication is the most challenging parts of the AFIM manufacturing. The laminated iron parts are preferable owing to the less core loss. The preparation of a slotted core using a same mechanical procedure as the stator is not acceptable for the AFIMs because of the low mechanical strength of the punched steel layers. The low mechanical strength of the punched layers increases the risk of rotor explosion especially at higher speeds due to the unbalance centrifugal forces exerted on the different lamination layers. Hence, this section focuses on the fabrication of the rotor from a solid steel sheet.

To make sure that the solid rotor does not reduce the performance of the AFIM, the machine performance parameters are calculated using 3D FEA and compared with each other (see Fig. 8.6). As it was expected, the consideration of solid stator is not reasonable because of the large airgap flux density drop resulted from the high amount of the eddy current on the solid steel of the stator.

The low frequency of the rotor bar currents at smaller slips allows to use the solid rotor. As shown in the presented 3-D FEA results in Fig. 8.6, the performance of the AFIM with solid rotor and laminated stator in smaller slips is similar (see Figs. 8.6a, 8.6b, and 8.6c). The output power in larger slips is dropped due to the reduction of airgap flux density and consequently the produced torque. The reduction of the airgap flux density results from the increment of the induced eddy current on the rotor steel. However, Fig. 8.6f shows the efficiency of the solid and laminated rotors are same. It allows to use the solid rotor AFIM instead of a laminated rotor to guarantee the rotor mechanical strength.

The available mechanical processes for manufacturing of metals are divided to subtractive and additive methods. The computerized numerical control (CNC) milling, laser-jet cutting, waterjet cutting, and electrical discharge machining (EDM) are the available subtractive methods. The laser beam melting known as the 3-D printing is the available additive method for fabrication of a metal component.

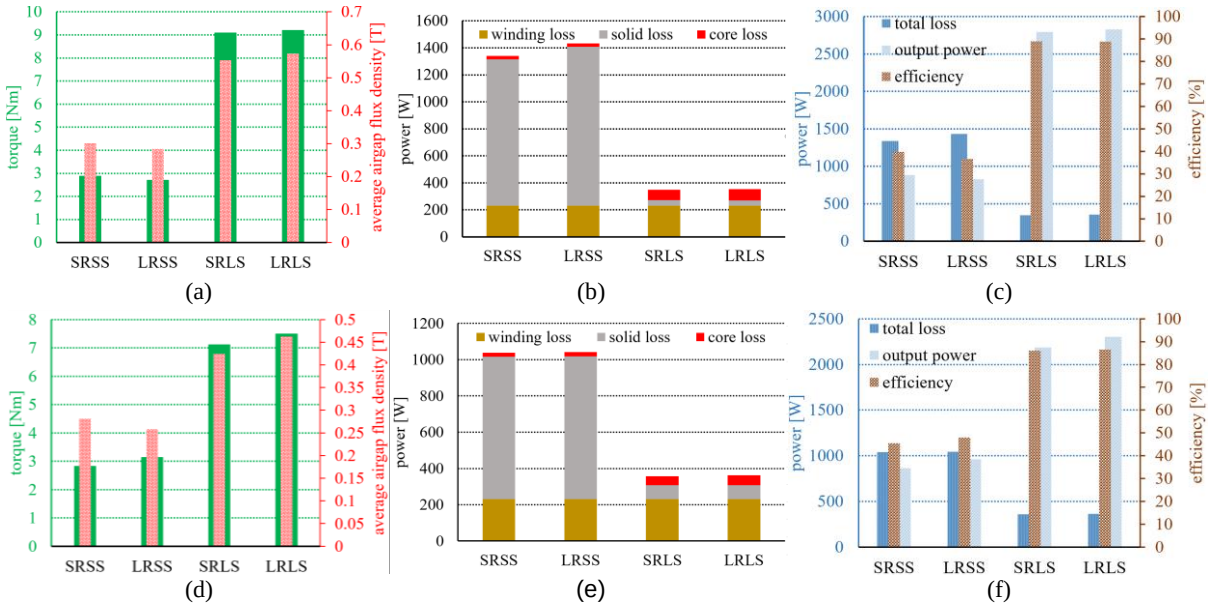

Fig. 8.6. 3D FEA results of the AFIM design in two different slips when the stator windings are supplied by 85A current. (a) the torque and airgap flux density values at 4955 rpm rotating speed and 333Hz supply frequency. (b) different loss components at 4955 rpm rotating speed and 333Hz supply frequency. (c) total loss, output power, and efficiency at 4955 rpm rotating speed and 333Hz supply frequency. (d) the torque and airgap flux density values at 4900 rpm rotating speed and 333Hz supply frequency. (e) different loss components at 4900 rpm rotating speed and 333Hz supply frequency. (f) total loss, output power, and efficiency at 4900 rpm rotating speed and 333Hz supply frequency. Solid rotor solid stator motor core loss distribution is shown by (SRSS). Laminated rotor with solid stator is shown by (LRSS). SRLS and LRLS are the solid rotor laminated stator and laminated rotor laminated stator core loss distribution.

The CNC milling is a popular method for metal machining. However, it has some limitations and cannot be used for all geometries. The length of the standard mill tools is 4mm. In large depths (larger than 35mm depth), the mill tool losses its stability and start bouncing which will lead to break of the tool. So, the axial length of the rotor slots should not be larger than 30mm to make sure that the milling tool is not at the break risk. Moreover, the circuital rotation of the milling tool will damage the possible sharp edges of the slots. So, the circular edges should be considered for the rotor slots.

Laser-jet cutting is a powerful technique for cutting the metals. However, its maximum possible depth of cut for the commercialized laser-jets is less than 15mm. So, this cutting technique is not an option for the construction of rotor.

Waterjet cutting, blasts a high pressure (>400MPa) water stream through the metals. It cuts the metal from one side and needs a water pass to collect the water in the pool. However, it is not a proper option for AF rotor because the waterjet will destroy another side of the disk. Moreover, the commercial water-jets machines do not have a proper CNC function to automatically move the work piece for preparation of proper slots as per design.

Conventional EDM named as plunge EDM uses an electrode in a distinctive shape which is usually made from copper. The metal piece is used as the second electrode. An electrical field is created between the two electrodes, which is separated by a dielectric fluid. When the dielectric breaks down, current flows, sparks discharge and material is removed very precisely from the work piece. The shaped electrode is CNC controlled and is plunged repeatedly up and down into the material and the electrode arcs and cuts a negative impression of its shape. The work piece must conduct electricity. The copper electrodes are machined based on the given drawing. The copper electrodes are eroded during the EDM and should be substituted by new electrodes during the manufacturing. So, EDM plunge machining is precise, albeit slow and expensive process (see Table 9. 2). It should be highlighted that the low electrical conductivity of the steel materials used in electrical machines leads to the increase of the EDM time.

Wire EDM is an electro-thermal cutting process, also known as wire spark EDM or wire cutting. It uses single thin single copper wire as an electrode that moves through the metal to cut a particular shape via electrical discharges, or sparks. During wire EDM cutting the wire constantly unspools from an automated feeder and is ultimately disposed of, as it can only be used once. The dielectric fluid, deionized water, acts as the conductor. As shown in Table II, like EDM plunge, the EDM wire cutting is precise but expensive (see Table 8.2).

As it is discussed the CNC milling and EDM are the proper available techniques for rotor manufacturing. It was mentioned that the EDM methods are expensive compared to the CNC. For the comparison purpose, the cost of the CNC and EDM collected from local companies in Adelaide are tabulated in Table 8.2.

TABLE 8.2. THE COMPARISON OF THE MANUFACTURING COSTS OF DIFFERENT METHODS FOR THE DESIGNED ROTOR.

Method	EDM plunge	EDM wire cutting	CNC milling
Cost (AU$)	5500	5000	1940

8.4.2. Approaches of rotor cage fabrication

The aluminum diecast is a well-known technique to fabricate the induction cage. The diecast is carried out at 640°C. The aluminum uniform distribution through the slots and the rotor iron shape changes due to the high temperature of the casting process need to be investigated during the manufacturing. The die-casting of pure aluminum is impossible because it will not be spread uniformly in whole rotor slots areas. Hence, an aluminum alloy (e.g., EA401) containing approximately 12% silicon, 0.16% lead, and other trace elements is used to improve aluminum diffusion through the slots. The closed slot rotor topology is preferable in the design of induction machines for EVs which helps to the reduction of torque ripple. The slot opening is closed by a thin steel layer with a thickness of less than 0.5mm. This thin layer is vulnerable when a high-temperature process is applied to the rotor. To protect the thin layer against possible damage, a 2mm thicker rotor is manufactured from the steel sheet. It allows to have a thicker steel layer before die-casting and this additional part is removed during a machining process after die-casting.

8.5. Construction of Design and Testing

8.5.1. Construction of designed AFIM

The laminated stator which is chosen from the available commercial design is shown in Fig. 8.5a. A view of the preparation of winding for the stator is presented in Fig. 8.5b. As explained in the CNC milling section, the rotor can be fabricated using milling devices for small axial lengths (i.e., <35mm). So, the designed rotor is constructed through the CNC milling process on a solid rotor piece. As shown in Fig. 8.7c. the upper and lower section of the slots are drilled before milling. Then, the milling process to shape the rotor slots is executed on each rotor slots (see Fig. 8.5d).

For the aluminium die-casting, a 3-D printed mold which entirely covers the considered end ring is provided. The rotor is heat up to 640°C and the melted aluminium alloy is die-casted into the created aluminium mold and slots regions. The constructed rotor cage after die-cast is shown in Fig. 8.5e. The die-casted cage needs to be smoothed.

The constructed shaft is shown in Fig. 8.5g. The dimensions of the shaft are chosen based on the housing of the commercial design. A slotted end based on a frame size of IEC90 (Frame 90L) conforming to IEC 60034-1 is investigated for the shaft. As shown in Fig. 8.5f, there are four holes on the shaft plate which are used to screw the shaft to the rotor. The assembled shaft on the rotor with smoothed end rings are shown in Fig. 8.5h.

Fig. 8.7. The fabricated parts of the designed AFIM. (a) stator with the insulator layers prepared for winding. (b) wounded stator. (c) the initial step for the rotor slots milling. (d) rotor iron. (e) the die-casted cage on rotor (the aluminium circles on the rotor are the inlet and outlets of the casting process). (f) shaft. (g) the assembled shaft on rotor.

Axial force is an important factor for determination of the bearing in axial flux machines. An axial force analysis is conducted to firstly understand the effect of the laminated and solid rotor on the amount of force, and secondly determine the size of bearing. Fig. 8.8 shows that the AFIM axial force with solid rotor is a bit smaller than the laminated rotor AFIM. It happens due to the reduction of the airgap flux density in presence of solid rotor (see the reported flux density values in Figs. 8.6a and

8.6d). According to Fig. 8.6, the AFIM axial force 1.55kN which is in a same range of the AFPMSM commercial design.

The simple design of deep groove ball bearings which consist of an inner ring, outer ring, and steel balls have made them popular in industrial applications such as electric machines. These bearings offer a high load capacity with a low noise and small friction losses. Hence, two deep groove ball bearings are selected for the drive end and non-drive end of the machine.

The bearings are NTN 6006LU for drive end and smaller NSK 6202DU for the non-drive end. The 6006DU is a single row, single seal, radial ball bearing with a 30mm bore ID, 55mm OD, and 13mm width, and dynamic load rating of 7.65kN. The 6006LU is a single seal, deep groove ball bearing with a 15mm bore ID, 35mm OD, and 11mm width, and dynamic load rating of 7.74kN. Considering the calculated axial forces and the ratings of the bearings in load handling, they are suitable options for the designed EM.

The assembled AFIM design is installed on the test rig for experimental investigation and analysis (see Fig. 8.9). It is found out that the rotor touches the stator even at small currents. Further investigation is conducted in the continuation of this chapter to find the main reason of this failure.

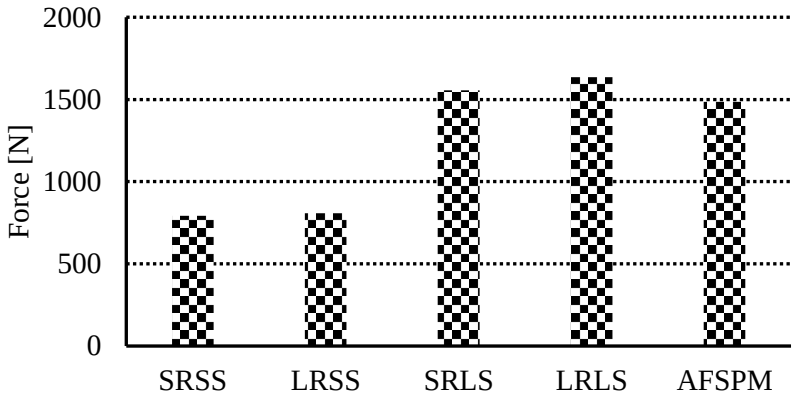

Fig. 8.8. The axial force of the AFIM with different type of rotor and stator and a simple comparison with AFSPMSM.

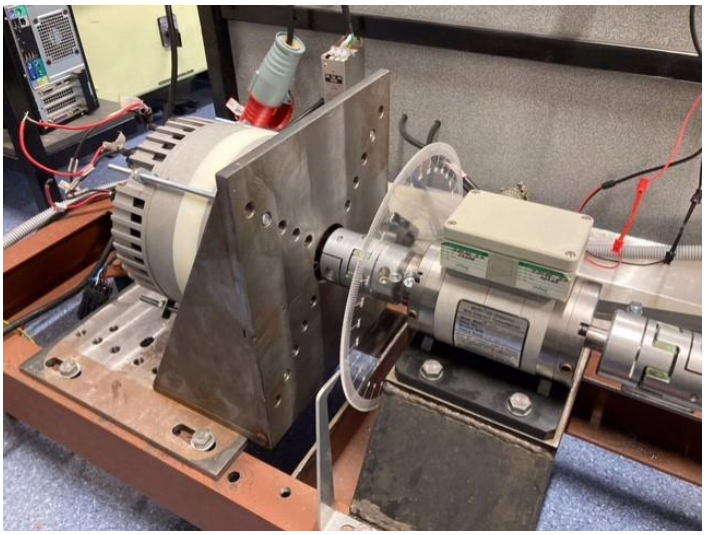

Fig. 8.9. The installed AFIM on the test rig.

8.5.2. Axial stiffness test and analysis

8.5.2.1. Introduction of experimental setup

Axial stiffness is defined as the variation of the force with airgap length (i.e., slope of the force vs. airgap length line). This phenomenon was ignored in the initial design of the machine. The design of the machine at large stiffness is not reasonable because the amount of axial force can be changed hugely in any transient and unbalance situation. The rotor field in the AFPMSM is more uniform as compared to the AFIM because the generated field by the rotor bars is not uniform in the entire airgap region.

An experimental test using a high precision extensometer is planned to measure the axial force of both machines in different airgaps. The considered axial stiffness experiment measures the force at no-load condition. The prepared experimental setup is shown in Fig. 8.10.

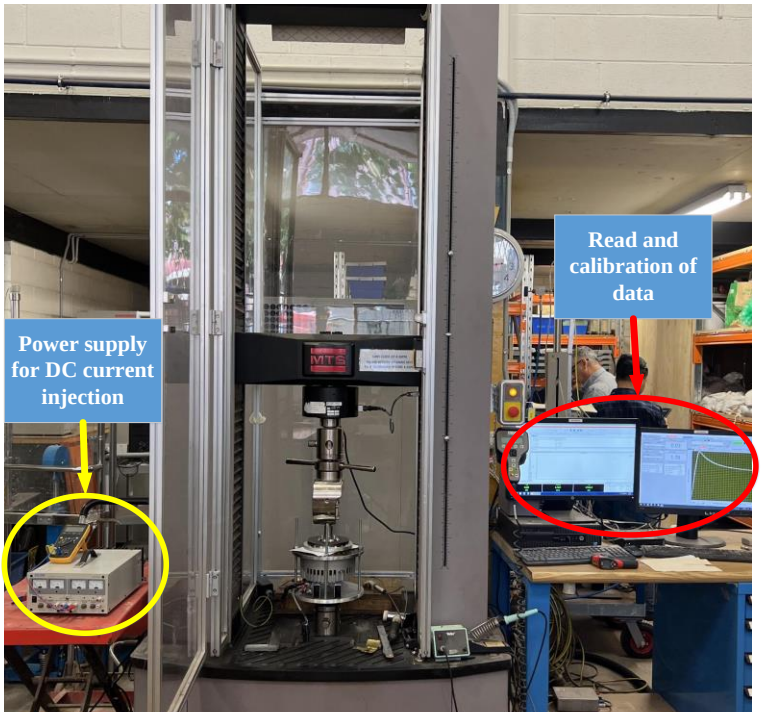

Fig. 8.10. The extensometer setup and the required equipment for axial force and stiffness measurement.

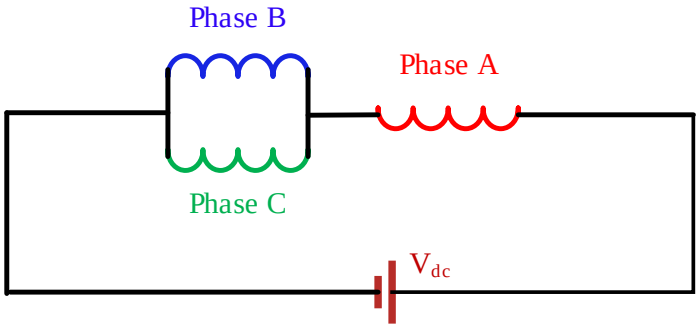

Fig. 8.11. The connection of the phases to inject current into the winding during force measurement.

(a)

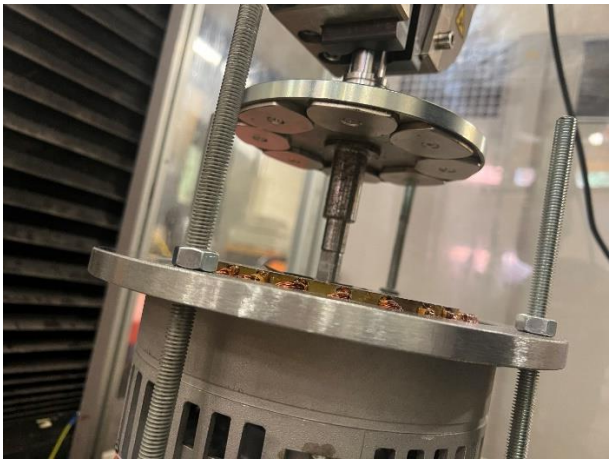

(b)

Fig. 8.12. (a) and (b) are the views of the test setup when AFIM and AFPMSM rotors are connected to the upper jaws, respectively.

To emulate the AFIM no-load condition in a static test, one of the phases is supplied by a DC current which is equal to the peak of the no-load current of the AFIM. Half of the peak no-load current is injected to the other windings of the machine. This current distribution between windings is achieved when two phases are connected in series with each other, and the remaining phase is connected in parallel with them (see Fig. 8.11). It should be highlighted that this current injection emulates the *d*-axis current which results in the *d*-axis flux (magnetizing flux when the rated voltage is injected to the winding). Fig. 8.12a shows the connection of the connection of the stator and rotors to the MTS extensometer jaws. It is shown that the stator is stiffly mounted on the lower jaw using a frame and the rotor is hanged by connection to the moving jaw of the extensometer.

The process of the no-load force measurement of the AFPMSM is more straight forward and there is no need of injection of the current into the winding. Like the AFIM test, the stator of the AFPMSM is fixed on the bottom of the extensometer where the rotor is moved using the upper jaw (see Fig. 12b).

8.5.2.2. Update stator design to lower the current

The initial AFIM design is a low-voltage and high current design (i.e., phase voltage 40V and 80A). For this reason, the no-load current which is required to be injected during the stiffness measurement is about 40A which needs a large and expensive DC power supply. Hence, the stator winding is updated to a design with rated phase voltage of 240V.

The low-voltage AFIM its voltage limit at 248Hz during operation at rated current. This design is converted to a 240V, 50Hz stator using (8-1). This equation is derived from the emf equation formulated in (5-2).

$$N_{ph,new} = \frac{N_{ph,old} \times f_{old}}{V_{ph,rms,old}} \times \frac{V_{ph,rms,new}}{f_{new}} \quad (8\text{-}1)$$

In (8-1), the number of turns of the first design (high speed design) and the updated design are respectively shown by $N_{ph,old}$ and $N_{ph,new}$. The rated frequencies of the initial and new design are shown by f_{old} and f_{new}, respectively. The rated phase voltage of the high-speed design and updated design are shown by $V_{ph,rms,old}$ and $V_{ph,rms,new}$. Considering (8-1), the number of turns per phase of the updated 50Hz design should be equal to 832 turns. The no-load V-I curve of the updated design collected from 3-D FEA is shown in Fig. 8.13. According to this figure, the peak of the no-load current at the rated voltage is 3.51A. The phase resistance of the updated design at 60°C is 7.48Ω. Thus, a 60V DC power supply can inject about 1.5 times of the peak no-load current using the winding connection shown in Fig. 8.11.

8.5.2.3. Data collection and discussion

The experimental tests explained in 8.5.2.1 are executed and the collected data are compared with 3-D FEA results. The discussion on the results determines the optimum airgap length for the machine.

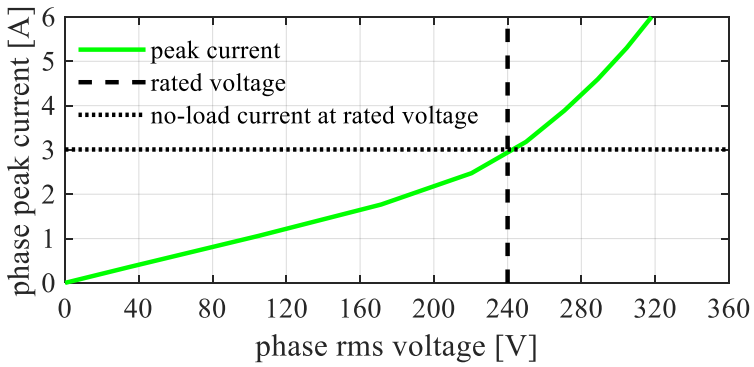

Fig. 8.13. The 3-D FEA collected data of the high-voltage low current design used in the experimental measurement of the axial force.

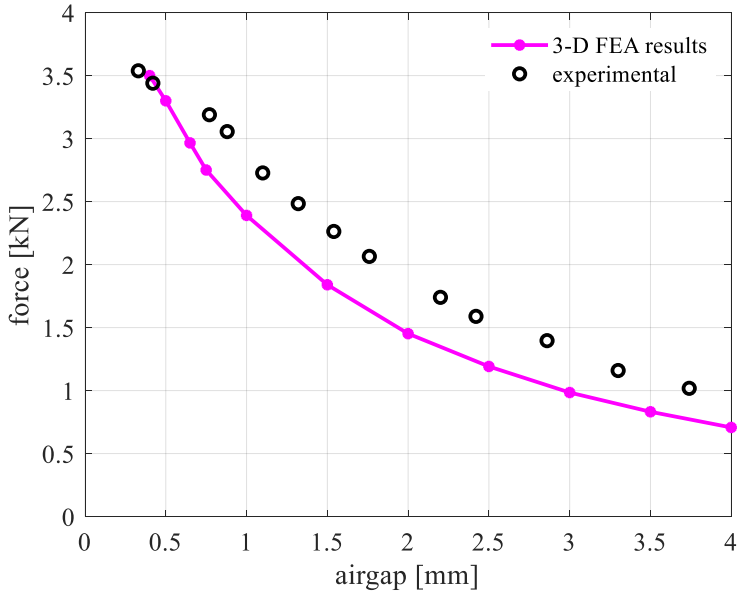

Fig. 8.14. The 3-D FEA results of the axial force in different airgap lengths of the commercialized AFPMSM.

In the first step, the force of the commercialized AFPMSM machine at the no-load condition in different airgap lengths is obtained. Fig. 8.14 shows the maximum difference between the predicted forces via 3-D FEA with experimental results is 25% which occurs at the middle of the plotted curve. This difference is acceptable and validates the capability and reliability of the 3-D FEA in the prediction of the axial force in AFPMSM. This figure shows the risk of the selection of small airgap lengths for this machine due to the high stiffness. It should be highlighted that the slope of the force variation vs. airgap is about 0.95 around the rated airgap of the machine (2mm). Thus, the bearing can successfully handle the stiffnesses smaller than this value.

The results of the 3-D FEA analysis in different DC currents and airgap lengths are presented in Fig. 8.15. This figure shows the high level of saturation in smaller airgaps. According to this figure, the rate of the variation of the axial force by the current increase is dropped by the increase of the airgap length. It is mainly because of the increase of the reluctance and flux density drop in the airgap. This observation from the results of 3-D FEA is validated using the experimental results shown in Fig. 8.16.

As mentioned in the previous section, the peak of the no-load current of the AFIM with 0.5mm airgap is 3.20A. The variation of the force versus airgap length is plotted in Fig. 8.17 to show the stiffness. According to this figure, the stiffness (slope of the line) is large until 0.70mm airgap. It is observed that the slope starts to reduce significantly after this point. The stiffness reduction is continued by the increase of the airgap. It is seen that the slope of the line between 0.9mm and 1mm airgap reaches 0.95 which is in the same range as the AFPMSM machine. Hence, the airgap length of 1mm is selected for updating the AFIM design.

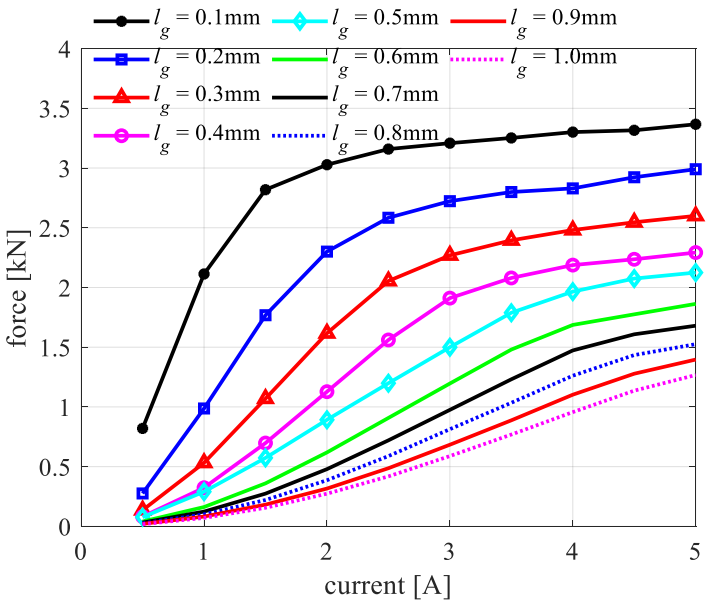

Fig. 8.15. The 3-D FEA results of the axial force in different airgap length and excitation currents.

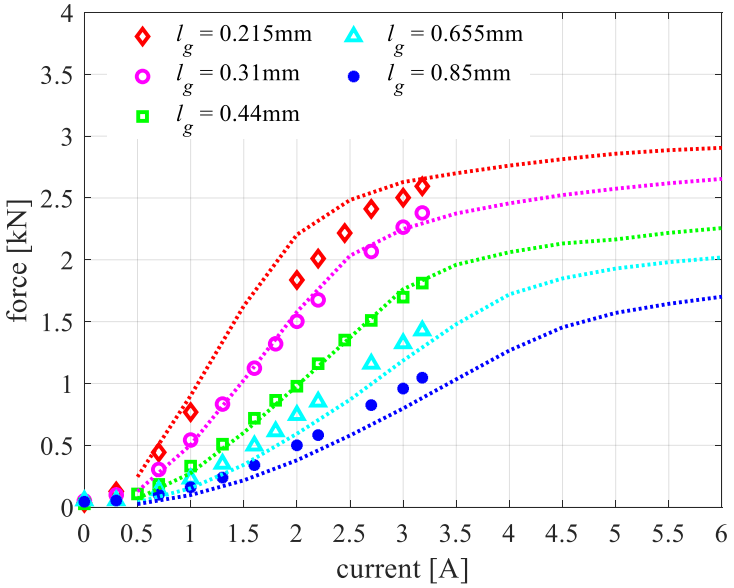

Fig. 8.16. The comparison and validation of the 3-D FEA results (dot-lines) against experimental results (symbols).

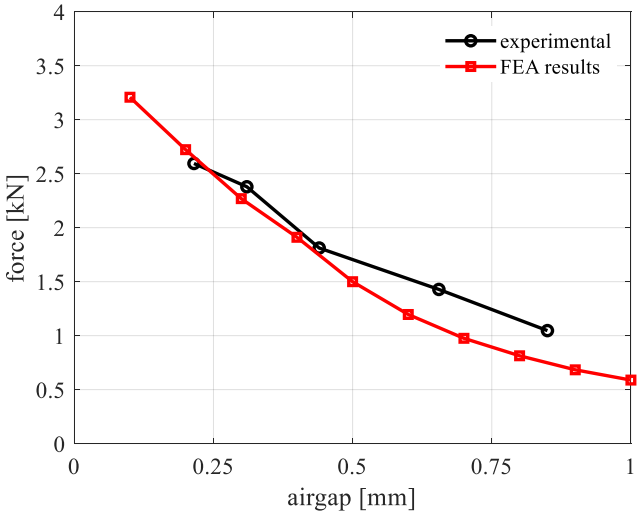

Fig. 8.17. The force variation vs. airgap of the AFIM when 3.20A current is injected to the winding using the winding structure shown in Fig. 8.11.

8.5.2.4. Locked rotor test

The locked rotor test is executed in 0.5mm and 1mm airgaps to see the effect of airgap length on the equivalent circuit parameters and validate the 3-D FEA results. The utilized experimental setup for the locked rotor test includes an autotransformer, power analyser, and the AFIM rotor and stator (see Fig. 8.18). The 816 turns stator is used for this purpose because the rated current of the available autotransformer is 10A. Table 8.3 tabulates the experimentally collected data at 0.5mm and 1mm airgap of AFIM as well as the 3-D FEA results. According to this figure, the predicated leakage inductances and rotor resistance are in a good agreement with 3-D FEA results.

TABLE 8.3. LOCKED ROTOR TEST RESULTS COLLECTED FROM 3-D FEA AND EXPERIMENTAL TEST AT 50HZ AND 60°C.

	1mm airgap		0.5mm airgap	
	Experimental test	3-D FEA	Experimental test	3-D FEA
R_s [Ω]	7.48	7.48	7.48	7.48
R_r' [Ω]	6.65	6.48	8.82	9.08
X_s [mH]	63.3	77.7	59.1	75.1
X_r' [mH]	63.3	77.7	59.1	75.1

Fig. 8.18. The experimental setup, consisting of autotransformer, power analyser, and the AFIM, for carrying out the locked rotor test at 50Hz.

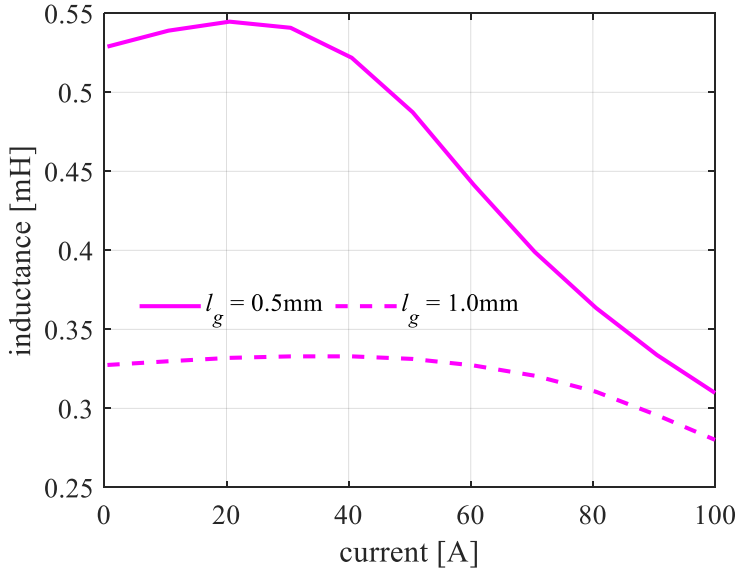

Fig. 8.19. Comparison of the inductance variation of the AFIM with 0.5mm and 1mm airgap lengths.

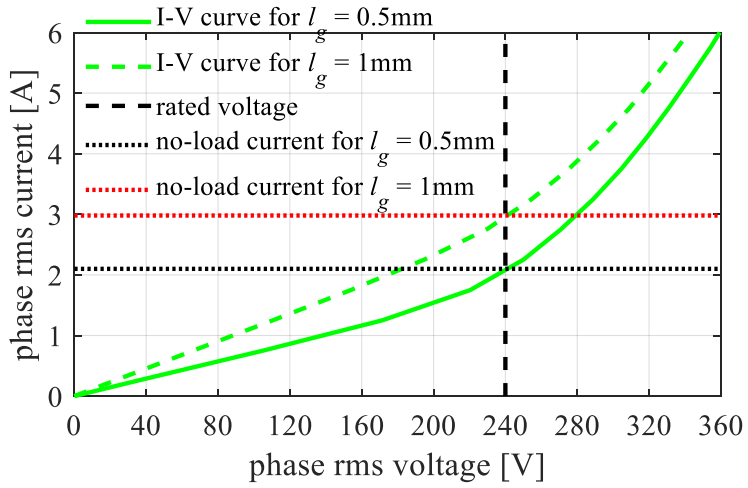

Fig. 8.20. Comparison of the inductance variation of the AFIM with 0.5mm and 1mm airgap lengths.

8.6. AFIM with larger airgap

Based on the conclusion of the previous section, the AFIM should be capable of operation by increasing the airgap length to 1mm where the stiffness of the machine comes to a reasonable range. The airgap length of the low voltage high current AFIM designed in section 8.3 is increased from 0.5mm to 1mm. Initially, the no-load 3-D FEA simulation is executed to find the inductance of the machine in different excitation current. Comparison of the inductance of the AFIM with 0.5mm and 1mm airgap lengths demonstrates a large drop of the inductance value by increase of the airgap (see Fig. 8.19). The inductance drop will increase the magnetizing current of the machine (see Fig. 8.20) which in turn leads to the performance parameters drop in a certain frequency.

The performance parameters of the AFIM with 1mm airgap length in the torque-speed envelope is presented in Fig. 21. The comparison of the EffMs of the AFIM with 0.5mm airgap in Fig. 8.5a and the AFIM with 1mm airgap in Fig. 21a shows 32% torque drop by 0.5mm increase of the airgap length. The efficiency at higher speeds in larger airgap is 1% lower than the AFIM with 0.5mm airgap length owing to its higher ohmic losses. The reduction of the rotor resistance transferred to the stator side in the AFIM allows to have a wider constant torque region for the design with 1mm airgap. The constant torque region of the updated AFIM ends at 12Nm torque and 5600rpm speed where the maximum torque of the 0.5mm design is 17.67Nm at 3860rpm. The power map results (Figs. 8.21b and 8.5b) show the machine with 1mm airgap can reach 7kW power at the end of its constant torque region which is only 100W less than the maximum power of AFIM with 0.5mm airgap.

The AFIM with 1mm airgap does not offers 18.7% less torque compared the commercial AFPMSM in a same current density (see Figs. 8.21 and 8.5). Its maximum efficiency is 1% less than the maximum efficiency of AFPMSMs. The comparison of the power maps of these two machines shows higher power of the AFIM at the constant power region. It should be highlighted that these results are collected with ignorance of rotor thermal issues of the AFIM. In practice, the rotor temperature of AFIM will reduce the current limit leading to the reduction of torque and power density.

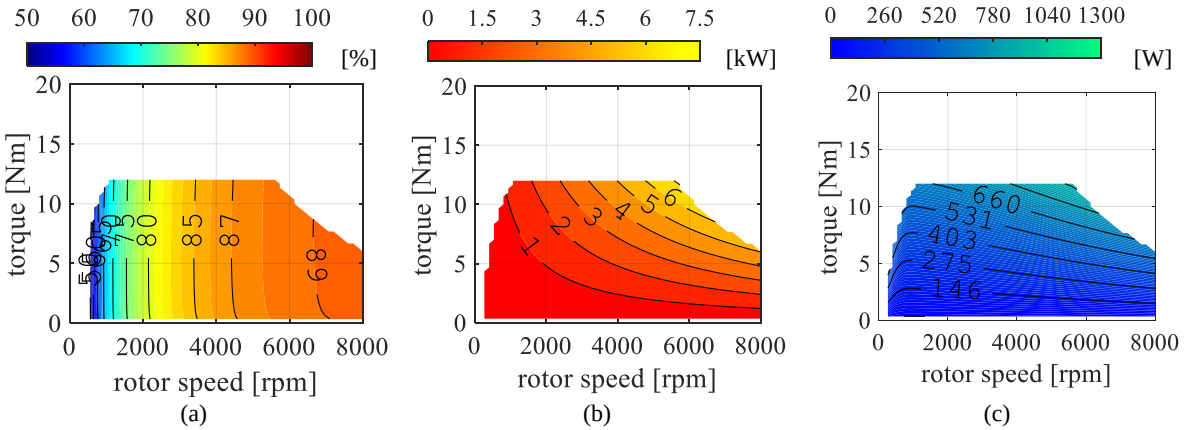

(a) (b) (c)

Fig. 8.21. Performance parameters of the updated AFIM design with 1mm airgap length computed through 3-D FEA. (a) EffM, (b) power map, (c) total loss map

8.7. Conclusion

A 4.5kW commercialized AFPMSM is selected and a AFIM was designed in a same size as the AFPMSM. The optimum number of rotor bars which gives the minimum torque ripple was selected for the rotor. The effect of the consideration of the solid rotor for AFIM design was discussed and it was shown that the solid rotor can be a proper choice for inverter driven AFIMs. The 3-D FEA results demonstrated the high performance of the designed AFIM with 0.5mm airgap length over a wide torque-speed range compared to the benchmark AFPMSM.

The challenges and difficulties of the construction of AFIM were discussed and the possible mechanical solution for fabrication of the rotor were described. Based on the machine geometry the cheapest possible method for fabrication of the rotor was introduced (i.e., CNC milling). The procedure of the construction of the motor was explained and the AFIM was prototyped for experimental studies.

Although the bearings were selected based on the estimated axial forces, the initial AFIM design (i.e., the design with 0.5mm airgap length) was jammed after excitation on the test rig. The axal force analysis using in different airgaps were conducted using a high precision extensometer. It was understood that the negative stiffness at smaller airgap lengths is high which is responsible for unsuccessful operation of the bearings. It was found out that the AFIM stiffness reaches a reasonable value at 1mm airgap length.

The AFIM airgap is increased to 1mm and the locked rotor test was performed to validate the 3-D FEA results. The 3-D FEA model was used to predict the performance parameters of the of the AFIM with 1mm airgap length in the torque-speed envelope. The obtained results showed the reduction of the torque density by increment of the airgap length which was expectable. Despite the reduction of the torque density the power density remains constant because of the higher torque of higher torque of the AFIM with 1mm airgap at higher speeds.

It was explained that the presented results are valid when the effect of the rotor over heating is ignored. In fact, the designed AFIM can deliver the reported power from the electromagnetic perspective. However, its rotor losses are much larger than the AFPMSM rotor loss which leads to the increase of the rotor temperature. Considering this, further experimental loading results is required to determine a new current limit for the AFIM.

Chapter 9. Conclusion and Future works

9.1. Conclusion

The importance of electric vehicles and the relationship of the design of electric motors with the performance of electric vehicles were discussed in the first chapter. The efficiency map was defined and the necessity of the investigation of efficiency maps for the study of electric machine performance used in EVs were clarified. It was concluded that the efficiency map not only helps to understand the torque-speed capability of an EM, but also it helps to estimate the energy consumption of the EMs over driving cycles.

The significance of each type of loss in the calculation of the efficiency and the sources of the losses were studied and summarized in the second chapter. The procedure of the calculation, estimation, modelling, and measurement of these losses were described. The important factors which play determinative roles in the amount of loss in various operating points were explained. The results of the loss analysis and study demonstrated that a large portion of the drivetrain system losses occur in the electric machines of the EVs and HEVs. So, the design of the electric machines and loss reduction is the focus of the thesis.

To design the electric machines for EVs/HEVs, the accurate estimation of their efficiency maps is important. Hence, the details of the efficiency map calculation and the required considerations to provide an accurate efficiency map were reported in Chapter 3. The control methods and different operating regions of the electric machines were described. The different methods for calculation of the EffMs of AC electric machines were discussed in detail. The differences of the calculated efficiency maps obtained through each method were highlighted. The experimental methods for the calculation of the EffM were explained. To validate the suggested method for the efficiency map estimation of the induction machines, an experimental test setup was prepared, and the maximum efficiency point was obtained for a number of operating points. This chapter provides a comprehensive tutorial on the estimation of the efficiency map. It compares the different techniques in terms of accuracy and computational effort, and assists in selection of suitable methods for EffM calculation in different situations.

Chapter four was dedicated to the design of 100kW IM and IPMSM to show the design procedure of electric machines and compare their in the torque-speed envelope. A FEA based step-by-step design process for fast design of IPMSMs and IMs was proposed. The proposed method covered both the electromagnetic and thermal behaviour of the EMs. The importance of the optimum selection of the number of poles to meet the temperature limits were highlighted. The superiority of the V-shape PMs over the other PM shapes for interior PMSMs was described. It was shown that a deep V-shape PM topology achieves higher torque and lower voltage THD. The effect of the optimum selection of the number of rotor bars was another subject of the study. It was shown that the torque ripple is minimized when the number of rotor bars equals the number of stator slots plus two or four.

The 100kW machines were designed and their performance parameters were obtained. The results of the analysis showed the IPMSM torque is about 50% more than the IM. A 2% higher efficiency and 30% higher power factor of the IPMSM were other advantages versus It was shown that both machines can operate safely (within the temperature limit) at 2 times of the rated current for 30 seconds which meets the required overload characteristics.

The proposed step-by-step design process was employed for the design of the axial flux permanent magnet machines in Chapter Five. Three different AFPMSM designs including a double rotor single stator design and a double stator with single rotor, were investigated to understand which structure is more promising for the AFPMSM. The slightly higher torque production capability and cooling simplicity of the double stator AFPMSM were the reasons to select this topology for further design and analysis. The effect of the number of slots, different winding structures, and skewing were analysed to obtain a low THD back-emf and small cogging torque. Designs with 36 and 72 slots were considered and the rotor eddy current loss in each design was studied. The demagnetization analysis was executed for the designs to show the PMs will not be demagnetized under short circuit or over current conditions. An equivalent radial flux machine for each design was provided to conduct the thermal analysis at full load. A radial flux machine was designed to show the difference of the size and performance with the designed AFPMSM. A surrogate multi-objective optimization was executed on the 72-slot design to find the optimal design with the minimum length and minimum PM volume.

An interior PM topology was studied to improve the performance of the AFPMSM in the field weakening region. It was demonstrated that this design suffers from a low power factor which leads to the increase of the rated current and hence slot depth and machine axial length which is not desirable. Fractional slot stator windings were investigated and found to improve the power density but increase the rotor loss. The selected 12-pole 36-slot design offers a reasonable rotor loss for the 100kW machine with a suitable performance in the FW region. A multi-objective optimization was executed to find the optimum design with minimum loss and a value of characteristic current to obtain the required performance in the FW region.

Next the design of a 200kW AFPMSM with the capability of operation up to 4 times of the rated speed was considered. It was demonstrated that the rotor eddy losses for larger number of slots per pole is in a reasonable range. Hence, it was decided to study a lower number of poles with different numbers of slots per pole. The results of the analysis showed an 8-pole machine with 48 slots offers the required FW performance with a reasonable eddy current loss for the 200kW AFPMSM. This study was completed by optimization of the 200kW design with the objectives of the minimum loss and achievement of a characteristic current close to rated current.

The lack of a fast and accurate analytical model for IMs was highlighted as a research gap. The benefits of an analytical model in the prediction of the performance of the IMs were explained in Chapter Six. An analytical model based on subdomain modelling was developed and validated using

2-D and 3-D FEA, and experimental results. The analysis of the effect of inter-bar currents on the performance of induction machines was studied. It was shown that the proposed analytical model is successful in estimating the IM performance at different load and speeds. A sensitivity analysis was carried out to demonstrate the capability of the model in the prediction of the IM performance with different geometries and power ratings.

The seventh chapter utilizes the proposed analytical model in an optimization study. An optimization procedure was introduced to design IMs over a driving cycle. A lumped circuit thermal model was developed to predict the machine performance during operation over a driving cycle. Two optimizations, with and without consideration of the overload, were performed to find the optimal designs for operation over three different driving cycles. The optimal designs were compared in terms of the power density and efficiency. The results showed that a machine designed with consideration of the overload can offer a power density which is 4 times of a machine designed without consideration of the overload. However, the increase in the power density leads to increased energy consumption of the machine due to the reduced efficiency.

The design and construction of a small single-stator single-rotor axial flux IM was the subject of Chapter 8. The AFIM was designed using 3-D FEA analysis, and the effect of the number of rotor bars on torque ripple of the AFIM was analysed. The designed AFIM was analysed with both a solid rotor and a laminated rotor, and the losses in the solid rotor were slightly higher. The performance parameters of the designed AFIM were compared with a baseline commercial AFPMSM in the torque-speed envelope. The maximum torque of the AFPMSM at low speeds was larger than the AFIM but the AFIM can offer comparable power at higher speeds. The procedure used for the construction of the AFIM and the difficulties of the manufacturing were described. An experimental setup was prepared to determine the dependence of the axial forces on the airgap length. Based on the results the airgap of the AFIM design was increased. To validate the 3-D FEA results, a locked rotor test was conducted at the new airgap. The performance parameters of the design were compared with the AFPMSM to highlight their differences.

9.2. Discussion

This thesis contributed to the field of EV technology by focusing on the design and analysis of the electric machines. As EV demand grows, there is an urgent need to develop electric vehicles that are not only more efficient and reliable, but also cost-effective and scalable. This thesis addressed these issues by description of the losses over the drivetrain of EVs, discussion on the efficiency map of EMs, and introduction of EM design and modelling approaches.

A systematic design procedure was introduced and employed in Chapters 4 and 5 for designing IPMSM, IM, and AFPSMSMs. The proposed method uses FEA and lumped circuit thermal modelling which are the most accurate available techniques for EM modelling and performance analysis. As the

designed machines performance using the proposed technique were comparable with the performance of the available commercial designs, it can be pointed out that the proposed design approach is suitable for preparation of base-line designs.

A fast and accurate subdomain model was proposed for IM performance prediction in this thesis. Such a technique is useful for defining an optimization problem over driving cycles. A comprehensive optimization problem was defined to find the optimal designs with and without consideration of the effect of overload capability. The results of the optimization study demonstrated that the consideration of OL for IMs can increase the power density up to 4 times of the normal design but increases the energy consumption by 30% in urban driving cycles. The energy consumption increase for the highway driving cycles is about 5%. Thus, it is important to investigate the OL during the design and consider the power density and energy consumption trade-offs.

Axial flux machines are popular due to their higher power density compared to the radial flux machines. The difficulty of the construction of the AFIM and feasibility of the implementation of the small airgaps have not been covered adequately in literature. The FEA and experimental analysis of the axial forces to show the limitations in selection of small airgaps was another important topic which was discussed. It was shown that the use of small airgaps may not be practical due to the high axial stiffness at small airgaps. The provided results and descriptions in Chapter 8 helps designers to take more attention on the axial force during their design.

In this thesis, several axial flux and radial flux devices were designed. Considering the manufacturing difficulties associated with axial flux machines, radial flux machines are preferred for applications where the axial length is not a constraint. Therefore, radial flux machines are suitable for the drivetrain of EVs, as there is no engine in the system and there is sufficient space to accommodate a long stack length. In the drive train of HEVs, both the engine and the electric machine should be installed. Therefore, the axial length is a crucial installation limit for the motor. Therefore, the axial flux machine is the superior option for HEV systems.

This thesis is completed by design of PMSM and IM. The higher power density, power factor, and efficiency of the PM machines against IM make them a suitable choice for utilization of them in scooters and electric motor bikes. However, the availability of the PM materials increases their cost. For this reason, it is more reasonable to use the non-PM machines to reduce the cost of EV and HEV. As discussed in Chapter 7, it is possible to use IM machines in passenger cars if there is enough space for placing the electrical machine and cooling system. Due to the large size of the EMs in heavy trucks and busses, the amount and cost of PM is high. So, it is more reasonable to use IM machines in heavy trucks and buses where the machine size is not limited by the space and the cooling system can be embedded in both of rotor and stator of IMs.

In a nutshell, this thesis helps to improve the development of more effective and environmentally friendly EVs, by providing a thorough and in-depth analysis of the important factors that affect the performance and efficiency of electric machines in this application. The thesis's observations and conclusions will be of interest to academics and engineers in the field.

9.3. Future Work

The performance improvement of EMs used in EVs/HEVs is a popular cutting-edge subject. Although recent EM designs offer significantly improved performance, there are research gaps which need investigation in future work. The potential studies in this field as the continuation of the work shown in this thesis are presented in this section.

9.3.1. More precise core loss models

As discussed in the third chapter, the prediction of the core loss in presence of high order harmonics (i.e., inverter harmonics) is a challenge. Using FEA can solve this issue, but it increases the time of simulation dramatically. Thus, introduction of more precise core loss models with the capability of loss prediction can help to improve the accuracy of the predicted efficiency map of electric machines.

9.3.2. Proximity losses of the windings using an analytical model

It was explained that stator winding ohmic losses are changed by temperature, skin effect, and proximity effect. There are accurate and straightforward analytical models to investigate temperature and skin depth in the estimation of the loss. The proximity effect can have a significant effect on the losses at higher frequencies. The available finite element models are computationally expensive. Thus, it seems reasonable to conduct studies on analytical and statistical modelling of the proximity effect to increase the speed of the proximity loss estimation.

9.3.3. PM loss modelling and estimation

The PM losses are estimated using 2-D and 3-D FEA. To find the induced eddy current in the PMs. Hence, the transient FEA should be executed with small size meshes and time steps to estimate the eddy current losses with an acceptable accuracy, which is time consuming. The study of the PM loss analytical modelling and estimation can thus be useful.

9.3.4. EV drivetrain modelling

Electric machines are the heart of the drivetrain of EVs and HEVs. This thesis focused mainly on the electromagnetic and thermal characteristics of electric machine for optimal designs. The optimal design can be more reliable if an accurate and comprehensive drivetrain model is developed. Although there are some numerical and analytical models for each drivetrain component, there is a lack of a comprehensive model covering all details of the drivetrain components.

9.3.5. Analytical model for machines

An accurate and fast analytical model with the capability of saturation level prediction was introduced for IMs in this thesis. It was shown that the speed of the analytical model allows using it in an optimization study. Although the literature has introduced analytical models for PM machines, there is room for improving their speed and accuracy. The available PM models which can investigate saturation are slow which makes them less useful for utilization as a tool for design of EMs for EVs and HEVs. So, the available analytical models for PM machines for use in optimization can be improved in accuracy in the future.

9.3.6. Study of different materials for electric machines

SmCo and NdFe are two types of rare-earth magnets with high residual magnetic flux density which are studied in the designed machines in the thesis. The rotor loss analysis showed a high value of the eddy current loss on the rotor of the designed machines in chapter 5. It is possible to substitute the utilized PMs with other magnetic materials such as ferrite which has a lower electrical conductivity. However, the limited magnetic energy density of ferrite will need further investigation to understand the feasibility of utilization of ferrite instead of SmCo.

The investigate M250-50 steel can be substituted with more modern steels or advanced magnetic materials such as soft magnetic composites (SMCs) with lower core losses to increase the machine efficiency and reduce overall temperature of the machine. For instance, replacement of the M250-50 with 50mm thickness by M250-35 with 35mm thickness helps to reduce the core losses effectively. Although the eddy current losses of SMC are lower than laminated materials, their hysteresis loss is normally higher. On the other hand, the SMC saturation point is smaller than the laminated materials saturation point. These limitations necessitate further detailed investigations to propose these materials as a substitute for M250-50 studied in the designed machines in this thesis.

The winding loss is another source of loss in the electric machines discussed in this chapter. This thesis investigates the stranded copper windings to reduce the effect of skin effect on the copper wires. The hairpin windings and carbon nanotubes are some other alternatives which has been introduced for winding of electric machines. Further investigations can be conducted to highlight the difference and effect of these alternatives instead of the stranded windings.

9.3.7. Design procedure for other machines

The proposed step-by-step design procedure for the PMSM and IMs explained in Chapters 4 and 5 can be extended and developed for other type of machines such as PM vernier, synchronous reluctance, and flux switching machines. The examination and development of such design procedure to achieve a reliable base-line design can be the subject of study in future works.

APPENDIX I

The written equations written in Table 6.2. are solved to find the Fourier coefficients in each subdomain. According to (I) in (4-22) shown in (AI-1), A^{Ik} just has the coefficients of the co-sinusoidal terms of a Fourier transform.

$$\sum_{n_2} A_{n_2}^{Ik}\cos\left(\frac{n_2\pi}{\theta_s}(\theta-\theta_s^{0k})\right) = \begin{cases}\displaystyle\sum_{n_1}\left(A_{n_1}^{IIk}\frac{n_1\pi}{\theta_{so}}\frac{2}{\mathrm{E}\left(\frac{n_1\pi}{\theta_{so}},r_5,r_4\right)}+B_{n_1}^{IIk}\frac{n_1\pi}{\theta_{so}}\frac{\mathrm{P}}{\mathrm{E}}\left(\frac{n_1\pi}{\theta_{so}},r_4,r_5\right)\right)\cos\left(\frac{n_1\pi}{\theta_{so}}(\theta-\theta_{so}^{0k})\right)+b_{2k}+\frac{1}{2}j_{kv}\mu_0(r_4^2-r_5^2) & \\ \frac{1}{2}j_{kv}\mu_0(r_4^2-r_5^2)\end{cases} \quad \text{(AI-1)}$$

Thus, the integration of the constant values must be zero to guarantee that the DC component of this equation in the Fourier transform is zero. The b_{2k} constant is obtained as follows:

$$\frac{1}{\theta_s}\int_{\theta_{so}^{0k}}^{\theta_{so}^{0k}+\theta_{so}} b_2\,\mathrm{d}\theta+\frac{1}{\theta_s}\int_{\theta_s^{0k}}^{\theta_s^{0k}+\theta_s}\left[\frac{1}{2}j_{kv}\mu_0(r_4^2-r_5^2)\right]\mathrm{d}\theta=0\rightarrow b_2=-\frac{\theta_s}{2\theta_{so}}j_{kv}\mu_0(r_4^2-r_5^2)\rightarrow b_{2k}=-\frac{\mu_0 I_{ks}}{\theta_{so}} \quad \text{(AI-2)}$$

According to (AI-1), the co-sinusoidal term of the right-hand side equation is equal to $A_{n_2}^{Ik}$. So, this term of the Fourier transform is sought as below:

$$\begin{aligned}\rightarrow A_{n_2}^{Ik}=\frac{2}{\theta_s}\Bigg[&\sum_{n_1}\Bigg(A_{n_1}^{IIk}\frac{n_1\pi}{\theta_{so}}\frac{2}{\mathrm{E}\left(\frac{n_1\pi}{\theta_{so}},r_5,r_4\right)}\\ &+B_{n_1}^{IIk}\frac{n_1\pi}{\theta_{so}}\frac{\mathrm{P}}{\mathrm{E}}\left(\frac{n_1\pi}{\theta_{so}},r_4,r_5\right)\Bigg)\int_{\theta_{so}^{0k}}^{\theta_{so}^{0k}+\theta_{so}}\cos\left(\frac{n_2\pi}{\theta_s}(\theta-\theta_s^{0k})\right)\cos\left(\frac{n_1\pi}{\theta_{so}}(\theta-\theta_{so}^{0k})\right)\mathrm{d}\theta\\ &+\int_{\theta_{so}^{0k}}^{\theta_{so}^{0k}+\theta_{so}} b_2\cos\left(\frac{n_2\pi}{\theta_s}(\theta-\theta_s^{0k})\right)\mathrm{d}\theta+\int_{\theta_s^{0k}}^{\theta_s^{0k}+\theta_s}\frac{1}{2}j_{kv}\mu_0(r_4^2-r_5^2)\cos\left(\frac{n_2\pi}{\theta_s}(\theta-\theta_s^{0k})\right)\mathrm{d}\theta\Bigg]\end{aligned} \quad \text{(AI-3)}$$

The right hand side of the above equation has four terms. The last two terms which has a simple co-sinusoidal in their body are considered first to find the results of these integrals:

$$\begin{aligned}&\frac{2}{\theta_s}\int_{\theta_{so}^{0k}}^{\theta_{so}^{0k}+\theta_{so}} b_2\cos\left(\frac{n_2\pi}{\theta_s}(\theta-\theta_s^{0k})\right)\mathrm{d}\theta+\frac{2}{\theta_s}\int_{\theta_s^{0k}}^{\theta_s^{0k}+\theta_s}\frac{1}{2}j_{kv}\mu_0(r_2^2-r_1^2)\cos\left(\frac{n_2\pi}{\theta_s}(\theta-\theta_s^{0k})\right)\mathrm{d}\theta\\ &=b_2\frac{2}{n_2\pi}\left[\sin\left(\frac{n_2\pi}{\theta_s}(\theta_{so}^{0k}+\theta_{so}-\theta_s^{0k})\right)-\sin\left(\frac{n_2\pi}{\theta_s}(\theta_{so}^{0k}-\theta_s^{0k})\right)\right]\\ &=-\frac{\mu_0 I_{ks}}{\theta_{so}}\frac{2}{n_2\pi}\left[sin\left(\frac{n_2\pi}{\theta_s}(\theta_{so}^{0k}+\theta_{so}-\theta_s^{0k})\right)-sin\left(\frac{n_2\pi}{\theta_s}(\theta_{so}^{0k}-\theta_s^{0k})\right)\right]\end{aligned} \quad \text{(AI-4)}$$

The results of (AI-4) is a portion of the specific solution of this equation. The answer of the first two term of (AI-3) is divided into two parts when $\frac{n_1\pi}{\theta_{so}}=\frac{n_2\pi}{\theta_s}$ and $\frac{n_1\pi}{\theta_{so}}\neq\frac{n_2\pi}{\theta_s}$. So, the results are derived as below:

$$\frac{2}{\theta_s}\sum_{n_1}\left(A_{n_1}^{IIk}\frac{n_1\pi}{\theta_{so}}\frac{2}{\mathrm{E}\left(\frac{n_1\pi}{\theta_{so}},r_5,r_4\right)}+B_{n_1}^{IIk}\frac{n_1\pi}{\theta_{so}}\frac{\mathrm{P}}{\mathrm{E}}\left(\frac{n_1\pi}{\theta_{so}},r_4,r_5\right)\right)\int_{\theta_{so}^{0k}}^{\theta_{so}^{0k}+\theta_{so}}\cos\left(\frac{n_2\pi}{\theta_s}(\theta-\theta_s^{0k})\right)\cos\left(\frac{n_1\pi}{\theta_{so}}(\theta-\theta_{so}^{0k})\right)\mathrm{d}\theta$$

If $\frac{n_1\pi}{\theta_{so}}=\frac{n_2\pi}{\theta_s}$:

$$\int_{\theta_{so}^{0k}}^{\theta_{so}^{0k}+\theta_{so}}\cos\left(\frac{n_2\pi}{\theta_s}(\theta-\theta_s^{0k})\right)\cos\left(\frac{n_1\pi}{\theta_{so}}(\theta-\theta_{so}^{0k})\right)\mathrm{d}\theta=\frac{\theta_{so}}{2}\cos\left(\frac{n_1\pi}{\theta_{so}}(\theta_s^{0k}-\theta_{so}^{0k})\right)$$

$$\rightarrow A_{n_2}^{Ik}=\sum_{n_1}\frac{\theta_{so}}{\theta_s}\left(A_{n_1}^{IIk}\frac{n_1\pi}{\theta_{so}}\frac{2}{E\left(\frac{n_1\pi}{\theta_{so}},r_5,r_4\right)}+B_{n_1}^{IIk}\frac{n_1\pi}{\theta_{so}}\frac{P}{E}\left(\frac{n_1\pi}{\theta_{so}},r_4,r_5\right)\right)cos\left(\frac{n_1\pi}{\theta_{so}}(\theta_s^{0k}-\theta_{so}^{0k})\right) \quad \text{(AI-5)}$$

If $\frac{n_1\pi}{\theta_{so}}\neq\frac{n_2\pi}{\theta_s}$: the co-sinusoidal multiplication is expanded as below:

$$\int_{\theta_{so}^{0k}}^{\theta_{so}^{0k}+\theta_{so}}\cos\left(\frac{n_2\pi}{\theta_s}(\theta-\theta_s^{0k})\right)\cos\left(\frac{n_1\pi}{\theta_{so}}(\theta-\theta_{so}^{0k})\right)\mathrm{d}\theta$$
$$=\frac{1}{2}\int_{\theta_{so}^{0k}}^{\theta_{so}^{0k}+\theta_{so}}\left[\cos\left(\frac{n_2\pi}{\theta_s}(\theta-\theta_s^{0k})+\frac{n_1\pi}{\theta_{so}}(\theta-\theta_{so}^{0k})\right)\right.$$
$$\left.+\cos\left(\frac{n_2\pi}{\theta_s}(\theta-\theta_s^{0k})-\frac{n_1\pi}{\theta_{so}}(\theta-\theta_{so}^{0k})\right)\right]\mathrm{d}\theta$$

Then, the result of the integration is found as below:

$$\int_{\theta_{so}^{0k}}^{\theta_{so}^{0k}+\theta_{so}}\cos\left(\frac{n_2\pi}{\theta_s}(\theta-\theta_s^{0k})+\frac{n_1\pi}{\theta_{so}}(\theta-\theta_{so}^{0k})\right)\mathrm{d}\theta$$
$$=\frac{\theta_{so}\theta_s}{n_1\pi\theta_s+n_2\pi\theta_{so}}\sin\left(\frac{n_2\pi}{\theta_s}(\theta-\theta_s^{0k})+\frac{n_1\pi}{\theta_{so}}(\theta-\theta_{so}^{0k})\right)\Bigg|_{\theta_{so}^{0k}}^{\theta_{so}^{0k}+\theta_{so}}$$
$$=\frac{\theta_{so}\theta_s}{n_1\pi\theta_s+n_2\pi\theta_{so}}\left[(-1)^{n_1}\sin\left(\frac{n_2\pi}{\theta_s}(\theta_{so}+\theta_{so}^{0k}-\theta_s^{0k})\right)-\sin\left(\frac{n_2\pi}{\theta_s}(\theta_{so}^{0k}-\theta_s^{0k})\right)\right] \quad \text{(AI-6)}$$

$$\int_{\theta_{so}^{0k}}^{\theta_{so}^{0k}+\theta_{so}}\cos\left(\frac{n_2\pi}{\theta_s}(\theta-\theta_s^{0k})-\frac{n_1\pi}{\theta_{so}}(\theta-\theta_{so}^{0k})\right)\mathrm{d}\theta$$
$$=\frac{\theta_{so}\theta_s}{n_2\pi\theta_{so}-n_1\pi\theta_s}\sin\left(\frac{n_2\pi}{\theta_s}(\theta-\theta_s^{0k})-\frac{n_1\pi}{\theta_{so}}(\theta-\theta_{so}^{0k})\right)\Bigg|_{\theta_{so}^{0k}}^{\theta_{so}^{0k}+\theta_{so}}$$
$$=\frac{\theta_{so}\theta_s}{n_2\pi\theta_{so}-n_1\pi\theta_s}\left[(-1)^{n_1}\sin\left(\frac{n_2\pi}{\theta_s}(\theta_{so}+\theta_{so}^{0k}-\theta_s^{0k})\right)-\sin\left(\frac{n_2\pi}{\theta_s}(\theta_{so}^{0k}-\theta_s^{0k})\right)\right]$$

$$\int_{\theta_{so}^{0k}}^{\theta_{so}^{0k}+\theta_{so}}\cos\left(\frac{n_2\pi}{\theta_s}(\theta-\theta_s^{0k})\right)\cos\left(\frac{n_1\pi}{\theta_{so}}(\theta-\theta_{so}^{0k})\right)\mathrm{d}\theta$$
$$=\frac{n_2\pi\theta_{so}^2\theta_s}{(n_2\pi\theta_{so})^2-(n_1\pi\theta_s)^2}\left[(-1)^{n_1}\sin\left(\frac{n_2\pi}{\theta_s}(\theta_{so}+\theta_{so}^{0k}-\theta_s^{0k})\right)-\sin\left(\frac{n_2\pi}{\theta_s}(\theta_{so}^{0k}-\theta_s^{0k})\right)\right]$$

Therefore, A^{Ik} is summarized in (AI-7). As shown in AI-7, the calculated A^{Ik} depends on the values of the AII and BII which are the constant unknowns of the adjacent subdomain.

$$\rightarrow A_{n_2}^{Ik}$$

$$= \begin{cases} \sum_{n_1}\left(A_{n_1}^{IIk}\frac{2}{E\left(\frac{n_1\pi}{\theta_{so}},r_5,r_4\right)}+B_{n_1}^{IIk}\frac{P}{E}\left(\frac{n_1\pi}{\theta_{so}},r_4,r_5\right)\right)\frac{2n_2n_1\theta_{so}((-1)^{n_1}-1)}{(n_2\theta_{so})^2-(n_1\theta_s)^2}sin\left(\frac{n_2\pi}{\theta_s}(\theta_{so}^{0k}-\theta_s^{0k})\right) & \boldsymbol{\frac{n_1\pi}{\theta_{so}}\neq\frac{n_2\pi}{\theta_s}} \\ \sum_{n_1}\left(A_{n_1}^{IIk}\frac{2}{E\left(\frac{n_1\pi}{\theta_{so}},r_5,r_4\right)}+B_{n_1}^{IIk}\frac{P}{E}\left(\frac{n_1\pi}{\theta_{so}},r_4,r_5\right)\right)\frac{n_1\pi}{\theta_s}cos\left(\frac{n_1\pi}{\theta_{so}}(\theta_s^{0k}-\theta_{so}^{0k})\right) & \boldsymbol{\frac{n_1\pi}{\theta_{so}}=\frac{n_2\pi}{\theta_s}} \end{cases} \quad \text{(AI-7)}$$

$$-\frac{\mu_0 I_{ks}}{\theta_{so}}\frac{2}{n_2\pi}\left[sin\left(\frac{n_2\pi}{\theta_s}(\theta_{so}^{0k}+\theta_{so}-\theta_s^{0k})\right)-sin\left(\frac{n_2\pi}{\theta_s}(\theta_{so}^{0k}-\theta_s^{0k})\right)\right]$$

Eq. II in (4-22) is employed to find the B^{IIk} relationship with A^{Ik}. As shown in this equation, the relationship is with the sinusoidal term of the Fourier transform of the right hand-side equation presented in (AI-8). Therefore, the equation is expanded (see (AI-9)) and solved for two different condition which are $\frac{n_1\pi}{\theta_{so}}=\frac{n_2\pi}{\theta_s}$ and $\frac{n_1\pi}{\theta_{so}}\neq\frac{n_2\pi}{\theta_s}$.

$$\sum_{n_1}\frac{n_1\pi}{\theta_{so}}B_{n_1}^{IIk}\,sin\left(\frac{n_1\pi}{\theta_{so}}(\theta-\theta_{so}^{0k})\right)=\sum_{n_2}A_{n_2}^{Ik}\frac{P}{E}\left(\frac{n_2\pi}{\theta_s},r_5,r_4\right)sin\left(\frac{n_2\pi}{\theta_s}(\theta-\theta_s^{0k})\right) \quad \text{(AI-8)}$$

$$\rightarrow B_{n_1}^{IIk}=\sum_{n_2}A_{n_2}^{Ik}\frac{2}{n_1\pi}\frac{\mathrm{P}}{\mathrm{E}}\left(\frac{n_2\pi}{\theta_s},r_5,r_4\right)\int_{\theta_{so}^{0k}}^{\theta_{so}^{0k}+\theta_{so}}\sin\left(\frac{n_2\pi}{\theta_s}(\theta-\theta_s^{0k})\right)\sin\left(\frac{n_1\pi}{\theta_{so}}(\theta-\theta_{so}^{0k})\right)\mathrm{d}\theta \quad \text{(AI-9)}$$

If $\boldsymbol{\frac{n_1\pi}{\theta_{so}}=\frac{n_2\pi}{\theta_s}}$:

$$\int_{\theta_{so}^{0k}}^{\theta_{so}^{0k}+\theta_{so}}\sin\left(\frac{n_2\pi}{\theta_s}(\theta-\theta_s^{0k})\right)\sin\left(\frac{n_1\pi}{\theta_{so}}(\theta-\theta_{so}^{0k})\right)\mathrm{d}\theta=\frac{\theta_{so}}{2}\cos\left(\frac{n_1\pi}{\theta_{so}}(\theta_s^{0k}-\theta_{so}^{0k})\right) \quad \text{(AI-10)}$$

$$\rightarrow B_{n_1}^{IIk}=\sum_{n_2}A_{n_2}^{Ik}\frac{P}{E}\left(\frac{n_2\pi}{\theta_s},r_5,r_4\right)\frac{\theta_s}{n_2\pi}cos\left(\frac{n_1\pi}{\theta_{so}}(\theta_s^{0k}-\theta_{so}^{0k})\right)$$

If $\boldsymbol{\frac{n_1\pi}{\theta_{so}}\neq\frac{n_2\pi}{\theta_s}}$:

$$\int_{\theta_{so}^{0k}}^{\theta_{so}^{0k}+\theta_{so}}\sin\left(\frac{n_2\pi}{\theta_s}(\theta-\theta_s^{0k})\right)\sin\left(\frac{n_1\pi}{\theta_{so}}(\theta-\theta_{so}^{0k})\right)\mathrm{d}\theta$$

$$=\frac{1}{2}\int_{\theta_{so}^{0k}}^{\theta_{so}^{0k}+\theta_{so}}\left[\cos\left(\frac{n_2\pi}{\theta_s}(\theta-\theta_s^{0k})-\frac{n_1\pi}{\theta_{so}}(\theta-\theta_{so}^{0k})\right)\right.$$

$$\left.-\cos\left(\frac{n_2\pi}{\theta_s}(\theta-\theta_s^{0k})+\frac{n_1\pi}{\theta_{so}}(\theta-\theta_{so}^{0k})\right)\right]\mathrm{d}\theta \quad \text{(AI-11)}$$

$$\int_{\theta_{so}^{0k}}^{\theta_{so}^{0k}+\theta_{so}}\cos\left(\frac{n_2\pi}{\theta_s}(\theta-\theta_s^{0k})+\frac{n_1\pi}{\theta_{so}}(\theta-\theta_{so}^{0k})\right)\mathrm{d}\theta$$

$$=\frac{\theta_{so}\theta_s}{n_1\pi\theta_s+n_2\pi\theta_{so}}\sin\left(\frac{n_2\pi}{\theta_s}(\theta-\theta_s^{0k})+\frac{n_1\pi}{\theta_{so}}(\theta-\theta_{so}^{0k})\right)\Bigg|_{\theta_{so}^{0k}}^{\theta_{so}^{0k}+\theta_{so}}$$

$$=\frac{\theta_{so}\theta_s}{n_1\pi\theta_s+n_2\pi\theta_{so}}\left[(-1)^{n_1}\sin\left(\frac{n_2\pi}{\theta_s}(\theta_{so}+\theta_{so}^{0k}-\theta_s^{0k})\right)-\sin\left(\frac{n_2\pi}{\theta_s}(\theta_{so}^{0k}-\theta_s^{0k})\right)\right]$$

$$\int_{\theta_{so}^{0k}}^{\theta_{so}^{0k}+\theta_{so}} \cos\left(\frac{n_2\pi}{\theta_s}(\theta-\theta_s^{0k})-\frac{n_1\pi}{\theta_{so}}(\theta-\theta_{so}^{0k})\right)\mathrm{d}\theta$$

$$=\frac{\theta_{so}\theta_s}{n_2\pi\theta_{so}-n_1\pi\theta_s}\sin\left(\frac{n_2\pi}{\theta_s}(\theta-\theta_s^{0k})-\frac{n_1\pi}{\theta_{so}}(\theta-\theta_{so}^{0k})\right)\Bigg|_{\theta_{so}^{0k}}^{\theta_{so}^{0k}+\theta_{so}}$$

$$=\frac{\theta_{so}\theta_s}{n_2\pi\theta_{so}-n_1\pi\theta_s}\left[(-1)^{n_1}\sin\left(\frac{n_2\pi}{\theta_s}(\theta_{so}+\theta_{so}^{0k}-\theta_s^{0k})\right)-\sin\left(\frac{n_2\pi}{\theta_s}(\theta_{so}^{0k}-\theta_s^{0k})\right)\right]$$

$$\int_{\theta_{so}^{0k}}^{\theta_{so}^{0k}+\theta_{so}} \sin\left(\frac{n_2\pi}{\theta_s}(\theta-\theta_s^{0k})\right)\sin\left(\frac{n_1\pi}{\theta_{so}}(\theta-\theta_{so}^{0k})\right)\mathrm{d}\theta$$

$$=\frac{n_1\pi\theta_{so}\theta_s^2}{(n_2\pi\theta_{so})^2-(n_1\pi\theta_s)^2}\left[(-1)^{n_1}\sin\left(\frac{n_2\pi}{\theta_s}(\theta_{so}+\theta_{so}^{0k}-\theta_s^{0k})\right)-\sin\left(\frac{n_2\pi}{\theta_s}(\theta_{so}^{0k}-\theta_s^{0k})\right)\right]$$

Considering, the (AI-10) and (AI-11), the B^{IIk} is summarized as follows:

$$\rightarrow B_{n_1}^{IIk}$$

$$=\begin{cases}\displaystyle\sum_{n_2} A_{n_2}^{Ik}\frac{P}{E}\left(\frac{n_2\pi}{\theta_s},r_2,r_1\right)\frac{2\theta_{so}\theta_s^2\left((-1)^{n_1}\,sin\left(\frac{n_2\pi}{\theta_s}(\theta_{so}+\theta_{so}^{0k}-\theta_s^{0k})\right)-sin\left(\frac{n_2\pi}{\theta_s}(\theta_{so}^{0k}-\theta_s^{0k})\right)\right)}{(n_2\pi\theta_{so})^2-(n_1\pi\theta_s)^2} & \frac{n_1\pi}{\theta_{so}}\neq\frac{n_2\pi}{\theta_s}\\ \displaystyle\sum_{n_2} A_{n_2}^{Ik}\frac{P}{E}\left(\frac{n_2\pi}{\theta_s},r_2,r_1\right)\frac{\theta_s}{n_2\pi}cos\left(\frac{n_1\pi}{\theta_{so}}(\theta_s^{0k}-\theta_{so}^{0k})\right) & \frac{n_1\pi}{\theta_{so}}=\frac{n_2\pi}{\theta_s}\end{cases} \quad \text{(AI-12)}$$

After calculation of the unknowns for the slot and slot opening, the airgap unknowns of the Fourier transform are calculated by means of (4-23).

$$\sum_n B_n^{III}\sin nN_p\theta+D_n^{III}\cos nN_p\theta$$

$$=\begin{cases}\displaystyle\sum_{n_1}\left(A_{n_1}^{IIk}\frac{n_1\pi}{\theta_s}\frac{\mathrm{P}}{\mathrm{E}}\left(\frac{n_1\pi}{\theta_{so}},r_4,r_3\right)+B_{n_1}^{IIk}\frac{n_1\pi}{\theta_{so}}\frac{2}{\mathrm{E}\left(\frac{n_1\pi}{\theta_{so}},r_3,r_4\right)}\right)\cos\left(\frac{n_1\pi}{\theta_{so}}(\theta-\theta_{so}^{0k})\right)+b_{2k}\\ 0\end{cases} \quad \text{(AI-13)}$$

According to (AI-13), B^{III} and D^{III} are the coefficient of the sinusoidal and co-sinusoidal terms of the Fourier transform of the right-hand side equation. Therefore, B^{III} is found when the sinusoidal term of the Fourier transform is driven from the right-hand side of (AI-13).

$$\rightarrow B_n^{III}=\frac{N_p}{\pi}\sum_k\left[\sum_{n_1}\left(A_{n_1}^{IIk}\frac{n_1\pi}{\theta_{so}}\frac{\mathrm{P}}{\mathrm{E}}\left(\frac{n_1\pi}{\theta_{so}},r_4,r_3\right)\right.\right.$$

$$\left.+B_{n_1}^{IIk}\frac{n_1\pi}{\theta_{so}}\frac{2}{\mathrm{E}\left(\frac{n_1\pi}{\theta_{so}},r_3,r_4\right)}\right)\int_{\theta_{so}^{0k}}^{\theta_{so}^{0k}+\theta_{so}}\sin nN_p\theta\cos\left(\frac{n_1\pi}{\theta_{so}}(\theta-\theta_{so}^{0k})\right)\mathrm{d}\theta \quad \text{(AI-14)}$$

$$\left.+\int_{\theta_{so}^{0k}}^{\theta_{so}^{0k}+\theta_{so}} b_2\sin nN_p\theta\,\mathrm{d}\theta\right]$$

In this equation, b_2 which has been calculated in (AI-2) is a excitation dependent variable. For this reason, the sinusoidal term and co-sinusoidal term of (AI-13) are calculated separately for the b_2 integration. So, B^{III} is calculated as below when $n_1\pi=nN_p\theta_{so}$.

$$\int_{\theta_{so}^{0k}}^{\theta_{so}^{0k}+\theta_{so}}\sin nN_p\theta\cos\left(\frac{n_1\pi}{\theta_{so}}(\theta-\theta_{so}^{0k})\right)\mathrm{d}\theta=\frac{1}{2}\int_{\theta_{so}^{0k}}^{\theta_{so}^{0k}+\theta_{so}}\sin nN_p\theta_{so}^{0k}\,\mathrm{d}\theta=\frac{\theta_{so}}{2}\sin nN_p\theta_{so}^{0k} \quad \text{(AI-15)}$$

$$B_n^{III} = \sum_k \sum_{n_1} \left(A_{n_1}^{IIk} \frac{P}{E}\left(\frac{n_1\pi}{\theta_{so}}, r_4, r_3\right) + B_{n_1}^{IIk} \frac{2}{E\left(\frac{n_1\pi}{\theta_{so}}, r_3, r_4\right)} \right) \frac{n_1 N_p}{2} sin\, nN_p\theta_{so}^{0k}$$

When $n_1\pi \neq nN_p\theta_{so}$ B^{III} is found as follow:

$$\int_{\theta_{so}^{0k}}^{\theta_{so}^{0k}+\theta_{so}} \sin nN_p\theta \cos\left(\frac{n_1\pi}{\theta_{so}}(\theta - \theta_{so}^{0k})\right) \mathrm{d}\theta$$

$$= \frac{1}{2}\int_{\theta_{so}^{0k}}^{\theta_{so}^{0k}+\theta_{so}} \left[\sin\left(nN_p\theta + \frac{n_1\pi}{\theta_{so}}(\theta - \theta_{so}^{0k})\right) + \sin\left(nN_p\theta - \frac{n_1\pi}{\theta_{so}}(\theta - \theta_{so}^{0k})\right)\right] \mathrm{d}\theta$$

$$\int_{\theta_{so}^{0k}}^{\theta_{so}^{0k}+\theta_{so}} \sin\left(nN_p\theta + \frac{n_1\pi}{\theta_{so}}(\theta - \theta_{so}^{0k})\right) \mathrm{d}\theta = -\frac{\theta_{so}}{n_1\pi + nN_p\theta_{so}} \left[\cos\left(nN_p\theta + \frac{n_1\pi}{\theta_{so}}(\theta - \theta_{so}^{0k})\right)\right]_{\theta_{so}^{0k}}^{\theta_{so}^{0k}+\theta_{so}}$$

$$= \frac{\theta_{so}}{n_1\pi + nN_p\theta_{so}} \left[\cos\left(nN_p\theta_{so}^{0k}\right) - (-1)^{n1} \cos\left(nN_p(\theta_{so}^{0k} + \theta_{so})\right)\right] \quad \text{(AI-16)}$$

$$\int_{\theta_{so}^{0k}}^{\theta_{so}^{0k}+\theta_{so}} \sin\left(nN_p\theta - \frac{n_1\pi}{\theta_{so}}(\theta - \theta_{so}^{0k})\right) \mathrm{d}\theta = \frac{\theta_{so}}{n_1\pi - nN_p\theta_{so}} \left[\cos\left(nN_p\theta - \frac{n_1\pi}{\theta_{so}}(\theta - \theta_{so}^{0k})\right)\right]_{\theta_{so}^{0k}}^{\theta_{so}^{0k}+\theta_{so}}$$

$$= -\frac{\theta_{so}}{n_1\pi - nN_p\theta_{so}} \left[\cos\left(nN_p\theta_{so}^{0k}\right) - (-1)^{n1} \cos\left(nN_p(\theta_{so}^{0k} + \theta_{so})\right)\right]$$

$$\rightarrow \int_{\theta_{so}^{0k}}^{\theta_{so}^{0k}+\theta_{so}} \sin n\theta \cos\left(\frac{n_1\pi}{\theta_{so}}(\theta - \theta_{so}^{0k})\right) \mathrm{d}\theta = \frac{nN_p\theta_{so}^2 \left[(-1)^{n1} \cos\left(n(\theta_{so}^{0k} + \theta_{so})\right) - \cos(n\theta_{so}^{0k})\right]}{n_1^2\pi^2 - n^2N_p^2\theta_{so}^2}$$

Then, B^{III} is summarized in (AI-17) using the calculated values in (AI-15) and (AI-16).

$$B_n^{III} = \begin{cases} \sum_k \sum_{n_1} \left(A_{n_1}^{IIk} \frac{P}{E}\left(\frac{n_1\pi}{\theta_{so}}, r_4, r_3\right) + B_{n_1}^{IIk} \frac{2}{E\left(\frac{n_1\pi}{\theta_{so}}, r_3, r_4\right)} \right) \frac{n_1 nN_p^2\theta_{so} \left[(-1)^{n1} cos\left(nN_p(\theta_{so}^{0k} + \theta_{so})\right) - cos\left(nN_p\theta_{so}^{0k}\right)\right]}{n_1^2\pi^2 - n^2N_p^2\theta_{so}^2} & n_1\pi \neq nN_p\theta_{so} \\ \sum_k \sum_{n_1} \left(A_{n_1}^{IIk} \frac{P}{E}\left(\frac{n_1\pi}{\theta_{so}}, r_4, r_3\right) + B_{n_1}^{IIk} \frac{2}{E\left(\frac{n_1\pi}{\theta_{so}}, r_3, r_4\right)} \right) \frac{n_1 N_p}{2} sin\, nN_p\theta_{so}^{0k} & n_1\pi = nN_p\theta_{so} \end{cases} \quad \text{(AI-17)}$$

The co-sinusoidal term of (AI-13) is written as follows:

$$D_n^{III} = \frac{1}{\pi} \sum_k \left[\sum_{n_1} \left(A_{n_1}^{IIk} \frac{n_1\pi}{\theta_{so}} \frac{\mathrm{P}}{\mathrm{E}}\left(\frac{n_1\pi}{\theta_{so}}, r_3, r_2\right) + B_{n_1}^{IIk} \frac{n_1\pi}{\theta_{so}} \frac{2}{\mathrm{E}\left(\frac{n_1\pi}{\theta_{so}}, r_2, r_3\right)} \right) \int_{\theta_{so}^{0k}}^{\theta_{so}^{0k}+\theta_{so}} \cos n\theta \cos\left(\frac{n_1\pi}{\theta_{so}}(\theta - \theta_{so}^{0k})\right) \mathrm{d}\theta + \int_{\theta_{so}^{0k}}^{\theta_{so}^{0k}+\theta_{so}} b_{2k} \cos n\theta \, \mathrm{d}\theta \right] \quad \text{(AI-18)}$$

Thus, D^{III} is found by (AI-19) when $n_1\pi = n\,\theta_{so}$.

$$\int_{\theta_{so}^{0k}}^{\theta_{so}^{0k}+\theta_{so}} \cos n\theta \cos\left(\frac{n_1\pi}{\theta_{so}}(\theta - \theta_{so}^{0k})\right) \mathrm{d}\theta = \frac{1}{2}\int_{\theta_{so}^{0k}}^{\theta_{so}^{0k}+\theta_{so}} \cos n\theta_{so}^{0k} \, \mathrm{d}\theta = \frac{\theta_{so}}{2} \cos n\theta_{so}^{0k}$$

$$D_n^{III} = \sum_k \sum_{n_1} \left(A_{n_1}^{IIk} \frac{P}{E}\left(\frac{n_1\pi}{\theta_{so}}, r_3, r_2\right) + B_{n_1}^{IIk} \frac{2}{E\left(\frac{n_1\pi}{\theta_{so}}, r_2, r_3\right)} \right) \frac{n_1}{2} cos\, n\theta_{so}^{0k} \quad \text{(AI-19)}$$

And this value is calculated by (AI-20) when $n_1\pi \neq n\,\theta_{so}$.

$$\int_{\theta_{so}^{0k}}^{\theta_{so}^{0k}+\theta_{so}} \cos n\theta \cos\left(\frac{n_1\pi}{\theta_{so}}(\theta-\theta_{so}^{0k})\right)\mathrm{d}\theta = \frac{1}{2}\int_{\theta_{so}^{0k}}^{\theta_{so}^{0k}+\theta_{so}} \left[\cos\left(n\theta+\frac{n_1\pi}{\theta_{so}}(\theta-\theta_{so}^{0k})\right)+\cos\left(n\theta-\frac{n_1\pi}{\theta_{so}}(\theta-\theta_{so}^{0k})\right)\right]\mathrm{d}\theta$$

$$\int_{\theta_{so}^{0k}}^{\theta_{so}^{0k}+\theta_{so}} \cos\left(n\theta+\frac{n_1\pi}{\theta_{so}}(\theta-\theta_{so}^{0k})\right)\mathrm{d}\theta = \frac{\theta_{so}}{n_1\pi+n\theta_{so}}\left[\sin\left(n\theta+\frac{n_1\pi}{\theta_{so}}(\theta-\theta_{so}^{0k})\right)\right]_{\theta_{so}^{0k}}^{\theta_{so}^{0k}+\theta_{so}}$$

$$= \frac{\theta_{so}}{n_1\pi+n\theta_{so}}\left[(-1)^{n1}\sin\big(n(\theta_{so}^{0k}+\theta_{so})\big)-\sin(n\theta_{so}^{0k})\right]$$

$$\int_{\theta_{so}^{0k}}^{\theta_{so}^{0k}+\theta_{so}} \cos\left(n\theta-\frac{n_1\pi}{\theta_{so}}(\theta-\theta_{so}^{0k})\right)\mathrm{d}\theta = \frac{\theta_{so}}{n\theta_{so}-n_1\pi}\left[\sin\left(n\theta-\frac{n_1\pi}{\theta_{so}}(\theta-\theta_{so}^{0k})\right)\right]_{\theta_{0}^{ks}}^{\theta_{0}^{ks}+\theta_{s}}$$

$$= -\frac{\theta_{so}}{n_1\pi-n\theta_{so}}\left[(-1)^{n1}\sin\big(n(\theta_{so}^{0k}+\theta_{so})\big)-\sin(n\theta_{so}^{0k})\right] \tag{AI-20}$$

$$\rightarrow \int_{\theta_{so}^{0k}}^{\theta_{so}^{0k}+\theta_{so}} \cos n\theta \cos\left(\frac{n_1\pi}{\theta_{so}}(\theta-\theta_{so}^{0k})\right)\mathrm{d}\theta = \frac{n\theta_{so}^2\left[(-1)^{n1}\sin\big(n(\theta_{so}^{0k}+\theta_{so})\big)-\sin(n\theta_{so}^{0k})\right]}{n^2\theta_{so}^2-n_1^2\pi^2}$$

Considering (AI-19) and (AI-20). The D^{III} is retrieved in (AI-21).

$$\rightarrow D_n^{III} = \begin{cases} \sum_k\sum_{n_1}\left(-A_{n_1}^{IIk}\frac{P}{E}\left(\frac{n_1\pi}{\theta_{so}},r_3,r_2\right)-B_{n_1}^{IIk}\frac{2}{E\left(\frac{n_1\pi}{\theta_{so}},r_2,r_3\right)}\right)\frac{n_1nN_p^2\theta_{so}\left[(-1)^{n1}sin\left(nN_p(\theta_{so}^{0k}+\theta_{so})\right)-sinN_p(n\theta_{so}^{0k})\right]}{n_1^2\pi^2-n^2N_p^2\theta_{so}^2} & n_1\pi\neq nN_p\theta_{so} \\ \sum_k\sum_{n_1}\left(A_{n_1}^{IIk}\frac{P}{E}\left(\frac{n_1\pi}{\theta_{so}},r_3,r_2\right)+B_{n_1}^{IIk}\frac{2}{E\left(\frac{n_1\pi}{\theta_{so}},r_2,r_3\right)}\right)\frac{n_1N_p}{2}cos\,nN_p\theta_{so}^{0k} & n_1\pi=nN_p\theta_{so} \end{cases} \tag{AI-21}$$

The value of the excitation dependent integral for the sinusoidal and co-sinusoidal equations presented in (AI-14) and (AI-18) are calculated by (AI-22) and (AI-23) to consider them in the excitation matrix when required.

$$\frac{N_p}{\pi}\sum_k\int_{\theta_{so}^{0k}}^{\theta_{so}^{0k}+\theta_{so}} b_{2k}\,sin\,nN_p\theta\,d\theta = \frac{1}{\pi n}\sum_k b_{2k}\left[cos\,nN_p\theta_{so}^{0k}-cos\,nN_p(\theta_{so}^{0k}+\theta_{so})\right]$$

$$\triangleq \frac{\mu_0}{\pi n\theta_{so}}\sum_k I_{ks}\left[cos\,nN_p(\theta_{so}^{0k}+\theta_{so})-cos\,nN_p\theta_{so}^{0k}\right] \tag{AI-22}$$

$$\frac{1}{\pi}\sum_k\int_{\theta_{so}^{0k}}^{\theta_{so}^{0k}+\theta_{so}} b_{2k}\,cos\,nN_p\theta\,d\theta = \frac{1}{\pi n}\sum_k b_{2k}\left[sin\,nN_p(\theta_{so}^{0k}+\theta_{so})-sin\,nN_p\theta_{so}^{0k}\right]$$

$$\triangleq -\frac{\mu_0}{\pi n\theta_{so}}\sum_k I_{ks}\left[sin\,nN_p(\theta_{so}^{0k}+\theta_{so})-sin\,nN_p\theta_{so}^{0k}\right] \tag{AI-23}$$

The relationship between A^{II} and A^{III}, B^{III}, D^{III}, and C^{III} is found by means of the equation IV of (4-23) shown in (AI-24).

$$\sum_{n_1}\frac{n_1\pi}{\theta_{so}}A_{n_1}^{IIk}\sin\left(\frac{n_1\pi}{\theta_{so}}(\theta-\theta_{so}^{0k})\right)$$

$$= \sum_n -A_n^{III}\frac{2}{\mathrm{E}(nN_p,r_2,r_3)}\cos nNp\theta - B_n^{III}\frac{\mathrm{P}}{\mathrm{E}}(nN_p,r_3,r_2)\cos nNp\theta$$

$$+ C_n^{III}\frac{2}{\mathrm{E}(nN_p,r_2,r_3)}\sin nNp\theta + D_n^{III}\frac{\mathrm{P}}{\mathrm{E}}(nN_p,r_3,r_2)\sin nNp\theta \tag{AI-24}$$

According to (AI-24), A^{II} is the constant coefficient of the sinusoidal term of the Fourier transform of the right-hand side equation. Therefore, it is written as follow:

$$A_{n_1}^{IIk}=\frac{2N_p}{n_1\pi}\sum_n\int_{\theta_{so}^{0k}}^{\theta_{so}^{0k}+\theta_{so}}\Big[-A_n^{III}\frac{2}{\mathrm{E}(n,r_2,r_3)}\cos nN_p\theta-B_n^{III}\frac{\mathrm{P}}{\mathrm{E}}(n,r_3,r_2)\cos nN_p\theta+C_n^{III}\frac{2}{\mathrm{E}(n,r_2,r_3)}\sin nN_p\theta$$
$$+D_n^{III}\frac{\mathrm{P}}{\mathrm{E}}(n,r_3,r_2)\sin nN_p\theta\Big]\sin\left(\frac{n_1\pi}{\theta_{so}}(\theta-\theta_{so}^{0k})\right)\mathrm{d}\theta \qquad \text{(AI-25)}$$

A^{II} is found after the simplification of all four right hand side equations of (AI-25). For the first two terms, the equation is simplified as follow:

$$I=-A_n^{III}\frac{2}{\mathrm{E}(n,r_2,r_3)}\frac{2N_p}{n_1\pi}\int_{\theta_{so}^{0k}}^{\theta_{so}^{0k}+\theta_{so}}\cos nN_p\theta\sin\left(\frac{n_1\pi}{\theta_{so}}(\theta-\theta_{so}^{0k})\right)\mathrm{d}\theta \qquad \text{(AI-26)}$$

If $n_1\pi=nN_p\theta_{so}$:

$$\int_{\theta_{so}^{0k}}^{\theta_{so}^{0k}+\theta_{so}}\cos(nN_p\theta)\sin\left(\frac{n_1\pi}{\theta_{so}}(\theta-\theta_{so}^{0k})\right)\mathrm{d}\theta=-\frac{\theta_{so}}{2}\sin(nN_p\theta_{so}^{0k}) \qquad \text{(AI-27)}$$
$$\rightarrow I=\sum_n A_n^{III}\frac{2}{E(nN_p,r_2,r_3)}\frac{1}{n}sin(nN_p\theta_{so}^{0k})$$

If $n_1\pi\neq nN_p\theta_{so}$:

$$\int_{\theta_{so}^{0k}}^{\theta_{so}^{0k}+\theta_{so}}\cos(nN_p\theta)\sin\left(\frac{n_1\pi}{\theta_{so}}(\theta-\theta_{so}^{0k})\right)\mathrm{d}\theta$$
$$=\frac{1}{2}\int_{\theta_{so}^{0k}}^{\theta_{so}^{0k}+\theta_{so}}\left[\sin\left(\frac{n_1\pi}{\theta_{so}}(\theta-\theta_{so}^{0k})+nN_p\theta\right)+\sin\left(\frac{n_1\pi}{\theta_{so}}(\theta-\theta_{so}^{0k})-nN_p\theta\right)\right]\mathrm{d}\theta$$

$$\int_{\theta_{so}^{0k}}^{\theta_{so}^{0k}+\theta_{so}}\sin\left(\frac{n_1\pi}{\theta_{so}}(\theta-\theta_{so}^{0k})+nN_p\theta\right)\mathrm{d}\theta=-\frac{\theta_{so}}{n\theta_{so}+n_1N_p\pi}\cos\left(\frac{n_1\pi}{\theta_{so}}(\theta-\theta_{so}^{0k})+nN_p\theta\right)\Bigg|_{\theta_{so}^{0k}}^{\theta_{so}^{0k}+\theta_{so}}$$
$$=-\frac{\theta_{so}}{nN_p\theta_{so}+n_1\pi}\left[(-1)^{n_1}\cos\left(nN_p(\theta_{so}+\theta_{so}^{0k})\right)-\cos(nN_p\theta_{so}^{0k})\right] \qquad \text{(AI-28)}$$

$$\int_{\theta_{so}^{0k}}^{\theta_{so}^{0k}+\theta_{so}}\sin\left(\frac{n_1\pi}{\theta_{so}}(\theta-\theta_{so}^{0k})-nN_p\theta\right)\mathrm{d}\theta=-\frac{\theta_{so}}{n_1\pi-nN_p\theta_{so}}\cos\left(\frac{n_1\pi}{\theta_{so}}(\theta-\theta_{so}^{0k})-nN_p\theta\right)\Bigg|_{\theta_{so}^{0k}}^{\theta_{so}^{0k}+\theta_{so}}$$
$$=\frac{\theta_{so}}{nN_p\theta_{so}-n_1\pi}\left[(-1)^{n_1}\cos\left(nN_p(\theta_{so}+\theta_{so}^{0k})\right)-\cos(nN_p\theta_{so}^{0k})\right]$$

$$\int_{\theta_{so}^{0k}}^{\theta_{so}^{0k}+\theta_{so}}\cos(nN_p\theta)\sin\left(\frac{n_1\pi}{\theta_{so}}(\theta-\theta_{so}^{0k})\right)\mathrm{d}\theta$$
$$=\frac{n_1\pi\theta_{so}}{(nN_p\theta_{so})^2-(n_1\pi\theta_s)^2}\left[(-1)^{n_1}\cos\left(nN_p(\theta_{so}+\theta_{so}^{0k})\right)-\cos(nN_p\theta_{so}^{0k})\right]$$

Thus,

$$I=\begin{cases}A_n^{III}\dfrac{2}{E(nN_p,r_2,r_3)}\dfrac{2\theta_{so}\left[(-1)^{n1}cos\left(nN_p(\theta_{so}^{0k}+\theta_{so})\right)-cos(nN_p\theta_{so}^{0k})\right]}{n_1^2\pi^2-n^2N_p^2\theta_{so}^2} & n_1\pi\neq nN_p\theta_{so}\\ A_n^{III}\dfrac{1}{nN_p}\dfrac{2}{E(nN_p,r_2,r_3)}sin(nN_p\theta_{so}^{0k}) & n_1\pi=nN_p\theta_{so}\end{cases} \qquad \text{(AI-29)}$$

and the same for II which is related to B^{II} is:

$$II \triangleq \begin{cases} B_n^{III}\dfrac{P}{E}(nN_p, r_3, r_2)\dfrac{2\theta_{so}\left[(-1)^{n1}\,cos\left(nN_p(\theta_{so}^{0k}+\theta_{so})\right)-cos\left(nN_p\theta_{so}^{0k}\right)\right]}{n_1^2\pi^2-n^2N_p^2\theta_{so}^2} & n_1\pi \neq nN_p\theta_{so} \\ B_n^{III}\dfrac{1}{nN_p}\dfrac{P}{E}(nN_p, r_3, r_4)\,sin\left(nN_p\theta_{so}^{0k}\right) & n_1\pi = nN_p\theta_{so} \end{cases} \quad \text{(AI-30)}$$

For the third and fourth terms of (AI-25) the equation is expanded as follow:

$$III = C_n^{III}\frac{2}{n_1\pi}\frac{2}{\mathrm{E}\left(nN_p, r_2, r_3\right)}\int_{\theta_{so}^{0k}}^{\theta_{so}^{0k}+\theta_{so}} \sin nN_p\theta \sin\left(\frac{n_1\pi}{\theta_{so}}(\theta-\theta_{so}^{0k})\right)\mathrm{d}\theta \quad \text{(AI-31)}$$

If $n_1\pi = nN_p\theta_{so}$:

$$\int_{\theta_{so}^{0k}}^{\theta_{so}^{0k}+\theta_{so}} sin\left(nN_p\theta\right) sin\left(\frac{n_1\pi}{\theta_{so}}(\theta-\theta_{so}^{0k})\right)d\theta = \frac{\theta_{so}}{2}cos\left(nN_p\theta_{so}^{0k}\right) \quad \text{(AI-32)}$$

$$\rightarrow III = \sum_n C_n^{III}\frac{2}{E(n, r_3, r_2)}\frac{1}{nN_p}cos\left(nN_p\theta_{so}^{0k}\right)$$

If $n_1\pi \neq n\theta_{so}$:

$$\int_{\theta_{so}^{0k}}^{\theta_{so}^{0k}+\theta_{so}} \sin(n\theta)\sin\left(\frac{n_1\pi}{\theta_{so}}(\theta-\theta_{so}^{0k})\right)\mathrm{d}\theta$$
$$= \frac{1}{2}\int_{\theta_{so}^{0k}}^{\theta_{so}^{0k}+\theta_{so}}\left[\cos\left(n\theta-\frac{n_1\pi}{\theta_{so}}(\theta-\theta_{so}^{0k})\right)-\cos\left(n\theta+\frac{n_1\pi}{\theta_{so}}(\theta-\theta_{so}^{0k})\right)\right]\mathrm{d}\theta$$

$$\int_{\theta_{so}^{0k}}^{\theta_{so}^{0k}+\theta_{so}} \cos\left(nN_p\theta+\frac{n_1\pi}{\theta_{so}}(\theta-\theta_{so}^{0k})\right)\mathrm{d}\theta = \frac{\theta_{so}}{nN_p\theta_{so}+n_1\pi}\sin\left(\frac{n_1\pi}{\theta_{so}}(\theta-\theta_{so}^{0k})+nN_p\theta\right)\Bigg|_{\theta_{so}^{0k}}^{\theta_{so}^{0k}+\theta_{so}}$$
$$= \frac{\theta_{so}}{nN_p\theta_{so}+n_1\pi}\left[(-1)^{n_1}\sin\left(nN_p(\theta_{so}+\theta_{so}^{0k}-\theta_s^{0k})\right)-\sin\left(nN_p(\theta_{so}^{0k}-\theta_s^{0k})\right)\right] \quad \text{(AI-33)}$$

$$\int_{\theta_{so}^{0k}}^{\theta_{so}^{0k}+\theta_{so}} \cos\left(nN_p\theta-\frac{n_1\pi}{\theta_{so}}(\theta-\theta_{so}^{0k})\right)\mathrm{d}\theta = \frac{\theta_{so}}{nN_p\theta_{so}-n_1\pi}\sin\left(\frac{n_1\pi}{\theta_{so}}(\theta-\theta_{so}^{0k})-nN_p\theta\right)\Bigg|_{\theta_{so}^{0k}}^{\theta_{so}^{0k}+\theta_{so}}$$
$$= \frac{\theta_{so}}{nN_p\theta_{so}-n_1\pi}\left[(-1)^{n_1}\sin\left(nN_p(\theta_{so}+\theta_{so}^{0k}-\theta_s^{0k})\right)-\sin\left(nN_p(\theta_{so}^{0k}-\theta_s^{0k})\right)\right]$$

$$\int_{\theta_{so}^{0k}}^{\theta_{so}^{0k}+\theta_{so}} \cos\left(nN_p\theta\right)\sin\left(\frac{n_1\pi}{\theta_{so}}(\theta-\theta_{so}^{0k})\right)\mathrm{d}\theta$$
$$= \frac{n_1\pi\theta_{so}}{\left(nN_p\theta_{so}\right)^2-(n_1\pi\theta_s)^2}\left[(-1)^{n_1}\sin\left(nN_p(\theta_{so}+\theta_{so}^{0k}-\theta_s^{0k})\right)-\sin\left(nN_p(\theta_{so}^{0k}-\theta_s^{0k})\right)\right]$$

Then, the third and fourth terms are summarized as follow:

$$III = \begin{cases} C_n^{III}-\dfrac{2}{E\left(nN_p, r_2, r_3\right)}\dfrac{2\theta_{so}\left[(-1)^{n1}\,sin\left(nN_p(\theta_{so}^{0k}+\theta_{so})\right)-sin\left(nN_p\theta_{so}^{0k}\right)\right]}{n_1^2\pi^2-n^2N_p^2\theta_{so}^2} & n_1\pi \neq nN_p\theta_{so} \\ C_n^{III}\dfrac{1}{nN_p}\dfrac{2}{E\left(nN_p, r_4, r_3\right)}cos\left(nN_p\theta_{so}^{0k}\right) & n_1\pi = nN_p\theta_{so} \end{cases} \quad \text{(AI-34)}$$

$$IV \triangleq \begin{cases} D_n^{III}-\dfrac{P}{E}(nN_p, r_3, r_2)\dfrac{2\theta_{so}\left[(-1)^{n1}\,sin\left(nN_p(\theta_{so}^{0k}+\theta_{so})\right)-sin\left(nN_p\theta_{so}^{0k}\right)\right]}{n_1^2\pi^2-n^2N_p^2\theta_{so}^2} & n_1\pi \neq nN_p\theta_{so} \\ D_n^{III}\dfrac{1}{nN_p}\dfrac{P}{E}(nN_p, r_3, r_2)\,cos\left(nN_p\theta_{so}^{0k}\right) & n_1\pi = nN_p\theta_{so} \end{cases} \quad \text{(AI-35)}$$

The form of the equations in (4-24) and (4-25) are similar to the (4-22) and (4-23) which has been solved in this Appendix. To be concise, just the final solution after simplification of each equation is presented for these equations.

For the rotor bars and rotor slots opening equation which VII and VIII in (4-25) are extended like (AI-1) and (AI-8) and the unknowns' relationship is briefed as below:

From VII in (4-25)

$$\sum_{n_2} A_{n_2}^{Vk} \cos\left(\frac{n_1\pi}{\theta_r}(\theta-\theta_r^{0k})\right) = \begin{cases} \sum_{n_1}\left(A_{n_1}^{IVk}\frac{n_1\pi}{\theta_{ro}}\frac{2}{\mathrm{E}\left(\frac{n_1\pi}{\theta_{ro}},r_1,r_2\right)}+B_{n_1}^{IVk}\frac{n_1\pi}{\theta_{ro}}\frac{\mathrm{P}}{\mathrm{E}}\left(\frac{n_1\pi}{\theta_{ro}},r_2,r_1\right)\right)\cos\left(\frac{n_1\pi}{\theta_{ro}}(\theta-\theta_{ro}^{0k})\right)+b_{4k}+\frac{1}{2}j_{kv}\mu_0(r_1^2-r_0^2) \\ \frac{1}{2}j_{kv}\mu_0(r_1^2-r_0^2) \end{cases} \quad \text{(AI-36)}$$

$$b_{4k}=\frac{\mu_0 I_{kr}}{\theta_{ro}} \quad \text{(AI-37)}$$

$$A_{n_2}^{Vk}=\begin{cases} \sum_{n_1}\left(A_{n_1}^{IVk}\frac{2}{E\left(\frac{n_1\pi}{\theta_{ro}},r_1,r_2\right)}+B_{n_1}^{IVk}\frac{P}{E}\left(\frac{n_1\pi}{\theta_{ro}},r_2,r_1\right)\right)\frac{2n_2n_1\theta_{ro}((-1)^{n_1}-1)}{(n_2\theta_{ro})^2-(n_1\theta_r)^2}sin\left(\frac{n_2\pi}{\theta_r}(\theta_{ro}^{0k}-\theta_r^{0k})\right) & \frac{n_1\pi}{\theta_{ro}}\neq\frac{n_2\pi}{\theta_r} \\ \sum_{n_1}\left(A_{n_1}^{IVk}\frac{2}{E\left(\frac{n_1\pi}{\theta_{ro}},r_1,r_2\right)}+B_{n_1}^{IVk}\frac{P}{E}\left(\frac{n_1\pi}{\theta_{ro}},r_2,r_1\right)\right)\frac{n_1\pi}{\theta_r}cos\left(\frac{n_1\pi}{\theta_{ro}}(\theta_r^{0k}-\theta_{ro}^{0k})\right) & \frac{n_1\pi}{\theta_{ro}}=\frac{n_2\pi}{\theta_r} \end{cases} \quad \text{(AI-38)}$$

$$+\frac{\mu_0 I_{kr}}{\theta_{ro}}\frac{2}{n_2\pi}\left[sin\left(\frac{n_2\pi}{\theta_r}(\theta_{ro}^{0k}+\theta_{ro}-\theta_r^{0k})\right)-sin\left(\frac{n_2\pi}{\theta_r}(\theta_{ro}^{0k}-\theta_r^{0k})\right)\right]$$

From VIII in (4-25):

$$\sum_{n_1}\frac{n_1\pi}{\theta_{ro}}B_{n_1}^{IVk}\sin\left(\frac{n_1\pi}{\theta_{ro}}(\theta-\theta_{ro}^{0k})\right)=\sum_{n_2}\frac{n_2\pi}{\theta_r}A_{n_2}^{Vk}\frac{\theta_r}{n_2\pi}\frac{\mathrm{P}}{\mathrm{E}}\left(\frac{n_2\pi}{\theta_r},r_1,r_0\right)\sin\left(\frac{n_2\pi}{\theta_r}(\theta-\theta_r^{0k})\right) \quad \text{(AI-39)}$$

$$\rightarrow B_{n_1}^{IVk}=\begin{cases} \sum_{n_2}A_{n_2}^{Vk}\frac{P}{E}\left(\frac{n_2\pi}{\theta_r},r_5,r_6\right)\frac{2\theta_{ro}\theta_r^2\left((-1)^{n_1}sin\left(\frac{n_2\pi}{\theta_r}(\theta_{ro}+\theta_{ro}^{0k}-\theta_r^{0k})\right)-sin\left(\frac{n_2\pi}{\theta_r}(\theta_{ro}^{0k}-\theta_r^{0k})\right)\right)}{(n_2\pi\theta_{ro})^2-(n_1\pi\theta_r)^2} & \frac{n_1\pi}{\theta_{ro}}\neq\frac{n_2\pi}{\theta_r} \\ \sum_{n_2}A_{n_2}^{Vk}\frac{P}{E}\left(\frac{n_2\pi}{\theta_r},r_5,r_6\right)\frac{\theta_r}{n_2\pi}cos\left(\frac{n_1\pi}{\theta_{ro}}(\theta_r^{0k}-\theta_{ro}^{0k})\right) & \frac{n_1\pi}{\theta_{ro}}=\frac{n_2\pi}{\theta_r} \end{cases} \quad \text{(AI-40)}$$

The unknowns of the rotor slot opening at the boundary of airgap are obtained as follows (like the procedure of the calculation of BIII and DIII from (AI-13) to (AI-21)).

From V in (4-24):

$$\sum_n A_n^{III}\sin nN_p\theta+C_n^{III}\cos nN_p\theta = \begin{cases} \sum_{n_1}\left(A_{n_1}^{IVk}\frac{n_1\pi}{\theta_{ro}}\frac{\mathrm{P}}{\mathrm{E}}\left(\frac{n_1\pi}{\theta_{ro}},r_3,r_2\right)+B_{n_1}^{IVk}\frac{n_1\pi}{\theta_{ro}}\frac{2}{\mathrm{E}\left(\frac{n_1\pi}{\theta_{ro}},r_2,r_3\right)}\right)\cos\left(\frac{n_1\pi}{\theta_{ro}}(\theta-\theta_{ro}^{0k})\right)+b_{4k} \\ 0 \end{cases} \quad \text{(AI-41)}$$

$$\sum_n A_n^{III}\sin n\theta + C_n^{III}\cos n\theta$$

$$= \begin{cases} \sum_{n_1}\left(A_{n_1}^{IVk}\frac{n_1\pi}{R_m\theta_{ro}}coth\frac{n_1\pi}{R_m\theta_{ro}}(r_2-r_3) + B_{n_1}^{IVk}\frac{n_1\pi}{R_m\theta_{ro}}csch\frac{n_1\pi}{R_m\theta_{ro}}(r_3-r_2)\right)cos\left(\frac{n_1\pi}{\theta_{ro}}(\theta-\theta_{ro}^{0k})\right)+b_4 \\ 0 \end{cases}$$

$$\rightarrow A_n^{III} \tag{AI-42}$$

$$= \begin{cases} \sum_k\sum_{n_1}\left(A_{n_1}^{IVk}\frac{P}{E}\left(\frac{n_1\pi}{\theta_{ro}},r_3,r_2\right)+B_{n_1}^{IVtk}\frac{2}{E\left(\frac{n_1\pi}{\theta_{ro}},r_2,r_3\right)}\right)\frac{n_1 n\,\theta_{ro}\left[(-1)^{n1}cos\left(n(\theta_{ro}^{0k}+\theta_{ro})\right)-cos(n\,\theta_{ro}^{0k})\right]}{n_1^2\pi^2-n^2\theta_{ro}^2} & n_1\pi\neq n\,\theta_{ro} \\ \sum_k\sum_{n_1}\left(A_{n_1}^{IVk}\frac{P}{E}\left(\frac{n_1\pi}{\theta_{ro}},r_3,r_2\right)+B_{n_1}^{IVtk}\frac{2}{E\left(\frac{n_1\pi}{\theta_{ro}},r_2,r_3\right)}\right)\frac{n_1}{2}sin\,n\,\theta_{ro}^{0k} & n_1\pi=n\,\theta_{ro} \end{cases}$$

$$\sum_n A_n^{III}\sin n\theta + C_n^{III}\cos n\theta$$

$$= \begin{cases} \sum_{n_1}\left(A_{n_1}^{IVk}\frac{n_1\pi}{\theta_{ro}}\frac{P}{E}\left(\frac{n_1\pi}{\theta_{ro}},r_3,r_2\right)+B_{n_1}^{IVtk}\frac{n_1\pi}{\theta_{ro}}\frac{2}{E\left(\frac{n_1\pi}{\theta_{ro}},r_2,r_3\right)}\right)cos\left(\frac{n_1\pi}{\theta_{ro}}(\theta-\theta_{ro}^{0k})\right)+b_{4k} \\ 0 \end{cases}$$

$$\rightarrow C_n^{III} \tag{AI-43}$$

$$= \begin{cases} \sum_k\sum_{n_1}\left(A_{n_1}^{IVk}\frac{P}{E}\left(\frac{n_1\pi}{\theta_{ro}},r_3,r_2\right)+B_{n_1}^{IVk}\frac{2}{E\left(\frac{n_1\pi}{\theta_{ro}},r_2,r_3\right)}\right)\frac{n_1 n\,\theta_{ro}\left[(-1)^{n1}sin\left(n(\theta_{ro}^{0k}+\theta_{ro})\right)-sin(n\,\theta_{ro}^{0k})\right]}{n^2\theta_{ro}^2-n_1^2\pi^2} & n_1\pi\neq n\,\theta_{ro} \\ \sum_k\sum_{n_1}\left(A_{n_1}^{IVk}\frac{P}{E}\left(\frac{n_1\pi}{\theta_{ro}},r_3,r_2\right)+B_{n_1}^{IVk}\frac{2}{E\left(\frac{n_1\pi}{\theta_{ro}},r_5,r_4\right)}\right)\frac{n_1}{2}cos\,n\,\theta_{ro}^{0k} & n_1\pi=n\,\theta_{ro} \end{cases}$$

The value of the excitation dependent integral for the sinusoidal and co-sinusoidal equations form the explanation of (AI-41) are found as follow:

$$\frac{1}{\pi}\sum_k\int_{\theta_{ro}^{0k}}^{\theta_{ro}^{0k}+\theta_{ro}} b_{4k}\sin n\theta\,d\theta = \frac{1}{\pi n}\sum_k b_{4k}[\cos n\,\theta_{ro}^{0k}-\cos n(\theta_{ro}^{0k}+\theta_{ro})]$$
$$\triangleq -\frac{\mu_0}{\pi n\,\theta_{ro}}\sum_k I_{kr}[\cos n(\theta_{ro}^{0k}+\theta_{ro})-\cos n\,\theta_{ro}^{0k}] \tag{AI-44}$$

$$\frac{1}{\pi}\sum_k\int_{\theta_{ro}^{0k}}^{\theta_{ro}^{0k}+\theta_{ro}} b_{4k}\cos n\theta\,d\theta = \frac{1}{\pi n}\sum_k b_{4k}[\sin n(\theta_{ro}^{0k}+\theta_{ro})-\sin n\,\theta_{ro}^{0k}]$$
$$\triangleq \frac{\mu_0}{\pi n\,\theta_{ro}}\sum_k I_{kr}[\sin n(\theta_{ro}^{0k}+\theta_{ro})-\sin n\,\theta_{ro}^{0k}] \tag{AI-45}$$

The unknowns of the general solutions of the calculated vector potentials in Table 6. 2 on are finalized by simplification of VI in (4-24)

From (4-24):

$$\sum_{n_1}\frac{n_1\pi}{\theta_{ro}}A_{n_1}^{IVk}\sin\left(\frac{n_1\pi}{\theta_{ro}}(\theta-\theta_{ro}^{0k})\right)$$
$$= \sum_n -A_n^{III}\frac{\mathrm{P}}{\mathrm{E}}(nN_p,r_2,r_3)\cos nNp\theta - B_n^{III}\frac{2}{\mathrm{E}(nN_p,r_3,r_2)}\cos nNp\theta$$
$$+ C_n^{III}\frac{\mathrm{P}}{\mathrm{E}}(nN_p,r_2,r_3)\sin nNp\theta + D_n^{III}\frac{2}{\mathrm{E}(nN_p,r_3,r_2)}\sin nNp\theta \tag{AI-46}$$

Then the relationship of the four right hand side coefficients with A^{IV} is as follows:

$$I \triangleq \begin{cases} A_n^{III}\dfrac{P}{E}(n,r_2,r_3)\dfrac{2\theta_{ro}\left[(-1)^{n1}\cos\left(n(\theta_{ro}^{0k}+\theta_{ro})\right)-\cos(n\,\theta_{ro}^{0k})\right]}{n_1^2\pi^2-n^2\theta_{ro}^2} & n_1\pi \neq n\,\theta_{ro} \\ A_n^{III}\dfrac{1}{n}\dfrac{P}{E}(n,r_2,r_3)\sin n\,\theta_{ro}^{0k} & n_1\pi = n\,\theta_{ro} \end{cases}$$

$$II \triangleq \begin{cases} B_n^{III}\dfrac{2}{E(n,r_3,r_2)}\dfrac{2\theta_{ro}\left[(-1)^{n1}\cos\left(n(\theta_{ro}^{0k}+\theta_{ro})\right)-\cos(n\,\theta_{ro}^{0k})\right]}{n_1^2\pi^2-n^2\theta_{ro}^2} & n_1\pi \neq n\,\theta_{ro} \\ B_n^{III}\dfrac{1}{n}\dfrac{2}{E(n,r_3,r_2)}\sin n\,\theta_{ro}^{0k} & n_1\pi = n\,\theta_{ro} \end{cases}$$

$$III \triangleq \begin{cases} -C_n^{III}\dfrac{P}{E}(n,r_2,r_3)\dfrac{2\theta_{ro}\left[(-1)^{n1}\sin\left(n(\theta_{ro}^{0k}+\theta_{ro})\right)-\sin(n\,\theta_{ro}^{0k})\right]}{n_1^2\pi^2-n^2\theta_{ro}^2} & n_1\pi \neq n\,\theta_{ro} \\ C_n^{III}\dfrac{1}{n}\dfrac{P}{E}(n,r_2,r_3)\cos n\,\theta_{ro}^{0k} & n_1\pi = n\,\theta_{ro} \end{cases}$$

$$IV \triangleq \begin{cases} -D_n^{III}\dfrac{2}{E(n,r_3,r_2)}\dfrac{2\theta_{ro}\left[(-1)^{n1}\sin\left(n(\theta_{ro}^{0k}+\theta_{ro})\right)-\sin(n\,\theta_{ro}^{0k})\right]}{n_1^2\pi^2-n^2\theta_{ro}^2} & n_1\pi \neq n\,\theta_{ro} \\ D_n^{III}\dfrac{1}{n}\dfrac{2}{E(n,r_3,r_2)}\cos n\,\theta_{ro}^{0k} & n_1\pi = n\,\theta_{ro} \end{cases} \quad \text{(AI-47)}$$

The all other unknown values in the general solution of the calculated vector potentials are obtained using the equations presented in Table 6. 1 and consideration of the continuity at the boundary of each subdomain.

From (4-18) and (4-19) at r = r_4:

$$b_{2k}\ln r_3 + a_{2k} = \sum_n \left[A_n^{III}\frac{1}{nN_p}\frac{\mathrm{P}\left(nN_p,r,r_4\right)}{\mathrm{E}\left(nN_p,r_3,r_4\right)}\sin nNp\theta + B_n^{III}\frac{1}{nN_p}\frac{\mathrm{P}\left(nN_p,r,r_3\right)}{\mathrm{E}\left(nN_p,r_4,r_3\right)}\sin nNp\theta + C_n^{III}\frac{1}{nN_p}\frac{\mathrm{P}\left(nN_p,r,r_4\right)}{\mathrm{E}\left(nN_p,r_3,r_4\right)}\cos nNp\theta + D_n^{III}\frac{1}{nN_p}\frac{\mathrm{P}\left(nN_p,r,r_3\right)}{\mathrm{E}\left(nN_p,r_4,r_3\right)}\cos nNp\theta\right] \quad \text{(AI-48)}$$

From (AI-2): $b_{2k} = -\frac{\mu_0 I_{ks}}{\theta_{so}}$, then

$$a_{2k} = \frac{\mu_0 I_{ks}}{\theta_{so}}ln\, r_3 - \frac{1}{\theta_{so}N_p^2n^2}\left[A_n^{III}\frac{2}{E\left(nN_p,r_3,r_4\right)} + B_n^{III}\frac{P\left(nN_p,r_4,r_3\right)}{E\left(nN_p,r_4,r_3\right)}\right]\left(cos\left(nNp(\theta_{so}+\theta_{so}^{0k})\right) - cos(nNp\theta_{so}^{0k})\right) + \frac{1}{\theta_{so}N_p^2n^2}\left[C_n^{III}\frac{2}{E\left(nN_p,r_3,r_4\right)} + D_n^{III}\frac{P\left(nN_p,r_4,r_3\right)}{E\left(nN_p,r_4,r_3\right)}\right]\left(sin\left(nNp(\theta_{so}+\theta_{so}^{0k})\right) - sin(nNp\theta_{so}^{0k})\right) \quad \text{(AI-49)}$$

From (4-17) and (4-18) at r=r4:

$$\begin{aligned} b_{2k}\ln r_4 + a_{2k} &= a_{1k} - \mu_0 j_v\left(\frac{1}{4}r_4^2 - \frac{1}{2}r_1^2\ln r_5\right) + \sum_n A_n^{Ik}\frac{\theta_s}{n\pi}\frac{\mathrm{P}\left(\frac{n\pi}{\theta_s},r_5,r_4\right)}{\mathrm{E}\left(\frac{n\pi}{\theta_s},r_4,r_5\right)}\frac{1}{\theta_{so}}\int_{\theta_{so}^{0k}}^{\theta_{so}+\theta_{so}^{0k}}\cos\left(\frac{n\pi}{\theta_s}(\theta-\theta_s^{0k})\right)\mathrm{d}\theta \\ &= a_{0k} - \mu_0 j_v\left(\frac{1}{4}r_4^2 - \frac{1}{2}r_1^2\ln r_5\right) \\ &\quad + \sum_n A_n^{Ik}\frac{1}{\theta_{so}}\left(\frac{\theta_s}{n\pi}\right)^2\frac{\mathrm{P}\left(\frac{n\pi}{\theta_s},r_5,r_4\right)}{\mathrm{E}\left(\frac{n\pi}{\theta_s},r_4,r_5\right)}\left(\sin\left(\frac{n\pi}{\theta_s}(\theta_{so}+\theta_{so}^{0k}-\theta_s^{0k})\right)-\sin\left(\frac{n\pi}{\theta_s}(\theta_{so}^{0k}-\theta_s^{0k})\right)\right) \end{aligned} \quad \text{(AI-50)}$$

$$\mu_0 j_v\left(\frac{1}{4}r_4^2 - \frac{1}{2}r_5^2\ln r_4\right) = \frac{I_k\mu_0}{\theta_s(r_4^2-r_5^2)}\left(\frac{1}{2}r_4^2 - r_5^2\ln r_2\right)$$

$$\rightarrow\ a_{1k} = a_{2k} - \frac{\mu_0 I_{ks}}{\theta_{so}} ln\, r_4 - \sum_n A_n^{Ik} \frac{1}{\theta_{so}} \left(\frac{\theta_s}{n\pi}\right)^2 \frac{P\left(\frac{n\pi}{\theta_s}, r_5, r_4\right)}{E\left(\frac{n\pi}{\theta_s}, r_4, r_5\right)} \left[sin\left(\frac{n\pi}{\theta_s}(\theta_{so} + \theta_{so}^{0k} - \theta_s^{0k})\right) - sin\left(\frac{n\pi}{\theta_s}(\theta_{so}^{0k} - \theta_s^{0k})\right)\right] + \frac{I_k \mu_0}{\theta_s (r_4^2 - r_5^2)} \left(\frac{1}{2} r_4^2 - r_5^2\, ln\, r_4\right) \quad \text{(AI-51)}$$

In the same procedure for the rotor side constant and using (4-20) and (4-21), a_{4k} and a_{5k} are attained as below:

$$a_{4k} = -\frac{\mu_0 I_{kr}}{\theta_{ro}} ln\, r_2 - \frac{1}{\theta_{ro} N_p^2 n^2} \left[A_n^{III} \frac{P\left(nN_p, r_2, r_3\right)}{E\left(nN_p, r_2, r_3\right)} + B_n^{III} \frac{2}{E\left(nN_p, r_3, r_2\right)}\right] \left(cos\left(nNp(\theta_{ro} + \theta_{ro}^{0k})\right) - cos(nNp\theta_{ro}^{0k})\right) + \frac{1}{\theta_{ro} N_p^2 n^2} \left[C_n^{III} \frac{P\left(nN_p, r_2, r_3\right)}{E\left(nN_p, r_2, r_3\right)} + D_n^{III} \frac{2}{E\left(nN_p, r_3, r_2\right)}\right] \left(sin\left(nNp(\theta_{ro} + \theta_{ro}^{0k})\right) - sin(nNp\theta_{ro}^{0k})\right) \quad \text{(AI-52)}$$

$$a_{5k} = a_{4k} + \frac{\mu_0 I_{kr}}{\theta_{ro}} ln\, r_1 - \sum_n A_n^{Vk} \frac{1}{\theta_{ro}} \left(\frac{\theta_r}{n\pi}\right)^2 \frac{P\left(\frac{n\pi}{\theta_r}, r_1, r_0\right)}{E\left(\frac{n\pi}{\theta_r}, r_1, r_0\right)} \left[sin\left(\frac{n\pi}{\theta_r}(\theta_{ro} + \theta_{ro}^{0k} - \theta_r^{0k})\right) - sin\left(\frac{n\pi}{\theta_r}(\theta_{ro}^{0k} - \theta_r^{0k})\right)\right] + \frac{I_k \mu_0}{\theta_r (r_0^2 - r_1^2)} \left(\frac{1}{2} r_1^2 - r_0^2\, ln\, r_5\right) \quad \text{(AI-53)}$$

APPENDIX II

To calculate A_1 and A_2, the magnetic vector potential equation at the stator slot (i. e. equation (4-17) at the middle of the slots with the radius of $\frac{r_4+r_5}{2}$ is investigated. (AII-1) shows the required MVP for calculation of A_1 and A_2. Note that these values are not equal because of the current distribution in all the stator slots.

$$A_{1,2}^{k} = \sum_{n} A_n^{Ik} \frac{\theta_s}{n\pi} \frac{\mathrm{P}\left(\frac{n\pi}{\theta_s}, \frac{r_5+r_6}{2}, r_6\right)}{\mathrm{E}\left(\frac{n\pi}{\theta_s}, r_5, r_6\right)} \cos\left(\frac{n\pi}{\theta_s}\left(\theta - \theta_s^{0k}\right)\right) + a_{1k} - \mu_0 j_v \left(\frac{1}{4}\left(\frac{r_5+r_6}{2}\right)^2 - \frac{1}{2} r_5^2 \ln\left(\frac{r_5+r_6}{2}\right)\right) \tag{AII-1}$$

Where j_v is the current density of the slot and a_{1k} is obtained using the following equation:

$$a_{1k} = a_{2k} - \frac{\mu_0 I_{ks}}{\theta_{so}} \ln r_5 - \sum_{n} A_n^{Ik} \frac{1}{\theta_{so}} \left(\frac{\theta_s}{n\pi}\right)^2 \frac{\mathrm{P}\left(\frac{n\pi}{\theta_s}, r_5, r_6\right)}{\mathrm{E}\left(\frac{n\pi}{\theta_s}, r_5, r_6\right)} \left[\sin\left(\frac{n\pi}{\theta_s}\left(\theta_{so} + \theta_{so}^{0k} - \theta_s^{0k}\right)\right) - \sin\left(\frac{n\pi}{\theta_s}\left(\theta_{so}^{0k} - \theta_s^{0k}\right)\right)\right] + \frac{I_{ks}\mu_0}{\theta_s(r_6^2 - r_5^2)} \left(\frac{1}{2} r_5^2 - r_6^2 \ln r_5\right) \tag{AII-2}$$

and a_{2k} which depends on the MVPs at the airgap subdomain (i.e. equation (4-19)) is achieved by (AII-3).

$$a_{2k} = \frac{\mu_0 I_{ks}}{\theta_{so}} \ln r_4 - \frac{1}{\theta_{so} N_p^2 n^2} \left[A_n^{III} \frac{2}{\mathrm{E}\left(nN_p, r_4, r_3\right)} + B_n^{III} \frac{\mathrm{P}\left(nN_p, r_3, r_4\right)}{\mathrm{E}\left(nN_p, r_3, r_4\right)}\right] \left(\cos\left(nNp\left(\theta_{so} + \theta_{so}^{0k}\right)\right) - \cos\left(nNp\theta_{so}^{0k}\right)\right) + \frac{1}{\theta_{so} N_p^2 n^2} \left[C_n^{III} \frac{2}{\mathrm{E}\left(nN_p, r_4, r_3\right)} + D_n^{III} \frac{\mathrm{P}\left(nN_p, r_3, r_4\right)}{\mathrm{E}\left(nN_p, r_3, r_4\right)}\right] \left(\sin\left(nNp\left(\theta_{so} + \theta_{so}^{0k}\right)\right) - \sin\left(nNp\theta_{so}^{0k}\right)\right) \tag{AII-3}$$

A_3 is another required vector potential to calculate the saturation factor which is derived from the stator slots MVPs. Equation (4-17) is used to find A_3 by consideration of the maximum radius in adjacency of the stator yoke. So, A_3 is attained using (AII-4).

$$A_3^k = \sum_n A_n^{Ik} \frac{\theta_s}{n\pi} \frac{2}{\mathrm{E}\left(\frac{n\pi}{\theta_s}, r_5, r_6\right)} \cos\left(\frac{n\pi}{\theta_s}\left(\theta - \theta_s^{0k}\right)\right) + a_{1k} - \mu_0 j_v \left(\frac{1}{2}(r_6)^2 - \frac{1}{2} r_6^2 \ln(r_6)\right) \quad \text{(AII-4)}$$

The saturation study is conducted in the no-load condition where the rotor current is zero. So, the excitation related term of the equation (4-21) is zero and A_{1r} and A_{2r} for the saturation consideration is obtained using (AII-5).

$$A_{1r,2r}^k = \sum_n A_n^{Vk} \frac{\theta_r}{n\pi} \frac{\mathrm{P}\left(\frac{n\pi}{\theta_r}, \frac{r_1 + r_2}{2}, r_1\right)}{\mathrm{E}\left(\frac{n\pi}{\theta_r}, r_2, r_1\right)} \cos\left(\frac{n\pi}{\theta_r}\left(\theta - \theta_r^{0k}\right)\right) + a_{5k} \quad \text{(AII-5)}$$

Where a_{5k} is calculated using (AII-6).

$$a_{5k} = a_{4k} + \frac{\mu_0 I_{kr}}{\theta_{ro}} \ln r_2 - \sum_n A_n^{Vk} \frac{1}{\theta_{ro}} \left(\frac{\theta_r}{n\pi}\right)^2 \frac{\mathrm{P}\left(\frac{n\pi}{\theta_r}, r_2, r_1\right)}{\mathrm{E}\left(\frac{n\pi}{\theta_r}, r_2, r_1\right)} \left[\sin\left(\frac{n\pi}{\theta_r}\left(\theta_{ro} + \theta_{ro}^{0k} - \theta_r^{0k}\right)\right) - \sin\left(\frac{n\pi}{\theta_r}\left(\theta_{ro}^{0k} - \theta_r^{0k}\right)\right)\right] + \frac{I_{kr}\mu_0}{\theta_r(r_2^2 - r_1^2)}\left(\frac{1}{2} r_2^2 - r_1^2 \ln r_2\right) \quad \text{(AII-6)}$$

Based on the solutions of the Maxwell equations, a_{4k} is calculated using the following equation:

$$\begin{aligned} a_{4k} = {} & -\frac{\mu_0 I_{kr}}{\theta_{ro}} \ln r_3 \\ & - \frac{1}{\theta_{ro} N_p^2 n^2} \left[A_n^{III} \frac{\mathrm{P}\left(nN_p, r_4, r_3\right)}{\mathrm{E}\left(nN_p, r_4, r_3\right)} + B_n^{III} \frac{2}{\mathrm{E}\left(nN_p, r_3, r_4\right)} \right] \left(\cos\left(nNp\left(\theta_{ro} + \theta_{ro}^{0k}\right)\right) - \cos\left(nNp\theta_{ro}^{0k}\right)\right) \\ & + \frac{1}{\theta_{ro} N_p^2 n^2} \left[C_n^{III} \frac{\mathrm{P}\left(nN_p, r_4, r_3\right)}{\mathrm{E}\left(nN_p, r_4, r_3\right)} + D_n^{III} \frac{2}{\mathrm{E}\left(nN_p, r_3, r_4\right)} \right] \left(\sin\left(nNp\left(\theta_{ro} + \theta_{ro}^{0k}\right)\right) - \sin\left(nNp\theta_{ro}^{0k}\right)\right) \end{aligned} \quad \text{(AII-7)}$$

In (AII-6) and (AII-7) the value of the I_{kr}, which represents the rotor current, is zero for the calculation of the saturation factor because the saturation factor is determined based on the no-load condition.

REFERENCES

[1] "Climate Change Act 2008," *UK Public General Acts*, 2008. https://www.legislation.gov.uk/ukpga/2008/27/contents.

[2] I. Staffell *et al.*, "The role of hydrogen and fuel cells in the global energy system," *Energy Environ. Sci.*, vol. 12, no. 2, pp. 463–491, 2019.

[3] I. E. A. G. E. V Outlook, "Scaling-up the transition to Electric Mobility," *IEA London, UK*, 2019.

[4] G. Hill, O. Heidrich, F. Creutzig, and P. Blythe, "The role of electric vehicles in near-term mitigation pathways and achieving the UK's carbon budget," *Appl. Energy*, vol. 251, p. 113111, 2019, doi: https://doi.org/10.1016/j.apenergy.2019.04.107.

[5] Oak Ridge National Laboratory, "All-Electric Vehicles," *the U.S. Department of Energy and the U.S. Environmental Protection Agency*. https://www.fueleconomy.gov/feg/evtech.shtml.

[6] E. Roshandel, A. Mahmoudi, S. Kahourzade, A. Tahir, and N. Fernando, "Propulsion System of Electric Vehicles: Review," in *2021 Australasian Universities Power Engineering Conference*, 2021.

[7] J. C. Son, J. Y. Kim, J. W. Choi, D. K. Lim, and H. K. Yeo, "Performance Enhancement of the IPMSM for HEV Applications Using Grain-Oriented Electrical Steel and Design Optimization," *IEEE Access*, vol. 10, pp. 46599–46607, 2022, doi: 10.1109/ACCESS.2022.3170896.

[8] M. Scarfogliero *et al.*, "Lithium-ion batteries for electric vehicles: A review on aging models for vehicle-to-grid services," in *2018 International Conference of Electrical and Electronic Technologies for Automotive*, 2018, pp. 1–6.

[9] W. Cai, X. Wu, M. Zhou, Y. Liang, and Y. Wang, "Review and Development of Electric Motor Systems and Electric Powertrains for New Energy Vehicles," *Automot. Innov.*, vol. 4, no. 1, pp. 3–22, 2021.

[10] A. Salem and M. Narimani, "A review on multiphase drives for automotive traction applications," *IEEE Trans. Transp. Electrif.*, vol. 5, no. 4, pp. 1329–1348, 2019.

[11] S. Shivam, R. Singh, R. R. Singh, and R. Sitharthan, "A Review on Power Electronics and Drives in Electric Propulsion System," in *IOP Conference Series: Materials Science and Engineering*, 2020, vol. 937, no. 1, p. 12050.

[12] N. Kunihiro, T. Todaka, and M. Enokizono, "Loss evaluation of an induction motor model core by vector magnetic characteristic analysis," *IEEE Trans. Magn.*, vol. 47, no. 5, pp. 1098–1101, 2011, doi: 10.1109/TMAG.2010.2072910.

[13] Y. Yamashita and Y. Okamoto, "Design Optimization of Synchronous Reluctance Motor for Reducing Iron Loss and Improving Torque Characteristics Using Topology Optimization Based on the Level-Set Method," *IEEE Trans. Magn.*, vol. 56, no. 3, pp. 2–5, 2020, doi: 10.1109/TMAG.2019.2954468.

[14] J. Du, X. Wang, and H. Lv, "Optimization of Magnet Shape Based on Efficiency Map of IPMSM for EVs," *IEEE Trans. Appl. Supercond.*, vol. 26, no. 7, pp. 1–7, Oct. 2016, doi: 10.1109/TASC.2016.2594834.

[15] S. Kahourzade, A. Mahmoudi, W. L. Soong, N. Ertugrul, and G. Pellegrino, "Estimation of PM Machine Efficiency Maps from Limited Data," *IEEE Trans. Ind. Appl.*, vol. 56, no. 3, pp. 2612–2621, 2020, doi: 10.1109/TIA.2020.2979975.

[16] S. Kahourzade, A. Mahmoudi, W. L. Soong, N. Ertugrul, and G. Pellegrino, "Estimation of PM Machine Efficiency Maps from Limited Experimental Data," in *2018 IEEE Energy Conversion Congress and Exposition (ECCE)*, Sep. 2018, pp. 4315–4322, doi: 10.1109/ECCE.2018.8557885.

[17] S. Kahourzade, A. Mahmoudi, W. L. Soong, S. Ferrari, and G. Pellegrino, "Correction of finite-element calculated efficiency map using experimental measurements," *2019 IEEE Energy Convers. Congr. Expo. ECCE 2019*, pp. 5629–5636, 2019, doi: 10.1109/ECCE.2019.8913235.

[18] J. Larminie and J. Lowry, *Electric vehicle technology explained*. John Wiley & Sons, 2012.

[19] E. Dlala *et al.*, "Efficiency map simulations for an interior PM motor with experimental comparison and investigation of magnet size reduction," in *2013 International Electric*

Machines & Drives Conference, May 2013, pp. 23–29, doi: 10.1109/IEMDC.2013.6556124.
[20] E. Roshandel, A. Mahmoudi, S. Kahourzade, and W. Soong, "Analytical Model and Performance Prediction of Induction Motors using Subdomain Technique," in *2020 IEEE Energy Conversion Congress and Exposition (ECCE)*, 2020, pp. 3815–3822, doi: 10.1109/ECCE44975.2020.9235826.
[21] A. Mahmoudi, W. L. Soong, G. Pellegrino, and E. Armando, "Efficiency maps of electrical machines," in *2015 IEEE Energy Conversion Congress and Exposition (ECCE)*, Sep. 2015, pp. 2791–2799, doi: 10.1109/ECCE.2015.7310051.
[22] J. F. Gieras, *Permanent magnet motor technology: design and applications*. CRC press, 2002.
[23] P. Roy *et al.*, "Thermal Representation of Interior and Surface Mounted PMSMs for Electric Vehicle Application," in *IECON 2019-45th Annual Conference of the IEEE Industrial Electronics Society*, 2019, vol. 1, pp. 1411–1416.
[24] E. Roshandel, S. M. Gheasaryan, and S. M. Saghaian-Nejad, "A novel control strategy based on fuzzy logic for switched reluctance machine in battery charging mode," in *Conference Proceedings of 2015 2nd International Conference on Knowledge-Based Engineering and Innovation, KBEI 2015*, 2016, doi: 10.1109/KBEI.2015.7436149.
[25] A. Mahmoudi, S. Kahourzade, E. Roshandel, and W. L. Soong, "Axial-Flux Synchronous Reluctance Motors: Introduction of a New Machine," in *2020 IEEE International Conference on Power Electronics, Drives and Energy Systems (PEDES)*, 2020, pp. 1–6.
[26] E. Roshandel, M. M. Namazi, A. Rashidi, S. M. Saghaian-Nejad, and J.-W. Ahn, "SSC strategy for SRG to achieve maximum power with minimum current ripple in battery charging," *IET Electr. Power Appl.*, vol. 11, no. 7, 2017, doi: 10.1049/iet-epa.2016.0770.
[27] Z. Yang, F. Shang, I. P. Brown, and M. Krishnamurthy, "Comparative study of interior permanent magnet, induction, and switched reluctance motor drives for EV and HEV applications," *IEEE Trans. Transp. Electrif.*, vol. 1, no. 3, pp. 245–254, 2015, doi: 10.1109/TTE.2015.2470092.
[28] A. Rassolkin, H. Heidari, A. Kallaste, T. Vaimann, J. P. Acedo, and E. Romero-Cadaval, "Efficiency Map Comparison of Induction and Synchronous Reluctance Motors," *2019 26th Int. Work. Electr. Drives Improv. Effic. Electr. Drives, IWED 2019 - Proc.*, pp. 26–29, 2019, doi: 10.1109/IWED.2019.8664334.
[29] E. Roshandel, A. Mahmoudi, S. Kahourzade, and W. L. Soong, "Design and Analysis of Small Aspect-Ratio Switched Reluctance Motor," in *2020 IEEE International Conference on Power Electronics, Drives and Energy Systems (PEDES)*, 2020, pp. 1–6.
[30] Z. Q. Zhu, W. Q. Chu, and Y. Guan, "Quantitative comparison of electromagnetic performance of electrical machines for HEVs/EVs," *CES Trans. Electr. Mach. Syst.*, vol. 1, no. 1, pp. 37–47, 2017.
[31] D. U. Thakar and R. A. Patel, "Comparison of Advance and Conventional Motors for Electric Vehicle Application," in *2019 3rd International Conference on Recent Developments in Control, Automation & Power Engineering (RDCAPE)*, 2019, pp. 137–142.
[32] J. Goss, M. Popescu, and D. Staton, "A comparison of an interior permanent magnet and copper rotor induction motor in a hybrid electric vehicle application," in *2013 International Electric Machines & Drives Conference*, 2013, pp. 220–225.
[33] C. Zhou, X. Huang, Y. Fang, and L. Wu, "Comparison of PMSMs with different rotor structures for EV application," in *2018 XIII International Conference on Electrical Machines (ICEM)*, 2018, pp. 609–614.
[34] M. Ehsani, Y. Gao, S. Longo, and K. M. Ebrahimi, *Modern electric, hybrid electric, and fuel cell vehicles*. CRC press, 2018.
[35] K. Bayar, "Performance comparison of electric-vehicle drivetrain architectures from a vehicle dynamics perspective," *Proc. Inst. Mech. Eng. Part D J. Automob. Eng.*, vol. 234, no. 4, pp. 915–935, 2020.
[36] Q. Chen, C. Liao, A. Ouyang, X. Li, and Q. Xiao, "Research and development of in-wheel motor driving technology for electric vehicles," *Int. J. Electr. Hybrid Veh.*, vol. 8, no. 3, pp. 242–254, 2016.
[37] M. Roozegar and J. Angeles, "The optimal gear-shifting for a multi-speed transmission system for electric vehicles," *Mech. Mach. Theory*, vol. 116, pp. 1–13, 2017.

[38] M. S. R. Mousavi and B. Boulet, “Modeling, simulation and control of a seamless two-speed automated transmission for electric vehicles,” in *2014 American control conference*, 2014, pp. 3826–3831.
[39] S. B. Bhat, S. P. Nikam, and B. G. Fernandes, “Design and analysis of ferrite based permanent magnet motor for electric assist bicycle,” in *2014 International Conference on Electrical Machines (ICEM)*, 2014, pp. 106–111.
[40] H. Neudorfer, N. Wicker, and A. Binder, “Comparison of three different electric powertrains for the use in hybrid electric vehicles,” in *4th IET International Conference on Power Electronics, Machines and Drives (PEMD 2008)*, 2008, no. 538 CP, pp. 510–514, doi: 10.1049/cp:20080574.
[41] H. Laitinen, A. Lajunen, and K. Tammi, “Improving electric vehicle energy efficiency with two-speed gearbox,” in *2017 IEEE Vehicle Power and Propulsion Conference (VPPC)*, 2017, pp. 1–5.
[42] A. Morozov, K. Humphries, T. Zou, S. Martins, and J. Angeles, “Design and optimization of a drivetrain with two-speed transmission for electric delivery step van,” in *2014 IEEE International Electric Vehicle Conference (IEVC)*, 2014, pp. 1–8.
[43] A. Sorniotti *et al.*, “Analysis and simulation of the gearshift methodology for a novel two-speed transmission system for electric powertrains with a central motor,” *Proc. Inst. Mech. Eng. Part D J. Automob. Eng.*, vol. 226, no. 7, pp. 915–929, 2012.
[44] Y. Fang, J. Ruan, P. Walker, and N. Zhang, “Comparison of effect on motor among 2-, 3-and 4-speed transmission in electric vehicle,” in *2017 IEEE International Conference on Mechatronics (ICM)*, 2017, pp. 455–459.
[45] C.-M. Chang and J.-C. Siao, “Performance Analysis of EV Powertrain system with/without transmission,” *World Electr. Veh. J.*, vol. 4, no. 3, pp. 629–634, 2010.
[46] J. W. Shin, H. Y. Jung, and S. H. Oh, “A study on 2-speed transmission of electric vehicle by using inventogram,” *J. Mech. Sci. Technol.*, vol. 31, no. 5, pp. 2543–2548, 2017.
[47] P. G. Anselma and G. Belingardi, “Comparing battery electric vehicle powertrains through rapid component sizing,” *Int. J. Electr. Hybrid Veh.*, vol. 11, no. 1, pp. 36–58, 2019.
[48] J. W. Shin, J. O. Kim, J. Y. Choi, and S. H. Oh, “Design of 2-speed transmission for electric commercial vehicle,” *Int. J. Automot. Technol.*, vol. 15, no. 1, pp. 145–150, 2014.
[49] L. Zhang, X. Zhang, Z. Han, J. Chen, and J. Liu, “A novel multi-parameter coordinated shift control strategy for an automated manual transmission based on fuzzy inference,” *Proc. Inst. Mech. Eng. Part D J. Automob. Eng.*, vol. 231, no. 5, pp. 684–699, 2017.
[50] C.-Y. Tseng and C.-H. Yu, “Advanced shifting control of synchronizer mechanisms for clutchless automatic manual transmission in an electric vehicle,” *Mech. Mach. Theory*, vol. 84, pp. 37–56, 2015.
[51] C.-H. Yu and C.-Y. Tseng, “Research on gear-change control technology for the clutchless automatic–manual transmission of an electric vehicle,” *Proc. Inst. Mech. Eng. Part D J. Automob. Eng.*, vol. 227, no. 10, pp. 1446–1458, 2013.
[52] J. Pentzer and S. Brennan, “Investigation of the effect of continuously variable transmissions on ground robot powertrain efficiency,” in *2012 American Control Conference (ACC)*, 2012, pp. 4245–4250.
[53] T. Hofman, M. Steinbuch, R. Van Druten, and A. Serrarens, “Rule-based energy management strategies for hybrid vehicles,” *Int. J. Electr. Hybrid Veh.*, vol. 1, no. 1, pp. 71–94, 2007.
[54] N. Srivastava and I. Haque, “A review on belt and chain continuously variable transmissions (CVT): Dynamics and control,” *Mech. Mach. theory*, vol. 44, no. 1, pp. 19–41, 2009.
[55] Q. Ren, D. A. Crolla, and A. Morris, “Effect of transmission design on Electric Vehicle (EV) performance,” in *2009 IEEE vehicle power and propulsion conference*, 2009, pp. 1260–1265.
[56] I. W. Y. Arta, Z. Arifin, and A. Yudantoko, “The Effect of CVT Rollers Weight on Power and Torque of Honda Vario 125 Engine in Garuda Hybrid Car 2017,” in *Journal of Physics: Conference Series*, 2020, vol. 1700, no. 1, p. 12064.
[57] C.-T. Chung, C.-H. Wu, and Y.-H. Hung, “A design methodology for selecting energy-efficient compound split e-CVT hybrid systems with planetary gearsets based on electric circulation,” *Energy*, vol. 230, p. 120732, 2021.
[58] N. S. Patil, E. Malekipour, and H. El-Mounayri, “Development of a Cone CVT by SDPD and

Topology Optimization," SAE Technical Paper, 2019.
[59] P. Spanoudakis, N. C. Tsourveloudis, L. Doitsidis, and E. S. Karapidakis, "Experimental research of transmissions on electric vehicles' energy consumption," *Energies*, vol. 12, no. 3, p. 388, 2019.
[60] J. Ruan, P. Walker, and N. Zhang, "Comparison of power consumption efficiency of CVT and multi-speed transmissions for electric vehicle," *Int. J. Automot. Eng.*, vol. 9, no. 4, pp. 268–275, 2018.
[61] J. Ruan, P. Walker, and N. Zhang, "A comparative study energy consumption and costs of battery electric vehicle transmissions," *Appl. Energy*, vol. 165, pp. 119–134, 2016, doi: https://doi.org/10.1016/j.apenergy.2015.12.081.
[62] A. Yildiz and M. A. Özel, "A Comparative Study of Energy Consumption and Recovery of Autonomous Fuel-Cell Hydrogen–Electric Vehicles Using Different Powertrains Based on Regenerative Braking and Electronic Stability Control System," *Appl. Sci.*, vol. 11, no. 6, p. 2515, 2021.
[63] R. Mistry, W. R. Finley, and T. Gaerke, "Comparison of IEC and NEMA Requirements to Ensure Proper Specification and Design of Induction Motors & Generators for Global use-part 2: Copyright Material IEEE, Paper No. PCIC-2017-04," in *2018 IEEE Petroleum and Chemical Industry Technical Conference (PCIC)*, 2018, pp. 29–38.
[64] I. E. Commission, "IEC 60034-1: rotating electrical machines, Part 1: Rating and performance." 2010.
[65] I. E. Commission, "Rotating electrical machines–Part 2-1: Standard 430 methods for determining losses and efficiency from tests (excluding machines for traction vehicles), Standard No," IEC 60034-2-1, International Electrotechnical Commission, 2014.
[66] A. T. I, "Energy Efficiency Regulation of Electric Motors," Sydney. [Online]. Available: https://www.energyrating.gov.au/sites/default/files/2020-01/motors_issues_paper_-_january_2020_0.pdf.
[67] W. Gu, X. Zhu, L. Quan, and Y. Du, "Design and optimization of permanent magnet brushless machines for electric vehicle applications," *Energies*, vol. 8, no. 12, pp. 13996–14008, 2015.
[68] A. Mahmoudi, N. A. Rahim, and W. P. Hew, "An analytical complementary FEA tool for optimizing of axial-flux permanent-magnet machines," *Int. J. Appl. Electromagn. Mech.*, vol. 37, no. 1, pp. 19–34, 2011.
[69] B. Dianati, S. Kahourzade, and A. Mahmoudi, "Axial-Flux Induction Motors for Electric Vehicles," in *2019 IEEE Vehicle Power and Propulsion Conference (VPPC)*, Oct. 2019, pp. 1–6, doi: 10.1109/VPPC46532.2019.8952278.
[70] E. Roshandel, S. M. Gheasaryan, and S. M. Saghaian-Nejad, "A novel control strategy based on fuzzy logic for switched reluctance machine in battery charging mode," in *2015 2nd International Conference on Knowledge-Based Engineering and Innovation (KBEI)*, 2015, pp. 813–818.
[71] B. Sarlioglu, C. T. Morris, D. Han, and S. Li, "Benchmarking of electric and hybrid vehicle electric machines, power electronics, and batteries," in *2015 Intl Aegean Conference on Electrical Machines & Power Electronics (ACEMP), 2015 Intl Conference on Optimization of Electrical & Electronic Equipment (OPTIM) & 2015 Intl Symposium on Advanced Electromechanical Motion Systems (ELECTROMOTION)*, 2015, pp. 519–526, doi: 10.1109/OPTIM.2015.7426993.
[72] E. Roshandel, A. Mahmoudi, S. Kahourzade, A. Yazdani, and G. M. Shafiullah, "Losses in efficiency maps of electric vehicles: An overview," *Energies*, vol. 14, no. 22, 2021, doi: 10.3390/en14227805.
[73] S. Kahourzade, A. Mahmoudi, W. L. Soong, N. Ertugrul, and G. Pellegrino, "Estimation of PM Machine Efficiency Maps From Limited Data," *IEEE Trans. Ind. Appl.*, vol. 56, no. 3, pp. 2612–2621, May 2020, doi: 10.1109/TIA.2020.2979975.
[74] K. Yamazaki and A. Abe, "Loss investigation of interior permanent-magnet motors considering carrier harmonics and magnet eddy currents," *IEEE Trans. Ind. Appl.*, vol. 45, no. 2, pp. 659–665, 2009, doi: 10.1109/TIA.2009.2013550.
[75] K. Yamazaki and S. Kuramochi, "Additional harmonic losses of induction motors by PWM inverters: Comparison between result of finite element method and IEC/TS 60034," *Proc.* -

2012 20th Int. Conf. Electr. Mach. ICEM 2012, vol. 1, no. Im, pp. 1552–1558, 2012, doi: 10.1109/ICElMach.2012.6350085.

[76] K. Yamazaki and S. Watari, "Loss analysis of permanent-magnet motor considering carrier harmonics of PWM inverter using combination of 2-D and 3-D finite-element method," *IEEE Trans. Magn.*, vol. 41, no. 5, pp. 1980–1983, 2005, doi: 10.1109/TMAG.2005.846278.

[77] R. Wrobel, P. H. Mellor, M. Popescu, and D. A. Staton, "Power loss analysis in thermal design of electrical machines," *Proc. - 2015 IEEE Work. Electr. Mach. Des. Control Diagnosis, WEMDCD 2015*, pp. 118–126, 2015, doi: 10.1109/WEMDCD.2015.7194519.

[78] C. C. Chan, K. T. Chau, J. Z. Jiang, W. Xia, M. Zhu, and R. Zhang, "Novel permanent magnet motor drives for electric vehicles," *IEEE Trans. Ind. Electron.*, vol. 43, no. 2, pp. 331–339, Apr. 1996, doi: 10.1109/41.491357.

[79] R. Palka, P. Paplicki, M. Wardach, and M. Bonislawski, "Hybrid excited machine for electric vehicles propulsion," *2018 Int. Symp. Electr. Mach. SME 2018*, pp. 21–24, 2018, doi: 10.1109/ISEM.2018.8442700.

[80] X. Liu, Z. Q. Zhu, and D. Wu, "Evaluation of efficiency optimized variable flux reluctance machine for EVs/HEVs by comparing with interior PM machine," in *2014 17th International Conference on Electrical Machines and Systems (ICEMS)*, Oct. 2014, pp. 2648–2654, doi: 10.1109/ICEMS.2014.7013948.

[81] J. An and A. Binder, "Design of interior permanent magnet synchronous machine for two-drive-transmission," *Electr. Syst. Aircraft, Railw. Sh. Propulsion, ESARS*, vol. 2015-May, pp. 1–6, 2015, doi: 10.1109/ESARS.2015.7101507.

[82] R. Vincent, V. Emmanuel, G. Lauric, and G. Laurent, "Optimal sizing of an electrical machine using a magnetic circuit model: Application to a hybrid electrical vehicle," *IET Electr. Syst. Transp.*, vol. 6, no. 1, pp. 27–33, 2016, doi: 10.1049/iet-est.2015.0008.

[83] J. S. Hsu *et al.*, "16,000-RPM Interior Permanent Magnet Reluctance Machine with Brushless Field Excitation," in *2008 IEEE Industry Applications Society Annual Meeting*, Oct. 2008, pp. 1–6, doi: 10.1109/08IAS.2008.67.

[84] M. Ciampolini, G. Ferrara, L. Fazzini, L. Pugi, and L. Berzi, "Simplified Approach for Developing Efficiency Maps of High-Speed PMSM Machines for Use in EAT Systems Starting from Single-Point Data," 2020.

[85] R. B. Sepe, J. M. Miller, and A. R. Gale, "Intelligent efficiency mapping of a hybrid electric vehicle starter/alternator using fuzzy logic," in *Gateway to the New Millennium. 18th Digital Avionics Systems Conference. Proceedings (Cat. No.99CH37033)*, 1999, vol. B.6-6 vol., pp. 8.B.2-1-8.B.2-8, doi: 10.1109/DASC.1999.822007.

[86] D. F. Gosden, "Drive system design for an electric vehicle based on alternative motor types," in *Proceedings of 5th International Conference on Power Electronics and Variable-Speed Drives*, 1994, vol. 1994, no. 399, pp. 710–715, doi: 10.1049/cp:19941052.

[87] H. Mokhtari and E. Tara, "Efficiency map of a Switched Reluctance Motor using Finite Element Method in vehicular applications," in *2007 7th Internatonal Conference on Power Electronics*, Oct. 2007, pp. 644–649, doi: 10.1109/ICPE.2007.4692467.

[88] S. Yajima, M. Takemoto, Y. Tanaka, A. Chiba, and T. Fukao, "Total Efficiency of a Deeply Buried Permanent Magnet Type Bearingless Motor Equipped with 2-pole Motor Windings and 4-pole Suspension Windings," in *2007 IEEE Power Engineering Society General Meeting*, Jun. 2007, pp. 1–7, doi: 10.1109/PES.2007.386109.

[89] R. Liu, H. Zhao, P. Zheng, X. Gan, R. Zhao, and B. Kou, "Experimental evaluation of a radial-radial-flux compound-structure permanent-magnet synchronous machine used for HEVs," in *2008 14th Symposium on Electromagnetic Launch Technology*, 2008, pp. 1–5.

[90] P. Zheng, R. Liu, Q. Wu, C. Tong, and Z. Tang, "Compound-structure permanent-magnet synchronous machine used for HEVs," *Proc. 11th Int. Conf. Electr. Mach. Syst. ICEMS 2008*, pp. 2916–2920, 2008, [Online]. Available: https://ieeexplore.ieee.org/document/4771252.

[91] S. Kahourzade, A. Mahmoudi, W. L. Soong, S. Ferrari, and G. Pellegrino, "Correction of Finite-Element Calculated Efficiency Map using Experimental Measurements," in *2019 IEEE Energy Conversion Congress and Exposition (ECCE)*, Sep. 2019, pp. 5629–5636, doi: 10.1109/ECCE.2019.8913235.

[92] H. C. Jung, D. J. Kim, S. Y. Jung, and D. Lee, "Optimization Method to Maximize Efficiency

Map of a Drive Motor with Electrical Winding Changeover Technique for Hybrid EV," *IEEE Trans. Appl. Supercond.*, vol. 30, no. 4, 2020, doi: 10.1109/TASC.2020.2987016.

[93] Q. Li, T. Fan, X. Wen, X. Tai, Y. Li, and G. Zhang, "Modeling of the efficiency MAP of surface permanent magnet machine for electrical vehicles," *2013 Int. Conf. Electr. Mach. Syst. ICEMS 2013*, pp. 1222–1225, 2013, doi: 10.1109/ICEMS.2013.6713361.

[94] S. A. Rahman and A. M. Knight, "Performance and core loss of concentrated winding IPMSM with different core treatment," in *2014 IEEE Energy Conversion Congress and Exposition (ECCE)*, Sep. 2014, pp. 5587–5594, doi: 10.1109/ECCE.2014.6954166.

[95] W. Q. Chu *et al.*, "Comparison of electrically excited and interior permanent magnet machines for hybrid electric vehicle application," in *2014 17th International Conference on Electrical Machines and Systems (ICEMS)*, Oct. 2014, pp. 401–407, doi: 10.1109/ICEMS.2014.7013504.

[96] W. Q. Chu, Z. Q. Zhu, J. Zhang, X. Liu, D. A. Stone, and M. P. Foster, "Investigation on operational envelops and efficiency maps of electrically excited machines for electrical vehicle applications," *IEEE Trans. Magn.*, vol. 51, no. 4, 2015, doi: 10.1109/TMAG.2014.2359008.

[97] T. Kato, M. Minowa, H. Hijikata, K. Akatsu, and R. D. Lorenz, "Design Methodology for Variable Leakage Flux IPM for Automobile Traction Drives," *IEEE Trans. Ind. Appl.*, vol. 51, no. 5, pp. 3811–3821, 2015, doi: 10.1109/TIA.2015.2439642.

[98] K. Zhou, A. Ivanco, Z. Filipi, and H. Hofmann, "Finite-Element-Based Computationally Efficient Scalable Electric Machine Model Suitable for Electrified Powertrain Simulation and Optimization," *IEEE Trans. Ind. Appl.*, vol. 51, no. 6, pp. 4435–4445, 2015, doi: 10.1109/TIA.2015.2451094.

[99] A. Mahmoudi, W. L. Soong, G. Pellegrino, and E. Armando, "Loss Function Modeling of Efficiency Maps of Electrical Machines," *IEEE Trans. Ind. Appl.*, vol. 53, no. 5, pp. 4221–4231, Sep. 2017, doi: 10.1109/TIA.2017.2695443.

[100] S. Stipetic and J. Goss, "Calculation of efficiency maps using scalable saturated flux-linkage and loss model of a synchronous motor," *Proc. - 2016 22nd Int. Conf. Electr. Mach. ICEM 2016*, pp. 1380–1386, 2016, doi: 10.1109/ICELMACH.2016.7732704.

[101] S. Stipetic, J. Goss, D. Zarko, and M. Popescu, "Calculation of Efficiency Maps Using a Scalable Saturated Model of Synchronous Permanent Magnet Machines," *IEEE Trans. Ind. Appl.*, vol. 54, no. 5, pp. 4257–4267, 2018, doi: 10.1109/TIA.2018.2837672.

[102] P. Dück and B. Ponick, "A novel iron-loss-model for permanent magnet synchronous machines in traction applications," *2016 Int. Conf. Electr. Syst. Aircraft, Railw. Sh. Propuls. Road Veh. Int. Transp. Electrif. Conf. ESARS-ITEC 2016*, 2016, doi: 10.1109/ESARS-ITEC.2016.7841432.

[103] S. B. Shah and A. Arkkio, "Efficiency map prediction of flux switching machine," *2015 18th Int. Conf. Electr. Mach. Syst. ICEMS 2015*, no. 2, pp. 1490–1493, 2016, doi: 10.1109/ICEMS.2015.7385276.

[104] K. Hruska and P. Dvorak, "The validity range of PMSM efficiency map regarding its equivalent circuit parameters," 2016, pp. 1–7, [Online]. Available: https://ieeexplore.ieee.org/document/7827817.

[105] M. Ruba, F. Jurca, and C. Martis, "Analysis of synchronous reluctance machine for light electric vehicle applications," *2016 Int. Symp. Power Electron. Electr. Drives, Autom. Motion, SPEEDAM 2016*, pp. 1138–1143, 2016, doi: 10.1109/SPEEDAM.2016.7525841.

[106] C. Lu, S. Ferrari, and G. Pellegrino, "Two Design Procedures for PM Synchronous Machines for Electric Powertrains," *IEEE Trans. Transp. Electrif.*, vol. 3, no. 1, pp. 98–107, 2017, doi: 10.1109/TTE.2016.2646738.

[107] M. H. Mohammadi and D. A. Lowther, "A Computational Study of Efficiency Map Calculation for Synchronous AC Motor Drives Including Cross-Coupling and Saturation Effects," *IEEE Trans. Magn.*, vol. 53, no. 6, 2017, doi: 10.1109/TMAG.2017.2661994.

[108] K. Li, S. Cui, A. Bouscayrol, and M. Hecquet, "Analytical derivation of efficiency map of an induction machine for electric vehicle applications," *2018 IEEE Veh. Power Propuls. Conf. VPPC 2018 - Proc.*, no. 1, pp. 1–6, 2019, doi: 10.1109/VPPC.2018.860495000.

[109] D. B. Pinhal and Di. Gerling, "Performance Map Calculation of a Salient-Pole Synchronous Motor with Hairpin Winding," *IEEE Int. Symp. Ind. Electron.*, vol. 2019-June, pp. 359–365, 2019, doi: 10.1109/ISIE.2019.8781339.

[110] A. He, C. Zhou, X. Huang, J. Shen, Y. Fang, and Q. Lu, “Evaluation of fractional slot concentrated winding permanent magnet synchronous machine for electric vehicle application,” *2019 IEEE Int. Electr. Mach. Drives Conf. IEMDC 2019*, no. 51877196, pp. 988–992, 2019, doi: 10.1109/IEMDC.2019.8785223.

[111] G. Bacco, C. Babetto, M. Bonfante, M. Carbonieri, and N. Bianchi, “Efficiency Maps Computation and Comparison Including Thermal Limits,” *2019 IEEE Energy Convers. Congr. Expo. ECCE 2019*, pp. 4846–4852, 2019, doi: 10.1109/ECCE.2019.8912730.

[112] A. G. Gonzalez, A. K. Jha, Z. Li, P. Upadhayay, and P. Rasmussen, “Validation of efficiency maps of an outer rotor surface mounted permanent magnet machine for evaluation of recyclability of magnets,” *2018 IEEE Int. Magn. Conf. INTERMAG 2018*, pp. 1–6, 2018, doi: 10.1109/INTMAG.2018.8508142.

[113] P. N. Materu and R. Krishnan, “Estimation of switched reluctance motor losses,” *IEEE Trans. Ind. Appl.*, vol. 28, no. 3, pp. 668–679, 1992, doi: 10.1109/28.137456.

[114] C. Lopez-Torres, C. Colls, A. Garcia, J. R. Riba, and L. Romeral, “Development of a Behavior Maps Tool to Evaluate Drive Operational Boundaries and Optimization Assessment of PMa-SynRMs,” *IEEE Trans. Veh. Technol.*, vol. 67, no. 8, pp. 6861–6871, 2018, doi: 10.1109/TVT.2018.2823339.

[115] J. Sepe, C. M. Morrison, J. M. Miller, and A. R. Gale, “High efficiency operation of a hybrid electric vehicle starter/generator over road profiles,” *Conf. Rec. - IAS Annu. Meet. (IEEE Ind. Appl. Soc.*, vol. 2, no. C, pp. 921–925, 2001, doi: 10.1109/ias.2001.955562.

[116] G. Pugsley, C. Chillet, A. Fonseca, and A.-L. Bui-Van, “New modeling methodology for induction machine efficiency mapping for hybrid vehicles,” in *IEEE International Electric Machines and Drives Conference, 2003. IEMDC’03.*, 2003, vol. 2, pp. 776–781, doi: 10.1109/IEMDC.2003.1210324.

[117] T. Finken, M. Hombitzer, and K. Hameyer, “Study and comparison of several permanent-magnet excited rotor types regarding their applicability in electric vehicles,” in *2010 Emobility - Electrical Power Train*, Nov. 2010, no. c, pp. 1–7, doi: 10.1109/EMOBILITY.2010.5668074.

[118] Z. Li and A. Miotto, “Concentrated-winding fractional-slot synchronous surface PM motor design based on efficiency map for in-wheel application of electric vehicle,” in *2011 IEEE Vehicle Power and Propulsion Conference*, Sep. 2011, pp. 1–8, doi: 10.1109/VPPC.2011.6043087.

[119] F. Stanislav, B. Jan, and L. Jiri, “Analytical derivation of induction machine efficiency map,” in *4th International Conference on Power Engineering, Energy and Electrical Drives*, May 2013, no. May, pp. 1206–1210, doi: 10.1109/PowerEng.2013.6635784.

[120] S. M. Lukic and A. Emado, “Modeling of electric machines for automotive applications using efficiency maps,” in *Proceedings: Electrical Insulation Conference and Electrical Manufacturing and Coil Winding Technology Conference (Cat. No.03CH37480)*, 2003, no. Figure I, pp. 543–550, doi: 10.1109/EICEMC.2003.1247945.

[121] Y. Guan, Z. Q. Zhu, I. A. A. Afinowi, J. C. Mipo, and P. Farah, “Calculation of torque-speed characteristic of induction machine for electrical vehicle application using analytical method,” *Proc. - 2014 Int. Conf. Electr. Mach. ICEM 2014*, pp. 2715–2721, 2014, doi: 10.1109/ICELMACH.2014.6960572.

[122] M. Novak, J. Novak, and Z. Novak, “Methodology for efficiency mapping of permanent magnet synchronous motors,” *Int. Conf. Electical Drives Power Electron.*, vol. 2017-Octob, pp. 205–210, Oct. 2017, doi: 10.1109/EDPE.2017.8123234.

[123] M. Novak, J. Novak, Z. Novak, J. Chysky, and O. Sivkov, “Efficiency mapping of a 100 kW PMSM for traction applications,” *IEEE Int. Symp. Ind. Electron.*, pp. 290–295, 2017, doi: 10.1109/ISIE.2017.8001262.

[124] M. Golzar, H. Van Khang, M. M. Hubert Choux, and A. M. Midtbo Versland, “Experimental investigation of efficiency map for an inverter-fed surface-mount permanent magnet synchronous motor,” *8th Int. Conf. Renew. Energy Res. Appl. ICRERA 2019*, pp. 551–556, 2019, doi: 10.1109/ICRERA47325.2019.8996549.

[125] M. Novak and J. Novak, “Test Setup with a Permanent Magnet Synchronous Machine for Efficiency Maps of an Electric Vehicle,” *Proc. - 2018 23rd Int. Conf. Electr. Mach. ICEM 2018*, pp. 1698–1703, 2018, doi: 10.1109/ICELMACH.2018.8507249.

[126] T. Endress and M. Bragard, “Recording of efficiency-maps of low-power electric drive systems using a flexible Matlab-based test bench,” *58th Annu. Int. Sci. Confererence Power Electr. Eng. Riga Tech. Univ. RTUCON 2017 - Proc.*, vol. 2017-Novem, pp. 1–5, 2017, doi: 10.1109/RTUCON.2017.8124775.
[127] Qianfan Zhang and Xiaofei Liu, “Permanent Magnetic Synchronous Motor and drives applied on a mid-size hybrid electric car,” in *2008 IEEE Vehicle Power and Propulsion Conference*, Sep. 2008, pp. 1–5, doi: 10.1109/VPPC.2008.4677807.
[128] A. M. Bazzi and P. T. Krein, “Comparative evaluation of machines for electric and hybrid vehicles based on dynamic operation and loss minimization,” in *2010 IEEE Energy Conversion Congress and Exposition*, Sep. 2010, pp. 3345–3351, doi: 10.1109/ECCE.2010.5617782.
[129] M. Takeno, S. Ogasawara, A. Chiba, M. Takemoto, and N. Hoshi, “Power and efficiency measurements and design improvement of a 50kW switched reluctance motor for Hybrid Electric Vehicles,” in *2011 IEEE Energy Conversion Congress and Exposition*, Sep. 2011, pp. 1495–1501, doi: 10.1109/ECCE.2011.6063958.
[130] M. Morandin, M. Ferrari, and S. Bolognani, “Power-Train Design and Performance of a Hybrid Motorcycle Prototype,” *IEEE Trans. Ind. Appl.*, vol. 51, no. 3, pp. 2216–2226, 2015, doi: 10.1109/TIA.2014.2360955.
[131] M. Morandin, M. Ferrari, and S. Bolognani, “Design and performance of a power train for mild-hybrid motorcycle prototype,” in *2013 International Electric Machines & Drives Conference*, May 2013, pp. 1–8, doi: 10.1109/IEMDC.2013.6556121.
[132] F. Aguilera, P. M. De La Barrera, and C. H. De Angelo, “Induction machine models for efficiency studies in EV design applications,” *2012 10th IEEE/IAS Int. Conf. Ind. Appl. INDUSCON 2012*, no. 1, pp. 1–7, 2012, doi: 10.1109/INDUSCON.2012.6452497.
[133] F. Aguilera, P. M. de la Barrera, and C. H. De Angelo, “Selection of Induction Machine Models for Efficiency Evaluation in Electric Vehicles,” *IEEE Lat. Am. Trans.*, vol. 11, no. 1, pp. 334–340, Feb. 2013, doi: 10.1109/TLA.2013.6502826.
[134] S. Williamson, M. Lukic, and A. Emadi, “Comprehensive drive train efficiency analysis of hybrid electric and fuel cell vehicles based on motor-controller efficiency modeling,” *IEEE Trans. Power Electron.*, vol. 21, no. 3, pp. 730–740, May 2006, doi: 10.1109/TPEL.2006.872388.
[135] P. J. Kollmeyer, J. D. McFarland, and T. M. Jahns, “Comparison of class 2a truck electric vehicle drivetrain losses for single- and two-speed gearbox systems with IPM traction machines,” pp. 1501–1507, 2016, doi: 10.1109/iemdc.2015.7409261.
[136] G. Haines, N. Ertugrul, and W. L. Soong, “Autonomously obtaining system efficiency maps from motor drive systems,” *Proc. IEEE Int. Conf. Ind. Technol.*, vol. 2019-Febru, pp. 231–236, 2019, doi: 10.1109/ICIT.2019.8755199.
[137] M. Ade and A. Binder, “Modeling the drive train for two parallel Hybrid Electric Vehicles in MATLAB/Simulink,” in *2009 IEEE Vehicle Power and Propulsion Conference*, Sep. 2009, pp. 592–600, doi: 10.1109/VPPC.2009.5289795.
[138] Wang Xiaoxu, Wang Sibo, Chen Mingjian, and Zhao Huichao, “Efficiency testing technology and evaluation of the electric vehicle motor drive system,” in *2014 IEEE Conference and Expo Transportation Electrification Asia-Pacific (ITEC Asia-Pacific)*, Aug. 2014, pp. 1–5, doi: 10.1109/ITEC-AP.2014.6941059.
[139] C. Depature, W. Lhomme, A. Bouscayrol, P. Sicard, and L. Boulon, “Efficiency Map of the Traction System of an Electric Vehicle from an On-Road Test Drive,” in *2014 IEEE Vehicle Power and Propulsion Conference (VPPC)*, Oct. 2014, pp. 1–6, doi: 10.1109/VPPC.2014.7007056.
[140] L. Sun, M. Cheng, H. Wen, and L. Song, “Motion Control and Performance Evaluation of a Magnetic-Geared Dual-Rotor Motor in Hybrid Powertrain,” *IEEE Trans. Ind. Electron.*, vol. 64, no. 3, pp. 1863–1872, 2017, doi: 10.1109/TIE.2016.2627018.
[141] C. T. Krasopoulos, M. E. Beniakar, and A. G. Kladas, “Multicriteria PM motor design based on ANFIS evaluation of EV driving cycle efficiency,” *IEEE Trans. Transp. Electrif.*, vol. 4, no. 2, pp. 525–535, 2018, doi: 10.1109/TTE.2018.2810707.
[142] M. Cosovic and S. Smaka, “Design of initial topology of interior permanent magnet

synchronous machine for hybrid electric vehicle," *Proc. - 2015 IEEE Int. Electr. Mach. Drives Conf. IEMDC 2015*, pp. 1658–1664, 2016, doi: 10.1109/IEMDC.2015.7409286.
[143] S. Kahourzade, A. Mahmoudi, W. L. Soong, and G. Pellegrino, "A Practical Method for Estimating Efficiency Maps for PM Machines Using a Reduced Number of Tests," in *2019 IEEE Vehicle Power and Propulsion Conference (VPPC)*, Oct. 2019, pp. 1–6, doi: 10.1109/VPPC46532.2019.8952286.
[144] "Ansys® Electromagnetics." 2021, [Online]. Available: https://www.ansys.com/academic/terms-and-conditions.
[145] X. Nan and C. R. Sullivan, "An improved calculation of proximity-effect loss in high-frequency windings of round conductors," *PESC Rec. - IEEE Annu. Power Electron. Spec. Conf.*, vol. 2, pp. 853–860, 2003, doi: 10.1109/pesc.2003.1218168.
[146] C. P. Steinmetz, "On the law of hysteresis," *Proc. IEEE*, vol. 72, no. 2, pp. 197–221, 1984.
[147] J. Li, T. Abdallah, and C. R. Sullivan, "Improved calculation of core loss with nonsinusoidal waveforms," in *Conference Record of the 2001 IEEE Industry Applications Conference. 36th IAS Annual Meeting (Cat. No. 01CH37248)*, 2001, vol. 4, pp. 2203–2210.
[148] K. Venkatachalam, C. R. Sullivan, T. Abdallah, and H. Tacca, "Accurate prediction of ferrite core loss with nonsinusoidal waveforms using only Steinmetz parameters," in *2002 IEEE Workshop on Computers in Power Electronics, 2002. Proceedings.*, 2002, pp. 36–41.
[149] R. H. Pry and C. P. Bean, "Calculation of the energy loss in magnetic sheet materials using a domain model," *J. Appl. Phys.*, vol. 29, no. 3, pp. 532–533, 1958.
[150] G. Bertotti, "Physical interpretation of eddy current losses in ferromagnetic materials. I. Theoretical considerations," *J. Appl. Phys.*, vol. 57, no. 6, pp. 2110–2117, 1985.
[151] G. Bertotti, "Physical interpretation of eddy current losses in ferromagnetic materials. II. Analysis of experimental results," *J. Appl. Phys.*, vol. 57, no. 6, pp. 2118–2126, 1985.
[152] W. A. Pluta, "Some properties of factors of specific total loss components in electrical steel," *IEEE Trans. Magn.*, vol. 46, no. 2, pp. 322–325, 2010.
[153] B. Dianati, S. Kahourzade, and A. Mahmoudi, "Analytical Design of Axial-Flux Induction Motors," in *2019 IEEE Vehicle Power and Propulsion Conference (VPPC)*, Oct. 2019, pp. 1–6, doi: 10.1109/VPPC46532.2019.8952172.
[154] Z.-Q. Zhu *et al.*, "Evaluation of iron loss models in electrical machines," *IEEE Trans. Ind. Appl.*, vol. 55, no. 2, pp. 1461–1472, 2018.
[155] M. Sippola and R. E. Sepponen, "Accurate prediction of high-frequency power-transformer losses and temperature rise," *IEEE Trans. Power Electron.*, vol. 17, no. 5, pp. 835–847, 2002.
[156] H. N. Ji, Z. W. Lan, Z. Y. Xu, H. W. Zhang, J. X. Yu, and M. Q. Li, "Effects of second milling time on temperature dependence and improved Steinmetz parameters of low loss MnZn power ferrites," *IEEE Trans. Appl. Supercond.*, vol. 24, no. 5, pp. 1–4, 2014.
[157] Z. Zhao, X. Hu, Z. Bi, M. Xu, X. Ma, and P. Zhang, "Calculation of core loss under distorted flux density with minor hysteresis loops for laminated steel structure," *AIP Adv.*, vol. 10, no. 7, p. 75001, 2020.
[158] I. D. Mayergoyz, *Mathematical models of hysteresis and their applications*. Academic Press, 2003.
[159] D. C. Jiles and D. L. Atherton, "Theory of ferromagnetic hysteresis," *J. Magn. Magn. Mater.*, vol. 61, no. 1–2, pp. 48–60, 1986.
[160] L. R. Dupre, R. Van Keer, and J. A. A. Melkebeek, "An iron loss model for electrical machines using the Preisach theory," *IEEE Trans. Magn.*, vol. 33, no. 5, pp. 4158–4160, 1997.
[161] A. Benabou, S. Clenet, and F. Piriou, "Comparison of Preisach and Jiles–Atherton models to take into account hysteresis phenomenon for finite element analysis," *J. Magn. Magn. Mater.*, vol. 261, no. 1–2, pp. 139–160, 2003.
[162] E. Roshandel, A. Mahmoudi, S. Kahourzade, and W. L. Soong, "Saturation Consideration in Modeling of the Induction Machine Using Subdomain Technique to Predict Performance," *IEEE Trans. Ind. Appl.*, vol. 58, no. 1, pp. 261–272, Jan. 2022, doi: 10.1109/TIA.2021.3125915.
[163] Ansys Motor-CAD, "Electric Machine Design Software." 2021, [Online]. Available: https://www.ansys.com/products/electronics/ansys-motor-cad.
[164] JMAG, "JMAG: simulation technology for electromechanical design." JAPAN, 2021,

[Online]. Available: https://www.jmag-international.com/wp-content/uploads/products/pdf/catalog_en.pdf.
[165] J. Corporation, "JMAG version 12 user's manual solver," Osaka/ 2-2-4 Tosabori; Nishi-ku; Osaka; 550-0001 Japan, 2013.
[166] A. Krings, S. Nategh, A. Stening, H. Grop, O. Wallmark, and J. Soulard, "Measurement and modeling of iron losses in electrical machines," in *5th International Conference Magnetism and Metallurgy WMM'12, June 20th to 22nd, 2012, Ghent, Belgium*, 2012, pp. 101–119.
[167] S. Kahourzade, A. Mahmoudi, E. Roshandel, and Z. Cao, "Optimal design of Axial-Flux Induction Motors based on an improved analytical model," *Energy*, vol. 237, p. 121552, 2021, doi: https://doi.org/10.1016/j.energy.2021.121552.
[168] Z. Cao, A. Mahmoudi, S. Kahourzade, and W. Soong, "Surface Permanent Magnet Machines: A Comparative Study (4-pole vs. 40-pole motor)," in *2020 IEEE International Conference on Power Electronics, Drives and Energy Systems (PEDES)*, 2020, pp. 1–6.
[169] P. Naderi, M. Heidary, and M. Vahedi, "Performance analysis of ladder-secondary-linear induction motor with two different secondary types using Magnetic Equivalent Circuit," *ISA Trans.*, vol. 103, pp. 355–365, 2020.
[170] F. Tao, L. Jian, W. Xuhui, and L. Xiaofeng, "A new sizing equation and it's application in electrical machine design," in *2011 International Conference on Electric Information and Control Engineering*, 2011, pp. 3890–3893.
[171] B. Dianati, S. Kahourzade, and A. Mahmoudi, "Optimization of Axial-Flux Induction Motors for the Application of Electric Vehicles Considering Driving Cycles," *IEEE Trans. Energy Convers.*, vol. 35, no. 3, pp. 1–1, 2020, doi: 10.1109/TEC.2020.2976625.
[172] G. J. Park, B. Son, S. Y. Jung, and Y. J. Kim, "Reducing computational time strategy for estimating core loss with spatial and temporal periodicity," *2016 IEEE Transp. Electrif. Conf. Expo, Asia-Pacific, ITEC Asia-Pacific 2016*, no. 2, pp. 460–464, 2016, doi: 10.1109/ITEC-AP.2016.7512998.
[173] W. Eberle, Z. Zhang, Y.-F. Liu, and P. C. Sen, "A simple analytical switching loss model for buck voltage regulators," in *2008 Twenty-Third Annual IEEE Applied Power Electronics Conference and Exposition*, 2008, pp. 36–42.
[174] E. Gurpinar and B. Ozpineci, "Loss analysis and mapping of a sic mosfet based segmented two-level three-phase inverter for ev traction systems," in *2018 IEEE Transportation Electrification Conference and Expo (ITEC)*, 2018, pp. 1046–1053.
[175] M. Thoben, D. Siepe, and K. Kriegel, "Use of Power electronics for HEV at elevated temperature," *Braunschweiger Hybridsymposium*, 2008.
[176] X. Wu, R. Wrobel, P. H. Mellor, and C. Zhang, "A computationally efficient PM power loss derivation for surface-mounted brushless AC PM machines," in *2014 International Conference on Electrical Machines (ICEM)*, 2014, pp. 17–23.
[177] X. Wu, R. Wrobel, P. H. Mellor, and C. Zhang, "A computationally efficient PM power loss mapping for brushless AC PM machines with surface-mounted PM rotor construction," *IEEE Trans. Ind. Electron.*, vol. 62, no. 12, pp. 7391–7401, 2015.
[178] S. T. Lundmark and P. R. Fard, "Two-dimensional and three-dimensional core and magnet loss modeling in a radial flux and a transverse flux PM traction motor," *IEEE Trans. Ind. Appl.*, vol. 53, no. 3, pp. 2028–2039, 2017.
[179] S. Kahourzade, N. Ertugrul, and W. L. Soong, "Loss analysis and efficiency improvement of an axial-flux PM amorphous magnetic material machine," *IEEE Trans. Ind. Electron.*, vol. 65, no. 7, pp. 5376–5383, 2017.
[180] Z. Cao, A. Mahmoudi, S. Kahourzade, W. L. Soong, and J. R. Summers, "A Comparative Study of Axial-Flux versus Radial-Flux Induction Machines," in *2020 IEEE International Conference on Power Electronics, Drives and Energy Systems (PEDES)*, 2020, pp. 1–6.
[181] A. Mlot, M. Łukaniszyn, and M. Korkosz, "Magnet loss analysis for a high-speed PM machine with segmented PM and modified tooth-tips shape," *Arch. Electr. Eng.*, vol. 65, no. 4, 2016.
[182] J.-W. Lim, Y.-J. Kim, and S.-Y. Jung, "Numerical investigation on permanent-magnet eddy current loss and harmonic iron loss for pm skewed ipmsm," *J. Magn.*, vol. 16, no. 4, pp. 417–422, 2011.
[183] P. Su, W. Hua, M. Hu, Z. Chen, M. Cheng, and W. Wang, "Analysis of PM eddy current loss

in rotor-PM and stator-PM flux-switching machines by air-gap field modulation theory," *IEEE Trans. Ind. Electron.*, vol. 67, no. 3, pp. 1824–1835, 2019.
[184] A. Rahideh and T. Korakianitis, "Analytical magnetic field distribution of slotless brushless permanent magnet motors–Part I. Armature reaction field, inductance and rotor eddy current loss calculations," *IET Electr. Power Appl.*, vol. 6, no. 9, pp. 628–638, 2012.
[185] S. Kanazawa, N. Takahashi, and T. Kubo, "Measurement and analysis of AC loss of NdFeB sintered magnet," *Electr. Eng. Japan*, vol. 154, no. 4, pp. 8–15, 2006.
[186] G. Yang and C. Zhang, "Computationally Efficient PM Power Loss Mapping for PWM Drive Surface-Mounted Permanent Magnet Synchronous Machines," *Appl. Sci.*, vol. 11, no. 7, p. 3246, 2021.
[187] G. Burnand, D. M. Araujo, C. Koechli, and Y. Perriard, "Validation by measurements of a windage losses model for very-high-speed machines," in *2017 20th International Conference on Electrical Machines and Systems (ICEMS)*, Aug. 2017, pp. 1–4, doi: 10.1109/ICEMS.2017.8056273.
[188] R. Wrobel, G. Vainel, C. Copeland, T. Duda, D. Staton, and P. H. Mellor, "Investigation of mechanical loss components and heat transfer in an axial-flux PM machine," *IEEE Trans. Ind. Appl.*, vol. 51, no. 4, pp. 3000–3011, 2015.
[189] Y. ITOH, K. SAKAI, and Y. MAKINO, "In-wheel motor system," *NTN Tech. Rev.*, no. 79, 2011.
[190] B.-R. Höhn, K. Michaelis, and M. Hinterstoißer, "Optimization of gearbox efficiency," *Goriva i Maz.*, vol. 48, no. 4, p. 462, 2009.
[191] P. Lynwander, *Gear drive systems: Design and application*. CRC Press, 2019.
[192] J.-W. Biermann, "Measurement system for CV joint efficiency," *SAE Trans.*, pp. 1724–1730, 1999.
[193] F. M. F. Novo, M. M. de Souza, J. Savoy, and M. A. do Carmo Silva, "Analysis of the vibration modes of an automotive propeller shaft using FEM and analytical models," SAE Technical Paper, 2012.
[194] S. Foulard, S. Rinderknecht, M. Ichchou, and J. Perret-Liaudet, "Automotive drivetrain model for transmission damage prediction," *Mechatronics*, vol. 30, pp. 27–54, 2015.
[195] V. Ripard, "Tribological characterization of greased drive-shaft: Evaluation of constant velocity joint durability." Université de Lyon, 2019.
[196] M. Cirelli, O. Giannini, M. Cera, F. De Simoni, P. P. Valentini, and E. Pennestrì, "The mechanical efficiency of the Rzeppa transmission joint," *Mech. Mach. Theory*, vol. 164, p. 104418, 2021.
[197] H. Lohse-Busch *et al.*, "Automotive fuel cell stack and system efficiency and fuel consumption based on vehicle testing on a chassis dynamometer at minus 18° C to positive 35° C temperatures," *Int. J. Hydrogen Energy*, vol. 45, no. 1, pp. 861–872, 2020.
[198] Y.-L. Lei, Y.-Z. Jia, Y. Fu, K. Liu, Y. Zhang, and Z.-J. Liu, "Car fuel economy simulation forecast method based on CVT efficiencies measured from bench test," *Chinese J. Mech. Eng.*, vol. 31, no. 1, pp. 1–16, 2018.
[199] J. Ruan, P. D. Walker, J. Wu, N. Zhang, and B. Zhang, "Development of continuously variable transmission and multi-speed dual-clutch transmission for pure electric vehicle," *Adv. Mech. Eng.*, vol. 10, no. 2, p. 1687814018758223, 2018.
[200] B. Fu, Y. Zhou, C. Cao, Q. Li, and F. Zhang, "Research on Power Loss of Continuously Variable Transmission Based on Driving Cycles," in *IOP Conference Series: Earth and Environmental Science*, 2018, vol. 108, no. 5, p. 52054.
[201] M. S. Jneid, P. Harth, and P. Ficzere, "In-wheel-motor electric vehicles AND their associated drivetrains," *Int. J. Traffic Transp. Eng.*, vol. 10, no. 4, 2020.
[202] M. Nell, J. Lenz, and K. Hameyer, "Scaling laws for the FE solutions of induction machines," *Arch. Electr. Eng.*, vol. 68, no. 3, 2019.
[203] Y. Wan, S. Cui, S. Wu, and L. Song, "Electromagnetic design and losses analysis of a high-speed permanent magnet synchronous motor with toroidal windings for pulsed alternator," *Energies*, vol. 11, no. 3, 2018, doi: 10.3390/en11030562.
[204] T. Raminosoa and T. Aytug, "Impact of ultra-conducting winding on the power density and performance of non-heavy rare earth traction motors," *2019 IEEE Int. Electr. Mach. Drives*

Conf. IEMDC 2019, pp. 2107–2114, 2019, doi: 10.1109/IEMDC.2019.8785295.
[205] C. Axtmann, J. Kolb, and M. Braum, "Efficiency map computation of arbitrary converter topologies in EV powertrains," in *2016 IEEE 2nd Annual Southern Power Electronics Conference (SPEC)*, Dec. 2016, pp. 1–6, doi: 10.1109/SPEC.2016.7846079.
[206] H. Kärkkäinen, L. Aarniovuori, M. Niemelä, and J. Pyrhönen, "Converter-fed induction motor losses in different operating points," in *2016 18th European Conference on Power Electronics and Applications (EPE'16 ECCE Europe)*, 2016, pp. 1–8.
[207] H. Karkkainen, L. Aarniovuori, M. Niemela, and J. Pyrhonen, "Converter-fed induction motor efficiency: Practical applicability of IEC methods," *IEEE Ind. Electron. Mag.*, vol. 11, no. 2, pp. 45–57, 2017.
[208] R. E. Machines—Part, "Part 2-3: Specific Test Methods for Determining Losses and Efficiency of Converter-Fed AC Induction Motors," *IEC TS*, pp. 60032–60034, 2013.
[209] A. Boglietti, A. Cavagnino, M. Cossale, A. Tenconi, and S. Vaschetto, "Efficiency determination of converter-fed induction motors: Waiting for the IEC 60034–2–3 standard," in *2013 IEEE Energy Conversion Congress and Exposition*, 2013, pp. 230–237.
[210] G. R. Slemon and X. Liu, "Core losses in permanent magnet motors," *IEEE Trans. Magn.*, vol. 26, no. 5, pp. 1653–1655, 1990.
[211] N. Yogal, C. Lehrmann, and M. Henke, "Magnetic loss measurement of surface-mounted permanent magnet synchronous machines used in explosive environments," *J. Eng.*, vol. 2019, no. 17, pp. 3760–3765, 2019.
[212] G. G. Haines, "Integrated Motor System Estimation Using Efficiency Maps." University of Adelaide, Adelaide, 2020.
[213] Y. Loayza, A. Reinap, and M. Alakula, "Performance and efficiency evaluation of FPGA controlled IPMSM under dynamic loading," in *8th IEEE Symposium on Diagnostics for Electrical Machines, Power Electronics & Drives*, Sep. 2011, pp. 550–555, doi: 10.1109/DEMPED.2011.6063677.
[214] K. Li, S. Han, S. Cui, and A. Bouscayrol, "Sizing of modular cascade machines system for electric vehicles," *IEEE Trans. Veh. Technol.*, vol. 68, no. 2, pp. 1278–1287, 2019, doi: 10.1109/TVT.2018.2886402.
[215] E. Roshandel, A. Mahmoudi, S. Kahourzade, and W. L. Soong, "Efficiency Maps of Electrical Machines: A Tutorial Review," *IEEE Trans. Ind. Appl.*, vol. 59, no. 2, pp. 1263–1272, Mar. 2023, doi: 10.1109/TIA.2022.3210077.
[216] S. Ferrari, P. Ragazzo, G. Dilevrano, and G. Pellegrino, "Flux-Map Based FEA Evaluation of Synchronous Machine Efficiency Maps," in *2021 IEEE Workshop on Electrical Machines Design, Control and Diagnosis (WEMDCD)*, 2021, pp. 76–81.
[217] M. Popescu, D. M. Ionel, A. Boglietti, A. Cavagnino, C. Cossar, and M. I. McGilp, "A general model for estimating the laminated steel losses under PWM voltage supply," *IEEE Trans. Ind. Appl.*, vol. 46, no. 4, pp. 1389–1396, 2010, doi: 10.1109/TIA.2010.2049810.
[218] M. Carbonieri, N. Bianchi, and L. Alberti, "A Fast and Direct Analysis of Three-Phase Induction Motors Using Finite Element," in *2018 XIII International Conference on Electrical Machines (ICEM)*, 2018, pp. 18–24, doi: 10.1109/ICELMACH.2018.8506897.
[219] O. Stiscia, S. Rubino, S. Vaschetto, A. Cavagnino, and A. Tenconi, "Accurate Induction Machines Efficiency Mapping Computed by Standard Test Parameters," *IEEE Trans. Ind. Appl.*, 2022.
[220] M. Carbonieri, N. Bianchi, and L. Alberti, "Induction motor mapping using rotor field-oriented analysis technique," *2019 IEEE Energy Convers. Congr. Expo. ECCE 2019*, pp. 2321–2328, 2019, doi: 10.1109/ECCE.2019.8912787.
[221] H. V. Khang, A. K. Repo, and A. Arkkio, "Resistive loss identification of an inverter-fed deep-bar induction motor," *SPEEDAM 2010 - Int. Symp. Power Electron. Electr. Drives, Autom. Motion*, no. 2, pp. 105–110, 2010, doi: 10.1109/SPEEDAM.2010.5544776.
[222] M. Carbonieri, N. Bianchi, and L. Alberti, "Direct analysis of induction motor using finite element," in *2018 IEEE Energy Conversion Congress and Exposition (ECCE)*, 2018, pp. 277–283.
[223] G. Von Pfingsten, S. Steentjes, and K. Hameyer, "Operating Point Resolved Loss Calculation Approach in Saturated Induction Machines," *IEEE Trans. Ind. Electron.*, vol. 64, no. 3, pp.

2538–2546, Mar. 2017, doi: 10.1109/TIE.2016.2597761.
[224] P. H. Mellor, R. Wrobel, and D. Holliday, “A computationally efficient iron loss model for brushless AC machines that caters for rated flux and field weakened operation,” in *2009 IEEE International Electric Machines and Drives Conference*, May 2009, pp. 490–494, doi: 10.1109/IEMDC.2009.5075251.
[225] K. Zhou, J. Pries, and H. Hofmann, “Computationally Efficient 3-D Finite-Element-Based Dynamic Thermal Models of Electric Machines,” *IEEE Trans. Transp. Electrif.*, vol. 1, no. 2, pp. 138–149, 2015, doi: 10.1109/TTE.2015.2456429.
[226] K. Selvam and S. Sahoo, “Effect of temperature rise in magnetic materials and deviation of torque in permanent magnet synchronous motor,” in *2016 XXII International Conference on Electrical Machines (ICEM)*, Sep. 2020, vol. 2220, no. May 2020, p. 110015, doi: 10.1063/5.0001534.
[227] O. Bilgin and F. A. Kazan, “The effect of magnet temperature on speed, current and torque in PMSMs,” in *2016 XXII International Conference on Electrical Machines (ICEM)*, Sep. 2016, no. 1, pp. 2080–2085, doi: 10.1109/ICELMACH.2016.7732809.
[228] C. Lungoci and D. Stoia, “TEMPERATURE EFFECTS ON TORQUE PRODUCTION AND EFFICIENCY OF MOTORS WITH NdFeB,” *Rev. Roum. Sci. Techn.-Électrotechn. Énerg*, vol. 53, no. 1, pp. 445–454, 2008.
[229] Z. Q. Zhu *et al.*, “Evaluation of Iron Loss Models in Electrical Machines,” *IEEE Trans. Ind. Appl.*, vol. 55, no. 2, pp. 1461–1472, 2019, doi: 10.1109/TIA.2018.2880674.
[230] G. Du, N. Huang, H. He, G. Lei, and J. Zhu, “Parameter Design for a High-Speed Permanent Magnet Machine under Multiphysics Constraints,” *IEEE Trans. Energy Convers.*, vol. 35, no. 4, pp. 2025–2035, 2020, doi: 10.1109/TEC.2020.3000054.
[231] S. Kim and D. P. Neikirk, “Compact equivalent circuit model for the skin effect,” in *1996 IEEE MTT-S International Microwave Symposium Digest*, 1996, vol. 3, pp. 1815–1818.
[232] I. Boldea and S. A. Nasar, *The induction machines design handbook*. CRC press, 2018.
[233] M. Carbonieri, L. DI Leonardo, N. Bianchi, M. Tursini, M. A. Villani, and M. Popescu, “Cage Losses in Induction Motors Considering Harmonics: A New Finite Element Procedure and Comparison with the Time-Domain Approach,” *IEEE Trans. Ind. Appl.*, vol. 58, no. 2, pp. 1931–1940, 2022, doi: 10.1109/TIA.2021.3138366.
[234] R. Bojoi, E. Armando, M. Pastorelli, and K. Lang, “Efficiency and loss mapping of AC motors using advanced testing tools,” in *2016 XXII International Conference on Electrical Machines (ICEM)*, Sep. 2016, vol. 1, pp. 1043–1049, doi: 10.1109/ICELMACH.2016.7732654.
[235] K. Stockman, S. Dereyne, D. Vanhooydonck, W. Symens, J. Lemmens, and W. Deprez, “Iso efficiency contour measurement results for variable speed drives,” in *The XIX International Conference on Electrical Machines - ICEM 2010*, Sep. 2010, pp. 1–6, doi: 10.1109/ICELMACH.2010.5608035.
[236] T. J. E. Miller and D. A. Staton, *Electric Machine Design using SPEED and Motor-CAD*. Motor Design, 2013.
[237] K. Kiyota and A. Chiba, “Design of switched reluctance motor competitive to 60-kW IPMSM in third-generation hybrid electric vehicle,” *IEEE Trans. Ind. Appl.*, vol. 48, no. 6, pp. 2303–2309, 2012.
[238] T. A. Lipo, “Introduction to AC Machine Design,” *Introd. to AC Mach. Des.*, pp. 193–250, 2017, doi: 10.1002/9781119352181.
[239] S. Li, Y. Li, W. Choi, and B. Sarlioglu, “High-Speed Electric Machines: Challenges and Design Considerations,” *IEEE Trans. Transp. Electrif.*, vol. 2, no. 1, pp. 2–13, 2016, doi: 10.1109/TTE.2016.2523879.
[240] R. Qu and T. A. Lipo, “Sizing Equations and Power Density Evaluation of Dual-Rotor, Radial-Flux, Toroidally Wound, Permanent-Magnet Machines,” *IEEE Trans. Ind. Appl.*, vol. 39, no. 2, 2004.
[241] D. M. Ionel and M. Popescu, “Finite-element surrogate model for electric machines with revolving field-application to IPM motors,” *IEEE Trans. Ind. Appl.*, vol. 46, no. 6, pp. 2424–2433, 2010, doi: 10.1109/TIA.2010.2073671.
[242] I. Eroglu, L. Horlbeck, M. Lienkamp, and C. M. Hackl, “Increasing the overall efficiency of induction motors for BEV by using the overload potential through downsizing,” *2017 IEEE*

Int. Electr. Mach. Drives Conf. IEMDC 2017, 2017, doi: 10.1109/IEMDC.2017.8002040.
[243] B. Hannon, P. Sergeant, and L. Dupré, "2-D Analytical Subdomain Model of a Slotted PMSM With Shielding Cylinder," *IEEE Trans. Magn.*, vol. 50, no. 7, 2014, doi: 10.1109/TMAG.2014.2309325.
[244] Z. Djelloul-Khedda, K. Boughrara, R. Ibtiouen, and F. Dubas, "NonLinear analytical calculation of magnetic field and torque of switched reluctance machines," *Proc. 2016 Int. Conf. Electr. Sci. Technol. Maghreb, Cist. 2016*, vol. 53, no. 7, 2017, doi: 10.1109/CISTEM.2016.8066773.
[245] W. Tong, S. Wang, S. Dai, S. Wu, and R. Tang, "A quasi-three-dimensional magnetic equivalent circuit model of a double-sided axial flux permanent magnet machine considering local saturation," *IEEE Trans. Energy Convers.*, vol. 33, no. 4, pp. 2163–2173, 2018, doi: 10.1109/TEC.2018.2853265.
[246] M. Amrhein and P. T. Krein, "Induction machine modeling approach based on 3-D magnetic equivalent circuit framework," *IEEE Trans. Energy Convers.*, vol. 25, no. 2, pp. 339–347, 2010.
[247] B. O. Tak and J. S. Ro, "Analysis and design of an axial flux permanent magnet motor for in-wheel system using a novel analytical method combined with a numerical method," *IEEE Access*, vol. 8, pp. 203994–204011, 2020, doi: 10.1109/ACCESS.2020.3036666.
[248] C. Lu, S. Ferrari, and G. Pellegrino, "Two Design Procedures for PM Synchronous Machines for Electric Powertrains," *IEEE Trans. Transp. Electrif.*, vol. 3, no. 1, pp. 98–107, 2017, doi: 10.1109/TTE.2016.2646738.
[249] J. Lai, J. Li, and T. Xiao, "Design of a Compact Axial Flux Permanent Magnet Machine for Hybrid Electric Vehicle," *IEEE Trans. Ind. Electron.*, vol. 68, no. 8, pp. 6630–6639, 2021, doi: 10.1109/TIE.2020.3008358.
[250] J. Du, X. Wang, and H. Lv, "Optimization of Magnet Shape Based on Efficiency Map of IPMSM for EVs," *IEEE Trans. Appl. Supercond.*, vol. 26, no. 7, 2016, doi: 10.1109/TASC.2016.2594834.
[251] H.-C. Jung, G.-J. Park, D.-J. Kim, and S.-Y. Jung, "Optimal design and validation of IPMSM for maximum efficiency distribution compatible to energy consumption areas of HD-EV," *IEEE Trans. Magn.*, vol. 53, no. 6, pp. 1–4, 2017.
[252] H. Chen and C. H. T. Lee, "Parametric Sensitivity Analysis and Design Optimization of an Interior Permanent Magnet Synchronous Motor," *IEEE Access*, vol. 7, pp. 159918–159929, 2019, doi: 10.1109/ACCESS.2019.2950773.
[253] S. G. Min and B. Sarlioglu, "Analysis and Comparative Study of Flux Weakening Capability in Fractional-Slot Concentrated Windings," *IEEE Trans. Energy Convers.*, vol. 33, no. 3, pp. 1025–1035, 2018, doi: 10.1109/TEC.2017.2781718.
[254] G. Choi and G. Bramerdorfer, "Comprehensive Design and Analysis of an Interior Permanent Magnet Synchronous Machine for Light-Duty Passenger EVs," *IEEE Access*, vol. 10, pp. 819–831, 2022, doi: 10.1109/ACCESS.2021.3137897.
[255] Y. Yang *et al.*, "Design and Comparison of Interior Permanent Magnet Motor Topologies for Traction Applications," *IEEE Trans. Transp. Electrif.*, vol. 3, no. 1, pp. 86–97, 2017, doi: 10.1109/TTE.2016.2614972.
[256] X. Liu, H. Chen, J. Zhao, and A. Belahcen, "Research on the Performances and Parameters of Interior PMSM Used for Electric Vehicles," *IEEE Trans. Ind. Electron.*, vol. 63, no. 6, pp. 3533–3545, 2016, doi: 10.1109/TIE.2016.2524415.
[257] Y. Zhang, W. Cao, S. McLoone, and J. Morrow, "Design and Flux-Weakening Control of an Interior Permanent Magnet Synchronous Motor for Electric Vehicles," *IEEE Trans. Appl. Supercond.*, vol. 26, no. 7, 2016, doi: 10.1109/TASC.2016.2594863.
[258] K. C. Kim, K. Kim, H. J. Kim, and J. Lee, "Demagnetization analysis of permanent magnets according to rotor types of interior permanent magnet synchronous motor," *IEEE Trans. Magn.*, vol. 45, no. 6, pp. 2799–2802, 2009, doi: 10.1109/TMAG.2009.2018661.
[259] P. Gao, X. Sun, D. Gerada, C. Gerada, and X. Wang, "Improved V-shaped interior permanent magnet rotor topology with inward-extended bridges for reduced torque ripple," *IET Electr. Power Appl.*, vol. 14, no. 12, pp. 2404–2411, 2020, doi: 10.1049/iet-epa.2019.0850.
[260] S.-C. Wang, Y.-C. Nien, and S.-M. Huang, "Multi-Objective Optimization Design and

Analysis of V-Shape Permanent Magnet Synchronous Motor," *Energies*, vol. 15, no. 10, p. 3496, 2022, doi: 10.3390/en15103496.
[261] S. Chakraborty, S. V. Nair, and K. Hatua, "Effect of v Angle Variation and Strengthening Rib on Performance Characteristics of IPMSM Motor for Electric Vehicles," *ICPEE 2021 - 2021 1st Int. Conf. Power Electron. Energy*, 2021, doi: 10.1109/ICPEE50452.2021.9358664.
[262] G. Joksimović, E. Levi, A. Kajević, M. Mezzarobba, and A. Tessarolo, "Optimal Selection of Rotor Bar Number for Minimizing Torque and Current Pulsations Due to Rotor Slot Harmonics in Three-Phase Cage Induction Motors," *IEEE Access*, vol. 8, pp. 228572–228585, 2020.
[263] D. Zhang, C. S. Park, and C. S. Koh, "A new optimal design method of rotor slot of three-phase squirrel cage induction motor for NEMA class D speed-torque characteristic using multi-objective optimization algorithm," *IEEE Trans. Magn.*, vol. 48, no. 2, pp. 879–882, 2012.
[264] T. T. To, E. Roshandel, A. Mahmoudi, Z. Cao, and S. Kahourzade, "Optimization of IM Rotor Bars Inclination Angle using Analytical Model in Free FEA Software," in *2021 IEEE Energy Conversion Congress and Exposition (ECCE)*, 2021, pp. 4119–4126.
[265] S. Pao-La-Or, P., Peaiyoung, S., Kulworawanichpong, T., & Sujitjorn, "Effects of the Geometry of the Rotor Slots on the Mechanical Vibration of Three-phase Induction Motors," *Proc. 7th WSEAS Int. Conf. Simulation, Model. Optim.*, no. 1, pp. 434–438, 2007.
[266] M. J. Akhtar, R. K. Behera, and S. K. Parida, "Optimized rotor slot shape for squirrel cage induction motor in electric propulsion application," in *2014 IEEE 6th India International Conference on Power Electronics (IICPE)*, 2014, pp. 1–5.
[267] A. Lordoglu, M. O. Gulbahce, and D. A. Kocabas, "A comprehensive disturbing effect analysis of multi-sectional rotor slot geometry for induction machines in electrical vehicles," *IEEE Access*, vol. 9, pp. 49590–49600, 2021, doi: 10.1109/ACCESS.2021.3068821.
[268] Y. Hasegawa, K. Nakamura, and O. Ichinokura, "Optimization of a Switched Reluctance Motor Made of Permendur," *IEEE Trans. Magn.*, vol. 46, no. 6, pp. 1311–1314, Jun. 2010, doi: 10.1109/TMAG.2010.2041903.
[269] Z. Hao, W. Zhou, T. Ji, X. Huang, and C. Zhang, "Multi-Objective Optimization of Double Primary Tubular Permanent Magnet Synchronous Linear Motor in Wide Temperature Range Environment Based on Pareto Front Method," *IEEE Access*, vol. 8, pp. 207193–207203, 2020, doi: 10.1109/ACCESS.2020.3026040.
[270] E. T. Kartal and F. K. Arabul, "A Comparison between IM and IPMSM with Same Stator Core for EV and Performance Analysis of IPMSM," *Avrupa Bilim ve Teknol. Derg.*, no. 38, pp. 165–172, 2022.
[271] J. Kim, H. Kim, J. Bae, D. Kim, J. S. Eo, and K. K. K. Kim, "Economic nonlinear predictive control for real-time optimal energy management of parallel hybrid electric vehicles," *IEEE Access*, vol. 8, pp. 177896–177920, 2020, doi: 10.1109/ACCESS.2020.3027024.
[272] Y. Gai *et al.*, "Cooling of automotive traction motors: Schemes, examples, and computation methods," *IEEE Trans. Ind. Electron.*, vol. 66, no. 3, pp. 1681–1692, 2019, doi: 10.1109/TIE.2018.2835397.
[273] X. Yang, A. Fatemi, T. Nehl, L. Hao, W. Zeng, and S. Parrish, "Comparative Study of Three Stator Cooling Jackets for Electric Machine of Mild Hybrid Vehicle," *IEEE Trans. Ind. Appl.*, vol. 57, no. 2, pp. 1193–1201, 2021, doi: 10.1109/TIA.2020.3046195.
[274] M. Popescu, D. A. Staton, A. Boglietti, A. Cavagnino, D. Hawkins, and J. Goss, "Modern Heat Extraction Systems for Power Traction Machines - A Review," *IEEE Trans. Ind. Appl.*, vol. 52, no. 3, pp. 2167–2175, 2016, doi: 10.1109/TIA.2016.2518132.
[275] N. Boubaker, D. Matt, P. Enrici, F. Nierlich, and G. Durand, "Measurements of iron loss in PMSM stator cores based on CoFe and SiFe lamination sheets and stemmed from different manufacturing processes," *IEEE Trans. Magn.*, vol. 55, no. 1, pp. 1–9, 2019, doi: 10.1109/TMAG.2018.2877995.
[276] J. Rao, Y. Gao, D. Li, and R. Qu, "Performance Analysis of Interior Permanent Magnet Motor Using Overlapping Windings with Fractional Ratio of Slot to Pole Pair," *IEEE Trans. Appl. Supercond.*, vol. 26, no. 7, 2016, doi: 10.1109/TASC.2016.2599206.
[277] M. Soltani, S. Nuzzo, D. Barater, and G. Franceschini, "A Multi-Objective Design

Optimization for a Permanent Magnet Synchronous Machine with Hairpin Winding Intended for Transport Applications," *Electronics*, vol. 10, no. 24, p. 3162, 2021.
[278] J.-W. Chin, K.-S. Cha, M.-R. Park, S.-H. Park, E.-C. Lee, and M.-S. Lim, "High Efficiency PMSM With High Slot Fill Factor Coil for Heavy-Duty EV Traction Considering AC Resistance," *IEEE Trans. Energy Convers.*, vol. 36, no. 2, pp. 883–894, 2021, doi: 10.1109/TEC.2020.3035165.
[279] M. Farahani, E. Gockenbach, H. Borsi, K. Schäfer, and M. Kaufhold, "Behavior of machine insulation systems subjected to accelerated thermal aging test," *IEEE Trans. Dielectr. Electr. Insul.*, vol. 17, no. 5, pp. 1364–1372, 2010, doi: 10.1109/TDEI.2010.5595537.
[280] Y. Yang *et al.*, "Design and comparison of interior permanent magnet motor topologies for traction applications," *IEEE Trans. Transp. Electrif.*, vol. 3, no. 1, pp. 86–97, 2016.
[281] R. Thomas, L. Garbuio, L. Gerbaud, and H. Chazal, "Modeling and design analysis of the Tesla Model S induction motor," in *2020 International Conference on Electrical Machines (ICEM)*, 2020, vol. 1, pp. 495–501.
[282] G. Joksimovic, A. Kajevic, M. Mezzarobba, and A. Tessarolo, "Optimal rotor bars number in four pole cage induction motor with 36 stator slots - Part II: Results," *Proc. - 2020 Int. Conf. Electr. Mach. ICEM 2020*, pp. 509–514, 2020, doi: 10.1109/ICEM49940.2020.9270690.
[283] Yasa Motor, "YASA." https://www.yasa.com/products/.
[284] EMRAX, "Manual for EMRAX Motors / Generators," 2020. [Online]. Available: https://emrax.com/wp-content/uploads/2020/03/manual_for_emrax_motors_version_5.4.pdf.
[285] J. Chang and C. Wang, "Electromagnetic thermal coupling analysis for a novel cooling system of an axial flux hub motor," *IET Electr. Power Appl.*, vol. 16, no. 4, pp. 421–433, 2022, doi: 10.1049/elp2.12164.
[286] T. C Cano *et al.*, "Future of Electrical Aircraft Energy Power Systems: An Architecture Review," *IEEE Trans. Transp. Electrif.*, vol. 7, no. 3, pp. 1915–1929, 2021, doi: 10.1109/TTE.2021.3052106.
[287] N. Chiodetto, N. Bianchi, and L. Alberti, "Improved Analytical Estimation of Rotor Losses in High-Speed Surface-Mounted PM Synchronous Machines," *IEEE Trans. Ind. Appl.*, vol. 53, no. 4, pp. 3548–3556, Jul. 2017, doi: 10.1109/TIA.2017.2693178.
[288] S. Ruoho and A. Arkkio, "Partial demagnetization of permanent magnets in electrical machines caused by an inclined field," *IEEE Trans. Magn.*, vol. 44, no. 7, pp. 1773–1778, 2008.
[289] S. Sjökvist and S. Eriksson, "Experimental verification of a simulation model for partial demagnetization of permanent magnets," *IEEE Trans. Magn.*, vol. 50, no. 12, pp. 1–5, 2014.
[290] J. F. Liu and M. H. Walmer, "Thermal stability and performance data for SmCo 2:17 high-temperature magnets on PPM focusing structures," *IEEE Trans. Electron Devices*, vol. 52, no. 5, pp. 899–902, 2005, doi: 10.1109/TED.2005.845868.
[291] S. N. Lophaven, H. B. Nielsen, and J. Søndergaard, *DACE: a Matlab kriging toolbox*, vol. 2. Citeseer, 2002.
[292] T. M. Jahns, "Flux-Weakening Regime Operation of an Interior Permanent-Magnet Synchronous Motor Drive," *IEEE Trans. Ind. Appl.*, vol. IA-23, no. 4, pp. 681–689, 1987, doi: 10.1109/TIA.1987.4504966.
[293] P. F. Hawley, "Determination of the Mutual Inductance of End Turns of Induction Motors." California Institute of Technology, 1933.
[294] E. Devillers, J. Le Besnerais, T. Lubin, M. Hecquet, and J. P. Lecointe, "A review of subdomain modeling techniques in electrical machines: Performances and applications," *Proc. - 2016 22nd Int. Conf. Electr. Mach. ICEM 2016*, no. July, pp. 86–92, 2016, doi: 10.1109/ICELMACH.2016.7732510.
[295] N. Boules, "Two-dimensional field analysis of cylindrical machines with permanent magnet excitation," *IEEE Trans. Ind. Appl.*, no. 5, pp. 1267–1277, 1984.
[296] E. Bolte and K. Oberretl, "Three-dimensional analysis of linear motor with solid iron secondary," in *International Conference on Electrical Machines (ICEM)*, 1980, pp. 68–75.
[297] D. Zarko, D. Ban, and T. A. Lipo, "Analytical calculation of magnetic field distribution in the slotted air gap of a surface permanent-magnet motor using complex relative air-gap permeance," *IEEE Trans. Magn.*, vol. 42, no. 7, pp. 1828–1837, 2006.

[298] X. Wang, Q. Li, S. Wang, and Q. Li, “Analytical calculation of air-gap magnetic field distribution and instantaneous characteristics of brushless DC motors,” *IEEE Trans. Energy Convers.*, vol. 18, no. 3, pp. 424–432, 2003.
[299] F. Dubas and K. Boughrara, “New scientific contribution on the 2-D subdomain technique in Cartesian coordinates: taking into account of iron parts,” *Math. Comput. Appl.*, vol. 22, no. 1, p. 17, 2017.
[300] F. Dubas and C. Espanet, “Analytical solution of the magnetic field in permanent-magnet motors taking into account slotting effect: No-load vector potential and flux density calculation,” *IEEE Trans. Magn.*, vol. 45, no. 5, pp. 2097–2109, 2009.
[301] Z. Q. Zhu, L. J. Wu, and Z. P. Xia, “An accurate subdomain model for magnetic field computation in slotted surface-mounted permanent-magnet machines,” *IEEE Trans. Magn.*, vol. 46, no. 4, pp. 1100–1115, 2009.
[302] V. Z. Faradonbeh, A. Rahideh, M. M. Ghahfarokhi, E. Amiri, A. D. Aliabad, and G. A. Markadeh, “Analytical Modeling of Slotted, Surface-Mounted Permanent Magnet Synchronous Motors With Different Rotor Frames and Magnet Shapes,” *IEEE Trans. Magn.*, vol. 57, no. 1, pp. 1–13, 2020.
[303] T. Lubin, S. Mezani, and A. Rezzoug, “Analytic calculation of eddy currents in the slots of electrical machines: Application to cage rotor induction motors,” *IEEE Trans. Magn.*, vol. 47, no. 11, pp. 4650–4659, 2011.
[304] K. Boughrara, N. Takorabet, R. Ibtiouen, O. Touhami, and F. Dubas, “Analytical Analysis of Cage Rotor Induction Motors in Healthy, Defective, and Broken Bars Conditions,” *IEEE Trans. Magn.*, vol. 51, no. 2, p. 8200317, 2015, doi: 10.1109/TMAG.2014.2349480.
[305] L. Roubache, K. Boughrara, and R. Ibtiouen, “Analytical electromagnetic analysis of multi-phases cage rotor induction motors in healthy, broken bars and open phases conditions,” *Prog. Electromagn. Res.*, vol. 70, pp. 113–130, 2016.
[306] R. L. J. Sprangers, B. L. J. Gysen, J. J. H. Paulides, J. Waarma, and E. A. Lomonova, “Calculation of induced rotor current in induction motors using a slotted semi-analytical harmonic model,” in *2014 International Conference on Electrical Machines (ICEM)*, 2014, pp. 2709–2714.
[307] R. L. J. Sprangers, J. J. H. Paulides, B. L. J. Gysen, E. A. Lomonova, and J. Waarma, “Electric circuit coupling of a slotted semi-analytical model for induction motors based on harmonic modeling,” in *2014 IEEE Energy Conversion Congress and Exposition (ECCE)*, 2014, pp. 1301–1308.
[308] E. Devillers, J. Le Besnerais, T. Lubin, M. Hecquet, and J.-P. Lecointe, “An improved 2-D subdomain model of squirrel-cage induction machine including winding and slotting harmonics at steady state,” *IEEE Trans. Magn.*, vol. 54, no. 2, pp. 1–12, 2018.
[309] M. Carbonieri, N. Bianchi, and L. Alberti, “Direct Analysis of Three-Phase Induction Motor Considering Rotor Parameters’ Variation and Stator Belt Harmonics Effect,” *IEEE Trans. Ind. Appl.*, vol. 56, no. 4, pp. 3559–3570, 2020.
[310] T. Lubin, S. Mezani, and A. Rezzoug, “2-D exact analytical model for surface-mounted permanent-magnet motors with semi-closed slots,” *IEEE Trans. Magn.*, vol. 47, no. 2 PART 2, pp. 479–492, 2011, doi: 10.1109/TMAG.2010.2095874.
[311] T. YAMAGUCHI, Y. KAWASE, M. SHIBATA, T. FURUKAWA, and H. KAWANO, “3-D finite element analysis of interbar current of V-skewed squirrel-cage induction motor taking into account of contact resistance,” *J. Japan Soc. Appl. Electromagn. Mech.*, vol. 27, no. 1, pp. 146–151, 2019.
[312] Z. Gmyrek, A. Cavagnino, and S. Vaschetto, “FEM analysis of the inter-bar currents in induction motors aimed at estimating contact resistance,” *2019 IEEE Int. Electr. Mach. Drives Conf. IEMDC 2019*, pp. 1532–1538, 2019, doi: 10.1109/IEMDC.2019.8785101.
[313] G. S. Liew, “Analysis and design of single-sided, slotted AMM axial-field permanent magnet machines.” 2009.
[314] D. Troncon, M. Carbonieri, L. Alberti, and N. Bianchi, “Measures and Simulations of Induction Machines Flux Linkage Characteristics Based on Rotor Field Orientation,” *IEEE Trans. Ind. Appl.*, vol. 57, no. 5, pp. 4686–4693, 2021, doi: 10.1109/TIA.2021.3089662.
[315] T.-V. Tran, E. Negre, K. Mikati, P. Pellerey, and B. Assaad, “Optimal Design of TEFC

Induction Machine and Experimental Prototype Testing for City Battery Electric Vehicle," *IEEE Trans. Ind. Appl.*, vol. 56, no. 1, pp. 635–643, Jan. 2020, doi: 10.1109/TIA.2019.2943447.

[316] K. Li, A. Bouscayrol, S. Cui, and Y. Cheng, "A Hybrid Modular Cascade Machines System for Electric Vehicles Using Induction Machine and Permanent Magnet Synchronous Machine," *IEEE Trans. Veh. Technol.*, vol. 70, no. 1, pp. 273–281, 2021, doi: 10.1109/TVT.2020.3047219.

[317] A. Cavagnino, S. Vaschetto, L. Ferraris, Z. Gmyrek, E. Agamloh, and G. Bramerdorfer, "Towards an IE4 efficiency class for induction motors with minimal manufacturer impact," in *2018 IEEE Energy Conversion Congress and Exposition (ECCE)*, 2018, pp. 289–296.

[318] A. G. Sarigiannidis, M. E. Beniakar, and A. G. Kladas, "Fast Adaptive Evolutionary PM Traction Motor Optimization Based on Electric Vehicle Drive Cycle," *IEEE Trans. Veh. Technol.*, vol. 66, no. 7, pp. 5762–5774, Jul. 2017, doi: 10.1109/TVT.2016.2631161.

[319] T. Wu *et al.*, "Multiobjective optimization of a tubular coreless LPMSM based on adaptive multiobjective black hole algorithm," *IEEE Trans. Ind. Electron.*, vol. 67, no. 5, pp. 3901–3910, 2019.

[320] R. C. P. Silva, T. Rahman, M. H. Mohammadi, and D. A. Lowther, "Multiple Operating Points Based Optimization: Application to Fractional Slot Concentrated Winding Electric Motors," *IEEE Trans. Ind. Electron.*, vol. 65, no. 2, pp. 1719–1727, 2018, doi: 10.1109/TIE.2017.2756586.

[321] Q. Wang, F. Zhao, and K. Yang, "Analysis and Optimization of the Axial Electromagnetic Force for an Axial-Flux Permanent Magnet Vernier Machine," *IEEE Trans. Magn.*, vol. 57, no. 2, pp. 7–11, 2021, doi: 10.1109/TMAG.2020.3005216.

[322] K. Diao, X. Sun, G. Bramerdorfer, Y. Cai, G. Lei, and L. Chen, "Design optimization of switched reluctance machines for performance and reliability enhancements: A review," *Renew. Sustain. Energy Rev.*, vol. 168, p. 112785, 2022.

[323] R. C. P. Silva, M. Li, T. Rahman, and D. A. Lowther, "Surrogate-based MOEA/D for electric motor design with scarce function evaluations," *IEEE Trans. Magn.*, vol. 53, no. 6, pp. 1–4, 2017.

[324] Y. Ma, J. Wang, L. Zhou, and K. Shuai, "Surrogate-assisted optimization of a five-phase SPM machine with quasi-trapezoidal PMs," *IEEE Trans. Ind. Electron.*, vol. 69, no. 1, pp. 202–212, 2021.

[325] G. Lei, G. Bramerdorfer, B. Ma, Y. Guo, and J. Zhu, "Robust Design Optimization of Electrical Machines: Multi-Objective Approach," *IEEE Trans. Energy Convers.*, vol. 36, no. 1, pp. 390–401, 2021, doi: 10.1109/TEC.2020.3003050.

[326] G. Watthewaduge, E. Sayed, M. Bakr, A. Emadi, and B. Bilgin, "An optimization study for a switched reluctance motor using magnetic equivalent circuit and space mapping techniques," *2020 IEEE Transp. Electrif. Conf. Expo, ITEC 2020*, no. 3, pp. 1025–1030, 2020, doi: 10.1109/ITEC48692.2020.9161619.

[327] J. Hou, W. Geng, Q. Li, and Z. Zhang, "3-D Equivalent Magnetic Network Modeling and FEA Verification of a Novel Axial-Flux Hybrid-Excitation In-wheel Motor," *IEEE Trans. Magn.*, vol. 57, no. 7, 2021, doi: 10.1109/TMAG.2021.3081830.

[328] J. Gao, L. Dai, and W. Zhang, "Improved genetic optimization algorithm with subdomain model for multi-objective optimal design of SPMSM," *CES Trans. Electr. Mach. Syst.*, vol. 2, no. 1, pp. 160–165, 2020, doi: 10.23919/tems.2018.8326463.

[329] S. A. Mohd Shafri *et al.*, "Design and Optimization of Electromagnetic Torque for a Surface-Mounted PMSM by using Subdomain Model and GA in Electric Vehicle Application," *ICEMS 2021 - 2021 24th Int. Conf. Electr. Mach. Syst.*, pp. 11–16, 2021, doi: 10.23919/ICEMS52562.2021.9634680.

[330] S. P. Emami, E. Roshandel, A. Mahmoudi, and S. Khaourzade, "IPM Motor Optimization for Electric Vehicles Considering Driving Cycles," in *2021 31st Australasian Universities Power Engineering Conference (AUPEC)*, 2021, pp. 1–5.

[331] E. Roshandel, A. Mahmoudi, and S. Kahourzade, "2D Subdomain Model of the Ladder Linear Induction Machine with considering Saturation Effect," *2021 IEEE Energy Convers. Congr. Expo. ECCE 2021 - Proc.*, pp. 4127–4134, 2021, doi: 10.1109/ECCE47101.2021.9595612.

[332] R. L. J. Sprangers, J. J. H. Paulides, B. L. J. Gysen, and E. A. Lomonova, “Magnetic saturation in semi-analytical harmonic modeling for electric machine analysis,” *IEEE Trans. Magn.*, vol. 52, no. 2, pp. 1–10, 2015.
[333] P. Liang, F. Chai, Y. Li, and Y. Pei, “Analytical prediction of magnetic field distribution in spoke-type permanent-magnet synchronous machines accounting for bridge saturation and magnet shape,” *IEEE Trans. Ind. Electron.*, vol. 64, no. 5, pp. 3479–3488, 2016.
[334] N. Flaherty, “Radial flux motors,” *E-mobility Engineering*, 2022. https://www.emobility-engineering.com/radial-flux-motors/.
[335] X. Ding, M. Bhattacharya, and C. Mi, “Simplified Thermal Model of PM Motors in Hybrid Vehicle Applications Taking into Account Eddy Current Loss in Magnets,” *J. Asian Electr. Veh.*, vol. 8, no. 1, pp. 1337–1343, 2010, doi: 10.4130/jaev.8.1337.
[336] S. K. Chowdhury and P. K. Baski, “A simple lumped parameter thermal model for electrical machine of TEFC design,” *2010 Jt. Int. Conf. Power Electron. Drives Energy Syst. PEDES 2010 2010 Power India*, pp. 1–7, 2010, doi: 10.1109/PEDES.2010.5712385.
[337] D. A. Staton and A. Cavagnino, “Convection heat transfer and flow calculations suitable for electric machines thermal models,” *IEEE Trans. Ind. Electron.*, vol. 55, no. 10, pp. 3509–3516, 2008, doi: 10.1109/TIE.2008.922604.
[338] W. Brown and Y. Liu, “Modeling and Simulation of an Electric Vehicle with Independent Rear Motors to Estimate the Fuel Economy during EPA Drive Cycles.,” *Int. J. Veh. Struct. Syst.*, vol. 12, no. 5, 2020.
[339] K.-L. Du and M. N. S. Swamy, “Particle swarm optimization,” in *Search and optimization by metaheuristics*, Springer, 2016, pp. 153–173.
[340] M. A. Jarrahi, E. Roshandel, M. Allahbakhshi, and M. Ahmadi, “Cost-optimal as a tool for helping in designing distribution transformer using particle swarm optimization,” *COMPEL - Int. J. Comput. Math. Electr. Electron. Eng.*, vol. 38, no. 2, pp. 862–877, Mar. 2019, doi: 10.1108/COMPEL-06-2017-0229.
[341] Y.-L. Chen, J. Cheng, C. Lin, X. Wu, Y. Ou, and Y. Xu, “Classification-based learning by particle swarm optimization for wall-following robot navigation,” *Neurocomputing*, vol. 113, pp. 27–35, 2013.
[342] M. Polat, A. Yildiz, and R. Akinci, “Performance Analysis and Reduction of Torque Ripple of Axial Flux Permanent Magnet Synchronous Motor Manufactured for Electric Vehicles,” *IEEE Trans. Magn.*, vol. 57, no. 7, 2021, doi: 10.1109/TMAG.2021.3078648.
[343] M. Ashari *et al.*, “Design and Implementation of Axial Flux Induction Motor Single Stator - Single Rotor for Electric Vehicle Application,” *IPTEK J. Proc. Ser.*, vol. 0, no. 1, pp. 0–5, Jul. 2015, doi: 10.12962/j23546026.y2014i1.250.
[344] A. K. Kalo, A. Dwivedi, R. K. Srivastava, and D. K. Banchhor, “Experiences with Axial-Flux induction motor,” in *2015 International Conference on Energy, Power and Environment: Towards Sustainable Growth (ICEPE)*, Jun. 2015, pp. 1–6, doi: 10.1109/EPETSG.2015.7510124.
[345] M. A. Tapia, W. Jara, R. Wallace, and J. A. Tapia, “Parameters Identification of an Axial Flux Induction Machine Using Field Equations,” *Proc. - 2018 23rd Int. Conf. Electr. Mach. ICEM 2018*, pp. 351–357, 2018, doi: 10.1109/ICELMACH.2018.8506891.
[346] N. Bianchi, *Electrical machine analysis using finite elements*. CRC press, 2017.